Fast frequency control in low-inertia power systems

Krpan, Matej

Doctoral thesis / Disertacija

2023

Degree Grantor / Ustanova koja je dodijelila akademski / stručni stupanj: **University of Zagreb, Faculty of Electrical Engineering and Computing / Sveučilište u Zagrebu, Fakultet elektrotehnike i računarstva**

Permanent link / Trajna poveznica: https://urn.nsk.hr/urn:nbn:hr:168:493685

Rights / Prava: In copyright/Zaštićeno autorskim pravom.

Download date / Datum preuzimanja: **2024-06-27**

Repository / Repozitorij:

FER Repository - University of Zagreb Faculty of Electrical Engineering and Computing repozitory

University of Zagreb

FACULTY OF ELECTRICAL ENGINEERING AND COMPUTING

Matej Krpan

FAST FREQUENCY CONTROL IN LOW-INERTIA POWER SYSTEMS

DOCTORAL THESIS

Zagreb, 2023

University of Zagreb

FACULTY OF ELECTRICAL ENGINEERING AND COMPUTING

Matej Krpan

FAST FREQUENCY CONTROL IN LOW-INERTIA POWER SYSTEMS

DOCTORAL THESIS

Supervisor: Professor Igor Kuzle, Ph.D.

Zagreb, 2023

Sveučilište u Zagrebu

FAKULTET ELEKTROTEHNIKE I RAČUNARSTVA

Matej Krpan

BRZA REGULACIJA FREKVENCIJE U ELEKTROENERGETSKIM SUSTAVIMA SA SMANJENOM KONSTANTOM TROMOSTI

DOKTORSKI RAD

Mentor: Prof. dr. sc. Igor Kuzle

Zagreb, 2023.

About the supervisor

Igor Kuzle (`www.fer.unizg.hr/en/igor.kuzle`) is a Full professor and Head of the Smart Grids Laboratory at the Department of Energy and Power Systems of the University of Zagreb's Faculty of Electrical Engineering and Computing. He is a member of two scientific councils of the Croatian Academy of Sciences and Arts (Scientific Council for Technological Development and Scientific Council for Crude Oil and Gas Economy and Power Supply). He has been a member of the Croatian Academy of Engineering since 2017. Prof. Kuzle has received numerous awards for his scientific work: University of Zagreb annual award "Fran Bošnjaković" for the academic year 2022/2023; Croatian Academy of Engineering: annual award "Rikard Podhorsky" for the year 2020; Croatian Academy of Sciences and Arts: Excellence in Engineering Award for the year 2019; Republic of Croatia: National Science Award for the year 2017.

Since 2017, he has been a member of the Scientific Field Committee for Electrical Engineering and Computer Science of the Croatian Agency for Science and Higher Education (the committee makes the final decisions on the appointment of university professors). Prof. Kuzle has established the university research Smart Grids Laboratory, which enables practical and simulation investigations in the field of advanced grid technologies. His scientific interests include problems of dynamics and control of electric power systems, smart grids and integration of renewable energy sources. as well as maintenance of electric equipment.

He acts as an Editor-in-Chief of two journals: Electrical Engineering journal (ISSN: 0948-7921) and Journal of Energy (ISSN: 0013-7448) and serves on 8 journal editorial boards. Igor Kuzle published 4 books (one of them is official textbook of University of Zagreb) and more than 220 journal and conference papers, over 300 technical studies and reports for utilities and companies (project leader in more than 100 technical projects). He chaired 8 international conferences and participated in more than 70 conferences in international scientific/technical or steering committees and gave more than 20 keynote lectures.

He is a very active member of the IEEE, where he has held several leadership positions. He was a member of the IEEE PES Governing Board and Region 8 Chapters Representative (2021-2022), IEEE Region 8 Vice Chair for technical activities (2015-2016), IEEE Croatia Section Chair (2009-2012). Prof. Kuzle is a member of the professional association CIGRE (2009-2012 he was a member of the Croatian National Committee CIGRE Executive Board). Since 2019 he is a member of the Steering Committee of the Croatian Maintenance Society.

O mentoru

Igor Kuzle (`www.fer.unizg.hr/igor.kuzle`) je redoviti profesor u trajnom zvanju i voditelj Laboratorija za napredne elektroenergetske mreže na Zavodu za visoki napon i energetiku, Sveučilišta u Zagrebu Fakulteta elektrotehnike i računarstva (FER). Diplomirao je, magistrirao i doktorirao u polju elektrotehnike 1991., 1997. odnosno 2002. godine na FER-u, gdje u kontinuietu radi od srpnja 1992. godine. Član je dva znanstvena vijeća Hrvatske akademije znanosti i umjetnosti (HAZU), Znanstvenog vijeća za tehnološki razvoj i Znanstvenog vijeća za naftno-plinsko gospodarstvo i energetiku. Redoviti je član Akademije tehničkih znanosti Hrvatske.

Prof. Kuzle je nagrađen s više nagrada za svoj znanstveni rad: 2023. nagrada Sveučilišta u Zagrebu "Fran Bošnjaković" za akademsku godinu 2022./2023. - za ostvarene znanstveno-nastavne rezultate u promicanju znanstvenih disciplina i struke, te prijenosa znanja i odgoj mladih stručnjaka u tehničkom području; 2020. nagrada Akademije tehničkih znanosti Hrvatske "Rikard Podhorsky" - za razvoj i primjenu naprednih mreža; 2019. nagrada Hrvatske akademije znanosti i umjetnosti za najviša znanstvena i umjetnička dostignuća za područje tehičkih znanosti - za primjenu različitih koncepata upravljanja naprednim elektroenergetskim mrežama u svrhu povećanja fleksibilnosti elektroenergetskog sustava te omogućavanja masovne integracije OIE; 2017. godišnja Državna nagrada za znanost za doprinos znanosti u područuju naprednih mreža u prijenosnom sustavu.

Član je Matičnog odbora za elektrotehniku i računarstvo Nacionalnog vijeća za znanost, visoko obrazovanje i tehnološki razvoj. Na Sveučilištu u Zagrebu ustrojio je istraživački Laboratorij za napredne elektroenergetske mreže koji omogućava praktična i simulacijska istraživanja iz predmetnog područja. Istražuje probleme iz područja dinamike i regulacije elektroenergetskih sustava, naprednih mreža, integracije OIE te održavanja elektroenergetske opreme.

Sudjelovao je na više međunarodnih i nacionalnih znanstvenih projekata od čega je ili bio voditelj jednog Horizon Europe, jednog H2020 i tri međunarodna bilateralna projekta, jednog inovacijsko-razvojnog (IRI) projekta Europskog fonda za regionalni razvoj i dva projekta Hrvatske zaklade za znanost (HRZZ). Glavni je urednik dva znanstvena časopisa: Electrical Engineering, ISSN: 0948-792 (Springer) i Journal od Energy, ISSN: 0013-7448 (HEP i HRO CIGRE), a član je uredničkih odbora osam znanstvenih časopisa. Objavio je jedan sveučilišni udžbenik i tri knjige, više od 220 radova u časopisima i na konferencijama, te više od 300 tehničkih studija i elaborate za komunalne tvrtke i industriju (voditelj više od 100 projekata za gospodarstvo). Bio je predsjedavajući osam međunarodnih konferencija i član u više od 70 međunarodnih programskih/ tehničkih ili upravnih odbora znanstvenih konferencija, a održao je i više od 20 plenarnih predavanja.

Posebno je aktivan u udruzi IEEE gdje je obnašao više vodećih dužnosti. Bio je: član

Upravnog odbora PES i predstavnik svih PES odjela u Regiji 8 (2021.-2022.); dopredsjednik za tehničke aktivnosti IEEE Regije 8 (2015.-2016.); predsjednik Hrvatske sekcije IEEE (2009.-2012.). Član je hrvatskog ogranka stručne udruge CIGRE (2009-2012 - član izvršnog odbora HRO CIGRE). Od 2019. član je Upravnog odbora Hrvatskog društva održavatelja (HDO).

Progress is not possible without deviation

Frank Zappa

Abstract

The increasing share of power converters in power systems is changing the power system dynamics. Increased penetration of converter-interfaced renewable energy sources reduces the inertia of the power system and introduces new interactions among the converters and the rest of the power system. This thesis is aimed at evaluating the impact of increased penetration of power converters on the dynamic behaviour of power system frequency through the development of reduced-order dynamic models of converter-interfaced sources and loads. The particular focus is on modelling wind turbine generators and supercapacitor energy storage for dynamic simulations of a power system with a high share of power electronic devices. The final goal of the research is to develop a reduced-order dynamic model of a power system with a high share of power converters for studying the power system frequency dynamics. This low-order system frequency response model would encapsulate the relevant dynamics of converter-interfaced elements participating in frequency control of a low-inertia power system. This model could be used as a basis for frequency simulators and unit commitment of large power systems with a high share of power converters. Additionally, fast acting capabilities of converters are exploited to design a coordinated control method for provision of fast frequency control by a hybrid system of a wind turbine and a supercapacitor energy storage. Finally, some remarks on the feasibility of distributed control of energy storage assets for frequency regulation are provided based on experimental verification and testing in the University of Zagreb's Smart Grid Laboratory.

Keywords: grid frequency control, power system inertia, power system dynamics, power system stability, supercapacitor, low-order models, system frequency response modelling, wind turbine generators, power electronics; distributed control; energy storage

Brza regulacija frekvencije u elektroenergetskim sustavima sa smanjenom konstantom tromosti

Moderni elektroenergetski sustavi proživljavaju drastičnu transformaciju vođenu integracijom obnovljivih izvora energije i ostalih niskougljičnih tehnologija. Tradicionalno je poimanje elektroenergetskog sustava u kojem su velike konvencionalne hidroelektrane i termoelektrane centralizirane na relativno malom broju lokacija i s jednosmjernim tokovima snaga od proizvođača do potrošača, to to poimanje se mijenja i prelazi u sustav s velikim brojem manjih nekonvencionalnih vjetroelektrana i solarnih fotonaponskih elektrana decentraliziranih na velikom broju lokacija, od kojih su mnoge na distribucijskoj razini, te tako i tokovi snaga postaju dvosmjerni. Veća ovisnost proizvodnje ovih elektrana o lokalnim vremenskim uvjetima temporalno mijenja centre proizvodnje te vođenje i upravljanje elektroenergetskim sustavom postaje sve zahtjevnije. Vjetroelektrane, solarne fotonaponske elektrane, kao i spremnici energije, ali sve češće i potrošači, priključuju se asinkrono na elektroenergetski sustav preko sučelja energetske elektronike (pretvarača) koja efektivno razdvaja ponašanje uređaja od uvjeta u izmjeničnoj mreži. Isključenje konvencionalnih elektrana s mreže s ciljem oslobađanja kapaciteta za prihvat novih izvora energije prvenstveno smanjuje tromost elektroenergetskog sustava i snagu kratkog spoja kojima doprinose sinkroni i asinkroni strojevi. Obje veličine su pokazatelji otpornosti elektroenergetskog sustava na poremećaje te imaju značajan utjecaj na dinamiku i stabilnost. S druge strane, pretvarači imaju značajno brži odziv od konvencionalnih sinkronih agregata te se mogu iskoristiti za brzu regulaciju frekvencije koja može kompenzirati smanjenje tromosti. Značajan udio novih tehnologija također zahtijeva i nove modele za računalnu simulaciju koja je neizostavan dio planiranja, vođenja i upravljanja elektroenergetskim sustavom.

Disertacija se bavi problematikom regulacije i stabilnosti frekvencije, koja je jedan od glavnih pokazatelja stabilnosti elektroenergetskog sustava jer ukazuje na trenutnu ravnotežu proizvodnje i potrošnje, a na koju izravno utječe smanjenje tromosti zbog integracije pretvarača. U tom kontekstu, disertacija pokušava odgovoriti na sljedeća pitanja:

- Kako modelirati pretvarače u simulacijskim modelima smanjenog reda za dinamičku simulaciju frekvencije elektroenergetskog sustava?
- Možemo li zanemariti utjecaj elektromehaničke dinamike vjetroagregata koji sudjeluju u regulaciji frekvencije bez obzira na to što su priključeni preko pretvarača?
- Koji su najznačajniji parametri sustava koji utječu na dinamičko ponašanje frekvencije nakon poremećaja u kontekstu smanjene konstante tromosti sustava?
- Kako modelirati superkondenzatorski spremnik energije za dinamičke simulacije i kako upravljati njime za potrebe regulacije frekvencije?
- Kako iskoristiti superkondenzatorski spremnik energije za poboljšanje virtualnog inercijskog odziva vjetroagregata u uvjetima slabog i jakog vjetra?

- Koji su praktični problemi implementacije distribuiranog upravljanja spremnicima energije temeljenog na konsenzusu za sekundarnu i tercijarnu regulaciju frekvencije?

Obzirom na navedeno, disertacija ima tri izvorna znanstvena doprinosa:

1. Metodologija za vrednovanje utjecaja povećane penetracije energetskih pretvarača na dinamičko vladanje frekvencije elektroenergetskog sustava.

2. Modeli smanjenog reda vjetroagregata i superkondenzatorskog spremnika energije za dinamičke simulacije elektroenergetskog sustava, priključenih putem pretvarača.

3. Metoda za koordinirano sudjelovanje vjetroelektrane i superkondenzatorskog spremnika energije u brzoj regulaciji frekvencije.

Prvo poglavlje uvodi u temu istraživanja. Opisana je problematika integracije pretvarača u elektroenergetski sustav u kontekstu dinamike, regulacije i stabilnosti te je sažeta nova IEEE klasifikacija stabilnosti elektroenergetskog sustava. U nastavku je dan pregled literature iz sljedećih područja: dinamika i regulacija elektroenergetskih sustava male konstante tromosti, modeli smanjenog reda tehnologija temeljenih na pretvaračima za simulaciju frekvencije, modeliranje superkondenzatora, te distribuirano upravljanje spremnicima energije za pomoćne usluge sustavu.

Drugo poglavlje daje pregled tehnika za dinamičku simulaciju elektroenergetskog sustava. Opisane su razlike između elektromagnetske i fazorske simulacije, te usrednjene simulacije i simulacije sa upravljanjem poluvodičkim sklopkama, kao i njihova primjenjivost u simulacijskim domenama: statički i dinamički fazori, trofazna (*abc*) domena i rotirajuća (*dqo*) domena.

Posebna pažnja posvećena je razlici između fazorske i elektromagnetske simulacije te sposobnosti fazorskih simulacija da precizno opišu sve veće frekvencije oscilacija, gdje je zaključeno da bi fazorska simulacija trebala biti primjenjiva i do 200 Hz uz zahtjev da se veličina koraka integracije adekvatno smanji. Ovo ne znači da su sve pojave do te širine pojasa obuhvaćene fazorskom simulacijom, nego samo da su frekvencijske oscilacije kontroliranog izvora izmjenične struje bile precizno simulirane u usporedbi s referentnim elektromagnetskim modelom.

Također je ilustrirano kako simulacija u domeni dq0 ubrzava vrijeme simulacije 3–4,5 puta u balansiranim sustavima, dok su performanse za simulaciju asimetričnih trofaznih sustava nešto sporije, ovisno o vrsti numeričke metode za rješavanje diferencijalnih jednadžbi. Također je prikazano kako asimetrični uvjeti stvaraju oscilirajuće komponente u dq0 varijablama.

Dinamički fazori i fazorsko-elektromagnetska ko-simulacija ukratko su predstavljeni kao rješenja za ubrzanje simulacije sustava temeljenih na pretvaračima, pri čemu su dinamički fazori još uvijek ograničeni na akademska istraživanja, dok se ko-simulacijske metode mogu pronaći i u komercijalnom softveru.

Treće poglavlje opisuje modeliranje pretvarača, koji se prema glavnoj veličini u istosmjernom međukrugu mogu klasificirati kao pretvarači s naponskim ulazom i pretvarači sa strujnim

ulazom. Disertacija se fokusira na pretvarače s naponskim ulazom, stoga je predstavljena generička struktura koja se sastoji od primarnog sustava (uređaja) za pretvorbu energije, dva *back-to-back* pretvarača (jedan na strani uređaja i drugi na strani mreže) s odgovarajućim upravljačkim sustavima, istosmjernog međukruga i filtera na izmjeničnoj strani.

Svaki podsustav detaljno je opisan s odgovarajućim jednadžbama, čime se postavlja matematički okvir koji se koristi u ostatku disertacije. Posebna pažnja posvećena je upravljačkim podsustavima, različitim načinima održavanja ravnoteže snage i sinkronizaciji pretvarača s mrežom. Objašnjene su razlike između pretvarača koji slijede mrežu (*grid-following*) i pretvarača koji tvore mrežu (*grid-forming*), kao i njihove posebnosti u pogledu emulacije tromosti sinkronog stroja. Razvijene su prijenosne funkcije niskog reda temeljene na jednadžbama ravnoteže snage za opis odnosa snaga-snaga i snaga-napon. Na kraju je napravljena usporedba različitih načina upravljanja pretvaračem na temelju simulacija u vremenskom domeni.

Četvrto poglavlje usmjereno je na razumijevanje dinamike frekvencije elektroenergetskog sustava kroz prizmu modela smanjenog reda (SFR modeli) inspiriranih radom Andersona i Mirheydara. Pretpostavke na koje se takvi modeli oslanjaju ponovno su razmotrene i proširene u kontekstu elektroenergetskog sustava dominiranog pretvaračima. Svi izvedeni modeli potvrđeni su usporedbom s detaljnim elektromagnetskim modelima u programskom okruženju DIgSILENT PowerFactory.

Prvo je izveden konvencionalni SFR model za sustav koji se sastoji samo od sinkronih generatora. Ovdje je otkriven potencijalni utjecaj stabilizatora elektroenergetskog sustava na frekvenciju, iako se takvi uređaji obično ne razmatraju jer su dio sustava uzbude. Međutim, modulacija struje uzbude na temelju signala frekvencije utjecat će na armaturni napon i stoga izlaznu snagu u prijelaznim uvjetima. Zatim je analiziran utjecaj karakteristike mehaničkog opterećenja sinkronih i asinkronih motora na dinamiku frekvencije u kontekstu dobro poznatog parametra D u SFR modelima. Nadalje, pokazano je da dok konstanta tromosti sinkronog motora izravno doprinosi efektivnoj konstanti tromosti sustava, konstanta tromosti asinkronog generatora nema trenutačni utjecaj zbog klizanja, odnosno, s njom je povezano određeno vremensko kašnjenje.

Zatim su predstavljeni pretvarači koji slijede mrežu. Pokazano je kako dinamika fazno-zaključane petlje (PLL) može dovesti do nestabilnosti frekvencije te kako širina pojasa PLL-a i dodatno filtriranje trebaju biti pažljivo odabrani. Izveden je model PLL-a za SFR analize, te su izvedeni i SFR modeli dva upravljačka sustava pretvarača koji slijede mrežu (iz trećeg poglavlja). Izvedeni modeli pokazuju poboljšanu preciznost u predviđanju ponašanja frekvencije, iako se preciznost smanjuje kod udjela pretvarača iznad 80%. Ipak, izvedeni modeli su konzervativni jer SFR model predviđa lošije uvjete nego detaljni elektromagnetski model.

Također su izvedeni i SFR modeli za tri upravljačka sustava pretvarača koji tvore mrežu. SFR model virtualnog sinkronog stroja precizan je do 100% prodiranja pretvarača. SFR model

neizravnog usklađivanja potpuno je precizan samo u slučaju 100% prodiranja pretvarača kada su svi uređaji isti. U svim ostalim slučajevima pogreška nije značajna, ali postoji zbog činjenice da ovaj način upravljanja u kombinaciji sa sinkronim generatorima rezultira neujednačenom frekvencijom tijekom početnog prijelaznog stanja. Utvrđeno je da shema ViSynC ne funkcionira dobro u čistom načinu oblikovanja mreže u scenarijima s niskom inercijom jer su odstupanja frekvencije mreže bila najveća (do 3%–4%) i sustav je bio nestabilan za razine prodiranja veće od 80%. Stoga je SFR model sheme ViSynC bio precizan do 50% u razmatranim slučajevima.

Učinak virtualne tromosti u pretvaračima koji tvore mrežu može se smatrati trenutačnim kao kod sinkronih strojeva, dok učinak virtualne tromosti pretvarača koji slijede mrežu nije trenutačan zbog vremenskog kašnjenja u mjerenju frekvencije uzrokovanog PLL-om.

Konačno, u svim slučajevima rezultati elektromagnetske simulacije uspoređeni su s rezultatima fazorske simulacije i utvrđeno je da je fazorski model i dalje prikladan za dinamičku simulaciju frekvencije za sve razine prodiranja pretvarača, pod uvjetom da ne postoji nestabilnost uzrokovana PLL-om za koju je moguće da se neće vidjeti u fazorskoj simulaciji. Uzrok nestabilnosti jest previsoka efektivna propusnost PLL-a zbog koje vremenska derivacija signala procijenjene mrežne frekvencije uzrokuje nestabilnost u upravljačkoj petlji emuliranja tromosti.

U prvom dijelu petog poglavlja provedena je analiza osjetljivosti performansi regulacije frekvencije na parametre DFIG-a koji slijedi mrežu. Ti parametri uključuju: početnu radnu točku, parametre upravljačkog sustava pretvarača na strani generatora i pretvarača na strani mreže, parametre regulacije zakreta lopatica te parametre PLL-a.

Utjecaj brzine vjetra na snagu inercijskog odziva ovisi o načinu upravljanja pretvaračem na strani generatora. Za vjetroagregate s regulacijom snage, odziv je slabiji s povećanjem brzine vjetra, dok je za regulaciju brzine s inverznom karakteristikom praćenja maksimalne snage odziv jači s povećanjem brzine vjetra. Kada regulacija zakreta lopatica postane aktivna, maksimalna vrijednost odziva je u početku nešto viša nego u trenutku prije aktivacije regulatora lopatica. Nadalje, odziv postaje slabiji s povećanjem brzine vjetra. S druge strane, primarna regulacija frekvencije rezultira većim odstupanjem snage za isti poremećaj dok je regulacija zakreta lopatica aktivna.

Male vrijednosti pojačanja PI regulatora PLL-a rezultirat će oscilirajućim ponašanjem i slabim prigušenjem lokalnog moda. Nakon poremećaja, snaga DFIG-a se privremeno smanjuje, dodatno pogoršavajući frekvenciju mreže, iako je stvarna vršna vrijednost veća. S druge strane, velike vrijednosti pojačanja rezultiraju snažnim praćenjem frekvencije i nema oscilacija u odzivu snage. Općenito, dinamiku PLL-a možemo zanemariti ako je PLL brz i modovi su dobro prigušeni. S druge strane, previše agresivno podešavanje PLL-a može dovesti do nestabilnosti, no to također ovisi o karakteristikama sustava. Kao što je prikazano u poglavlju 4, simulirani sustav može biti stabilan u fazorskoj simulaciji, a nestabilan u elektromagnetskoj

simulaciji. U sustavima s niskom konstantom tromosti, PLL se ne smije zanemariti.

Vanjska upravljačka petlja pretvarača na strani generatora ima utjecaj na pružanje regulacije frekvencije. Ako vanjska petlja ima manja pojačanja PI regulatora, izlazna snaga je jača, a vrijeme vršnog odziva je kraće. To je zbog toga što će trebati više vremena da slabiji regulator suzdrži promjene snage prema postavljenoj vrijednosti. Unutarnja regulacijska petlja oba pretvarača, regulacijski krug DC napona i dinamika istosmjernog međukruga mogu se zanemariti u studijama regulacije frekvencije jer imaju vrlo brzi odziv.

Među svim parametrima regulacije kuta zakreta lopatica, proporcionalno pojačanje PI regulatora ima najznačajniji utjecaj. Veće proporcionalno pojačanje rezultirat će većom izlaznom snagom. Performanse regulacije frekvencije nisu značajno osjetljive na pojačanje integracijskog člana niti na vremensku konstantu servomehanizma za zakret lopatica u analiziranim slučajevima. Bez obzira na to, premala pojačanja regulatora lopatica mogu rezultirati neželjenim njihanjem statora i rotora koje nije vidljivo u njihovom ukupnom zbroju.

U svakom slučaju, teško je donijeti generalizirane zaključke o dinamici vjetroagregata jer uvelike ovisi o dizajnu upravljačkog sustava radne snage, koji može značajno varirati među pojedinim proizvođačima, ali i u znanstvenoj literaturi.

U drugom dijelu petog poglavlja izveden je SFR model generičkog vjetroagregata s promjenjivom brzinom vrtnje, u kojem se primarna regulacija frekvencije postiže isključivo putem upravljanja kutom zakreta lopatica. Korišteni nelinearni model pojednostavljen je zanemarivanjem brzih upravljačkih petlji pretvarača sukladno zaključcima iz prvog dijela petog poglavlja. Preciznost SFR modela provjerena je naspram pojednostavljenog nelinearnog modela u otvorenoj petlji, kao i naspram punog nelinearnog fazorskog modela u zatvorenoj petlji simulacijom u programskom paketu DIgSILENT PowerFactory.

Izvedene su tri prijenosne funkcije: prva koja povezuje promjenu brzine vjetra s promjenom izlazne snage, druga koja povezuje promjenu referentne vrijednosti snage virtualnog inercijskog odziva s promjenom izlazne snage, te treća koja povezuje promjenu referentne vrijednosti snage primarne regulacije frekvencije s promjenom izlazne snage. Sve prijenosne funkcije u svom najopćenitijem obliku trećeg su reda i, nažalost, analitički oblik ne pruža intuitivan uvid u dinamičko ponašanje. Međutim, red prijenosne funkcije može se smanjiti ovisno o tome je li regulator kuta zakreta lopatica aktivan ili ne. Ovdje je najzanimljiviji rezultat za slučaj virtualnog inercijskog odziva pri brzinama vjetra ispod nazivne, gdje je pokazano da vjetroagregat djeluje kao visokopropusni filtar, pri čemu vremenska konstanta ovisi o inerciji vjetroagregata, početnoj brzini vrtnje generatora i karakteristikama krivulje praćenja maksimalne snage (MPPT). Stoga je nevažeća konvencionalna pretpostavka u literaturi da je svaki sustav priključen preko pretvarača opisan prijenosnom funkcijom prvog reda. U ovom konkretnom primjeru, moduliranje referentne vrijednosti maksimalne snage na temelju odstupanja frekvencije rezultira smanjenjem brzine turbine, što pak smanjuje izlaznu snagu. Drugim riječima, elektromehanička di-

namika vjetroagregata postaje povezana s dinamikom mreže.

U svim analiziranim slučajevima predloženi model precizniji je od konvencionalnog pristupa u literaturi jer on daje preoptimistične rezultate. Međutim, za veće poremećaje (više od 10%), SFR model gubi preciznost zbog nelinearnosti modela turbine i podsustava regulatora kuta zakreta lopatica.

Šesto poglavlje predstavlja ujedinjeni SFR model elektroenergetskog sustava smanjene konstante tromosti na temelju analize u poglavljima 3 – 5. SFR model uključuje relevantnu dinamiku sinkronih i asinkronih strojeva, dinamiku stabilizatora elektroenergetskog sustava, generičku dinamiku pretvarača koji slijede mrežu i tvore mrežu, te dinamiku vjetroagregata s promjenjivom brzinom kao posebnog slučaja sustava koji slijedi mrežu. U ovom poglavlju sažete su ključne točke svakog od navedenih podsustava. SFR model nije sveobuhvatan jer ne uzima u obzir specifično dinamičko ponašanje drugih uređaja poput solarnih fotonaponskih panela, agregata s pretvaračima koji tvore mrežu, spremnika energije itd.

Koristeći razvijeni SFR model, provela su se razna istraživanja karakteristika dinamike frekvencije sustava smanjene konstante tromosti. Definirana je razlika između fizičke konstante tromosti i virtualne konstante tromosti pretvarača koji tvore mrežu. Pokazano je da je, za dovoljno male korake diskretizacije, virtualna konstanta tromosti pretvarača koji tvore mrežu praktički identična fizičkoj konstanti tromosti. Međutim, vidljivo je mjerenje snage na stezaljkama pretvarača i širina propusnosti filtra mogu imati utjecaj na navedeno, što zahtijeva dodatnu analizu.

Nakon što je kvantificirana tromost različitih izvora energije i opisana analogija između rotacijske tromosti (agregati) i elektromagnetske tromosti (pretvarači), raspravljalo se o važnosti konstante tromosti. Pokazano je da smanjena konstanta tromosti nije nužno važna s gledišta stabilnosti za male poremećaje jer njeno smanjenje povećava prigušenje elektromehaničkih modova. Ipak, problem leži u povećanju RoCoF-a (eng. *Rate-of-Change-of-Frequency*) koji može aktivirati zaštitne releje gdje vremenski prozor za procjenu RoCoF-a ima važnu ulogu. Povećanje vremenskog prozora smanjit će prosječnu procijenjenu vrijednost kako se pojedinačne brzine generatora približavaju jedinstvenoj vrijednosti. Ako oprema može privremeno izdržati visok RoCoF, tada se zahtjevi mogu relaksirati i učinak smanjene konstante tromosti ne bi trebao biti značajan. Glavna je poanta da se učinak smanjene konstante tromosti može nadoknaditi malim vremenskim konstantama sustava (puno brzih pretvarača) u smislu ograničenja odstupanja frekvencije. Početnu vrijednost RoCoF-a nije moguće smanjiti ničim drugim osim inercijom; međutim, mala vremenska konstanta osigurat će da se početni prijelazni RoCoF brzo priguši. Dakle, oprema u sustavima s izuzetno niskom konstantom tromosti trebala bi podnijeti visoki RoCoF samo u prvih nekoliko stotina milisekundi nakon velikog poremećaja. Međutim, smanjena konstanta tromosti rezultira većim oscilacijama frekvencije koje mogu izazvati druge rezonancije u sustavu koje su izvan primjenjivosti SFR modela.

Zatim je pokazano kako kombinacija propusnosti PLL-a, statičnosti i smanjene konstante tromosti može uzrokovati nestabilnost frekvencije, te su izračunata područja nestabilnosti za određene kombinacije parametara. Nadalje, analiziran je utjecaj širine pojasa PLL-a i dodatnog filtriranja na RoCoF sustava. Dokazano je da emuliranje tromosti pretvaračima koji slijede mrežu ne može zamijeniti sinkronu tromost tijekom početnog prijelaznog stanja zbog inherentnog vremenskog kašnjenja u procjeni frekvencije.

Pokazano je i da agregiranje samoregulacije potrošnje u konstantu D daje konzervativne rezultate. U stvarnosti, asinkroni strojevi više će doprinijet smanjenju odstupanja frekvencije i RoCoF-a. Međutim, budući da se većina motora u industriji priključuje preko frekvencijskih pretvarača, ovi učinci danas nisu relevantni niti će biti u budućnosti. Upravljanje tim pretvaračima u svrhu regulacije frekvencije bit će potrebno u budućnosti, te su stoga izneseni zaključci o različitoj dinamici pretvarača i dalje primjenjivi.

Nadalje, ilustrirano je kako dinamika vjetroagregata koji slijedi mrežu može poboljšati odziv frekvencije sustava u uvjetima visoke konstante tromosti, ali s druge strane može destabilizirati frekvenciju u uvjetima niske konstante tromosti, ovisno o radnoj točki.

Konačno, uspoređeno je pet analiziranih načina upravljanja pretvaračem (dva koja slijede mrežu i tri koja tvore mrežu). Što se tiče sustava koji slijede mrežu, regulacija DC napona na pretvaraču na strani mreže može rezultirati slabije prigušenim ponašanjem ili čak nestabilnošću u uvjetima niske konstante tromosti zbog dodatne dinamike drugog reda u petlji negativne povratne veze. Što se tiče sustava s pretvaračima koji tvore mrežu, emuliranje velike konstante tromosti na pretvaraču sa strane mreže zahtijeva vrlo brzu regulaciju DC napona, kao i brzi izvor energije koji ovaj regulator regulira. S druge strane, usklađivanje virtualne tromosti s energijom istosmjernog međukruga u druga dva *grid-forming* načina upravljanja inherentno znači da je efektivna konstanta inercije izuzetno niska, što značajno povećava početni RoCoF. Postavljanje vrlo velikih konstanti virtualne tromosti nije izvedivo u tim slučajevima jer će rezultirati slomom DC napona i posljedičnim prestankom rada pretvarača.

U sedmom poglavlju predstavljen je jednostavan i precizan model superkondenzatorske baterije i njenog upravljačkog sustava za upotrebu u dinamičkim simulacijama. Polazeći od detaljnog modela superkondenzatorske ćelije temeljenog na RC krugu, model je postupno pojednostavljen do najjednostavnijeg prikaza koji i dalje precizno opisuje dinamiku superkondenzatora, što je potvrđeno simulacijama. Predloženi model opisan je samo sa četiri parametra koji su lako dostupni iz tehničkih podataka: početni kapacitet, naponski ovisan kapacitet, DC otpor i visokofrekvencijski otpor. Performanse predstavljenog modela uspoređene su s idealnim modelom u IEEE 14-bus testnom sustavu u scenarijima regulacije frekvencije i prolaska kroz kvar.

Za regulaciju frekvencije, idealni model ne predstavlja uvijek precizno nelinearni model, ovisno o početnom naponu superkondenzatora i veličini poremećaja. Za poremećaj koji uzrokuje

pad frekvencije, potpuno do djelomično napunjen superkondenzator može biti dovoljno dobro modeliran idealnim modelom u smislu odziva frekvencije sustava, ali približavanjem donje granice napunjenosti, idealni model može davati optimistične ili pesimistične rezultate (razlika u najvećem odstupanju frekvencije može biti veća od 0,1 Hz, ovisno o vrijednosti kapaciteta idealnog kondenzatora). Slično ponašanje primjećuje se i kod poremećaja koji uzrokuju porast frekvencije. Općenito, ekvivalentni serijski otpor i serija paralelnih RC krugova u prvoj grani smanjuju učinkovitost superkondenzatora, dok naponsko ovisni kapacitet mijenja količinu pohranjene energije tijekom punjenja i pražnjenja, i utječe na brzinu punjenja i pražnjenja. Promatrana prosječna apsolutna relativna pogreška u vremenu pražnjenja između idealnog i nelinearnog modela kreće se od 9% do 16% za promjenjivi kapacitet od 10% te od 10% do 25% za promjenjivi kapacitet od 40%, dok maksimalna apsolutna relativna pogreška u vremenu pražnjenja može ići do 27% za promjenjivi kapacitet od 10% te 43% za promjenjivi kapacitet od 40%. Najbolji idealni model za većinu promatranih slučajeva za oba tipa korištenih upravljačkih sustava regulacije frekvencije je idealni model s kapacitetom postavljenim između minimalnog i prosječnog kapaciteta superkondenzatora, pri čemu je idealni model s prosječnim kapacitetom obično precizniji za visoko početno stanje napunjenosti. Gubici i nelinearna dinamika napona otežavaju prikazivanje stvarnog superkondenzatora idealnim modelom za sve radne točke.

Za prolazak kroz kvar, utjecaj modeliranja nije značajan te će idealni model biti dovoljan, iako bi za nelinearni model podnaponska i prenaponska zaštita mogla biti ranije aktivirana. Zatim je predstavljen jednostavan iterativni postupak za dimenzioniranje superkondenzatorskog spremnika energije koji koristi aproksimaciju modela i detaljnije simulacije. Također je dana rasprava o karakteristikama superkondenzatora i kako različiti pristupi modeliranju utječu na predviđene performanse superkondenzatora:

- Varijabilni kapacitet superkondenzatorske ćelije može značajno utjecati na količinu pohranjene energije te stoga i na dinamiku napona tijekom punjenja i pražnjenja.
- Superkondenzatorske ćelije elementi su vrlo niskog napona koji se moraju povezati u seriju za primjenu u tehnikama visokog napona. Međutim, to povećava gubitke, pa je potrebno postići ravnotežu s paralelnim nizovima kako bi se smanjili gubici.
- Konstantna operacija snage može se postići samo u ograničenom rasponu napona zbog ograničenja struje—oko 75% energije može se iskoristiti od polovine do punog nazivnog napona.

Nadalje, predložena je shema koordiniranog upravljanja vjetroelektranom i superkondenzatorom kako bi se poboljšalo pružanje virtualnog inercijskog odziva vjetroelektrane tijekom niskih i visokih brzina vjetra. Tijekom niskih brzina vjetra, virtualni inercijski odziv vjetroelektrane onemogućen je kako se ne bi prekoračila donja granica minimalne brzine rotora, a virtualni inercijski odziv preuzima superkondenzator. Tijekom visokih (iznad nazivnih) brzina vjetra, generator i pretvarač rade na nazivnoj snazi, a dodatna raspoloživa snaga ograničena je

termičkim granicama pretvarača i/ili generatora (maksimalna struja). Nedostatak predloženog rješenja jest to što se vjetroelektrana modelira kao agregirani sustav identičnih vjetroagregata.

Konačno, predloženo je modelsko prediktivno upravljanje (MPC) za optimizaciju pogona superkondenzatorske baterije u svrhu regulacije frekvencije. MPC algoritam temelji se na linearnom prediktivnom modelu superkondenzatora, dok se nelinearni model koristi kao simulacijski model za provjeru algoritma. Predložen je autonomni regulator frekvencije temeljen na referentnoj putanji napona i MPC-u, te je uspoređen s tri klasična PID rješenja za različite veličine poremećaja u slučajevima sa i bez sekundarne regulacije frekvencije u elektroenergetskom sustavu. Predloženi regulator autonomno i postupno ponovno puni superkondenzator u stacionarnom stanju mijenjanjem ograničenja MPC formulacije, pružajući snažan neprekidni odziv tijekom poremećaja. Glavni zaključak je da MPC osigurava glađe smanjenje snage i poboljšava odziv sustava na frekvenciju (u smislu odstupanja frekvencije i RoCoF-a), budući da uzima u obzir ograničenja brzine promjene snage pražnjenja. Za simulirane slučajeve, predloženi MPC regulator smanjuje maksimalno odstupanje frekvencije između 10% i 30%. S druge strane, iako je početni RoCoF za MPC kontroler veći za 6% do 25%, on se brže prigušuje. Osim toga, ovo ponešto inferiornije ponašanje proizlazi iz činjenice da korišteni PID regulatori imaju d/dt izraz koji snažnije reagira na RoCoF. Naposljetku, agresivno podešavanje PID regulatora može rezultirati neželjenim oscilatornim ponašanjem i iznenadnim gubitkom snage nakon što se energija iscrpi, izazivajući još jedan poremećaj frekvencije i 50% do 100% veći RoCoF u tom trenutku. Ovo ponašanje je ublaženo korištenjem predloženog MPC regulatora koji se ponaša dosljedno u svim simuliranim slučajevima. Također, glatko smanjenje snage sprječava probleme s prenaponima koji mogu nastati u pretvaraču zbog nagle promjene struje. Dodatna prednost predloženog MPC algoritma jest i ta što se temelji samo na izravnim mjerenjima (naponu na stezaljkama superkondenzatora i izlaznoj snazi), pa stoga nije potrebna estimacija stanja, što ga čini manje računski zahtjevnim.

U osmom poglavlju, eksperimentalno je potvrđen koncept distribuiranog upravljanja temeljenog na konsenzusu za pružanje usluga automatske i ručne regulacije frekvencije koristeći malu laboratorijsku virtualnu elektranu koja se sastoji od 6 uređaja. Rezultati su pokazali da virtualna elektrana regulirana korištenjem predloženog algoritma zadovoljava mrežna pravila jer je postignuto praćenje zadane snage ispod 1 minute, a frekvencija otočnog sustava može se obnoviti u manje od 15 minuta. Eksperimentalno je pokazano da distribuirano upravljanje može postići optimalno raspoređivanje portfelja virtualne elektrane na računski učinkovit način, uz istodobno zadovoljenje zahtjeva postavljenih na cijelu virtualnu elektranu. Stoga distribuirano upravljanje omogućuje da se sekundarna i tercijarna regulacija događa u istom vremenskom periodu, pod uvjetom da se provodi ispravna sinkronizacija stanja.

Glavni izazovi identificirani tijekom laboratorijskih eksperimenata bili su problemi s propagacijom pogrešnih stanja između pojedinih uređaja koji mogu uzrokovati oscilacije i/ili ne-

točnost praćenja referenci zbog neujednačenih vremenskih kašnjenja. Stoga je izrazito bitno da algoritmi postizanja konsenzusa budu otporni na pogreške kako bi bili u skladu s mrežnim pravilima. Sinkronizacija stanja, globalni konsenzus o vremenu ili postojanje globalne vremenske reference osiguravaju precizno djelovanje algoritma postizanja konsenzusa. Čak i vrlo osnovna shema sinkronizacije stanja može postići zadanu snagu u manje od 1 minute, što je znatno ispod maksimalnog vremena pune aktivacije sekundarne i tercijarne rezerve. Odabir najprikladnijeg komunikacijskog protokola zahtijeva daljnja istraživanja.

U ovoj disertaciji istraživano je dinamičko ponašanje frekvencije elektroenergetskog sustava s viskom udjelom elektroničkih energetskih pretvarača. Glavni cilj bio je procijeniti primjenjivost modela odziva frekvencije sustava niskog reda u kontekstu visokog udjela pretvarača, te preispitati postojeće pretpostavke i predložiti rješenja koja mogu proširiti područje primjenjivosti SFR modela. Glavna motivacija istraživanja leži u činjenici da se određeni dijelovi upravljanja pretvaračem odvijaju na elektromagnetskoj vremenskoj skali i mogu nepovoljno djelovati na elektroenergetski sustav. Iako se regulacija frekvencije tradicionalno odvija na sporijoj vremenskoj skali od elektromagnetske, nove usluge brze regulacije frekvencije pomoću pretvarača mogu je donekle pomaknuti prema elektromagnetskoj vremenskoj skali.

Pokazano je da će dinamičko ponašanje frekvencije postati sve kompliciranije s povećanjem udjela pretvarača. Konvencionalne pretpostavke o svemogućim i brzim pretvaračima više neće biti prikladne kako konstanta tromosti sustava opada. Glavna zapreka za pretvarače koji slijede mrežu jest fazno zaključana petlja ili bilo koje drugo rješenja za procjenu frekvencije, dok je za upravljanje koje tvori mrežu glavno ograničenje stabilnost DC napona. Bez obzira na vrstu upravljanja, dinamika primarnog sustava pretvorbe energije iza pretvarača postaje povezana s ponašanjem mreže i treba ju uzeti u obzir kako bismo imali potpunu sliku o ravnoteži snage (kao što je ilustrirano primjerom vjetroelektrane). Na kraju, navodimo nekoliko smjernica za daljnja istraživanja:

- analiziranje i kvantificiranje utjecaja impedancije mreže i podešavanja regulatora na performanse pretvarača;
- analiziranje utjecaja različitih načina upravljanja pretvaračem na regulaciju frekvencije, uzimajući u obzir specifičnu dinamiku uređaja (vjetroturbina, solarni PV panel, pohrana energije, HVDC itd.) i identificiranje ograničenja za pružanje usluga regulacije frekvencije pod uvjetima stabilnosti napona istosmjernog međukruga i stabilnosti uređaja;
- razvijanje bržih i robusnijih načina procjene frekvencije sustava;
- daljnja istraživanja za poboljšanje preciznosti predloženih modela odziva frekvencije sustava koji poboljšavaju točnost procjene frekvencije mreže do određene mjere, ovisno o dizajnu upravljanja pretvaračem;
- više eksperimentalnih istraživanja u identifikaciji i dizajniranju robusnih komunikacijskih protokola za konzistentno upravljanje geografski distribuiranim spremnicima energije.

Ključne riječi: regulacija frekvencije EES-a, tromost EES-a, dinamika EES-a, stabilnost EES-a, superkondenzator, modeli smanjenog reda, modeliranje odziva frekvencije EES-a, vjetroagregati, energetska elektronika; distribuirano upravljanje; spremnici energije

Contents

Chapter 1

Introduction

The way we know and understand power systems is changing. Nowadays, the electric power system is undergoing a massive transformation—a substantial number of devices based on power electronics have been installed at dispersed locations, thus changing the overall system layout from a traditional hierarchical structure to a highly decentralised one. This major paradigm shift is graphically illustrated in Fig. 1.1, and is mostly linked with the spread of renewable energy sources (RES), electric vehicles (EVs) and energy storage systems (ESS). Nevertheless, any power plant today and in the near future can be connected through an inverter interface ranging from micro hydro power plants to thermal power plants, regardless of the type of energy resource. Similarly, power system loads are also increasingly connected through power electronic interfaces.

Traditionally, power plants are dislocated from the consumers, and electric power is first transmitted over long distances via high-voltage lines to consumption centres. Then, voltages are stepped-down to medium and low voltage levels and distributed to the consumers. Today, we are witnessing a radically different structure: The penetration of devices at medium and low voltage levels both in utility networks and behind-the-meter is increasing, not only through wind and solar photovoltaic (PV) systems, but also in small/micro hydro, gas, and steam turbines, as well as controllable loads. Distribution grids are active, and the whole grid is shifting towards a more decentralised structure where 100% inverter-based islands or autonomous microgrids may, and likely will, occur.
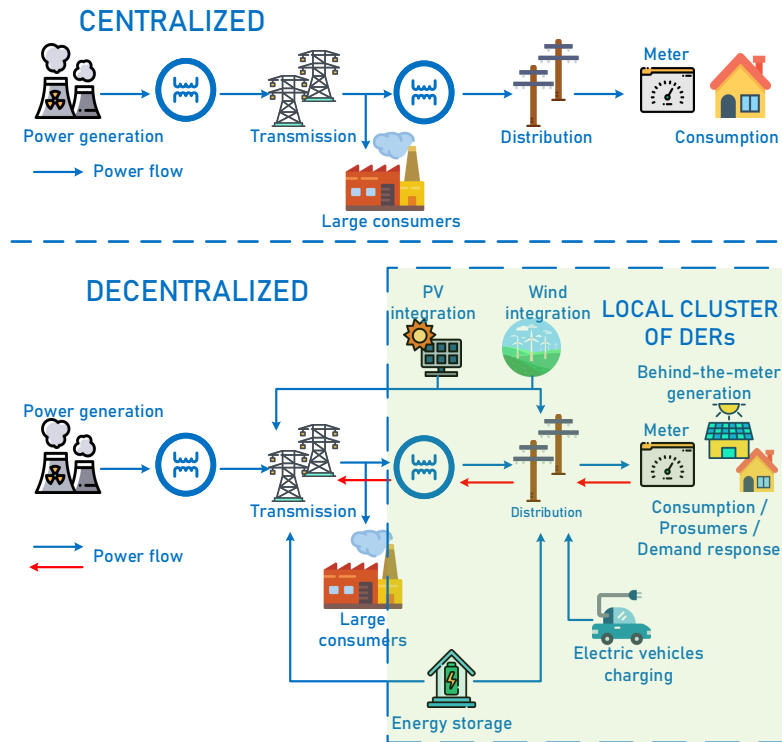
Figure 1.1: Power system paradigm shift.

1.1 Background

The aforementioned evolution greatly changes the attributes of a power grid. New characteristics include faster dynamics, shorter time delays, weakened damping ability and reduction of synchronous inertia [1–4]. The key issues of a massive integration of power electronic equipment into the bulk power system are [5, 6]:

- Most grid-connected inverters today are grid-following, meaning that they require a strong grid as the source of frequency and voltage reference, traditionally provided by synchronous generators (SGs). Displacing synchronous generation with stochastic, converter-interfaced RES eventually leads to the unstable operation of grid-following inverters, thus grid-forming control strategies must be employed: virtual synchronous generators, synchronverters, and other alternative synchronisation techniques, e.g. [7–10].

- The time scales of power electronic converter actuation and control are very small (on a microsecond and millisecond levels), which is much faster than the electromechanical dynamics which traditionally dominate the power grid due to synchronous turbine-generators (from hundreds of milliseconds to tens of seconds). In this sense, the converter dynamics are much closer to the electromagnetic dynamics of switching transients. The faster the dynamics of power electronic converters are and the bigger their share in the system is, the stronger the coupling between a converter and the grid is. New models are

required which will consider key dynamics without being too computationally intensive.

- Time delays related to measurements, signal processing and control actions are accentuated in the usage of power converters. These delays may have a significant impact on the dynamics and stability of the power grid.

Therefore, the main topic is that the power system dynamics, stability and control are changing due to increasing share of power electronic devices, so much so that the original definition of power system stability [11] has been revisited and extended by the IEEE PES Task Force in 2021 [12] to include resonance stability and converter-driven stability, as shown in Fig. 1.2.
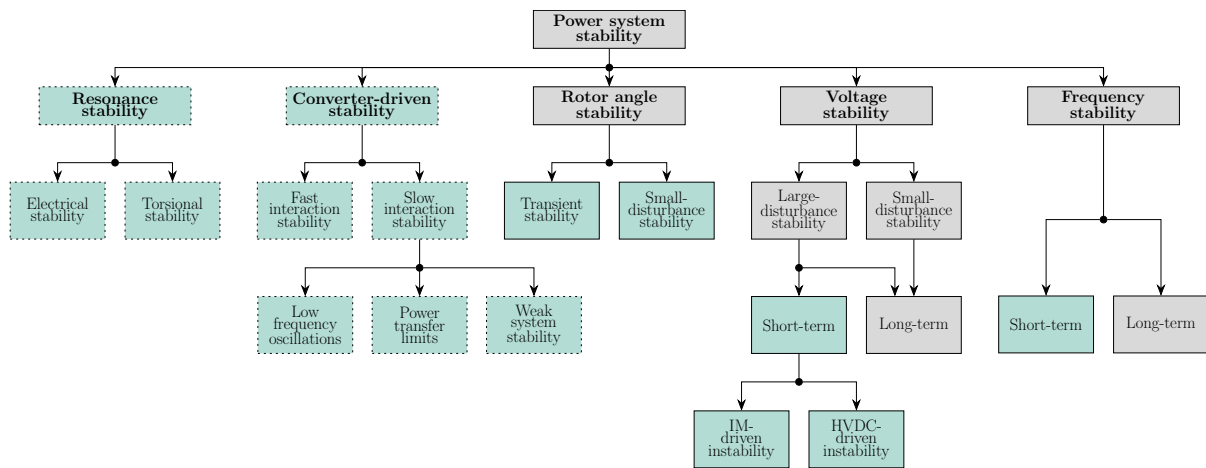
Figure 1.2: Extended classification of power system stability, based on [12]: green blocks with dashed border are newly added categories, while green blocks with solid border are updated subcategories to include the effects of converter-interfaced devices.

The main definitions of rotor angle stability, voltage stability and frequency stability remain unaffected (as in [11]), but their subcategories have been updated to reflect the effects of converter-interfaced devices (CID).

Firstly, the impact of CID on small-signal and transient rotor stability is mainly reflected through the displacement of SGs and consequently the reduction of system inertia and damping. Additional impact of CID is through the fault ride-through behavior. The time period of interest in rotor angle stability studies is in the order of several seconds.

Secondly, the effect of CID on short-term voltage stability is driven by unstable HVDC links with line-commutated converters (LCCs). The time period of interest in short-term voltage stability studies is in the order of several seconds, as well.

Thirdly, the impact of CID on short-term frequency stability mainly comes through the reduction of synchronous inertia and spinning reserves that increase the size of frequency excursions. However, CID have a much faster response rate and can use smaller droop values since in many cases (e.g., PV, batteries) they are not limited by mechanical subsystems. Instability due to HVDC and due to induction machines (IM) has been separated compared to [11]. The time period of interest in short-term frequency stability studies is up to 30 seconds after a

disturbance.

The first newly added category is the resonance stability, further subdivided into torsional and electrical stability. In both cases, the term resonant stability encompasses only the sub-synchronous resonance (SSR), with the only difference being the equipment that interacts with each other. Torsional stability is concerned with the torsional SSR which happens because of the interactions between the power grid and the (synchronous) turbine-generator mechanical shaft. More specifically, the torsional resonance happens either due to the series-compensated lines or because of the interactions with fast-acting FACTS devices (e.g., HVDC, STATCOM, SVC), and PSS. On the other hand, electrical resonance is driven by the subsynchronous resonance between the stator of a doubly-fed induction generator (DFIG) and a series-compensated lines. In this type of resonance, the induction generator stator inductance forms a resonant circuit at subsynchronous frequencies with the series capacitor for line compensation. This causes an apparent net negative resistance of this circuit and unstable behaviour further exacerbated by the DFIG converter control. This type of SSR is also called subsynchronous control interaction (SSCI).

The second newly added category is the converter-driven stability. This category has been added due to the fact that the converter control encompasses a wide bandwidth ranging from several kHz (converter gate signal modulation, e.g., PWM) up to a few Hz (active and reactive power control) [6]. Therefore, the converter control can cross-couple with both the electromagnetic phenomena of the grid and the electromechanical dynamics of synchronous machines. Fast interaction stability involves interactions between fast control loops of power-electronic converters and power system components with very small time constants (transmission lines, SG stator impedance, and other power-electronic equipment). These interactions result in high-frequency resonances ranging from a hundred Hz to several kHz. The power electronics community refers to this type of (in)stability as harmonic (in)stability. Slow interaction stability involves interactions between slower converter control loops (PLL, active/reactive power control, outer voltage control loops) and electromechanical dynamics of synchronous generators and SG controllers (AVR , PSS and turbine-governors). In this context, there is a differentiation between low frequency oscillations (due to converter controller interaction), weak system stability (due to the diminished capability of PLLs to synchronise with grid voltage in weak grids) and power transfer limits (because of the thermal limitations of converters due to which the converter current saturates).

The overview of characteristic time scales and bandwidths of power system phenomena is shown in Fig. 1.3. Starting from the bottom, the time scales of broader-categorised physical phenomena are shown (wave phenomena being the fastest and thermodynamic phenomena being the slowest). Above the physical phenomena (in green), the physical phenomena are further subdivided into phenomena specific for power systems. Above that (in pink), the time scales

of different high-level power system control mechanisms are visible. Finally, the time scales of device-level control (in orange and teal) are at the very top, shown only for synchronous generators and voltage-sourced converters since they are the focus of this thesis. Note that the time scales of device-level control are related to the time constants of different controllers and turbines, while the time scales of power system control, power system phenomena and physical phenomena are more related to the time periods of interest for observation after a disturbance . The time scales of interest in this thesis are shaded in blue.
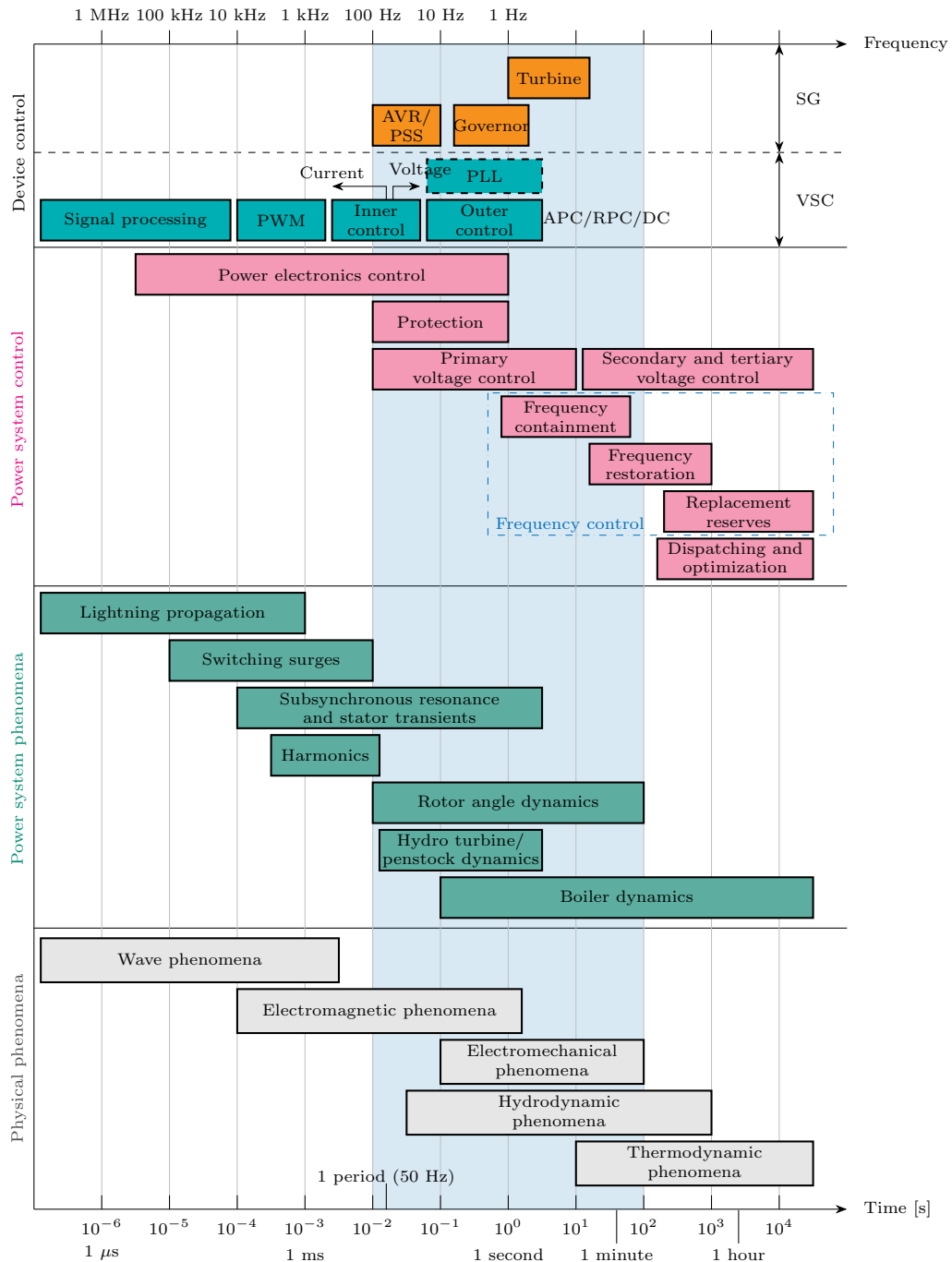

Figure 1.3: Overview of characteristic time scales in power systems, based on data from [6, 12–17].

1.2 Motivation, scope, objectives and contributions

Now that the background has been set, the motivation behind this thesis stems from the changing frequency dynamics due to CID, specifically. The conducted research has been closely related to the activities of two projects: *Wind Energy Integration in Low-Inertia Power System* (WINDLIPS) [18], funded by the Croatian Science Foundation; and *CROSS BOrder management of variable renewable energies and storage units enabling a transnational Wholesale market* (CROSSBOW) [19], funded by the European Commission (Horizon2020 program).

The first idea and motivation for this thesis started back in 2015/2016 during my master's studies when I was trying to develop a low-order system frequency response model of different types of WTGs. I continued to work on this when I started my PhD degree in 2017. Although we published several papers on this topic in the period between 2017 and 2018, I quickly realised that I lack the fundamentals of dynamic modelling of electric machines and power electronic devices to conduct a comprehensive analysis. While catching up on these skills and simultaneously reading up on the state-of-the-art literature on synthetic/virtual inertial response by converter-interfaced WTGs, the scope of my research naturally expanded to converter-dominated power systems as this has become a very hot topic in the last five years. Therefore, the scope of this thesis expanded to trying to develop a generalised low-order SFR model which would include the effects of generic CID in order to update the soon-to-be-obsolete SFR models that are based on the seminal work by Anderson and Mirheydar [20] which only includes slow thermal/hydro turbine dynamics.

Concurrently, I started working on the CROSSBOW project where my activities intensified in the 2018–2022 period when, among other things, I worked on the development of supercapacitor dynamic models and the experimental setup at the Smart Grid Laboratory (SGLab) [21] for validation of distributed control algorithms in collaboration with The University of Manchester. With all this said, this thesis tries to bring together all the aforementioned work in the last 6 years. In the following paragraphs, the main goals of this thesis are introduced.

The first goal of this thesis is to understand the impact of CID on frequency dynamics and quantify this impact through appropriate mathematical modelling and simulation techniques. The second goal is to utilise the fast response of CID to provide fast frequency control services to the system operator via development of novel control algorithms. **In this context, there are three main contributions of this thesis:**

1. **Evaluation of the impact of CID penetration on power system frequency dynamics.**
2. **Development of reduced-order models of a converter-interfaced wind turbine-generator (WTG) and supercapacitor bank for power system dynamics simulation.**
3. **Algorithm for coordinated control of a wind turbine-generator and a supercapacitor bank for providing a fast frequency control ancillary service.**

The term "fast frequency control" is not to be confused with specific products such as National Grid ESOs *dynamic containment* services [22, 23]. In this thesis, it is used as a blanket term which encompasses the inertial response and primary frequency control by CID which generally have a faster response than conventional synchronous turbine-generators. Moreover, the term "power system dynamics simulation" refers to three types of simulations in this thesis:

1. Electromagnetic transient (EMT) simulation in which the network is modeled by differential equations. Balanced network conditions are assumed.

2. Fundamental frequency simulation (also called RMS or phasor simulations) in which the power network is modeled by steady-state (algebraic, phasor) equations. Balanced network conditions are assumed.

3. Low-order system frequency response (SFR) simulations in which a power system is aggregated in a single machine with equivalent inertia, damping, and the relevant active power control mechanisms (turbine-governors, under-frequency load shedding, synthetic inertia, etc.). Only electromechanical dynamics defined by the largest time constants are considered in this model.

Additionally, this thesis attempts to derive a unified low-order SFR model that takes into account the impact of CID (both grid-following and grid-forming, including WTGs, energy storage units, as well as converter-interfaced loads). Low-order SFR models are especially useful since they provide a simple way to simulate the behaviour of average system frequency by using a small number of key parameters, therefore avoiding the need to model a complex power system with many elements like generators, lines and transformers which require knowledge of a large set of parameters. Furthermore, SFR models are linear and can be easily integrated into power system optimisation problems. Finally, experimental validation results of distributed control of energy storage units for secondary and tertiary frequency control are discussed at the end of this thesis.

1.3   Thesis outline

In summary, this thesis is structured as follows: Chapter 1 introduces the topic and motivation for this thesis, and reviews the state-of-the-art technologies. Chapters 2 and 3 systematise and discuss the modelling and simulation of power system dynamics contextualised to the presence of power electronic devices. Chapter 4 defines the mathematical framework for the modelling of conventional synchronous turbine-generators, power system loads and CID based on voltage-sourced converters (VSC) after which the fundamentals of frequency dynamics in the presence of CID are explained. In Chapter 5, a low-order (small-signal) model of converter-interfaced WTG with frequency support capabilities is derived for integration into low-order SFR models. In Chapter 6, the results of chapters 4 and 5 are used to synthesise a unified low-order SFR

model of a system with a high share of CID. Chapter 7 deals with deriving a reduced-order (but large-signal) model of a supercapacitor bank suitable for use in power system fundamental frequency simulations. Additionally, two algorithms are developed: (i) for coordinated control of a WTG and SC bank for providing synthetic inertial response and (ii) a model predictive control approach to the operation optimisation of an SC bank for frequency control. Chapter 8 presents the experimental validation results of distributed control of a laboratory-scale virtual storage plant (VSP) in the Smart Grid Laboratory [21]. Chapter 9 concludes the thesis.

1.4 A brief overview of the state-of-the-art

In order to better position the scope and contributions of this thesis, a brief overview of the state-of-the-art will be given in this section. The overview is divided into subsections based on the topics covered in this thesis.

1.4.1 Operation, dynamics and control of low-inertia power systems

Two excellent PhD theses have been written in the last five years, one by Dr. Pieter Tielens at KU Leuven [24], and the other by Dr. Uroš Marković at ETH Zürich [25]. These are not the only theses that deal with the topic of low-inertia systems, but arguably, they can be considered seminal based on their timeliness and novel contributions to the prospective field of converter-dominated power systems. Some of the conclusions and challenges stated in [1, 24, 25] are summarised below:

1.4.1.1 Inertia estimation and load inertia:

Inertia estimation is a daunting task to accomplish. On the one hand, post-mortem estimation is sensitive to factors: accuracy and location of the frequency measurement, identification of the exact size and start time of an disturbance, correcting for control reactions (turbine governors, power control, load-shedding, etc.) and dependency of load on voltage and frequency. On the other hand, real-time inertia estimation requires plenty of information on generator inertia which was found unreliable or often missing. Load inertia is often either assumed fixed or not considered at all. Simplified load models are generally used in the industry. Such an approach is understandable since the sheer number of different load types and their stochastic nature, and spatio-temporal distribution make it impractical to estimate the exact share of each load type.

1.4.1.2 Transient and small-signal stability:

It was observed that the instability will first occur due to the negative interactions between converter inner control loops and the SG's AVR/PSS system, not due to frequency instability.

Thus, voltage control scheme plays an important role in system stability. There is no general consensus on the impact of CID on system eigenvalues (which can be both positive or negative) since the results are often limited to the specific benchmark systems used in simulation studies.

1.4.1.3 Impact of inertia is over-exaggerated:

Low rotational inertia impacts the system stability only to a certain extent. Insufficient damping in the system is what actually exacerbates the stability problem. Increase in the system damping can be achieved by increasing droop gains and PSS responsiveness.

1.4.1.4 Frequency stability:

Inertia does affect frequency dynamics in terms of increased frequency deviation and ROCOF which can in turn trigger frequency protection schemes. This can be combated by units with fast frequency control capabilities. Other countermeasures include modifications of grid codes to allow for wider tolerance on frequency and ROCOF excursions, and incentivizing operation of synchronous units such as generators and compensators.

1.4.1.5 Maximum penetration of CID:

Contrary to the popular belief, maximum penetration of CID does not depend on inertia, but on voltage control scheme and network topology. Regardless whether the CID are of grid-following or grid-forming type, the maximum penetration in a network with SGs does not differ very much. Grid-forming converters remove the frequency instability problem at higher penetrations assuming there is a large enough energy buffer behind the converter. Still, the instability occurs due to inadequacy of system voltage stabilisation. Frequency instability can occur with grid-following converters when PLL and APC cannot track the grid frequency anymore to achieve proper synchronisation.

1.4.1.6 Impact of transmission line dynamics, network topology and system operating point:

Transmission line dynamics improve the stability margin and maximum grid-following converter penetration in a 100% converter-based system as inductive and capacitive components of transmission lines act as energy buffers slowing down the system dynamics. However, transmission line dynamics have a limited impact on a mixed SG/converter system since the issue still lies in the AVR/PSS design thus the maximum CID penetration stays the same. Inclusion of transmission line dynamics implies that phasor-based (RMS) modelling approach will not be sufficient in converter-based power systems since the system dynamics shift towards the electromagnetic time scale and the coupling with the grid becomes important. Operating

point (dispatch) of the units can significantly affect the unstable modes and a single metric of converter penetration is not sufficient to prescribe stability margins. Increasing connectivity between generators increases permissible converter penetration levels. 100% inverter-based grid is lee prone to instability than a mixed system, while the placement of grid-forming converters might prove to be highly important.

1.4.1.7   Operating a low-inertia system:

A system comprising solely of CID (grid-forming and grid-following) is less prone to instability than a low-inertia system. Transition towards 100% RES-based power systems dominated by CID requires coordination between all stakeholders. In that context, operating a low synchronous inertia power system may be more challenging than operating a 100% converter-based system (*inertialess*). Grid-following control will become very challenging in weak grids and the stability issues related to PLLs will be pronounced. Thus, grid-forming control techniques will be indispensable in the future, but they imply that a sufficient energy buffer is available. Still, converter thermal limit (maximum permissible converter current) is the main limitation of converter-based power systems.

1.4.1.8   Provision of synthetic inertia by RES:

Besides static energy storage systems such as batteries, only WTGs have a sufficient amount of energy to provide virtual inertia support without the need for deloading to provide an energy buffer like PV plants, for example. The amount of stored energy in the DC link is two to three orders of magnitude smaller than conventional SGs, although a comparable amount of energy can be extracted for small frequency deviations.

1.4.1.9   Capabilities of grid-forming and grid-following converters:

On the one hand, grid-forming converter does not require a PLL, but its "forming" capability is inferior to the one of a traditional SG. On the other hand, synchronous reference frame PLL (SRF-PLL) is inadequate during distorted and unbalanced conditions, thus more elaborate PLL structures should be used. Increasing PLL bandwidth marginally improves the stability while it reduces passivity of the converter.

1.4.1.10   The role of frequency in an *inertialess* system:

Synchronous machines naturally react to power unbalances which manifests as the change in the machine mechanical speed due to the rotational inertia of the machines. In a synchronous system the frequency is consistent throughout the interconnection (with negligible differences

between measuring points) which makes the frequency a convenient global signal which indicates the generation-load balance. If there are no synchronous machines in the system, then there is no element that naturally responds to generation-load unbalance. Likewise, the frequency is not a physical property anymore related to the mechanical rotation of masses, but a product of converter control software.

1.4.2 Low-order modelling of converter-interfaced devices for system frequency response studies

SFR models simplify the analysis of frequency dynamics of large power systems (or islanded portions thereof) after sudden load disturbances. The basic concept of a simple SFR model is based on the idea of averaging inter-machine oscillations so that the system frequency can be described by a single, uniform quantity: the average system frequency. Conceptually, SFR model averages individual machine dynamics into an equivalent single machine. The most widely accepted and used SFR model is derived by Anderson and Mirheydar in [20] which assumes a system dominated by steam reheat turbine-generators. Since the phenomena of interest is machine mechanical speed dynamics, electromagnetic dynamics of synchronous generators are considered too fast, while thermodynamics of the boiler system are too slow, leaving only the dynamics of speed governor, turbine and aggregated turbine-generator inertia. All but the largest time constants are neglected since they will dominate the dynamic response. In this case, the largest time constant is related to the steam reheater. Later, the original model has been expanded to include the dynamics of hydro turbine-generators [26, 27], gas turbines [28], combined-cycle plants [29, 30] and demand response [31]. An analytical method for aggregating multiple machines into a single machine low-order model is proposed in [32].

As the share of wind power increased worldwide, more papers started focusing on participation of wind turbine generators in frequency control services. Naturally, some papers aimed to develop reduced-order SFR models of wind turbine generators, e.g. [33–36], including our own attempts [37, 38, 38, 39]. The main drawback of all these papers is that the analysis and models are not generic due to the vast amount of approaches to WTG modelling and control (e.g. torque [35, 40] or power control [36, 40, 41], role of machine-side and grid-side converter [40, 42], different operating modes [36, 39] and deloading techniques [34, 36, 43]). The resulting models are often convoluted and provide no intuitive insight into the inner workings of the WTG. Additionally, these models do not differentiate between grid-forming and grid-following operation nor do they include the effects of phase-locked loop. Another issue is the aggregation of spatially-distributed wind turbines in a wind farm into an equivalent turbine, but this is beyond the scope of this thesis.

Similarly, literature on reduced order modelling of PV plants for SFR studies is relatively

scarce. Derived small-signal models [44–47] are generally used to design specific inner controllers, while SFR models usually reduce to generic first-order transfer function describing the fast actuation of inverter and implemented frequency support function [48–50]. A detailed derivation and analysis is missing in literature that would encapsulate the idiosyncrasies of a PV system, if any exist. As in WTG SFR models, these models do not differentiate between grid-forming and grid-following operation nor do they include the effects of phase-locked loop.

A generic low-order model of grid-following and grid-forming converters has been presented in [51]. Notwithstanding the simplicity of the models, they do not discern between different types of devices behind the DC link of the converter, as pointed out in [25].

This thesis will go into more detail about the different technologies behind the VSC in order to develop SFR models which capture the characteristics of each technology while still being analytically tractable.

1.4.3   Supercapacitors in power systems: modelling and applications

Supercapacitor (SC) ESS can be used both as a standalone ESS for grid support or as a combination with other storage systems or CID as part of a hybrid energy (storage) system. Its high power density, in particular, as well as hundreds of thousands of charging/discharging cycles and fast discharge naturally make it most applicable during grid frequency excursions when a fast injection or absorption of active power is necessary. Similarly, it can be used to quickly stabilise intermittent output of solar and wind generation. There are several reasons for using SC systems for fast injection of high power instead of other storage devices, e.g. batteries or flywheels [52, 53]: i) SC bank can be fully charged or discharged in the time scale of several tens of seconds or faster while the rated power can be reached within a few milliseconds; ii) SCs have bigger power density than batteries and flywheels, i.e. a SC system of the same power rating will be much smaller than equivalent battery or flywheel system; iii) SCs can withstand significantly more (hundreds of thousands) charging/discharging cycles; iv) SCs have smaller operation and maintenance costs than batteries and flywheels.

SC technology has often been used for electric vehicle applications in the past, e.g., [54], with the focus on numerical modelling and/or energy management. SCs are often paired with wind and/or solar generation systems for power smoothing, virtual inertial response or low-voltage ride through (LVRT) [55–58] and in these papers the SC is usually used in the DC link of voltage source converters. On larger scale applications, SC is often used as a part of a hybrid ESS in microgrids, e.g. [59], or isolated power systems [60–65] for levelling out intermittent RES or for grid ancillary services such as frequency and voltage support.

All of the surveyed papers have one or more similarities: i) SC is modelled as an ideal capacitor which is not always appropriate as the capacitance, and therefore the stored energy as well, varies with the applied voltage [66]; ii) SC energy storage system model is not applicable for

power system dynamic studies as the supercapacitor model is either given in its RC/RLC form (not a block diagram with defined inputs and outputs), e.g. [63,67] or the complete control system is only given functionally on a higher level with actual details on subsystem implementation missing which makes it difficult to integrate in power system simulation software, e.g. [64]. One outlier from the reviewed literature is a simplified model by Egido *et al.* [65] which neglects any capacitor dynamics and is described only with an initial state-of-charge (SoC) estimation and a simplified control system which seems to agree fairly well with field measurements. However, the used disturbances were smaller than the size of a fully charged supercapacitor and the time scale was not long enough to observe the differences in time-to-discharge (i.e. when the stored energy is depleted).

Based on our work in [68–70], this thesis aims to investigate the adequate complexity level of a supercapacitor model for power system dynamics studies, and derive a suitable SC bank model that can be easily integrated in commercially available power system simulation software. Furthermore, two control designs for enhancing system frequency control performance are presented:

1. A model predictive control (MPC) of SC based on (DC) voltage-frequency droop for enhancing supercapacitor performance [71].

2. A coordinated control of a SC and WTG for enhancing WTG virtual inertia provision during low and above-rated wind speeds [72].

1.4.4 Distributed control of energy storage for ancillary services

It can be easily envisaged that in the future a great amount of flexibility may come from a large number of dispersed, small-scale storage units (e.g. thousands of small-scale residential batteries) as an alternative to centralised bulk storage. If that is going to be the case, then the existing centralised or decentralised control schemes will not be adequate anymore to coordinate such a large number of assets [73]. Drawbacks of the centralised approach are sensitivity to noise, vulnerability to single point failures, huge computational and communication requirements and therefore objectionable scalability. On the other hand, drawbacks of the decentralised approach are instability and sub-optimality which is not adequate since we have coordination goals, and units must cooperate to achieve a common goal. Furthermore, there is also coupling in the constraints since the agents are interconnected.

On the other hand, consensus-based distributed control in the multi-agent system is a viable alternative to solving the aforementioned issues of large-scale integration of small, dispersed storage devices due to lighter computational and hardware requirements [73–78]. However, possible drawbacks of distributed control can be higher sensitivity of performance to communication delays, bugs during operation or malicious attacks, which can cause incorrect syncing between the units and needs to be tackled carefully.

The literature on distributed control for power systems applications (active power & frequency control) can be divided into three groups. Articles in the first group [74, 75, 79–84] are mainly focused on setting the theoretical framework and deriving the sufficient conditions for stability, optimality, robustness, etc. These papers are heavy on the mathematical formalities and the validation is mostly done on simple low-order power system simulation models that assume an ideal communication system. Therefore, any delays in the control or communication, packet losses, bandwidth issues are ignored. Primary and/or secondary and/or tertiary frequency control is discussed in these papers. In the cases of tertiary control, no system dynamics are usually assumed. The simulation examples were focused on validating the theoretical framework, thus practical issues of performance and implementation were not analysed.

The second group of papers [73, 85–95] is more applications oriented. However, all validation setups are completely based on computer simulation. Some of these papers assume ideal communication and control systems [73, 85, 88, 92], but most simulate the effect of delays. Others arguably fall outside distributed control, contrary to their usage of the term, in a sense that there is no interaction between the agents [85, 90, 91]. In some setups [86, 89], the multi-agent system is modelled in JADE environment which allows for a more detailed simulation of the communication system, but these papers focused on unit scheduling and fault detection. Furthermore, it is still a simulation in perfectly controllable centralised environment. In summary, none of the above papers investigated the feasibility of different tiers of frequency control in a physically distributed manner, i.e. that the corresponding framework is run on a real set of devices that are interconnected and that their operation must be synchronised.

The third group of papers [96–100] validated their respective distributed control systems (DCS) on some sort of hardware-in-the-loop (HIL) setup, and they represent the validation of highest fidelity of all the reviewed literature. Prodanović *et al.* [96] focused on improving the parallel operation of inverters through an additional signal that is calculated centrally and distributed to the inner control loops of the inverters. Du *et al.* [97, 98] focused on the development of a general HIL platform for microgrid distributed control and the validation effort was focused on transitioning between on-grid and off-grid microgrid operation. Finally, [99, 100] proposed alternative paradigms of primary and secondary control of active and reactive power in AC microgrids based on cooperative distributed control. The drawback of the validation methodology is that the control routines and the communication channels were modelled on a single processor board, thus basically simulating the DCS on a central computer. Nevertheless, the results show the feasibility of DCS for performing primary and secondary control actions. Additionally, authors in [101] focused on showing the technical capabilities of real-time simulation of a complex microgrid along with its communication network during grid-connected and islanding operation.

The existing literature so far has proven the feasibility of distributed control for power sys-

tem applications mostly by computer simulations. On the other hand, papers that have shown feasibility of DCS for automatic frequency control using a HIL setup implemented the control schemes and the communication network on a single processor board thus simulating the distributed structure. Other papers that used true distributed communication between controllers did not investigate the automatic frequency control. Therefore, there were no papers that investigated the feasibility of different tiers of frequency control using commercial storage devices for which the DCS is implemented on real and distributed controllers. This thesis aims to bridge this gap by going one step further and implementing such a distributed consensus control approach for operating a laboratory-scale VSP using commercially available devices.

Chapter 2

Simulation of power system dynamics in converter-rich power systems

Dynamics of power electronic converters are driven by fast-acting control actions and high-frequency switching of semi-conductors. The timescales are much faster and closer to the electromagnetic time domain. On the one hand, this means that more detailed models of power electronic devices are needed to capture the relevant phenomena. On the other hand, power system time-domain analysis often deals with simulation of complex power networks consisting of hundreds and thousands of buses. In this case, high-fidelity models would be infeasible as they would take a very long time to solve (and would require many parameters to be known). Therefore, very detailed models are limited to single-device infinite bus systems or small systems with a few buses since they are computationally intensive.

This chapter will provide a primer of a converter-based power system simulation based on the recent research [3, 25, 102–105]. The two basic types of dynamic simulations in power system analysis are RMS (root mean square, or fundamental frequency simulation) and EMT (electromagnetic transient). They mainly differ in the modelling approach which is summarised in Table 2.1. Moreover, they differ also in the method of numerically solving the systems of differential-algebraic equations [105], but this is beyond the scope of this thesis.

First consider a generic representation of a three-phase signal

$$\mathbf{x^{abc}}(t) = \begin{pmatrix} x^a(t) & x^b(t) & x^c(t) \end{pmatrix}^\top \in \mathbb{R}^3 \wedge t \in \mathbb{R}_{\geq 0}$$

where phase signals $x^a \in \mathbb{R}$, $x^b \in \mathbb{R}$, and $x^c \in \mathbb{R}$ are defined in (2.1). For brevity, let $\mathbf{X_0^{abc}}(t) = \mathbf{A_0^{abc}}(t) + \boldsymbol{\varepsilon}_{\mathbf{A_0^{abc}}}(t)$ where $\mathbf{A_0^{abc}}(t) \in \mathbb{R}^3$ and $\boldsymbol{\varepsilon}_{\mathbf{A_0^{abc}}}(t) \in \mathbb{R}^3$ are defined by (2.2a) and (2.2b), respectively; $\boldsymbol{\Theta_0^{abc}}(t) = \boldsymbol{\Omega_0}(t) + \boldsymbol{\theta_0^{abc}} + \boldsymbol{\varepsilon}_{\boldsymbol{\theta_0^{abc}}}(t)$ where $\boldsymbol{\Omega_0}(t) \in \mathbb{R}^3$, $\boldsymbol{\theta_0^{abc}} \in \mathbb{R}^3$ and $\boldsymbol{\varepsilon}_{\boldsymbol{\theta_0^{abc}}}(t) \in \mathbb{R}^3$ are defined by (2.2c), (2.2d) and (2.2e), respectively; $\boldsymbol{\zeta^{abc}}(t) \in \mathbb{R}^3$ is defined by (2.2f). Let $\mathbf{A} \odot \mathbf{B}$ be the Hadamard product of matrices $\mathbf{A} \in \mathbb{R}^{N \times M}$ and $\mathbf{B} \in \mathbb{R}^{N \times M}$ for $(N, M) \in \mathbb{N}^2$; let

Table 2.1: Comparison of modelling approaches and dynamic simulation types.

| | Type of simulation | | |
| | EMT | | RMS |
Modelling approach	Switching	Average	Average
static phasors	✗	✗	✓
abc	✓	✓	✗
dq0	✗	✓	✓
dynamic phasors	✓(abc)	✓	✓

$\cos_\odot \mathbf{C}_{N \times 1} := (\cos c_1 \quad \cos c_2 \quad \dots \quad \cos c_n)^\top$. Then, (2.1a)–(2.1c) can be written in a compact form (2.3).

$$x^a(t) = \left[A_0^a(t) + \varepsilon_{A_0^a}(t) \right] \cos \left[\int_{t_0}^t (\omega_0(\tau) + \varepsilon_{\omega_0}(\tau))\, d\tau + \theta_0^a + \varepsilon_{\theta_0^a}(t) \right] + \zeta^a(t) \tag{2.1a}$$

$$x^b(t) = \left[A_0^b(t) + \varepsilon_{A_0^b}(t) \right] \cos \left[\int_{t_0}^t (\omega_0(\tau) + \varepsilon_{\omega_0}(\tau))\, d\tau + \theta_0^b + \varepsilon_{\theta_0^b}(t) - \frac{2\pi}{3} \right] + \zeta^b(t) \tag{2.1b}$$

$$x^c(t) = \left[A_0^c(t) + \varepsilon_{A_0^c}(t) \right] \cos \left[\int_{t_0}^t (\omega_0(\tau) + \varepsilon_{\omega_0}(\tau))\, d\tau + \theta_0^c + \varepsilon_{\theta_0^c}(t) + \frac{2\pi}{3} \right] + \zeta^c(t) \tag{2.1c}$$

$$\mathbf{A_0^{abc}}(t) = \left(A_0^a(t) \quad A_0^b(t) \quad A_0^c(t) \right)^\top \tag{2.2a}$$

$$\boldsymbol{\varepsilon}_{\mathbf{A_0^{abc}}}(t) = \left(\varepsilon_{A_0^a}(t) \quad \varepsilon_{A_0^b}(t) \quad \varepsilon_{A_0^c}(t) \right)^\top \tag{2.2b}$$

$$\boldsymbol{\Omega_0}(t) = \begin{pmatrix} \int_{t_0}^t (\omega_0(\tau) + \varepsilon_{\omega_0}(\tau))\, d\tau \\ \int_{t_0}^t (\omega_0(\tau) + \varepsilon_{\omega_0}(\tau))\, d\tau \\ \int_{t_0}^t (\omega_0(\tau) + \varepsilon_{\omega_0}(\tau))\, d\tau \end{pmatrix} \tag{2.2c}$$

$$\boldsymbol{\theta_0^{abc}} = \begin{pmatrix} \theta_0^a \\ \theta_0^b - \frac{2\pi}{3} \\ \theta_0^c + \frac{2\pi}{3} \end{pmatrix} \tag{2.2d}$$

$$\boldsymbol{\varepsilon}_{\boldsymbol{\theta_0^{abc}}}(t) = \left(\varepsilon_{\theta_0^a}(t) \quad \varepsilon_{\theta_0^b}(t) \quad \varepsilon_{\theta_0^c}(t) \right)^\top \tag{2.2e}$$

$$\boldsymbol{\zeta^{abc}}(t) = \left(\zeta^a(t) \quad \zeta^b(t) \quad \zeta^c(t) \right)^\top \tag{2.2f}$$

$$\mathbf{x^{abc}}(t) = \mathbf{X_0^{abc}}(t) \odot \cos_\odot \mathbf{\Theta_0^{abc}}(t) + \mathbf{\zeta^{abc}}(t) \tag{2.3}$$

Form (2.3) completely describes a generic three-phase signal, both balanced and unbalanced, and containing other disturbances. $\mathbf{A_0^{abc}}(t)$ is the time-varying amplitude of the fundamental component (indice $(\cdot)_0$); $\mathbf{\varepsilon_{A_0^{abc}}}(t)$ models the amplitude modulations of the fundamental component (e.g. voltage dips); $\omega_0(t)$ is the time-varying fundamental frequency; $\varepsilon_{\omega_0}(t)$ models the modulation of the fundamental frequency (e.g. frequency oscillations); $\mathbf{\theta_0^{abc}}(t)$ models the initial phase angle of the fundamental component with respect to the reference node; $\mathbf{\varepsilon_{\theta_0^{abc}}}(t)$ models the phase angle modulations of the fundamental component (e.g. phase jumps); $\mathbf{\zeta^{abc}}(t)$ is a generic function that can be used to model the presence of higher harmonics, DC bias, noise, etc., per each phase.

2.1 Modelling in *abc* reference frame

EMT simulations use very detailed models of each component. The passive power network is modelled with differential equations ($L\frac{di}{dt}$ and $C\frac{dv}{dt}$). Electric machinery can be modelled using high-fidelity models and power electronic converters can be modelled either as switching models or average models (averaged over one switching period). The phenomena ranging from DC to hundreds of kHz can be simulated this way [102] and the bandwidth depends only on the fidelity of component models, and consequently the integration step size in the interval $(0.1, 1000)\,\mu$s. Ultimately, EMT simulations are very slow and limited to component-level simulation or very small-systems.

EMT simulations employ modelling in the natural three-phase *abc* domain (as introduced by (2.3)). Any kind of equipment can be modelled in the *abc* reference frame, and all the electrical quantities are represented with their three-phase instantaneous values in the time domain. Although closest to physical reality, the *abc* framework is not very efficient as it intrinsically does not have a steady-state (e.g., a balanced three-phase current in steady-state is still a three-phase sine wave oscillating in time with the fundamental frequency, meaning that the model is time-variant which in turn prevents using small-signal analysis tools [104]). Unbalanced systems are easily simulated and analysed in *abc* reference frame.

2.2 Modelling with static phasors

On the other hand, the *static phasors* approach (also known as *quasi-stationary phasors* or *time-varying phasors*) is used in RMS simulations. Its main characteristic is that the passive power network (i.e. branches and shunts) is modelled as constant impedances at the fundamental frequency [104]. This means that the network transients are neglected and the power grid

is described by algebraic equations. Furthermore, stator transients of electric machinery are neglected as well [106]. Power electronic devices are modelled using average models at fundamental frequency (higher harmonics are neglected) [103]. All other dynamics are modelled per desired level of detail.

In steady-state, phasor representation of a balanced three-phase signal consisting of fundamental frequency only ($\boldsymbol{\zeta}^{\mathbf{abc}} = \mathbf{0}$) is based on the assumption that $\mathbf{A}_0^{\mathbf{abc}}(t)$, $\omega_0(t)$ and $\boldsymbol{\theta}_0^{\mathbf{abc}}(t)$ are constant with respect to time ($\boldsymbol{\varepsilon}_{\mathbf{A}_0^{\mathbf{abc}}} = \boldsymbol{\varepsilon}_{\boldsymbol{\theta}_0^{\mathbf{abc}}} = \mathbf{0}$; $\varepsilon_{\omega_0} = 0$; $\omega_0(t) = 2\pi f_s$ where $f_s \in \mathbb{R}_{\geq 0}$ is the synchronous frequency). The phasor $\bar{\mathbf{x}}_0^{\mathbf{abc}}$ is defined as (2.4), where $e_\odot^{j\boldsymbol{\theta}_0^{\mathbf{abc}}}$ denotes the per-element exponentiation: $\left(e^{j\theta^a} \quad e^{j\left(\theta_0^b - \frac{2\pi}{3}\right)} \quad e^{j\left(\theta_0^c + \frac{2\pi}{3}\right)} \right)^\top$. Factor $\frac{1}{\sqrt{2}}$ is used to define the phasor magnitude with the RMS value instead of the peak value of the time-domain signal.

$$\bar{\mathbf{x}}_0^{\mathbf{abc}} = \frac{1}{\sqrt{2}}\mathbf{A}_0^{\mathbf{abc}} \odot e_\odot^{j\boldsymbol{\theta}_0^{\mathbf{abc}}} \tag{2.4}$$

More generally, a phasor defined as in (2.4) is the fundamental Fourier coefficient of $\mathbf{x}^{\mathbf{abc}}(t)$. Looking only at the phase a signal $x^a(t)$ (2.1a), it can be written as an an infinite sum of sinusoidal functions (2.5), where $\bar{\chi}_k^a$ (2.6) is the k-th Fourier coefficient. For $k = \pm 1$, the coefficient $\sqrt{2}\bar{x}_0^a = \bar{\chi}_1^a + \bar{\chi}_{-1}^a$ (2.7) is the fundamental frequency phasor of $x^a(t)$. If $x^a(t)$ is a pure cosine signal, then $\bar{\chi}_k^a = 0 \ \forall k \in \mathbb{Z}\backslash\{-1,1\}$.

$$x^a(t) = \sum_{k=-\infty}^{\infty} \bar{\chi}_k^a e^{j2\pi f_s k t}, \quad k \in \mathbb{Z} \tag{2.5}$$

$$\bar{\chi}_k^a = \frac{1}{T}\int_{t_0}^{t_0+T} x^a(\tau)e^{-j2\pi f_s k \tau}d\tau \tag{2.6}$$

$$\bar{x}_0^a = \frac{1}{\sqrt{2}}A_0^a e^{j\theta_0^a} \tag{2.7}$$

In transient conditions, however, the system is not in a state where amplitude, frequency and phase are constant. Instead, they are time-varying and the corresponding signals are nearly-periodic. The Fourier series approach can be extended to nearly-periodic signals [107, 108] to obtain time-varying phasors (2.8)–(2.9) since the interval under consideration slides as a function of time.

$$\bar{\chi}_k^a(t) = \frac{1}{T}\int_{t_0}^{t_0+T} x^a(\tau)e^{-j2\pi f_s k \tau}d\tau \tag{2.8}$$

$$\bar{x}_0^a(t) = \frac{1}{\sqrt{2}}A_0^a(t)e^{j\theta_0^a(t)} \tag{2.9}$$

This definition of a phasor using Fourier series expansions is convenient since the idea of dynamic phasors described in Section 2.6 is just an extension of the fundamental frequency phasor $\bar{x}_0$ to higher harmonics $\bar{x}_k$, $k \in \mathcal{K} \subseteq \mathbb{Z}\backslash\{-1,0,1\}$.

The main assumption here is that the grid frequency deviates very little around the fundamental frequency which makes the use of phasors to describe voltages and currents appropriate. Furthermore, it assumes that the high-bandwidth devices (control, switching) have no impact on the electromechanical dynamics [102]. These assumptions have two consequences: One is that the model is only appropriate for low-frequency phenomena (up to a few Hz) as dictated by the parameters of the system, although this also may not hold in certain cases [109]; the other is that the transfer of electric power happens in a narrow band around the fundamental frequency [110].

Unbalanced systems can be analysed in RMS simulations and there are two ways to achieve this. The first way is to use a three-phase system representation [16, 106] which is essentially a phasor of each phase per (2.4) (this approach is used by PowerFactory [111]). The second way is to use symmetrical components [112]) and appropriately interconnect positive, negative and zero sequence networks at the fault location [16, 106] (this approach is used by PSS/E [113]). Note that the second approach is used for simulating balanced systems which become unbalanced due to an asymmetrical fault. It cannot be used for systems which are inherently unbalanced, such as due to unbalanced loads, hence the first approach is required.

RMS simulations are still the key tool in bulk power system dynamics simulations as they use a relatively large integration step size in the interval $(1, 30)$ ms. Phasor models are also time-invariant. However, the assumptions that the RMS simulation is based on are currently being challenged in the power engineering community due to the fast dynamics introduced by power electronic converters.

2.3   EMT (*abc*) vs. RMS

Consider an ideal and controllable three-phase voltage source $\mathbf{x^{abc}} \to \mathbf{u^{abc}}$ connected to a pair of constant three-phase RL loads ($R_L \in \mathbb{R}_{\geq 0}, L_L \in \mathbb{R}_{\geq 0}$) through two parallel transmission lines (π-section model described by positive, negative and zero-sequence components in $R_l \in \mathbb{R}^3_{\geq 0}$, $L_l \in \mathbb{R}^3_{\geq 0}, C_l \in \mathbb{R}^3_{\geq 0}$) as shown by the single-line diagram in Fig. 2.1. The system is balanced and the three-phase source only has the fundamental component at constant frequency ($\boldsymbol{\varepsilon}_{\mathbf{A_0^{abc}}} = \boldsymbol{\varepsilon}_{\boldsymbol{\theta}_0^{abc}} = \mathbf{0}$; $\varepsilon_{\omega_0} = 0$; $\omega_0(t) = 2\pi f_s$). The line-to-line RMS voltage of the source is 400 kV ($\mathbf{A_0^{abc}}(t) = \mathbf{400}\frac{\sqrt{2}}{\sqrt{3}}$ kV). Internal impedance of $\mathbf{u^{abc}}$ is modelled as a series RL branch (R_s and L_s). The load is modelled as a delta-connected, series RL, constant impedance load such that it draws $P_L = 400$ MW and $Q_L = 100$ Mvar in the initial steady-state. The source, line and load data are provided in Table 2.2.
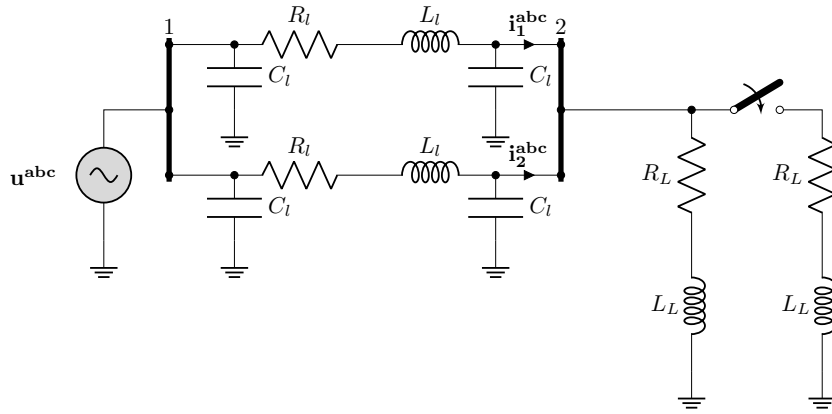
Figure 2.1: Single-line diagram of an ideal three-phase voltage source connected to a load through two parallel transmission lines.

Table 2.2: Parameters of the system from Fig. 2.1.

Parameter	Value
R_s	1 mΩ
L_s	100 μH
R_l	(0.03, 0.03, 0.3) mΩ km^{-1}
L_l	(1.05, 1.05, 3.5) mH km^{-1}
C_l	(0.011, 0.011, 0.0055) μF km^{-1}
Line length	100 km
R_L	366 Ω
L_L	0.291 H
f_s	50 Hz

2.3.1 Step change of load

At $t = 0.05$ s, the switch is closed, simulating a step load increase of $\approx 100\%$. Fig. 2.2 shows the instantaneous three-phase power measured at Bus 2. Due to the interactions between the L and C elements of the grid, there are high-frequency power oscillations not captured by the RMS model which neglects grid dynamics. The voltage phasor $\bar{\mathbf{u}}^{\mathbf{abc}}$ only captures the RMS value of the fundamental component of $\mathbf{u}^{\mathbf{abc}}$ (Fig. 2.3 only shows the magnitude, but the time-varying phase has an identical shape). Thus, the instantaneous voltage cannot be accurately reconstructed as shown by Fig. 2.3. The frequency spectrum captured by EMT (*abc*) and RMS simulation is shown in Fig. 2.4. The high-frequency component of around 750 Hz is clearly visible in the EMT spectrum.

Nonetheless, accuracy at high frequencies was hitherto not of concern for frequency dy-
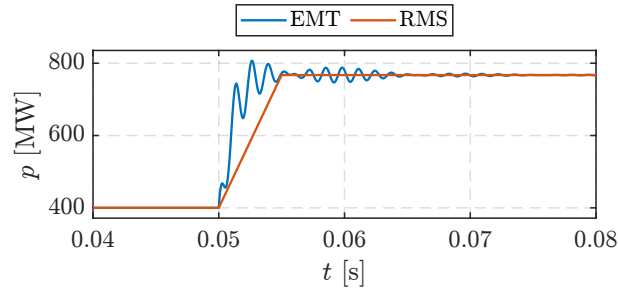
Figure 2.2: EMT vs. RMS simulation: instantaneous three-phase power at Bus 2 for a step increase in load.

namics as it was mostly governed by slow electromechanical dynamics centred inside a narrow band around the synchronous frequency f_s as shown in Fig. 2.4. Naturally, the question arises if RMS will be applicable to study frequency dynamics in converter-based power systems because such systems will be characterised by high RoCoF in the fundamental component, i.e., signal $\mathbf{\Omega_0}(t)$ (2.2c) can possibly contain frequency components in a wide band around ω_s.

2.3.2 Frequency modulation

A frequency modulation component (2.10) is added to the fundamental component $\omega_0(t) = 2\pi f_s$ of the three-phase source $\mathbf{u^{abc}}$ from Fig. 2.1, where $\Delta f_\infty \in \mathbb{R}_{\geq 0}$ is the post-disturbance steady-state frequency deviation; $D \in \mathbb{R}_{\geq 0}$ is the damping factor; $t_0 \in \mathbb{R}_{\geq 0}$ is the disturbance start time; $A \in \mathbb{R}_{\geq 1}$ is the oscillation amplitude; $f_{\mathrm{osc}} \in \mathbb{R}_{\geq 0}$ is the oscillation frequency.

$$\varepsilon_{\omega_0}(t) = \Delta f_\infty \left[1 - A e^{-D(t-t_0)} \cos\left(2\pi f_{\mathrm{osc}}(t-t_0) + \cos^{-1}\frac{1}{A} \right) \right] \tag{2.10}$$

A comparison of grid frequency estimation (at Bus 2) in the RMS and EMT simulation is conducted for $f_{\mathrm{osc}} \in \{0.1, 1, 10, 100, 200\}$ Hz for RMS integration step sizes $\Delta T \in \{0.1, 1, 10\}$ ms. The integration step size of EMT simulations is $\Delta T = 10 \ \mu$s for all simulations. In this study case, the switch (Fig. 2.1) remains open. Fundamental frequency modulation parameters are given in Table 2.3. It bares mentioning that the frequency is calculated from the difference between the current and previous bus voltage phase angle, divided by the integration step size (in RMS it is the phase angle of the positive sequence phasor) defined in (2.11). Since the system under study is balanced, phase voltage superscript (*abc*) notation is dropped. The EMT simulation is taken as the benchmark.

$$\tilde{f} = \frac{\theta_t - \theta_{t-1}}{\Delta T} \tag{2.11}$$

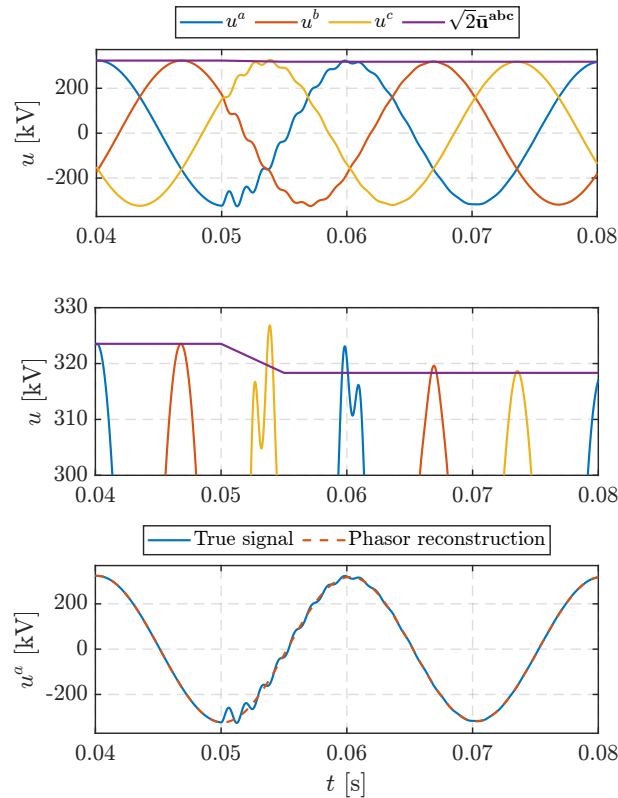Results in Fig. 2.5 show that even for low-frequency oscillations of 0.1 Hz and 1 Hz there

Figure 2.3: EMT vs. RMS simulation: instantaneous three-phase voltage (top), three-phase voltage phasor magnitude (middle), and phasor-reconstructed instantaneous phase a voltage at Bus 2 (bottom) for a step increase in load.

will be an error during the transient state between the EMT and RMS simulations for the standard integration step size of 10 ms. This error is caused by the fact that the change of a state variable due to a disturbance at $t = 0.1$ s will not be recorded until the next time step $t = 0.11$ s. Such a detail, however, is generally not of concern in frequency dynamics studies. It can be seen that a 10 ms step size will be accurate for oscillations up to 10 Hz, a 1 ms step size will be accurate for oscillations up to 100 Hz, while for oscillations up to around 200 Hz, a 0.1 ms time step is needed. There are not strict cut-off values, but rather a ballpark of required step sizes.

For even higher frequency oscillations (e.g. > 200 Hz), transmission line L and C dynamics come into play so the RMS simulation will not be applicable, i.e., it will not capture these dy-
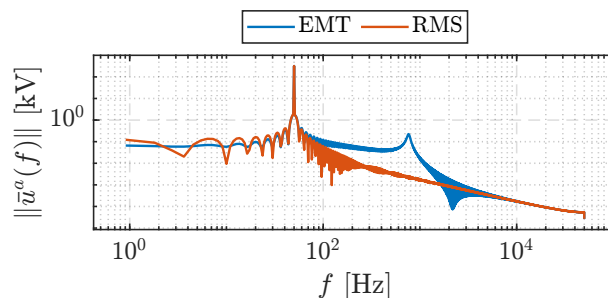
Figure 2.4: EMT vs. RMS simulation: frequency spectrum of $u^a(t)$ at Bus 2 for a step increase in load.

Table 2.3: RMS vs. EMT simulation: fundamental frequency modulation parameters.

Parameter	Value
Δf_∞	-0.1 Hz
A	1 Hz
D	5 s^{-1}
t_0	0.1 s

namics even for a 10 μs step size (Fig. 2.6). As active power control (including PLL dynamics) happens in the frequency range up to 100 Hz (Fig. 1.3), RMS simulation should still be applicable regardless of the possible existence of frequency components ≥ 10 Hz (just a smaller step size should be used). This can be explained by the Nyquist frequency criterion which states that in order to accurately reconstruct a signal with the highest frequency f, the sampling frequency (in this case it is the integration step size) should be **at least** $2f$. For $f_{\mathrm{osc}} = 10$ Hz, the sampling frequency should theoretically be 20 Hz, which translates to a 50 ms time step. However, Fig. 2.5 shows that even for a 10 ms step, there is an error in the calculated frequency. In practice, the integration step size is generally chosen to be an order of magnitude smaller than the theoretical minimum sampling frequency—therefore, for $f_{\mathrm{osc}} = 5$ Hz, the minimum sampling frequency should be 10 Hz. In other words, choosing a sampling frequency of 100 Hz (which translated to a 10 ms integration step size) should be accurate for frequencies up to 5 Hz, which is why it is said in literature that RMS studies are accurate for phenomena up to a few Hz (assuming the standard step size of 10 ms in most commercial solvers). The other way that the integration step is chosen in dynamic simulations is to be at least an order of magnitude smaller than the smallest time constant, which is similar to choosing it according to the Nyquist criterion.

This study indicates that RMS simulation should be conditionally adequate even for fast frequency transients that could theoretically appear in converter-based power systems during generation-load imbalances under the assumption that active power control phenomena will not be faster than ≈ 100 Hz. Appropriate reduction of the integration step size should be enough to accurately reconstruct the frequency signal from ideal node voltage measurements, while grid *LC* oscillations should not be relevant during normal frequency control, as also indicated in [102, 114]. However, the main drawback of the study is that the frequency dynamics were simulated by modulating the fundamental frequency of an ideal three-phase voltage source without a real load step change. RMS simulation fails only when grid dynamics interact with other elements, such as control systems and electric machinery, and is more pronounced during short-circuit faults [102, 114] and specific conditions when interactions happen at lower frequencies (e.g., subsynchronous resonances), which are beyond the scope of this thesis. Nevertheless, EMT and RMS simulations of multi-machine systems with detailed converter and synchronous

generator models during load disturbances will be conducted in the subsequent chapters.
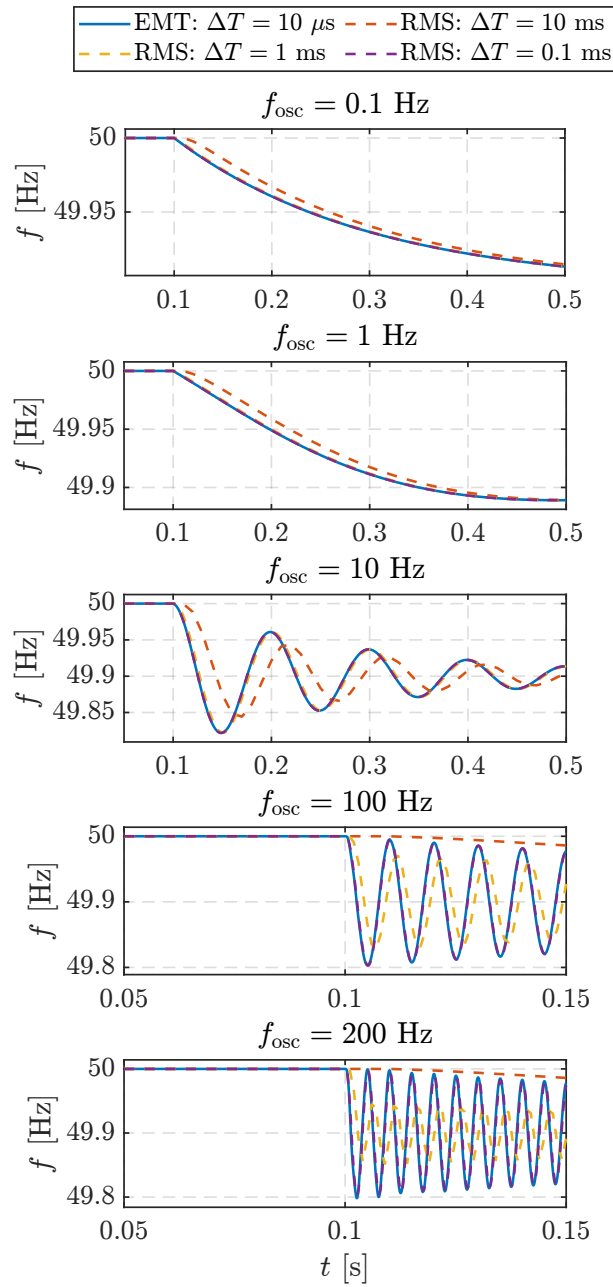

Figure 2.5: EMT vs RMS: estimation of frequency at Bus 2 for different integration step sizes ΔT and oscillation frequencies f_{osc} (up to 200 Hz) of the fundamental component.
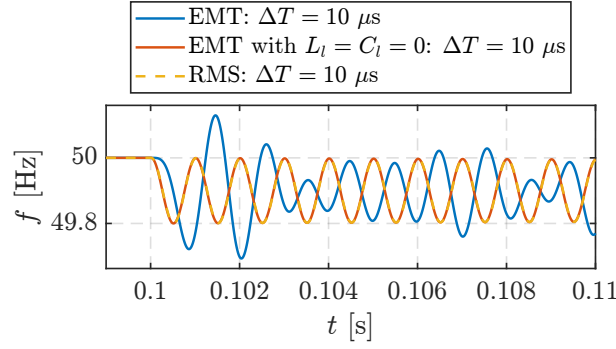
Figure 2.6: EMT vs RMS: estimation of frequency at Bus 2 for integration step size $\Delta T = 10 \ \mu s$ and $f_{osc} = 1$ kHz.

2.4 Modelling in $dq0$ reference frame

The next modelling tool is the representation of system components in the $dq0$ reference frame which is, historically, based on Park's transform [115] which is used to simplify analysis of electric machinery. Generally, all known transforms (e.g. Clarke's, Park's, etc.) can be subsumed under the transform to an *arbitrary reference frame*. In other words, all known transformations can be obtained by assigning the appropriate speed of rotation (including zero) to this *arbitrary reference frame*. The quantities in any frame are derived directly from the physical representation in *abc* frame by applying a transform $\mathbb{R}^3 \mapsto \mathbb{R}^3$ which maps three-phase signals to a reference frame rotating at an arbitrary angular speed $\omega^\bullet \in \mathbb{R}_{\geq 0}$ (2.12). Generally, Clarke's (or $\alpha\beta0$) transform is obtained for $\omega^\bullet = 0$. For $\omega^\bullet > 0$, the obtained transform is generically referred to as $dq0$ transform.

$$\mathbf{x^{dq0}} = \mathbf{T^{dq0}}(\theta^\bullet(t))\mathbf{x^{abc}} \tag{2.12a}$$

$$\mathbf{T^{dq0}}(\theta^\bullet(t)) = \frac{2}{3} \begin{pmatrix} \cos\theta^\bullet(t) & \cos\left(\theta^\bullet(t) - \frac{2\pi}{3}\right) & \cos\left(\theta^\bullet(t) + \frac{2\pi}{3}\right) \\ \sin\theta^\bullet(t) & \sin\left(\theta^\bullet(t) - \frac{2\pi}{3}\right) & \sin\left(\theta^\bullet(t) + \frac{2\pi}{3}\right) \\ \frac{1}{2} & \frac{1}{2} & \frac{1}{2} \end{pmatrix} \tag{2.12b}$$

$$\frac{d\theta^\bullet(t)}{dt} = \omega^\bullet(t) \tag{2.12c}$$

The $dq0$ transform using the definition of $\mathbf{T^{dq0}}$ in (2.12b) is referred to as a power-variant transform since the expression for instantaneous power in the $dq0$ coordinates has to be scaled by a factor of $\frac{3}{2}$ (2.13) in order to conserve the instantaneous power from the *abc* coordinates.

$$p^{abc}(t) = p^{dq0}(t) \tag{2.13a}$$

$$v^a i^a + v^b i^b + v^c i^c = \frac{3}{2}\left(v^d i^d + v^q i^q + 2v^0 i^0\right) \tag{2.13b}$$

(power-variant, if (2.12b) is used)

27

Alternatively, one can also define a power-invariant transform by defining $\mathbf{T^{dq0}}$ as (2.14), in which case the power balance equation equals to (2.15). Other alternatives also include the choice of whether the d-axis leads the q-axis or vice-versa [106, 115]. The rotation matrix $\mathbf{T^{dq0}}$, whether defined like (2.12b) or like (2.14) is such that the d-axis will lead the q-axis by $\frac{\pi}{2}$ assuming a space vector definition $x_d - jx_q$. For q-axis to lead the d-axis, the second row should be scaled by a factor of -1. In the end, the choice of the $\mathbf{T^{dq0}}$ form (power-variant or power-invariant, orientation of dq axis) comes down to personal preference and application. In any case, once the form is chosen, it must be consistently applied to have a consistent mathematical formulation, especially when quantities are transformed between multiple reference frames.

$$\mathbf{T^{dq0}}(\theta^{\bullet}(t)) = \sqrt{\frac{2}{3}} \begin{pmatrix} \cos\theta^{\bullet}(t) & \cos\left(\theta^{\bullet}(t) - \frac{2\pi}{3}\right) & \cos\left(\theta^{\bullet}(t) + \frac{2\pi}{3}\right) \\ \sin\theta^{\bullet}(t) & \sin\left(\theta^{\bullet}(t) - \frac{2\pi}{3}\right) & \sin\left(\theta^{\bullet}(t) + \frac{2\pi}{3}\right) \\ \frac{1}{\sqrt{2}} & \frac{1}{\sqrt{2}} & \frac{1}{\sqrt{2}} \end{pmatrix} \tag{2.14}$$

$$p^{abc}(t) = p^{dq0}(t) \tag{2.15a}$$
$$v^a i^a + v^b i^b + v^c i^c = v^d i^d + v^q i^q + v^0 i^0 \tag{2.15b}$$

(power-invariant, if (2.14) is used)

The inverse transform of (2.12b) and (2.14) is given by (2.16) and (2.17), respectively.

$$\left(\mathbf{T^{dq0}}(\theta^{\bullet}(t))\right)^{-1} = \begin{pmatrix} \cos\theta^{\bullet}(t) & \sin\theta^{\bullet}(t) & 1 \\ \cos\left(\theta^{\bullet}(t) - \frac{2\pi}{3}\right) & \sin\left(\theta^{\bullet}(t) - \frac{2\pi}{3}\right) & 1 \\ \cos\left(\theta^{\bullet}(t) + \frac{2\pi}{3}\right) & \sin\left(\theta^{\bullet}(t) + \frac{2\pi}{3}\right) & 1 \end{pmatrix} \tag{2.16}$$

$$\left(\mathbf{T^{dq0}}(\theta^{\bullet}(t))\right)^{-1} = \sqrt{\frac{2}{3}} \begin{pmatrix} \cos\theta^{\bullet}(t) & \sin\theta^{\bullet}(t) & \frac{1}{\sqrt{2}} \\ \cos\left(\theta^{\bullet}(t) - \frac{2\pi}{3}\right) & \sin\left(\theta^{\bullet}(t) - \frac{2\pi}{3}\right) & \frac{1}{\sqrt{2}} \\ \cos\left(\theta^{\bullet}(t) + \frac{2\pi}{3}\right) & \sin\left(\theta^{\bullet}(t) + \frac{2\pi}{3}\right) & \frac{1}{\sqrt{2}} \end{pmatrix} \tag{2.17}$$

The advantage of the $dq0$ transformation is two-fold [104]: firstly, it inherently preserves dynamic behaviour of the physical quantities in abc frame, which means that it is accurate for observing phenomena at higher frequencies. Secondly, a balanced three-phase signal in the abc domain maps to a quasi-stationary signal (DC) in the $dq0$ domain which has a defined steady-state value and small-signal analysis can be utilised. Hence, controllers are easier to implement

in the $dq0$ domain (PI controllers can be used) than in an *abc* or stationary reference frame (resonant controllers need to be used) [13].

Both RMS and EMT simulations can be done in the $dq0$ domain, and the RMS representation of system components is established by setting the appropriate time derivates to zero. Another advantage of the $dq0$ transformation is that the resulting quantities are orthogonal. On the one hand, if the system is in a balanced state, the $dq0$ transformation is significantly more efficient than the *abc* simulation, and larger step sizes can be used (since the positive sequence $dq0$ signals vary slower in time) [108]. On the other hand, if the system is in unbalanced state or if higher harmonics are present, negative and zero sequence components will introduce oscillations in the $dq0$ representation which reduces the maximum step size and hinders the interpretation of results [3, 108]. $dq0$ representation is most efficient in terms of simulation time around the frequency of transformation.

Multiple local reference frames are possible inside each power system component (e.g. control of DFIG in its own reference frame rotating with the rotor of the induction machine). In multi-machine systems, quantities in different reference frames need to be converted to the global reference frame in order to achieve a consistent mathematical formulation. In the context of power system analysis, the global reference frame most often rotates either at the constant synchronous frequency (which simplifies the problem formulation but introduces problems for system linearisation [25, 116]) or at the actual speed of some arbitrary machine/converter designated as the reference (which is preferred), although some additional options like aligning to the centre of inertia are available in some power system simulation software [111]. Transformation of variables from reference frame x to reference frame y is obtained by the rotation matrix $_x\mathbf{T}_y$ (2.18). More details on power system modelling in $dq0$ frame can be found in [104, 117, 118].

$$_x\mathbf{T}_y = \begin{pmatrix} \cos\left(\theta_y^\bullet - \theta_x^\bullet\right) & -\sin\left(\theta_y^\bullet - \theta_x^\bullet\right) & 0 \\ \sin\left(\theta_y^\bullet - \theta_x^\bullet\right) & \cos\left(\theta_y^\bullet - \theta_x^\bullet\right) & 0 \\ 0 & 0 & 1 \end{pmatrix} \tag{2.18}$$

The aforementioned advantages and disadvantages of $dq0$ transform are illustrated in section 2.5.

2.5 EMT (*abc*) vs. EMT(*dq*0)

2.5.1 Balanced system

The system from Fig. 2.1 is modelled in the *dq*0 frame rotating with the frequency of voltage source $\mathbf{u^{abc}}$ (50 Hz) in MATLAB-Simulink. Load flow calculation for initializing the dynamic model is computed using MATPOWER 7.1 [119–121]. The step load increase occurs at $t = 0.05$ s. Dynamics are preserved in the *dq*0 domain (Fig. 2.7, bottom) which is reflected in the oscillations of *dq* components. Quantities in the *abc* domain can be reconstructed by applying an inverse transform (2.16) to *dq*0 quantities. Reconstructed values from the MATLAB- Simulink *dq*0 simulation are identical to the values from the *abc* simulation in PowerFactory (dashed lines in Fig. 2.7, top). Fig. 2.8 shows the frequency spectrum of the Bus 2 voltages in both modelling approaches. Since the *dq*0 model rotates with the synchronous frequency, this part of the spectrum is shifted towards DC, but high frequency dynamics due to the *L* and *C* elements are preserved.
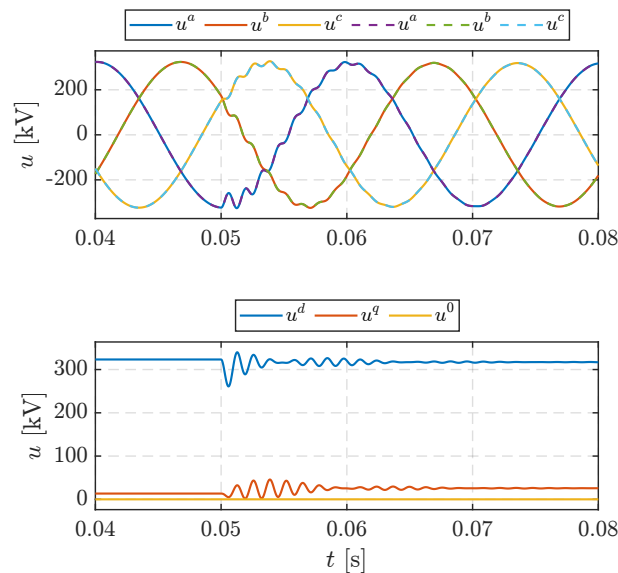
Figure 2.7: EMT (*abc*) vs. EMT (*dq*0) simulation: instantaneous three-phase voltage at Bus 2 in the *abc* domain (top), its reconstruction from the *dq*0 domain (top, dashed), and instantaneous three-phase voltage at Bus 2 in the *dq*0 domain (bottom).

Next, the same system was simulated in MATLAB-Simulink using the *abc* (Simscape Specialized Power Systems toolbox) and *dq*0 modelling approach. Both the fixed-step solver (`ode8`) and variable-step solver (`ode23tb`) were used. For the fixed-step solver, the integration step size ΔT was varied from 1 μs to 1 ms by factors of 10 ($\Delta T \in \{1, 10, 100, 1000\}$ μs). For the variable-step solver, ΔT was used as the maximum step size with the relative tolerance of state variables calculation set to 10^{-4}. The length of simulation time was set to 0.3 s in all cases. For each integration step size, the simulation was conducted 10 times and the average simulation speed was calculated as shown in Table 2.4. The integration step size of a fixed-step
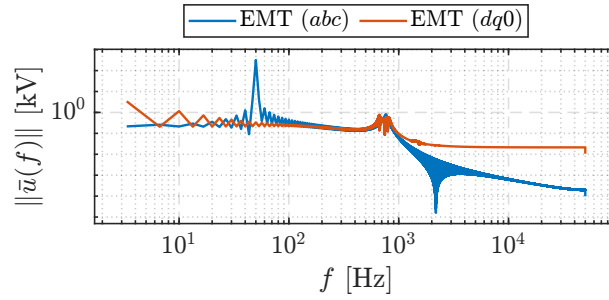
Figure 2.8: EMT (*abc*) vs. EMT (*dq*0) simulation: frequency spectrum of the *abc* and *dq*0 models.

solver is limited by the smallest time constants of the system, which is around 10 μs, determined by the L and C constants of transmission lines and the internal inductance of the voltage source. For a 1 μs step size, the *dq*0 simulation is 5.3 times faster than the *abc* simulation. For step-sizes $\geq$ 10 μs, the *abc* simulation does not numerically converge. Variable-step solvers automatically reduce the step size during fast state changes to increase accuracy, and increase the step size when states change slowly to improve computational efficiency. Even for a variable-step, the *dq*0 approach is 3–4.5 times faster than the *abc* simulation. The better performance of *dq*0 models is attributed to the fact steady-state values are essentially DC and there is no need to calculate state values for of each phase, which are oscillating in steady-state with a frequency of 50 Hz, which in turn limits the maximum integration step size. Therefore, the *dq*0 modelling framework is a good choice for EMT simulations of converter-based power systems.

Table 2.4: Average speed of the *abc* vs. *dq*0 EMT balanced simulations for a fixed-step / variable-step solver and different integration step sizes.

	Fixed-step solver (`ode8`)				Variable-step solver (`ode23tb`)			
	1 μs	10 μs	100 μs	1000 μs	1 μs	10 μs	100 μs	1000 μs
abc	72.3 s	✗	✗	✗	29.3 s	4.0 s	1.3 s	1.2 s
*dq*0	13.6 s	1.9 s	✗	✗	6.5	1.2	0.4	0.3

2.5.2 Unbalanced system

Consider the system from Fig. 2.1 such that the fundamental frequency amplitudes of $\mathbf{u^{abc}}$ are set as (2.19), i.e., the phase b voltage is reduced by 5%. This will cause negative and zero-sequence components to appear in the system. Consequently, an additional harmonic appears in the d and q components which rotates at double the synchronous frequency, and a harmonic that rotates at the synchronous frequency appears in the 0 component (Fig. 2.9). Table 2.5 shows that the unbalanced simulation is more computationally intensive, that is, due to oscillations in

the $dq0$ components, the minimum step size is limited, thus decreasing simulation speed.

$$\mathbf{U_0^{abc}}(t) = \left(400\sqrt{\frac{2}{3}} \quad 380\sqrt{\frac{2}{3}} \quad 400\sqrt{\frac{2}{3}} \right) \text{ kV} \tag{2.19}$$
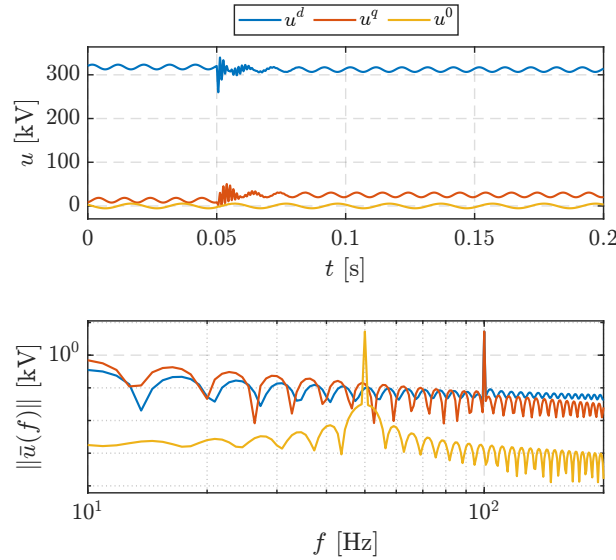

Figure 2.9: Bus 2 voltage $dq0$ components during an unbalanced simulation: time-domain (top) and frequency spectrum (bottom).

Table 2.5: Average speed of the $dq0$ EMT balanced/unbalanced simulation for a fixed-step / variable-step solver and different integration step sizes.

	Fixed-step solver (`ode8`)				Variable-step solver (`ode23tb`)			
	$1\ \mu s$	$10\ \mu s$	$100\ \mu s$	$1000\ \mu s$	$1\ \mu s$	$10\ \mu s$	$100\ \mu s$	$1000\ \mu s$
$dq0$ (balanced)	13.6 s	1.9 s	✗	✗	6.5	1.2	0.4	0.3
$dq0$ (unbalanced)	14.4 s	2.0 s	✗	✗	8.2	4.8	4.7	4.8

Consider a transformation to the $dq0$ frame rotating at (constant) synchronous speed. If $\mathbf{u^{abc}}$ is balanced, but there is an oscillation of the fundamental frequency component with the amplitude $A = 1$ Hz and $f_{\text{osc}} = 5$ Hz (2.10), then there will be a f_{osc} harmonic in the q component (e.g. 5 Hz) and f_{osc}, $2f_{\text{osc}}$ harmonics in the d component (e.g. 5 Hz and 10 Hz), as shown in Fig. 2.10.
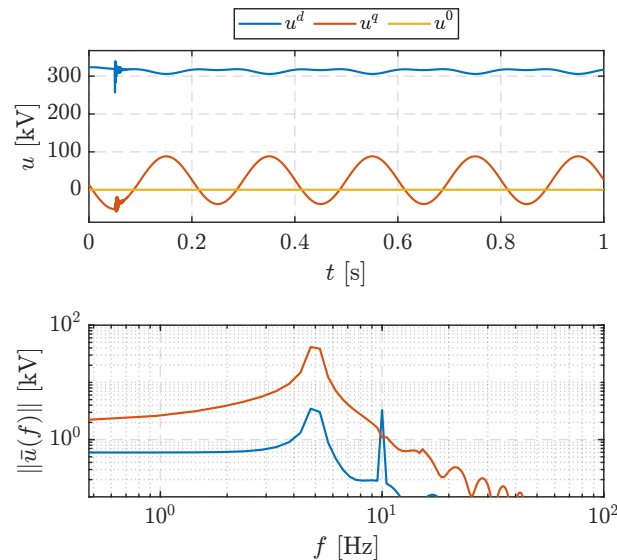
Figure 2.10: Bus 2 voltage $dq0$ components during fundamental frequency oscillation: time-domain (top) and frequency spectrum (bottom).

2.6 Modelling with dynamic phasors

The last modelling approach is commonly referred to as *dynamic phasors* in the power system literature [107]. It is also sometimes referred to as *baseband* representation or *analytic* representation, although the terminology may slightly vary depending on the source [3, 108]. There are also alternative approaches, such as using the Hilbert transform [110], depending on the nature of the original signal (narrow-band vs. broad-band). From a general perspective, all of these approaches are equivalent to some degree or have certain overlaps.

In the simplest case, a power system transient can be thought of as a signal whose frequency components are centred around the synchronous frequency ω_s. Such a signal is called a bandpass signal in the signal processing literature. Baseband representation of this signal consists of shifting its frequency spectrum by $-\omega_s$, thus essentially transforming the signal into a low-frequency one, which in turn enables larger integration step size in numerical solvers. However, the basic baseband approach loses its advantage if there are other harmonics present, as the maximum step size will be limited by the highest harmonic. An example of a baseband approach is the $dq0$ transform discussed in section 2.5.

The terminology in existing literature is somewhat confusing. A static or time-varying phasor is an extension of a fundamental frequency ($k = \pm 1$) steady-state phasor (2.5)–(2.6) to nearly periodic signals which are time-varying (2.8). The definition of a dynamic phasor [108, 122] is essentially (2.8) as well. However, use of dynamic phasors usually assumes a selection of multiple Fourier coefficients (k) along with the fundamental frequency coefficient ($k = \pm 1$). The selection of multiple coefficients covers a wider bandwidth in the frequency domain during transient simulations but decreases the performance.

Therefore, steady-state phasors (or just phasors) are used for steady-state AC circuit analysis at the fundamental frequency where amplitudes of electrical quantities are constant (Fourier coefficients are constant with respect to time). During dynamic simulations, electrical quantities vary in time. These time-varying phasors are called *static phasors* or *time-varying phasors* in fundamental frequency simulations because only the fundamental component is observed and all network-side transients are neglected. When multiple frequency components are chosen, then time-varying phasors are called *dynamic phasors*. However, *dynamic phasor* models can be derived from *abc* and *dq*0 models so they inherently preserve dynamics while in steady-state they degrade to constant values. Hence, they can be used for EMT simulations, while for RMS studies, network-side transients are neglected.

The main advantage of dynamic phasors is that they enable EMT simulation with larger time steps without noticeably degrading the accuracy [3] (especially in unbalanced systems and systems with higher harmonic content) at the expense of a larger number of dynamic equations. The dynamic phasor approach is still a concept mostly seen in academic research in custom frameworks [123–125], as we are unaware of any commercial software using this method for solving dynamic systems.

Although no special numerical integration solvers are needed for solving dynamic systems modelled in the dynamic phasor domain, choosing an appropriate solver can have a significant impact on the efficiency and accuracy of the simulation.

2.7   RMS/EMT co-simulation

Installation of power electronic devices in the bulk power system magnifies the dominance of fast transients which motivated great research efforts in increasing the simulation model detail while still being computationally efficient. One of the most accepted and widely used methods is the RMS/EMT co-simulation [126, 127] which is used in commercial software as well, e.g., DIgSILENT PowerFactory. The idea is that the parts of the network with a high-share of CID are simulated in the EMT domain, while those areas further apart are simulated in the RMS domain. Finding a way to accurately define this boundary is an ongoing research effort [128, 129].

2.8   Summary

This chapter briefly reviews power system dynamic simulation techniques in the context of power electronic devices. Similarities and differences between EMT, RMS, switching, and averaged simulations are defined as well as their applicability in different domains: static and dynamic phasors, *abc* and *dq*0.

Particular attention was given to the difference between RMS and EMT simulations and the ability of RMS simulations to capture power system frequency dynamics for frequency oscillations of increasing bandwidth where it was concluded that RMS simulations should still be applicable up to 200 Hz, under the requirement that the integration step size is adequately reduced. This does not mean that all phenomena up to that bandwidth are captured by the RMS simulation, just that the frequency oscillations of a controllable AC voltage source were accurately simulated compared to the EMT model.

It was also illustrated how $dq0$ speeds up the simulation time 3–4.5 times in balanced systems, while the performance for unbalanced simulations is somewhat slower depending on the solver type. It was also illustrated how unbalanced conditions create oscillating components in $dq0$ variables.

Dynamics phasors and RMS/EMT co-simulation were briefly introduced as solutions to speeding up converter-based systems simulation, with the former still being limited to academic research, while the latter can be seen in commercial software.

Chapter 3

Modelling of converter-interfaced devices

Besides extensive research on power system modelling and simulation discussed in chapter 2, a complementary research is ongoing which strives to find the appropriate level of CID modelling detail depending on the type of simulation and phenomena to be analysed [3, 6, 25, 102, 103].

There many types, configurations and control designs of power electronic converters that are used for interfacing AC systems. For better understanding of a general converter structure that will be used in the remainder of this thesis, we briefly introduce the main categorisation and configurations of DC/AC converters and how they can be subsumed under a unified model which facilitates further analysis.

DC/AC converters can be classified according to the waveform at the DC port. In current-sourced converters (CSCs) the DC current has constant polarity which is achieved by a large inductor. Therefore, the direction of power transfer is achieved by changing the voltage polarity at the DC port. In voltage-sourced converters (VSCs), the DC voltage has constant polarity which is achieved by a large capacitor. The direction of power transfer is achieved by changing the current polarity at the DC port. Line-commutated CSCs are mostly used in HVDC transmission [130] and industrial medium-voltage drives [131]. Force-commutated CSCs (e.g. PWM-switched) are not that widely used in power system applications because they require bipolar switches which are not commercially widespread so they are usually tailored for very specific high-power applications [13],e.g. industrial drives [131].

On the other hand, VSCs require reverse-conducting switches which are commercially readily available so they are more flexible and more convenient for general purpose power system applications (e.g. WTGs, PV plants, storage) [13]. An elementary configuration of VSC is based on a two-level topology which means that the output AC voltage waveform can take on one of two discrete values synthesised from the DC voltage. Since the voltage rating that can be obtained with a single converter is limited, two-level converters can be connected in series to increase the rating, or in parallel to increase the current rating. Another way to increase the voltage rating is to use multilevel converters. For power system applications, diode-clamped converters

are most widely used. The output AC voltage waveform can assume one of n discrete values synthesised from the DC-side voltage which is divided among $n-1$ DC link capacitors. Using the multilevel configuration reduces the harmonic content of AC-side voltage, so that a lower switching frequency can be used and a smaller AC-side filter is required [13]. Finally, modular multilevel converters (MMCs) consist of (multilevel) modules connected in series and parallel to increase voltage and current rating (like in two-level multimodule converters). MMCs are mostly used for HVDC applications [130, 132]. Regardless of the VSC configuration, the semi-conductor switches are mostly driven by the pulse-width modulation (PWM) strategy. The main exemption here are MMCs which would require as many PWM signals as there are switches which is computationally intensive, so other approaches exist. Nevertheless, this thesis focuses on PWM-commutated VSCs only.
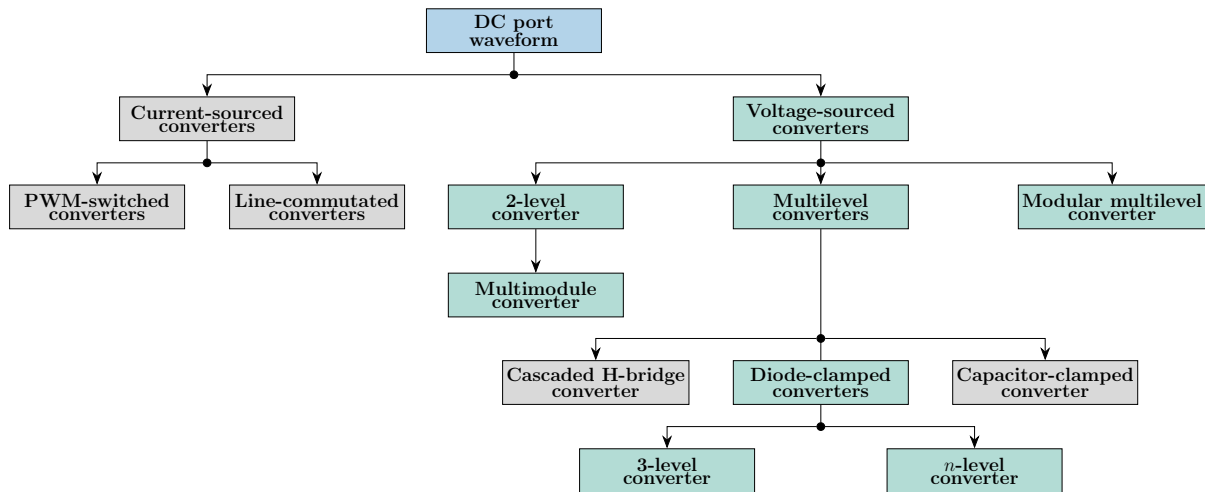
Figure 3.1: Classification of power converters according to the DC port waveform: green boxes are covered in this thesis.

A generic structure of a VSC-based CID is shown in Fig. 3.2. It consists of four main subsystems: a power conversion stage made up of grid-side (GSC) and device-side converter (DSC), and their respective control systems, an energy-conversion device (ECS), a DC link capacitor (C_{DC}) which is used as an interface between the DC ports of the converters, and an AC filter in a generic *LCL* configuration which reduces harmonic content on the AC-side. The presented structure is a higher-level representation of a generic CID structure than in [25, 103] as it considers device-side dynamics, while different control structures are subsumed under GSC/DSC control blocks (thus being compatible with [25, 103]).

The structure from Fig. 3.2 can be used to represent any standard CID. The GSC will always be a VSC, which is controlled by its control system, which takes a control input vector $\mathbf{x}_c^G \in \mathbb{R}^{N_c^G}$ and outputs a vector of modulating signals $\mathbf{m}^G \in \mathbb{R}^3$ (one signal per phase). The vector $\mathbf{m}^G$ is an input to a PWM generator that outputs a vector of gating signals $\mathbf{g}^G \in \{0, 1\}^{N_g^G}$ that command the semiconductor switches. N_c^G is the total number of controller inputs and
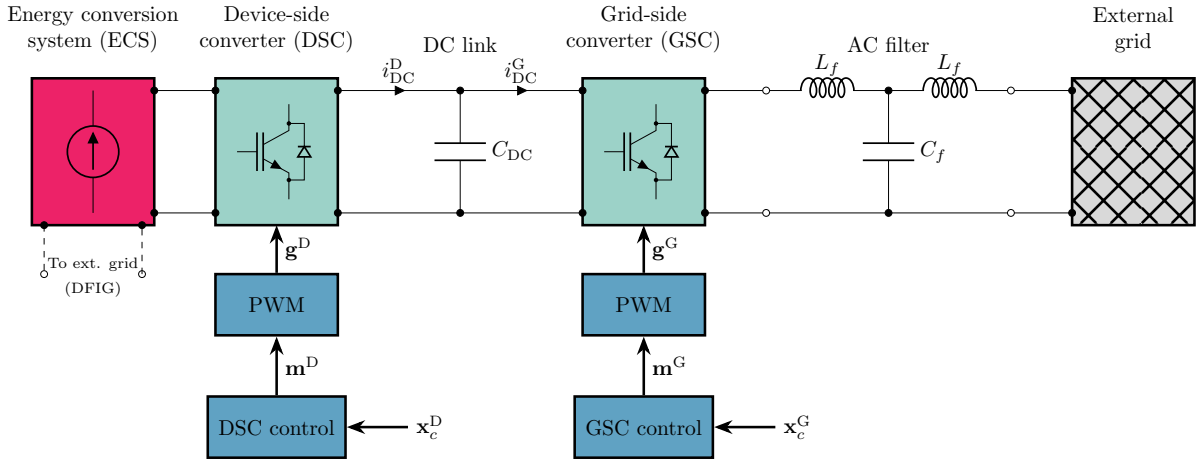
Figure 3.2: A generic structure of a CID: energy conversion system (red), control system (blue), power conversion stages (green) and DC link + AC filter (C_{DC}, C_f, L_f).

external measurements used to generate $\mathbf{m}^G$ which depends on the internal controller design, and N_g^G is the total number of gating signals which depends on the type of VSC configuration (2-level, 3-level, MMC).

The DSC can either be a VSC (e.g., in case of type-3 or type-4 WTGs) or a DC-DC converter (e.g., in case of PV arrays or DC energy storage systems). Regardless, it also takes a control input vector $\mathbf{x}_c^D \in \mathbb{R}^{N_c^D}$ and outputs a vector of modulating signals $\mathbf{m}^D \in \mathbb{R}^{N_m^D}$ that are used to generate gating signals $\mathbf{g}^D \in \{0,1\}^{N_g^D}$, where N_m^D, N_g^D depend on the type of converter (DC-DC, VSC). N_c^D depends on the combination of ECS and DSC, as well as on the implemented controller design.

The dashed port at the bottom of ECS block in Fig. 3.2 exists only in case where the ECS is a DFIG-based system (e.g., type-3 WTG or a DFIG-based pumped-hydro storage) since in those systems the stator of a motor/generator is directly connected to an external grid, while only the rotor is decoupled.

3.1 Modelling of VSCs in power conversion stage

Fig. 3.3 shows the circuit diagrams of most commonly used VSC configurations.

The three-phase two-level VSC (Fig. 3.3a) consists of three half-bridge DC/AC converters. Each half-bridge consists of two semiconductor switches (usually IGBT). The DC link consists of two series-connected DC capacitors with the midpoint used as a reference node. The instantaneous AC voltage is either $+\frac{v_{DC}}{2}$ or $-\frac{v_{DC}}{2}$. The number of switches that need to be controlled is 6 ($N_g^G = 6$, $\mathbf{g}^G \in \{0,1\}^6$).

The three-phase three-level VSC (Fig. 3.3b) consists of six half-bridge converters, i.e., each phase consists of two half-bridge converters where one half-bridge generates a positive AC voltage, and the other a negative one [13]. The DC link is identical to the one in the two-level

(a) Two-level VSC

(b) Three-level (neutral point clamped) VSC

(c) MMC
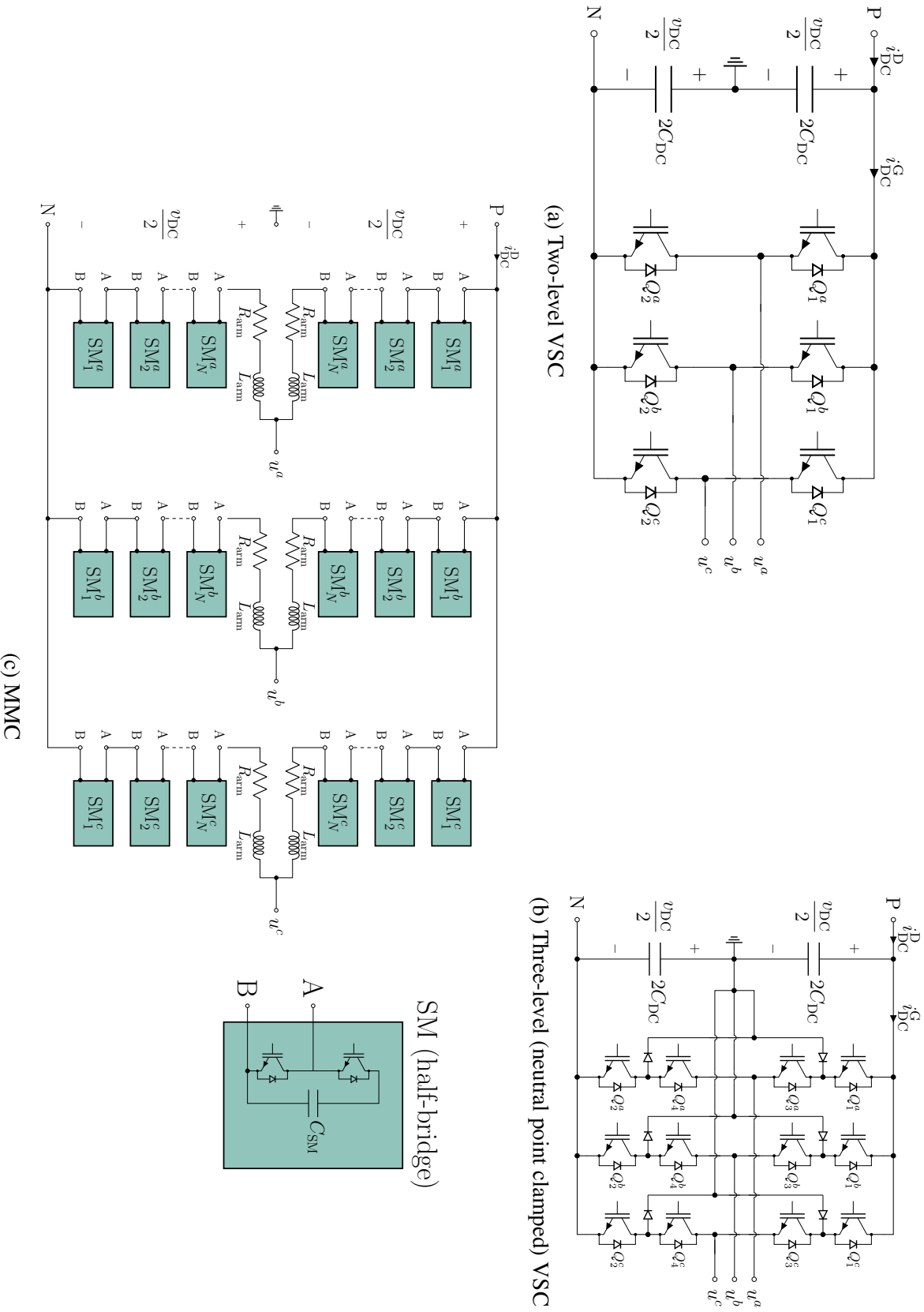
SM (half-bridge)

Figure 3.3: Circuit diagrams of common VSC configurations.

VSC, but the midpoint is connected to each half-bridge pair via two clamping diodes. Therefore, the instantaneous AC voltage is either $+\frac{v_{DC}}{2}$, $-\frac{v_{DC}}{2}$ or 0. The number of switches that need to be controlled is 12 ($N_g^G = 12$, $\mathbf{g}^G \in \{0, 1\}^{12}$).

Each phase leg of a three-phase MMC (Fig. 3.3c) consists of two arms (upper and lower) where each arm is comprised of N series-connected submodules (SMs) and an arm inductor. The submodules can be realised by different circuits, but a half-bridge converter is the most popular [132]. The DC link is not realised by two DC capacitors as in two-level and three-level configurations. Instead, the equivalent DC capacitance is equal to $C_{DC} = \frac{6C_{SM}}{N}$ [133, 134]. The number of instantaneous AC voltage levels is $N + 1$. The number of switches that need to be controlled is $12N$ ($N_g^G = 12N$, $\mathbf{g}^G \in \{0, 1\}^{12N}$). Additionally, instead of phase inductors (as part of AC filters in two-level and three-level VSC), the MMC utilizes arm inductors (R_{arm}, L_{arm} in Fig. 3.3c).

The diagrams in Fig. 3.3 represent the so-called switching models and as such can only be simulated in the *abc* domain (including dynamic phasors since they can be derived from any domain, see Table 2.1). There is no point in modelling the switches in *dq*0 domain since they are discrete elements switched at a very high frequency so any advantage of a rotating reference frame disappears. Switching models consist of semiconductor switch models and the PWM algorithm operating at a kHz level which in turn reduces the step size significantly. However, detailed switching models are not necessary for most power system applications [102, 103]: they are only required during analysis of specific phenomena such as converter faults, harmonic stability or during converter design.

In most cases, averaged models are sufficient. Averaged models are derived by averaging the voltage across semiconductor switches over one switching period. For example, in the two-level converter the output voltage of phase a $u^a(t)$ is equal to (3.1), where $g_1^a(t)$ and $g_2^a(t)$ are the gating signals calculated by the PWM control scheme as (3.2) and (3.3).

$$u^a(t) = \frac{v_{DC}}{2} g_1^a(t) - \frac{v_{DC}}{2} g_2^a(t) \tag{3.1}$$

$$g_1^a(t) = \begin{cases} 1 & \text{if } m^a(t) - c(t) > 0, \\ 0 & \text{if } m^a(t) - c(t) \leq 0 \end{cases} \tag{3.2}$$

$$g_2^a(t) = 1 - g_1^a(t) \tag{3.3}$$

The modulating signal $m^a(t) \in [-1, 1] \subseteq \mathbb{R}$ is a sine wave at the fundamental frequency f_0 (e.g. 50 Hz) while $c(t) \in [-1, 1] \subseteq \mathbb{R}$ is the carrier signal, a periodic waveform (usually triangular) at the switching frequency $f_{switch} = 1/T_{switch}$, $f_{switch} \gg f_0$. By applying the moving

average operator on (3.1), one obtains the average value of phase a voltage $\langle u^a \rangle(t)$ (3.4).

$$\langle u^a \rangle(t) = \frac{1}{T_{\text{switch}}} \int_{\tau - T_{\text{switch}}}^{\tau} u^a(\tau) d\tau = m^a(t) \frac{V_{\text{DC}}}{2} \tag{3.4}$$

Averaging enables us to neglect the PWM block (Fig. 3.2) and replace the switches with controlled voltage sources at the fundamental frequency. The internal dynamics between two-level, three-level and multilevel converters are different since multilevel converters require control schemes for DC voltage balancing between capacitors [13] and there are circulating currents in MMCs that need to be suppressed [132]. Fortunately, from the grid perspective in normal, balanced operation all these internal differences can be considered well-controlled. Therefore, the same control systems can be utilised for all three configurations and the averaged model of each configuration is identical to the averaged model of a two-level converter [134, 135]. The only difference is in the case of MMC, where the controllable voltage source is in series with the fictitious, SM-dependent capacitance C_{MMC} [136, 137], although this was neglected in previous studies [134, 135]. The unified averaged model of the two-level, three-level and MMC configurations is described by (3.5)–(3.7)* and shown in Fig. 3.4.

$$\mathbf{u}_{\text{c}}^{\mathbf{abc}}(t) = \begin{cases} \dfrac{v_{\text{DC}}}{2} \mathbf{m}^{\mathbf{abc}} & \text{for two-level, three-level VSC,} \\ \dfrac{v_{\text{DC}}}{2} \mathbf{m}^{\mathbf{abc}} - \mathbf{u}_{C_{\text{MMC}}}^{\mathbf{abc}} & \text{for MMC} \end{cases} \tag{3.5}$$

$$\begin{cases} \mathbf{u}_{C_{\text{MMC}}}^{\mathbf{abc}} = 0 & \text{for two-level, three-level VSC,} \\ \mathbf{i}_{\text{c}}^{\mathbf{abc}} = C_{\text{MMC}} \dfrac{d}{dt} \mathbf{u}_{C_{\text{MMC}}}^{\mathbf{abc}} & \text{for MMC} \end{cases} \tag{3.6}$$

$$C_{\text{MMC}} = \frac{C_{\text{SM}}}{N} \frac{64}{8 - 3\left[(m^d)^2 + (m^q)^2\right]} = \frac{C_{\text{SM}}}{N} \frac{64}{8 - 2\left[(m^a)^2 + (m^b)^2 + (m^c)^2\right]} \tag{3.7}$$

Consider a 1000 MW 400 kV grid-following VSC connected to an infinite bus through a low-impedance path. Fig. 3.5 illustrates the differences between the averaged and switching models for a two-level (Fig. 3.5a), three-level NPC (Fig. 3.5b) and MMC (Fig. 3.5c) topologies. It can be seen that the averaged models do not contain the high-frequency switching ripple. The switching ripple is not of concern in bulk power system simulations, especially for frequency control which has low bandwidth. Fig. 3.5d shows that all models behave essentially identically for a step change in active and reactive power reference. Therefore, all VSC topologies can essentially be represented by the same averaged model assuming a well-functioning inner control system without unwanted interactions.

---

*Brackets $\langle \cdot \rangle$ denoting averaged quantity have been dropped for clarity
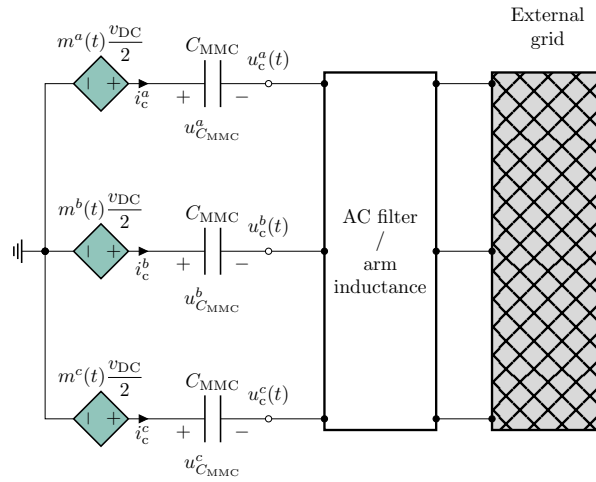
Figure 3.4: Unified averaged model of VSC power stage on the AC side.

(a) Two-level (2L) VSC

(b) Three-level NPC (3L) VSC

(c) MMC VSC

(d) 2L, 3L and MMC
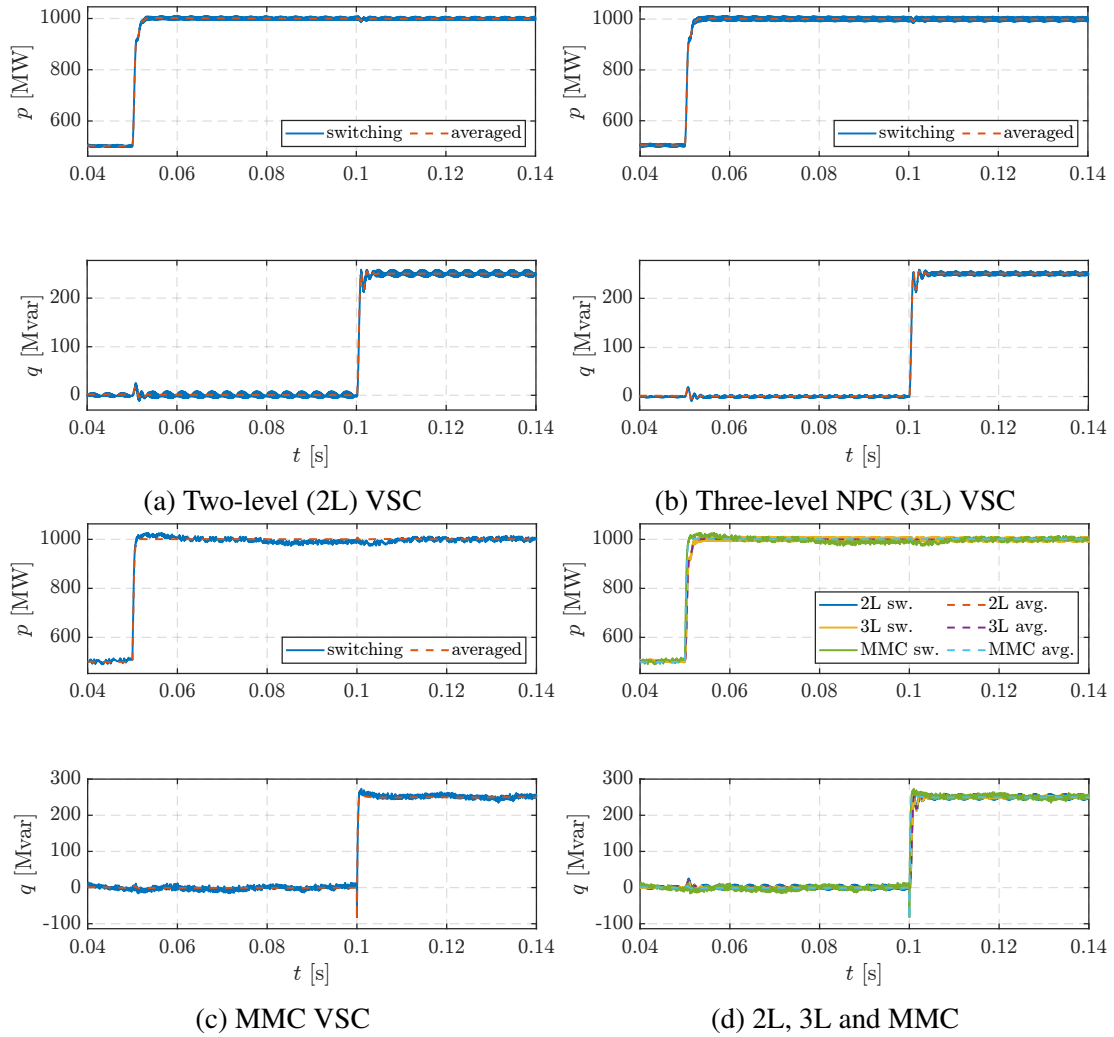
Figure 3.5: Switching vs. averaged VSC model response to step change in active (p) and reactive (q) power set-point.

3.2 GSC control systems

The GSC operation mode depends on its control system design. Referring back to Fig. 3.2, the GSC control system takes a control input vector $\mathbf{x}_c^G$ and outputs a modulation vector $\mathbf{m}^G$ which generates fundamental frequency AC voltage at the converter terminals by modulating the DC link voltage v_{DC}. From this standpoint, VSC is a controllable voltage source regardless of the internal control system. From a control standpoint, however, the control system determines whether the converter behaves like a controlled voltage source or a controlled current source. The most recognised classification of converter operation modes is the one by Rocabert *et al.* [7] and stems from microgrid operation. It classifies converters into *grid-forming*, *grid-feeding* and *grid-supporting*, as illustrated by Fig. 3.6.

(a) Grid-forming

(b) Grid-feeding

(c) Grid-supporting (voltage-source-based)

(d) Grid-supporting (current-source-based)
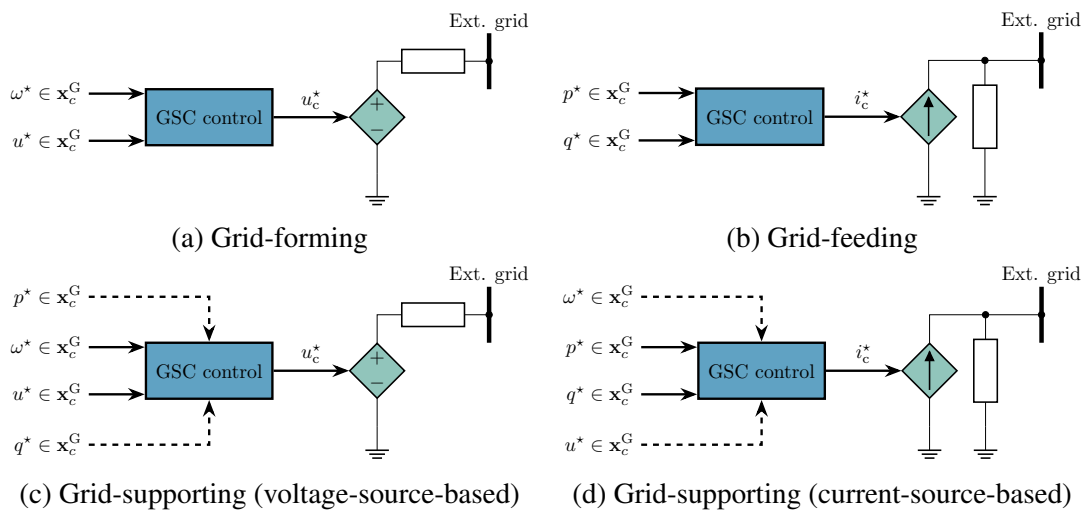
Figure 3.6: Traditional classification of converter operating modes according to [7].

The grid-forming (Fig. 3.6a) mode is characterised by directly setting the desired voltage amplitude $u^\star \in \mathbb{R}_{\geq 0}$ and frequency $\omega^\star \in \mathbb{R}_{\geq 0}$. Set-points $(u^\star, \omega^\star)$ are a subset of the control vector $\mathbf{x}_c^G$. The output of the GSC control is the converter terminal voltage reference $u_c^\star$. The grid-forming mode will define the AC voltage and frequency, and energise the grid. Since the converter behaves as a voltage source with low output impedance, its active and reactive power output will be determined by the load, thus the converter needs to be sized properly to deliver the desired power. Parallel operation of grid-forming converters requires either a very accurate synchronisation mechanism or some sort of a power-sharing algorithm (e.g. droop). Grid-forming mode is conceptually similar to a synchronous generator with an isochronous governor supplying an isolated load. An example of a grid-forming device is an uninterruptible power supply. A grid-forming system is referred to as a controlled-frequency system in [13].

The grid-feeding (Fig. 3.6b) mode is characterised by setting the desired active and reactive $(p^\star \in \mathbb{R}, q^\star \in \mathbb{R})$ power set-points. In reality, the GSC control output is a modulating vector that determines the converter terminal AC voltage output, but this voltage is controlled in a way to

deliver the specified power. Therefore, it is operating as a controlled current source with current reference $i_c^\star$ and a large parallel impedance. A grid-feeding converter cannot operate standalone, it requires an energised grid or a grid-forming converter which will define voltage amplitude and phase information which is used to calculate the current set-point. Grid-feeding converters can inherently operate in parallel with other grid-feeding converters. It is conceptually similar to a generator operating in PQ mode, and not participating in frequency and voltage support. An example of a grid-feeding system is a PV plant set to deliver the available active power at a constant power factor. A grid-feeding system is referred to as a grid-imposed system in [13].

The grid-supporting mode is in-between the grid-forming and grid-feeding modes, and can be based either on a controllable voltage source (Fig. 3.6c) or on a controllable current source (Fig. 3.6d). Essentially, a voltage-source-based grid-supporting converter is a grid-forming converter where the voltage and amplitude set-points $(u^\star, \omega^\star)$ are adjusted based on active and reactive power delivered to the grid $(p^\star, q^\star)$. Conceptually, it is similar to a grid-connected synchronous generator with a speed-droop governor and an AVR. Likewise, a current-source-based grid-supporting converter is a grid-feeding converter where its set-points $(p^\star, q^\star)$ are adjusted based on grid voltage amplitude and frequency $(u^\star, \omega^\star)$. Conceptually, it is similar to a grid-connected wind power plant with a defined power-frequency characteristic and operating in terminal voltage control.

Recently, the characterisation according to Fig. 3.6 has been criticised in literature as it is not practical for transmission-level application [25]. For example, a grid-forming converter has no dispatchable active and reactive power set-points so it's not suitable for grid-connection. On the other hand, the grid-feeding category is essentially obsolete as all grid codes require voltage and frequency support capabilities from converter-interfaced generators. All transmission-level grid-connected converters today are grid-supporting, the only difference being whether they can operate standalone or require a stiff grid for operation. Therefore, new terminology only differentiates between *grid-forming* and *grid-following* modes of operation.

3.2.1 General GSC control structure

Referring to Fig. 3.2, there are three control subsystems required for proper VSC operation:

1. DC voltage control (DCVC).
2. Reactive power and AC voltage control (RPC).
3. Active power and frequency control (APC).

DCVC is absolutely crucial for RPC and APC. For RPC, converter terminal AC voltage $\mathbf{u}_c^{\mathbf{abc}}$ is synthesised from the DC voltage v_{DC}. Therefore, DCVC ensures that the DC link voltage is stable: if the voltage is too low, the converter will saturate and the required AC voltage amplitude cannot be achieved. If it is too high, it can damage the DC capacitor. Only active power is passed through the DC link. A mismatch between DSC power consumption and GSC

power consumption results in a current flow through C_{DC} which will charge or discharge the capacitor as described by (3.8) (using current difference) or (3.9) (using power difference), both in per-unit form:

$$i_{DC}^{D} - i_{DC}^{G} = \omega_b^{-1} C_{DC} \frac{dv_{DC}}{dt} \tag{3.8}$$

$$p_{DC}^{D} - p_{DC}^{G} = \omega_b^{-1} C_{DC} v_{DC} \frac{dv_{DC}}{dt} = \frac{1}{2} \omega_b^{-1} C_{DC} \frac{dv_{DC}^2}{dt} \tag{3.9}$$

Similar to synchronous machine's frequency, the DC link indicates power imbalance. Therefore, DCVC ensures power balance between the power source and the grid. Although RPC can be realised independently of DCVC and APC (as a separate control system), DCVC and APC are mutually exclusive subsystems. That is, DCVC and APC cannot be realised simultaneously on the same converter: if GSC operates in APC mode, then DCVC must be ensured by the DSC or vice versa. An example of this is a type-3 WTG in which the DSC operates in APC (tracking the maximum power point) and provides excitation to the induction generator (RPC) such that no reactive power is exchanged through the stator, while GSC controls the DC voltage (DCVC) and ensures that the GSC operates with unity power factor (RPC) [42].

The uniform converter model proposed in [25] replaces the ECS and DSC (Fig. 3.2) with a controllable current source whose current reference is obtained through DCVC (see Fig. 3.7). On the one hand, it simplifies the analysis as all necessary control subsystems are subsumed under the GSC control. On the other hand, this structure does not discern between different types of energy sources on the DC-side (wind, solar, battery, etc.). Nevertheless, that structure is helpful for introducing each control subsystem in more detail.

In the shown structure, the power converter model encompasses the controllable DC current source, DC link model (3.8)–(3.9), PWM generator + VSC model (PWM generator is omitted in the averaged model, see Section 3.1), and the AC filter (see Section 3.3). The system-level and device-level control are subsumed under the GSC control from Fig. 3.2. The system-level control is an outer control structure in charge of controlling active power and frequency (APC) as well as reactive power and voltage (RPC), as shown in Fig. 3.7b. The system-level control takes the set-point input vector $\mathbf{x}^{s\star}$ (Fig. 3.7a), and the filter voltage and grid-side terminal current measurements $\{\mathbf{u}_f^{\mathbf{abc}}, \mathbf{u}_g^{\mathbf{abc}}, \mathbf{i}_g^{\mathbf{abc}}\}$, and outputs the internal set-point vector $\mathbf{x}^{d\star}$ for the device-level control (i.e., internal voltage and current references). The device-level control tracks the internal references $\mathbf{x}^{d\star}$ based on AC current and voltage measurement vectors $\{\mathbf{u}_f^{\mathbf{abc}}, \mathbf{u}_g^{\mathbf{abc}} \mathbf{i}_g^{\mathbf{abc}}, \mathbf{i}_f^{\mathbf{abc}}\}$ and outputs the modulation vector used to drive the semiconductor switches $\mathbf{m}^G$. Additionally, the device-level control regulates the DC voltage v_{DC} to its set-point $v_{DC}^{\star}$, and outputs the DC current source set-point $i_{DC}^{\star}$. Therefore, the GSC control input vector from Fig. 3.2 $\mathbf{x}_c^G = \mathbf{x}^{s\star} \cup \mathbf{x}^{d\star} \cup \{\mathbf{u}_f^{\mathbf{abc}}, \mathbf{u}_g^{\mathbf{abc}}, \mathbf{i}_g^{\mathbf{abc}}, \mathbf{i}_f^{\mathbf{abc}}\} \cup \{v_{DC}^{\star}, v_{DC}\}$. Note that in [25], only the AC filter voltage $\mathbf{u}_f^{\mathbf{abc}}$ is used because of the *LC* structure. In this thesis, however, an *LCL* structure is used so
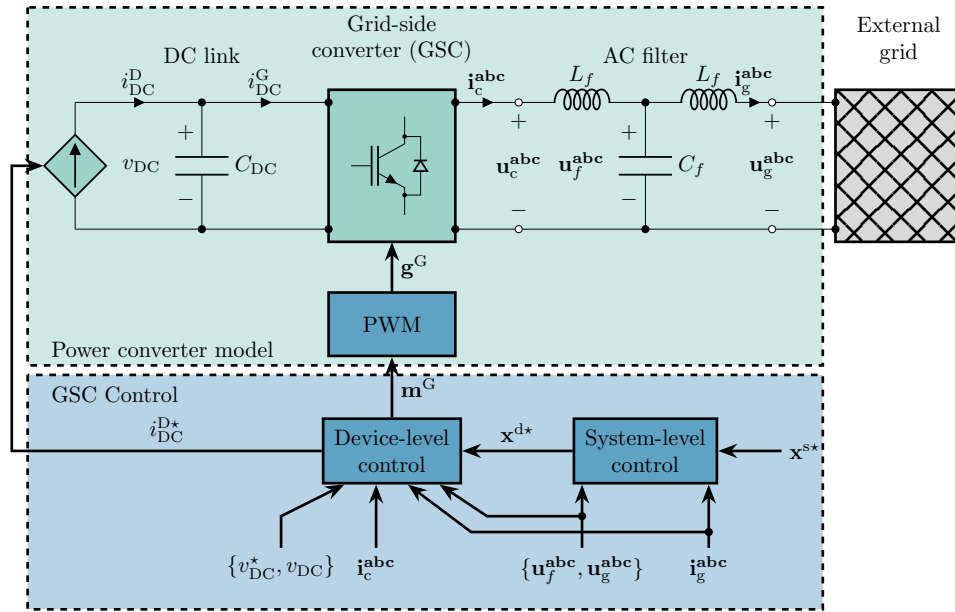
(a) Grid-connected VSC
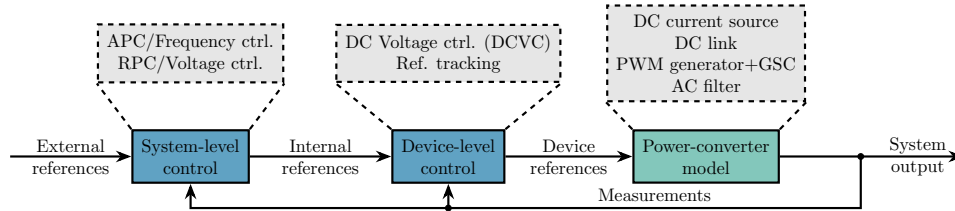
(b) Input-output block diagram of converter and its control system

Figure 3.7: Uniform GSC model structure proposed in [25].

grid-side voltage $\mathbf{u}_g^{\mathbf{abc}}$ is used instead. For completeness, we write this as a set of both vectors $\{\mathbf{u}_f^{\mathbf{abc}}, \mathbf{u}_g^{\mathbf{abc}}\}$ to denote that either one can be used, granted that the respective control system takes it into account appropriately [138].

3.2.2 System-level control

The system-level control defines whether the GSC behaves like a *grid-former* or a *grid-follower*. At the system-level control, we discern between control algorithms such as *virtual synchronous machine* [139], *synchronverter* [140], *grid-following virtual synchronous generators* [141], etc.

3.2.2.1 Grid-following mode

A control system for grid-following operation is shown in Fig. 3.8. External active and re-active power set-points $\{p^\star, q^\star\}$ are modulated by signals $\{\Delta p^\star, \Delta q^\star\}$ which depend on the measured grid frequency and voltage. According to a traditional classification of converter control (Fig. 3.6), this is a grid-following converter operating in grid-supporting mode (Fig. 3.6d). Generally, *Frequency control* and *Voltage control* blocks can contain arbitrary functionalities. However, most often a variation of frequency (3.10) and voltage (3.11) droop is implemented

(both expressions in per-unit):

$$\Delta p^\star = K_\omega \left(\omega_n - \omega^\star \right) - 2H_v \frac{d\omega^\star}{dt} \tag{3.10}$$

$$\Delta q^\star = K_u \left(u_g^\star - u_g^d \right) \tag{3.11}$$

where $K_\omega \in \mathbb{R}_{\geq 0}$ is the frequency droop gain, ω_n is the nominal grid frequency, $\omega^\star$ is the grid frequency estimated by the PLL ($\omega^\star := \hat{\omega}_g$), $K_u \in \mathbb{R}_{\geq 0}$ is the voltage droop gain, $u_g^\star \in \mathbb{R}_{\geq 0}$ is the desired amplitude of the PCC terminal voltage, $u_g^d \in \mathbb{R}_{\geq 0}$ is the measured PCC terminal voltage. It is assumed that $\{u_g^\star, u_g^d\}$ correspond to per-unit peak value of line-to-ground voltage in the shown control structure. The term $2H_v \dot{\omega}^\star$ is traditionally described as the *synthetic* or *virtual* inertia effect [14, 41], where $H_v \in \mathbb{R}_{\geq 0}$ is referred to as the virtual inertia constant. This control was also referred to as the *virtual synchronous generator* (VSG) in the early literature [10, 141], although today VSG or VSM (*virtual synchronous machine*) is a term used exclusively for grid-forming operation. Alternatively, outer PI loops that track the active and reactive power and generate internal current references can be used, as shown by Fig. 3.9.

Frequency and phase angle references $\{\omega^\star, \theta^\star\}$ are estimated by a PLL which is used for grid synchronisation, i.e., to inject a current into the grid at the correct phase angle which guarantees tracking the active and reactive power references $\{p^\star + \Delta p^\star, q^\star + \Delta q^\star\}$. The phase angle reference $\theta^\star$ is also used to transform *abc* quantities into the *dq* frame which enables decoupled control of active and reactive power. There are many types of synchronisation devices [7, 142–144], but the three-phase SRF-PLL is the most commonly used one in literature—shown in Fig. 3.10 and described by (3.12a)–(3.12c) in per-unit.

$$\frac{d\theta_g}{dt} = \omega_b \omega_g \tag{3.12a}$$

$$\frac{d\xi}{dt} = U_g \sin \left(\theta_g - \theta^\star \right) = u_g^q \tag{3.12b}$$

$$\frac{d\theta^\star}{dt} = K_p U_g \sin \left(\theta_g - \theta^\star \right) + K_i \xi = \omega_b \omega^\star \tag{3.12c}$$

where $\{\omega_g, \theta_g\}$ are the actual grid frequency and phase angle measured at the PCC, and U_g is the PCC voltage time-varying amplitude (per-unit peak value of line-to-ground voltage, assuming a balanced system $U_g^a = U_g^b = U_g^c = U_g$). PLL estimates the phase angle $\theta^\star = \theta^\star(t)$ such that the $abc \rightarrow dq$ transformation zeroes out the q component of voltage (u_g^q) which is passed through a proportional-integral (PI) controller to obtain the estimate of the grid angular frequency $\omega^\star$, which is then integrated by means of a voltage-controlled oscillator to obtain $\theta^\star$. In steady-state, $\omega_g = \omega^\star$, $\theta_g = \theta^\star$, $u_g^q = 0$, and $u_g^d = U_g$.

The internal per-unit current reference vector $\mathbf{i}_c^{dq\star} \in \mathbb{R}^2$ can be calculated directly from the power set-points and the d-component of terminal voltage (3.13)–(3.14) (in SI units, there is an
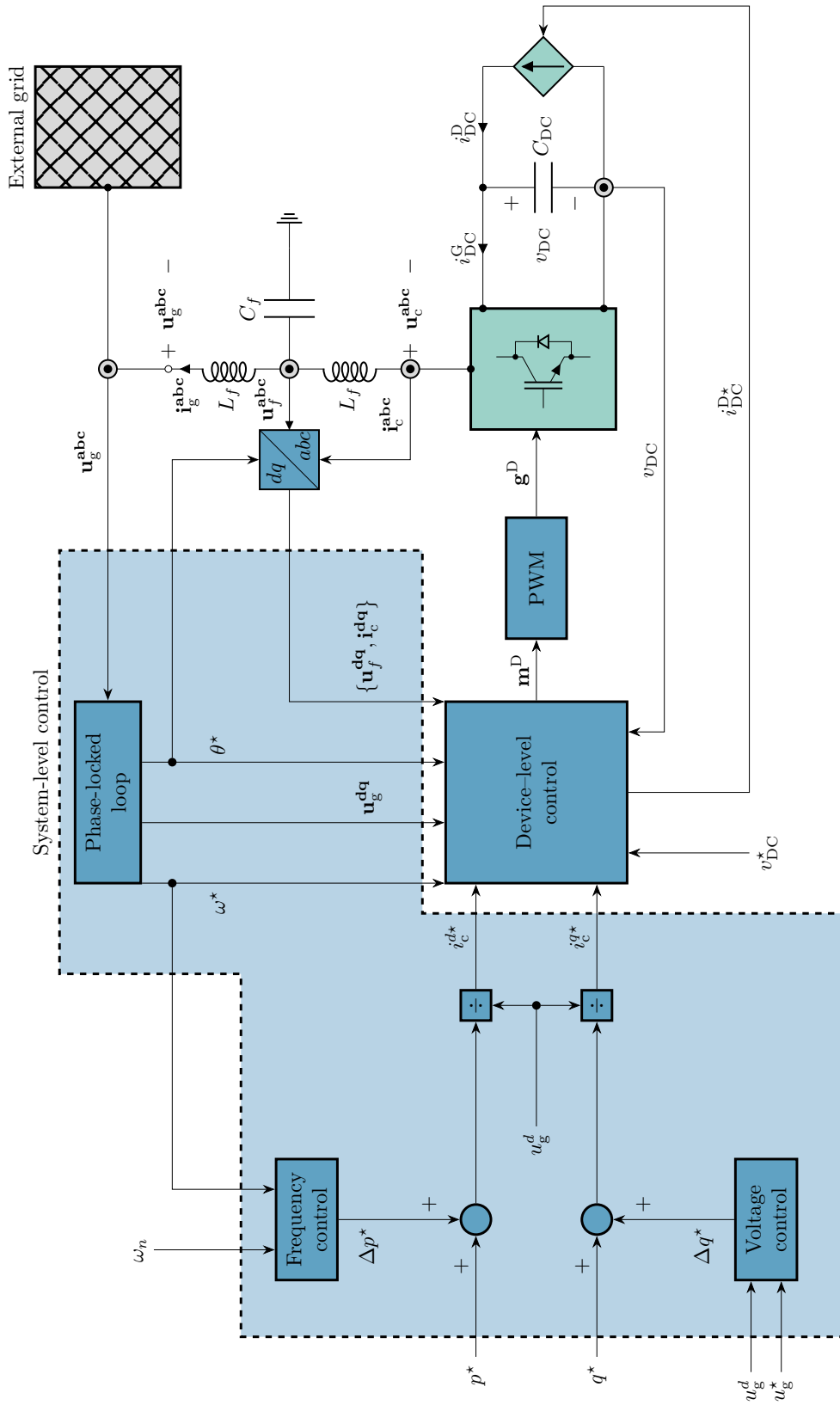
Figure 3.8: Grid-following system-level control (per-unit) with direct calculation of converter current reference.
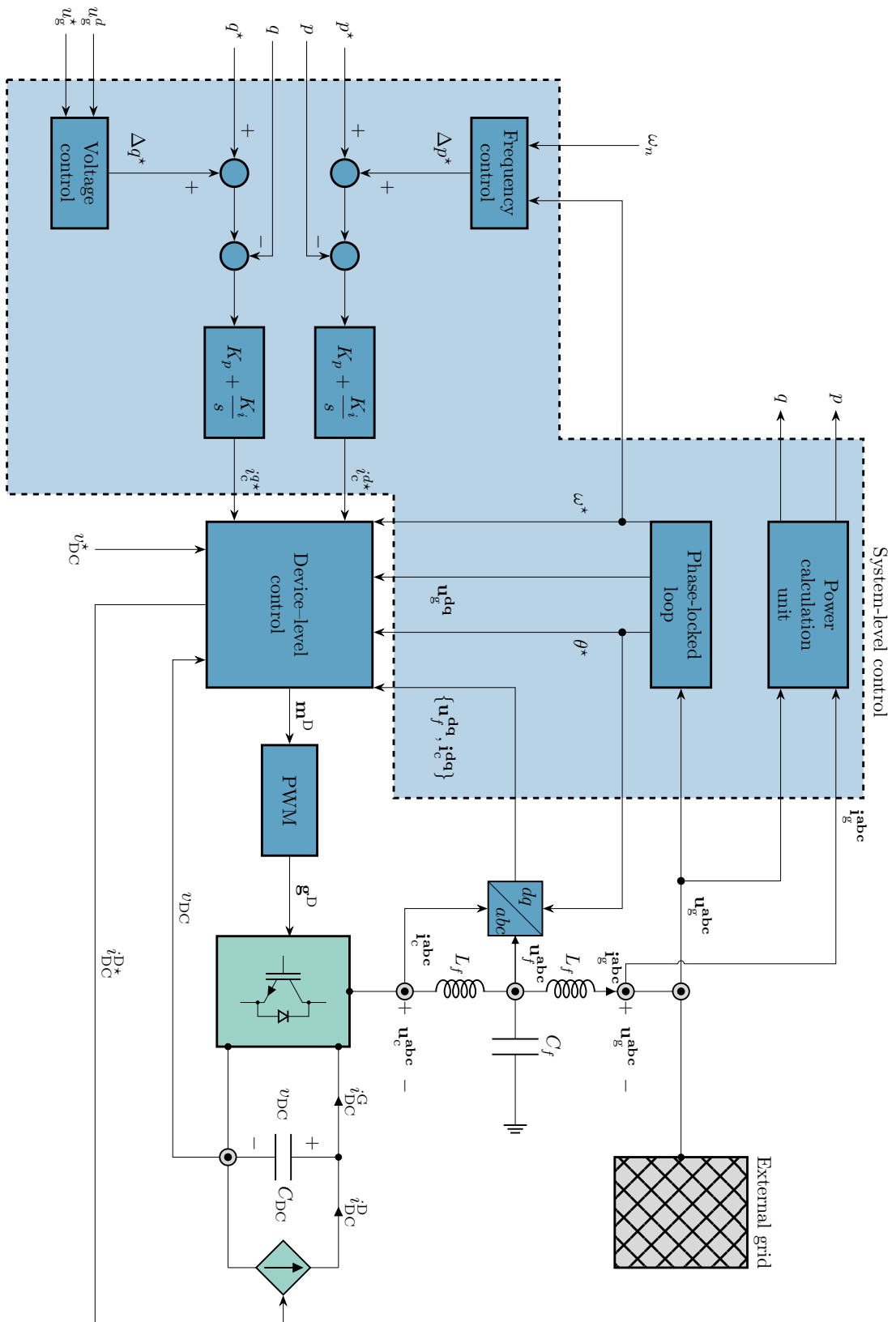
Figure 3.9: Grid-following system-level control (per-unit) with an outer PI controller for generating converter current reference.
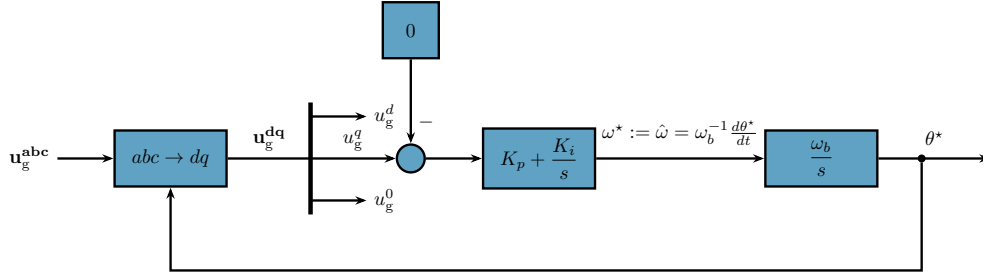
Figure 3.10: Three-phase SRF PLL block diagram (SI).

additional factor of $\frac{3}{2}$ multiplying the d-axis voltage):

$$i_c^{d\star} = \frac{p^\star + \Delta p^\star}{u_g^d} \tag{3.13}$$

$$i_c^{q\star} = \frac{q^\star + \Delta q^\star}{u_g^d} \tag{3.14}$$

3.2.2.2 Grid-forming mode based on the virtual synchronous machine

The grid-forming mode based on the virtual synchronous machine implementation is shown in Fig. 3.11. Compared to the grid-following mode, the input to device-level control are the converter voltage set-point $\mathbf{u}_c^{\mathbf{dq}\star}$ and frequency/phase-angle set-point pair $\{\omega^\star, \theta^\star\}$ instead of *dq* current references.

Instead of estimating $\{\omega^\star, \theta^\star\}$ using a PLL, these are calculated internally in the control software based on the swing equation: rearranging (3.10) and defining $\Delta p^\star := p - p^\star$ we obtain:

$$\frac{d\omega^\star}{dt} = \frac{1}{2H_v}\left[p^\star - p + K_\omega\left(\omega_n - \omega^\star\right)\right] \tag{3.15}$$

The internal angle reference $\theta^\star$ is then calculated as:

$$\frac{d\theta^\star}{dt} = \omega_b \omega^\star \tag{3.16}$$

An additional damping term can be introduced in (3.15) which acts on the difference between the internal converter frequency $\omega^\star$ and the external grid frequency estimated by a PLL $\hat{\omega}_g := \omega_{\text{PLL}}$, as described by (3.17). This term is not necessary as illustrated by dashed lines in Fig. 3.11, but it improves damping [139].

$$\frac{d\omega^\star}{dt} = \frac{1}{2H_v}\left[p^\star - p + K_\omega\left(\omega_n - \omega^\star\right) + K_D\left(\hat{\omega}_g - \omega^\star\right)\right] \tag{3.17}$$

Therefore, any difference between the external power set-point $p^\star$ and the measured power at the PCC p will drive the change in the internal converter frequency $\omega^\star$ (which can be thought of as a virtual rotor speed), which in turn drives the change of the internal converter phase angle

51
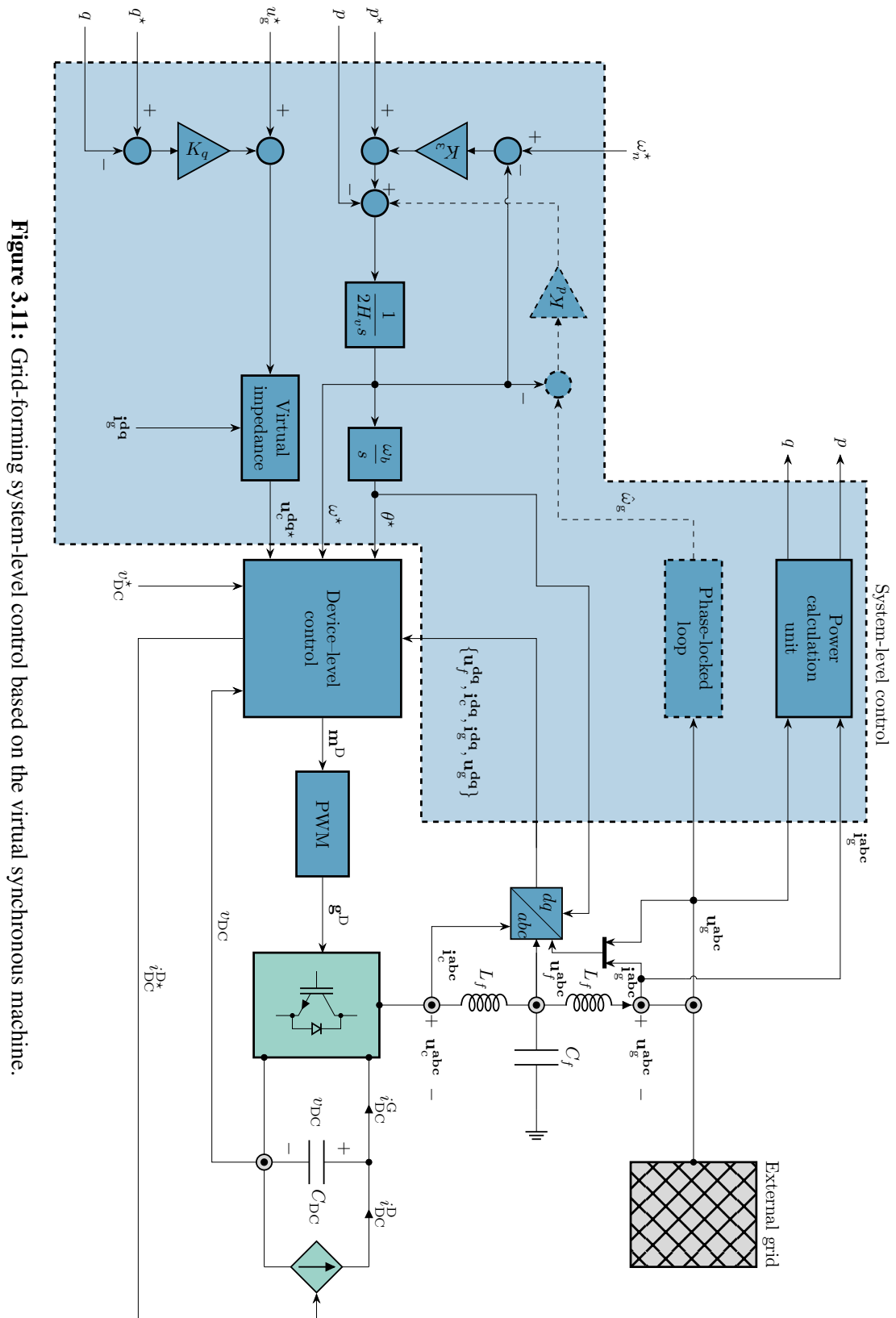
Figure 3.11: Grid-forming system-level control based on the virtual synchronous machine.

$\theta^\star$ (which can be thought of as a virtual load angle). Terms $K_\omega\left(\omega_n - \omega^\star\right)$ and $K_D\left(\hat{\omega}_g - \omega^\star\right)$ emulate droop control and damper windings, respectively.

Similarly to (3.11), voltage control of a VSM is achieved by drooping the reactive power instead of voltage:

$$u^\star = u_g^\star + K_q\left(q^\star - q\right) \tag{3.18}$$

where $u_g^\star$ is the external voltage reference and K_q is the reactive power droop gain. $u^\star$ is then passed through a virtual impedance block (Fig. 3.11) to obtain the internal converter voltage reference $\mathbf{u}_c^{\mathbf{dq}\star}$ (3.19):

$$u_c^{d\star} = u^\star - R_v i_g^d + \omega^\star \omega_b^{-1} L_v i_g^q \tag{3.19a}$$

$$u_c^{q\star} = 0 - R_v i_g^q - \omega^\star \omega_b^{-1} L_v i_g^d \tag{3.19b}$$

where R_v, L_v are the virtual resistance and inductance in per-unit, respectively. The virtual impedance block emulates the effect of a synchronous reactance of synchronous machines and improves the transient behaviour by reducing the control sensitivity to grid disturbances [7]. In low-voltage and medium-voltage networks where R/X is large, there is a stronger impact of reactive power on frequency and of active power on voltage which reduces the effectiveness of droop control. In such networks, virtual impedance virtually increases the system inductance as seen from the converter terminals in order to decouple voltage dynamics from frequency dynamics more effectively.

3.2.2.3 Other grid-forming modes

There are other ways of implementing a grid-forming control in a grid-side converter, such as: synchronisation based on DC voltage imbalance [145–147], virtual oscillator control [25], VSM0H [148, 149] or just simple droop control [3, 150]. However, under certain assumptions, all of these mechanisms can become equivalent [25, 150]. From a system-level perspective, synchronverter [140] differs from the VSM [139] only in the fact that it emulates a synchronous machine using a higher order model. Without going into specific details of each mode, Table 3.1 briefly summarizes the differences between various VSM implementations.

Table 3.1: Taxonomy of different VSM implementations.

Reference	Control strategy	Strengths	Weaknesses
[141]	VISMA	• fast current control • application in microgrids • direct limitations of current reference	• high frequency noise due to converter's switch activity • numerical instability
[151, 152]	VSG	• emulation of dynamic performance of SG • ability of absorbing or injecting power in the grid • fast response in tracking steady-state frequency • inherent overcurrent protection	• inability to operate in islanded mode • an internal model of the machine inertia is not established • instability due to PLL
[140]	Synchronverter	• ability to operate as SG and motor • possibility to choose the parameters that are impossible in conventional SG • only earlier versions required PLL • models without PLL are cheaper, easier in tuning and have lower computational time	• no inherent protection • protection is hard to implement • constraints of the converter are not included
[139, 153]	VSM	• fast frequency response • emulation of static and dynamic performance of SG • power-sharing ability • automatic synchronisation • ability of islanded operation • controllable and flexible protection strategies • PLL used only for synchronisation	• complex PLL implementation • limited flexibility during transient conditions due to fixed parameters • SG behaviour in the entire operating range is not covered
[154]	SEBIR	• no PLL • use of symmetric filters for frequency measurement	• slow response time • complicated algorithms and expensive communication network required

Table 3.1 – continued from previous page

Reference	Control strategy	Strengths	Weaknesses
[148, 149]	VSM0H	• no PLL • steady measured values during unbalanced scenarios • leads to a system with zero inertia in the future	• the RoCoF is not reduced right after the event • requires a boxcar filter for measurement • expensive communication network required • algorithms are computationally heavy
[155]	ST-VSM	• adapting the values of virtual inertia and damping coefficient • efficient control during transient conditions • use of online optimisation algorithms to find optimal parameters • emulation of SG behaviour in the entire operating range	• a greater discharge of ESS than VSM with fixed parameters • sufficient processing power should be provided • high computational burden
[145–147]	DC voltage balance	• no PLL required • maps virtual inertia to DC link energy • suitable for non-dispatchable sources to provide transient power	• negligible amount of energy can be extracted from the DC link • droop results in DC voltage deviation • [145] not suitable for standalone systems or systems with low inertia and low regulating energy
[8, 25, 156]	Virtual oscillator control	• no communication between inverters required • synchronisation from arbitrary initial conditions • existance of global asymptotic synchronisation conditions • working principle on time-domain signals instead of phasors	• non-dispatchable (requires extension to dVOC scheme for grid-connected applications [8, 25]) • worse dynamic behaviour than droop control for small frequency regulation range • nonlinear

3.2.3 Device-level control

The device-level control is subdivided into two parts:

1. Inner voltage and current control

2. DC link control

The first one is used to control the active and reactive power delivered to the grid based on the inputs from the system-level control, and the second one balances the power between the

device and grid-side converter.

3.2.3.1 Inner voltage and current control

Fig. 3.12 shows a current controller in the dq frame for a grid-following converter structure shown in Fig. 3.8 and Fig. 3.13. K_p and K_i are the proportional and integral gain of the current PI controller whose values depend on the AC filter impedance (refer to section 3.3). Reactive elements introduce cross-coupling between the d and q axes, therefore the terms $i_c^d \omega^\star L_f$ and $i_c^q \omega^\star L_f$ eliminate the cross-coupling between axes and improve transient performance. The AC filter capacitor generates reactive power, therefore in order to achieve the desired reactive power at the grid-side, the current references from system-level control $i_c^{d\star}$ and $i_c^{q\star}$ are compensated for the reactive current generated by the filter capacitor through the terms $u_f^d \omega^\star C_f$ and $u_f^q \omega^\star C_f$.

This controller is described by per-unit differential-algebraic equations (3.20):

$$\frac{d\zeta^d}{dt} = i_c^{d\star} - u_f^q \omega^\star C_f - i_c^d \tag{3.20a}$$

$$\frac{d\zeta^q}{dt} = i_c^{q\star} + u_f^d \omega^\star C_f - i_c^q \tag{3.20b}$$

$$v_{\text{DC}} m^d = K_p^i \frac{d\zeta^d}{dt} + K_i^i \zeta^d - i_c^q \omega^\star L_f + u_g^d \tag{3.20c}$$

$$v_{\text{DC}} m^q = K_p^i \frac{d\zeta^q}{dt} + K_i^i \zeta^q + i_c^d \omega^\star L_f + u_g^q \tag{3.20d}$$

The standard controller for the grid-forming converter in the literature is shown in Fig. 3.13. The difference compared to the current controller from Fig. 3.12 is the additional outer PI controller which acts on the dq voltage reference generated from the virtual impedance block (3.19a)–(3.19b). The bandwidth of the outer voltage controller should be sufficiently lower (e.g. 5–10 times) than the bandwidth of the inner current controller for a stable operation. The parameters of the inner current controller depend on the AC filter impedance as well.
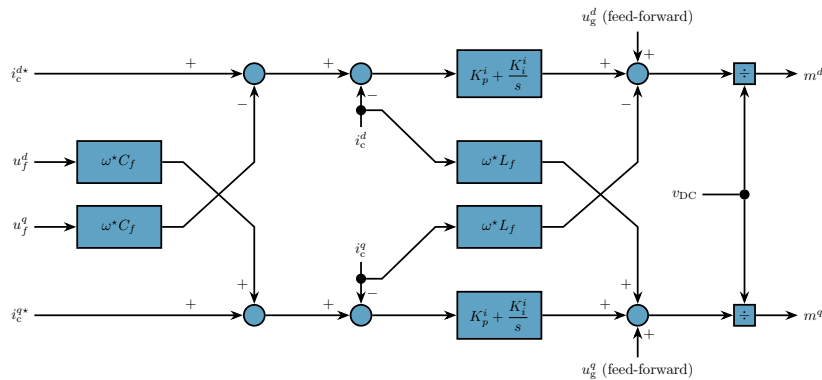
Figure 3.12: dq current controller for a grid-following converter.
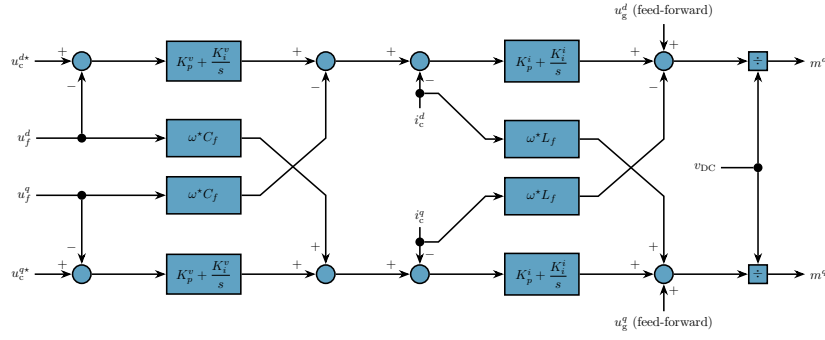
Figure 3.13: dq voltage and current controller for a grid-forming converter.

This controller is described by per-unit differential-algebraic equations (3.21):

$$\frac{d\chi^d}{dt} = u_c^{d\star} - u_f^d \tag{3.21a}$$

$$\frac{d\chi^q}{dt} = u_c^{q\star} - u_f^q \tag{3.21b}$$

$$i_c^{d\star} = K_p^v \frac{d\chi^d}{dt} + K_i^v \chi^d - u_f^q \omega^\star C_f \tag{3.21c}$$

$$i_c^{q\star} = K_p^v \frac{d\chi^q}{dt} + K_i^v \chi^q + u_f^d \omega^\star C_f \tag{3.21d}$$

$$\frac{d\zeta^d}{dt} = i_c^{d\star} - i_c^d \tag{3.21e}$$

$$\frac{d\zeta^q}{dt} = i_c^{q\star} - i_c^q \tag{3.21f}$$

$$v_{\mathrm{DC}} m^d = K_p^i \frac{d\zeta^d}{dt} + K_i^i \zeta^d - i_c^q \omega^\star L_f + u_g^d \tag{3.21g}$$

$$v_{\mathrm{DC}} m^q = K_p^i \frac{d\zeta^q}{dt} + K_i^i \zeta^q + i_c^d \omega^\star L_f + u_g^q \tag{3.21h}$$

3.2.3.2 DC link control

There are a few ways to realise the DC link control depending on whether it is implemented as part of a GSC or DSC. Regardless, it consists of a single PI controller acting on the DC link voltage deviation and generating a current/power reference as follows:

   a) Input: $\left(v_{\mathrm{DC}}^2 - v_{\mathrm{DC}}^{\star 2}\right)$; Output: $p^\star$
   b) Input: $\left(v_{\mathrm{DC}} - v_{\mathrm{DC}}^\star\right)$; Output: $i_c^{d\star}$
   c) Input: $\left(v_{\mathrm{DC}}^{\star 2} - v_{\mathrm{DC}}^2\right)$; Output: $p_{\mathrm{DC}}^\star$
   d) Input: $\left(v_{\mathrm{DC}}^\star - v_{\mathrm{DC}}\right)$; Output: $i_{\mathrm{DC}}^{\mathrm{D}\star}$

The block diagram of the DC link control describing all four implementations is shown in Fig. 3.14. This controller is described by equations (3.22).

$$\frac{d\zeta^{\mathrm{DC}}}{dt} = \begin{cases} v_{\mathrm{DC}}^2 - v_{\mathrm{DC}}^{\star 2} & \text{in case a)} \\ v_{\mathrm{DC}} - v_{\mathrm{DC}}^{\star} & \text{in case b)} \\ v_{\mathrm{DC}}^{\star 2} - v_{\mathrm{DC}}^2 & \text{in case c)} \\ v_{\mathrm{DC}}^{\star} - v_{\mathrm{DC}} & \text{in case d)} \end{cases} \tag{3.22a}$$

$$y = \begin{cases} p^{\star} & \text{in case a)} \\ i_c^{d\star} & \text{in case b)} \\ p_{\mathrm{DC}}^{\star} & \text{in case c)} \\ i_{\mathrm{DC}}^{\mathrm{D}\star} & \text{in case d)} \end{cases} \tag{3.22b}$$

$$y = K_p^{\mathrm{DC}} \frac{d\zeta^{\mathrm{DC}}}{dt} + K_i^{\mathrm{DC}} \zeta^{\mathrm{DC}} \tag{3.22c}$$

In case a), the DC link control is implemented as part of the GSC system-level control, i.e., it generates the GSC power reference $p^{\star}$ based on the difference of the squares of reference of the DC voltage and actual DC voltage (since power is proportional to the voltage square (3.9)). In this case the GSC active power is controlled indirectly, i.e., the DSC generates an arbitrary power, and the GSC tracks this power by controlling the DC voltage to nominal value. Case b) is similar to case a), only the d axis converter current reference is generated based on the DC voltage deviation (3.8). Controlling the power instead of current is more intuitive from a power engineer's perspective, and we are not aware of any other benefits or drawbacks of using one over the other. An example where the a), b) implementation is used is a PV system or a WTG generating intermittent power based on the ambient conditions (insolation, wind speed), and the GSC controls the power injected into the grid by tracking the power coming from the device-side.

In cases c) and d) the DC link balancing is implemented on the device-side, i.e., the GSC active power set-point is set directly, which means the DC link controller controls the power/current
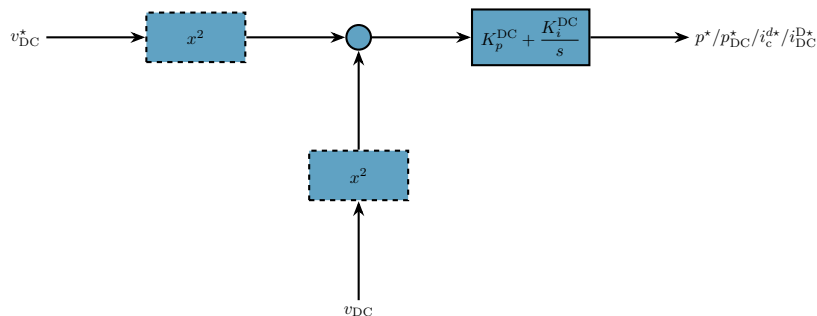
Figure 3.14: DC voltage controller.

coming from the DSC. Although this approach can be found in scientific literature [25], we are not aware of this structure actually being used in practice. The reason being that the device-side control must be faster than the GSC control in order to stabilise the DC link voltage sufficiently quickly. Alternatively, the GSC control must be appropriately slower than the DSC control. This has nothing to do with the DSC itself, but with the device dynamics behind the DSC. For example, a step power reference on the GSC will cause an immediate reduction of DC link voltage. DC link control responds immediately by generating a new device set-point (DSC). However, if the device itself has a large time constant like a wind turbine (meaning that there is a big time lag between the change of a set-point and actually achieving that power at the device terminals), large oscillations of the DC link voltage can occur, and consequently also DC link instability and converter system shutdown. Therefore, structures a) and b) make more sense from a control standpoint because the GSC is only used to transfer the power from the device-side which can be arbitrarily slow or fast, but it will always be slower than the GSC DC link control. Only in case of very fast devices like BESS could c) and d) be feasible.

3.3 Design and modelling of grid-side filters

A raw VSC output waveform contains harmonics around the switching frequency. To attenuate the high-frequency content and leave only the fundamental frequency component of the AC current and voltage, adequate filters need to be designed. Their main purpose is to make the VSC meet the grid code requirements regarding total harmonic distortion (THD), i.e., power quality requirements.

Lower converter switching frequency places greater requirements on the filter. On the other hand, higher switching frequency results in higher converter switching losses. A way to decrease the switching frequency while keeping the harmonic content low is to use more voltage levels. Therefore, MMCs have the lowest filter requirements; moreover, in the literature they usually don't have a dedicated filter as part of the model [135].

Passive filters come in L (Fig. 3.15a) or LC/LCL (Fig. 3.15b) form. An L filter only attenuates the current harmonics, but not the voltage harmonics. To also reduce voltage THD, an LC/LCL filter is required. Fig. 3.15 shows a single-line diagram which means that in reality there are three inductors L_f in total for an L filter, or in the case of LCL filter there are three inductors L_f on the converter-side, three inductors L_f on the grid-side and three wye-connected capacitors C_f with a damping resistor R_d in series.

Since there is usually a step-up transformer involved between the converter and the grid, the transformer inductance needs to be considered during the AC filter design. Hence, inductor requirements are lesser since the transformer itself can be utilised as a filter (in the case of an LCL, the inductor in question is the on the grid-side—between u_f and u_g). Likewise, if a VSC
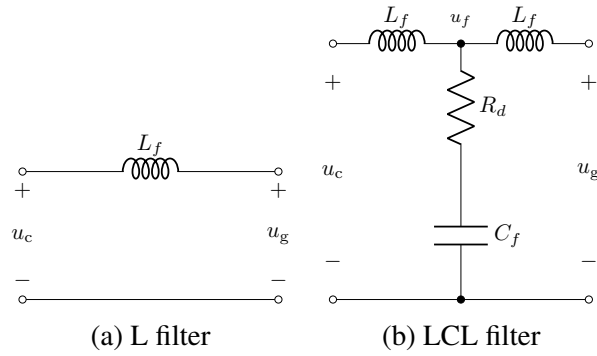
Figure 3.15: Single-line diagram of grid-side passive filters for VSCs.

is connected to a synchronous or induction machine, machine inductance can be utilised as a part of the filter. Additionally, parameters of L/LCL filters directly impact the current controller parameters of VSC, i.e., the converter PI controller is tuned according to the AC filter in order to achieve stable operation.

3.3.1 L filter

The size of the L filter total inductance L_f is around 0.1 p.u. to reduce AC voltage drop [138]. It is assumed L_f also includes the transformer inductance, if any. Then the proportional and integral gains of d-axis and q-axis current controllers are selected according to (3.23a)–(3.23b) [13]:

$$K_p = \frac{L_f \omega_b^{-1}}{\tau_i} \tag{3.23a}$$

$$K_i = \frac{R_f}{\tau_i} \tag{3.23b}$$

where τ_i is the desired time constant of the closed-loop control system (typically 0.5–5 ms) [13] and R_f is the total resistance of the branch: typically the sum of the filter inductor resistance (not shown in Fig. 3.15a) and the on-resistance of semiconductor switches. In (3.23a)–(3.23b), τ_i is in seconds, while L_f and R_f are assumed to be expressed in per-unit (if R_f, L_f are in SI then the base frequency factor ω_b is omitted from K_p).

The general procedure for selecting an L filter is summarised as follows:

1. With f_{switch} known, select L_f to obtain the desired current ripple on the converter-side.
2. Select τ_i such that $10\omega_n \lesssim \frac{1}{\tau_i} \lesssim \frac{2\pi f_{\text{switch}}}{5}$.
3. Check that $L_f \approx 0.1$ p.u. and $\tau_i \in [0.5, 5]$ ms. If not, go back to step 1.
4. Calculate K_p and K_i per (3.23a)–(3.23b).

3.3.2 *LCL* **filter**

The design of an *LCL* filter is generally both more complex and more iterative than the design of a simpler *L* filter [138, 157–165]. The presence of the filter capacitor can make the system unstable if not properly damped by the damping resistor R_d. Nevertheless, the impact of R_d, C_f can be neglected in controller tuning [138] so (3.23a)–(3.23b) can be used for the *LCL* as well. A quick-and-dirty guide for selecting filter parameters based on [13, 138, 162], assuming no grid-side transformer, can be summarised as follows:

1. With f_{switch} known, select converter-side L_f to obtain the desired current ripple on the converter-side. Set the grid-side L_f equal to converter-side L_f, such that $2L_f \approx 0.1$ p.u.
2. Select τ_i such that $10\omega_n \lessapprox \frac{1}{\tau_i} \lessapprox \frac{2\pi f_{\text{switch}}}{5}$. $\frac{1}{\tau_i} = \omega_{\text{res}}$ is the desired filter resonant frequency.
3. Select C_f such that the reactive power percentage x absorbed under rated conditions is $\leq 5\%$ of rated power, i.e., $C_f = x\frac{S_b}{\omega_n U_b^2} = 0.05C_b$, such that $x \leq 0.05$.
4. Check that the desired current ripple attenuation at the grid-side $\frac{1}{\|1+1-L_f x C_b \omega_{\text{switch}}^2\|}$ is achieved. If not, change the desired attenuation level or change x.
5. Check that the actual filter resonant frequency $\omega_{\text{res}} = \sqrt{\frac{2}{L_f C_f}}$ satisfies the criterion $10\omega_n \lessapprox \omega_{\text{res}} \lessapprox \frac{2\pi f_{\text{switch}}}{5}$. If not, choose different C_f or attenuation factor per step 3 and step 4, respectively.
6. Set R_d to be approximately equal to capacitor impedance at the resonant frequency, i.e., $R_d \approx \frac{1}{\omega_{\text{res}} C_f}$.
7. Calculate K_p and K_i per (3.23a)–(3.23b), where L_f and R_f are converter-side values only.

Using the steps above, inductor and capacitor values should result in $L_f \approx 0.05$ p.u. and $C_f \lessapprox 0.1$ p.u., respectively. For more detailed information on *LCL* filter design refer to [138].

3.3.3 **MMC**

Since MMC has many voltage levels, the voltage THD is much smaller and so are the C_f requirements. In fact, the *LCL* filter is not a part of MMC in a majority of the literature. Instead, MMC is represented as a controlled voltage source in series with half the arm inductance and half the arm resistance [136, 137] as shown in Fig. 3.16. Therefore, PI gain tuning of the current controller can be done in the same way as for the two-level and three-level VSCs with *L/LCL* filter.

Fig. 3.17 shows how the voltage at the converter terminals u_c differs from the voltage measured at the filter capacitor terminals u_f for two-level (Fig. 3.17a) and three-level (Fig. 3.17b) topologies. MMC is simulated without a dedicated filter, but it can be seen that its switched voltage waveform (Fig. 3.17c) is much closer to a pure sine wave compared to the two-level and three-level VSCs where u_c is essentially a square wave output.
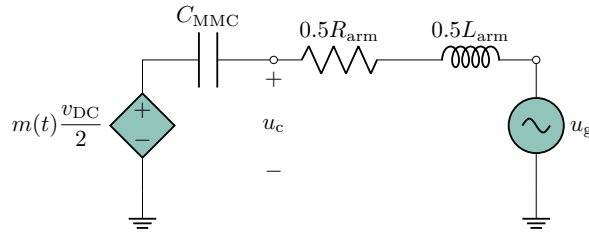
Figure 3.16: Single-line diagram of an AC-side averaged MMC model.

3.3.4 Considerations for frequency dynamics

Grid-tied VSCs with an *LCL* filter are more troublesome than VSCs with an *L* filter due to resonant modes introduced by the filter capacitor. Additionally, the VSC current control bandwidth is inevitably intertwined with the filter design. Therefore, a couple of detrimental challenges may arise during converter operation [166]:

1. Excitation of filter resonant modes may destabilise converter operation.

2. Weak power grid has a large impedance seen from the converter terminals which can impact the control bandwidth of the VSC resulting in instability.

So far, these issues were not of concern in frequency dynamics of bulk power systems for two reasons:

- Frequency dynamics were mainly driven by electromechanical dynamics and slower turbine control, while VSC filter interactions are a high-frequency phenomena.

- Grid impedance is small in well-interconnected bulk systems.

On the one hand, it may still very well hold that filter and inner control loops have no impact on frequency dynamics, assuming a strong grid, well-damped filter design, and layered control structures where slower outer control loops are in charge of power control (e.g., by emulating a synchronous generator). On the other hand, converters are not restricted by physical inertia so control algorithms for active power control may be even faster (e.g., [148, 149]) and these dynamics may play into account which will be examined in the remainder of this thesis.

(a) Two-level VSC

(b) Three-level VSC

(c) MMC (30 submodules per arm)
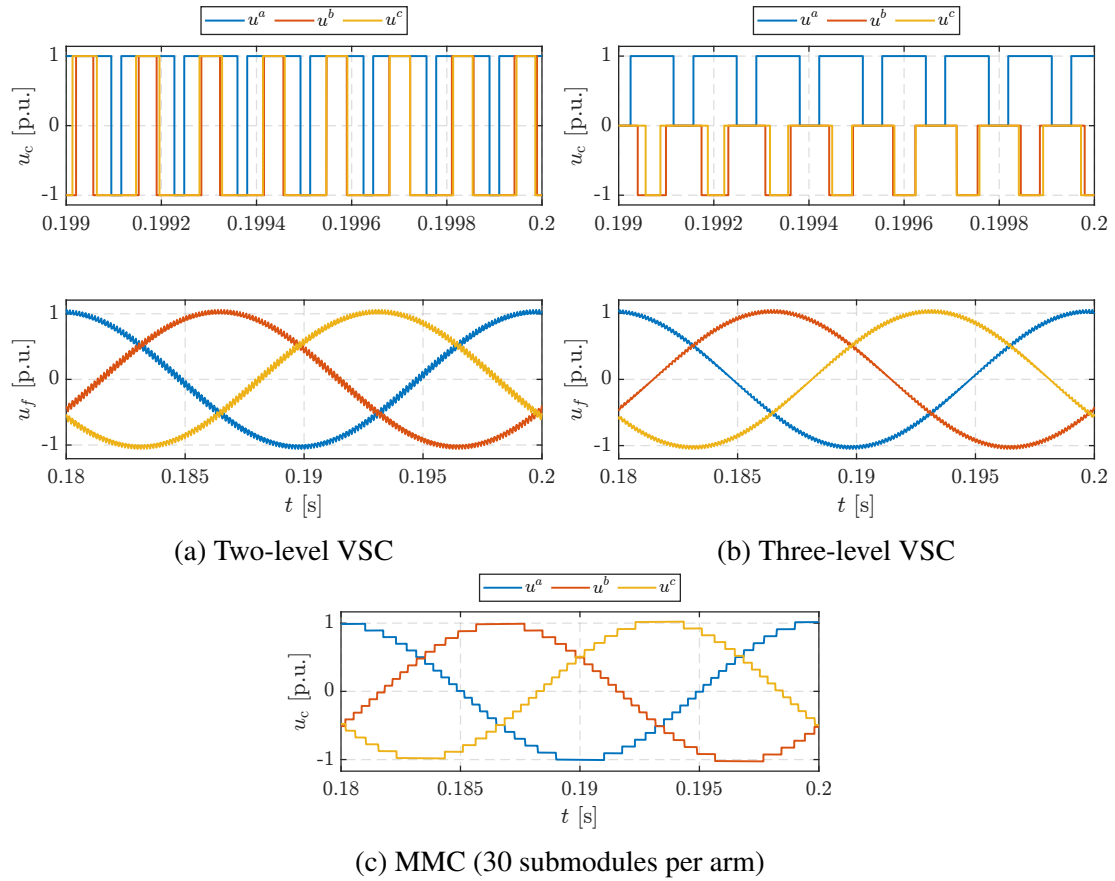
Figure 3.17: Voltage at the converter terminals (u_c) and at the filter capacitor terminals (u_f) for different VSC topologies.

3.4 DSC control systems and energy conversion system dynamics

Depending on the type of source connected, the actual realisation of the DSC is different. If we talk about a wind turbine system, then the DSC is another VSC which either connected to the rotor (type-3) or to the stator (type-4). If we talk about solar PV, then the DSC is a DC-DC converter which tries to impose optimal DC voltage on the solar PV panel in order to extract the maximum power. DC-DC converters may also be found in energy storage systems such as batteries and supercapacitors. In the context of industrial motor drives, DSC is usually also a VSC (more often called a frequency converter in that case). There are many possible combinations here with different dynamic behaviour which would take up too much space to properly explain so the specifics are omitted here. For the remainder of this chapter, as well as in Chapters 4, the ECS + DSC are modelled as an ideal controllable power source not to lose generality. Chapter 5, however, goes into detail of wind turbine dynamics and the consequences of neglecting it when studying grid frequency dynamics.

3.5 Comparison of different converter control modes

3.5.1 Grid-following converters: DC link control by the DSC vs. DC link control by the GSC

When the DC link is balanced on the device-side, any power requested by the GSC is immediately available on the DC-side through the controlled power source. This is similar to having a stiff DC voltage source in place of a DC link capacitor. All interactions between grid-side and device-side are completely decoupled. The control structure is designed in a way that active power and voltage/reactive power set-points are inputs to the GSC, while DC link voltage is controlled by the DSC+ECS: based on the DC link voltage deviation, DCVC generates the DC power set-point that is immediately realised on the device-side, as shown in Fig. 3.18 where $\mathbf{x}^{\text{s}\star}$ and $\mathbf{x}^{\text{d}\star}$ are defined by (3.24)–(3.25).
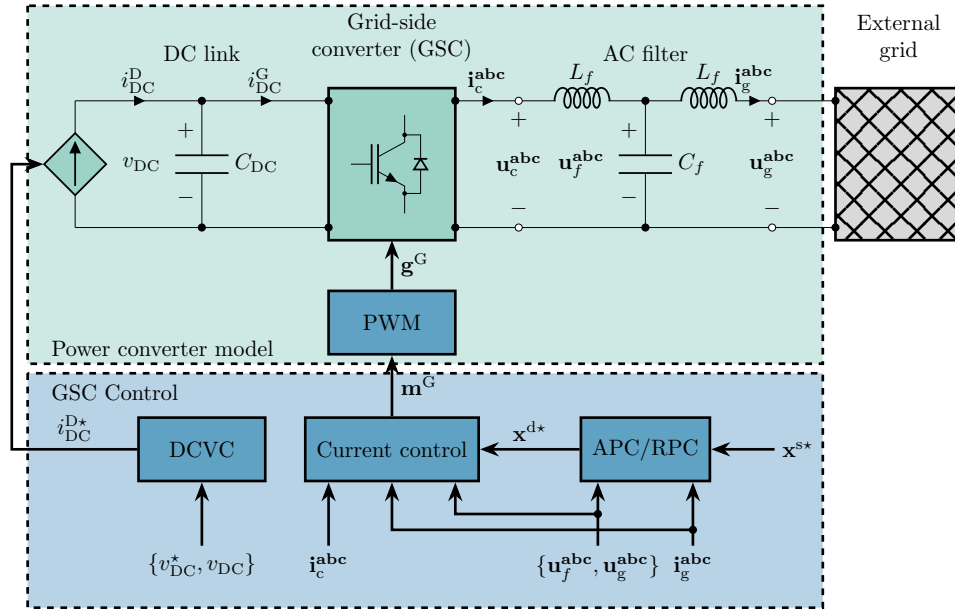
Figure 3.18: Grid-following converter with DC link balancing on the device-side.

$$\mathbf{x}^{\text{s}\star} = \{p^\star + \Delta p^\star, q^\star + \Delta q^\star\} \tag{3.24}$$

$$\mathbf{x}^{\text{d}\star} = \{i_{\text{c}}^{d\star}, i_{\text{c}}^{q\star}\} \tag{3.25}$$

When the DC link is balanced on the grid-side, any power generated or consumed on the device-side through externally set $p_{\text{DC}}^{\text{D}\star}/i_{\text{DC}}^{\text{D}\star}$ is balanced on the grid-side through DCVC which automatically generates the GSC active power set-point, as shown in Fig. 3.19 where $\mathbf{x}^{\text{s}\star}$ and $\mathbf{x}^{\text{d}\star}$ are defined by (3.26)–(3.27). Therefore, the GSC power reference is set indirectly through DC voltage control. The reactive power set-point is set directly like in the previous case.
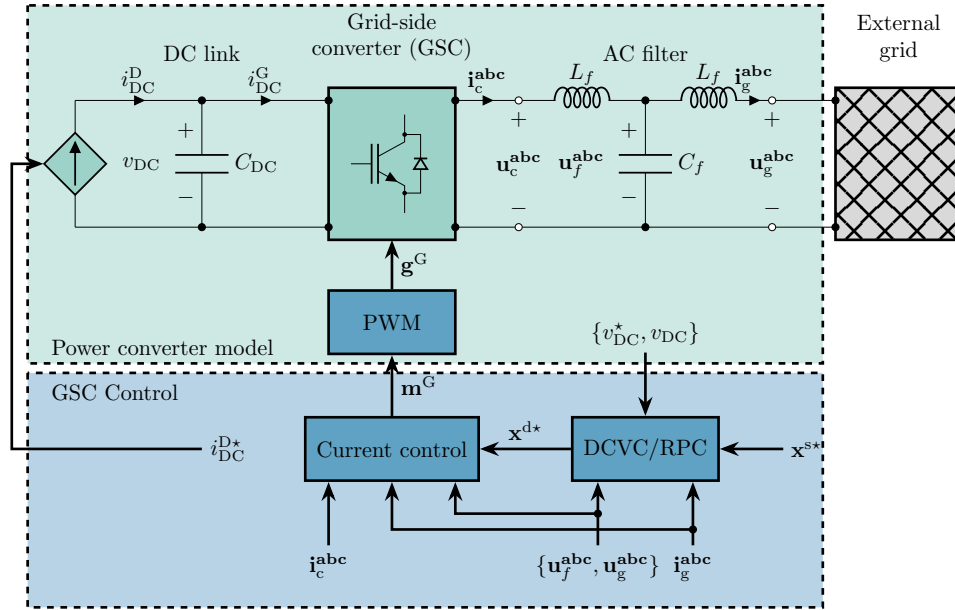
Figure 3.19: Grid-following converter with DC link balancing on the grid-side.

$$\mathbf{x}^{\mathrm{s}\star} = \left\{ p^\star = \left(v_{\mathrm{DC}}^2 - v_{\mathrm{DC}}^{\star 2} \right) \frac{K_p^{\mathrm{DC}} s + K_i^{\mathrm{DC}}}{s}, q^\star + \Delta q^\star \right\} \tag{3.26}$$

$$\mathbf{x}^{\mathrm{d}\star} = \left\{ i_{\mathrm{c}}^{d\star}, i_{\mathrm{c}}^{q\star} \right\} \tag{3.27}$$

Neglecting the AC filter capacitor, the simplified block diagram of the grid-following VSC in the d-axis is shown in Fig. 3.20a [13]. The PI controller is tuned according to (3.23) so that a first-order closed-loop response with time constant T_{GSC} is obtained. Assuming stiff grid voltage u_{g}^d, the closed-loop transfer function shown in Fig. 3.20b is obtained, which is the commonly found CID transfer function in the literature.

Taking into account DC link dynamics (3.9) and DC link controller (3.22), a simplified block diagram describing device-level dynamics of VSC systems from Fig. 3.18 and Fig.3.19 is shown in Fig. 3.21. The block diagram from Fig. 3.21 only considers the power balance and
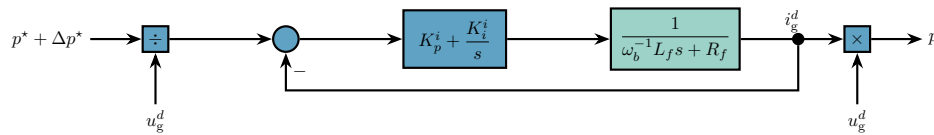
(a) Simplified block diagram of d-axis closed-loop control system of a grid-following VSC

(b) Closed-loop transfer function of a grid-following VSC

Figure 3.20: Simplified block diagrams of grid-following VSC for active power control.

65

neglects any disturbances emerging from grid voltage or grid current transients. Comparing Fig. 3.21a to Fig. 3.21b, one can see that regardless of whether the DC voltage is balanced on the grid-side or device-side, the same transfer function are used. The only difference is in the definition of inputs and outputs: for DCVC on the device-side the input is $p^\star + \Delta p^\star$ and the output is p where the input-output transfer function is defined as (3.28), input-to-DC voltage transfer function is defined as (3.29), and input-to-DC power is defined as (3.30). It can be seen that the AC-side dynamics are governed by a first order behaviour, while the DC voltage and power dynamics are described by third-order dynamic systems.

$$G_p(s) = \frac{\Delta p}{\Delta(p^\star + \Delta p^\star)} = \frac{1}{T_{\text{GSC}}s + 1} \tag{3.28}$$

$$G_{v_{\text{DC}}}(s) = \frac{\Delta v_{\text{DC}}^2}{\Delta(p^\star + \Delta p^\star)} = \frac{-s}{0.5\omega_b^{-1}C_{\text{DC}}s^2 + K_p^{\text{DC}}s + K_i^{\text{DC}}} \cdot \frac{1}{T_{\text{GSC}}s + 1} \tag{3.29}$$

$$G_{p_{\text{DC}}^\star}(s) = \frac{\Delta p_{\text{DC}}^\star}{\Delta(p^\star + \Delta p^\star)} = \frac{K_p^{\text{DC}}s + K_i^{\text{DC}}}{0.5\omega_b^{-1}C_{\text{DC}}s^2 + K_p^{\text{DC}}s + K_i^{\text{DC}}} \cdot \frac{1}{T_{\text{GSC}}s + 1} \tag{3.30}$$

On the other hand, when DCVC is on the grid-side, $p^\star$ is a state variable indirectly set to match the AC-side power p (system output) to the device-side power $p_{\text{DC}}^\star$ (system input). The transfer functions that describe this system are (3.31)–(3.32), where both the output power and DC voltage are described by a third-order dynamic system. The derived transfer functions (3.28)–(3.32) are shown in Fig. 3.22.

$$G_p(s) = \frac{\Delta p}{\Delta p_{\text{DC}}^\star} = \frac{K_p^{\text{DC}}s + K_i^{\text{DC}}}{0.5\omega_b^{-1}C_{\text{DC}}T_{\text{GSC}}s^3 + 0.5\omega_b^{-1}C_{\text{DC}}s^2 + K_p^{\text{DC}}s + K_i^{\text{DC}}} \tag{3.31}$$

$$G_{v_{\text{DC}}}(s) = \frac{\Delta v_{\text{DC}}^2}{\Delta p_{\text{DC}}^\star} = \frac{s(T_{\text{GSC}}s + 1)}{0.5\omega_b^{-1}C_{\text{DC}}T_{\text{GSC}}s^3 + 0.5\omega_b^{-1}C_{\text{DC}}s^2 + K_p^{\text{DC}}s + K_i^{\text{DC}}} \tag{3.32}$$

(a) DCVC on the device-side   (b) DCVC on the grid-side
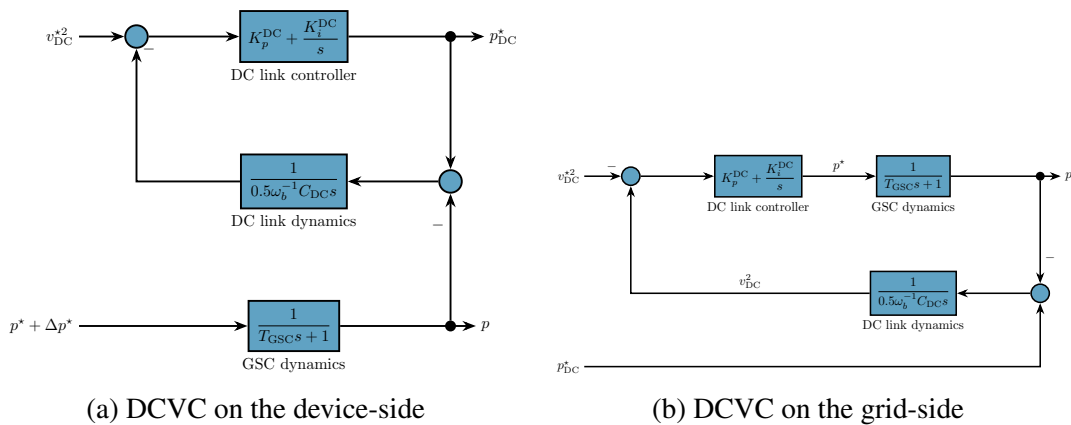
Figure 3.21: Simplified block diagram of a grid-following VSC considering DC link control.

Note that since T_{GSC} is small (order of magnitude $\approx 10^{-3}$), by neglecting it (3.31) exhibits a generic second-order system dynamics (3.33), where the natural frequency ω_n and damping factor ζ are defined as (3.34) and (3.35), respectively. T_i^{DC} is the integrator reset time. Therefore, by proper tuning of DCVC PI gains, the GSC will exhibit a well-damped behaviour similar to a first-order dynamic system (3.28).

$$\mathcal{G}(s) = \frac{2\zeta\omega_n s + \omega_n^2}{s^2 + 2\zeta\omega_n s + \omega_n^2} \tag{3.33}$$

$$\omega_n = \sqrt{\frac{K_i^{\text{DC}}}{0.5\omega_b^{-1}C_{\text{DC}}}} = \sqrt{\frac{K_p^{\text{DC}}}{0.5T_i^{\text{DC}}\omega_b^{-1}C_{\text{DC}}}} \tag{3.34}$$

$$\zeta = \frac{K_p^{\text{DC}}}{\omega_b^{-1}C_{\text{DC}}\omega_n} = \sqrt{\frac{K_p^{\text{DC}}T_i^{\text{DC}}}{2C_{\text{DC}}\omega_b^{-1}}} \tag{3.35}$$

Finally, note how $\Delta p^\star = 0$ in Fig. 3.21b. That is because in this scheme the GSC control always tries to balance out $P_{\text{DC}}^\star$, therefore this structure is not suitable for frequency droop control $\Delta p^\star = f(\Delta\omega_g)$ in the GSC. To achieve frequency droop capability, the device-side power should be modulated instead: $P_{\text{DC}}^\star \to P_{\text{DC}}^\star + \Delta p^\star$.

Fig. 3.23 shows the response of a converter connected to an infinite bus to a step-change of input power reference. It can be seen that for the same set of parameters ($T_{\text{GSC}} = 0.005$ s, $K_p^{\text{DC}} = 20$, $K_i^{\text{DC}} = 100$) the converter with DC link balancing on the grid-side has a slower response and an overshoot due to higher order dynamics (3.31)–(3.32). Δv_{DC}^2 has opposite signs because for the device-side DCVC the power is drawn from the DC link, while for the grid-side DCVC power is injected into the DC link since the input power reference is defined differently. In both cases, the derived small-signal models (Fig. 3.22) accurately describe DC link dynamics and output power dynamics. However, the two are not inherently equivalent and control parameters of the converter with DCVC on the grid-side should be re-tuned to achieve a behaviour closer to first-order dynamics.

(a) DCVC on the device-side: $\frac{\Delta p}{\Delta(p^\star + \Delta p^\star)}$

(b) DCVC on the device-side: $\frac{\Delta v_{\text{DC}}^2}{\Delta(p^\star + \Delta p^\star)}$

(c) DCVC on the grid-side: $\frac{\Delta p}{\Delta p_{\text{DC}}^\star}$

(d) DCVC on the grid-side: $\frac{\Delta v_{\text{DC}}^2}{\Delta p_{\text{DC}}^\star}$
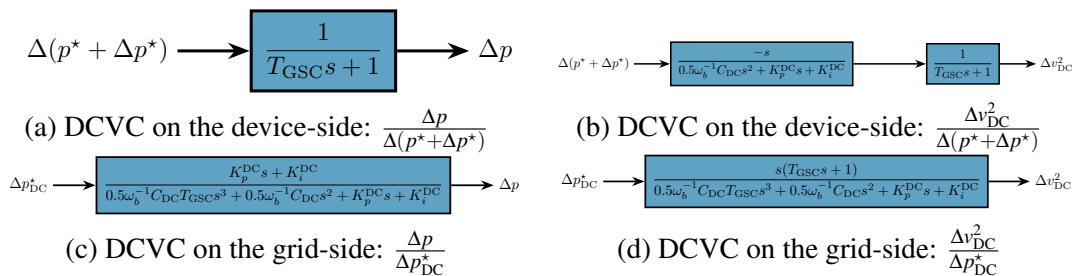
Figure 3.22: Transfer functions of grid-following VSC considering DC link dynamics & control.
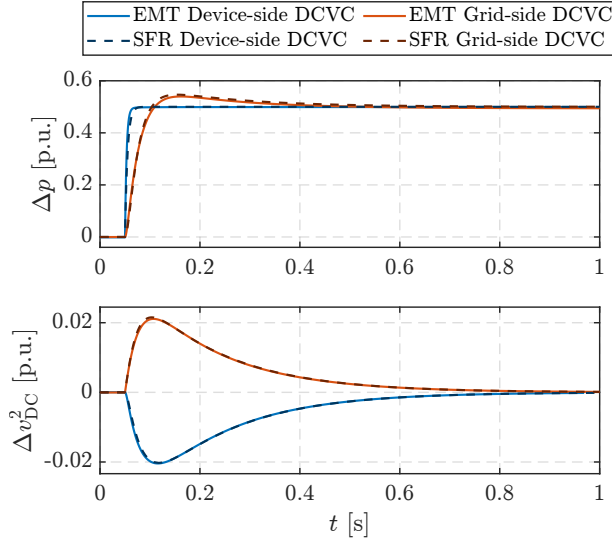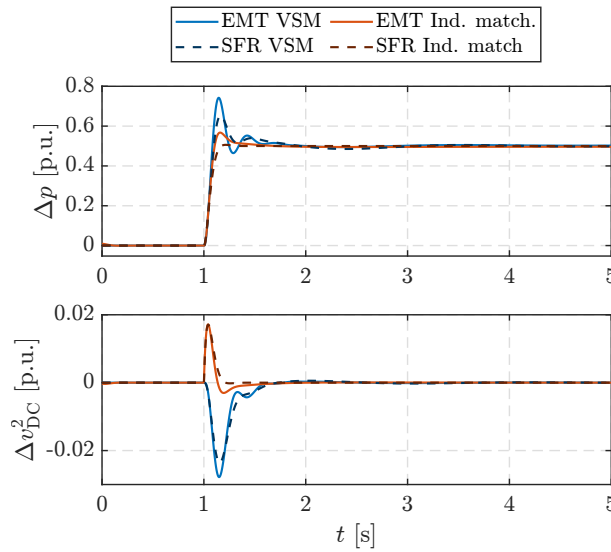
Figure 3.23: EMT vs. SFR model response of an infinite bus connected grid-following converter to a step change of power reference: power (top), square of DC voltage (bottom).

3.5.2 Grid-forming converters: synchronisation based on power imbalance vs. synchronisation based on DC link imbalance

Power imbalance synchronisation works on the principle of generating the internal voltage angle based on the difference between GSC power set-point and the measured output power. The DC link is controlled by the DSC. This structure is similar to the grid-following converter in which the DC link is controlled by the DSC, while the GSC directly receives the power set-point. The only difference is in how the set-point is realised: in grid-following the voltage angle is estimated by the PLL, while in grid-forming it is generated internally. Fig. 3.24 shows the grid-forming structure based on the power imbalance synchronisation where $\mathbf{x}^{s\star}$ and $\mathbf{x}^{d\star}$ are defined by (3.36) and (3.37). Standard VSM control is an example of a power imbalance synchronisation.

$$\mathbf{x}^{s\star} = \{p^\star, q^\star, u_g^\star\} \tag{3.36}$$

$$\mathbf{x}^{d\star} = \{u_c^{d\star}, u_c^{q\star}, \omega^\star, \theta^\star\} \tag{3.37}$$

The control structure of DC link based synchronisation is shown in Fig. 3.25. Here, the internal voltage angle is generated proportionally to the DC voltage deviation, thus the power imbalance is considered indirectly. The power set-point ($i_{DC}^{D\star}$) is generated by the ECS and this reference is modified by the DSC DCVC to maintain power balance. The DCVC is a P controller instead of PI as in the *indirect matching* scheme. $\mathbf{x}^{s\star}$ and $\mathbf{x}^{d\star}$ are defined by (3.38) and (3.39). This type of control structure is more suitable for non-dispatchable ECS such as solar PV, but the contribution is limited since virtual inertia is matched to the DC link energy and
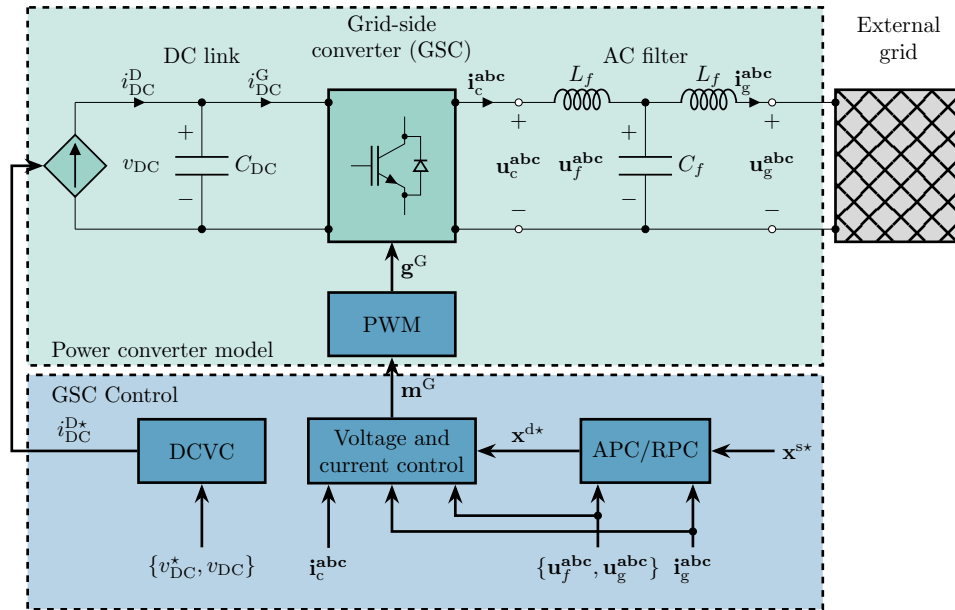
Figure 3.24: Grid-forming converter with power imbalance based synchronisation.

frequency deviation will result in DC voltage deviation, which needs to be tightly controlled.

$$\mathbf{x}^{\text{s}\star} = \{u_{\text{g}}^{\star}\} \tag{3.38}$$

$$\mathbf{x}^{\text{d}\star} = \{u_{\text{c}}^{d\star}, u_{\text{c}}^{q\star}, \omega^{\star}, \theta^{\star}\} \tag{3.39}$$
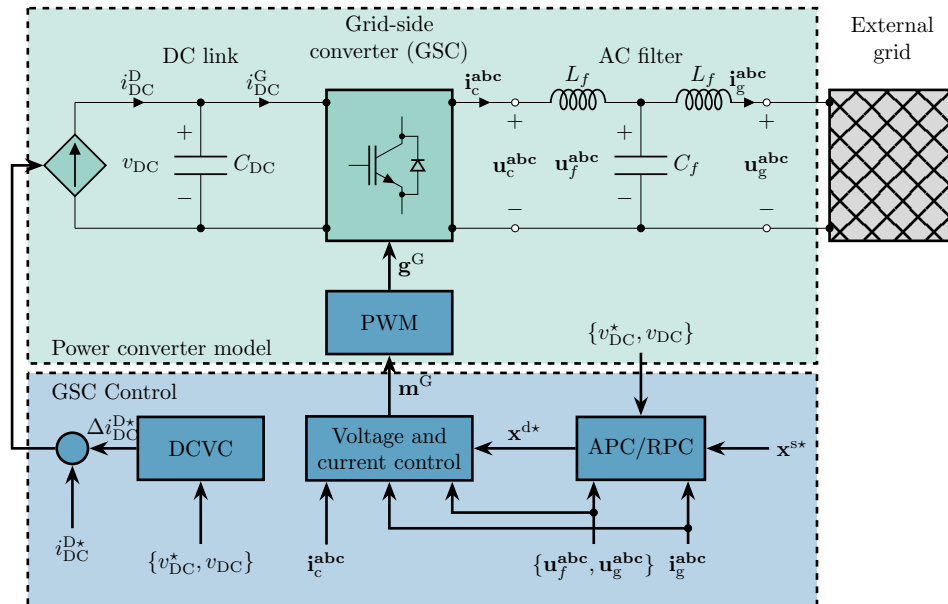
Figure 3.25: Grid-forming converter with DC link imbalance based synchronisation.

Considering only the virtual swing equation and DC link dynamics, and neglecting filter capacitance, virtual impedance and device-level control, a simplified model of a VSM connected to an infinite bus is written as (3.40), where *X* is the effective reactance between the converter

and PCC.

$$\frac{1}{\omega_b}\frac{d\theta^\star}{dt} = \omega^\star - 1 \tag{3.40a}$$

$$2H\frac{d\omega^\star}{dt} = p^\star(t) - p(t) - R^{-1}(\omega^\star - 1) + K_D(\omega_{\text{PLL}} - \omega^\star) \tag{3.40b}$$

$$p(t) = \frac{\|u_c\|\|u_g\|}{X}\sin\theta^\star \tag{3.40c}$$

$$p_{\text{DC}}^\star - p(t) = \frac{C_{\text{DC}}}{2\omega_b}\frac{dv_{\text{DC}}^2}{dt} \tag{3.40d}$$

$$p_{\text{DC}}^\star = K_p^{\text{DC}}\left(v_{\text{DC}}^{\star 2} - v_{\text{DC}}^2\right) + K_i^{\text{DC}}\lambda \tag{3.40e}$$

$$\frac{d\lambda}{dt} = v_{\text{DC}}^{\star 2} - v_{\text{DC}}^2 \tag{3.40f}$$

Linearizing (3.40) around the initial operating point transfer functions from the GSC set-point to power output and to DC voltage can be derived (Fig. 3.26), where $K_\theta = \|u_c\|\|u_g\|X^{-1}\cos\theta_0^\star$ (assuming stiff unity voltage $K_\theta \approx X^{-1}\cos\theta_0^\star$).

(a) VSM: $\frac{\Delta p}{\Delta p^\star}$

(b) VSM: $\frac{\Delta v_{\text{DC}}^2}{\Delta p^\star}$
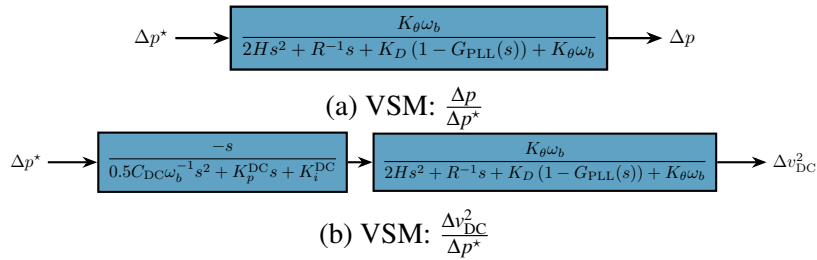
Figure 3.26: Transfer functions of grid-forming VSC (power imbalance synchronisation) considering DC link dynamics & control.

Similarly, a simplified model of the *indirect matching* scheme is described by (3.41), for which the transfer functions from the DSC set-point to the power output and DC voltage are shown in Fig. 3.27.

$$\frac{1}{\omega_b}\frac{d\theta^\star}{dt} = \omega^\star - 1 \tag{3.41a}$$

$$\omega^\star = 1 + R_{\text{DC}}\left(v_{\text{DC}}^2 - v_{\text{DC}}^{\star 2}\right) \tag{3.41b}$$

$$p(t) = \frac{\|u_c\|\|u_g\|}{X}\sin\theta^\star \tag{3.41c}$$

$$p_{\text{DC}}^\star + K_p^{\text{DC}}\left(v_{\text{DC}}^{\star 2} - v_{\text{DC}}^2\right) - p(t) = \frac{C_{\text{DC}}}{2\omega_b}\frac{dv_{\text{DC}}^2}{dt} \tag{3.41d}$$

Fig. 3.28 shows the step response of these two grid forming schemes to power set-point and validates the derived small-signal model which will be used later in this thesis. VSM has a larger overshoot due to SM emulation which can be damped through virtual impedance. Another difference is in the direction of the voltage deviation since the power set-point is requested at

(a) Indirect matching: $\frac{\Delta p}{\Delta p_{\mathrm{DC}}^\star}$ (b) Indirect matching: $\frac{\Delta v_{\mathrm{DC}}^2}{\Delta p_{\mathrm{DC}}^\star}$
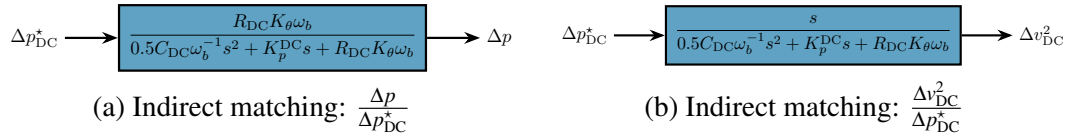
Figure 3.27: Transfer functions of grid-forming VSC (DC voltage imbalance synchronisation) considering DC link dynamics & control.

the GSC for VSM and at DSC for indirect matching control. Under certain conditions there is an equivalence between VSM and *indirect matching* which is covered in Section 4.6 and Section 6.2. Small-signal model formulation more suitable for SFR studies is derived in Section 4.5 and Section 4.6.

Figure 3.28: EMT vs. SFR model response of an infinite bus connected grid-forming converter to a step change of power reference: power (top), square of DC voltage (bottom).

3.6 Summary

Power electronics can be classified according to their DC port waveform into voltage-sourced and current-sourced converters. This thesis focuses on energy conversion systems interfaced to the grid via voltage-sourced converters. Therefore, a generic structure has been presented which consists of an energy conversion system, two power stages (device-side and grid-side converter) with corresponding control systems, the DC link and the AC filter.

Each subsystem has been described in detail with the governing equations, therefore setting up the modelling framework used in the remainder of the thesis. Particular attention has been given to control subsystems and to different ways of maintaining power balance and synchronizing the converter to the grid. Differences between grid-following and grid-forming modes have been explained, as well as their peculiarities in terms of synchronous machine inertia emulation. Low-order transfer functions based on power balance equations have been developed

for describing the power-to-power and power-to-voltage relationship. Consequently, different converter control modes were compared using time-domain simulations.

Chapter 4

Understanding power system frequency dynamics in the presence of converter-interfaced devices

Traditionally, power system frequency dynamics were determined largely by synchronous generators and their turbine governing systems and, to a lesser extent, by frequency-sensitive power system loads (synchronous and induction motors). In this chapter, we revisit the physical meaning of frequency and analyse how different conventional power system elements impact it. Then, we extend the analysis by introducing the converter-based devices introduced in Chapter 3 in order to understand their role in the physics of power system frequency.

In the following sections, all simulations are EMT simulations using:

- 9th-order round rotor synchronous generator model (3 diff. equations for stator transients, 4 diff. equations for rotor transients and 2 diff. equations for mechanical motion) and 8th-order salient pole synchronous generator model (current in the second q-axis is zero). Generator saturation is included. Associated turbine governing system, AVR and PSS are included.
- 17th-order grid-forming converter model and 15th-order grid-following converter model
- 5th-order induction motor model
- In EMT simulations, all general loads are modelled as purely passive loads (RLC combination). Frequency and voltage sensitive loads are modelled as synchronous or induction motors. Other types of loads are not considered.

All the RMS and EMT simulations are done on a modified IEEE 9-bus system in DIgSILENT PowerFactory shown in Fig. 4.1.
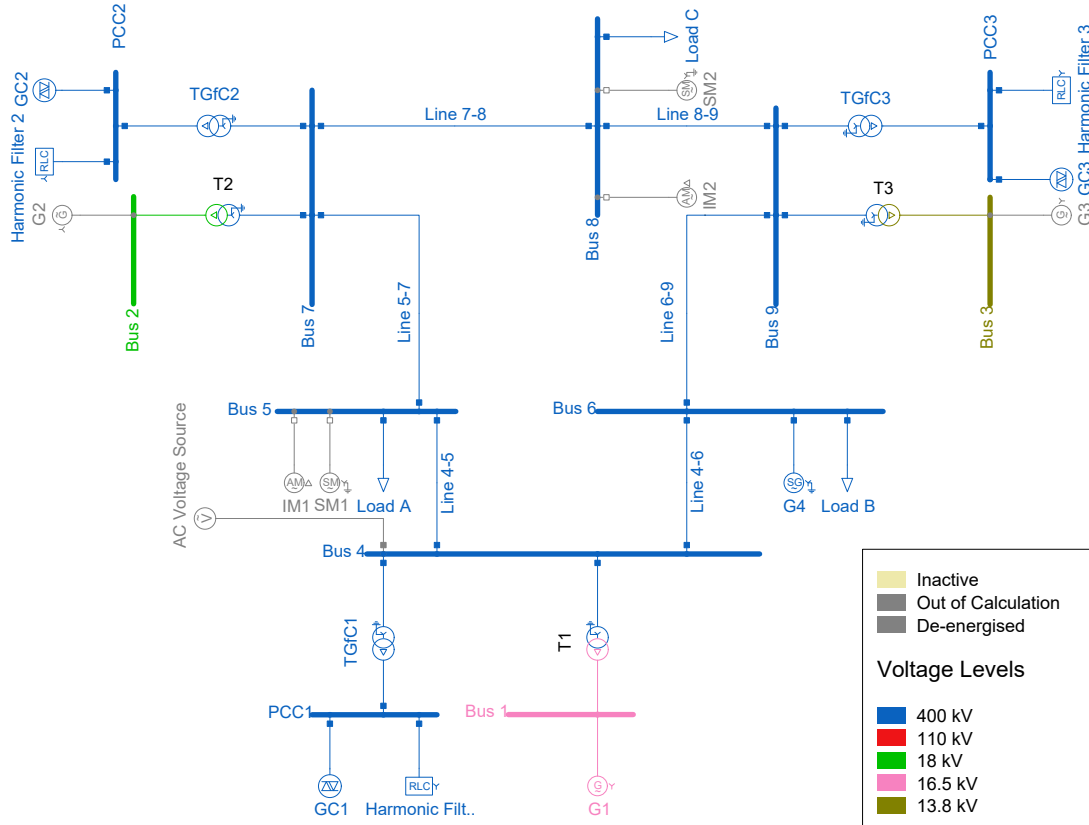
Figure 4.1: Modified IEEE nine bus system.

4.1 Systems based on synchronous generators and frequency-independent loads

The 9-bus system consists of three synchronous plants with their main parameters shown in Table 4.1. In the simplest case, neglecting synchronous generator damping due to friction or any other explicit speed damping source (some damping is implicitly provided by the damper

Table 4.1: Synchronous generator plant data.

Plant i	Type	Number of parallel machines N_i	Machine inertia H_i	Base power $S_{b,i}$	Turbine	Excitation	PSS
1	Hydro	5	9.55 s	247.5 MW	*HYGOV*	*IEEET1S*	*STAB1*
2	Thermal	5	3.92 s	163.2 MW	*TGOV1*	*IEEET1S*	*STAB1*
3	Thermal	5	2.77 s	108.8 MW	*TGOV1*	*IEEET1S*	*STAB1*

windings), the swing equation of generator i can be written as:

$$2H_i\omega_i\frac{d\omega_i}{dt} = p_{m,i}(t) - p_{e,i}(t) \tag{4.1}$$

where $p_{m,i}(t)$ is the SG mechanical power input determined by the turbine-governing system and $p_{e,i}(t)$ is the SG electrical power output determined by the SG model including AVR and PSS. H_i is the inertia constant of SG i defined as:

$$H_i = \frac{J_i\omega_{s,m,i}^2}{2S_{b,i}} = \frac{J_i\frac{\omega_{s,i}^2}{p_i^2}}{2S_{b,i}} \tag{4.2}$$

where J_i is the combined moment of inertia of the generator and turbine, $\omega_{s,m,i}$ is the synchronous mechanical speed, $\omega_{s,i}^2$ is the synchronous electrical speed and p_i is the number of pole pairs. $S_{b,i}$ is the base power of SG i on which H_i is expressed (rated apparent power, rated real power, etc.). Equation (4.1) assumes a single-mass model of the turbine-generator, but a multi-mass model can be defined as well.

If Load B is suddenly switched on, the frequency will start to fall before primary control action stabilizes it at a new value. Firstly, although generator speeds differ during the transient period depending on their inertia (Fig. 4.2), individual variations are not vastly different (generator with lower inertia will have larger excursions of speed and vice versa). After a few seconds, all generator speeds converge towards a uniform system frequency (assuming no loss of synchronism occurred). This enables the aggregation of individual machines into a single equivalent machine of inertia H_{eq} and turbine governing system. Fig. 4.3 shows that the SFR model accurately describes the grid frequency compared to an EMT model. The error is mostly caused by the linearised hydro turbine model (*HYGOV* is a nonlinear model compared to *TGOV1*) because its effective water starting time constant T_W' depends on the operating point, therefore it loses accuracy during larger excursions from the initial operating point [15] (this can be seen in the G1 mechanical power plot in Fig. 4.3).

The equivalent machine inertia constant can be analytically determined by summing up individual SG inertias and dividing by a common power base S_b (which can be completely
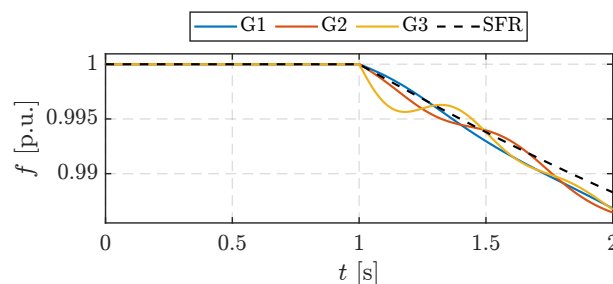
Figure 4.2: Initial transient period when individual (groups of) machines swing against each other.
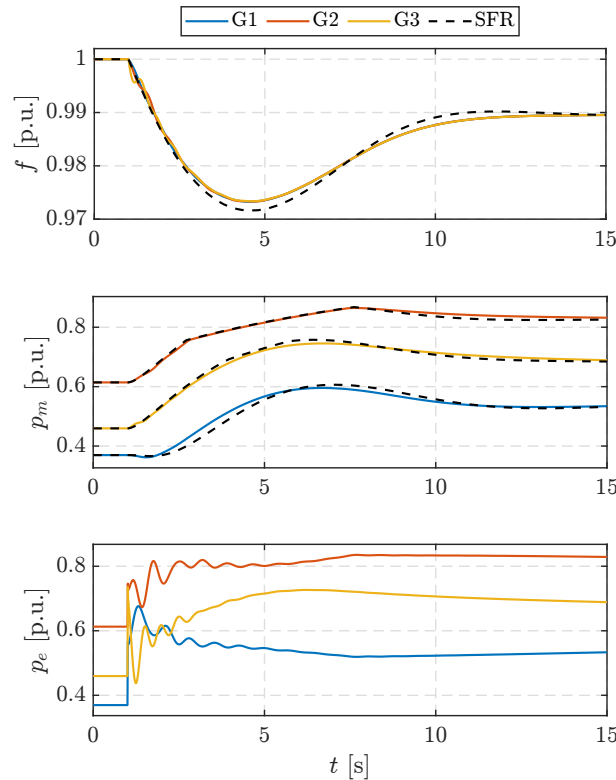
Figure 4.3: EMT vs. SFR model for simulating power system frequency (PSS neglected).

arbitrary):

$$H_{\text{eq}} = \frac{\sum_{i \in \mathcal{N}_{\text{SG}}} H_i S_{b,i}}{S_b} \tag{4.3}$$

where $\mathcal{N}_{\text{SG}}$ is a set of online SGs. Therefore, the term $\sum_{i \in \mathcal{N}_{SG}} H_i S_{b,i}$ is equal to the total kinetic energy of all online SGs. The SFR model which describes this system is shown in Fig. 4.4. The first branch corresponds to the turbine of SG 1 (linearised hydraulic turbine-governor based on the HYGOV model). Branches 2 and 3 correspond to turbines of SG 2 and SG 3, respectively (both based on the linear TGOV1 turbine-governor model). $H_{\text{eq}} \rightarrow H$ is the equivalent system inertia per (4.3). Each branch i assumes N_i identical parallel machines in plant i, which is taken into account in the base conversion factor. All parameters are expressed on a single-machine base.

Equation (4.3) can be proven through the swing equation (4.1) by summing over the set of online SGs (4.4):

$$\sum_{i \in \mathcal{N}_{\text{SG}}} 2H_i \omega_i \frac{d\omega_i}{dt} = \sum_{i \in \mathcal{N}_{\text{SG}}} p_{m,i}(t) - \sum_{i \in \mathcal{N}_{\text{SG}}} p_{e,i}(t) \tag{4.4}$$

$\sum_{i \in \mathcal{N}_{\text{SG}}} p_{m,i}(t) = p_m$ is the total generation and $\sum_{i \in \mathcal{N}_{\text{SG}}} p_{e,i}(t) = p_e$ is the total load (including losses). In a well-synchronised system, individual generator speeds converge towards a uniform system frequency $\omega_i \rightarrow \omega$, $\forall i \in \mathcal{N}_{\text{SG}}$ as $t \rightarrow \infty$. Therefore, (4.4) becomes (4.5):

$$\omega \frac{d\omega}{dt} \sum_{i \in \mathcal{N}_{\text{SG}}} 2H_i = p_m(t) - p_e(t) = 2H\omega\frac{d\omega}{dt} \tag{4.5}$$
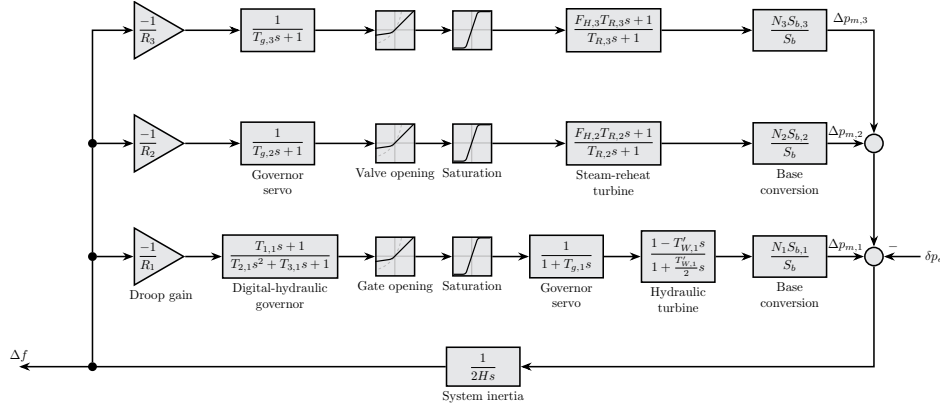
Figure 4.4: SFR model of a system consisting only of SGs (PSS disabled).

Linearising (4.5) and converting to the Laplace domain results in the transfer function which relates generator-load imbalance to system frequency deviation (4.6):

$$\Delta\omega(s) = \frac{\Delta p_m(s) - \Delta p_e(s)}{2Hs} \tag{4.6}$$

It should be noted that the existence of PSSs in the grid can also impact transient frequency dynamics during large excursions. This is due to the fact that a PSS modulates the excitation voltage in phase with the generator speed deviation in order to reduce machine acceleration. Consequently, the generator output power is affected. Generally, the existence of a PSS will improve frequency dynamics since the accelerating power is reduced, assuming well-tuned parameters. This is illustrated in Fig. 4.5 where the SFR model from Fig. 4.4 is used.

The accuracy of the SFR model can be improved by including the PSS model as shown in Fig. 4.6 and Fig. 4.7. The validity of adding PSSs in the SFR model can be justified as follows: Assuming a classical SG model (voltage behind reactance), the generator electrical power is proportional to the internal EMF v_e, terminal voltage v_t, equivalent reactance between the generator and generator terminal x_i and load angle δ_i (4.7). The internal EMF is an output of the excitation system whose inputs are the terminal voltage and PSS signal (4.8)–(4.9). Assuming linearity of the excitation system and PSS, one can deduce from (4.7)–(4.9) that the generator power modulation is proportional to the PSS excitation voltage modulation signal ($\Delta p_{e,i} \propto \Delta v_{\text{pss}} \propto \Delta\omega_i$).

Obviously, this only partially improves the accuracy of the SFR model because the dynamics of the excitation system itself are neglected, as well as the impact of generator model and terminal voltage dynamics. Furthermore, in a realistic bulk power system, not all generators are equipped with a PSS. This extreme example is used to illustrate that an excitation system equipped with a PSS can impact transient frequency dynamics during large disturbances. The factor α_i in Fig. 4.6 can be introduced to tune the PSS contribution to the SFR model more

77
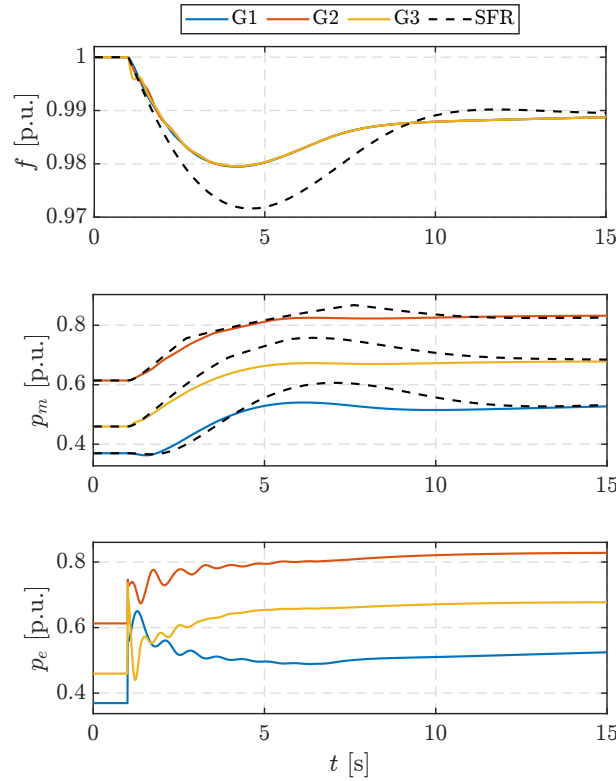
Figure 4.5: EMT vs. SFR model for simulating power system frequency (PSS enabled, but not considered in SFR model).

accurately. In this case, $\alpha_i = 1, \forall i$.

$$p_{e,i} = \frac{\|v_{e,i}\| \cdot \|v_{t,i}\|}{x_i} \sin \delta_i \Rightarrow \frac{\partial p_{e,i}}{\partial \|v_{e,i}\|} \propto \Delta v_{e,i} \tag{4.7}$$

$$v_{e,i} = f(v_{\text{pss},i}, v_{t,i}) \Rightarrow \Delta v_{e,i} \propto \Delta v_{\text{pss}} \text{ (assuming an LTI system)} \tag{4.8}$$

$$v_{\text{pss},i} = f(\omega_i) \Rightarrow \Delta v_{\text{pss}} \propto \Delta \omega_i \text{ (assuming an LTI system)} \tag{4.9}$$

The maximum relative error of frequency between EMT and SFR model is 0.2% in the case of disabled PSS, while in the case of enabled PSS without additional SFR model tuning, the error is 0.3%. In the worst-case scenario (PSS enabled, but not considered in the SFR model), the error is 0.8%. Regardless of the SFR model used (Fig. 4.4 or Fig. 4.6), there are two important conclusions which can be drawn from the SFR model regarding two characteristic operating points: (1) initial RoCoF ($t \rightarrow 0^+$) is also the maximum RoCoF and it depends only on the total system inertia and the size of the initial disturbance (see Eq.(4.10)), and (2) the post-disturbance steady-state ($t \rightarrow \infty$) frequency deviation depends only on the equivalent system droop and the size of the initial disturbance (see Eq. (4.11), where R'_i denotes that all individual droops are expressed on the common power base S_b). Equation (4.11) neglects turbine saturation, i.e., gate
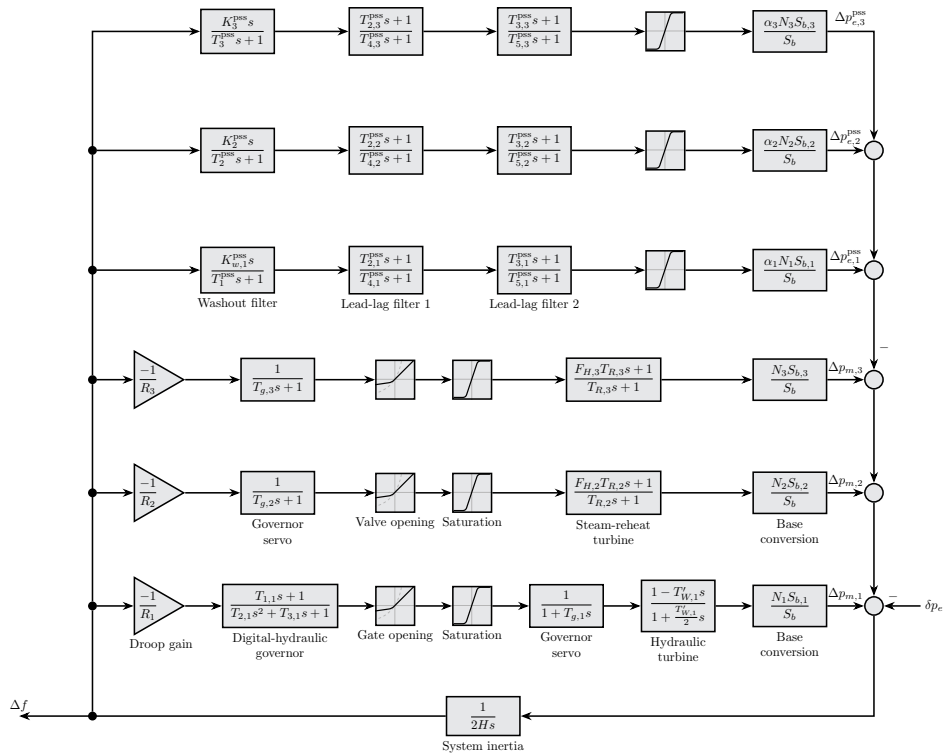
Figure 4.6: SFR model of a system consisting only of SGs (PSS enabled and considered in SFR model).
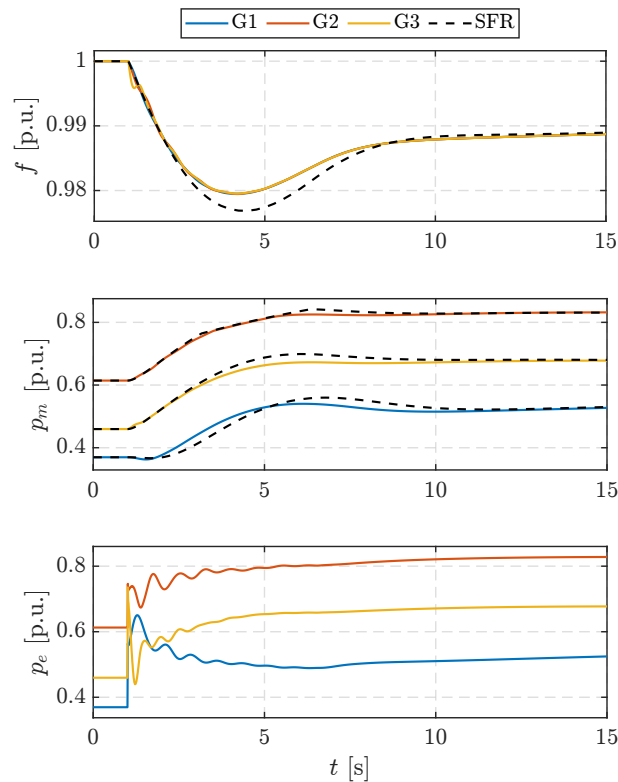
Figure 4.7: EMT vs. SFR model for simulating power system frequency (PSS enabled and considered in SFR model).

or valve maximum opening and closing, which will reduce the equivalent system droop.

$$\text{RoCoF}_{\text{max}} = \left.\frac{df}{dt}\right|_{t\to0^+} = \lim_{s\to\infty} s^2 \Delta f(s) = \frac{-\delta p_e}{2H} \tag{4.10}$$

$$\Delta f(t\to\infty) = \lim_{s\to0} s\Delta f(s) = \frac{-\delta p_e}{\sum_{i\in\mathcal{N}_{SG}} \frac{1}{R'_i}} \tag{4.11}$$

In between the two extreme operating points, $t \in (0^+, \infty)$, the frequency trajectory depends on all parameters and is too complicated to write analytically for any but the simplest systems [20].

4.2 Systems based on synchronous generators and frequency-dependent loads

Frequency-dependent loads are essentially synchronous motors and induction motors directly connected to the grid. Their contribution to the system frequency is two-fold: (1) they contribute to overall system inertia and (2) their electrical power consumption is inherently self-regulated to an extent, depending on the mechanical load characteristics.

A few things should be noted. Firstly, the most widespread type of AC drive is an induction motor due to its simplicity of construction. Large synchronous motors are not that common in the industry because starting-up is more complicated than for induction motors [167]. They can mostly be found in pumped-hydro plants for driving pumps or as synchronous condensers [167]. One of their benefits is reactive power control through the excitation, and they might see an increase of synchronous condenser application in the future for provision of inertia and short-circuit strength. Secondly, regardless of whether the drives are synchronous or induction, nowadays they are rarely being directly interfaced to grid because the speed is limited. Most applications require variable-speed drives so synchronous and induction motors are interfaced via frequency converters and essentially decoupled from the grid. Frequency converters also enable soft-starting and reactive power supply to the motor for magnetisation. Nevertheless, for the sake of completeness, we will cover both synchronous and induction motors directly interfaced to the power grid.

4.2.1 Synchronous motors

We start our analysis by replacing Load A and Load C with equivalent industrial plants each consisting of 10 synchronous motors. Plants are equivalent to Load A and Load C in terms of active and reactive power consumption in the initial load flow.

Table 4.2: Synchronous motor plant data.

Plant j	Type	Number of parallel machines N_j	Machine inertia H_j	Base power $S_{b,j}$	Mech. load torque t_m	Excitation	PSS
1	Syn.mot.	6	5 s	100 MW	$1 \cdot \omega^{\kappa}$	IEEET1S	-
2	Syn.mot.	10	5 s	100 MW	$0.6 \cdot \omega^{\kappa}$	IEEET1S	-

A synchronous motor uses the same model as a synchronous generator, the only difference being in the direction of power consumption: It consumes electrical power in order to drive a mechanical load. The mechanical swing equation of machine j in the motor mode is then (4.12), where H_j is the combined inertia of the motor and mechanical load.

$$2H_j\omega_j\frac{d\omega_j}{dt} = -p_{m,j}(t) + p_{e,j}(t) \tag{4.12}$$

Therefore, if mechanical power increases, the rotor will slow down. In a synchronous system, individual synchronous machine speeds do not vary significantly. Therefore, synchronous motor inertia can be simply added to the synchronous generator inertia (4.13):

$$H_{\mathrm{eq}} = H_{\mathrm{SG}} + H_{\mathrm{SM}} = \frac{\sum_{i\in\mathcal{N}_{\mathrm{SG}}} H_i S_{b,i}}{S_b} + \frac{\sum_{j\in\mathcal{N}_{\mathrm{SM}}} H_j S_{b,j}}{S_b} \tag{4.13}$$

where $\mathcal{N}_{\mathrm{SM}}$ is a set of online SGs. Motor self-regulation depends on the mechanical load torque characteristic which can be most simply modelled as a power function of speed:

$$t_{m,j} = T_0\omega_j^{\kappa} \tag{4.14}$$

where $T_0 \in \mathbb{R}_{\geq 0}$ is the proportional factor and $\kappa \in \mathbb{R}_{\geq 0}$ the exponential factor. Usually, T_0 is the torque at synchronous speed and $\kappa \in \{-1, 0, 1, 2\}$ depending on the load type as described by (4.15) and Fig. 4.8a. Constant power load (4.15a) has a torque inversely proportional to speed (e.g. paper rolling mills). In constant torque loads (4.15b), power varies linearly proportional to speed (e.g. cranes, elevators, conveyor belts). In linear torque loads (4.15c), power varies with the square of speed (e.g. eddy current brakes, smoothing machines). Finally, the most commonly found industrial loads are quadratic torque loads (4.15d) in which power varies with

the cube of speed (e.g. fans, centrifugal pumps, compressors).

$$t_m = T_0\omega^{-1} \Leftrightarrow p_m = T_0 \qquad \text{(Constant power)} \tag{4.15a}$$

$$t_m = T_0 \qquad \Leftrightarrow p_m = T_0\omega \qquad \text{(Constant torque)} \tag{4.15b}$$

$$t_m = T_0\omega \qquad \Leftrightarrow p_m = T_0\omega^2 \qquad \text{(Linear torque)} \tag{4.15c}$$

$$t_m = T_0\omega^2 \qquad \Leftrightarrow p_m = T_0\omega^3 \qquad \text{(Quadratic torque)} \tag{4.15d}$$

Therefore, in order to estimate how much motor consumption changes with its speed (in steady-state $p_m = p_e$), (4.15a)–(4.15d) can be linearised with respect to ω (4.16). Assuming $\omega_0 \approx \omega_s$ and $T_0 \in (0,1]$ p.u., D_{SM} varies between 0 and 3 p.u. Generally, if mechanical load torque is defined by (4.14), the self-regulation constant D_{SM} can be defined as (4.17).

$$\frac{\Delta p_e}{\Delta \omega} = \left.\frac{\partial p_m}{\partial \omega}\right|_{\omega_0} = D_{\mathrm{SM}} = \begin{cases} 0 & \text{(for constant power load)} \\ T_0 & \text{(for constant torque load)} \\ 2T_0\omega_0 & \text{(for linear torque load)} \\ 3T_0\omega_0^2 & \text{(for quadratic torque load)} \end{cases} \tag{4.16}$$

$$D_{\mathrm{SM}}(T_0, \kappa, \omega_0) = (\kappa + 1)T_0\omega_0^{\kappa} \tag{4.17}$$

In a strongly synchronised system, all individual synchronous machine speeds converge towards a uniform system frequency: $\omega_i, \omega_j \to \omega$ as $t \to \infty$. Let $D_{\mathrm{SM},j} \to D_j$. Then, $D_j\Delta\omega_j \to D_j\Delta\omega$. Then, the aggregated power of all synchronous motors equals (4.18).

$$\Delta p_m = \sum_{j\in\mathcal{N}_{\mathrm{SM}}} \Delta p_{m,j} = \Delta\omega \sum_{j\in\mathcal{N}_{\mathrm{SM}}} D_j = D\Delta\omega = D_{\mathrm{SM}}\Delta\omega \tag{4.18}$$
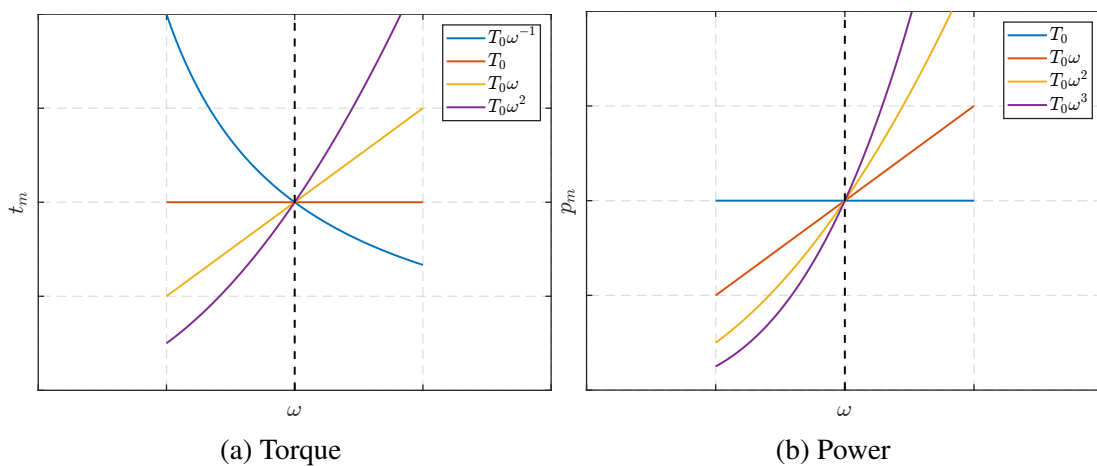
(a) Torque

(b) Power

Figure 4.8: Mechanical load torque/power characteristics. Dashed black line represents the synchronous motor torque/power characteristic.

Eq. (4.13) and Eq. (4.18) can be shown to be true in a similar way to (4.4)–(4.6). We start by summing (4.12) over the set of all synchronous motors $\mathcal{N}_{SM}$:

$$\sum_{j \in \mathcal{N}_{SM}} 2H_j \omega_j \frac{d\omega_j}{dt} = - \sum_{j \in \mathcal{N}_{SM}} p_{m,j}(t) + \sum_{j \in \mathcal{N}_{SM}} p_{e,j}(t) \tag{4.19}$$

Notice that the total generator power $\sum_{i \in \mathcal{N}_{SG}} p_{e,i}(t)$ from (4.4) must consist of total electrical power consumed by the synchronous motors and residual load p_e^R:

$$\sum_{i \in \mathcal{N}_{SG}} p_{e,i}(t) = \sum_{j \in \mathcal{N}_{SM}} p_{e,j}(t) + \sum_{i \in \mathcal{N}_{SG}} p_{e,i}^R(t) \tag{4.20}$$

where $p_{e,i}^R$ is the residual load of generator i that includes losses and other frequency-insensitive load share. Combining (4.4), (4.15), (4.19) and (4.20), we obtain (4.21):

$$\sum_{i \in \mathcal{N}_{SG}} 2H_i \omega_i \frac{d\omega_i}{dt} = \sum_{i \in \mathcal{N}_{SG}} p_{m,i}(t) - \left\{ \sum_{j \in \mathcal{N}_{SM}} 2H_j \omega_j \frac{d\omega_j}{dt} + \sum_{j \in \mathcal{N}_{SM}} T_{0,j} \omega_j^{\kappa_j+1} + \sum_{i \in \mathcal{N}_{SG}} p_{e,i}^R(t) \right\} \tag{4.21}$$

Assuming $\omega_i, \omega_j \to \omega, \forall i,k$ as $t \to \infty$ and rearranging (4.21) results in (4.22):

$$\omega \frac{d\omega}{dt} \left\{ \sum_{i \in \mathcal{N}_{SG}} 2H_i + \sum_{j \in \mathcal{N}_{SM}} 2H_j \right\} = \sum_{i \in \mathcal{N}_{SG}} p_{m,i}(t) - \sum_{i \in \mathcal{N}_{SG}} p_{e,i}^R(t) - \sum_{j \in \mathcal{N}_{SM}} T_{0,j} \omega^{\kappa_j+1} \tag{4.22a}$$

$$2(H_{SG} + H_{SM}) \omega \frac{d\omega}{dt} = p_m(t) - p_e^R(t) - \sum_{j \in \mathcal{N}_{SM}} T_{0,j} \omega^{\kappa_j+1} \tag{4.22b}$$

Linearising (4.22) around the initial operating point and converting to the Laplace domain yields (4.23), where $H_{SG} + H_{SM} = H$ per (4.13), $\sum_{j \in \mathcal{N}_{SM}} (\kappa_j + 1) T_{0,j} \omega_0^{\kappa_j} = D_{SM} = D$ per (4.18) and we dropped the superscript R for brevity $\Delta p_e^R(s) \to \Delta p_e(s)$. Eq. (4.23d) is the well-known form of the linearised swing equation for SFR studies.

$$2(H_{SG} + H_{SM}) s \Delta\omega(s) = \Delta p_m(s) - \Delta p_e^R(s) - \sum_{j \in \mathcal{N}_{SM}} (\kappa_j + 1) T_{0,j} \omega_0^{\kappa_j} \Delta\omega \tag{4.23a}$$

$$2(H_{SG} + H_{SM}) s \Delta\omega(s) = \Delta p_m(s) - \Delta p_e^R(s) - D_{SM} \Delta\omega \tag{4.23b}$$

$$\Delta\omega(s) = \frac{\Delta p_m(s) - \Delta p_e^R(s)}{2(H_{SG} + H_{SM}) s + D_{SM}} \tag{4.23c}$$

$$= \frac{\Delta p_m(s) - \Delta p_e(s)}{2Hs + D} \tag{4.23d}$$

Going back to our modified 9-bus system with 16 synchronous motors, we analyse the system responses for different types of mechanical loads on the motors. For simplicity, in each case all 16 motors will have the same load type. Nevertheless, if there was a mix of mechanical loads it would not impact the model because SFR is linear so the individual damping constants

would simply add up (4.23). Fig. 4.9 shows the grid frequency for different types of mechanical loads on the synchronous motors. It can be seen that higher κ is more beneficial for the system frequency because self-regulation is greater for those types of loads, i.e., centrifugal pumps are better for frequency dynamics than paper mills. As κ increases, RoCoF, nadir and steady-state deviation decrease.

Eq. (4.24) describes the steady-stage frequency deviation in the presence of synchronous motors. The contribution of synchronous motors to a decrease in steady-state frequency deviation is more clearly illustrated in Fig. 4.10. Obviously, loads that are more sensitive to frequency will have a larger change in their power consumption for the same frequency deviation. Strictly mathematically speaking, load self-regulation has the same effect as the turbine droop gain since these gains can be algebraically added. However, in practice $D << \sum_{i \in \mathcal{N}_{SG}} \frac{1}{R_i'}$ so the contribution is usually not significant compared to those of SGs with primary control action. Damping constant D has no effect on the initial RoCoF so the expression is the same as (4.10) (with motor inertia included in H). The power deviation of a single synchronous motor in plant 1 and plant 2 is shown in Fig. 4.11. Power is expressed on a single machine power rating. It can be seen that the reduction is larger for bigger κ. Moreover, as κ increases, so does the error between the SFR and nonlinear model.

$$\Delta f(t \to \infty) = \lim_{s \to 0} s\Delta f(s) = \frac{-\delta p_e}{\sum_{i \in \mathcal{N}_{SG}} \frac{1}{R_i'} + D} \tag{4.24}$$

4.2.2 Induction motors

The main difference compared to a synchronous machine is that the rotor is not excited through an external DC source. This means large reactive power is needed from the grid to induce a magnetic field in the air gap. Thus, the rotor of an induction motor will not rotate at the grid frequency, but at a slightly lower frequency in order to produce torque in the air gap. The
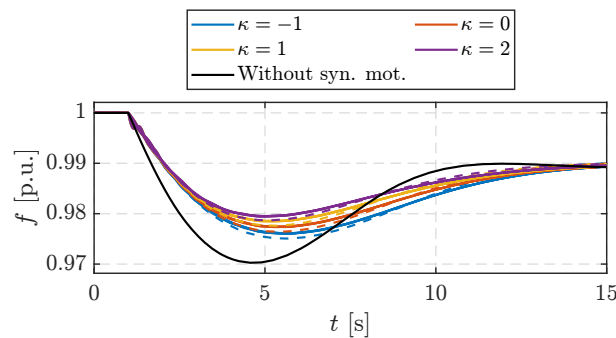
Figure 4.9: System frequency response for different types of synchronous motor mechanical loads. Dashed lines represent the corresponding response of SFR model.
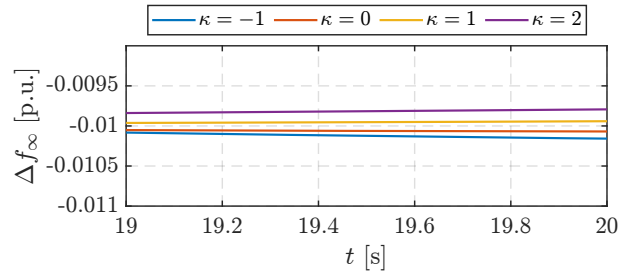
Figure 4.10: Steady-state frequency deviation for different types of synchronous motor mechanical loads.
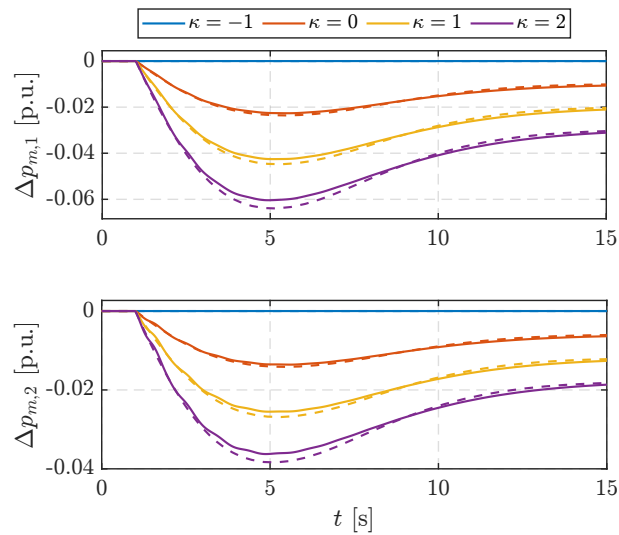
Figure 4.11: Reduction of synchronous motor power for a reduction in system frequency (syn. motor 1—top, syn. motor 2—bottom). Dashed lines represent the corresponding response of the SFR model.

relative difference between stator field mechanical angular frequency ω and rotor mechanical angular frequency ω_r is called the slip (4.25), usually denoted with s, but here we will denote it with σ not to confuse it with the Laplace operator.

$$\sigma = \frac{\omega - \omega_r}{\omega} \tag{4.25}$$

The two main types of induction machines are squirrel cage and wound rotor. The rotor of the former consists of short-circuited rotor bars resembling a cage. Rotor windings of the latter are connected in series with an external variable resistance. Both types of induction machines can be represented by the same single-cage model which is suitable for full-load studies [168], as shown by Fig. 4.12, where R_s, X_s are per-unit stator resistance and inductance, X_m is the per-unit magnetizing inductance, X_r' is the per-unit rotor inductance referred to the stator side and $\frac{R_r'}{\sigma} = R_r' + R_r'\frac{1-\sigma}{\sigma}$ is the per-unit slip-dependent variable rotor resistance.

The equivalent circuit shown in Fig. 4.12 is expressed in a dq frame rotating with the grid frequency $\omega^\bullet \to \omega$ in (2.12b) (i.e., speed of the reference machine in per-unit). Since X_s, X_m and X_r' are expressed on the nominal (base) frequency, terms ωX_s, ωX_m and $\omega X_r'$ account for the change of induction machine impedance due to a change in grid frequency during transient and quiescent states. Stator and rotor voltage and current space vectors are defined by (4.26), while the voltage equations of the equivalent circuit are defined by (4.27):

$$i_s = i_s^d + j i_s^q \tag{4.26a}$$

$$i_r' = i_r'^d + j i_r'^q \tag{4.26b}$$

$$u_s = u_s^d + j u_s^q \tag{4.26c}$$

$$u_r' = u_r'^d + j u_r'^q \tag{4.26d}$$

$$u_s = (R_s + j\omega X_s)\, i_s + j\omega X_m \left(i_s + i_r'\right) + \frac{1}{\omega_b}\frac{d}{dt}\left(\psi_s^d + j\psi_s^q\right) \tag{4.27a}$$

$$0 = \frac{u_r'}{\sigma} = \left(\frac{R_r'}{\sigma} + j\omega X_r'\right) i_r + j\omega X_m \left(i_s + i_r'\right) + \frac{1}{\omega_b\sigma}\frac{d}{dt}\left(\psi_r'^d + j\psi_r'^q\right) \tag{4.27b}$$

where ψ_s^d, ψ_s^q, $\psi_r'^d$, $\psi_r'^q$ are stator and rotor flux linkages per second (since the equations are
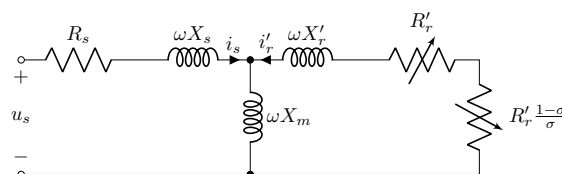
Figure 4.12: Single cage induction motor equivalent electric circuit with rotor variables referred to the stator side.

described in terms of reactances instead of inductances, so flux linkages become flux linkages per second, which are in this case in per-unit voltage units):

$$\psi_s^d = X_s i_s^d + X_m \left(i_s^d + i_r'^d \right) \tag{4.28a}$$

$$\psi_s^q = X_s i_s^q + X_m \left(i_s^q + i_r'^q \right) \tag{4.28b}$$

$$\psi_r'^d = X_r i_r'^d + X_m \left(i_s^d + i_r'^d \right) \tag{4.28c}$$

$$\psi_r'^q = X_r i_r'^q + X_m \left(i_s^q + i_r'^q \right) \tag{4.28d}$$

In Fig. 4.12, $\frac{R_r'}{\sigma}$ is split into R_r' and $R_r' \frac{1-\sigma}{\sigma}$ because $\|i_r'\|^2 R_r'$ represents rotor resistance loss which does not participate in the electromechanical conversion. Therefore, $\|i_r'\|^2 R_r' \frac{1-\sigma}{\sigma}$ represents the electrical power that drives the shaft. Finally, the electromagnetic torque developed by the induction motor is (4.29):

$$t_e = \frac{p_e}{\omega_r} = \|i_r'\|^2 R_r' \frac{1-\sigma}{\sigma} \frac{1}{\omega_r} = \|i_r'\|^2 \frac{R_r'}{\sigma \omega} \tag{4.29}$$

where $\|i_r'\|^2$ in steady-state can be expressed via stator voltage u_s (by setting flux transients to zero):

$$\|i_r'\|^2 = \frac{\|u_s\|^2}{\left(K_r R_s + K_s \frac{R_r'}{\sigma} \right)^2 + \left(\omega X_s - \frac{R_s R_r'}{\omega X_m \sigma} + K_s \omega X_r' \right)^2} \tag{4.30}$$

where K_s and K_r are defined as:

$$K_s = \frac{X_s + X_m}{X_m} \tag{4.31a}$$

$$K_r = \frac{X_r + X_m}{X_m} \tag{4.31b}$$

Finally, by replacing $\|i_r'\|^2$ in (4.29) with (4.30), (4.29) becomes (4.32) which is equivalent to similar, but more well-known expressions in [106, 115, 167]:

$$t_e = \frac{p_e}{\omega_r} = \frac{\|u_s\|^2}{\left(K_r R_s + K_s \frac{R_r'}{\sigma} \right)^2 + \left(\omega X_s - \frac{R_s R_r'}{\omega X_m \sigma} + K_s \omega X_r' \right)^2} \frac{R_r'}{\sigma \omega} \tag{4.32}$$

Induction machine rotor acceleration is described by the swing equation:

$$2 H_{\text{IM}} = t_e - t_m = \frac{p_e - p_m}{\omega_r} \tag{4.33}$$

where H_{IM} is the combined inertia constant of the induction machine and mechanical load, and t_m is the mechanical load torque characteristic identical to the one described for synchronous motors (4.15).

Finally, the total active power drawn from the grid by the induction motor is the sum of mechanical power and rotor and stator losses:

$$p_{\text{IM}} = p_e + p_{r,\text{loss}} + p_{s,\text{loss}} = \|i'_r\|^2 R'_r \frac{1-\sigma}{\sigma} + \|i'_r\|^2 R'_r + \|i'_s\|^2 R'_s \qquad (4.34)$$

Fig. (4.13) shows the torque-speed characteristic for different values of R'_r. Compared to a synchronous motor which can provide any desired torque at the synchronous speed, the induction motor torque has a lower gradient meaning that a change in machine speed results in smaller changes of electromagnetic torque. Fig. 4.13 shows that the greater the R'_r, the greater the change in rotor speed for the same change of load torque. On the one hand, allowing the rotor to speed up or slow down more reduces the induced currents and mechanical forces. On the other hand, it significantly increases losses which is why induction motors are designed to operate at low slip $< 5\%$ to achieve high efficiency. Old Type 1 WTGs which employ squirrel cage induction generators experienced large mechanical strains on the whole turbine-generator structure during wind gusts because the rotor could not speed up significantly. Therefore, Type 2 WTGs use variable slip technology by inserting a variable resistance in the rotor circuit of a wound rotor induction generator on the account of increased losses. Both are now phased out by Type 3 and Type 4 WTGs which use power electronic converters to decouple the rotor from the grid and achieve variable speed operation.

Fig. 4.14 shows that a change of grid frequency ω shifts the torque-speed characteristic left or right while also scaling the magnitude (assuming constant stator voltage). By observing Fig. 4.13 and Fig. 4.14, one can deduce that the value of R'_r will dictate the magnitude of inertial response of an induction machine which is more clearly illustrated in Fig. 4.15. Let the load torque be constant and equal to $t_m = 1$ p.u. as shown by the solid black line. IM with R'_r operates in point A with $\omega_r = 0.99$ p.u. and 1% slip on the characteristic shown by the solid blue line. If the grid frequency suddenly changes from $\omega = 1.00$ p.u. to $\omega = 0.99$ p.u., the IM jumps to point
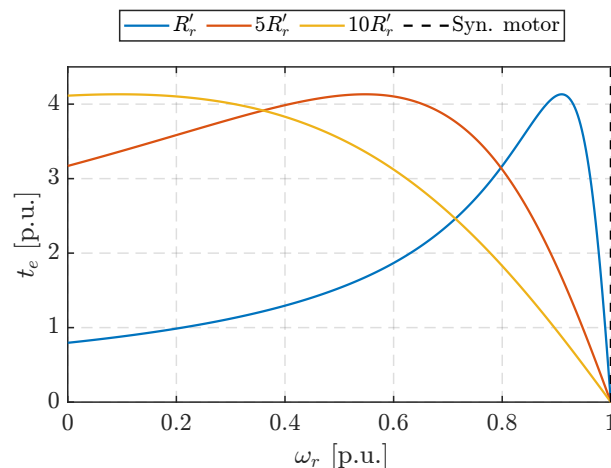
Figure 4.13: Induction motor torque-speed characteristic for different values of R'_r.
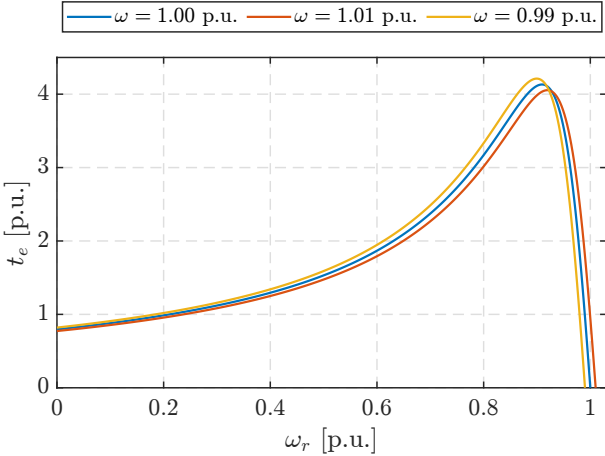
Figure 4.14: Induction motor torque-speed characteristic for different values of grid frequency ω.
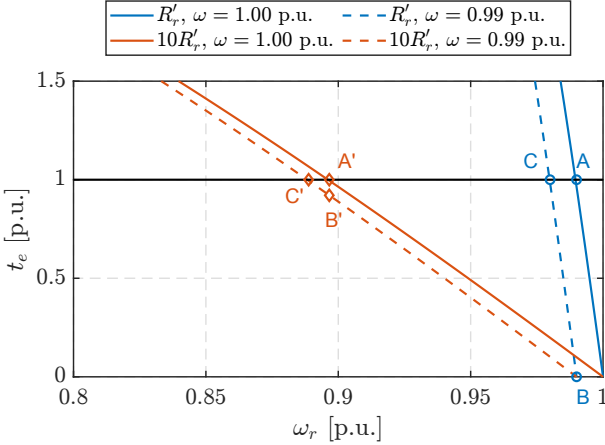
Figure 4.15: Induction motor torque-speed characteristic for different values of ω and R'_r.

B on the dashed blue line with $\omega_r = 0.99$ and $t_e = 0$ (because the rotor speed cannot change instantaneously due to inertia). At point B, the electromagnetic torque is smaller than the load torque so the rotor slows down and the speed increases until it stabilizes in point C with $t_e = 1$ p.u. and $\omega_r = 0.98$ p.u. On the other hand, IM with $10R'_r$ initially operates in point A' with $\omega_r \approx 0.9$ p.u. and 10% slip. After a step reduction of the grid frequency, the electromagnetic torque moves to point B' with $\omega_r \approx 0.9$ p.u. and $t_e \approx 0.92$ p.u. before stabilizing in point C' with $\omega_r \approx 0.89$ p.u. Clearly, $\Delta T_{AB} \gg \Delta T_{A'B'}$ and $\Delta \omega_{rAC} \approx \Delta \omega_{rA'C'}$. Since $\Delta P_e = T_0 \Delta \omega_r + \omega_{r0} \Delta T$, and immediately after a disturbance $\Delta \omega_r = 0$, it follows:

$$\frac{\Delta P}{\Delta P'} = \frac{\omega_{rA} \Delta T_{AB}}{\omega_{rA'} \Delta T_{A'B'}} \gg 1 \tag{4.35}$$

i.e., IM with a lower rotor resistance R'_r has a stronger inertial response following a grid frequency disturbance (larger initial change of power), but it also reaches the new steady-state speed faster.

By neglecting stator impedance, magnetizing reactance and rotor reactance, and assuming $\|u_s\| = \text{const.}$, the initial response ratio (4.35) can be further simplified to:

$$\frac{\Delta P}{\Delta P'} \approx \frac{R''_r}{R'_r} \frac{\omega_{rA} (2\omega_{rA} - 1)}{\omega_{rA'} (2\omega_{rA'} - 1)} \approx \frac{R''_r}{R'_r} \tag{4.36}$$

that is, IM response to a change in grid frequency is inversely proportional to its rotor resistance. In this particular case, $\frac{\Delta P}{\Delta P'} \approx \frac{10R'_r}{R'_r} = 10$. Fig 4.16 illustrates the time-domain response of synchronous and induction motors to a step decrease of infinite bus frequency. Clearly, the synchronous machine has the strongest response followed by the induction machine with small R'_r, and then by the induction machine with the largest $R'r$.

If we replace the infinite bus with a synchronous turbine-generator, the responses will be as shown in Fig. 4.17. Maximum RoCoF ($t = 0^+$) is lowest in the system with the synchronous motor, followed by the induction motor with a small R'_r, and then by the induction machine with the largest $R'r$. Interestingly enough, as time goes on post-disturbance, the frequency nadir is slightly better for the system with the bigger R'_r IM since a larger slip allows for a longer reduction of transient power consumption (Fig. 4.16). One could conclude from Fig. 4.17 that induction motors contribute to the initial RoCoF, however, that is not the case: as will be shown later, induction motors in the power grid behave as a combination of a low-pass and a high-pass filter and as such do not have impact on $t = 0^+$ because of their inherent time lag caused by the slip.

Consider the generic IM torque expression (4.32). If we neglect stator resistance ($R_s \to 0$) and assume $R'_r \sigma^{-1} \gg \omega X_s + K_s \omega X'_r$ which is generally true for low slip around synchronous
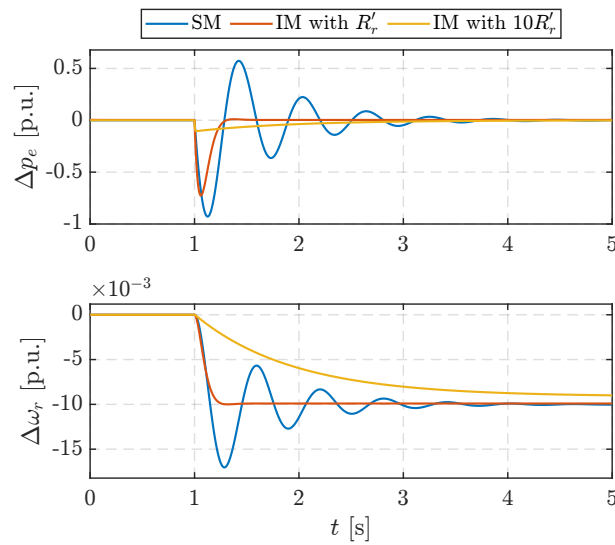
Figure 4.16: Synchronous vs. induction motor electric power (top) and rotor speed (bottom) deviation following a step reduction of infinite bus frequency.
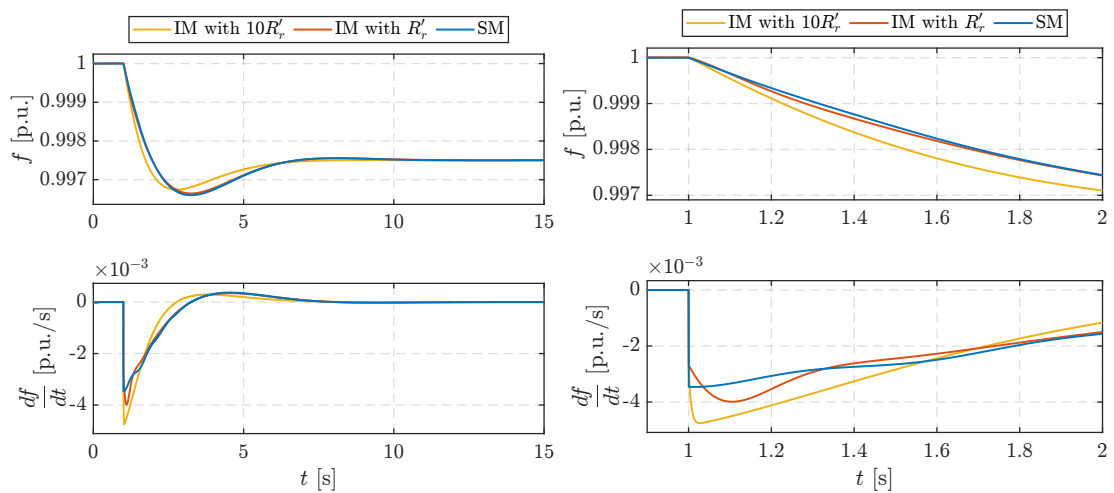
(a) Frequency (top) and RoCoF (bottom)

(b) Detail of 4.17a for $t \in [1,2]$ s

Figure 4.17: Frequency and RoCoF of a two-machine system with synchronous/induction motor and a synchronous turbine-generator.

frequency, p_e and t_e can then be approximated as:

$$p_e \approx \frac{\|u_s\|^2}{\frac{R'_r K_s}{\sigma}} \frac{1-\sigma}{\sigma} = \frac{\|u_s\|^2}{K_s^2 R'_r} \sigma (1-\sigma) = K_p \frac{\omega_r \omega - \omega_r^2}{\omega^2} \quad (4.37a)$$

$$t_e = p_e \omega_r^{-1} \approx K_p \frac{\omega - \omega_r}{\omega^2} \quad (4.37b)$$

where $K_p = \|u_s\|^2 K_s^{-2} R'_r{}^{-1}$. Since in practice $\|u_s\| \approx 1$ p.u. and $K_s = (X_m + X_s) X_m^{-1} \approx 1$ because $X_m \gg X_s$, K_p can be further simplified to $K_p \approx R'_r{}^{-1}$. Furthermore, total electrical power (4.34) is approximately equal to the sum of mechanical power and rotor losses:

$$p_{\mathrm{IM}} \approx p_e + p_{r,\mathrm{loss}} \approx K_p \frac{\omega - \omega_r}{\omega} \quad (4.38)$$

Error introduced by the simplification (4.37a) compared to a full characteristic (4.32) is $\approx 5\%$ around the rated speed regardless of R'_r as shown by Fig. 4.18.

With these approximations, we can write the simplified induction motor swing equation:

$$2H_{\mathrm{IM}} \omega_r \frac{d\omega_r}{dt} = p_e - p_m(\omega_r) \quad (4.39a)$$

$$= K_p \frac{\omega - \omega_r}{\omega^2} - p_m(\omega_r) \quad (4.39b)$$

where it can be seen more clearly how the IM rotor speed dynamics are a function of both rotor speed ω_r and grid frequency ω, assuming constant terminal voltage: $\dot{\omega}_r = f(\omega_r, \omega)$. Linearising (4.39a) and (4.37a) around $\{\omega_{r0}, \omega_0 \approx 1.0\}$ yields in the Laplace domain:

$$2H_{\mathrm{IM}} \omega_{r0} s \Delta \omega_r = K_p \left[(1 - 2\omega_{r0}) \Delta \omega_r + \omega_{r0} (2\omega_{r0} - 1) \Delta \omega_s \right] - D_{\mathrm{IM}} \Delta \omega_r \quad (4.40)$$

where $\Delta p_m = D_{\mathrm{IM}} \Delta \omega_r$ and D_{IM} depends on the mechanical load characteristic analogously to (4.16), where the initial synchronous speed ω_0 is replaced by the initial IM speed ω_{r0}. After

(a) $R'_r = 0.01$ p.u. (b) $R'_r = 0.1$ p.u.
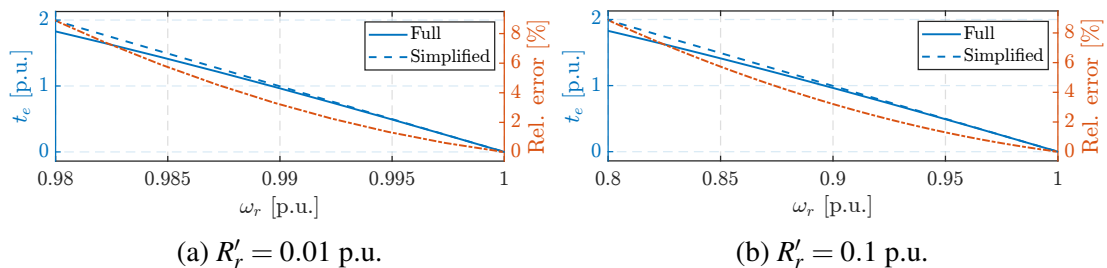
Figure 4.18: Full torque characteristic vs. simplified torque characteristic (Blue lines and left y-axis) and relative error (orange line and right y-axis).

algebraic manipulation, $\Delta\omega_r$ can be written as a function of grid frequency $\Delta\omega$:

$$\Delta\omega_r(s) = \frac{KD_s\Delta\omega}{2H_{\text{IM}}\omega_{r0}s + (KD_r + D_{\text{IM}})} \tag{4.41}$$

where coefficients D_s and D_r are defined as:

$$D_r = 2\omega_{r0} - 1 \qquad D_s = \omega_{r0}D_r = \omega_{r0}(2\omega_{r0} - 1) \tag{4.42}$$

Therefore, eq. (4.41) tells us that the IM acts as a low-pass filter to grid frequency where the time constant $T_{\text{IM}} = \frac{2H_{\text{IM}}\omega_{r0}}{KD_r + D_{\text{IM}}}$ and $K_{\text{IM}} = \frac{KD_s}{KD_r + D_{\text{IM}}}$ depend on the initial speed ω_{r0}, rotor resistance R'_r and mechanical load type D_{IM}. Comparing (4.23) and (4.41) one can see that just as the grid frequency cannot change instantaneously due to a step load disturbance because of synchronous inertia, the rotor speed of an induction machine cannot change instantaneously due to a step frequency disturbance because of IM inertia, i.e., the response of IM speed to a load disturbance in the grid is governed by a second order behaviour.

Fig. 4.19 shows the accuracy of the developed IM SFR model for a step change in grid frequency for an IM with constant mechanical power load. It can be seen that the SFR model accurately represents the rotor speed deviation with negligible error. On the other hand, electrical power deviation in the transient period is accurate for the IM with the larger R'_r with negligible error, while inaccurate for the model with the small R'_r with a relative error of 37.5% for the maximum power deviation ($R'_r = 0.01$ p.u. in this case). This is because the linearisation of (4.38) around $\{\omega_{r0}, \omega_0 \approx 1.0\}$ yields $\Delta p_{\text{IM}} = K(\omega_{r0}\Delta\omega - \Delta\omega_r)$ and since rotor speed cannot change instantaneously due to inertia, it follows that at $t = 0^+$ $\Delta p_{\text{IM,max}} = K\omega_{r0}\Delta\omega$, i.e., there is no time lag associated with the power change which is proportional to the step change in grid frequency. However, the power cannot change instantaneously because the rotor current cannot change instantaneously due to rotor inductance. And since the IM rotor is essentially a series RL circuit, the time constant L'_r/R'_r is larger for a small R'_r and smaller for a large R'_r enough so that the error of the described linear model increases significantly as R'_r decreases; e.g., for $X'_r = 0.1$ p.u. L'_r/R'_r is approximately 0.03 s and 0.003 s for $R'_r = 0.01$ p.u and $R'_r = 0.1$ p.u, respectively. Nevertheless, this error will not be relevant in an actual system because grid frequency will never change in a stepwise manner due to synchronous inertia, and so the IM power change will be accurate enough regardless of the rotor resistance, as will be shown later.

Figure 4.20 shows how T_{IM} and K_{IM} depend on ω_{r0}, R'_r and D_m. It can be seen that a larger rotor resistance and slower initial speed increase the effective IM time constant (Fig. 4.20a), while K_{IM} is linearly proportional to speed (Fig. 4.20a). Increasing the dependence of mechanical load on the rotor speed decreases the time constant and gain (Fig. 4.20b).

To derive the contribution of IM to system frequency dynamics, we start with an equivalent SG representing the grid with equivalent inertia H and damping $D = 0$ powering an equally
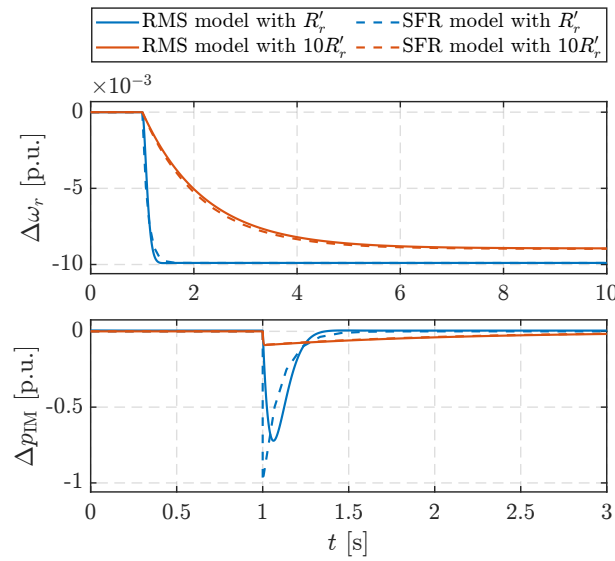
Figure 4.19: RMS vs. SFR induction machine model for different R'_r and a step change in synchronous frequency: rotor speed change (top) and electrical power change (bottom).

(a) varying R'_r and fixed D_m (b) fixed R'_r and varying D_m
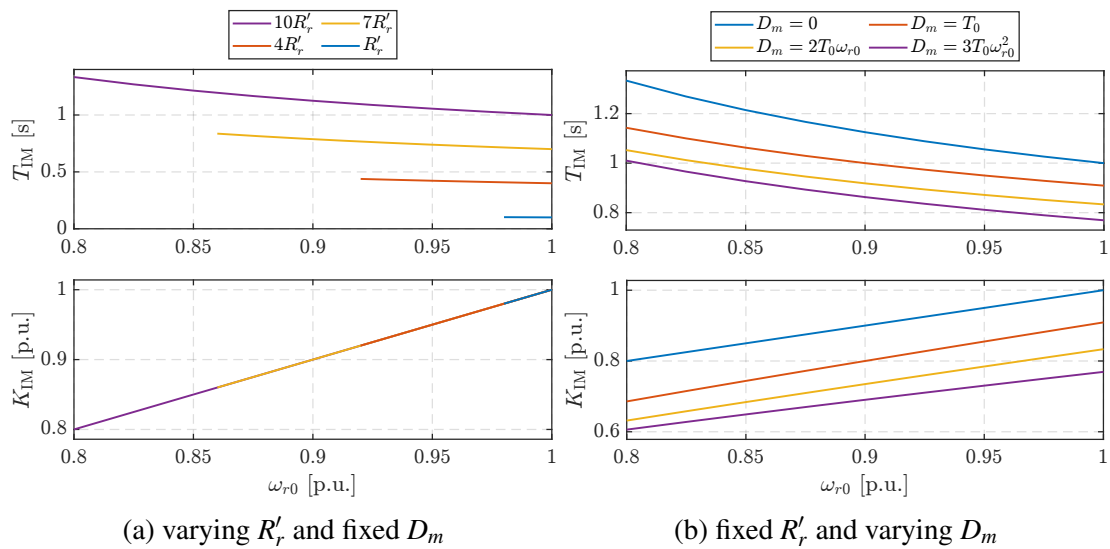
Figure 4.20: Dependence of T_{IM}, K_{IM} on: ω_{r0}, R'_r and D_m.

rated IM with the inertia constant H_{IM}. The swing equation can be written as:

$$2H\omega\frac{d\omega}{dt} = p_m(t) - p_e(t) \tag{4.43}$$

where p_e is the sum of the total IM power p_{IM} (4.38) and an external load disturbance $\Delta p_e(t)$. Note that the IM shaft power can be expressed as $2H_{\mathrm{IM}}\omega_r\frac{d\omega_r}{dt} + p_m(\omega_r)$ based on (4.39a). Therefore:

$$2H\omega\frac{d\omega}{dt} = p_m(t) - \Delta p_e(t) - \left(2H_{\mathrm{IM}}\omega_r\frac{d\omega_r}{dt} + p_m(\omega_r) + p_{r,\mathrm{loss}}\right) \tag{4.44}$$

Linearising (4.44) around ω_{r0} and $\omega_0 = 1$ and transforming it into the frequency domain yields:

$$2Hs\Delta\omega(s) = \Delta p_m(s) - \Delta p_e(s) - \left(2H_{\mathrm{IM}}\omega_{r0}s\Delta\omega_r + D_{\mathrm{IM}}\Delta\omega_r + \Delta p_{r,\mathrm{loss}}(s)\right) \tag{4.45}$$

where:

$$p_{r,\mathrm{loss}} = K_p\left(\frac{\omega - \omega_r}{\omega}\right)^2 \Rightarrow \Delta p_{r,\mathrm{loss}} = 2K_p(1-\omega_{r0})\left[\omega_{r0}\Delta\omega - \Delta\omega_r\right] = K_pD_{\mathrm{loss}}\left[\omega_{r0}\Delta\omega - \Delta\omega_r\right] \tag{4.46}$$

Combining (4.45), (4.46) and expressing $\Delta\omega_r(s) = f(\Delta\omega(s))$ from (4.41) we arrive to a final expression for IM contribution to grid frequency dynamics after some algebraic manipulation:

$$\Delta\omega(s) = \frac{\Delta p_m(s) - \Delta p_e(s)}{2Hs + K_pD_{\mathrm{loss}}\omega_{r0} + K_pD_s\dfrac{2H'_{\mathrm{IM}}s + D''}{2H'_{\mathrm{IM}}s + 1}} \tag{4.47}$$

where:

$$H'_{\mathrm{IM}} = H_{\mathrm{IM}}\frac{\omega_{r0}}{K_pD_r + D_{\mathrm{IM}}} \qquad D'' = \frac{D_{\mathrm{IM}} - K_pD_{\mathrm{loss}}}{K_pD_r + D_{\mathrm{IM}}}$$

$$D_r = 2\omega_{r0} - 1 \qquad D_s = \omega_{r0}D_r = \omega_{r0}(2\omega_{r0} - 1) \qquad D_{\mathrm{loss}} = 2(1 - \omega_{r0})$$

$$D_{\mathrm{IM}} = (\kappa + 1)T_0\omega_{r0}^\kappa$$

$$K_p \approx R_r'^{-1} \tag{4.48}$$

Table 4.3 provides a standard range of parameter values for a fully loaded IM (operating under rated torque $t_e \approx 1$ p.u.) where it holds $\|R_r'\| \approx \|1 - \omega_{r0}\|$.

Eq. 4.47 shows that an IM acts as a combination of a low-pass filter and a high-pass filter in which the terms $K_pD_{\mathrm{loss}}\omega_{r0}$, $K_pD_s\frac{2H'_{\mathrm{IM}}s}{2H'_{\mathrm{IM}}s+1}$, and $K_pD_s\frac{D''}{2H'_{\mathrm{IM}}s+1}$ describe the change in motor power loss due to a change in system frequency, the change in motor power due to an inertial response and the change in motor power due to a change in rotor speed, respectively. It can be

Table 4.3: Standard range of induction motor system frequency response model parameters.

R'_r	K_p	$\dfrac{\omega_{r0}}{K_pD_r+D_{\text{IM}}}$	D''	$K_pD_{\text{loss}}\omega_{r0}$	K_pD_s
0.01	100.0	0.0098–0.010	-0.02–0.010	1.98	97.0
0.025	40.0	0.024–0.026	-0.053–0.021	1.95	37.0
0.05	20.0	0.045–0.053	-0.111–0.034	1.9	17.0
0.075	13.0	0.066–0.082	-0.176–0.041	1.85	10.5
0.1	10.0	0.086–0.1125	-0.25–0.041	1.8	7.2

shown that the following is true:

$$\Delta\omega\left(t=0^+\right)=\lim_{s\to\infty}s^2\Delta\omega(s)=\frac{\Delta p_m-\Delta p_e}{2H} \tag{4.49}$$

$$\Delta\omega\left(t\to\infty\right)=\lim_{s\to0}s\Delta\omega(s)=\frac{\Delta p_m-\Delta p_e}{K_pD_{\text{loss}}\omega_{r0}+K_pD_sD''}$$

$$=\frac{\Delta p_m-\Delta p_e}{\dfrac{D_{\text{IM}}}{K_pD_r+D_{\text{IM}}}\left(K_pD_{\text{loss}}\omega_{r0}+K_pD_s\right)}$$

$$\approx\frac{\Delta p_m-\Delta p_e}{D_{\text{IM}}} \tag{4.50}$$

$$\tag{4.51}$$

Therefore, there is no contribution of induction machines to initial RoCoF, while the contribution in post-disturbance steady-state approximately depends on the mechanical load coefficient just like for the synchronous motors. In the transient period, IM's effect is similar to that of synchronous generators.

To verify the derived IM SFR model, consider the same model as in 4.2.1 where the two synchronous motors are replaced by equivalent induction motors in terms of inertia and active power consumption in the initial load flow. The motors are loaded by a constant power load. First, Fig. 4.21 shows the differences in system frequency response between synchronous and induction motors compared to the base case with no frequency sensitive loads. Fig. 4.21 (top) shows that during the initial decline, the system with synchronous motors has the smallest gradient, followed closely by the IM with smallest R'_r (insignificant difference), then by the IM with largest R'_r. This is further illustrated by Fig. 4.21 (middle) and Fig. 4.21 (bottom): in the initial moments after the disturbance there is no difference between the cases with IM and the case with no motors (visible around 1.004 s mark). Then, after the initial electromagnetic transients diminish after around 100 ms, it is clearly visible how the smallest RoCoF is for the

case with SM, then IM with small R'_r followed by the IM with large R'_r and then finally the base case. In terms of nadir, the contribution of IM is similar to that of SM since enough time has passed after the disturbance for IM electromechanical dynamics to play into account: The case with small R'_r has a slightly larger nadir than the case with SM, while the case with large R'_r has a slightly smaller nadir than the case with SM, but the differences are negligible (absolute difference is in the range $2.7 \cdot 10^{-4}$–$8.2 \cdot 10^{-4}$ p.u./s or 15–40 mHz/s).

Fig. 4.22 and Fig. 4.23 show that the developed SFR model of an induction machine accurately represents the full EMT model in a large power system, although the SFR model of an IM with a large R'_r (Fig. 4.23) has a bigger speed deviation absolute error in steady-state of about $1 \cdot 10^{-3}$ p.u., yet it is not relevant for the system response, as shown in the grid frequency plots of Fig. 4.22 and Fig. 4.23.

Finally, (4.47) can be generalised for an arbitrary number of IMs:

$$\Delta\omega(s) = \frac{\Delta p_m(s) - \Delta p_e(s)}{2Hs + \sum_{k \in \mathcal{N}_{\mathrm{IM}}} K_{p,k} D_{\mathrm{loss},k} \omega_{r0,k} + \sum_{k \in \mathcal{N}_{\mathrm{IM}}} K_{p,k} D_{s,k} \dfrac{2H'_{\mathrm{IM},k}s + D''_k}{2H'_{\mathrm{IM},k}s + 1}} \tag{4.52}$$

where $\mathcal{N}_{\mathrm{IM}}$ is the set of all induction machines in the system. A block diagram of an SFR model of a system with synchronous and induction motors is shown in Fig. 4.24, where H, D are the inertia and damping of synchronous generators and motors, respectively. $K^{\mathrm{IM}}_{1,k} = K_{p,k} D_{s,k}$ and $K^{\mathrm{IM}}_{2,k} = K_{p,k} D_{\mathrm{loss},k} \omega_{r0,k}$ per (4.52), $k \in \{1...\|\mathcal{N}_{\mathrm{IM}}\|\}$.
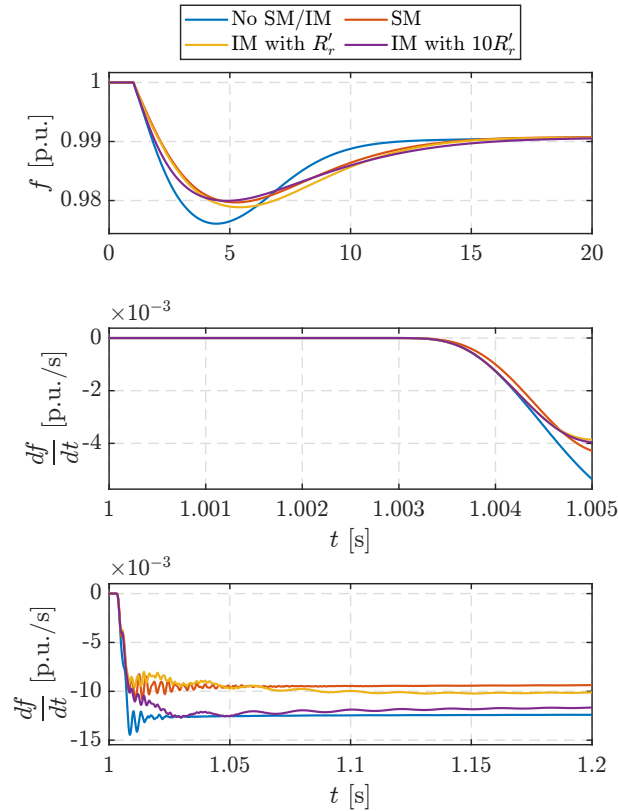
Figure 4.21: Impact of synchronous and induction machines on centre-of-inertia frequency (top) and centre-of-inertia RoCoF (middle, bottom).
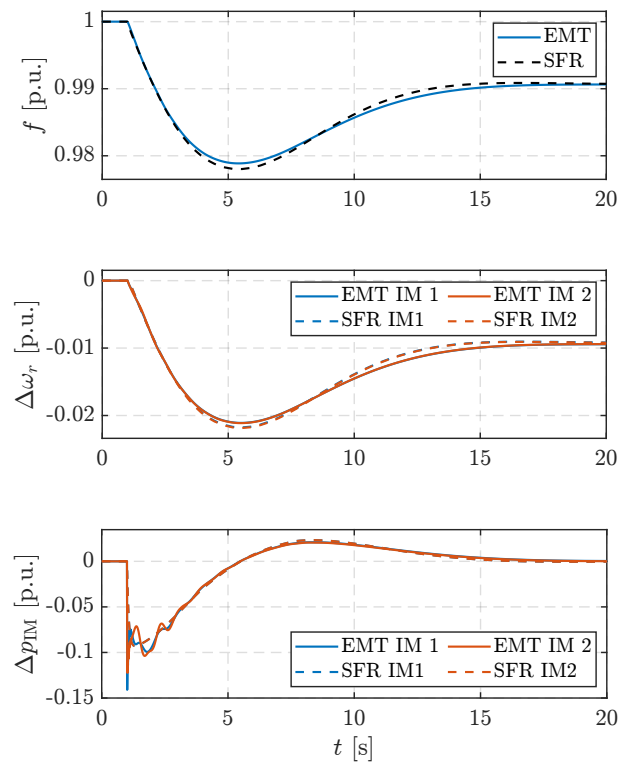
Figure 4.22: EMT vs. SFR model of a system with induction motors with $R'_r = 0.01$ p.u.: system frequency (top), IM speed deviation (middle) and IM power response (bottom).
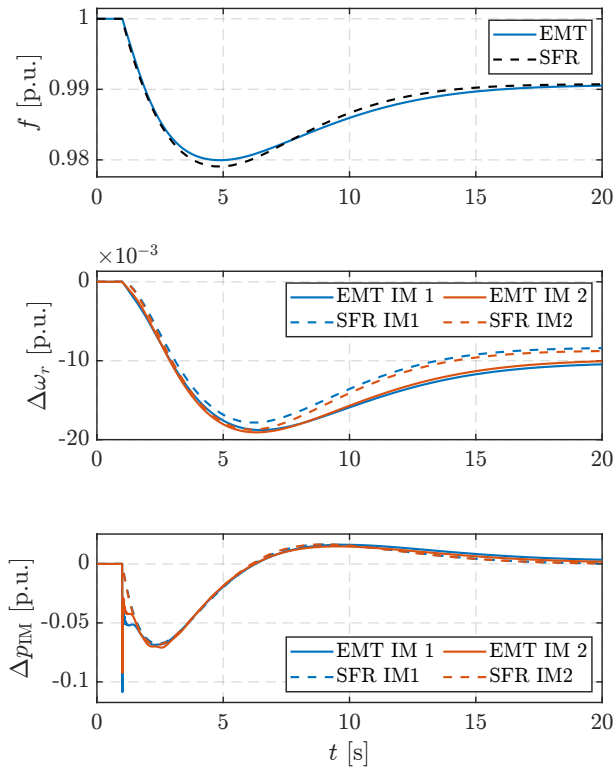
Figure 4.23: EMT vs. SFR model of a system with induction motors with $R'_r = 0.1$ p.u.: system frequency (top), IM speed deviation (middle) and IM power response (bottom).
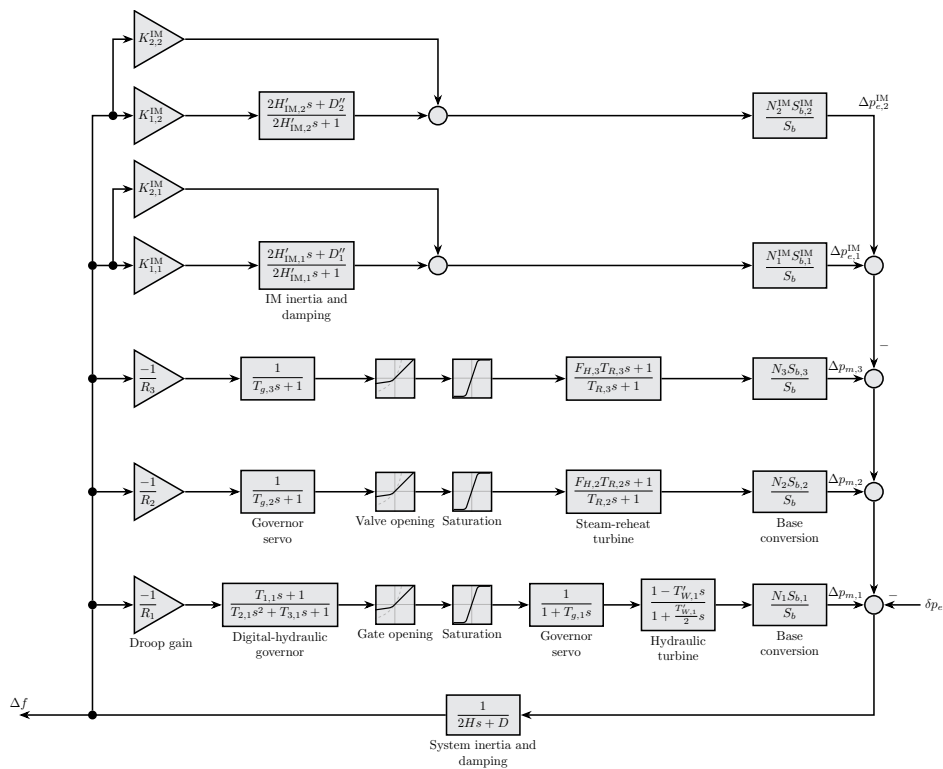
Figure 4.24: SFR model of a system consisting of SGs, SMs and IMs.

4.3 Systems based on synchronous generators and grid-following converters with a controlled device-side power source

Here, we will analyse the most common representation of CID in system frequency dynamic studies. Characteristics of the energy conversion system (Fig. 3.2) are neglected and ECS+DSC are replaced by a controlled power (current) source as shown in Fig. 3.7a.

The PLL will have a significant impact on overall system stability and performance. The majority of literature assumes perfect frequency tracking, but the reality is more complicated than that. Consider a converter providing only frequency droop control $p^\star + \Delta p^\star \rightarrow p^\star - R^{-1}(\omega^\star - \omega_n)$, where $\omega^\star := \omega_{\text{PLL}}$. In one case, PLL PI gains are tuned to $K_p = 100$ p.u. and $K_i = 300$ p.u. (referred to as fast PLL), while in the other case $K_p = 10$ p.u. and $K_i = 30$ (referred to as slow PLL). There is an outage of generator G4 at $t = 1$ s.

Fig. 4.25 shows that in the RMS simulation both the slow and fast PLL behave identically and track the frequency quickly. However, the EMT simulation actually shows unstable behaviour for the fast PLL. Moreover, the EMT simulation for the slow PLL shows brief oscillations due to an oscillation of the PCC voltage. Therefore, the RMS simulation shows a larger tolerance to a higher PLL bandwidth. Fig. 4.26 shows the impact of PLL gains for various penetration levels η_c of grid-following converters providing droop control: $\eta_c = \{26\%, 41\%, 51\%, 59\%, 71\%, 93\%\}$, where η_c is defined as:

$$\eta_c = \frac{\sum_{l \in \mathcal{N}_{\text{GfC}}} S_{b,l}}{\sum_{l \in \mathcal{N}_{\text{GfC}}} S_{b,l} + \sum_{i \in \mathcal{N}_{\text{SG}}} S_{n,i}} \tag{4.53}$$

where $\mathcal{N}_{\text{GfC}}$ is the set of grid-following converters, and $S_{b,l}$ is the rated power of each converter.

It can be seen that too aggressive PLL tuning results in frequency oscillations before the disturbance even happens, which is visible only in the EMT simulations (right side of Fig. 4.26), and in frequency instability for $\eta_c = 93\%$. On the other hand, all RMS simulations are stable.

Next, we replace the droop control with virtual inertia control $p^\star + \Delta p^\star \rightarrow p^\star - 2H_v \frac{d}{dt}(\hat{\omega}^\star - \omega_n)$, where $\hat{\omega}^\star = \frac{\omega^\star}{T_f s + 1}$ is the low-pass filtered PLL frequency because an ideal derivative cannot be practically implemented. Additionally, a time derivative is an operation that inherently amplifies small disturbances and reduces stability. Fig. 4.27 (top) shows that for the same PLL gains $K_p = 10$ and $K_p = 30$ for which the droop control is stable, the virtual inertia controlled converter is unstable for $T_f = 10$ ms, i.e., a bandwidth of 100 Hz. For the converter to be stable (Fig. 4.27 bottom) with the same PLL gains, the bandwidth of the low-pass filter needs to be reduced (blue line). Alternatively, for the same low-pass filter bandwidth, the PLL gains need to be reduced (orange line).
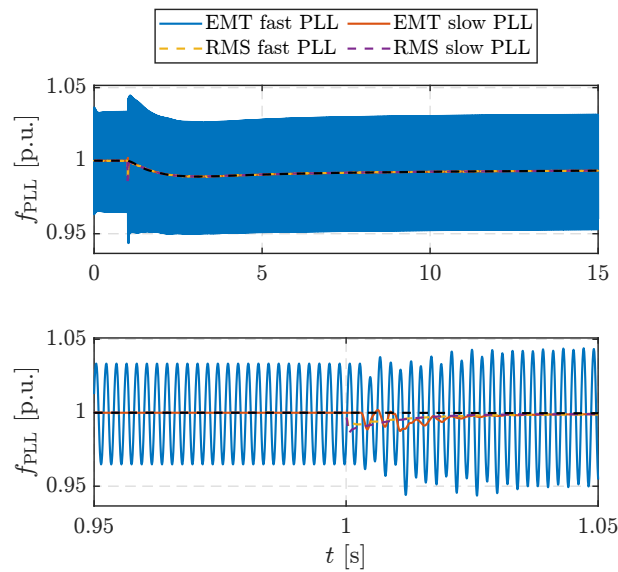
Figure 4.25: EMT vs. RMS: impact of PLL gains on frequency tracking performance. Black line represents actual grid frequency.
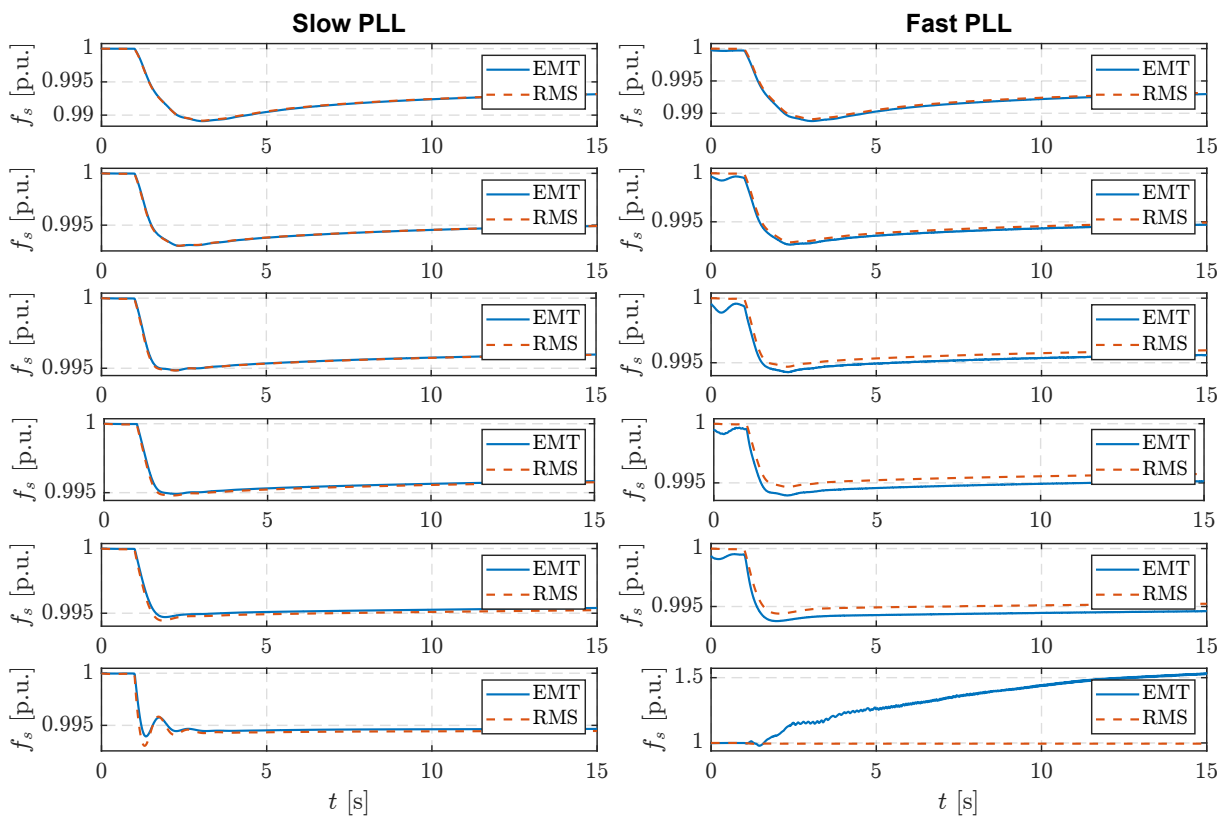
Figure 4.26: EMT vs. RMS: impact of PLL gains on system frequency. Top to bottom: $\eta_c = \{26\%, 41\%, 51\%, 59\%, 71\%, 93\%\}$.
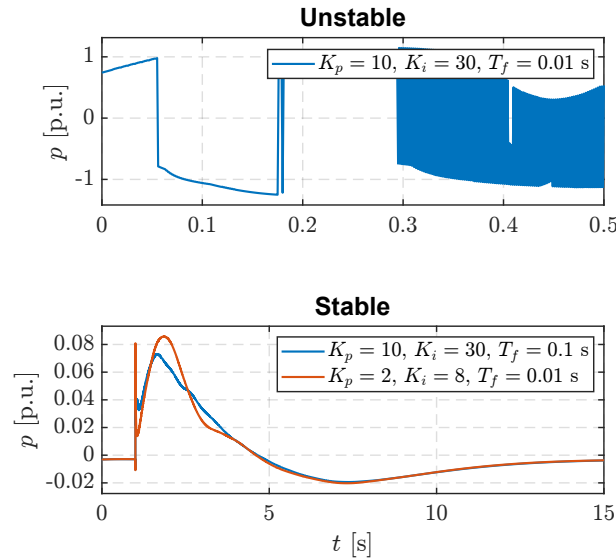
Figure 4.27: RMS simulation of the impact of PLL gains and virtual inertia on converter performance.

Therefore, grid-following converters do not contribute to the initial RoCoF analogous to induction machines. Additionally, note the spike in power immediately following the disturbance which originates from the PCC voltage transient. The physical mass of synchronous machines acts as a natural low-pass filter and such fast transients will not be transferred to the rotor. Moreover, a grid-following converter with the same inertia constant as an equivalent synchronous generator will have a weaker response exactly because of the low-pass filter that reduces the gain at higher frequencies (Fig. 4.28). However, since the virtual inertia constant does not have any physical meaning, it can be set to an arbitrary value in the control software to obtain a stronger or weaker response. Of course, the upper limit depends on system dynamics since too large a value can introduce instability. Fig. 4.29 shows that for $K_p = 10$, $K_i = 30$, $T_f = 0.1$ s, the RMS simulation is stable for all converter penetrations η_c. On the other hand, the EMT simulation behaves identically to the RMS simulation only in the first case for $\eta_c = 26\%$. For all other cases, there are large oscillations in the power output and the performance is unstable. This means that provision of synthetic inertia by grid-following converters requires adequate filtering of the PLL-estimated grid frequency: by reducing PLL gains, decreasing low-pass filter bandwidth or both. Fig. 4.30 shows the comparison of EMT and RMS models for $K_p = 2$, $K_i = 8$, $T_f = 0.1$ s where it can clearly be seen that both models behave identically. Therefore, grid-following converters cannot be considered as extremely fast first-order plants anymore since the dynamics of the PLL and filtering will slow down the response and make it more oscillatory as the share of converter-interfaced sources in a power system increases.

Thus, the hypothesis is that SFR models of CID only described by Fig. 3.22a are not adequate for systems with low rotational inertia and a high share of converters. More precisely, grid-following converters with droop & synthetic inertia described by Fig. 4.31a will produce
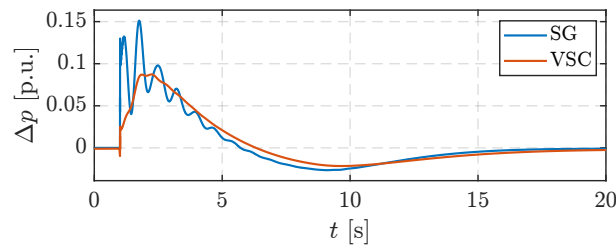
Figure 4.28: Comparison of an SG and grid-following VSC with equivalent inertia constants.
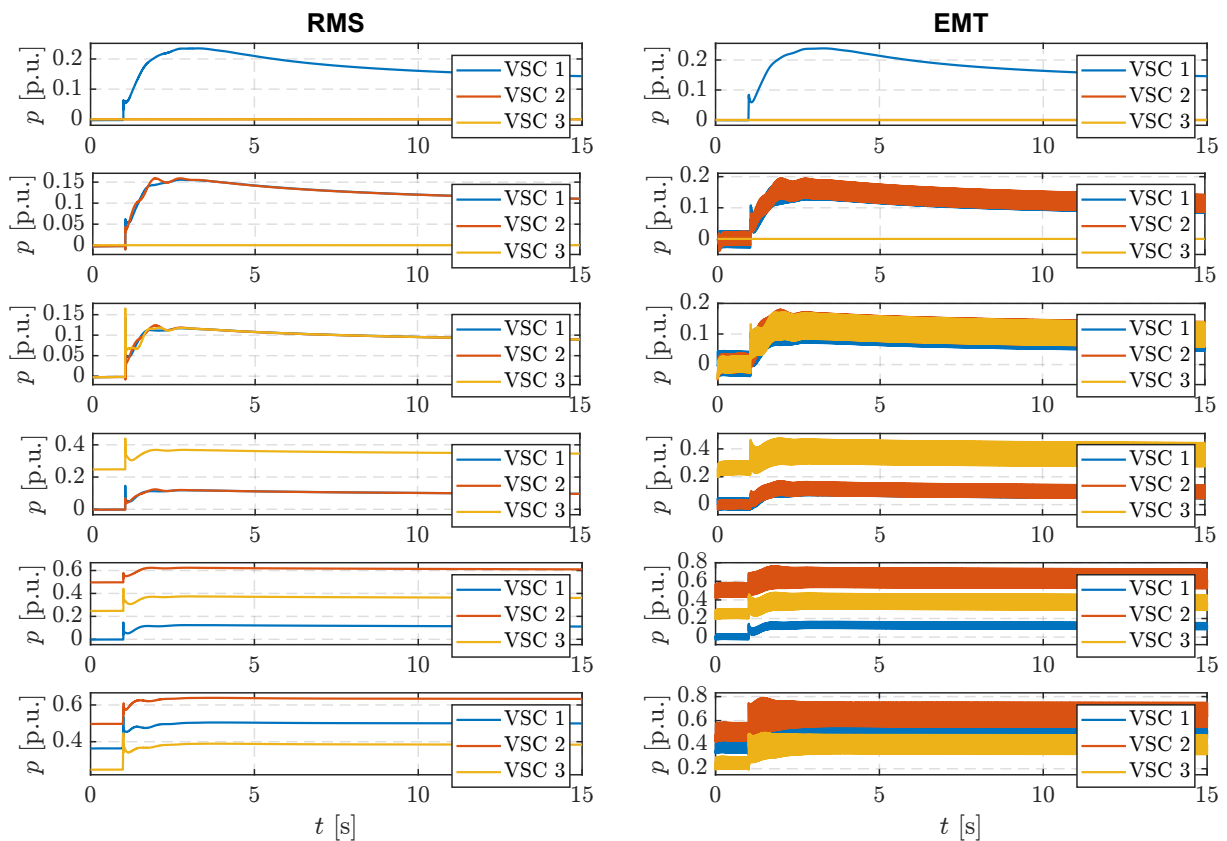
Figure 4.29: EMT vs. RMS: impact of droop + virtual inertia ($K_p = 10$, $K_i = 30$, $T_f = 0.1$ s) on converter performance. Top to bottom: $\eta_c = \{26\%, 41\%, 51\%, 59\%, 71\%, 93\%\}$.
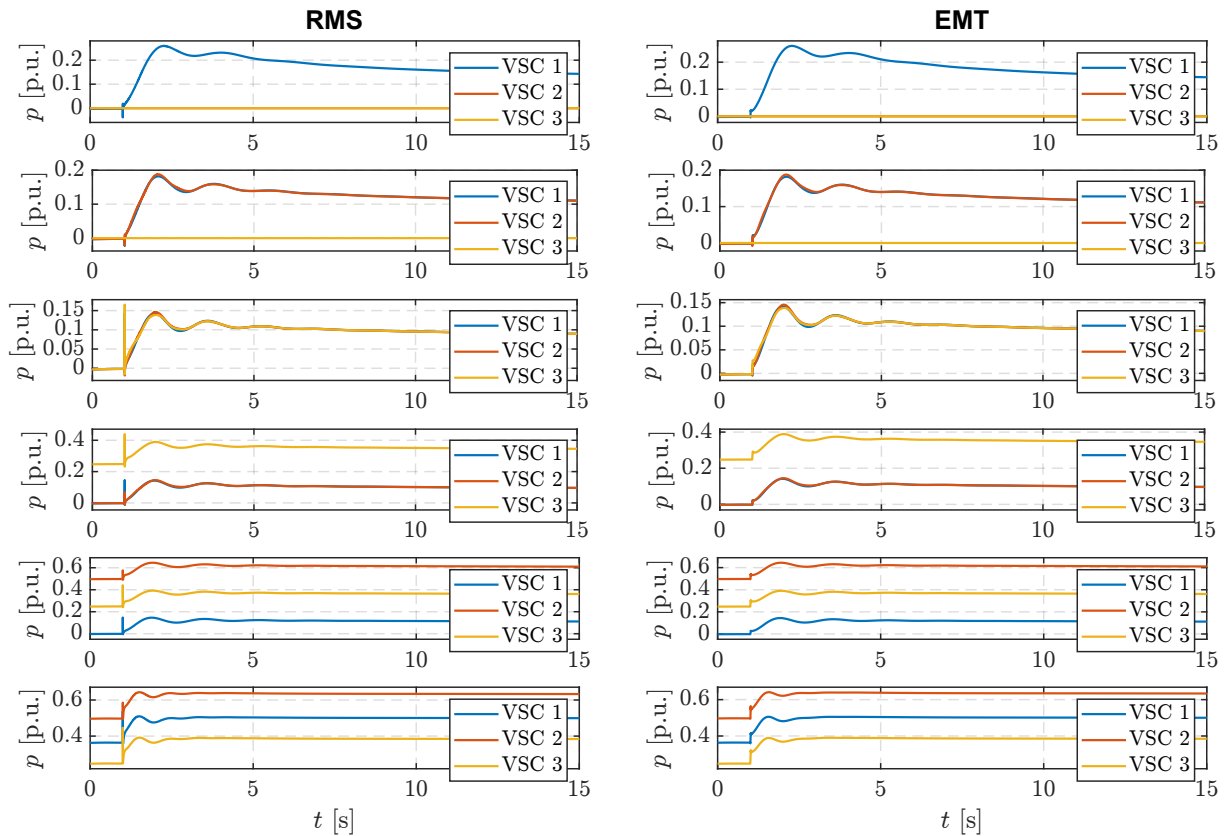
Figure 4.30: EMT vs. RMS: impact of droop + virtual inertia ($K_p = 2$, $K_i = 8$, $T_f = 0.1$ s) on converter performance. Top to bottom: $\eta_c = \{26\%, 41\%, 51\%, 59\%, 71\%, 93\%\}$.

overly optimistic results which are not realistic, as confirmed by detailed EMT simulations. A more accurate SFR model will have the structure illustrated by Fig. 4.31b.

4.3.1 Deriving the SFR model of a three-phase synchronous reference frame PLL

In this section, we shall derive the PLL transfer function $G_{\mathrm{PLL}}(s)$ for use in SFR models of low-inertia systems. The derivation is based on [169].

An analogy can be drawn between the conventional synchronous generators and the grid-following VSCs, as illustrated in Fig. 4.32. Voltage control / reactive power control is omitted from this illustration. SG machine speed ω is estimated by a speed transducer. Then, the estimated speed $\hat{\omega}$ is passed on to a turbine governor which modifies the gate or valve opening c (droop control). The turbine translates the gate/valve opening into the mechanical power output p_m at the turbine shaft.

In VSCs, on the other hand, a PLL estimates the grid frequency $\hat{\omega}$ from the measured voltage $\mathbf{u_{abc}}$ at the point of common coupling. If a VSC operates in the grid-supporting mode, then $\hat{\omega}$ can be used to modify the active power command p^* (e.g., droop control or virtual inertia). However, the main purpose of a PLL is to extract the phase angle of the grid voltage $\hat{\theta}$ in order

(a) Simplified model used in literature (inaccurate)

(b) Proposed SFR model (more accurate)
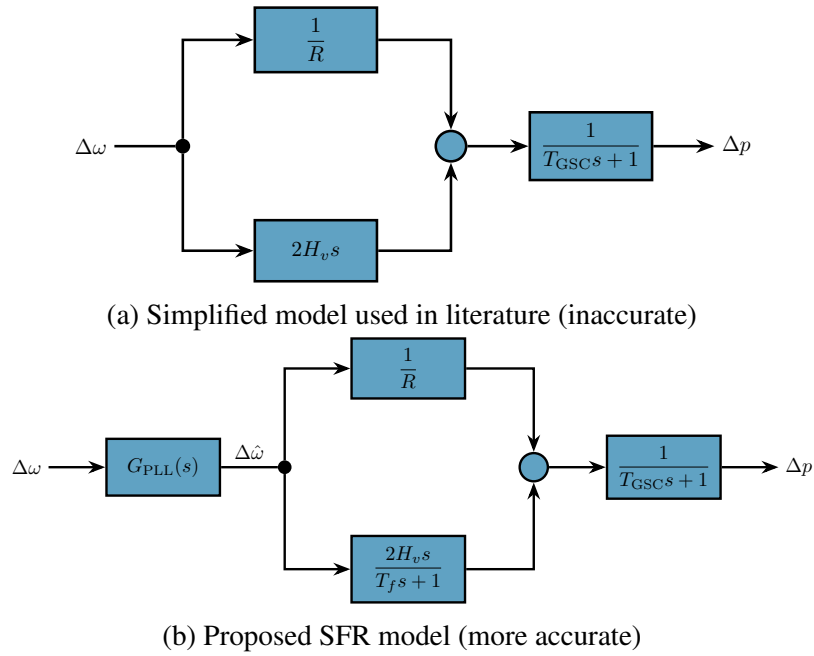
Figure 4.31: SFR models of grid-following VSC with droop and synthetic inertia.
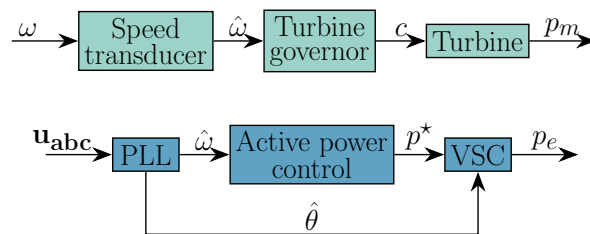
Figure 4.32: Analogy between synchronous generators and grid-following VSCs.

to synchronise with the grid. The VSC block in Fig. 4.32 contains the inner voltage and current control loops, as well as the PWM modulation for generating gate signals for the inverter. The output of the VSC is the electrical power p_e.

Generally, most generic dynamic models of turbines include the effect of the speed transducer and the governing system [16]. However, (modern) governing systems are much faster than turbine dynamics so their effect is often neglected in SFR models. On the other hand, the time scale of a PLL is also faster than the VSC active power control [6], so it can be inferred that it could also be neglected in SFR studies. However, depending on how PLL gains are tuned, the time lag it induces can have an effect on estimated frequency and, consequently, the performance of active power control [102, 103, 170, 171]—especially in low-inertia systems.

Regardless, since a PLL estimates the frequency from the measured instantaneous grid voltage, it is mostly susceptible to electromagnetic disturbances such as voltage unbalances, spikes and dips [142, 170]. This paper aims to derive a transfer function of a three-phase SRF PLL which relates the actual grid frequency to the estimated grid frequency suitable for implementation in SFR models which inherently do not capture the voltage dynamics. Such a transfer function essentially captures the time lag a PLL introduces into the closed-loop control. The derivation will be based on three assumptions: i) Three-phase voltages are balanced; ii) Voltage amplitudes are constant and close to the nominal value; iii) Only the simplest representation of an SRF PLL is used.

The first two assumptions are valid since SFR models do not consider voltage dynamics—they only model effects of global generation/load imbalance on a system's average frequency through the swing equation (generator inertia and load self-regulation) and control reactions (droop control, synthetic inertia, under-frequency load shedding, etc.). The last assumption is to simplify the analysis by using a textbook example of an SRF PLL system. It means that additional filters or more complex PLL structures used to improve rejection of grid voltage harmonics, unbalances and other disturbances are ignored (also, these phenomena are inherently not captured by SFR models).

The three-phase SRF PLL structure used to derive the small-signal model is shown in Fig. 3.10. The input is a three-phase voltage measurement at the grid connection point $\mathbf{u_{abc}}$ (4.54), where $\theta = \theta(t)$ is the grid voltage phase angle. The PLL estimates the phase angle $\hat{\theta} = \hat{\theta}(t)$ such that the $abc \rightarrow dq$ transformation zeroes out the q-component of voltage (v_q). The normalised (per-unit) component $\overline{u}_q$ is passed through a proportional-integral (PI) controller to obtain the estimate of the grid angular frequency $\hat{\omega}$, which is then integrated by means of a voltage-controlled oscillator to obtain $\hat{\theta}$. In steady-state, $\omega = \hat{\omega}$, $\theta = \hat{\theta}$, and $u_q = 0$.

$$\mathbf{u_{abc}}^{\top} = \begin{pmatrix} u_a(\theta(t)) & u_b(\theta(t)) & u_c(\theta(t)) \end{pmatrix} \tag{4.54}$$

We consider a three-phase system of AC voltages:

$$u_a = U_a \sin(\theta(t)) \tag{4.55a}$$

$$u_b = U_b \sin\left(\theta(t) - \frac{2\pi}{3}\right) \tag{4.55b}$$

$$u_c = U_c \sin\left(\theta(t) - \frac{4\pi}{3}\right) \tag{4.55c}$$

where U_a, U_b and U_c are the peak values of phase-to-ground voltages of each phase. $\theta(t)$ is the grid voltage phase angle described by (4.56). θ_0 is the initial phase angle and $\omega = \omega(t)$ is the grid angular frequency.

$$\theta(t) = \int \omega(\tau)d\tau + \theta_0 \tag{4.56a}$$

$$\frac{d\theta}{dt} = \omega \tag{4.56b}$$

The transformation from *abc* to *dq* coordinates (neglecting the 0-component for balanced systems) is achieved through the tensor $\mathbf{T_{dq}}$ [13]:

$$\begin{pmatrix} u_d \\ u_q \end{pmatrix} = \frac{2}{3}\mathbf{T_{dq}} \begin{pmatrix} u_a \\ u_b \\ u_c \end{pmatrix} \tag{4.57}$$

where $\mathbf{T_{dq}} = \mathbf{T_{dq}}(\hat{\theta}(t))$ is defined as:

$$\mathbf{T_{dq}} = \begin{pmatrix} \sin(\hat{\theta}(t)) & \sin(\hat{\theta}(t) - \frac{2\pi}{3}) & \sin(\hat{\theta}(t) - \frac{4\pi}{3}) \\ \cos(\hat{\theta}(t)) & \cos(\hat{\theta}(t) - \frac{2\pi}{3}) & \cos(\hat{\theta}(t) - \frac{4\pi}{3}) \end{pmatrix} \tag{4.58}$$

Obviously, the grid voltage angle extracted by the PLL is equal to:

$$\hat{\theta}(t) = \int \hat{\omega}(\tau)d\tau + \hat{\theta}_0 \tag{4.59a}$$

$$\frac{d\hat{\theta}}{dt} = \hat{\omega} \tag{4.59b}$$

107

After combining (4.55), (4.57) and (4.58), the component u_q is equal to:

$$u_q(t) = \begin{pmatrix} \cos(\hat{\theta}(t)) \\ \cos(\hat{\theta}(t) - \frac{2\pi}{3}) \\ \cos(\hat{\theta}(t) - \frac{4\pi}{3}) \end{pmatrix}^{\top} \begin{pmatrix} U_a \sin(\theta(t)) \\ U_b \sin(\theta(t) - \frac{2\pi}{3}) \\ U_c \sin(\theta(t) - \frac{4\pi}{3}) \end{pmatrix} \tag{4.60}$$

Assuming a balanced three-phase system with constant voltage amplitudes ($U_a = U_b = U_c = U$), expression (4.60) reduces to:

$$u_q(t) = U \sin\left(\theta(t) - \hat{\theta}(t)\right) \tag{4.61}$$

Equation (4.61) can be normalised to the voltage amplitude U to obtain the per-unit value of the q-component $\bar{u}_q$ from Fig. 3.10:

$$u_q(t) \mapsto \bar{u}_q(t) = \sin\left(\theta(t) - \hat{\theta}(t)\right) \tag{4.62}$$

The goal now is to eliminate of the voltage variable $\bar{u}_q$ (since there is no voltage in SFR models) and linearise the system to derive the transfer function from $\Delta\omega$ to $\Delta\hat{\omega}$. To achieve this, the nonlinear dynamical system of SRF PLL is described by a system of differential equations, as defined in (3.12), where K_p and K_i are the proportional and integral gain of the PI controller (Fig. 3.10) described by the transfer function $H(s) = K_p + K_i s^{-1}$.

$\Delta\bar{u}_q$ is a multivariate function linearised as follows:

$$\Delta\bar{u}_q \approx \left.\frac{\partial\bar{u}_q}{\partial\theta}\right|_{(\theta_0,\hat{\theta}_0)} \Delta\theta + \left.\frac{\partial\bar{u}_q}{\partial\hat{\theta}}\right|_{(\theta_0,\hat{\theta}_0)} \Delta\hat{\theta} \tag{4.63a}$$

$$= \cos\left(\theta_0 - \hat{\theta}_0\right)\Delta\theta - \cos\left(\theta_0 - \hat{\theta}_0\right)\Delta\hat{\theta} \tag{4.63b}$$

$$= \Delta\theta - \Delta\hat{\theta} \tag{4.63c}$$

since $\theta_0 = \hat{\theta}_0$ in the steady-state. Linearising Eq. (3.12a) results in (4.64), and $\Delta\omega$ is set as the input (perturbation) variable $\Delta u(t)$:

$$\frac{d\Delta\theta}{dt} = \Delta\omega = \Delta u(t) \tag{4.64}$$

Linearising (3.12c) results in (4.65), and $\Delta\hat{\omega}$ is set as the output variable $\Delta y(t)$:

$$\frac{d\Delta\hat{\theta}}{dt} = \Delta\hat{\omega} = \Delta y(t) \tag{4.65}$$

Finally, the state-space model can be written by combining (4.63)–(4.65):

$$\Delta \dot{\mathbf{x}} = \mathbf{A} \Delta \mathbf{x} + \mathbf{B} \Delta \mathbf{u} \tag{4.66a}$$

$$\Delta \mathbf{y} = \mathbf{C} \Delta \mathbf{x} + \mathbf{D} \Delta \mathbf{u} \tag{4.66b}$$

where $\Delta \mathbf{x}$, $\Delta \mathbf{u}$, $\Delta \mathbf{y}$, $\mathbf{A}$, $\mathbf{B}$, $\mathbf{C}$ and $\mathbf{D}$ are equal to:

$$\Delta \mathbf{x} = \begin{pmatrix} \Delta \theta & \Delta \xi & \Delta \hat{\theta} \end{pmatrix}^{\top} \tag{4.67a}$$

$$\Delta \mathbf{u} = \Delta u = \Delta \omega \tag{4.67b}$$

$$\Delta \mathbf{y} = \Delta y = \Delta \hat{\omega} \tag{4.67c}$$

$$\mathbf{A} = \begin{pmatrix} 0 & 0 & 0 \\ 1 & 0 & -1 \\ K_p & K_i & -K_p \end{pmatrix} \tag{4.67d}$$

$$\mathbf{B} = \begin{pmatrix} 1 & 0 & 0 \end{pmatrix}^{\top} \tag{4.67e}$$

$$\mathbf{C} = \begin{pmatrix} K_p & K_i & -K_p \end{pmatrix} \tag{4.67f}$$

$$\mathbf{D} = 0 \tag{4.67g}$$

The SRF PLL transfer function is now equal to (4.68), which corresponds to the form from [143], neglecting the voltage amplitude:

$$
\begin{aligned}
G_{\text{PLL}}(s) &= \frac{\Delta y(s)}{\Delta u(s)} = \frac{\Delta \hat{\omega}}{\Delta \omega} = \frac{\Delta \hat{f}}{\Delta f} \\
&= \mathbf{C} [s\mathbf{I} - \mathbf{A}]^{-1} \mathbf{B} + \mathbf{D} \\
&= \frac{K_p s + K_i}{s^2 + K_p s + K_i}
\end{aligned}
\tag{4.68}
$$

$G_{\text{PLL}}(s)$ exhibits a generic second-order system dynamics (3.33), where the natural frequency ω_n and damping factor ζ are defined as (4.69) and (4.70), respectively. T_i is the integrator reset time.

$$\omega_n = \sqrt{K_i} = \sqrt{\frac{K_p}{T_i}} \tag{4.69}$$

$$\zeta = \frac{K_p}{2\omega_n} = \sqrt{\frac{K_p T_i}{4}} \tag{4.70}$$

Depending on how the gains are tuned, the PLL will have more or less damped oscillatory behaviour. The input derivative ($2\zeta \omega_n s$ member in the numerator) mostly influences the high-frequency behaviour by introducing the $+90$ degree phase-shift and reducing the magnitude

fall-off by 20 dB/decade. The small-signal model of a three-phase SRF PLL (4.68) is compared against the large-signal model from Fig. 3.10 for a step change in frequency of $\Delta f = -0.2$ Hz. The PLL parameters are $K_p = 10$ and $K_i = 100$. K_p and K_i are tuned based on trial-and-error until a satisfying performance was achieved without being too aggressive, similar to [172]. Results show (Fig. 4.33) that the small-signal model perfectly describes the large-signal model, thus confirming the correctness of the small-signal model derivation.
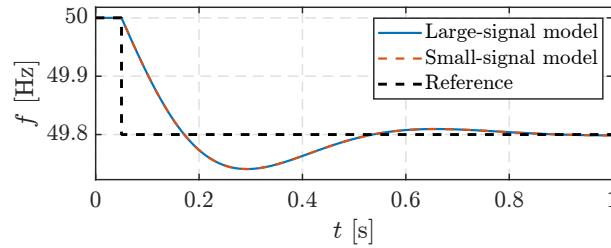
Figure 4.33: Validation of the small-signal SRF PLL model.

Finally, the hypothesised model from Fig. 4.31b is replaced by Fig. 4.34 for a three-phase SRF PLL operating in balanced conditions and assuming stiff voltage.
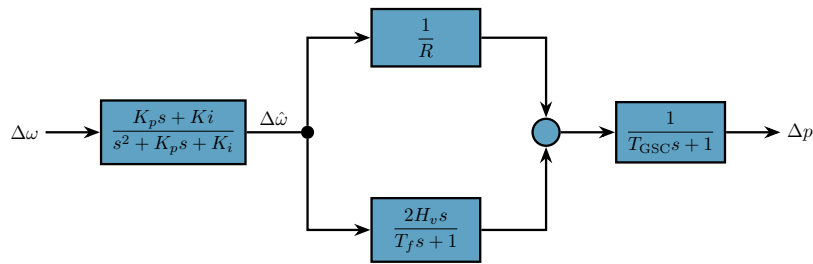
Figure 4.34: SFR model of a grid-following VSC (PQ-controlled GSC) with droop and virtual inertia, considering PLL dynamics and frequency filtering.

Fig. 4.35 compares the grid frequency estimated by the full EMT model to the frequencies estimated by the three SFR models: the simplified model with neglected PLL and grid frequency filtering (Fig. 4.31a), simplified model with included grid frequency filtering $T_f = 100$ ms and neglected PLL, and the proposed model which includes both the PLL dynamics and frequency low-pass filter. The results are shown for different shares of converter penetration η_c. It can be seen that for a low penetration rate of CID, the existing models are adequate. However, for $\eta_c \geq 41\%$) the existing models show a smaller RoCoF and more damped oscillations, i.e., more optimistic results. For the highest share $\eta_c = 93\%$, even the derived model (Fig. 4.34) is inaccurate compared to the EMT model since it shows more oscillatory behaviour which hints at the fact that in a real system there will be additional damping sources. This can be compensated in the SFR model by increasing the K_p gain of the PLL. Luckily, the derived model shows a more pessimistic behaviour, which means that it is on the safe side. Fig. 4.36 shows the corresponding converter output power.
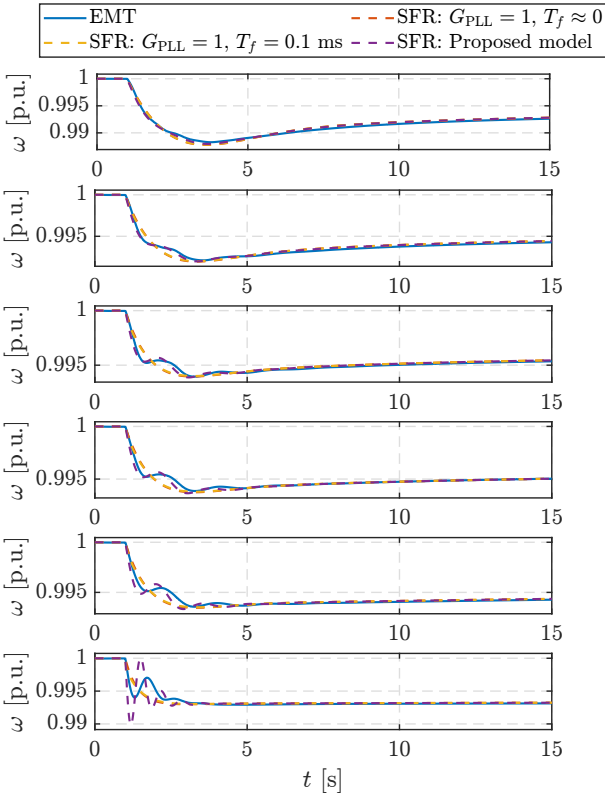
Figure 4.35: EMT vs. SFR: grid frequency for a grid-following VSC (PQ-controlled GSC) with droop and virtual inertia. Top to bottom: $\eta_c = \{26\%, 41\%, 51\%, 59\%, 71\%, 93\%\}$.
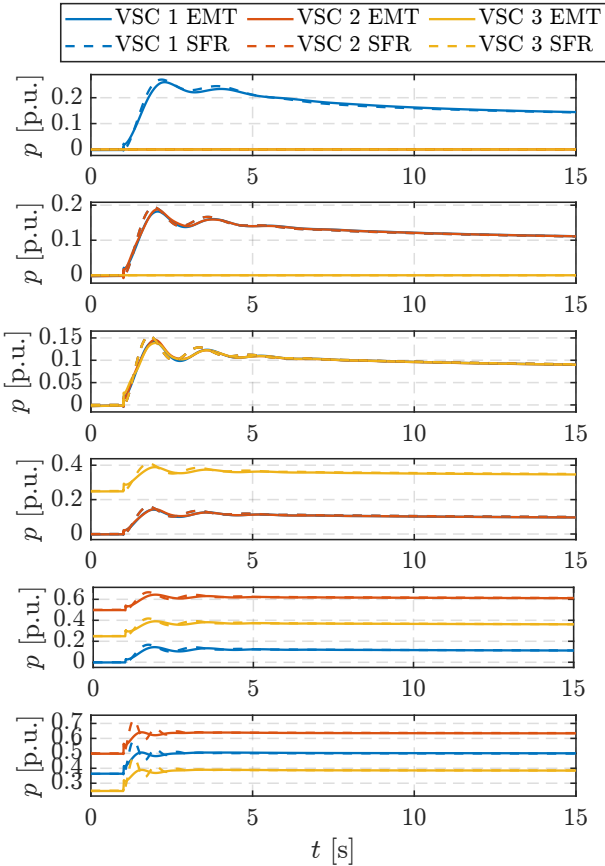
Figure 4.36: EMT vs. SFR: converter output power of a grid-following (PQ-controlled GSC) VSC with droop and virtual inertia. Top to bottom: $\eta_c = \{26\%, 41\%, 51\%, 59\%, 71\%, 93\%\}$.

4.4 Systems based on synchronous generators and grid-following converters with grid-side DCVC

When the DCVC is implemented in the GSC, all the conclusions from Section 4.3 are still valid. The only difference is that the GSC transfer function from Fig. 3.22a is replaced by the one from Fig. 3.22c, resulting in the SFR model illustrated by Fig. 4.37.
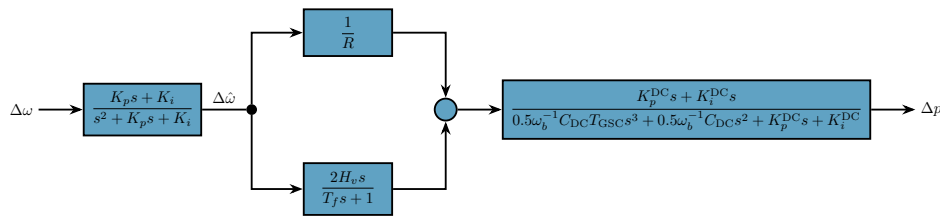
Figure 4.37: SFR model of a grid-following VSC (GSC-implemented DCVC) with droop and virtual inertia, considering PLL dynamics and frequency filtering.

The dynamic behaviour is similar to PQ-controlled GSC shown by Fig. 4.35 and Fig. 4.36. Fig. 4.38 compares the grid frequency estimated by the full EMT model to the frequencies estimated by the three SFR models: the simplified model with neglected PLL and grid frequency filtering (Fig. 3.22c), simplified model with included grid frequency filtering $T_f = 100$ ms and neglected PLL, and the proposed model which includes both PLL dynamics and a frequency low-pass filter. The results are shown for different shares of converter penetration η_c. It can be seen that for a low penetration rate of CID, the existing models are adequate. However, for $\eta_c \geq 41\%$) the existing models show a smaller RoCoF and more damped oscillations, i.e., more optimistic results. For the highest share $\eta_c = 93\%$, even the derived model (Fig. 4.34) is inaccurate compared to the EMT model since it shows more oscillatory behaviour, which hints at the fact that in a real system there would be additional sources of damping. This can be compensated in the SFR model by increasing the K_p gain of the PLL. Luckily, the derived model shows a more pessimistic behaviour, which means that it is on the safe side. Fig. 4.39 shows the corresponding converter output power.

Therefore, virtual inertia constant of grid-following converters cannot just be added to the synchronous inertia constant defined by synchronous generators and motors because its effect is not instantaneous due to PLL dynamics and low-pass filtering. This is similar to why inertia constants of synchronously connected induction machines cannot be added, strictly mathematically speaking. A low-order SFR model of a system consisting of grid-following VSCs with droop and virtual inertia (including both PQ-controlled GSC and DCVC-controlled GSC) is shown in Fig. 4.40. The SFR model is shown for N_1^{GSC} identical PQ-controlled VSCs and N_2^{GSC} identical DCVC-controlled VSCs, i.e., index $(\cdot)_1$ denotes PQ-controlled VSCs, and $(\cdot)_2$ denotes DCVC-controlled VSCs.
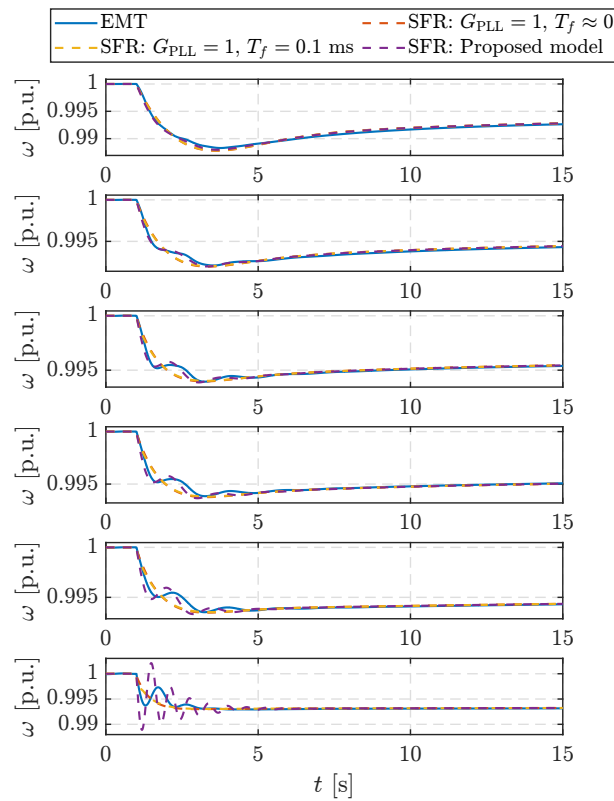
Figure 4.38: EMT vs. SFR model grid frequency for a grid-following VSC (GSC-implemented DCVC) with droop and virtual inertia. Top to bottom: $\eta_c = \{26\%, 41\%, 51\%, 59\%, 71\%, 93\%\}$.
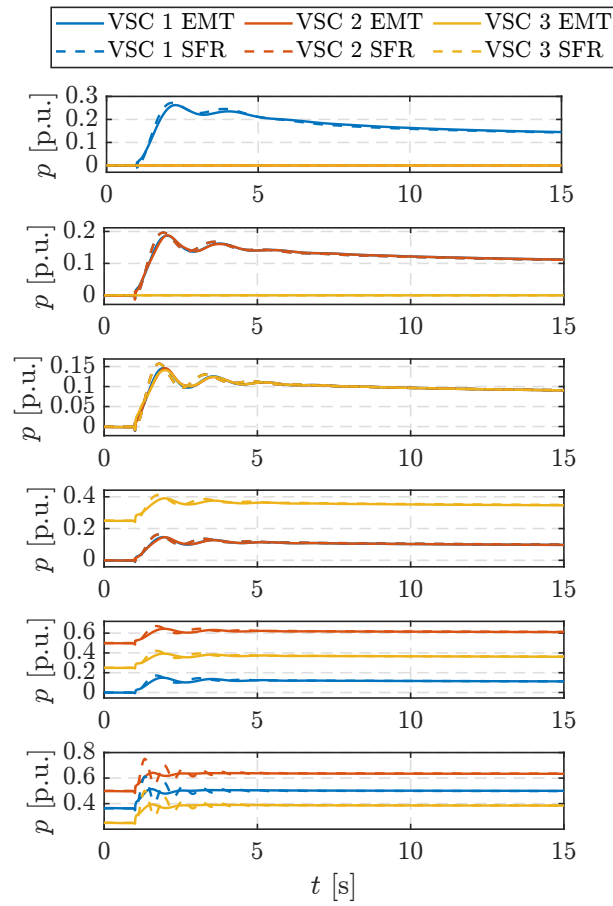
Figure 4.39: EMT vs. SFR model converter output power of a grid-following VSC (GSC-implemented DCVC) with droop and virtual inertia. Top to bottom: $\eta_c = \{26\%, 41\%, 51\%, 59\%, 71\%, 93\%\}$.
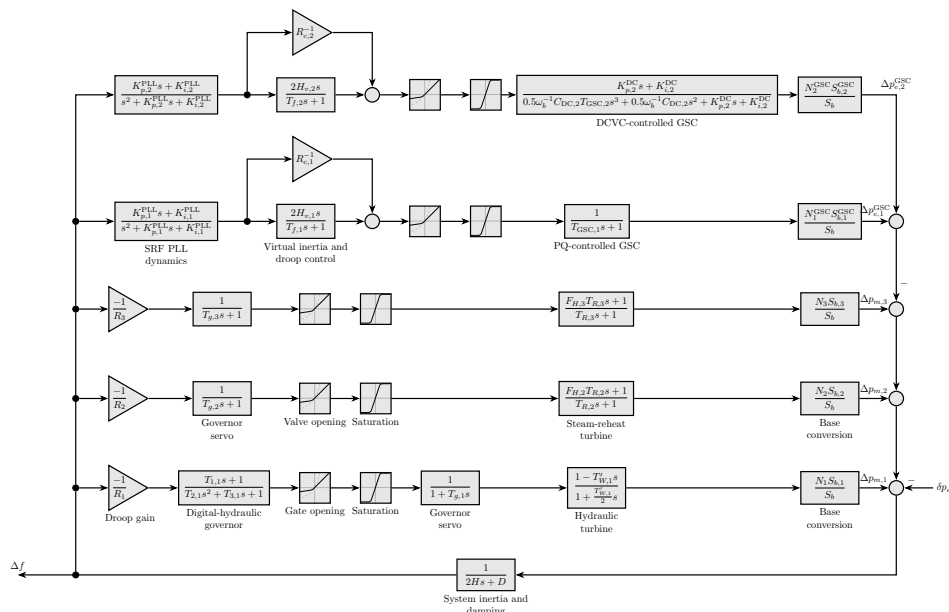
Figure 4.40: SFR model of a system consisting of SGs and grid-following PQ-controlled and DCVC-controlled GSCs.

4.5 Systems based on synchronous generators and grid-forming converters with controlled device-side power source

This section analyses the PQ-controlled GSC in the VSM scheme [139]. Same as in the grid-following PQ-controlled GSC discussed in section 4.3, the characteristics of the energy conversion system (Fig. 3.2) are neglected and ECS+DSC are replaced by a controlled power (current) source as shown in Fig. 3.7a.

The simulations are conducted for converter penetrations levels (4.53) of $\eta_c = \{26\%, 41\%, 51\%, 59\%, 71\%, 100\%\}$. Fig. 4.41 shows the converter power output comparison between the RMS and EMT models. It can be seen that both models behave identically for all shares of CID. Fig. 4.42 shows that the frequency is uniform except for minor differences during the transient state. It also shows good compatibility of the VSM scheme with traditional synchronous generators. If we compare the inertial response of an SG with an equivalent VSM (Fig. 4.43), we can see that the magnitude of the response is essentially identical, however VSM has larger oscillations. The reason for this is that a full SG has a larger damping due to the construction of the machine, as well as the effects of damper windings. On the other hand, the VSM scheme implemented in this paper [139] emulates an SG only with a second order model (swing equation only) and has a behaviour similar to the classical SG model. The oscillations can be mitigated to an extent by increasing the value of virtual inductance.

Analogous to the procedure shown for SGs in section 4.1, first we sum up the individual virtual (simplified) swing equations over the set of online grid-forming VSC operating in PQ-VSM mode ($\mathcal{N}_{\text{VSC}}^{\text{PQ}-\text{VSM}}$), as shown in (4.71):

$$\sum_{l \in \mathcal{N}_{\text{VSC}}^{\text{PQ}-\text{VSM}}} 2H_l \frac{d\omega_l}{dt} = \sum_{i \in \mathcal{N}_{\text{VSC}}^{\text{PQ}-\text{VSM}}} p_l^\star(t) - \sum_{l \in \mathcal{N}_{\text{VSC}}^{\text{PQ}-\text{VSM}}} p_l(t) \qquad (4.71)$$

Then, we assume a well-synchronised system in which all individual virtual speeds ω_l, that are used as the modulating signal for synthesizing the AC frequency, converge towards a uniform system frequency $\omega_l \to \omega, \forall l \in \mathcal{N}_{\text{VSC}}^{\text{PQ}-\text{VSM}}$ as $t \to \infty$. Therefore, (4.71) becomes (4.72):

$$\frac{d\omega}{dt} \sum_{l \in \mathcal{N}_{\text{VSC}}^{\text{PQ}-\text{VSM}}} 2H_l = p^\star(t) - p(t) = 2H_{\text{PQ}-\text{VSM}} \frac{d\omega}{dt} \qquad (4.72)$$

Now, since the virtual frequency defines the synthesised physical AC frequency that also converges towards a uniform value, the virtual swing equation can be algebraically added with the physical swing equation defined by synchronous machines (4.4)–(4.5) in order to describe the joint effect of synchronous inertia and grid-forming virtual inertia (4.73). Equation (4.73) can also be extended to include the effects of synchronous inertia due to synchronous motors,
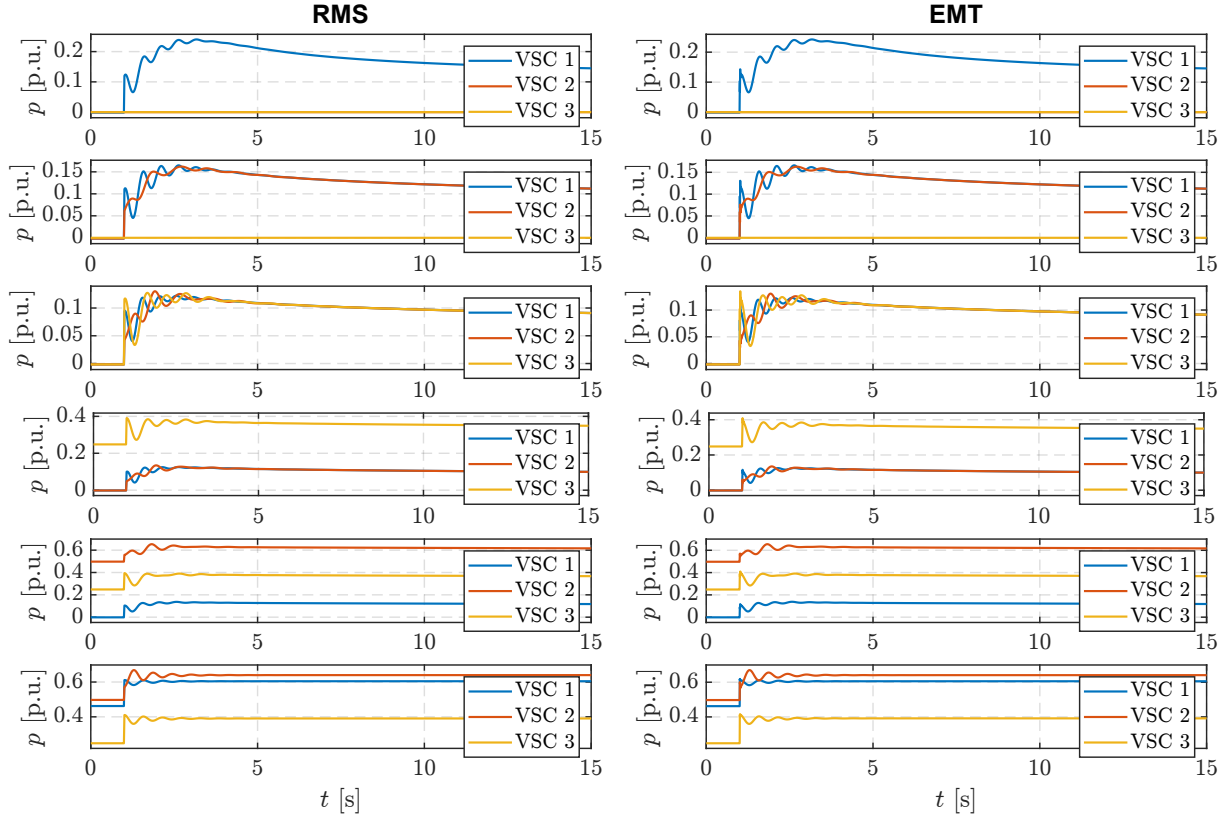
Figure 4.41: EMT vs. RMS: performance comparison of PQ-controlled GSC in VSM scheme. Top to bottom: $\eta_c = \{26\%, 41\%, 51\%, 59\%, 71\%, 100\%\}$.

as described in section 4.2.1.

$$p^\star(t) - p(t) + p_m(t) - p_e(t) = 2\left(H_{\text{PQ-VSM}} + H_{\text{SG}}\right)\frac{d\omega}{dt} = 2H \tag{4.73}$$

The converter power reference $p^\star$ is actually modulated by the frequency droop gain and damping per (3.17):

$$p^\star \rightarrow p^\star + K_\omega\left(\omega_n - \omega\right) + K_D\left(\hat{\omega} - \omega\right) \tag{4.74}$$

Linearizing (4.74) for a small disturbance and assuming $p^\star = \text{const.}$ yields in the frequency domain:

$$\Delta p_c = K_\omega\Delta\omega + K_D\left(\Delta\hat{\omega} - \Delta\omega\right) = K_\omega\Delta\omega + K_D\Delta\omega\left(G_{\text{PLL}}(s) - 1\right) \tag{4.75}$$

where $G_{\text{PLL}}(s)$ is defined by (4.68).

Finally, by combining (3.28), (4.72), and (4.75) we can obtain the small-signal model of a single PQ-VSM grid-forming converter $l \in \mathcal{N}_{\text{VSC}}^{\text{PQ-VSM}}$ shown by Fig. 4.44. Note that the model neglects the time constant of the device-level control. This is not precisely correct since the whole control system consists also of an outer voltage control loop and together with the LCL filter makes up a high-order dynamic system. Here, we neglected the higher-order behaviour assuming a well-controlled and well-damped device-level control so that the model can remain
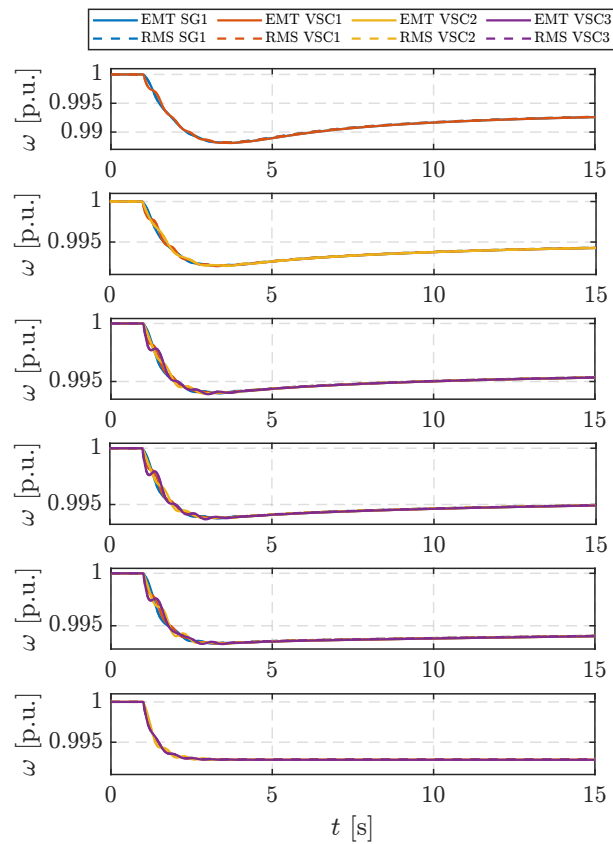
Figure 4.42: EMT vs. RMS: grid frequency the for PQ-controlled GSC in the VSM scheme. Top to bottom: $\eta_c = \{26\%, 41\%, 51\%, 59\%, 71\%, 100\%\}$.
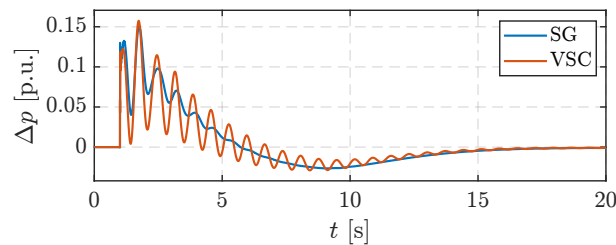
Figure 4.43: Comparison of an SG and grid-forming VSC (PQ-controlled GSC in VSM scheme) with equivalent inertia constants.

simple with as few parameters as possible. Because the frequency dynamics are slowed down by emulating SG inertia where the inertia constant is in the order of several seconds (several orders of magnitude larger than device-level control), this is justified for this particular case. In other words, active power dynamics are mostly governed by the slow phase angle dynamics, not fast voltage-current control.

To show that this simplification is valid, the SFR model is compared against a full-order EMT model of the nine-bus system consisting of multiple SGs and converters, for an outage of generator G4. The results are shown in Fig. 4.45–Fig. 4.46 for various converter penetration levels. The uniform SFR frequency is compared against SG1 and VSC1 which were used as a quick-and-dirty frequency reference to avoid recalculating the CoI frequency for each case. Fig. 4.45 shows that in all cases the SFR model accurately describes the system frequency. However, the SFR model does not capture small oscillations in system frequency which are the result of VSC output power oscillations shown in Fig. 4.46.

In these simulations $K_D = 0$. Fig. 4.47 and Fig. 4.48 show the impact of K_D on the converter power output response. When there is only one VSM in the system with SGs ($\eta_c = 23\%$, Fig. 4.47) it can be seen that the increase of K_D increases the amplitude of the initial power change and it slows down the oscillations. For a system completely consisting of PQ-VSMs ($\eta_c = 100\%$, Fig. 4.47) it can be seen that the fast oscillations were damped and slowed down for $K_D = 100$, but further increase to $K_D = 400$ if the frequency of oscillations is smaller, but the amplitude is higher. Therefore, the damping gain needs to be tuned carefully since the response of this control subsystem is dependent on the PLL that always has an associated time lag, as articulated in the section on grid-following converters (sections 4.3–4.4). Other results also show examples where the increase of K_D increases the oscillations of the VSM frequency and output power [10].

Finally, Fig. 4.49 shows the SFR model of the IEEE 9-bus system consisting of SGs and PQ-VSMs. The system inertia constant consists of SG inertia and PQ-VSM inertia per (4.73).
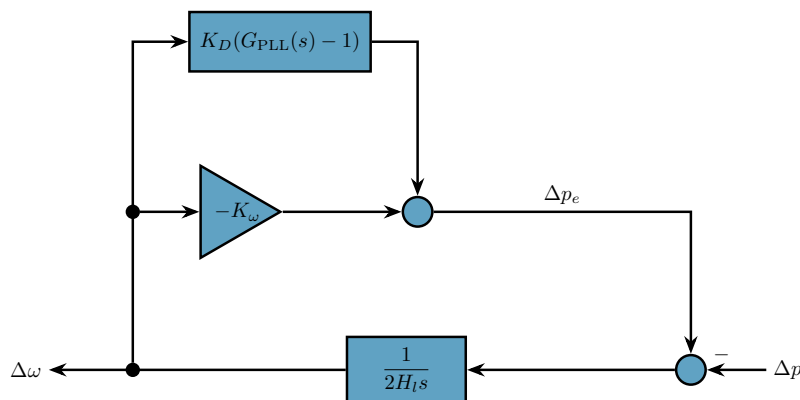
Figure 4.44: Small-signal model of a PQ-controlled GSC in the VSM scheme for frequency dynamics analysis.
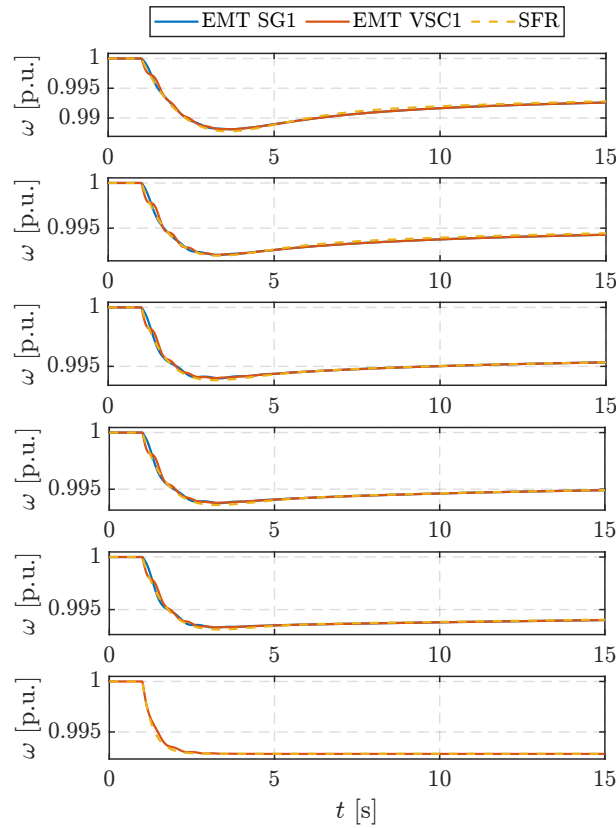
Figure 4.45: EMT vs. SFR: grid frequency for grid-forming VSC (PQ-controlled GSC in VSM scheme). Top to bottom: $\eta_c = \{26\%, 41\%, 51\%, 59\%, 71\%, 100\%\}$.

Regardless of the fact that the virtual and physical inertia are combined to define the system frequency, it is important to note that in this control scheme, in which the GSC is controlled as a PQ-VSM, the virtual inertia constant is an arbitrary number with no physical meaning. It relates in no way to the actual stored energy in the DC link and ECS. Therefore, if the DCVC on the device-side cannot balance the energy requested by the GSC, the DC voltage will collapse and the converter system will fail.
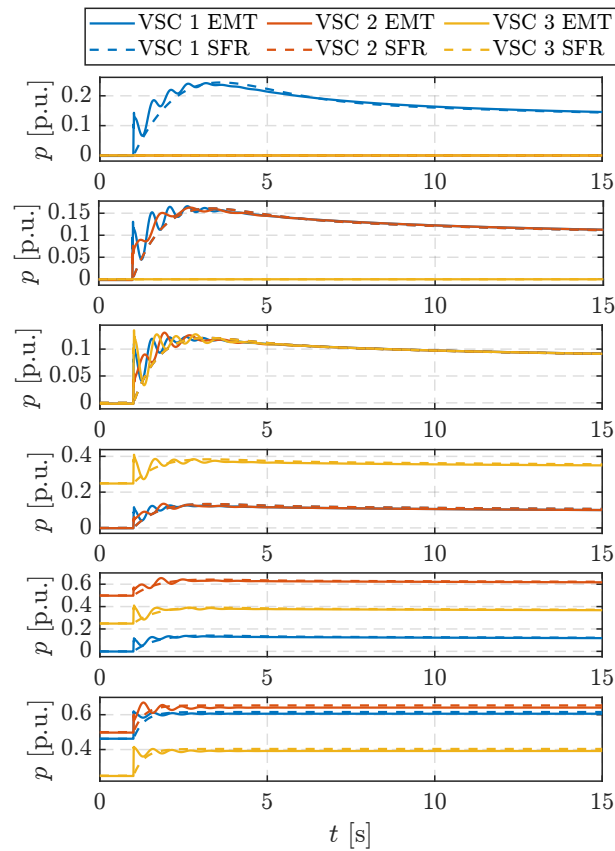
Figure 4.46: EMT vs. SFR: converter output power of a grid-forming VSC (PQ-controlled GSC in VSM scheme). Top to bottom: $\eta_c = \{26\%, 41\%, 51\%, 59\%, 71\%, 100\%\}$.
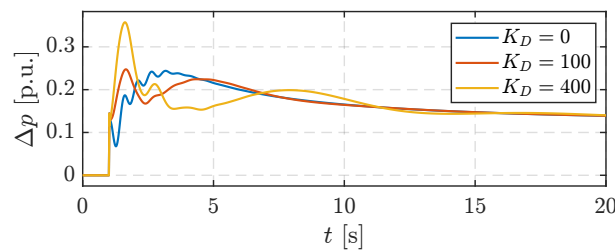
Figure 4.47: Impact of K_D on the power output of a grid-forming VSC (PQ-controlled GSC in VSM scheme); $\eta_c = 26\%$.
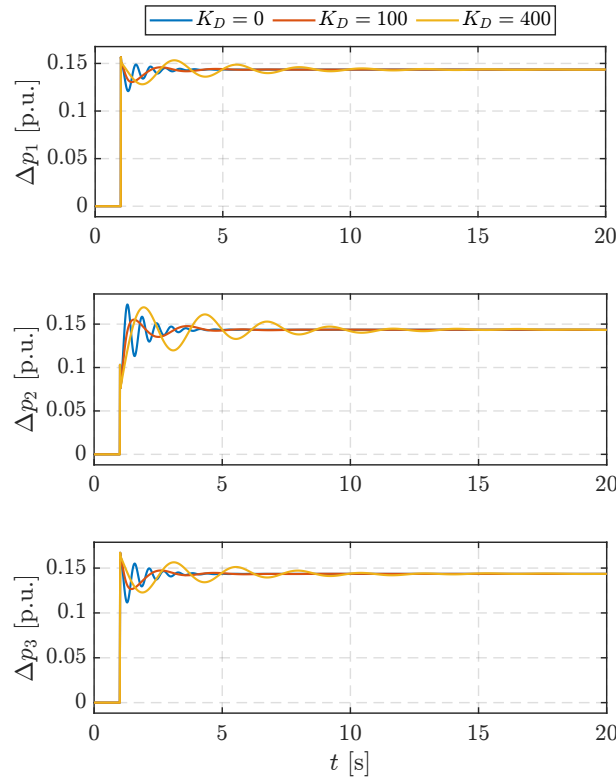
Figure 4.48: Impact of K_D on the power output of a grid-forming VSC (PQ-controlled GSC in VSM scheme); $\eta_c = 100\%$.
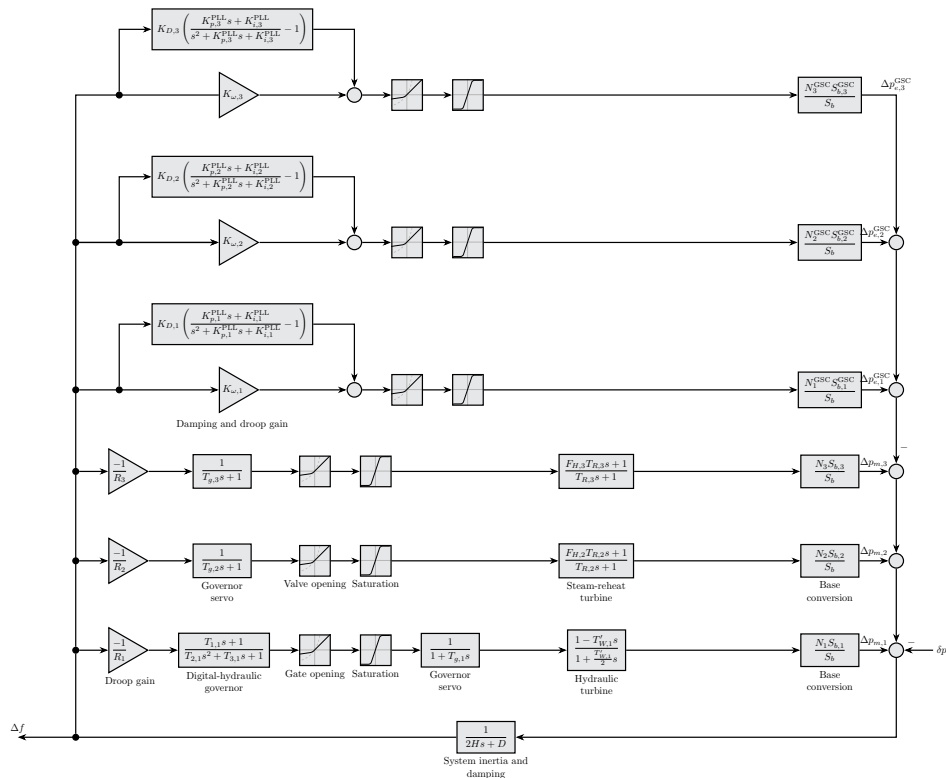
Figure 4.49: SFR model of a system consisting of SGs and grid-forming VSCs (PQ-controlled GSC in VSM scheme).

4.6 Systems based on synchronous generators and grid-forming converters with grid-side DCVC

In this section we shall describe VSM emulation schemes based on DC link power imbalance which explicitly link inertia and damping to the energy stored in the DC link capacitor.

4.6.1 Indirect matching control

First, we start with the *indirect matching control* (DCVC-IDM) described in [25], which we modify to be consistent with the DC power control we used so far (cases a) and c) in (3.22)) instead of DC current control (cases b) and d) in (3.22)). The GSC frequency reference is defined as:

$$\omega = \omega_n + R_{\text{DC}} \left(v_{\text{DC}}^2 - v_{\text{DC}}^{\star 2} \right) = \frac{d\theta}{dt} \tag{4.76}$$

i.e., the reference frequency $\omega = \omega^\star$ is modulated based on the DC voltage deviation from the DC voltage reference, where R_{DC} is the droop coefficient linking voltage imbalance and AC frequency.

On the DC-side, the DC link controller is modified by setting $K_i^{\text{DC}} = 0$. The DC balance equation is thus defined as:

$$\omega_b^{-1} \frac{C_{\text{DC}}}{2} \frac{dv_{\text{DC}}^2}{dt} = K_p^{\text{DC}} \left(v_{\text{DC}}^{\star 2} - v_{\text{DC}}^2 \right) + p_{\text{DC}}^\star - p \tag{4.77}$$

A simplified block diagram of the system (4.76)–(4.77) is shown in Fig. 4.50.

$x = v_{\text{DC}}^2$ is the only state variable in (4.76)–(4.77) (ignoring θ in aggregated SFR models). Therefore, by defining disturbance inputs as $\mathbf{u} = \left(p_{\text{DC}}^\star \ p \right)^\top$, setting $\Delta v_{\text{DC}}^{\star 2} = 0$ (DC voltage reference is constant) and linearising (4.76)–(4.77), the expressions for frequency deviation and DC
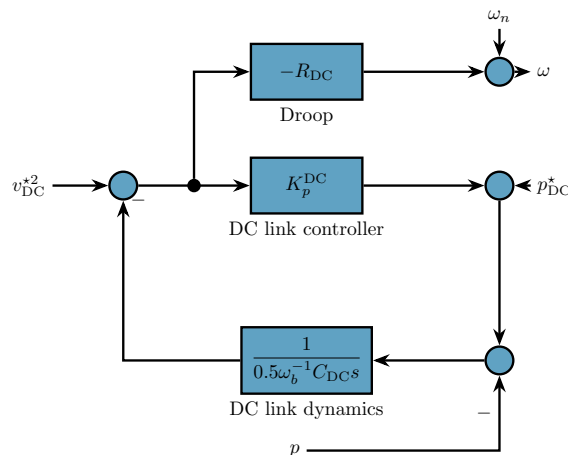
Figure 4.50: Simplified block diagram of a grid-forming VSM scheme based on *indirect matching*.

voltage deviation square are obtained:

$$\Delta v_{DC}^2 = \frac{\Delta p_{DC}^\star - \Delta p}{0.5\omega_b^{-1}C_{DC}s + K_p^{DC}} \tag{4.78}$$

$$\Delta\omega = \frac{\Delta p_{DC}^\star - \Delta p}{0.5\omega_b^{-1}C_{DC}R_{DC}^{-1}s + K_p^{DC}R_{DC}^{-1}} \tag{4.79}$$

One can see that eq. (4.79) has an equivalent form to the standard swing equation where the following relationship holds:

$$2H = \frac{\omega_b^{-1}C_{DC}}{2R_{DC}} \qquad \frac{K_p^{DC}}{R_{DC}} = \frac{1}{R} \tag{4.80}$$

where R^{-1} is the equivalent frequency droop gain (and damping). Therefore, R_{DC} and K_p^{DC} need to be carefully chosen based on the permissible DC voltage deviation under expected grid frequency deviations. By observing Fig. 4.50, one can notice that the power reference set on the device-side is simultaneously modulated by the DC link controller. Therefore, setting a large gain K_p^{DC} to reduce DC voltage deviations will deteriorate set-point tracking.

The simulations are conducted for converter penetrations levels (4.53) of $\eta_c = \{26\%, 41\%, 51\%, 59\%, 71\%, 100\%\}$. Fig. 4.51 shows the converter power output comparison between RMS and EMT models. It can be seen that both models behave identically for all shares of CID. Fig. 4.52 shows that the frequency is uniform in steady-state, however the differences between the SG and VSC frequencies are bigger during the transient state than for PQ-VSM control. It also shows good compatibility of the *indirect matching* scheme with traditional synchronous generators as there were no instability issues observed for different shares of VSCs in the system.

To aggregate the model, we use the same procedure as for the PQ-VSM and SGs described in section 4.5. First we sum up individual virtual (simplified) swing equations over the set of online grid-forming VSC operating in DCVC-IDM mode ($\mathcal{N}_{VSC}^{DCVC-IDM}$), as shown in (4.81). Furthermore, we utilise the relationship between inertia H, DC link capacitance C_{DC} and DC voltage frequency droop R_{DC} per (4.80)

$$\sum_{l\in\mathcal{N}_{VSC}^{DCVC-IDM}} \frac{\omega_b^{-1}C_{DC,l}}{2R_{DC,l}} \frac{d\omega_l}{dt} = \sum_{i\in\mathcal{N}_{VSC}^{DCVC-IDM}} p_l^\star(t) - \sum_{l\in\mathcal{N}_{VSC}^{DCVC-IDM}} p_l(t) \tag{4.81}$$

Then, we assume a well-synchronised system in which all individual virtual speeds ω_l, that are used as the modulating signal for synthesizing the AC frequency, converge towards a uniform system frequency $\omega_l \to \omega$, $\forall l \in \mathcal{N}_{VSC}^{DCVC-IDM}$ as $t \to \infty$. Therefore, (4.81) becomes
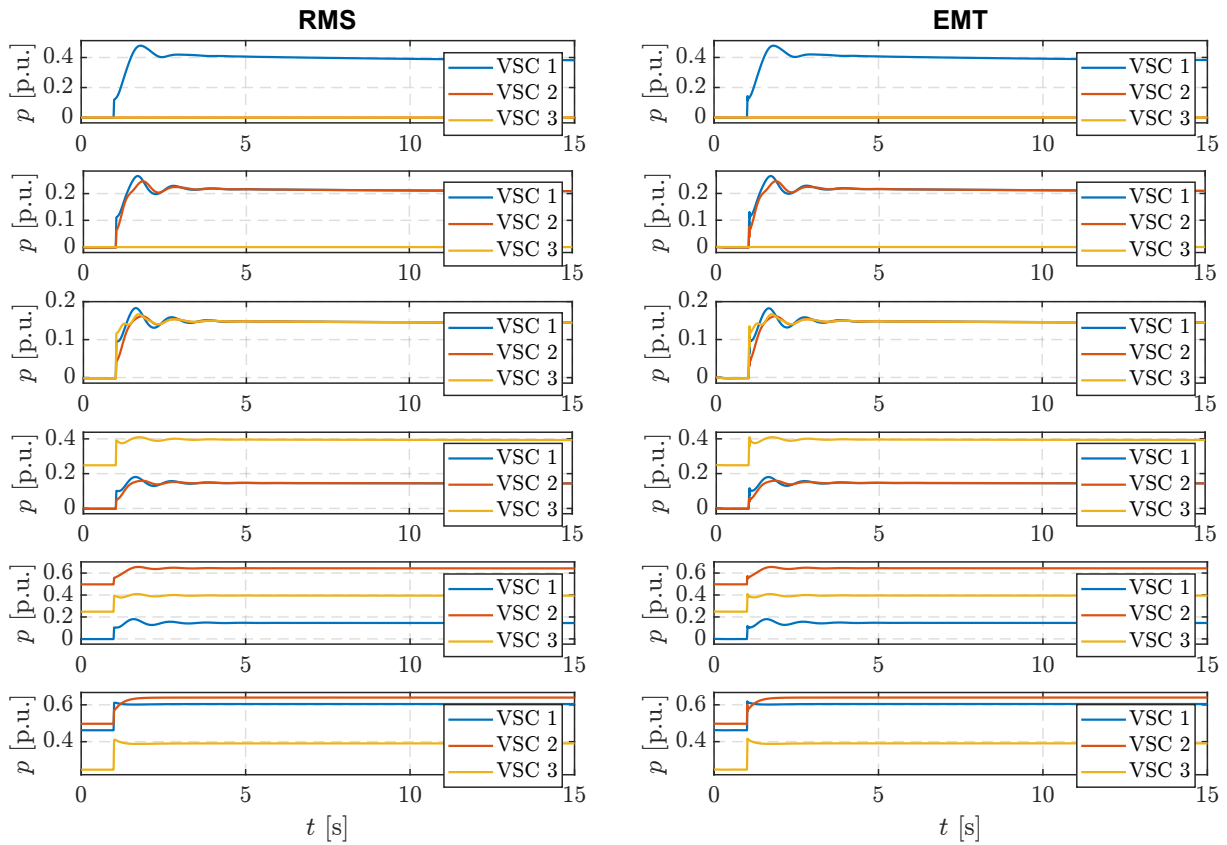
Figure 4.51: EMT vs. RMS: performance comparison of DCVC-controlled GSC (indirect matching) in the VSM scheme. Top to bottom: $\eta_c = \{26\%, 41\%, 51\%, 59\%, 71\%, 100\%\}$.
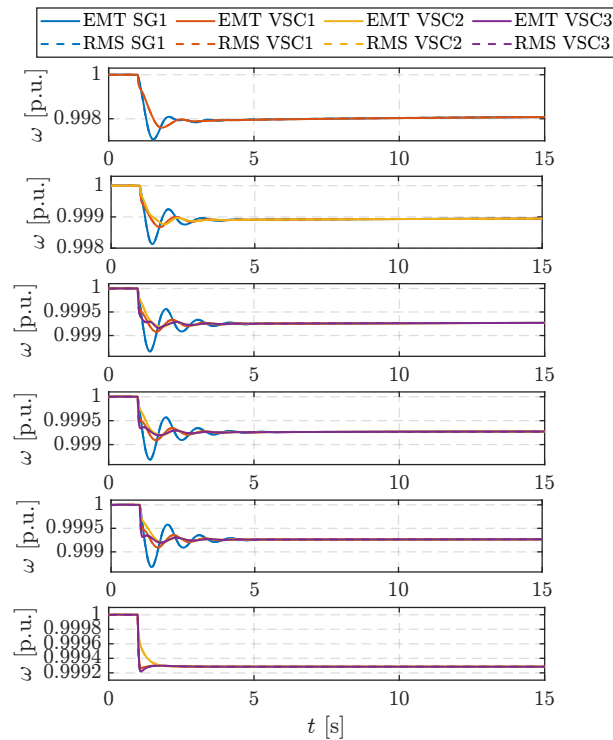
Figure 4.52: EMT vs. RMS: grid frequency for DCVC-controlled GSC (indirect matching) in the VSM scheme. Top to bottom: $\eta_c = \{26\%, 41\%, 51\%, 59\%, 71\%, 100\%\}$.

(4.82):

$$\frac{d\omega}{dt} \sum_{l \in \mathcal{N}_{\text{VSC}}^{\text{DCVC-IDM}}} \frac{\omega_b^{-1} C_{\text{DC},l}}{2R_{\text{DC},l}} = p^\star(t) - p(t) = 2H_{\text{DCVC-IDM}} \frac{d\omega}{dt} \tag{4.82}$$

This virtual inertia can be algebraically added to the synchronous inertia the same way as explained in section 4.5:

$$p^\star(t) - p(t) + p_m(t) - p_e(t) = 2\left(H_{\text{DCVC-IDM}} + H_{\text{SG}}\right) \frac{d\omega}{dt} = 2H \tag{4.83}$$

The DSC power reference $p_{\text{DC}}^\star$ is effectively modulated by the ratio of K_p^{DC} and R_{DC} per (4.80). Linearisation yields:

$$\Delta p_{\text{DC}}^\star \to p_{\text{DC}}^\star + \frac{K_p^{\text{DC}}}{R_{\text{DC}}} \Delta\omega \tag{4.84}$$

Finally, by combining (3.28), (4.82) and (4.84), an SFR model of a DCVC-IDM VSC is obtained, shown in Fig. 4.53.

To validate the SFR model, it is compared against a full-order EMT model of the nine-bus system consisting of multiple SGs and converters, for an outage of generator G4. The results are shown in Fig. 4.54–Fig. 4.55 for various converter penetration levels. The uniform SFR frequency is compared against SG1 and VSC1 which were used as a quick-and-dirty frequency reference. Fig. 4.54 shows that there is a larger discrepancy between SG speed and VSC speed due to the fact that a VSC in the indirect matching scheme has a strong damping in order to keep the DC voltage under permissible limits, which makes it settle more quickly with smaller oscillations. The derived SFR model does not capture these oscillations which is also visible in the power output in Fig. 4.55. Only for the case of $\eta_c = 100\%$ (bottom subfigure from Fig. 4.54), is the SFR model completely accurate.

Fig. 4.54 only shows the individual speed of SG1 and VSC1 which were used as global frequency references. A somewhat smaller error of the SFR model is achieved if its compared to the CoI frequency calculated from all 6 units (3 SGs and 3 VSCs), which is shown in Fig. 4.56. Oscillations still visibly persist in the CoI frequency that are not captured by the SFR model, however the maximum relative error between the SFR frequency and CoI frequency is
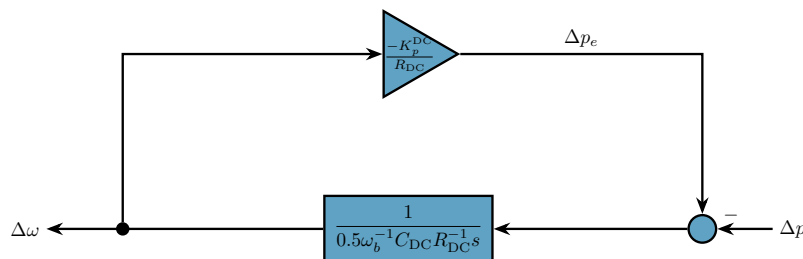
Figure 4.53: Small-signal model of a DCVC-controlled GSC in indirect matching scheme for frequency dynamics analysis.
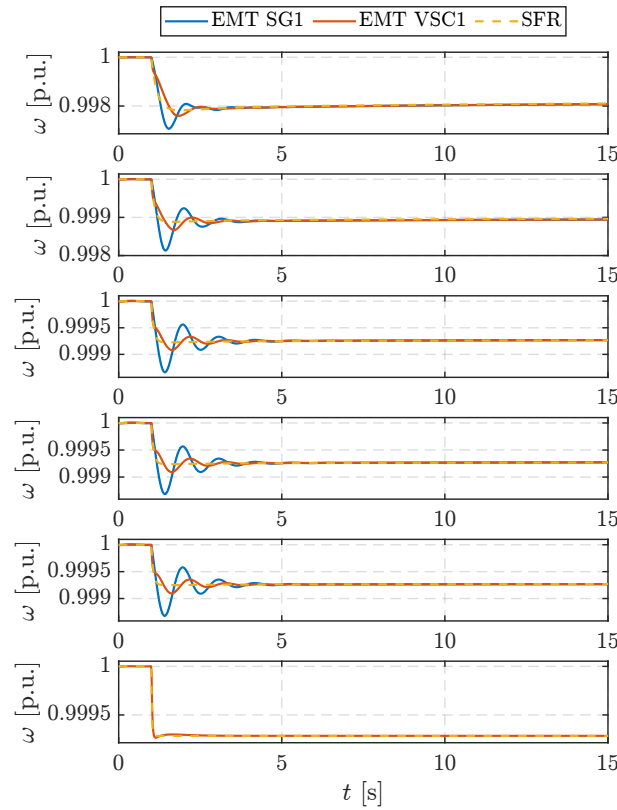
Figure 4.54: EMT vs. SFR: grid frequency for a grid-forming VSC (DCVC-controlled GSC in indirect matching scheme). Top to bottom: $\eta_c = \{26\%, 41\%, 51\%, 59\%, 71\%, 100\%\}$.

under 0.5% (24 mHz absolute error).

Finally, Fig. 4.57 shows the SFR model of the IEEE 9-bus system consisting of SGs and DCVC-VSMs. The system inertia constant is comprised of the SG inertia and DCVC (indirect matching) inertia per (4.82). Regardless of the fact that the virtual and physical inertia are combined to define the system frequency, it is important to note that in this control scheme, in which the GSC is controlled in the indirect matching scheme, the virtual inertia constant and droop gain are limited by the amount of stored energy in the DC link, and depend on the proportional gain of the DC voltage control.

4.6.2 DCVQ VSM (ViSynC)

The final grid-forming control we will analyse was proposed in [145]. Based on the DC link imbalance, it is similar to the *indirect matching* discussed in the previous section. The internal GSC frequency reference $\omega^\star := \omega$ is defined by the following control strategy:

$$\omega = \omega_n + m\left(\hat{\omega} - \omega_n\right) + \frac{s + K_T}{2Hs + K_D}\left(v_{\text{DC}}^2 - v_{\text{DC}}^{\star 2}\right) \tag{4.85}$$

where $m \in [0,1]$, $m \in \mathbb{R}$ is the weighting coefficient that will influence the DC link voltage deviation under grid frequency deviations. For $m = 1$, $v_{\text{DC}}^2 = v_{\text{DC}}^{\star 2}$, but the frequency reference
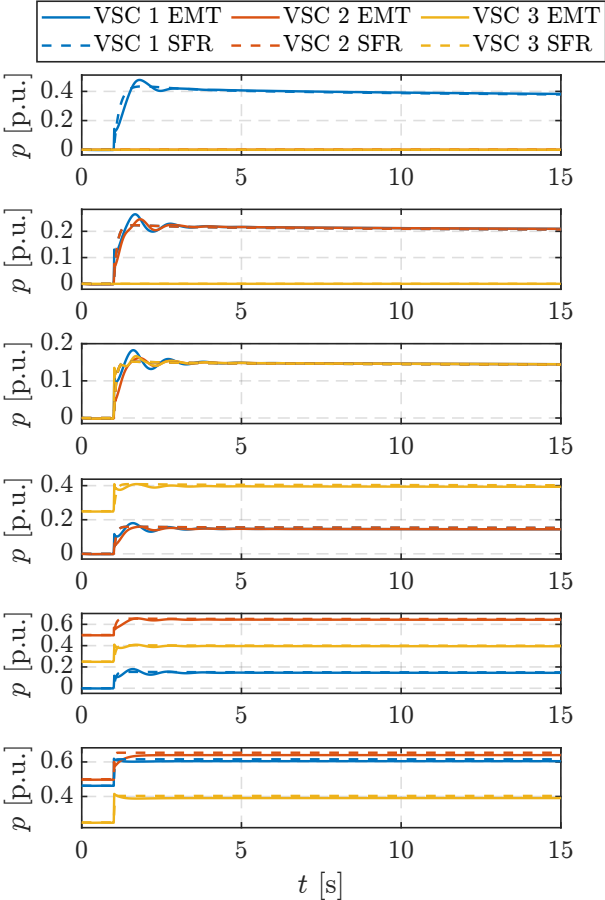
Figure 4.55: EMT vs. SFR: converter output power of a grid-forming VSC (DCVC-controlled GSC in indirect matching scheme). Top to bottom: $\eta_c = \{26\%, 41\%, 51\%, 59\%, 71\%, 100\%\}$.
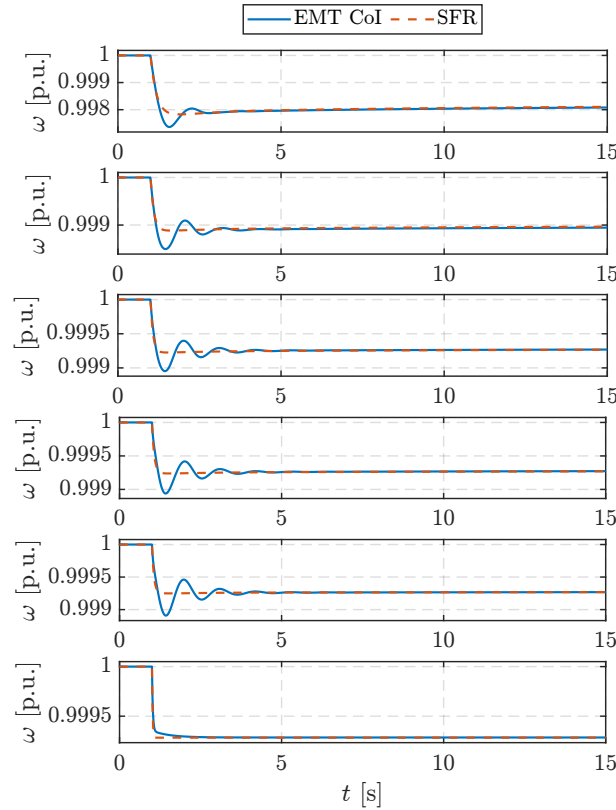
Figure 4.56: EMT vs. SFR: CoI frequency for grid-forming VSC (DCVC-controlled GSC in indirect matching scheme). Top to bottom: $\eta_c = \{26\%, 41\%, 51\%, 59\%, 71\%, 100\%\}$.

is largely impacted by the PLL dynamics. For $m = 0$, on the other hand, PLL has no impact on the VSC frequency reference, but the voltage deviations are larger so the gains need to be carefully tuned. In this section, we strictly focus on the PLL-less case $m = 0$. For $m \neq 0$, the PLL dynamics can be incorporated in the same way as described in section 4.3.

In (4.85), K_T is the voltage tracking coefficient that minimizes DC link voltage deviation; $2H$ emulates the inertia and K_D emulates the damping (droop gain). However, K_D will not actually provide steady-state continuous power change under grid frequency deviation. This control strategy is devised for non-dispatchable sources such as PV, i.e., the GSC will track the power coming from the DSC to balance the DC link. Therefore, it does not provide a spinning reserve that can be utilised from the GSC. Hence, this control strategy requires a stiff AC grid or other sources of flexibility that can provide a primary active power reserve. For ViSynC to provide grid balancing, the frequency droop control must be implemented in the DSC, as described in section 4.4.

To show that the standalone ViSynC is unstable, first we linearise (4.85):

$$\Delta\omega = \frac{s + K_T}{2Hs + K_D}\Delta v_{\mathrm{DC}}^2 \tag{4.86}$$

where we assumed $\Delta v_{\mathrm{DC}}^{\star 2} = 0$ (DC voltage reference is constant). Then, the DC voltage square

129
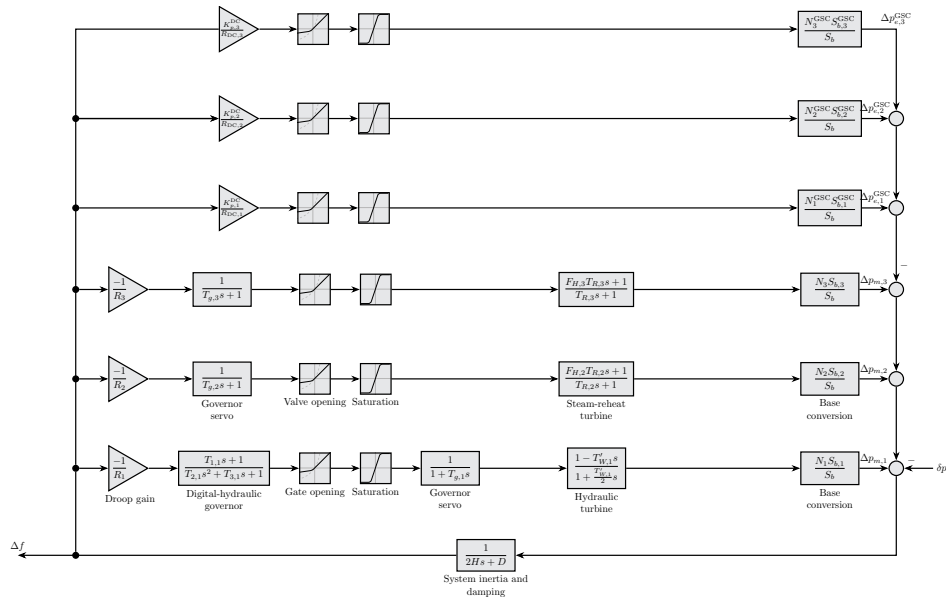
Figure 4.57: SFR model of a system consisting of SGs and grid-forming VSCs (DCVC-controlled GSC with indirect matching scheme).

deviation is expressed via linearised DC link dynamics (3.9):

$$\Delta\omega = \frac{s + K_T}{0.5\omega_b^{-1}C_{\text{DC}}s(2Hs + K_D)}\left(\Delta p_{\text{DC}}^\star - \Delta p\right) \tag{4.87}$$

Thus, for a finite and constant difference $\Delta p_{\text{DC}}^\star - \Delta p$, $\Delta\omega$ behaves according to a ramp because of an extra pole at zero, and this control law cannot stabilise the frequency assuming $\Delta p_{\text{DC}}^\star$ is insensitive to grid frequency deviations. In order to incorporate this control law into an SFR model, (4.87) is rewritten in terms of power output Δp and $\Delta p_{\text{DC}}^\star = 0$:

$$\Delta p = -0.5\omega_b^{-1}C_{\text{DC}}s\Delta\omega\frac{(2Hs + K_D)}{s + K_T} \tag{4.88}$$

Eq. (4.88) shows that ViSynC will provide a transient active power change for $\frac{d\Delta\omega}{dt} \neq 0$ and $\Delta p = 0$ once the frequency stabilizes ($\Delta\omega = $ const.) which inherently assumes that an additional source of frequency damping exists in the system. Generalizing (4.88) to a system with $\|\mathcal{N}_{\text{VSC}}^{\text{ViSynC}}\|$, where $\mathcal{N}_{\text{VSC}}^{\text{ViSynC}}$ is the set of ViSynC converters and $l \in \mathcal{N}_{\text{VSC}}^{\text{ViSynC}}$, (4.89) is obtained.

$$\Delta p_l = -0.5\omega_b^{-1}C_{\text{DC},l}s\Delta\omega\frac{(2H_ls + K_{D,l})}{s + K_{T,l}} \tag{4.89}$$

First, we show that the RMS and EMT models behave identically for converter penetration levels of $\eta_c = \{26\%, 41\%, 51\%, 59\%, 71\%, 80\%\}$. For $\eta_c > 80\%$, the system is not stable since there is not enough spinning reserve to cover the outage of generator G4, and ViSynC units do not participate in droop control due to the aforementioned reasons. One can see in Fig. 4.58 that the initial power transient (inertial response) is larger in the EMT simulation than in the

130

RMS simulation (up to 20% in certain cases). However, Fig. 4.59 shows that the frequency is uniform in both the quiescent and transient state.

We also notice that the frequency deviations are the largest of all analysed VSC control designs due to the lack of droop control by design in ViSynC. Maximum frequency deviations range between 2%–4% (1–2 Hz) which is well beyond the normal operating range and where underfrequency load shedding as well as generator tripping are activated. The virtual inertia and damping coefficients need to be sufficiently reduced for $m = 0$ in order to keep the DC voltage deviations in permissible limits, which in turn limits the contribution of ViSynC to frequency containment.

To validate the SFR model, it is compared against a full-order EMT model of the nine-bus system consisting of multiple SGs and converters, for an outage of generator G4. The results are shown in Fig. 4.60–Fig. 4.61 for various converter penetration levels. The uniform SFR frequency is compared against SG1 and VSC1, which were used as a quick-and-dirty frequency reference. Fig. 4.60 and Fig. 4.61 show that the accuracy of the SFR model is severely reduced for $\eta_c > 50\%$ in terms of nadir and the initial power transient, indicating that the behaviour needs to be analysed in more detail and closer to the EMT timescale. Additionally, the G1 providing primary frequency reserve experiences a large deviation from the initial operating point which reduces the accuracy of the linearised hydro-turbine governor model, which may be another reason for SFR model inaccuracy.

Finally, Fig. 4.62 shows the SFR model of the IEEE 9-bus system consisting of SGs and DCVC-VSMs. The system inertia constant is comprised only of the SG inertia because of higher order dynamics and a low-pass filter influence of DC voltage tracking $s + K_T$. In this control scheme, the tuning of H, K_D and K_T depends on the size of the DC link and there will be no contribution from ViSynC in steady-state. Note that (4.89) is, by itself, an improper transfer function. This is solved by multiplying the whole branch with $(T_{\mathrm{GSC}}s + 1)^{-1}$ which also takes into account the inherent converter time lag (the time constant is on the order of $\approx 10^{-3}$ s so it can often be ignored as it was done for the PQ-VSM and *indirect matching* scheme).
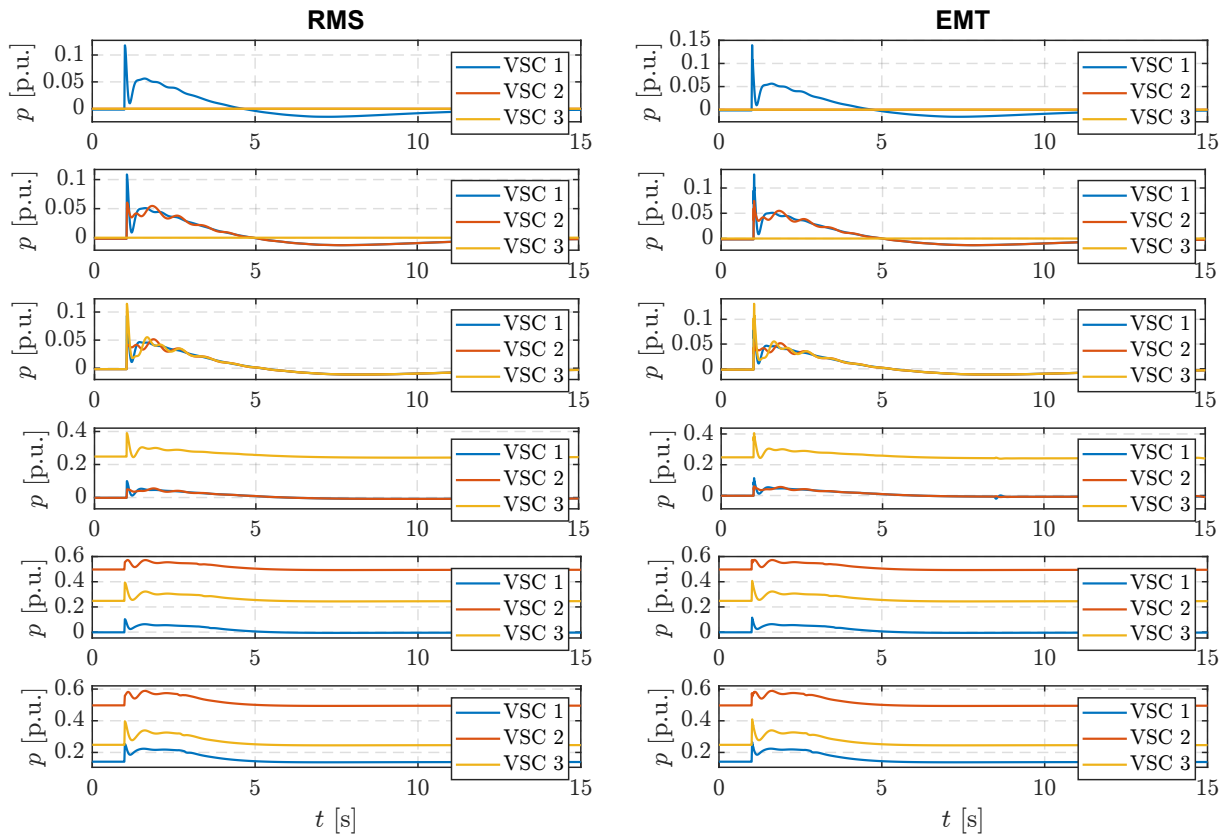
Figure 4.58: EMT vs. RMS: performance comparison of a DCVC-controlled GSC (ViSynC) in the VSM scheme. Top to bottom: $\eta_c = \{26\%, 41\%, 51\%, 59\%, 71\%, 80\%\}$.
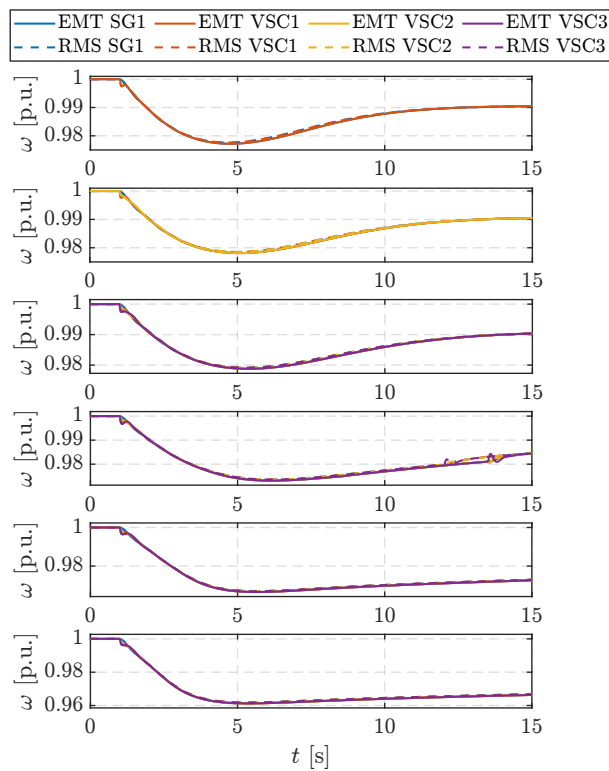
Figure 4.59: EMT vs. RMS: grid frequency for a DCVC-controlled GSC (ViSynC) in the VSM scheme. Top to bottom: $\eta_c = \{26\%, 41\%, 51\%, 59\%, 71\%, 80\%\}$.
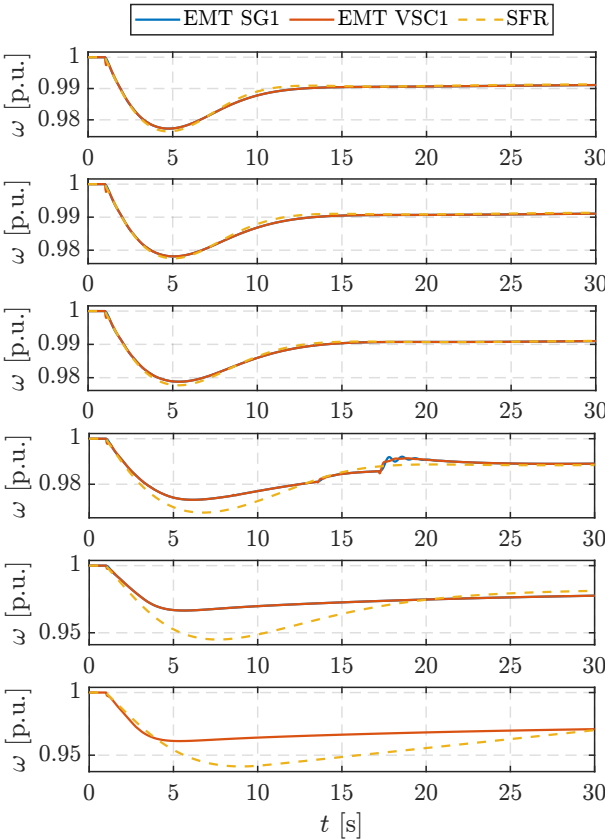
Figure 4.60: EMT vs. SFR: grid frequency for a grid-forming VSC (DCVC-controlled GSC in the ViSynC scheme). Top to bottom: $\eta_c = \{26\%, 41\%, 51\%, 59\%, 71\%, 80\%\}$.
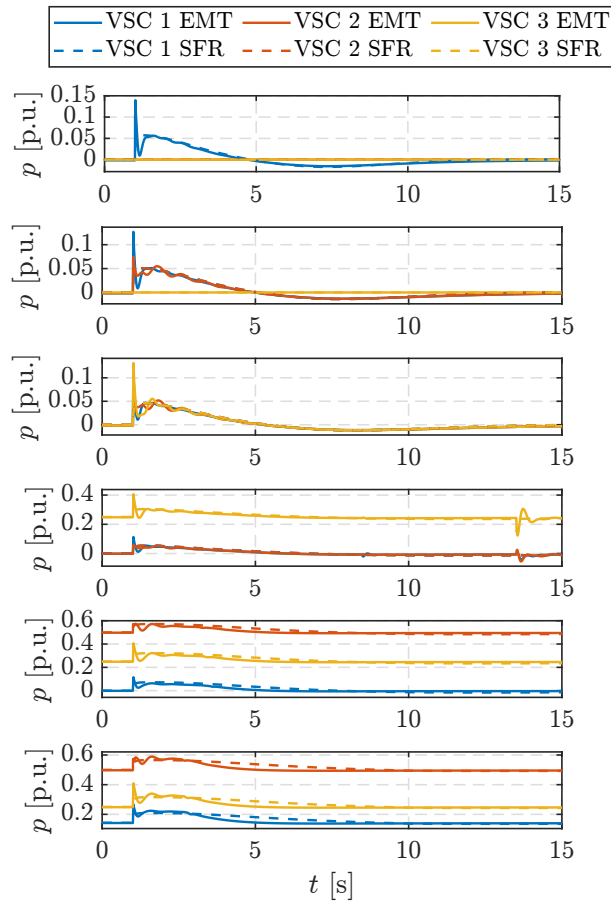
Figure 4.61: EMT vs. SFR: converter output power of a grid-forming VSC (DCVC-controlled GSC in the ViSynC scheme). Top to bottom: $\eta_c = \{26\%, 41\%, 51\%, 59\%, 71\%, 80\%\}$.
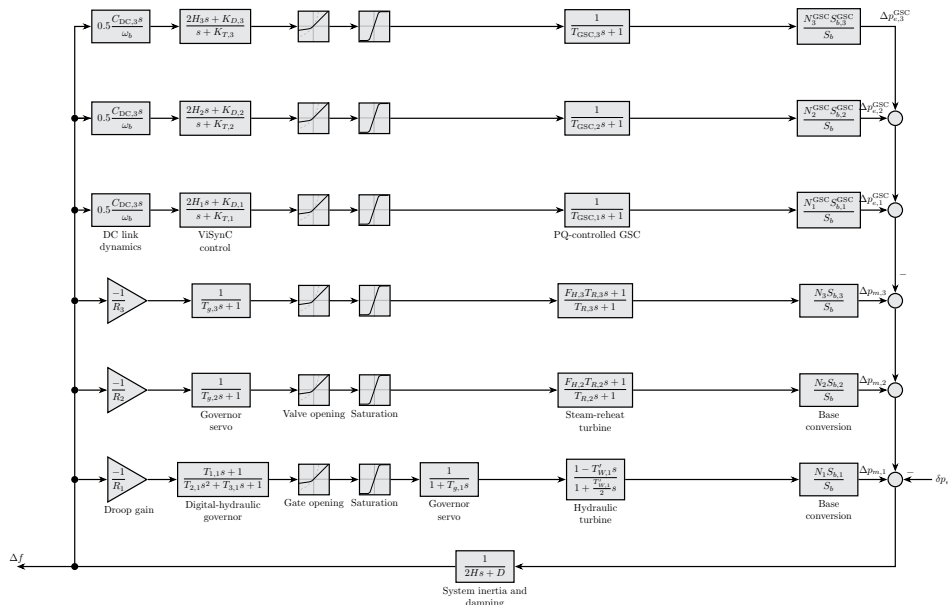
Figure 4.62: SFR model of a system consisting of SGs and grid-forming VSCs (DCVC-controlled GSC with the ViSynC scheme).

4.7 Summary

This chapter focused on understanding power system frequency dynamics through the lens of low-order models inspired by Anderson and Mirheydar [20]. The assumptions upon which such models rely have been revisited and extended in the context of converter-dominated power systems. All newly derived models have been validated against full EMT models in DIgSILENT PowerFactory.

First, the conventional SFR model has been derived for a system consisting of synchronous generators only. Here, the potential effect of power system stabilizers on frequency has been discovered even though such devices are not usually considered since they are a part of an excitation system. However, modulation of the excitation current based on the speed signal will impact the terminal voltage and therefore also the power output in transient conditions. Then, synchronous and induction motors were introduced as examples of most common frequency-dependent loads. The impact of their mechanical load characteristic on frequency dynamics has been analytically quantified and discussed in terms of the well-known D parameter (load self-regulation) in SFR models. Furthermore, it was shown that while synchronous motor inertia directly contributes to aggregated system inertia, the inertia of the induction generator is not instantaneous due to the slip characteristic, i.e., there is a certain time lag associated with it.

Next, the grid-following converters were introduced. It was shown how PLL dynamics can lead to frequency instability and how PLL bandwidth and additional filtering need to be carefully chosen. We have derived a model of a PLL for SFR studies as well as SFR models of two grid-following control schemes from Chapter 3. The derived models show improved accuracy in predicting grid frequency behaviour, although the accuracy is reduced for converter penetration levels $> 80\%$. Nevertheless, the inaccuracy is on the conservative side since the SFR model predicts a worse behaviour than the EMT model.

SFR models were derived for three grid-forming schemes as well, per Chapter 3. The SFR model of PQ-VSM is accurate up to 100% converter penetration. The SFR model of indirect matching scheme is completely accurate only in the case of 100% converter penetration when all units are the same. In all other cases the error is not significant, but exists due to the fact that this control design in mixture with synchronous generators results in a non-uniform frequency during the initial transient. It was found that the ViSynC scheme does not perform well in pure grid-forming mode in low inertia scenarios since grid frequency excursions were the largest (up to 3%–4%) and the system was unstable for penetration levels $> 80\%$. Consequently, the SFR model of the ViSynC scheme was accurate up to 50%.

The effect of grid-forming virtual inertia can be considered instantaneous like in synchronous machines, while grid-following virtual inertia is not instantaneous due to the time lag of PLL in frequency estimation.

Finally, in all simulations, the EMT results were compared to the RMS results and it was found that the RMS model is conditionally suitable for frequency dynamics simulations for all converter penetration levels. The condition under which the RMS simulation is still suitable is that the effective PLL bandwidth is low enough and won't cause any instability. The main source of instability was found to be the inertia emulation control loop which uses a time derivative operator on the estimated frequency signal.

Chapter 5

Reduced order modelling of wind turbine generators participating in synthetic inertial response and primary frequency control

In Chapter 4, we derived SFR models of power systems with various VSC control schemes. However, in all cases the ECS was replaced by a controllable or uncontrollable ideal power source which neglects any specific dynamics of an ECS, such as wind turbine generators or solar PV panels.

In this chapter, we shall analyse the electromechanical dynamics of generic converter interfaced WTGs (type III and IV) in order to quantify their impact on inertia emulation and provision of primary frequency control.

Most of today's commercial wind turbines are horizontal-axis wind turbines. Wind energy systems with this type of turbine can be divided into 4 types (Fig. 5.1) [40]. It is important to note that there are no significant differences in the turbine (mechanical, aerodynamic) part from the perspective of electric power systems, but these 4 types differ in the implementation of the generator/converter [40], as described below.

In the **Type I** configuration (Fig. 5.1, top), a squirrel-cage induction generator (SCIG) is used, directly connected to the grid through a block transformer. This type is also called a wind turbine (WT) with (quasi-)fixed rotational speed because the slip of the induction generator is less than 1% and is closely linked to the grid frequency. These wind power plants are usually designed for one or two wind speeds (in a double-generator implementation). The SCIG always takes reactive power from the grid to establish a magnetic field, so capacitor banks are used for reactive power compensation. The inrush current reduction during synchronisation to the grid is achieved using a *soft-starter* device.

In the **Type II** configuration (Fig. 5.1, second from the top), a wound-rotor induction generator (WRIG) is used, with rotor terminals connected to a variable resistor controlled by power electronics. The variable resistor allows for an increased slip range of about 10%, reducing mechanical stress during wind speed changes. This configuration also requires a *soft-starter* device for inrush current reduction during synchronisation and capacitor banks for reactive power compensation. The disadvantage is that the rotor's slip power is lost as heat dissipates in the variable resistor.

In the **Type III** configuration (Fig. 5.1, second from the bottom), a WRIG is also used, but the rotor terminals are connected to the grid through a frequency converter (usually a *back-to-back* voltage converter controlled by PWM) while the stator is directly connected to the grid. As the stator and rotor voltages are often different [173], a three-winding transformer is usually used as a solution through which the entire system is connected to the grid. The frequency converter is rated at approximately 30% of the generator's nominal power. This configuration allows for a wider speed range (from -40% to $+30\%$ of synchronous speed) and the same amount of active power can be transferred between the rotor and the grid (in both directions) via the converter. Furthermore, another advantage of this configuration is that the converter can also perform reactive power compensation and "softer" grid synchronisation, so separate devices for *soft-start* and reactive power compensation are not needed. Moreover, the frequency converter allows for independent control of active and reactive power, and the generator can inject reactive power into the grid (similar to an overexcited synchronous generator).

In the **Type IV** configuration (Fig. 5.1, bottom), the generator is completely separated from the grid via a frequency converter that transfers the generator's full nominal power. This configuration may or may not have a gearbox, depending on the generator implementation. Since the generator is completely separated from the grid, there are no restrictions on generator selection. Thus, in this configuration, a squirrel-cage induction generator or a wound-rotor induction generator can be used, as well as a permanent magnet synchronous generator (PMSG) with a gearbox implementation, or a multipole PMSG and a synchronous generator with an excitation winding (SG) in a gearbox-free implementation (i.e., *direct-drive* design) [174].

As elaborated in Chapter 1 and Chapter 2, the model fidelity depends on the type of phenomena observed. In particular, for power system frequency dynamics it is sufficient to use RMS simulations, even in scenarios of high shares of CID (up to 100%, as shown in Chapter 4). Therefore, in this chapter, we shall stick with RMS modelling for studying the impact of WTGs on system frequency dynamics. Wind turbines of type III and IV contain power electronic converters whose switching frequencies are on the order of kHz and would require a very small integration step, and whose electromagnetic phenomena are not of interest. Current controllers on converters act very quickly, and a new reference current value can be achieved within 10 milliseconds [175], which is a common integration step in dynamic simulations of interest.
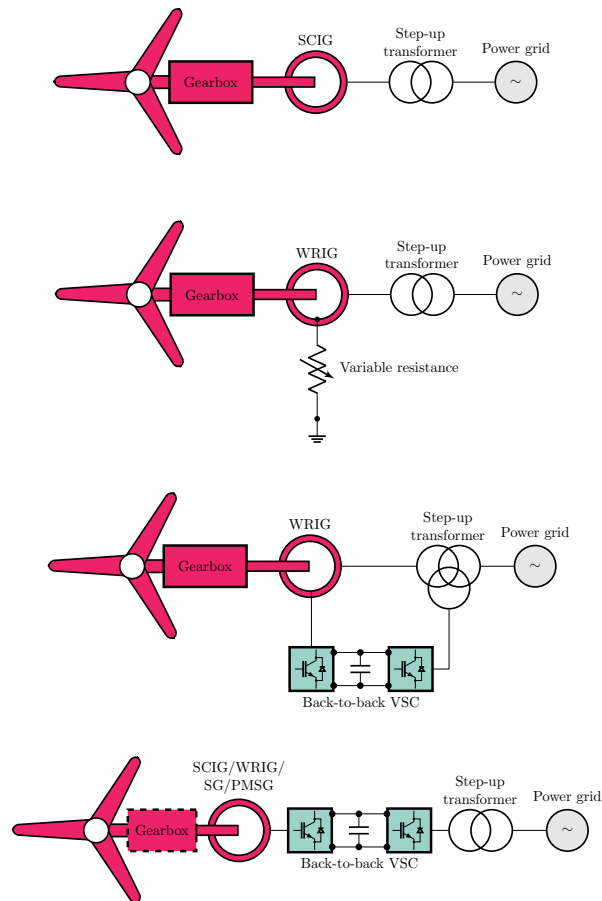
Figure 5.1: Wind turbine implementations, top-to-bottom: fixed-speed (Type I); variable slip (Type II); DFIG (Type III); Full converter (Type IV).

Therefore, the new current value is achieved within one integration step, which allows for the following simplifications:

- if rotor transients in the rotor equations of the induction generator in type III are neglected, frequency converters are modelled as dependent current sources. Otherwise, they are modelled as dependent voltage sources;

- stator and rotor transients in the equations of the *direct-drive* synchronous generator in type IV can be neglected.

The conditions under which these assumptions are valid are listed in [175], and for the purposes of frequency stability simulations, they can always be considered fulfilled. A more detailed discussion on wind turbine modelling for various purposes can be found in [40, 176]. It is also important to note that there are various approaches to wind turbine modelling and the development of generic models for the purpose of stability analysis of large systems, which have emerged as a result of research and industrial experience of many research groups, as well as international working groups, mostly organised by associations such as the IEC (based in Europe) and WECC (based in North America). Table 5.1 provides an overview of the literature dealing with wind turbine modelling for integration into software packages designed for simulating the

dynamics and stability of power systems. The IEC and WECC working groups continuously work on improving the generic wind turbine models, aiming for these generic models to eventually become standard models, just like other components in power systems. The mentioned generic models have been available for some time in power system analysis software packages such as PSS, NEPLAN, DIgSILENT PowerFactory, etc.

Table 5.1: Overview of generic wind turbine models.

Generic wind turbine models	References
IEC and WECC generic models	[40, 177–182]
General Electric (GE) generic models	[183]
Reduced-order generic models (no type II)	[40, 175, 184–186]
Modelling in DIgSilent PowerFactory software package	[42, 187–189]
Modelling in NEPLAN software package	[190]
Modelling in PSS/E software package	[191, 192]
Modelling in PSCAD/EMTDC software package	[193]
Initialisation of dynamic models	[173, 194, 195]

5.1 Primer on WTG modelling and control

The general structure of the wind energy conversion system (WECS) is shown in Fig. 5.2, where black lines illustrate the subsystems that are common to all 4 types of WECS, and blue dashed lines indicate the subsystems that are specific to variable-speed WECS (types III and IV). The individual subsystems are described in the following subsections based on [196].
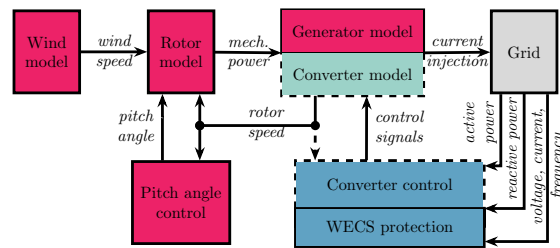
Figure 5.2: General WECS structure.

5.1.1 Wind model

The wind model represents a wind signal source that serves as an input variable for calculating wind power, i.e., the mechanical power developed on the turbine shaft. The wind speed signal can be obtained from measurements or generated from a mathematical model. The mathematical model is more flexible and encompasses all wind characteristics and can be adjusted as needed, which may not be the case for measured data [40]. The mathematical model for generating the wind speed signal is briefly described below according to [40, 175].

The wind speed signal consists of the sum of four components: the mean speed v_{mean}, the ramp v_{ramp} representing linear speed changes, gust v_{gust} representing sudden wind gusts, and the turbulence component v_{turb}.

$$v_w(t) = v_{\text{mean}} + v_{\text{ramp}}(t) + v_{\text{gust}}(t) + v_{\text{turb}}(t). \tag{5.1}$$

The mean wind speed v_{mean}, when the wind turbine operates below the rated power, is obtained by initializing the dynamic model by calculating power flows and solving the nonlinear equation (5.2) with a known mechanical rotor speed and blade pitch angle β of $0°$. If the wind turbine operates at rated power, the mean wind speed must be known in advance because it is not uniquely determined due to the blade pitch control. Expressions for $v_{\text{ramp}}(t)$, $v_{\text{gust}}(t)$, and $v_{\text{turb}}(t)$, as well as an example of a generated signal, can be found in [40, 175] and will not be reproduced here.

5.1.2 Rotor model

The rotor of a wind turbine is a complex aerodynamic system modelled using blade element theory, where it is necessary to use a field of wind speed signals distributed along the rotor blades as well as the rotor geometry [175]. This is very complex and computationally demanding, and such data is often not available to electrical engineers. Therefore, a simpler model is applied when it comes to simulating electrical phenomena, such as the dynamic behaviour of power systems.

The mechanical power developed on the turbine shaft is calculated according to (5.2):

$$p_t(\lambda, \beta, v_w) = \tfrac{1}{2}\rho R^2 \pi C_p(\lambda, \beta) v_w^3(t) \tag{5.2}$$

Where ρ is the air density, R is the rotor radius (blade length), and C_p is the aerodynamic coefficient whose theoretical upper limit is $16/27$, or 0.593 (Betz coefficient). The C_p of modern turbines is 0.52–0.55, but often includes mechanical and electrical losses. In this case, C_p ranges from 0.46 to 0.48 [40].

C_p is a function of the blade pitch angle β and the tip-speed ratio λ which is the ratio of the turbine rotor's tip (linear) speed $\omega_t R$ to the wind speed (5.3). C_p depends on the aerodynamic properties of a particular turbine and is important, among other things, for calculating energy yield. The differences between individual C_p curves of different turbines are negligible from the standpoint of power system dynamics [175, 186], and generic numerical approximations can be used (e.g., (5.4) according to [175]). The software implementation can be realised using the analytical expression (5.4), simpler polynomial approximations [40], or look-up tables. According to IEC/WECC models, there are three representations of the aerodynamic part [177], which

essentially represent the linearisation of aerodynamics (5.2)–(5.5) under the assumption of constant wind speed to reduce the number of parameters that are not known to system operators in principle.

$$\lambda(\omega_t, v_w) = \frac{\omega_t R}{v_w} \tag{5.3}$$

$$C_p(\lambda, \beta) = 0.73 \left(\frac{151}{\lambda_i} - 0.58\beta - 0.002\beta^{2.14} - 13.2 \right) e^{\frac{-18.4}{\lambda_i}} \tag{5.4}$$

$$\frac{1}{\lambda_i} = \frac{1}{\lambda - 0.02\beta} - \frac{0.003}{\beta^3 + 1} \tag{5.5}$$

There are two more effects that can be included in the rotor model; first, high frequencies in wind speed changes are of local character that are dampened over the entire rotor surface, which can be approximated by a low-pass filter (5.6) whose time constant τ depends on the rotor radius, turbulence intensity, and mean speed at hub height [197]. Second, tower shadow is a phenomenon that causes a brief reduction in torque each time a blade passes in front of the tower [40]. Tower shadow is approximated by adding periodic pulsations to the mechanical power (5.2). The transfer function of periodic pulsations $H_{\mathrm{RSF}}(s)$ (5.7) is defined in [197] and depends on the number of blades, rotation speed, and turbulence intensity. The amplitude of this pulsation is a few percent of the mechanical power and is important when investigating power quality and interactions between turbines that are electrically close to each other; tower shadow is more pronounced in the case of downwind facing wind turbines and types I and II, but it is not influential in the case of types III and IV due to power electronics that separate the mechanical and electrical actions.

$$v_{w,\mathrm{filt}}(s) = \frac{1}{s\tau + 1} v_w(s) \tag{5.6}$$

$$p_{t,\mathrm{filt}} = H_{\mathrm{RSF}}(s) p_t(s) \tag{5.7}$$

5.1.3   Mechanical model

The mechanical model refers only to the differential equations that describe the drivetrain: the inertial masses of the turbine and generator interconnected by shafts and a gearbox that connects the mechanical and electrical parts of the unit. Other oscillations and vibrations that can be excited in the mechanical structure of the unit (tower, blades) are in principle neglected as they do not have a significant impact from the grid side [177, 198]. The mechanical part is usually described by a single-mass or two-mass model, where it is usually required that type I and II wind turbines contain a two-mass model due to the rigid connection between rotor speed and electrical parameters of the asynchronous machine [198], while for types III and IV there is no strict consensus and a single-mass model can be used due to the separating effect of power electronics [40, 175, 177, 198]. On the other hand, it is suggested that in most cases a two-mass

model should be used [198], and IEC/WECC models provide the possibility to choose between a single-mass and two-mass model [177] by appropriately selecting parameters. A special case when type III should be described by a two-mass model is when simulating crowbar protection, which in principle briefly connects the rotor terminals [174], and at that moment the type III behaves like a type I.

The two-mass model is described by (5.8), the relationship between the rotational speed of the turbine and the mechanical rotational speed of the generator is defined by the transmission ratio of the gearbox N (5.9) (for direct-drive systems, $N = 1$), while the relationship between the mechanical rotational speed of the generator rotor and the electrical rotational speed is defined by the number of pole pairs p (5.10). H_t and H_g are the inertia constants of the turbine and generator, respectively; T_g and T_e are the mechanical torque on the turbine and the electromechanical torque of the generator, respectively; K_s and D_s are the stiffness and damping of the shaft; γ is the shaft twist angle (the difference in angle between the low-speed turbine shaft and the high-speed generator shaft); f_n is the nominal grid frequency.

$$
\begin{cases}
2H_t \dfrac{d\omega_t}{dt} = T_t - K_s\gamma - D_s\left(\omega_t - \omega_g\right) \\[2mm]
2H_g \dfrac{d\omega_g}{dt} = K_s\gamma + D_s\left(\omega_t - \omega_g\right) - T_g \\[2mm]
\dfrac{d\gamma}{dt} = 2\pi f_n\left(\omega_t - \omega_g\right)
\end{cases}
\tag{5.8}
$$

$$
\omega_t = \frac{\omega_g}{N}
\tag{5.9}
$$

$$
\omega_g = \frac{\omega_e}{p}
\tag{5.10}
$$

For completeness, the single-mass model is defined by (5.11), where all quantities are referred to the high-speed side, with $H = H_t/N^2 + H_g$.

$$
2H \frac{d\omega_g}{dt} = T_t - T_e
\tag{5.11}
$$

Since per-unit values are used in power system calculations, it is necessary to properly choose additional base mechanical quantities to keep the p.u. system consistent when converting mechanical quantities to electrical ones, as described in [40] (Appendix X).

5.1.4 Generator model

Various approaches to modelling generators for dynamic power system simulations can be found in the literature, and there is no strict standard applied: first, an overview of the standard generic models according to IEC/WECC and General Electric (GE) will be given, which

are commonly used in software packages. Then, the standard generator equations will be presented, allowing for the development of classical models.

For types I and II, the IEC/WECC working groups suggest using already integrated asynchronous generator models in power system simulation software packages, while the modelling of types III and IV has been a subject of discussion in recent years [177]. In short, Fig. 5.3 shows a block diagram of type III (without protection) and type IV generator models for dynamic power system simulations accepted by both working groups [177]. Fig. 5.4 shows the official GE unit model [183].
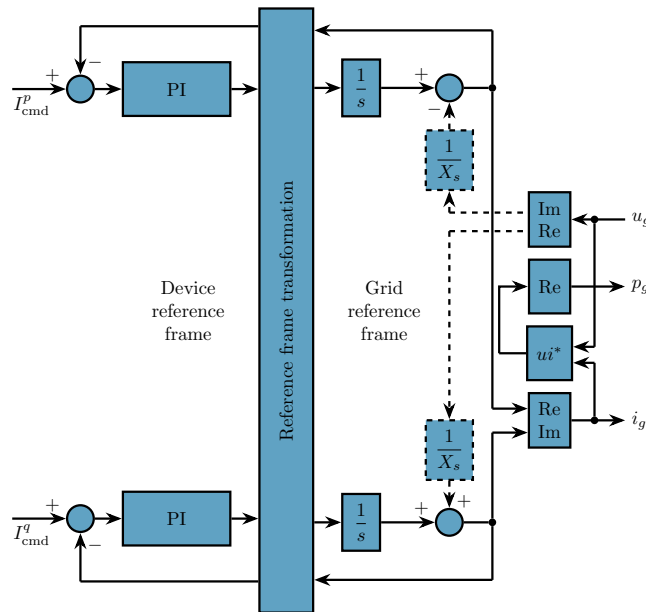
Figure 5.3: IEC/WECC type III and type IV generator models for dynamic power system simulations.
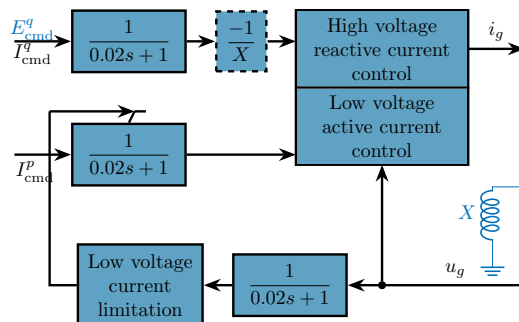
Figure 5.4: GE type III and type IV generator models for dynamic power system simulations.

From both figures, it is visible that the generator and converter are replaced with a control system whose output is the current i_g injected into the grid, and the inputs are control signals. From the shown models, it is evident that any dynamics from classical generator dynamic models have been neglected (rotor mechanical state variables, magnetic flux dynamics $d\psi/dt$), illustrating the fast response of the converter to control signals. The dynamic behaviour of type III and IV wind turbines is entirely determined by the converter, and the entire system behaves

as an algebraic, controllable current source towards the grid [183]. The difference between type III and IV is illustrated by the blue-dashed elements: the type III stator is directly connected to the grid, and a voltage change at the generator terminals will cause a change in the reactive power exchanged with the grid. This transient phenomenon is modelled by adding a reactance X to the generator/converter model [177]. Therefore, in the GE model, the reactive power control signal is voltage E_{cmd}^q instead of current.

On the other hand, there is also an approach where the generator equations and dynamics are included in the model of type III and IV wind turbines. For completeness, generator equations for all four types are shown in the $dq0$ system (generator direction of currents, transformation of abc quantities into a coordinate system rotating at synchronous speed $\omega = \omega_s$, d-axis is co-linear with the main magnetic flux and $\pi/2$ rad behind the q-axis). The equivalent circuit of an induction generator is shown in Fig. 5.5, and the generator equations are (5.12)–(5.15). All rotor quantities are referred to the stator side.
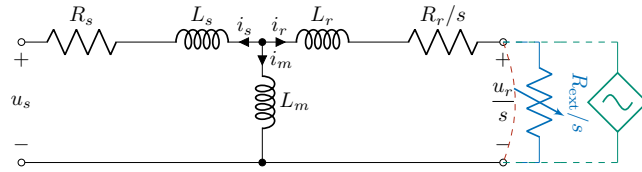
Figure 5.5: Equivalent circuit of induction generators used in type I–III WTGs.

$$u_s^d = -R_s i_s^d + \omega_s \left[(L_s + L_m) i_s^q + L_m i_r^q \right] \tag{5.12}$$

$$u_s^q = -R_s i_s^q - \omega_s \left[(L_s + L_m) i_s^d + L_m i_r^d \right] \tag{5.13}$$

$$u_r^d = -R_r i_r^d + s\omega_s \left[(L_r + L_m) i_r^q + L_m i_s^q \right] + \dot{\psi}_r^d \tag{5.14}$$

$$u_r^q = -R_r i_r^q - s\omega_s \left[(L_r + L_m) i_r^d + L_m i_s^d \right] + \dot{\psi}_r^q \tag{5.15}$$

In the case of a squirrel cage induction generator (Type I), the rotor bars are short-circuited, so $u_r = 0$, i.e., $u_r^d = u_r^q = 0$ (red dashed line in Figure 5.5). For a wound rotor induction generator with a rotor resistor (Type II), a controllable resistor R_{ext} is connected to the rotor terminals (blue dashed line in Figure 5.5). Type III injects currents into the rotor circuit via a dependent voltage source (green dashed line in Figure 5.5), i.e., u_r^d and u_r^q are defined by the converter.

Damper windings can be neglected when the synchronous generator is connected via a back-to-back voltage converter [40, 186]: (5.16)–(5.19) are equations of the synchronous generator with an excitation winding, and (5.16),(5.20) are equations of the synchronous generator with

permanent magnets (both in a reference frame rotating with the rotor $\omega = \omega_r$).

$$u_s^d = -R_s i_s^d + \omega_r \left(L_s + L_m^q \right) i_s^q \tag{5.16}$$

$$u_s^q = -R_s i_s^q + \omega_r \left[-\left(L_s + L_m^d \right) i_s^d + L_m^d i_f^d \right] \tag{5.17}$$

$$u_f^d = R_f^d i_f^d + \dot{\psi}_f^d \tag{5.18}$$

$$\psi_f^d = L_f^d i_f^d \tag{5.19}$$

For a rotor with permanent magnets, the expressions for u_f^d and ψ_f^d disappear as they relate to the excitation winding that the permanent magnet synchronous generator (PMSG) does not have, so equation (5.17) turns into (5.20):

$$u_s^q = -R_s i_s^q + \omega_r \left[-\left(L_s + L_m^d \right) i_s^d + \psi_{\text{pm}} \right] \tag{5.20}$$

In (5.12)–(5.20): u, i, ψ are voltage, current, and magnetic flux; R, L are resistance and inductance; s is the slip; indices s, r, d, q refer to stator, rotor, d and q axis. Transformation into the grid reference frame rotating at synchronous speed ω_s is performed using the appropriate transform (2.18).

More details on induction generator modelling are given in section 4.2. Generally, a good reference book on induction and synchronous machine modelling is [115]. Commercial power system simulation software packages like PSS/E or PowerFactory often do not have a PMSG as a built-in model. It is often modelled either as a standard SG with a constant excitation current [199] or a speed-dependent voltage source [200].

5.1.4.1 Converter + control model

In most literature, converters in the case of Type III or IV are modelled by control systems that generate the required signals. In some models, the DC link, the corresponding converter, and the control are not specifically modelled [40, 177, 183, 188, 189, 192], while in others they are [42, 187, 193]). In the former, only those control loops that control active and reactive power are considered.

For Type III, the rotor-side converter controls active and reactive power, while the grid-side converter controls the voltage of the DC link and maintains the unity power factor. For Type IV, the generator-side converter controls the voltage of the DC link, as well as the voltage and excitation of the generator, while the grid-side converter controls the active and reactive power exchanged with the grid. Regardless of the approach, when only the fundamental harmonic is considered, as in the case of power system stability simulations, the converter is modelled as a dependent voltage or current source without losses that obeys the conservation of active power between the AC and DC parts.

The active and reactive power of the converter (index c) for type III and IV wind turbines are calculated according to (5.21) and (5.22), respectively [186].

$$p_c = p_r = u_r^d i_r^d + u_r^q i_r^q = u_c^d i_c^d + u_c^q i_c^q \tag{5.21}$$
$$q_c = u_c^q i_c^d - u_c^d i_c^q = 0$$

$$p_c = p_s = u_s^d i_s^d + u_s^q i_s^q = u_c^d i_c^d + u_c^q i_c^q \tag{5.22}$$
$$q_c = u_c^q i_c^d - u_c^d i_c^q$$

In the literature, there are many approaches to control systems depending on the variables being controlled, the method of control, and the input and output signals between subsystems. In the following, some control structures for managing active and reactive power for types III and IV, as well as a control structure for managing active power through a variable resistor for type II, will be presented. Note that for simplicity we only show the simplified cascaded control structure without the cross-coupling compensation in inner control loops since the detailed converter modelling was covered in Chapter 3. Fig. 5.6 shows the power control structures for different types of wind turbines:

- Type II—rotor resistance control (Fig. 5.6 top): the control structure for Type II, based on [193], adjusts the rotor resistance to control the active power. The reference active power is generated based on the control characteristic of the power-speed relationship of the generator (slip). The reference effective rotor current is then generated based on the active power, which provides the required value of the rotor resistance.

- Type III—rotor voltage control (Fig. 5.6 middle): the control structure for the rotor converter in Type III wind turbines based on [40, 42] achieves optimal aerodynamic efficiency by measuring rotor speed and generating the maximum power (MPPT) that can be extracted at the current wind speed. Based on the active power, the reference rotor current in the q-axis is generated, which provides the required value of the rotor voltage in the q-axis. Reactive power control is identical, but the rotor quantities in the d-axis are controlled. The reactive power reference can be set directly or indirectly by controlling the voltage of a specific bus or power factor.

- Type IV—grid-side converter control (Fig. 5.6 bottom): the control structure is identical to Type III, with the only difference that the control is applied to the grid-side converter quantities [42]. In this case, since the reference frame is oriented such that the d-axis is collinear with the grid voltage, active power is controlled by the quantities in the d-axis, and reactive power is controlled by the quantities in the q-axis. In the literature, other control structures can be found, such as those in [40, 198], where active and reactive power is controlled through the generator-side converter, and the control variable for active power

is the load angle δ (the angle between stator and converter voltage).
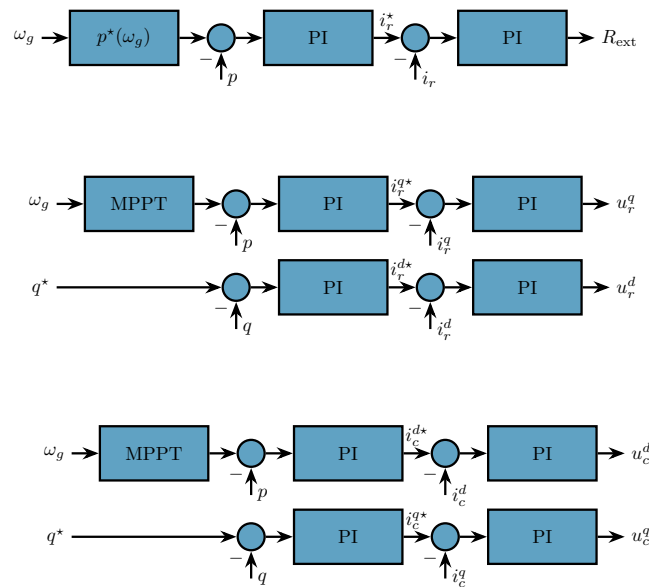
Figure 5.6: Power control of wind turbines: Type II rotor resistance control (top); Type III rotor voltage control (middle); Type IV grid-side converter control (bottom).

5.1.5 Pitch angle control model

The pitch control system is active at wind speeds higher than the rated speed, and its purpose is to limit the aerodynamic torque on the turbine shaft. In the literature, several implementations of the pitch control system have been mentioned, depending on the input variables [177, 201]: wind speed, generator rotational speed, or wind turbine active power.

However, wind speed measurement is not accurate [177, 201], so it is not commonly used in the literature. Therefore, implementations with measurements of generator rotational speed, generator power, or a hybrid version with power compensation can usually be found in the literature.

According to [42], there are two strategies for controlling a wind turbine:

1. If the converter controls power (Fig. 5.6 middle/bottom, where the active power reference is generated using the MPPT curve based on the generator rotational speed), the pitch control system controls the turbine speed;

2. It is possible for the converter to control the generator rotational speed: in this case, the speed reference is generated based on the inverse MPPT characteristic. In this implementation, the pitch control system controls the active power of the turbine.

A hybrid implementation that includes an additional loop for compensating the generator active power is also commonly used, although this additional loop can be neglected [177]. Figure 5.7 shows a hybrid implementation [177]. The two aforementioned implementations are

included in the hybrid implementation and each can be obtained by neglecting either the lower power control loop or the upper speed control loop. The factor K_{px} can also be 0 [191]. The integration elements in the PI controllers are usually blocked in certain situations to prevent the integrator windup. Therefore, the upper and lower limits of the integrators are set according to the limits of the servomechanism: the minimum and maximum blade positions β_{min}/β_{max} and the maximum rate of change of the blade pitch angle $|\dot{\beta}|$. In the literature, the following values can usually be found [28, 175, 191]: $\beta_{min} = 0°$; $\beta_{max} \approx 30°$; $\dot{\beta}max = -\dot{\beta}min \approx 10\frac{°}{s}$; the blades cannot be pitched instantly, and the servomechanism time constant T_β is on the order of 0.3 seconds. In [175], a simpler implementation with only a P controller is used, arguing that the wind turbine is never in a steady state since wind speed is always changing, so the advantage of the integration element (no steady-state error) is not applicable. A more general description of the pitch control system can be found in [28, 40, 42, 177, 201].
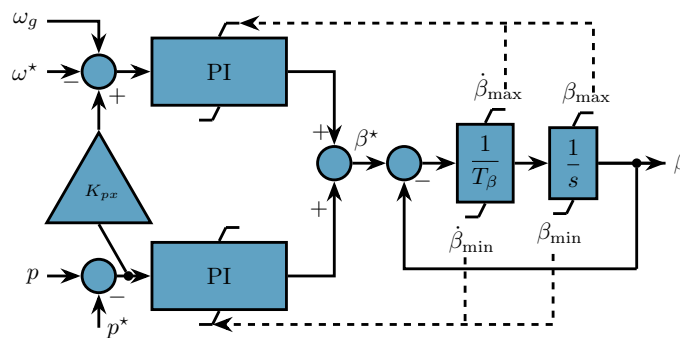
Figure 5.7: Pitch control system.

5.1.6 Protection system model

The protection system prevents damage to the wind turbine from excessive currents during short circuits and prevents islanding operation of the unit after a fault [40]. The protection system is also essential for types III and IV because it is necessary to protect the converters from excessive currents, overvoltages, and undervoltages. Honrubia-Escribano *et al.* [177] document that most discussions have revolved around modelling type III, which is only partially separated from the grid through the rotor converter. Older type III implementations used crowbar protection, which is essentially implemented through an impedance that short-circuits the rotor terminals immediately after fault detection; this bypasses the rotor converter, and then type III behaves like type I. Newer implementations use a chopper and/or a larger converter [177]. Protecting generator windings is not as significant an issue in type IV because the generator is completely separated from the grid.

Since the focus of the subsequent research will be on the participation of wind turbines in frequency regulation, normal operating conditions (except for frequency changes) are assumed,

and wind turbines operate within allowed limits, and short circuits and other major faults will not be considered. Therefore, modelling protection is not of excessive interest. Nevertheless, in the literature [183, 188, 192], it can be seen that protection in simulation models is applied in control systems as saturation blocks with upper and lower limits, and specific logic. Therefore, it is sufficient to act on control signals to simulate protective action [177]. Further discussion on the protection system can be found in [40, 175, 177].

5.2 Participation of WTGs in grid frequency control

5.2.1 Inertial response

Returning to the four main types of wind turbines, two inertial responses can be distinguished: the inertial response of types I and II and the inertial response of types III and IV. Although there are visible differences between individual responses, the responses of the first two types and the last two types are similar enough to be considered together. The inertial responses of the four types of wind turbines are shown in Fig. 5.8. Types I and II are directly connected to the grid, and their behaviour during a grid frequency drop is typical for an induction machine. Type I operates in a narrow oversynchronous region, and the speed change is on the order of 1%, which results in large mechanical stresses due to the power magnitude during the inertial response. This is less pronounced, but still significant in the case of type II, where rotor resistance control will still allow the kinetic energy to dissipate on the resistor. More on the dynamics of type I and II induction machines is shown in section 4.2. On the other hand, the inertial response of types III and IV is not significant due to the power electronic interface. In the case of type III, the frequency converter separates the rotor's mechanical frequency from the grid frequency, but the stator is still directly connected to the grid, so there will be a certain injection of active power into the grid immediately after the disturbance (depending on the PLL gain tuning). However, in Figure 5.8, it can be seen that this power amplitude is only a few percent of the initial value, and the entire transient phenomenon ends within 100 ms, with the released kinetic energy being negligible. The type IV generator is completely separated from the grid via a converter, so the inertial response is non-existent, as the behaviour of the wind turbine is entirely determined by
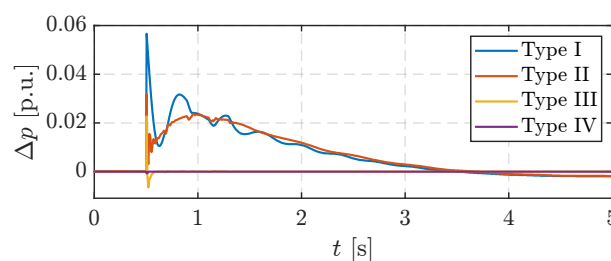
Figure 5.8: Inertial responses of different types of wind turbines.

the converter: from Figure 5.8, it can be seen that there is no injection of active power into the grid, i.e., a type IV wind turbine does not sense the grid frequency change, and the power remains constant.

Therefore, type I and II wind turbines have an inherent inertial response that cannot be controlled and is not of excessive interest in the literature [202–204]. Furthermore, these are older generation units, and their representation in systems is very small [28]. On the other hand, types III and IV wind turbines are the most represented on the market today because they enable maximum aerodynamic efficiency over a wide range of wind speeds, but on the other hand, their integration into the system reduces the system's inertia constant because types III and IV wind turbines have reduced or no inertial response due to the separating effect of frequency converters. However, the ability to flexibly control wind turbines with variable rotational speeds allows the addition of artificial inertial response using secondary control loops sensitive to RoCoF, which is referred to in the literature as virtual/synthetic inertia or fast frequency response. Therefore, the focus will be on virtual inertial response by types III and IV in the following sections.

5.2.1.1 Wind turbine inertia

Wind turbines have inertia comparable to conventional thermal/hydro units. The moment of inertia of a wind turbine can be approximated by an empirical expression according to (5.23) [205]:

$$J_t = 1.12 P_n^{2.135}, \tag{5.23}$$

where J_t is the moment of inertia of the turbine in 10^6 kgm^2; P_r is the rated power of the unit in MW. The generator's moment of inertia, J_g, is significantly smaller and ranges from 65 to 200 kgm^2 for 2–5 MW units according to data from [40, 205, 206]. The rotating mass of the turbine and the rotating mass of the generator are generally connected via the gearbox's transmission ratio. The equivalent moment of inertia, recalculated on the high-speed shaft, is calculated according to (5.24):

$$J = \frac{J_t}{n^2} + J_g, \tag{5.24}$$

where n is the gearbox's transmission ratio (for direct-drive systems, $n = 1$).

The inertia constant H is calculated according to the expression (5.25), where all quantities are converted to the electrical side:

$$H = \left(\frac{J_t}{n^2 p^2} + \frac{J_g}{p^2}\right)\frac{\omega_e^2}{2S_n}, \tag{5.25}$$

where p is the number of pole pairs, S_n is the rated power, and ω_e is the electrical rotational speed. The inertia constant H for several units of typical rated powers and rated rotational

speeds ω_r is shown in Table 5.2 [38] (the inertia constant is calculated assuming that the rated rotational speed ω_r is 20% higher than the synchronous speed $\omega_s = 2\pi f$). Unlike conventional units, the rotor speed of type III/IV wind turbines can vary significantly and even decrease by 50–60% of the rated speed, which reduces the inertia constant [38]. For example, the temporal inertia constant of a 5 MW wind turbine can vary between 1.5 and 6 seconds.

Table 5.2: Typical wind turbine generator mechanical constants.

S [MVA]	J_t [10^6 kgm^2]	J_g [kgm^2]	n	p	ω_r [rpm]	H [s]
1	1.121	70	75	2	24	4.78
2	4.924	130	100	2	18	5.52
5	34.83	200	150	2	12	6.21

5.2.1.2 Virtual inertia from wind turbine generators

The grid-following concept of controlling wind turbines with virtual inertia and droop is shown in Fig. 5.9. An additional control loop takes the estimated grid frequency deviation $\Delta \hat{f}$ and injects an additional signal Δp that modulates the optimal power reference $p^\star_{\text{MPPT}}$ to provide a new power set-point propagated into the converter control system.

Neglecting the droop control for a moment ($R^{-1} = 0$), T_v is called the virtual inertia constant and has no physical meaning, unlike the actual inertia constant [38]. Theoretically, T_v can be set to any value, and the virtual inertial response, unlike the actual one, is fully controllable: this means that type III/IV wind turbines can provide an even greater inertial response than conventional units [207]. However, the actual capabilities depend on the physical limitations of the unit, and the authors in [206] argue that the gain T_v should be set to a maximum of $1.85H$ to prevent the rotor speed from decreasing below the minimum, which can lead to turbine shutdown.
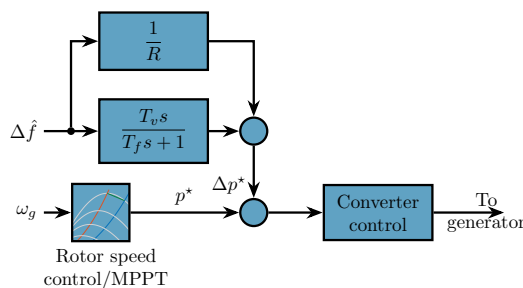
Figure 5.9: Virtual inertia and droop control concept for type III/IV.

Fig. 5.9 shows the so-called "natural" inertial response scheme because it is proportional to the RoCoF, which is analogous to an actual inertial response. In addition to the aforementioned

scheme, there are other schemes for providing virtual inertial response documented in [43]. What they all have in common is that the WTG is temporarily overloaded on the account of the rotor kinetic energy causing the wind turbine slow down, followed by a period of speeding up. Generally speaking, provision of virtual inertia does not require operating at a suboptimal power point (i.e. reserve) since the WTG returns to the initial operating point once the grid frequency is in steady-state (assuming stable operation under adequate wind speed).

5.2.2 Primary frequency control

Contrary to the provision of virtual inertial response, WTG needs to be deloaded in order to provide frequency droop control since a permanent power increase is required under grid frequency reduction. Type I and II wind turbines do not allow for flexible control due to their stiff connection to the grid, and there are not many studies in the literature dealing with primary frequency regulation from these two types [208]. Type I can be deloaded through the blade pitch system by increasing the blade pitch angle β. Type II can be deloaded through the variable resistor or blade pitching. However, the rotor resistor is active only at above-rated wind speeds, and its use is minimised to reduce losses (heat dissipation) [208]. Participation of types III and IV can also be achieved by pitching the blade angle. Nevertheless, frequency droop control by types I–IV through blade pitch control is achieved by modulating $p^\star$ from Fig. 5.7 based on frequency deviations (5.26):

$$p^\star := p^\star + \frac{1}{R}\Delta\hat{f} \tag{5.26}$$

However, converters in types III and IV allow for flexible rotor speed control at wind speeds below rated. The main task of this control is to regulate the optimal rotor speed at which the maximum currently available power is achieved (MPPT block in Fig. 5.6 and Fig. 5.9). The optimal power (or optimal rotor speed), which serves as the reference value propagated to the converter, is determined by (5.27) [174], expressed here in per-unit. ω_n is the rated electrical frequency of the grid, while $C_{p,\text{opt}}$, λ_{opt} are the optimal aerodynamic coefficient and tip-speed ratio, respectively, expressed as dimensionless units.

$$p^\star = K^g_{\text{mppt}}\omega_g^3 \tag{5.27a}$$

$$K_{\text{mppt}} = 0.5\rho R^5 \pi \frac{C_{p,\text{opt}}\omega_n^3}{\lambda_{\text{opt}}^3 n^3 p^3 S_n} \tag{5.27b}$$

The dependence of generator power on generator speed is shown in Figure 5.10. The grey curves in the background show the dependence of mechanical power on rotor speed for different wind speeds according to (5.2). The blue curve is the curve of optimal (maximum) power. Since the blade pitch controller is active only at higher wind speeds, a rotating reserve can be achieved either by accelerating or decelerating the rotor. In the literature, deloading by overspeeding is

commonly used for several reasons:

- greater kinetic energy released during frequency response;
- with deloading by underspeeding, the frequency response is weaker because part of the power must be expended to accelerate the rotor [209];
- deloading by underspeeding is unstable [206].
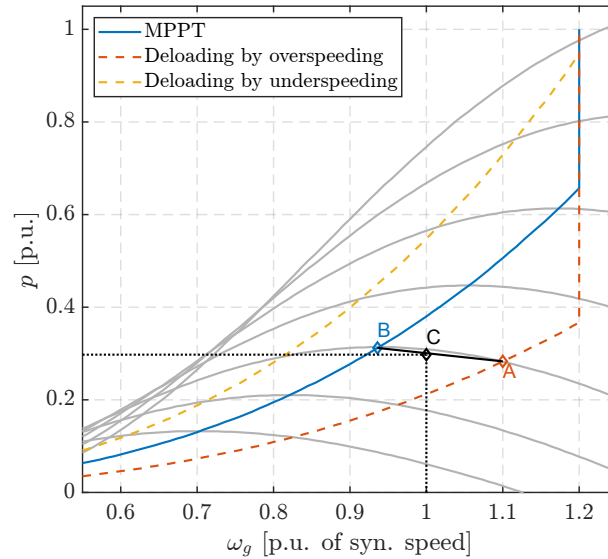
Figure 5.10: MPPT and deloaded curves.

An algorithm often found in the literature [206, 210, 211] is that the VA operates according to the deloading curve at point A (p_A, ω_A). During a frequency drop, the working power reference changes by $\Delta f / R$, and the operating point $(p^\star := p_C, \omega_g := \omega_C)$ shifts along the linear slope from point A towards point B (p_B, ω_B) as defined by (5.28).

$$p^\star(\omega_g, v_w) = P_A(v_w) + \frac{p_B(v_w) - p_A(v_w)}{\omega_B(v_w) - \omega_A(v_w)}(\omega_g - \omega_A(v_w)) + \frac{\Delta f}{R} \qquad (5.28)$$

This algorithm is supplemented with pitch control regulation that ensures the rotor speed does not exceed the maximum allowable value, which is typically around 1.2 p.u. of synchronous speed. Two implementations with this algorithm are presented in [206, 211]. From our own experience in modelling, the rotor speed control approach is not that simple to implement as sliding between the curves can lead to instability. Additionally, instantaneous rotor-effective wind speed needs to be known at all times and a large increase in speed is necessary for a small decrease in power output. Obtaining spinning reserve is more convenient via pitch angle control.

In the literature, some other approaches to primary frequency regulation can be found, such as: coordination of inertial response and spinning reserve [212], dynamic droop [213–215], and pitch control [216]. Table 5.3 shows a literature summary on the participation of WTGs in different levels of frequency control.

Table 5.3: Summary of literature on WTG participation in frequency control.

WTG type	Inertial response	Primary frequency control	Secondary and tertiary frequency control
Type I/II	[43, 202–204]	[208]	-
Type III	[43, 183, 203, 205, 209, 214, 215, 217–219]	[43, 206, 210, 211, 213, 217, 220–222]	[43, 209]
Type IV	[43, 183, 205, 217–219, 223, 224]	[43, 212, 216, 217]	[43]

5.3 Dynamic characteristics of virtual inertial response provision by variable-speed wind turbines

This section is based on [225, 226] and it will analyse sensitivity of various variable-speed wind turbine elements on virtual inertial response provision, namely: device-side converter (DSC) and grid-side converter (GSC) controller parameters, PLL parameters, pitch angle controller parameters and the initial operating point (initial wind speed). The main motivation is to understand how different elements of a WECS impact the provision of inertial response in order to facilitate further research regarding wind turbine control design, as well as to shed light onto the fact that different responses from wind farms may be expected during the frequency containment process. Although the analysis was done on a DFIG-based wind farm, very similar results are expected for type IV turbines as they behave identically in terms of active power control during frequency disturbances [41, 42, 175].

Fig. 5.11 shows the test system used in the simulations. It is a two-machine system consisting of a DFIG-based wind power plant (consisting of 15 aggregated 2 MVA turbines) and a 75 MVA synchronous generator interconnected through a series of lines and transformers. Wind power penetration is equal to 28.5% of total installed capacity. Loads are connected to bus 6. Although this is not a realistic bulk power system model, it is a simple, tractable model for studying frequency dynamics. The synchronous machine represents the rest of the bulk power system while isolating the average frequency dynamics from other factors such as grid topology, interaction between different controllers, different turbine types, etc. which are beyond the scope of this analysis. The standard model of the synchronous machine is used and it is equipped with a *TGOV1* turbine-governor model and a *IEEET1* automatic voltage regulator (AVR). In all test cases, a frequency disturbance is induced by connecting the 5 MW load at $t = 1$ s which is equal to 5% of the total generation capacity and 10% of pre-disturbance load.

Fig. 5.12 shows the overall DSC control system of the DFIG. MPPT or deloaded operation is set by setting the mode flag to 0 or 1, respectively. In this section we only analyse the inertial
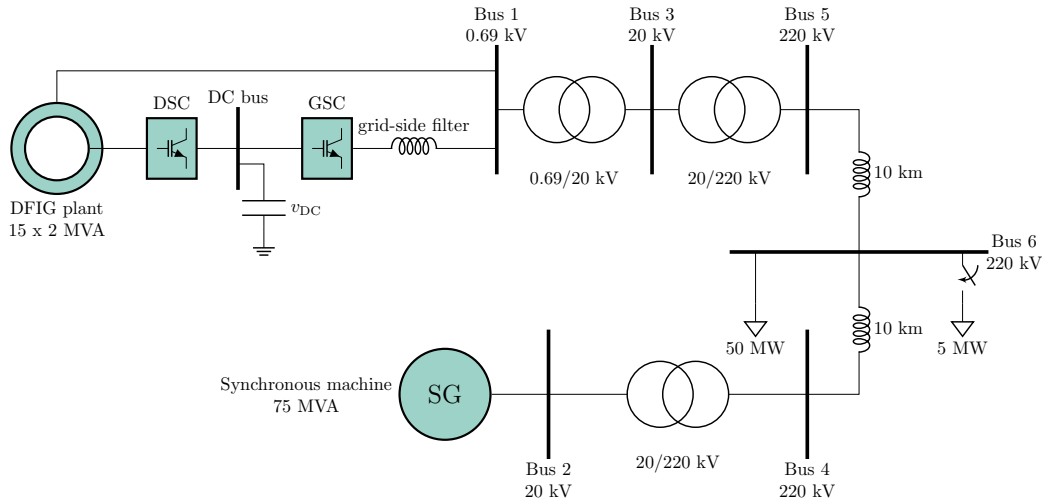
Figure 5.11: Two-machine test system.

response provision ($R^{-1} = 0$) so DFIG operates according to the MPPT curve (Fig. 5.10).
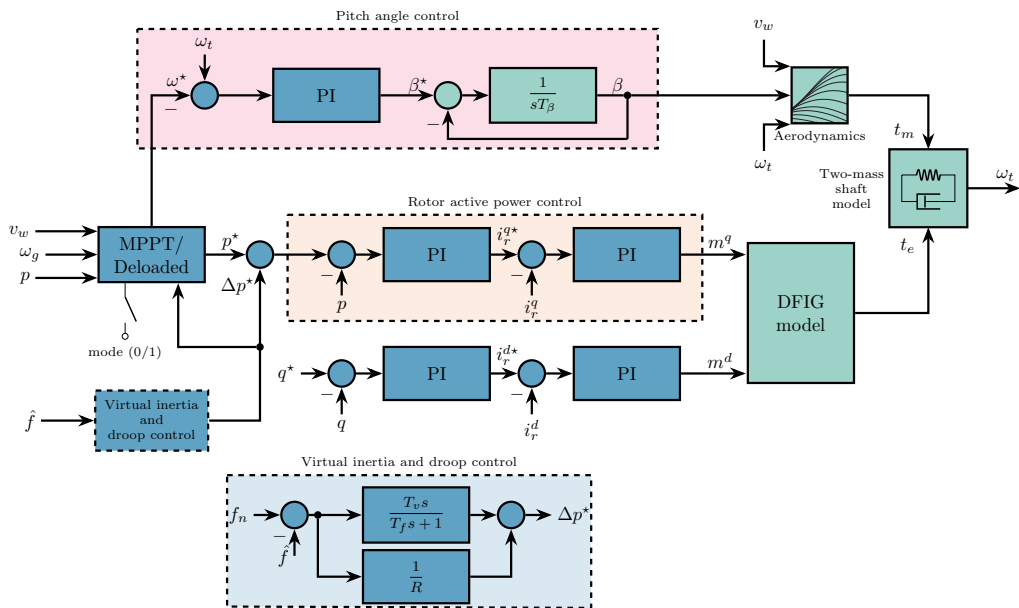
Figure 5.12: Wind-turbine generator model and rotor-side control system.

The following modelling aspects are considered:

- A two-mass shaft model is used (5.8).
- DC link dynamics are considered and GSC operates in the DCVQ mode (see section 3.2.3.2).
- The aerodynamic model from [175] is used, described by (5.2)–(5.5).
- The DFIG model is a built-in element in PowerFactory which consists of a standard fifth-order induction machine model and an integrated rotor-side converter.
- The DSC is controlled in the rotor reference frame, in which the d-axis is aligned with the stator flux (q-axis controls the active power).

Parameters of the complete wind turbine system are given in Appendix A.

5.3.1 Impact of initial wind speed

The wind speed is linearly increased from 7 m/s to 25 m/s. Pitch control becomes active around 12 m/s. Results are shown in Fig. 5.13 and Fig. 5.14. The main observable difference is that the undershoot is smaller for above-rated wind speeds.
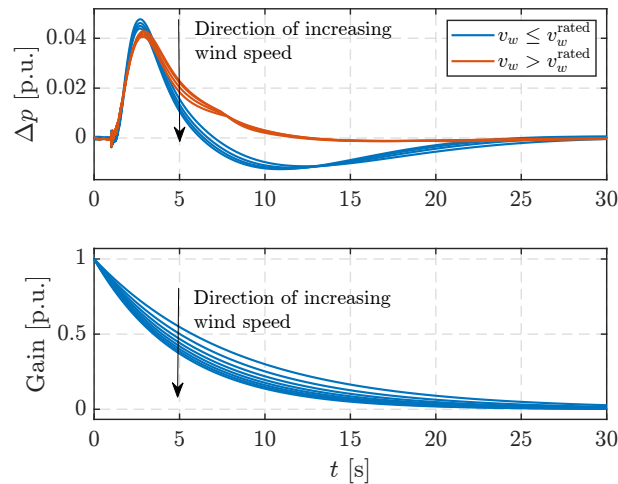
Figure 5.13: Impact of initial wind speed on the virtual inertial response: time-domain response (top) and gain of the WTG transfer function for below-rated wind speed.
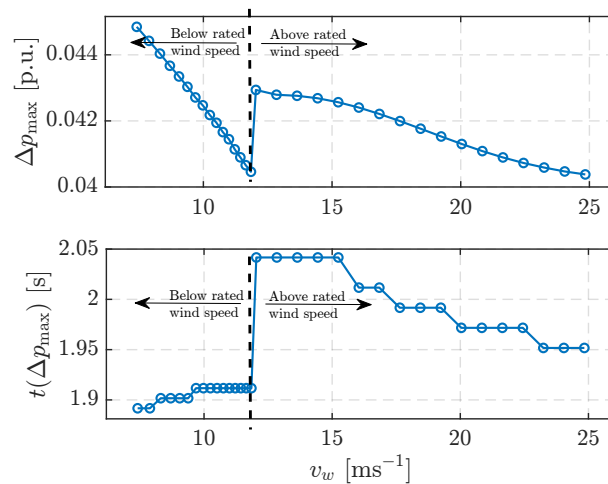
Figure 5.14: Impact of initial wind speed on the virtual inertial response: peak value (top) and peak time (bottom).

Below rated wind speed, the peak value of the inertial response falls linearly with the wind speed while there is no significant impact on the time when the peak value is reached. The explanation can be found in the small-signal stability model of the simplified one-mass wind turbine system which has been derived in [36, 39]; the transfer function $G(s)$ which relates the power set-point change $\Delta p^\star$ to the WTG power output Δp is (5.29) [39, 41]. The amplitude gain

of this transfer function falls with the increasing initial generator speed (i.e., wind speed) which has been illustrated in Fig. 5.14.

$$G(s) = \frac{\Delta p^\star}{\Delta p} = \frac{2Hs - (K_{\text{mppt}}\omega_0 + \frac{\partial T_m}{\partial \omega_g}|_0)}{2Hs + 2K_{\text{mppt}}\omega_0 - \frac{\partial T_m}{\partial \omega_g}|_0}. \tag{5.29}$$

Once the pitch control becomes active and the power reference and generator speed are controlled to be constant, there is a step increase in the peak value compared to the previous wind speed step when pitch control was inactive. Then, the peak value of the inertial response falls nonlinearly with respect to the increasing wind speed reflecting the nonlinear nature of the pitch angle in the aerodynamic model. Slower pitch control action is reflected in the peak time compared to when only rotor speed control is utilised: peak time jumps from 1.9 s to around 2.05 s and falls off with increasing wind speed. This fall-off can be attributed to the high nonlinearity of the aerodynamic part and the shortcomings of the analytical C_p curve at higher wind speeds [227]. The peak value of the inertial response can vary between 0.045 p.u. and 0.040 p.u. depending on the wind speed.

On the other hand, Hu *et al.* [35] used the speed-controlled DFIG model with inverse MPPT characteristics (rotor controller controls the speed rather than power) and they report a stronger inertial response at higher wind speed, which brings us to the following conclusion: inertial response sensitivity is not the same for total power controlled DFIG and for the speed-controlled DFIG. The value of the virtual inertia constant should be a function of the generator speed in order to achieve better inertial response and to achieve a consistent power injection, with respect to both the pre-disturbance power output and the rated power.

5.3.2 Impact of PLL parameters

We vary K_p^{PLL} and K_i^{PLL} linearly between 0.5–5, and 20–35, respectively. Fig. 5.15 shows the time domain response for a conservative and aggressive tuning of PLL gains. It can be seen that the peak value is higher for smaller PLL gains, but the total behaviour is more oscillatory and undesirable. Therefore, smaller PI gains resulted in worse tracking and stronger oscillations. On the other hand, if K_p^{PLL} and K_i^{PLL} are large enough, they do not have a significant impact on the strength of the inertial response (Fig. 5.16).

Secondly, for small PI gains, the DFIG model exhibits a behaviour similar to a non-minimal phase shift system which is visible through the initial undershoot in Fig. 5.15: in the initial moments following a disturbance, the DFIG output power is momentarily reduced, further aggravating the grid frequency dynamics which in turn results in a stronger response. Worse stator voltage angle tracking will indirectly influence the DFIG dynamics because this angle is used for transforming between the rotor reference frame and stator flux reference frame in the rotor-
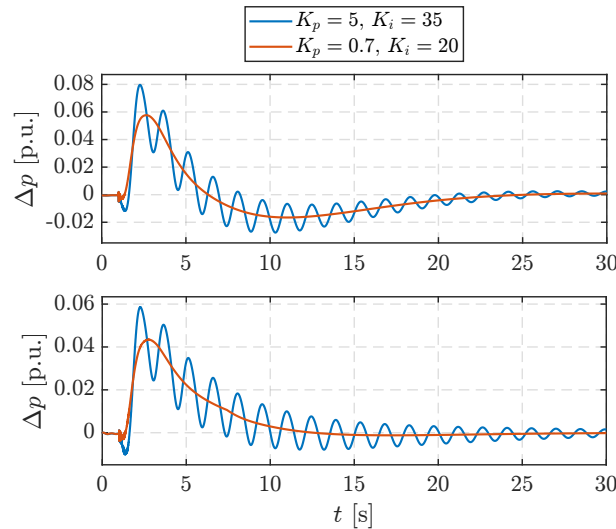
Figure 5.15: Time domain response of the impact of PLL gains on the virtual inertial response: below-rated wind speed (top) and above-rated wind speed (bottom).

side control system. Furthermore, with smaller PI gains the damped frequency of the PLL mode is close to that of the electromechanical modes of the system, which means that the PLL will participate in the electromechanical oscillations of the system.

To the contrary, Ma *et al.* [171] report a weaker inertial response under smaller PLL PI gains and well-damped behaviour. In their paper, they have investigated the impact of PLL dynamics on inter-area oscillations between two systems connected with a weak tie-line. We did not notice any such behaviour in our test system, even with increasing both line lengths from 10 km to 110 km. There can be multiple reasons for this discrepancy between the two results: grid topology, types of excitation systems and power system stabilizers, controller parameters, wind turbine generator models, etc. This behaviour is independent of whether or not the virtual inertial response is active, and it mostly depends on the PLL itself. The participation of PLL in electromechanical oscillations is visible by plotting the trajectories of the PLL mode and the system electromechanical mode (Fig. 5.17). The PLL mode is related to the PLL state variables ζ^{PLL} and $\hat{\theta}$. The synchronous generator (SG) mode has a frequency of around 1.5 Hz and can be considered a local mode. Fig. 5.17 shows that the parameters of the PLL PI controller do not have a significant impact on the SG mode. On the other hand, the PLL mode is close to the imaginary axis for small K_p^{PLL} values (weak damping) and this oscillatory behaviour will dominate the response as seen from Fig. 5.15. By increasing the proportional gain of the PLL, the damping of this mode is increased and, at a certain point, the PLL mode ceases to be oscillatory (it is completely damped). Fig. 5.18 shows that the participation factor of PLL state variables in the SG mode increases for larger K_p^{PLL} gain, but does not depend on the virtual inertia coefficient.

Even though PLL gains are typically large and the PLL mode is well damped [228], note that the PLL bandwidth cannot be arbitrarily high because it can cause instability during frequency
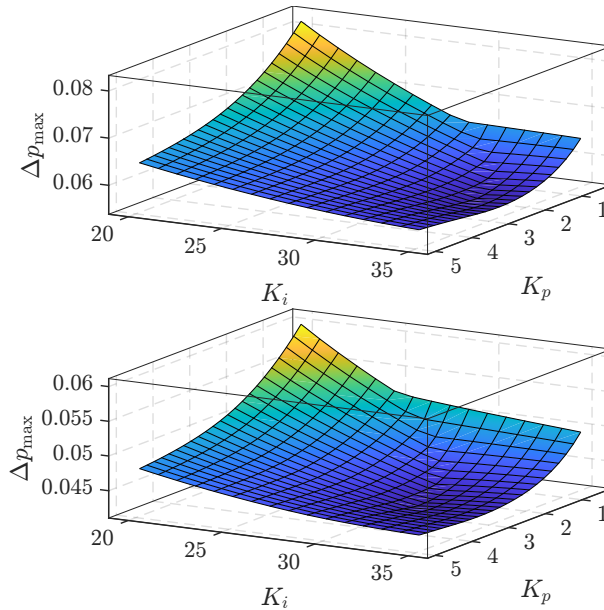
Figure 5.16: Sensitivity of the peak value of the virtual inertial response to PLL gains: below-rated wind speed (top) and above-rated wind speed (bottom).

excursions when the measured frequency is fed back to the active power controller for providing virtual inertia or droop control, as shown in sections 4.3 and 4.4. Since in this particular two-machine system, the DFIG is significantly smaller than the SG, the system is rather strong and such instabilities will likely not occur in RMS simulations.

In conclusion, PLL tuning has a visible impact on virtual inertial response provision by variable-speed wind turbines, but the extent of the impact depends on the grid-following converter penetration level, grid topology and the dynamics of synchronous generators. Nonetheless, PLL dynamics need to be considered, especially in weak or low-inertia systems.
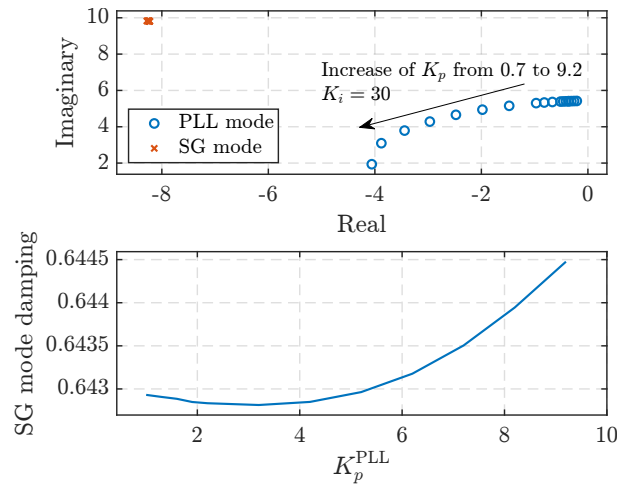
Figure 5.17: Impact of K_p^{PLL} on the PLL and SG modes: eigenvalues (top) and SG mode damping (bottom).
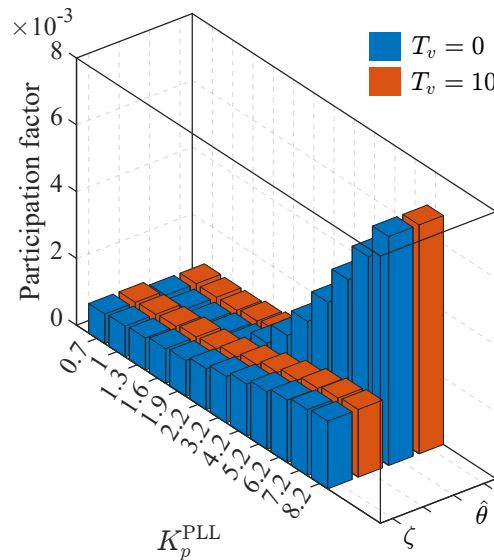
Figure 5.18: Participation factors of PLL state variables ζ and $\hat{\theta}$ in the SG mode for varying K_p^{PLL} and T_v.

5.3.3 Impact of the DSC outer power loop

K_p^{outer} and K_i^{outer} are linearly varied between 1.5–5, and 0.5–8, respectively. Fig. 5.19 illustrates the time domain response for two characteristic strong and weak combinations of PI gains. Fig. 5.20 show the sensitivity of the inertial response on DSC outer PI controller parameters. For smaller PI gains, the virtual inertial response is stronger (higher apex) for both the below-rated and above-rated wind speed. This is because the stronger action of the outer PI loop restrains the change of the generator power more [35]. This, in turn, results in a weaker power injection from DFIG. However, if the outer control loop is fast enough (large PI gains), there is no impact on the strength of the inertial response, as shown by the blue shaded areas in Fig. 5.20. In summary, this means that the dynamics of the slower outer loop should be considered when studying inertial response dynamics. It can be neglected if the PI gains are large, such that the

whole outer loop has faster set-point tracking.
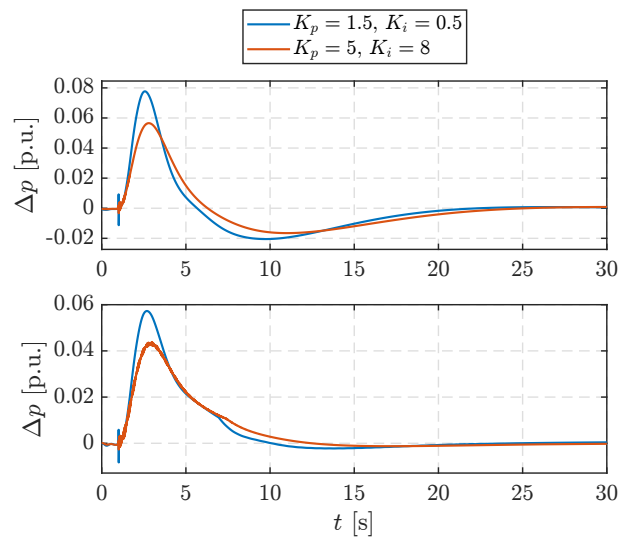
Figure 5.19: Time domain response of the impact of DSC outer loop gains on the virtual inertial response: below-rated wind speed (top) and above-rated wind speed (bottom).
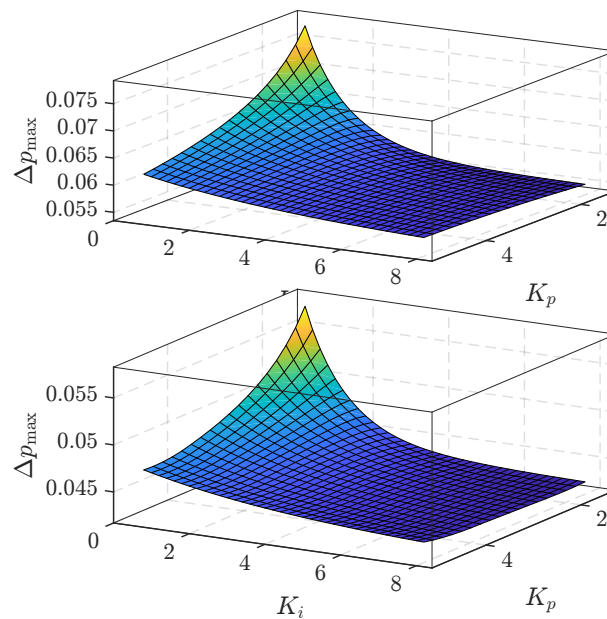
Figure 5.20: Sensitivity of the peak value of the virtual inertial response to DSC outer loop gains: below-rated wind speed (top) and above-rated wind speed (bottom).

5.3.4 Impact of the DSC inner current loop

K_p^{inner} and K_i^{inner} are linearly varied between 0.1–1.4, and 10–100, respectively. The impact of the much faster inner loop dynamics is negligible as shown in Fig. 5.22. The impact on the strength of the inertial response is in the order of 10^{-4}. Compared to the below-rated wind speed scenario when the pitch angle control is not active (Fig. 5.22 top), the strength of the

inertial response is much more sensitive to $K_p^{\text{inner}} > 1$ (Fig. 5.22 bottom), for about an order of the magnitude (10^{-3}). The only visible impact is in the initial fast transient, as shown in Fig. 5.21. Therefore, the dynamics of the inner loop can be neglected in DFIG inertial dynamics and they do not have an influence on the inertial response.
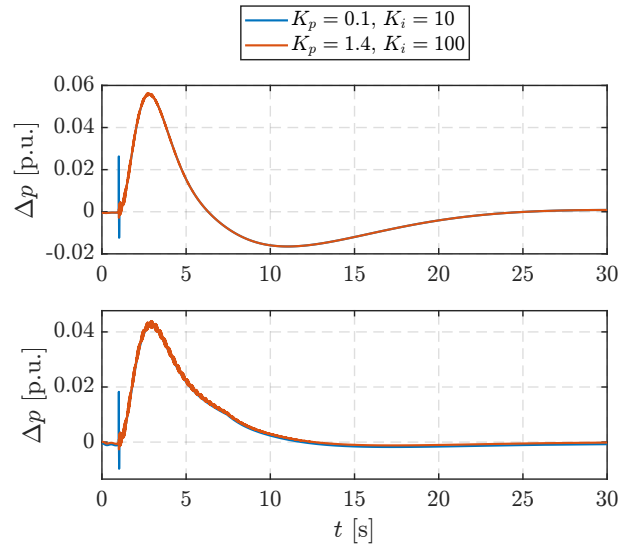
Figure 5.21: Time domain response of the impact of DSC inner loop gains on the virtual inertial response: below-rated wind speed (top) and above-rated wind speed (bottom).
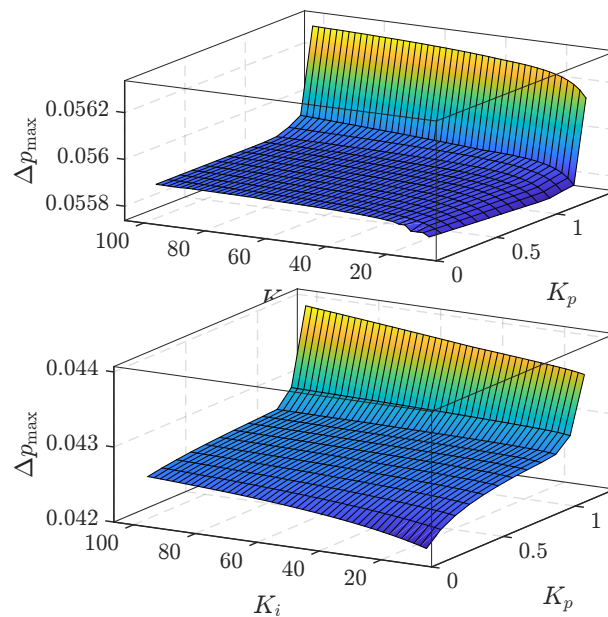
Figure 5.22: Sensitivity of the peak value of the virtual inertial response to DSC inner loop gains: below-rated wind speed (top) and above-rated wind speed (bottom).

5.3.5 Impact of pitch controller

Pitch control is active only at above rated wind speeds to keep the rotor from over-speeding. There are four main parameters which we have studied to see how they impact the DFIG inertial

163

response: proportional and integral gain of the PI controller (K_p^{pitch} and K_i^{pitch}, respectively) that generates the pitch servo reference $\beta^\star$, the time constant of the pitch servo mechanism T_s and the pitch rate limit. K_p^{pitch} and K_i^{pitch} are varied between 80–300 and 0–30, respectively. The pitch servo time constant T_s is varied between 100–500 ms, while the pitch rate limit is varied between 3–13 deg/s. Fig. 5.23 shows the inertial response for some combinations of the pitch PI gains and servo time constants.
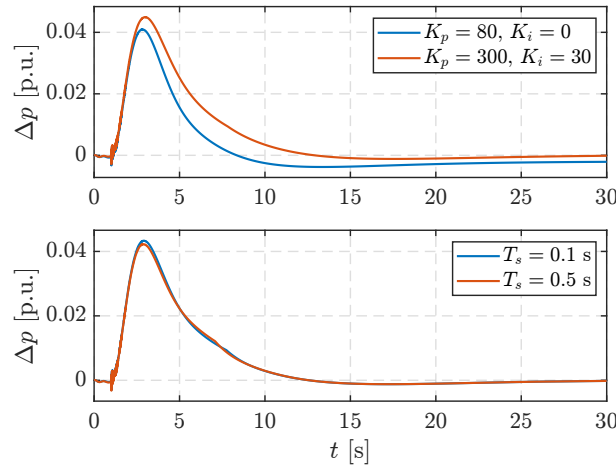
Figure 5.23: Time domain response of the impact of pitch controller parameters on the virtual inertial response: PI gains (top) and the servo time constant (bottom).

A stronger inertial response is achieved with larger K_p^{pitch}, while the K_i^{pitch} doesn't have a significant influence on the strength of the inertial response (Fig. 5.24 top). The time at which the peak of the active power injection occurs is longer for bigger K_p^{pitch} while the K_i^{pitch} does not have a significant contribution (Fig. 5.24 bottom).
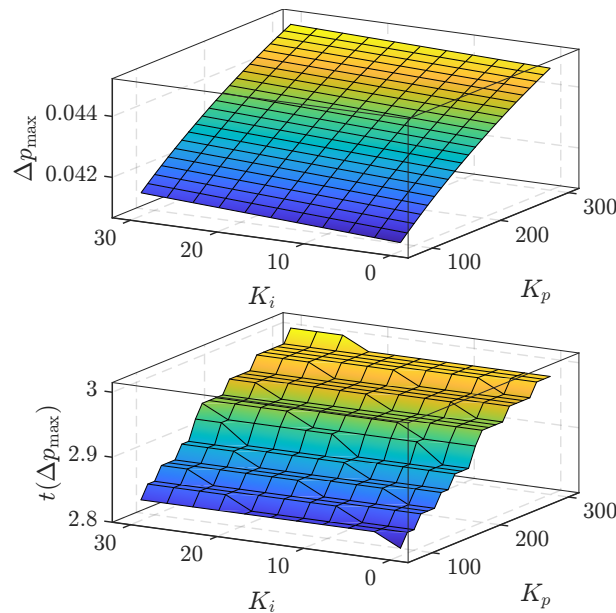
Figure 5.24: Sensitivity of the virtual inertial response to pitch controller PI gains: peak value (top) and peak time (bottom).

Fig. 5.23 (top) also shows that a reduction of K_p^{pitch} and K_i^{pitch} increases the undershoot during which the generator speeds up. On the other hand, the pitch servo time constant and the pitch rate limit do not have a significant influence on the peak value and peak time of the inertial response (Fig. 5.25 and Fig. 5.26).
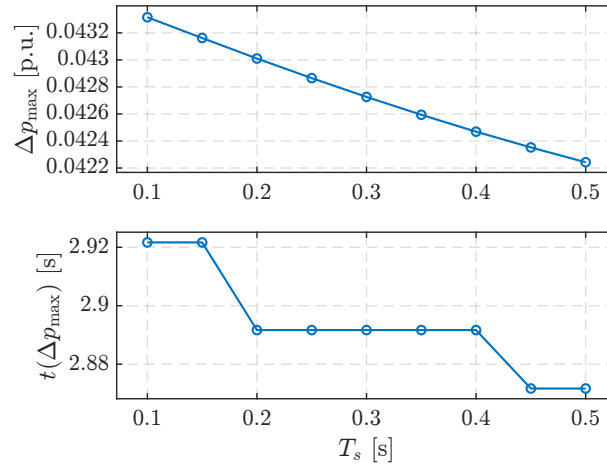
Figure 5.25: Impact of the pitch controller servo time constant on the virtual inertial response: peak value (top) and peak time (bottom).
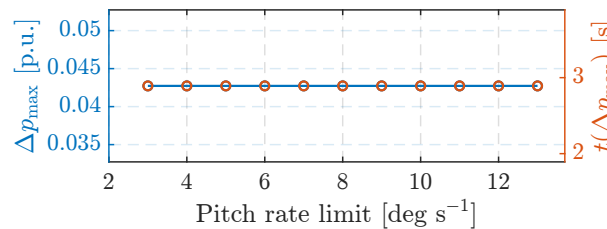
Figure 5.26: Impact of the pitch controller rate limit on the virtual inertial response.

Therefore, characteristics of pitch angle control have a small impact on virtual inertial response shaping, and should be taken into account if the controller has low bandwidth. Otherwise, its influence can be neglected based on the obtained results.

5.3.6 Impact of the GSC DC link controller and DC capacitor

The grid-side converter keeps the DC capacitor voltage constant and controls the power factor at the grid connection point. Inner current control loops will be disregarded in this section since they are fast and do not influence the inertial response as shown in section 5.3.4. Varying the GSC DCVC PI gains does not influence the inertial response of DFIG, as can be seen in Fig. 5.27.

Furthermore, Fig. 5.28 shows that the size of the DC link capacitor does not impact the inertial response dynamic, either. That is because the analysed WECS operates in the grid-following in which the slow active power control is done one the device side, while the fast DC
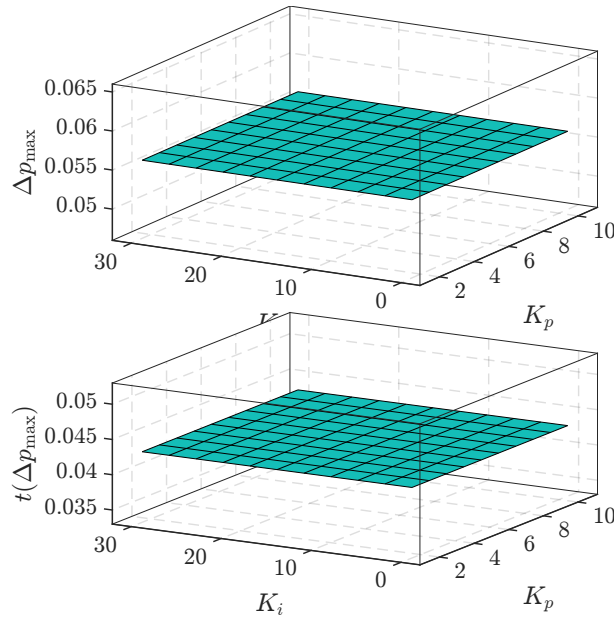
Figure 5.27: Sensitivity of the virtual inertial response to GSC DCVC PI gains: below-rated wind speed (top) and above-rate wind speed (bottom).

link control is done on the grid-side (GSC DCVC mode, section 4.4). Therefore, GSC only follows the DSC to balance the DC link and essentially no energy is extracted from the DC capacitor. GSC and DC link dynamics can be neglected in inertial response studies only if its fast and well-damped.
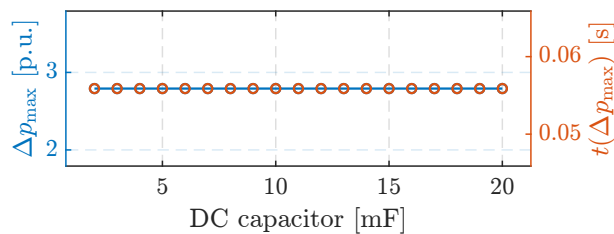
Figure 5.28: Impact of the DC link capacitor size on the virtual inertial response.

5.4 Dynamic characteristics of primary frequency control provision by variable-speed wind turbines

In [225], all the case studies introduced in section 5.3 were repeated for primary frequency control provision, although less comprehensive in terms of sensitivity analysis. The WTG was deloaded by employing overspeed principle and pitch angle control coordination [206], and $T_v = 0$ in these studies. All the conclusions from virtual inertial response sensitivity analysis are valid for primary frequency control as well. The main influence comes from the initial conditions where a $> 50\%$ difference in steady-state power output is observed (Fig. 5.29)

between the below-rated wind speed operation (pitch control inactive) and above-rated wind speed operation (pitch control active). Therefore, this indicates that different effects are at play during different operating conditions, which is why representing WTGs with only their frequency controller dynamics in system frequency response studies may not be accurate and requires further investigation.
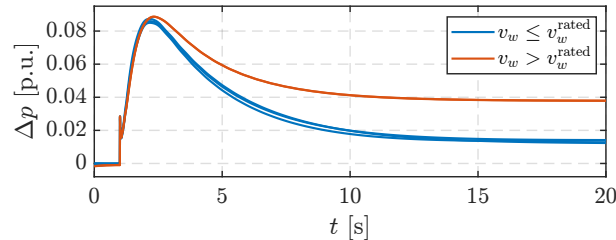
Figure 5.29: Impact of initial wind speed on primary frequency control activation.

Even though only a single-dimensional analysis was conducted (one parameter is varied while others are fixed to default values), the impact of other parameters was found to be insignificant: DSC outer loop (Fig. 5.30), DSC inner loop (Fig. 5.31), PLL gains (Fig. 5.32) and the pitch controller (Fig. 5.33). However, note that the parameter variation was not identical to the one in section 5.3. Finally, note that smaller pitch PI gains can result in large swings of stator and rotor power, even though the total power change $\Delta p = \Delta p_s + \Delta p_r$ remains unaffected as shown in Fig. 5.34, where indices s and r denote stator and rotor power, respectively.
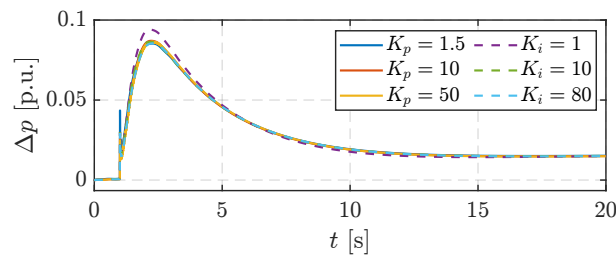
Figure 5.30: Impact of DSC outer loop parameters on primary frequency control activation.
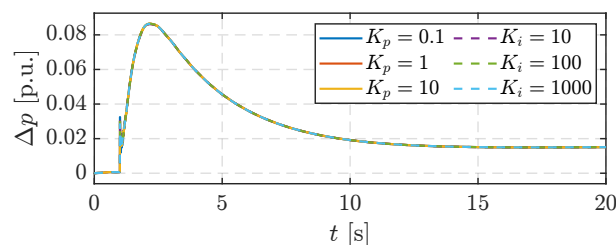
Figure 5.31: Impact of DSC inner loop parameters on primary frequency control activation.
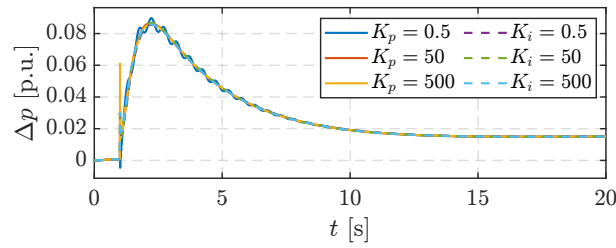
Figure 5.32: Impact of DSC PLL parameters on primary frequency control activation.
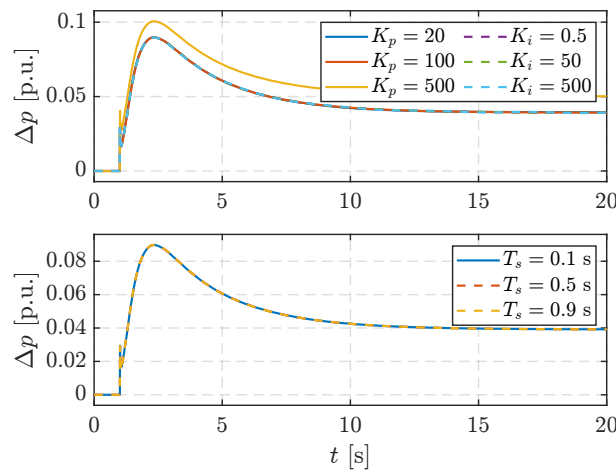
Figure 5.33: Impact of pitch controller parameters on primary frequency control activation: PI gains (top) and the servo time constant (bottom).
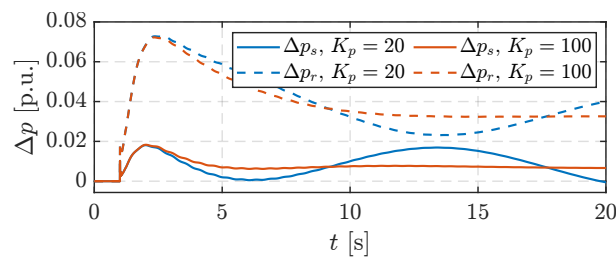
Figure 5.34: Swinging of stator and rotor power during primary frequency control activation due to pitch controller K_p gain variation.

5.5 Reduced-order modelling of variable-speed wind turbines for system frequency response studies

This section will expand and improve on the results from [37–39, 41]. In Chapter 4, we showed how different generic converter schemes contribute to grid frequency dynamics and we developed their SFR models. However, we neglected any device-side dynamics (ECS + DSC). In Chapter 5 so far, the time-domain parameter sensitivity analysis of a variable-speed wind turbine has shown that the impact of DSC/GSC control subsystems is negligible, except for the slower outer active power control loop of the DSC in certain cases.

5.5.1 Simplification of generator power curves and deloading by pitching instead of by overspeeding

Fig. 5.10 illustrated WTG power-speed control. However, a more realistic power-speed characteristic that exists in practice is shown in Fig. 5.35a [40, 175]. The MPT characteristic (blue) is divided into four zones. In zones $MPT - A$ and $MPT - C$ the torque is held constant and power is varied linearly (as described in section 4.2). In both zones a linear slope is used instead of a vertical line jump (Fig. 5.10) to reduce power fluctuations around those points. Zone $MPT - A$ controls the turbine around cut-in wind speed and the torque is held constant to prevent stalling. Zone $MPT - C$ exists due to aerodynamic characteristics of the rotor where sometimes the true MPT curve (zone $MPT - B$) cannot be tracked all the way to rated power because the maximum speed would be violated. Thus, the power is smoothly driven to the rated power and maximum speed via the slope in zone $MPT - C$. In zone $MPT - D$ the pitch control is active where both the wind turbine power and speed are held constant. Therefore, the true maximum power tracking is only in zone $MPT - B$.

A most often used deloading strategy is through overspeeding [206, 211, 220, 229]. A 10% deloaded characteristic is shown in orange in Fig. 5.35a, divided into four zones ($DEL - A - DEL - D$). However, this approach significantly complicates the control because zones do not necessarily overlap for the mechanical power curve at the same wind speed, which makes it difficult to consistently keep the constant power reserve. For instance, the 10% reserve is not obtained between points 1–1′. It is, however, obtained between points 2–2′ because both zones $MPT - B$ and $DEL - B$ overlap at that wind speed. Then, the reserve is again $\neq 10\%$ between points 3–3′ because point 3 is inside zone $MPT - B$, while point 3′ is inside zone $DEL - C$. To achieve 10% deloading at point 4, the pitch angle control needs to be activated as the deloaded characteristic does not have an inherently defined counter-point 4′.

An additional control complexity for deloading by modulating the generator power-speed curve (Fig. 5.35a) comes from the fact that two piecewise functions (consisting of four pieces

(a) Standard power curves and deloading by overspeeding

(b) Simplified power curve and deloading by pitch angle control
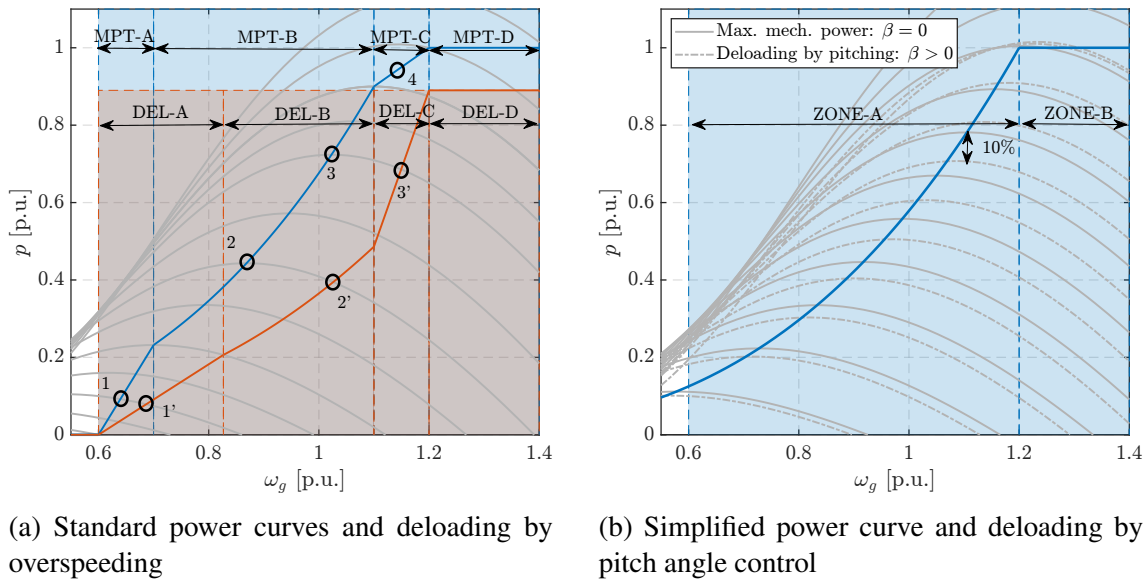
Figure 5.35: Standard and simplified WTG power characteristics.

each) need to be calculated and programmed into the rotor control system. Or, in a general case, since the reserve factor can be arbitrary the deloaded curve changes. Moreover, additional control logic is needed to transition between the zones, and pitch angle control still needs to be activated and coordinated with the rotor speed control, not to mention the difficulty in smoothly transitioning between deloaded and MPPT characteristics during normal operation, as well as during frequency excursions.

That being said, deriving small-signal models for SFR studies from the standard approach (Fig. 5.35a) is complicated since the mathematical model and the active control systems change for each operating zone and the mathematical model is inconsistent. Such an approach was tried in [36, 39, 41] and the end results are still disjoint and complex transfer functions with many parameters dependent on the initial conditions that are inconvenient to use. Furthermore, an operating point sweep and a comprehensive frequency-domain parameter sensitivity analysis was not conducted in [36, 39, 41], which means that a standard range of parameters was not provided. Therefore, the presented models are not plug & play and require manual calculation of initial conditions.

To build upon and simplify the existing results [37–39, 41], first we introduce a simplified power-speed curve shown in Fig. 5.35b. Zones MPT − A, MPT − B and MPT − C are merged into a single zone ZONE − A in which the generator power-speed curve operates according to the MPPT characteristic. Zone MPT − D corresponds to the zone ZONE − B. This approach gets rid of piecewise functions and the generator power reference is described by (5.27) in all operating conditions. Pitch control will automatically regulate the rotor speed and power at point $(\omega_{\max}, P_n) = (1.2, 1)$. Finally, the spinning reserve is consistently controlled without the need to jump between piecewise functions or additional logic (this is illustrated by the grey

dash-dot lines of reduced mechanical power at the corresponding wind speed).

Since deloading is not necessary for virtual inertial response, it is implemented as an additional signal $\Delta p_i^\star$ in the rotor-side converter (Fig. 5.36a). Deloading and frequency droop control is achieved via pitch control with the additional power control loop per Fig. 5.7 ($K_{px} = 0$) where the request for power change due to frequency deviations is denoted with $\Delta p_d^\star$ (Fig. 5.36b).

(a) Rotor speed controller with virtual inertia   (b) Pitch angle controller with frequency droop
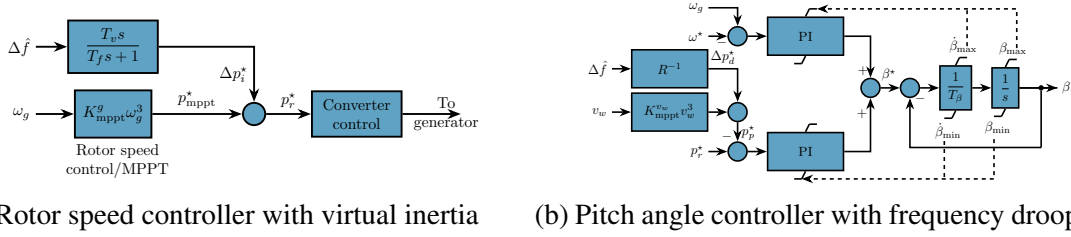
Figure 5.36: Standard and simplified WTG power characteristics.

5.5.2 Small-signal model

Finally, the electromechanical WTG model to be linearised is described by (5.30)–(5.37) which are expressed in per-unit of WTG nominal power S_n and synchronous electrical speed. λ is defined by (5.3)–(5.5), K_{mppt}^g is defined by (5.27) and $\alpha \in [0,1]$, $\alpha \in \mathbb{R}$ is the deloading factor (desired amount of spinning reserve relative to the instantaneously available wind power).

$$p_m(t) = \frac{\rho R^2 \pi}{2 S_n} C_p(\lambda, \beta) v_w^3 \tag{5.30}$$

$$p_e(t) = K_{\text{mppt}}^g \omega_g^3 + \Delta p_i^\star \tag{5.31}$$

$$2H \omega_g \frac{d\omega_g}{dt} = p_m(t) - p_e(t) \tag{5.32}$$

$$T_\beta \frac{d\beta}{dt} + \beta = \beta^\star \tag{5.33}$$

$$\beta^\star = \beta_\omega^\star + \beta_p^\star = K_p^\omega(\omega_g - \omega_g^\star) + K_i^\omega \beta_\omega + K_p^p(p_e - p_p^\star) + K_i^p \beta_p \tag{5.34}$$

$$\frac{d\beta_\omega}{dt} = \omega_g - \omega^\star \tag{5.35}$$

$$\frac{d\beta_p}{dt} = p_r^\star - p_p^\star \tag{5.36}$$

$$p_p^\star = \max \left\{ (1-\alpha) \frac{0.5 \rho R^2 \pi C_p^{\text{opt}}}{S_n} v_w^3, 1 \right\} + \Delta p_d^\star \tag{5.37}$$

$$= \max \left\{ K_{\text{mppt}}^{v_w} v_w^3, 1 \right\} + \Delta p_d^\star$$

Equations (5.30)–(5.37) describe a fourth-order nonlinear dynamic model of a single WTG. A single-mass shaft representation is used to further simplify the mathematical model so only one state is associated with the shaft dynamics. The remaining three states are associated with

the pitch control (two PI controller integrator states and one state of the pitch servo mechanism). The dynamics of the DC link, DSC and GSC are neglected since their time constants are much smaller as described in sections 5.3 and 5.4. Additionally, low-order converter dynamics were derived in chapter 4. Nonetheless, the small-signal model of equations (5.30)–(5.37) will be validated against a full RMS electromechanical model with a two-mass shaft (Fig. 5.12) whose rotor speed and pitch angle control subsystems have been modified to correspond to Fig. 5.36.

The state-space model ($\Delta\dot{\mathbf{x}} = \mathbf{A}\Delta\mathbf{x} + \mathbf{B}\Delta\mathbf{u}$; $\Delta\mathbf{y} = \mathbf{C}\Delta\mathbf{x} + \mathbf{D}\Delta\mathbf{u}$) can now be written down. The state vector $\Delta\mathbf{x}$, input vector $\Delta\mathbf{u}$ and output vector $\Delta\mathbf{y}$ are defined by (5.38). State, input, output and feed-forward matrices are defined by (5.39a)–(5.39d), respectively. The input-to-output transfer function is calculated as $\mathbf{C}(s\mathbf{I} - \mathbf{A})^{-1}\mathbf{B} + \mathbf{D}$.

$$\Delta\mathbf{x} = \begin{pmatrix} \Delta\omega_g \\ \Delta\beta \\ \Delta\beta_\omega \\ \Delta\beta_p \end{pmatrix} \qquad \Delta\mathbf{u} = \begin{pmatrix} \Delta v_w \\ \Delta p_i^\star \\ \Delta p_d^\star \end{pmatrix} \qquad \Delta\mathbf{y} = \Delta p_e \tag{5.38}$$

$$\mathbf{A} = \begin{pmatrix} \dfrac{K_m - K_e}{2H\omega_0} & \dfrac{K_\beta}{2H\omega_0} & 0 & 0 \\ \dfrac{K_p^\omega + K_p^p K_e}{T_\beta} & -\dfrac{1}{T_\beta} & \dfrac{K_i^\omega}{T_\beta} & \dfrac{K_i^p}{T_\beta} \\ 1 & 0 & 0 & 0 \\ K_e & 0 & 0 & 0 \end{pmatrix} \tag{5.39a}$$

$$\mathbf{B} = \begin{pmatrix} \dfrac{K_{v_w}}{2H\omega_0} & -\dfrac{1}{2H\omega_0} & 0 \\ -\dfrac{K_p^p K_p^\star}{T_\beta} & \dfrac{K_p^p}{T_\beta} & -\dfrac{K_p^p}{T_\beta} \\ 0 & 0 & 0 \\ -K_p^\star & 1 & -1 \end{pmatrix} \tag{5.39b}$$

$$\mathbf{C} = \begin{pmatrix} K_e & 0 & 0 & 0 \end{pmatrix} \tag{5.39c}$$

$$\mathbf{D} = \begin{pmatrix} 0 & 1 & 0 \end{pmatrix} \tag{5.39d}$$

Coefficients from (5.39a)–(5.39d) are calculated as:

$$K_m = \left.\frac{\partial p_m}{\partial \omega_g}\right|_{(\omega_0,\beta_0,v_0)} \qquad K_\beta = \left.\frac{\partial p_m}{\partial \beta}\right|_{(\omega_0,\beta_0,v_0)} \qquad K_{v_w} = \left.\frac{\partial p_m}{\partial v_w}\right|_{(\omega_0,\beta_0,v_0)} \tag{5.40a}$$

$$K_e = \left.\frac{\partial p_e}{\partial \omega_g}\right|_{\omega_0} = 3K_{\text{mppt}}^g \omega_0^2 \tag{5.40b}$$

$$K_p^\star = \left.\frac{\partial p_p^\star}{\partial v_w}\right|_{v_0} = \begin{cases} 3K_{\text{mppt}}^{v_w} v_0^2 = 3(1-\alpha)\dfrac{0.5\rho R^2 \pi C_p^{\text{opt}}}{S_n} v_0^2, & \text{for } v_0 \le 1 \text{p.u.} \\ 0, & \text{for } v_0 > 1 \text{p.u.} \end{cases} \tag{5.40c}$$

Analytical expressions for the three transfer functions (wind speed change to electrical power output, inertial response to electrical power output and droop response to electrical power output) are given by (5.41)–(5.43). Note that (5.42) and (5.43) are only the transfer functions that include the inherent WTG transient response to the respective disturbance inputs which do not include the dynamics of virtual inertia and droop controllers. But, since the model is now linear, these can be easily added by replacing $\Delta p_i^\star$ and $\Delta p_d^\star$ with the relevant transfer functions for inertial response and droop, and cascading them in series with (5.42) and (5.43).

$$G_{\text{WTG}}^{\text{wind}}(s) = \frac{\Delta p_e}{\Delta v_w} = \tag{5.41}$$

$$\frac{K_e K_{v_w} T_\beta s^2 + \left(K_e K_{v_w} - K_\beta K_e K_p^\star K_p^p\right) s - K_\beta K_e K_i^p K_p^\star}{2H\omega_0 T_\beta s^3 + \left(2H\omega_0 + K_e T_\beta - K_m T_\beta\right) s^2 + \left(K_e - K_m - K_\beta K_p^\omega - K_\beta K_e K_p^p\right) s - K_\beta \left(K_i^\omega + K_e K_i^p\right)}$$

$$G_{\text{WTG}}^{\text{inertia}}(s) = \frac{\Delta p_e}{\Delta p_i^\star} = \tag{5.42}$$

$$\frac{2H\omega_0 T_\beta s^3 + \left(2H\omega_0 - K_m T_\beta\right) s^2 - \left(K_m + K_\beta K_p^\omega\right) s - K_\beta K_i^\omega}{2H\omega_0 T_\beta s^3 + \left(2H\omega_0 + K_e T_\beta - K_m T_\beta\right) s^2 + \left(K_e - K_m - K_\beta K_p^\omega - K_\beta K_e K_p^p\right) s - K_\beta \left(K_i^\omega + K_e K_i^p\right)}$$

$$G_{\text{WTG}}^{\text{droop}}(s) = \frac{\Delta p_e}{\Delta p_d^\star} = \tag{5.43}$$

$$\frac{-K_\beta K_e \left(K_p^p s + K_i^p\right)}{2H\omega_0 T_\beta s^3 + \left(2H\omega_0 + K_e T_\beta - K_m T_\beta\right) s^2 + \left(K_e - K_m - K_\beta K_p^\omega - K_\beta K_e K_p^p\right) s - K_\beta \left(K_i^\omega + K_e K_i^p\right)}$$

As one can see, expressions (5.41)–(5.43) are still relatively complicated since the transfer functions coefficient depends on different combinations of many parameters. Secondly, these transfer functions are not yet plug & play because numerical information is missing, i.e., a standard range for these parameters. Therefore, a numerical analysis will be conducted in the following sections to further analyse the small-signal behaviour and simplify the corresponding small-signal model where possible.

A sensitivity analysis will be conducted for essentially the whole operating range between half the rated and twice the rated wind speed (rated wind speed is 12 ms^{-1}). This will provide

the power range between 10% and 100% rated power. First, Fig. 5.37 shows the WTG power as a function of the per-unit wind speed for 0%, 5% and 10% deloading ($\alpha \in \{0, 0.05, 0.1\}$). It can be clearly seen that the output power varies with the cube of wind speed up to the rated wind speed, after which the power output is constant. The blue curve is the MPPT curve, while the orange and yellow curves are deloaded curves for the corresponding deloading factors.
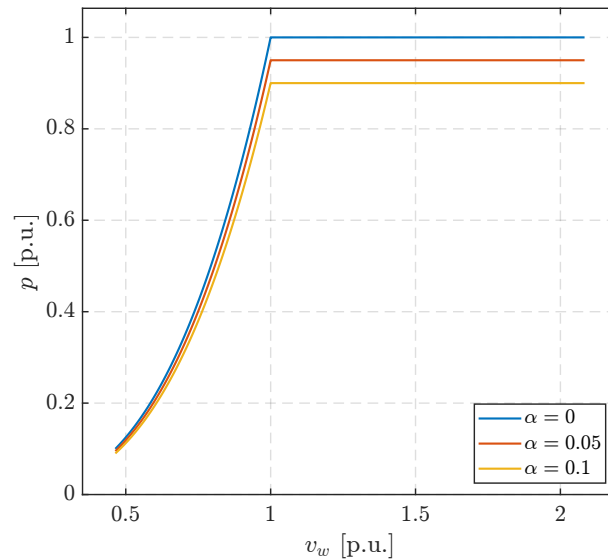
Figure 5.37: WTG power as a function of wind speed.

Fig. 5.38a shows a linear relationship between the rotor speed and below-rated wind speed due to the fact that the optimal tip-speed ratio is tracked (5.3). Above the rated wind speed, the rotor speed is held constant. The relationship to the WTG power is nonlinear, that is, proportional to the cubic root of power (5.31) as illustrated by Fig. 5.38b. What Fig. 5.38a reveals is that by utilizing deloading through the pitch control, the rotor speed will automatically be held under the maximum speed of 1.2 p.u. ($\omega_g < \omega_g^\star = 1.2$ p.u. in (5.35)). Consequently, $\omega_g - \omega_g^\star < 0$, but since β_ω and β_p are limited to positive numbers, only β_ω will be saturated at 0. Therefore, there will be no contribution from the speed control subsystem of the pitch controller. Since saturation is a nonlinearity that is neglected in the linearised model, this effect is taken into account by setting $K_p^\omega = K_i^\omega = 0$ which will further simplify the model.

Fig. 5.39a shows that the desired deloading below the rated wind speed is achieved by a fixed pitch angle (more clearly illustrated in Fig. 5.39b). Above the rated wind speed, the pitch angle changes nonlinearly. It is interesting to note that after a certain wind speed threshold (in this case $v_w \approx 1.7$ p.u.) the pitch angle starts decreasing again to keep the rotor speed constant. That is because of the aerodynamic characteristics of the blades determined by the $C_p(\lambda, \beta)$ (5.4) in which the passive stall effect is present around the cut-out wind speed [40].

Value ranges of the partial derivatives defined by (5.40) are shown in Fig. 5.40. Fig. 5.40a shows that the mechanical power barely changes for small variations in generator speed below the rated wind speed. That is because the maximum power point is tracked, where the aero-

(a) Rotor speed vs. wind speed

(b) Rotor speed vs. power
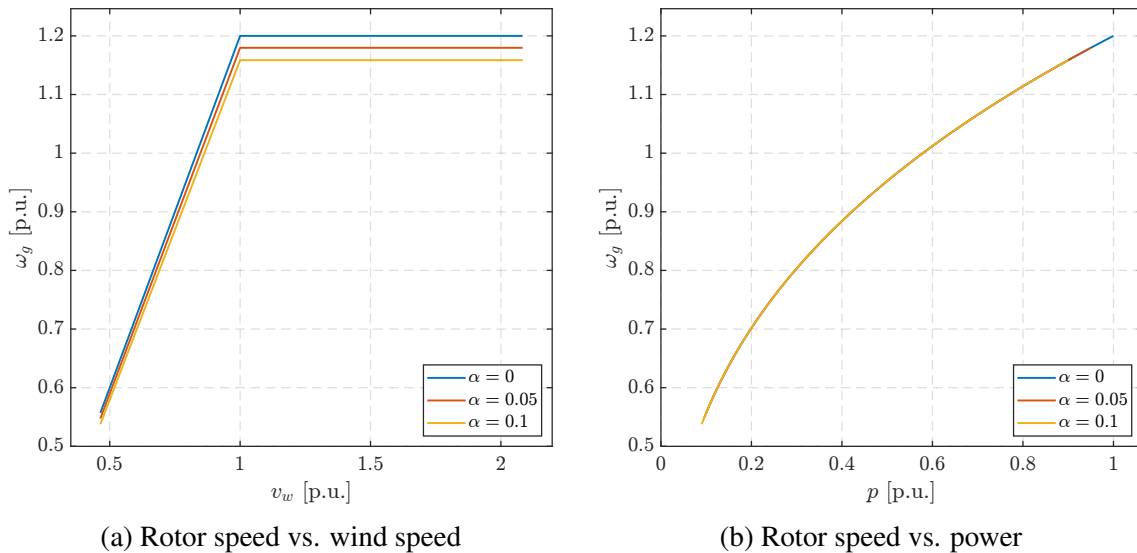
Figure 5.38: Rotor speed as a function of wind speed and WTG power.

(a) Pitch angle vs. wind speed

(b) Pitch angle vs. power
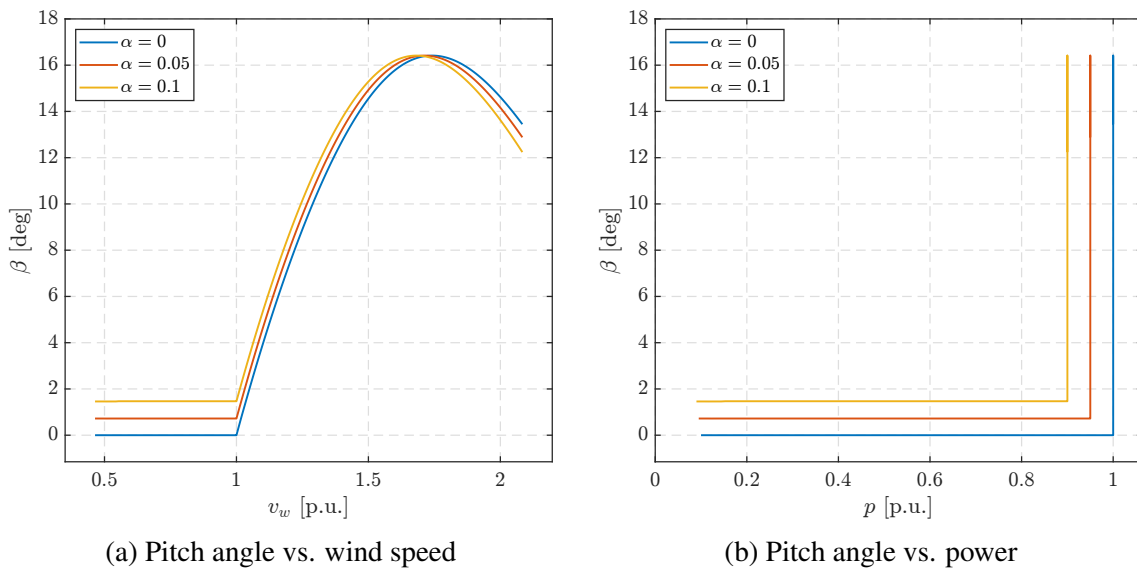
Figure 5.39: Pitch angle as a function of wind speed and WTG power.

dynamic power curves are relatively flat and the slope is zero. For $\alpha = 0 \Rightarrow K_m = 0$ because the generator power curve intersects the mechanical power point at its apex, while for $\alpha > 0$ the same generator power curve passes near the apex. This also reveals why the deloading by overspeed is relatively inefficient, since a large speed deviation is necessary for obtaining any meaningful reserve. Above the rated wind speed, K_m changes relatively steeply between 0 and 4 since the WTG generator curve intersects the mechanical curve at its steep part. The impact of the deloading factor α is not significant.

Sensitivity of p_m to β is shown in Fig. 5.40b. K_β is negative since the increase in β causes a decrease of p_m. K_β decreases strongly below the rated wind speed and $K_\beta \in [-0.08, -0.01]$. Above the rated wind speed, it slightly increases with increasing wind speed in the range $K_\beta \in [-0.08, -0.05]$. K_β essentially tells us how much the WTG power varies with each extra degree
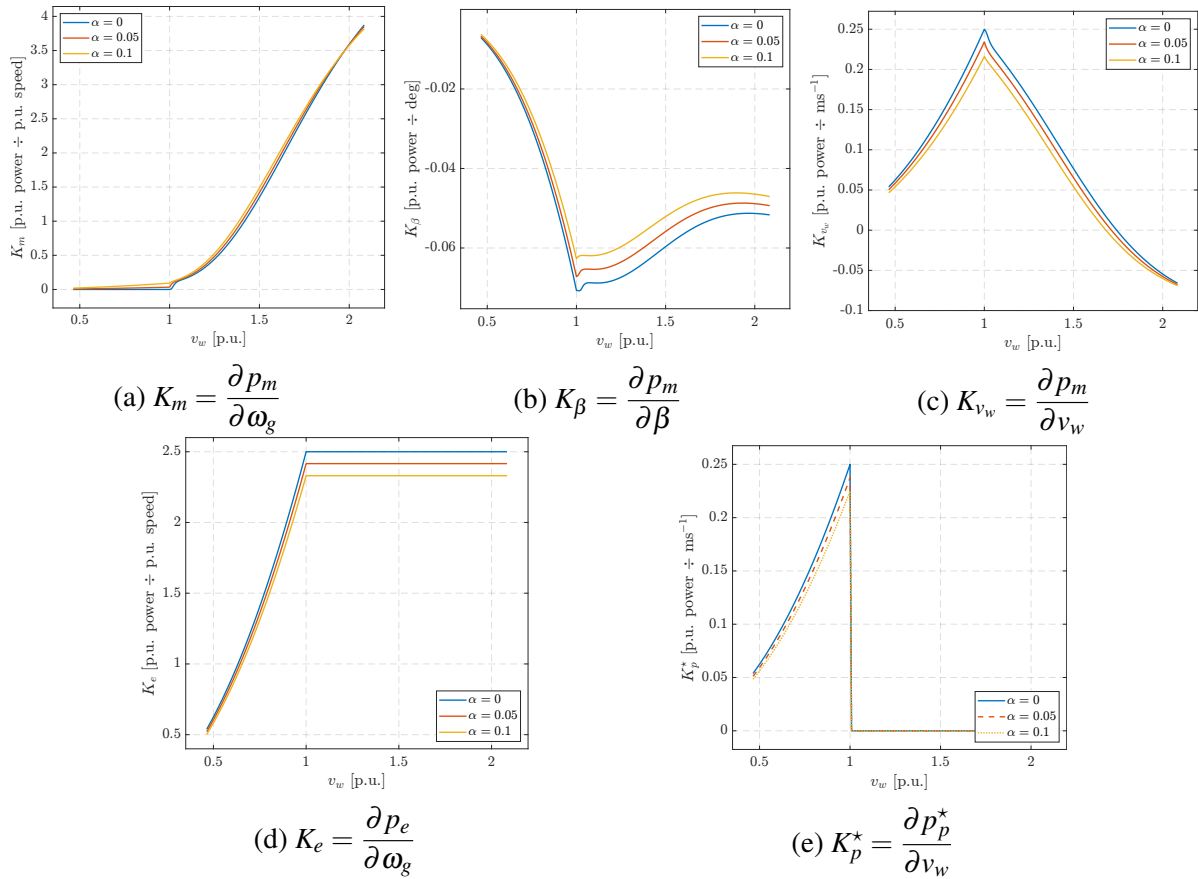
Figure 5.40: Value ranges of partial derivatives (5.40).

of blade pitch, and it is in the range of 1%–8%. The impact of the deloading factor is also not significant.

Fig. 5.40c shows that K_{v_w} increases with the increasing wind speed in the range $\in [0.05, 0.25]$ since p_m is proportional to the wind speed cube. Above the rated wind speed, the slope starts to taper out so K_{v_w} decreases again. Around $v_w = 1.7$ p.u., K_{v_w} becomes negative, which corresponds to the passive stall effect described by Fig. 5.39a. Further increase of wind speed causes a decrease of mechanical power. Therefore, $K_{v_w} \in [0.05, 0.25]$ below the rated wind speed and $K_{v_w} \in [-0.05, 0.25]$ above the rated wind speed.

$K_e \in [0.5, 2.5]$ below the rated wind speed (Fig. 5.40d) which makes sense since p_e is sensitive to ω_g^3, therefore $K_e \propto 3\omega_0^2$ and since $\omega_g \in [0.7, 1.2]$ K_e will significantly vary over the normal operating range. Above the rated wind speed, K_e does not change anymore since the power is held constant regardless of the wind speed / generator speed.

Finally, $K_p^\star$ changes proportionally to v_0^2 (5.40) below the rated wind speed as illustrated by Fig. 5.40e and it is additionally scaled by the factor $(1 - \alpha)$. $K_p^\star$ varies in the range $[0.05, 0.25]$. Above the rated wind speed, $K_p^\star = 0$ since constant power control is employed.

Table 5.4 summarizes the ranges of K_m, K_e, K_β, K_{v_w} and $K_p^\star$ for the deloading factor between 0% and 10%. Note that these coefficients cannot be arbitrarily chosen since they are

interdependent, i.e., they depend on the instantaneous wind speed. Therefore, they are provided as a function of initial wind speed. Additionally, they depend on the used wind turbine model and unit system. However, since standard generic models are similar and these coefficients are provided in per-unit in Table 5.4, it should be possible to readily use them as provided. Still, they might not be usable if control schemes other than the one used here are implemented.

Table 5.4: WTG small-signal model coefficients as functions of initial wind speed.

v_0	K_m [p.u.]	K_β [p.u.]	K_{v_w} [p.u.]	K_e [p.u.]	$K_p^\star$ [p.u.]
0.5	$[0.000, 0.024]$	$[-0.009, -0.008]$	$[0.055, 0.064]$	$[0.598, 0.642]$	$[0.058, 0.064]$
0.6	$[0.000, 0.034]$	$[-0.016, -0.014]$	$[0.079, 0.091]$	$[0.849, 0.911]$	$[0.082, 0.091]$
0.7	$[0.000, 0.045]$	$[-0.024, -0.021]$	$[0.105, 0.122]$	$[1.135, 1.218]$	$[0.110, 0.122]$
0.8	$[0.000, 0.060]$	$[-0.037, -0.033]$	$[0.140, 0.162]$	$[1.507, 1.617]$	$[0.145, 0.162]$
0.9	$[0.000, 0.075]$	$[-0.052, -0.046]$	$[0.175, 0.203]$	$[1.889, 2.027]$	$[0.182, 0.203]$
1.0	$[0.000, 0.093]$	$[-0.071, -0.062]$	$[0.216, 0.250]$	$[2.330, 2.500]$	$[0.225, 0.250]$
1.1	$[0.174, 0.208]$	$[-0.069, -0.062]$	$[0.186, 0.211]$	$[2.330, 2.500]$	0.000
1.2	$[0.329, 0.397]$	$[-0.068, -0.061]$	$[0.155, 0.181]$	$[2.330, 2.500]$	0.000
1.3	$[0.584, 0.684]$	$[-0.066, -0.058]$	$[0.122, 0.147]$	$[2.330, 2.500]$	0.000
1.4	$[0.930, 1.056]$	$[-0.063, -0.055]$	$[0.088, 0.112]$	$[2.330, 2.500]$	0.000
1.5	$[1.351, 1.489]$	$[-0.060, -0.052]$	$[0.054, 0.077]$	$[2.330, 2.500]$	0.000
1.6	$[1.818, 1.952]$	$[-0.056, -0.049]$	$[0.023, 0.043]$	$[2.330, 2.500]$	0.000
1.7	$[2.300, 2.413]$	$[-0.054, -0.047]$	$[-0.005, 0.012]$	$[2.330, 2.500]$	0.000
1.8	$[2.770, 2.848]$	$[-0.052, -0.046]$	$[-0.028, -0.015]$	$[2.330, 2.500]$	0.000
1.9	$[3.204, 3.237]$	$[-0.051, -0.046]$	$[-0.046, -0.037]$	$[2.330, 2.500]$	0.000
2.0	$[3.576, 3.591]$	$[-0.051, -0.046]$	$[-0.060, -0.055]$	$[2.330, 2.500]$	0.000

5.5.2.1 Inertial response under MPPT control below the rated wind speed

First, we shall consider a WTG operating at MPPT ($\alpha = 0$) and providing only the virtual inertial response ($R^{-1} = 0$). In this case, one can set $p_p^\star = 1$ p.u. to disable pitch control activation below the rated wind speed. Below the rated wind speed, the small-signal model (5.42) can thus be further simplified by setting $K_p^\omega = K_i^\omega = K_p^p = K_i^p = 0$ to account for the fact that the pitch control is inactive (which is handled in the full model by saturation on pitch PI controllers). Additionally, $K_m \approx 0$ per Fig. 5.40a. The simplified transfer function is then

described by (5.44).

$$G_{\text{WTG}}^{\text{inertia}}(s) = \frac{\dfrac{2H\omega_0}{K_e}s}{\dfrac{2H\omega_0}{K_e}s + 1} = \frac{T_{\text{WTG}}^{\text{inertia}}s}{T_{\text{WTG}}^{\text{inertia}}s + 1} \tag{5.44}$$

Therefore, regardless of the fact that the WTG is a converter-interfaced device, it does not act as an ideal power source without any dynamics besides the frequency controller. Adding a virtual inertial response disturbance input to the DSC (rotor-side converter) will impact the turbine mechanics which will be reflected on the grid-side due to rotor speed deviation from the optimal power point. The WTG acts as a high-pass filter with the time constant $T_{\text{WTG}}^{\text{inertia}}$ which depends on the mechanical inertia H, initial generator speed ω_0 and the generator power-speed curve scaling factor K_{mppt}^g.

$$T_{\text{WTG}}^{\text{inertia}} = \frac{2H\omega_0}{K_e} = \frac{2H}{3K_{\text{mppt}}^g\omega_0} \tag{5.45}$$

Equation (5.45) shows that the time constant reduces as the initial generator speed increases. For the normal operating range $\omega_0 \in [0.7, 1.2]$ p.u. $\Rightarrow T_{\text{WTG}}^{\text{inertia}} \in \left[\dfrac{5}{6}\dfrac{2H}{3K_{\text{mppt}}^g}, \dfrac{10}{7}\dfrac{2H}{3K_{\text{mppt}}^g}\right]$. For this particular WTG with $H = 6$ s and $K_{\text{mppt}}^g = 0.5787$ p.u., $T_{\text{WTG}}^{\text{inertia}}$ will vary between 6.9 s at the minimum speed and 4 s at the maximum speed. The pole-zero plot in Fig. 5.41 shows that the damping increases as wind speed increases since the poles lie on the x-axis and move away from the origin.
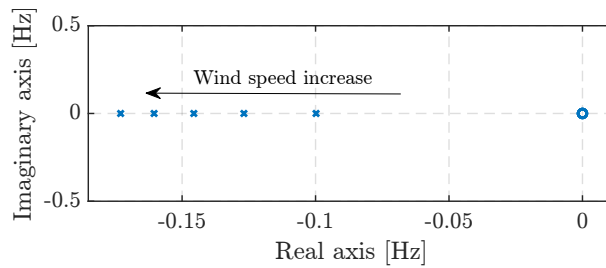
Figure 5.41: Pole-zero plot of $G_{\text{WTG}}^{\text{inertia}}(s)$: poles (xs) and zeros (os).

To show that the small-signal model is valid, we calculate the open-loop response of $G_{\text{WTG}}^{\text{inertia}}(s)$ to an arbitrary virtual inertia power change signal ($\Delta p_i^\star$ input) and compare it to the open-loop response of the nonlinear two-mass model to the same input. Results are shown in Fig. 5.42 and it can be seen that the small-signal model is very accurate for $v_0 \in [0.5, 1]$ p.u. (initial conditions did not affect the response significantly so the responses overlap to a large extent).

To show the effect of such additional dynamics, we compare the responses of the commonly used SFR model of CID where only the inertial controller is considered (Fig. 5.43a) and the proposed model (Fig. 5.43b) that also includes PLL and converter dynamics described by Fig. 4.31 in section 4.4. In this particular case, $G_{\text{WTG}}(s)$ is replaced by (5.44). The two SFR models are validated against a full RMS model in PowerFactory. The test system consists of a two-
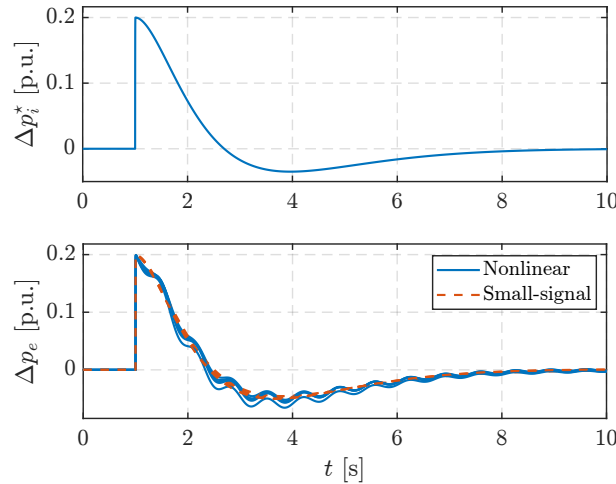
Figure 5.42: Comparison of open-loop responses of nonlinear and small-signal model up to the rated wind speed.

machine system from Fig. 5.11 which was modified so that the DFIG plant consists of 50x2 MVA DFIGs and 10x5 MVA SGs, which results in a converter penetration of $\eta_c = 66.7\%$. The 5 MW load is switched on at $t = 1$ s to induce a drop in frequency. The DFIG plant initially operates at $v_0 = 0.91$ p.u. which results in an output power of $p = 0.75$ p.u. To isolate only the contribution of the WTG dynamics, the GSC and PLL dynamics are fast enough to be neglected.

(a) Conventional
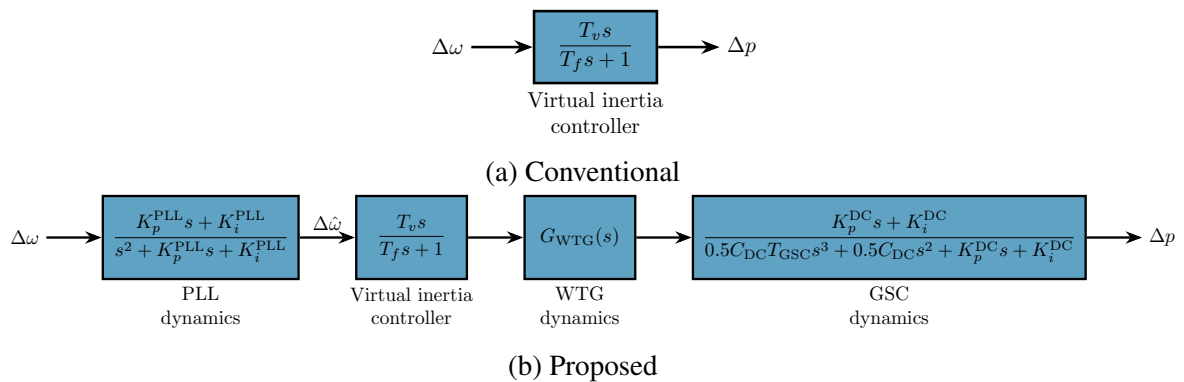
(b) Proposed

Figure 5.43: Conventional and proposed SFR model of a variable-speed wind turbine generator.

The results are shown in Fig. 5.44. It can be seen that the conventional model (orange dashed lines) gives overly optimistic results: the nadir is lower, there are fewer oscillations, and the system frequency settles more quickly. On the other hand, the proposed SFR model (yellow dashed lines) is more accurate compared to the conventional SFR model as it better captures the dynamics of the full RMS model. The maximum absolute frequency error occurs at the nadir point: the conventional SFR model estimates a $\approx 3 \cdot 10^{-3}$ p.u. (150 mHz) smaller nadir, while the error of the proposed model is only $\approx 6.5 \cdot 10^{-4}$ p.u. (30 mHz) which is a five times smaller error. The reason why the virtual inertial response is weaker is because $G_{\mathrm{WTG}}^{\mathrm{inertia}}(s)$ increases attenuation at lower frequencies, as shown by the Bode plot in Fig. 5.45.
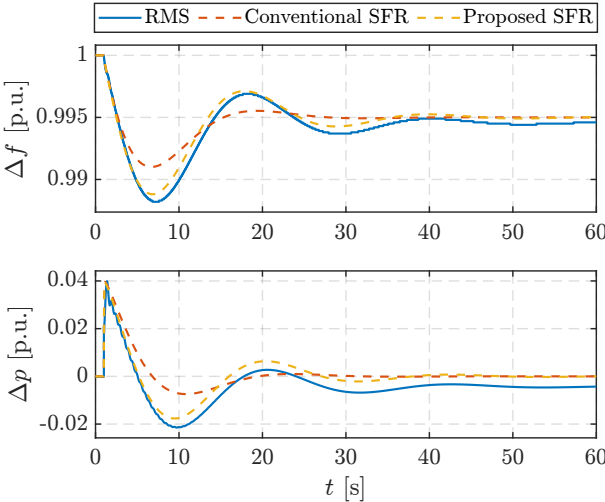
Figure 5.44: Comparison and validation of WTG inertial SFR models below the rated wind speed: system frequency (top) and WTG power output change (bottom).
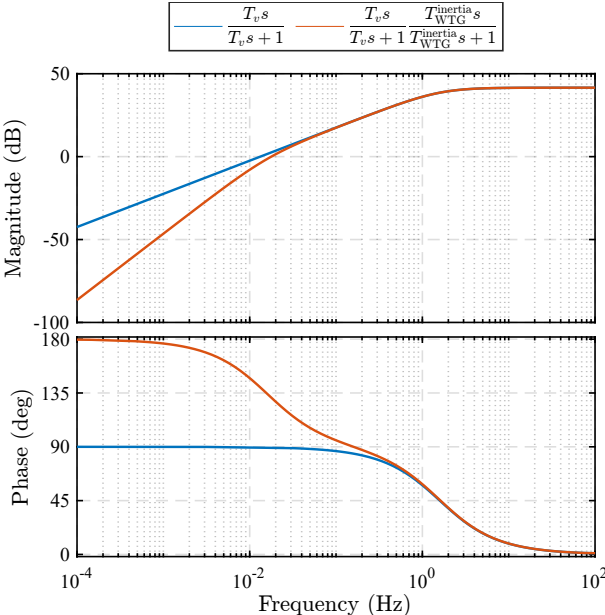
Figure 5.45: Bode plot of WTG inertial SFR models below the rated wind speed: magnitude (top) and phase (bottom).

5.5.2.2 Inertial response under MPPT control above the rated wind speed

During above-rated wind speeds, the pitch controller is active so the full transfer function (5.42) needs to be used in place of $G_{\text{WTG}}(s)$ from Fig. 5.43b. $K_p^\star = 0$ (Fig. 5.40e), while $K_m \neq 0$ (Fig. 5.40a). However, the power and speed pitch controllers may not be active at the same time since they are saturated depending on the initial speed, power and pitch angle, and that is where the small-signal model will lose its accuracy. To explain why, two cases are discerned here:

1. For an underfrequency event the generator will first slow down below the maximum speed due to injection of electrical power. Therefore, the speed control subsystem of the pitch controller will be inactive in this period, while the power control subsystem of the pitch controller will try to restore the power to 1 p.u. by increasing the pitch angle. However, once the speed starts recovering it will overshoot above the maximum speed limit and the speed control subsystem will turn on.

2. For an overfrequency event, the WTG will first accelerate over the rated speed due to a power reduction so the speed control subsystem of the pitch controller will be active, while the power control subsystem of the pitch controller will try to restore the power to 1 p.u. by decreasing the pitch angle.

To show that the small-signal model is valid, we calculate the open-loop response of $G_{\text{WTG}}^{\text{inertia}}(s)$ to an arbitrary virtual inertia power change signal ($\Delta p_i^\star$ input) and compare it to the open-loop response of the nonlinear two-mass model to the same input. Results are shown in Fig. 5.46 and it can be seen that the small-signal model is very accurate for $v_0 \in [1, 2]$ p.u. (initial conditions did not affect the response significantly so the responses overlap to a large extent).
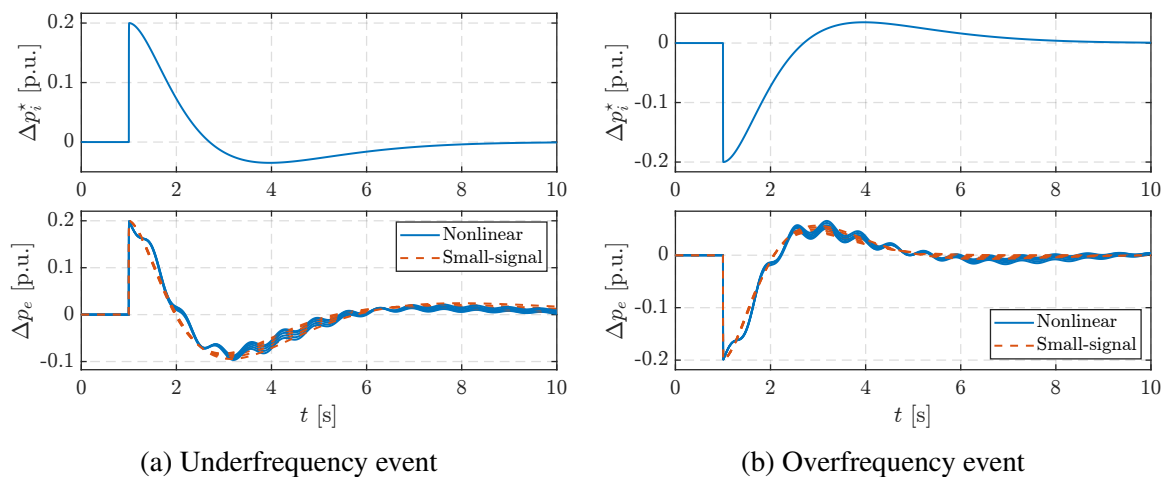
Figure 5.46: Comparison of open-loop responses of the nonlinear and small-signal model above the rated wind speeds.

However, the closed-loop response illustrates that the small-signal model loses accuracy, as visible in Fig. 5.47. The conventional SFR model estimates the most optimistic frequency behaviour, while the proposed model is slightly more accurate. The nonlinear pitch controller

dynamics are not captured by the SFR model. The largest difference can be observed around the nadir point—for an underfrequency event (Fig. 5.47a), the proposed SFR model predicts an approximately $6.3 \cdot 10^{-3}$ p.u. smaller maximum frequency deviation (300 mHz), while the conventional SFR model predicts an approximately $8.9 \cdot 10^{-3}$ p.u. smaller nadir (450 mHz). For an overfrequency event (Fig. 5.47b), the proposed SFR model predicts an approximately $3.5 \cdot 10^{-3}$ p.u. smaller maximum frequency deviation (175 mHz), while the conventional SFR model predicts an approximately $6.22 \cdot 10^{-3}$ p.u. smaller nadir (300 mHz).
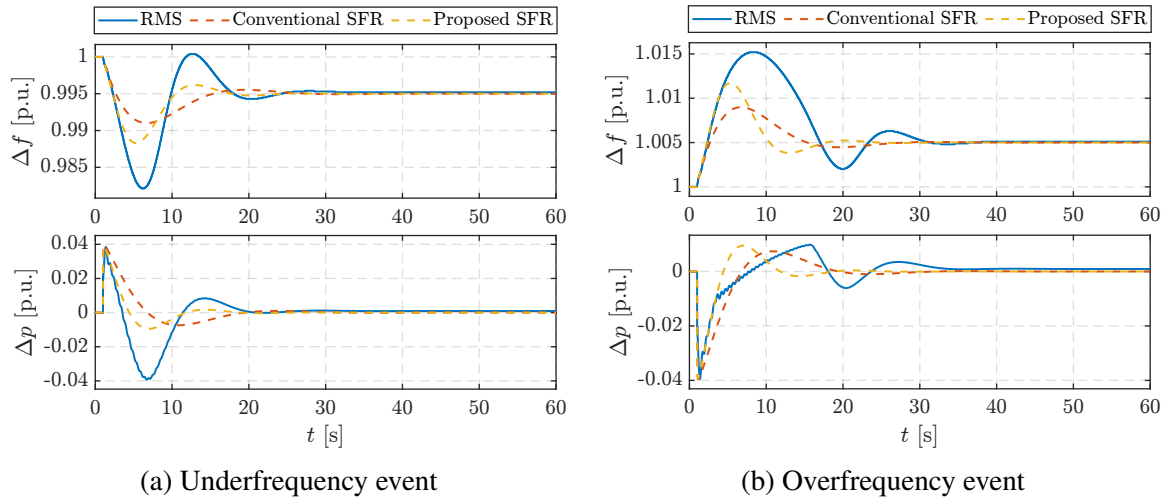
Figure 5.47: Comparison and validation of WTG SFR models above the rated wind speed: system frequency (top) and WTG power output change (bottom).

The influence of the pitch controller nonlinearity can be compensated by reducing the speed at which the subcontroller gains K_p^ω and K_i^ω to account for the fact that it is not active at all times. Reducing the gains by 60% in the SFR model compared to the actual model results in a response shown in Fig. 5.48, which is slightly more accurate in terms of average response, but more oscillatory. Fig. 5.49 shows how there is additional attenuation of the WTG response at low frequencies compared to just the inertial controller. Fig. 5.50 shows the magnitude and phase of $G_{\text{WTG}}^{\text{inertia}}(s)$ as a function of various above-rated wind speeds. It can be seen how the initial conditions affect the gain of the transfer function: between 10^{-2} Hz and 10^{-1} Hz the attenuation is increased with the increasing wind speed, and then it reduces with the increasing wind speed up to around 10^0 Hz when the unity gain is achieved, acting as a high-pass filter. Fig. 5.51 shows how the poles and zeros move around in the complex plane as a function of the pitch controller parameters K_p^ω, K_i^ω, K_p^p and K_i^p (root locus). One can see that reduction of K_p^ω results in complex-conjugate zeroes near the imaginary axis (weak damping) that will cause oscillatory behaviour. There are no complex-conjugate poles nor zeros for the observed ranges of other three parameters as all poles and zeroes lie on the real axis. Decreasing K_i^ω shifts the poles and zeros towards the imaginary axis. Decreasing K_p^p shifts the poles and zeros slightly away from the imaginary axis, thus increasing damping, while decreasing K_i^i shifts the poles

and zeros slightly towards the imaginary axis, thus decreasing damping.
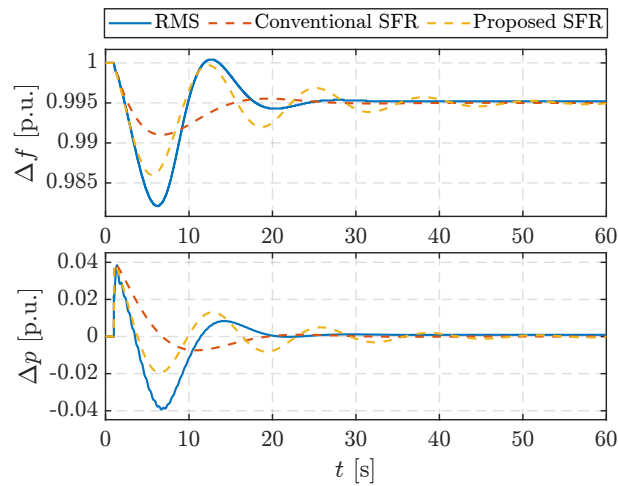
Figure 5.48: Improving the accuracy of the proposed WTG SFR model above the rated wind speed by reducing K_p^ω and K_i^ω: system frequency (top) and WTG power output change (bottom).
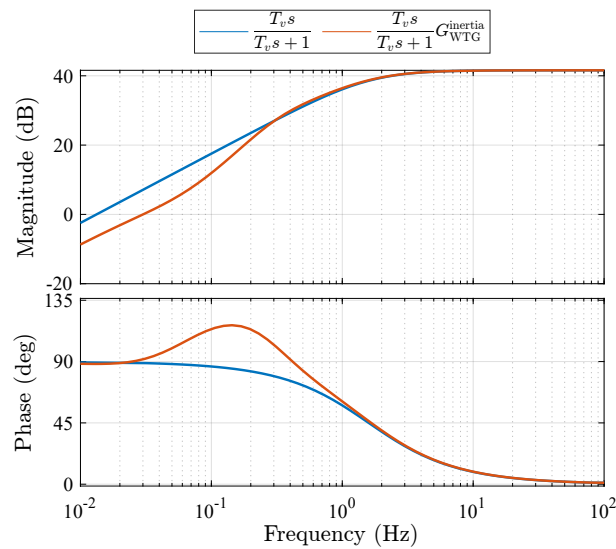
**Figure 5.49:** Bode plot of WTG inertial SFR models above the rated wind speed: magnitude (top) and phase (bottom).
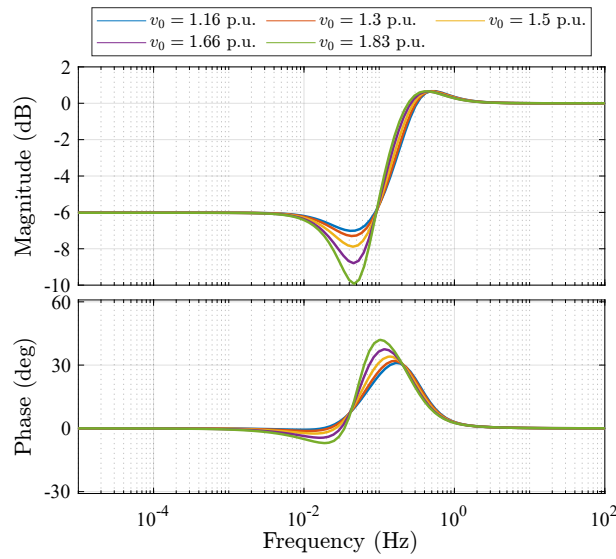
Figure 5.50: Bode plot of $G_{\mathrm{WTG}}^{\mathrm{inertia}}(s)$ sensitivity to v_0 for above-rated wind speeds: magnitude (top) and phase (bottom).
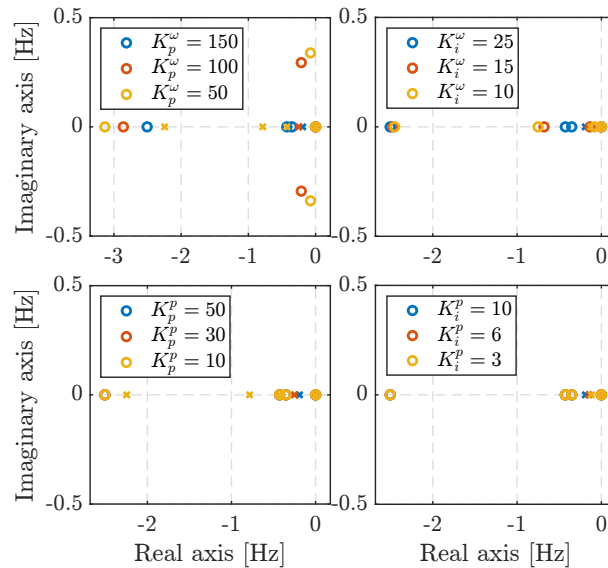
Figure 5.51: Root locus of $G_{\mathrm{WTG}}^{\mathrm{inertia}}(s)$ as a function of pitch controller parameters: K_p^ω (top left), K_i^ω (top right), K_p^p (bottom left) and K_i^p (bottom right).

5.5.2.3 Droop response under deloaded control below the rated wind speed

Below the rated wind speed, the pitch angle controller will be in charge of deloading the WTG to provide the required upwards spinning reserve. Since the speed will always be less than the maximum speed, $K_p^\omega = K_i^\omega = 0$ and the transfer function for small-disturbances (5.43) reduces to (5.46). The open-loop validation of the small-signal model is shown in Fig 5.52a.

$$G_{\text{WTG}}^{\text{droop}}(s) = \frac{-K_\beta K_e \left(K_p^p s + K_i^p \right)}{2H\omega_0 T_\beta s^3 + \left(2H\omega_0 + K_e T_\beta - K_m T_\beta \right) s^2 + \left(K_e - K_m - K_\beta K_e K_p^p \right) s - K_\beta K_e K_i^p}$$

(a) Small-disturbance   (b) Large disturbance
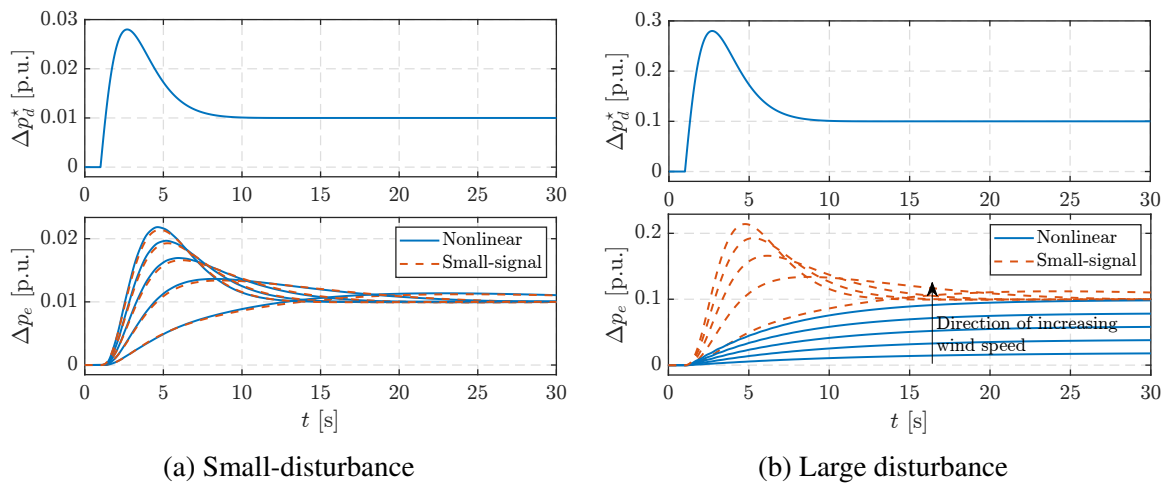
Figure 5.52: Comparison of droop control open-loop responses of the nonlinear and small-signal model up to the rated wind speed.

However, for a large disturbance when the power request is greater than the available reserve, the small-signal model fails, as shown in Fig. 5.52b. That is because the pitch controller will saturate since $\beta^\star$ cannot be < 0. The nonlinear model behavior differs for different wind speeds since a different amount of reserve is available (reserve is expressed as a fixed percentage of the available power). Essentially, what happens is that $\beta^\star$ experiences a step change to zero degrees since the controller is relatively fast. Therefore, the states $\Delta\beta_\omega$ and $\Delta\beta_p$ from (5.33)–(5.36) can be discarded and $\Delta p_d^\star \to \beta^\star$ in (5.33)–(5.34). The state-space model (5.38)–(5.39) then reduces to (5.46)–(5.47), which results in a second-order transfer function (5.48).

$$\Delta\mathbf{x} = \begin{pmatrix} \Delta\omega_g \\ \Delta\beta \end{pmatrix} \qquad \Delta\mathbf{u} = \begin{pmatrix} \Delta v_w \\ \Delta p_i^\star \\ \Delta p_d^\star \end{pmatrix} \qquad \Delta\mathbf{y} = \Delta p_e \tag{5.46}$$

$$\mathbf{A} = \begin{pmatrix} \dfrac{K_m - K_e}{2H\omega_0} & \dfrac{K_\beta}{2H\omega_0} \\ 0 & -\dfrac{1}{T_\beta} \end{pmatrix} \tag{5.47a}$$

$$\mathbf{B} = \begin{pmatrix} \dfrac{K_{v_w}}{2H\omega_0} & -\dfrac{1}{2H\omega_0} & 0 \\ 0 & 0 & \dfrac{1}{T_\beta} \end{pmatrix} \tag{5.47b}$$

$$\mathbf{C} = \begin{pmatrix} K_e & 0 \end{pmatrix} \tag{5.47c}$$

$$\mathbf{D} = \begin{pmatrix} 0 & 1 & 0 \end{pmatrix} \tag{5.47d}$$

$$G_{\text{WTG}}^{\text{droop}}(s) = \frac{\Delta p_e}{\Delta p_d^\star} = \frac{K_\beta K_e}{2H\omega_0 T_\beta s^2 + \left(2H\omega_0 + K_e T_\beta - K_m T_\beta\right)s + K_e - K_m} \tag{5.48}$$

The open-loop validation is shown in Fig. 5.53 which illustrates a more accurate response of the small-signal model when the nonlinear model saturates. To account for the fact that $\Delta p_d^\star$ will cause a step decrease of pitch angle to 0 degrees, it is multiplied by a large negative gain (illustrated by the $-\infty$ block) and saturated per Fig. 5.54c, where $\hat{\omega}$ is the estimated grid frequency (from PLL) and $G_{\text{WTG}}(s)$ is replaced by (5.48). Otherwise, for small-disturbances, the block diagram is shown by Fig. 5.54b, where $G_{\text{WTG}}(s)$ is replaced by (5.46). The conventional SFR model often used in literature is shown by Fig. 5.54a.

Fig. 5.55 shows the closed-loop validation of the proposed SFR model (Fig. 5.54b) for a 3 MW step load increase in the two-machine system. It can be seen that the conventional model (Fig. 5.54a) calculates a significantly more optimistic result than the benchmark full RMS model: the nadir is approximately 0.999 p.u. (49.95 Hz) compared to the RMS model, which estimates it around 0.993 p.u. (49.65 Hz), resulting in a difference of 300 mHz. On
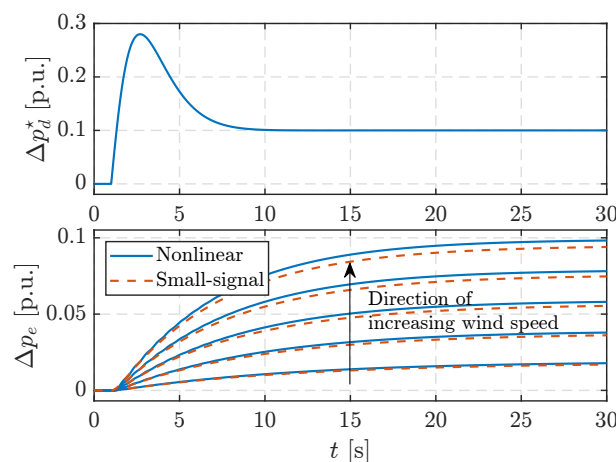
Figure 5.53: Droop control open-loop response validation of a modified small-signal model for larger disturbances up to the rated wind speed.

(a) Conventional

(b) Proposed—small disturbances

(c) Proposed—larger disturbances
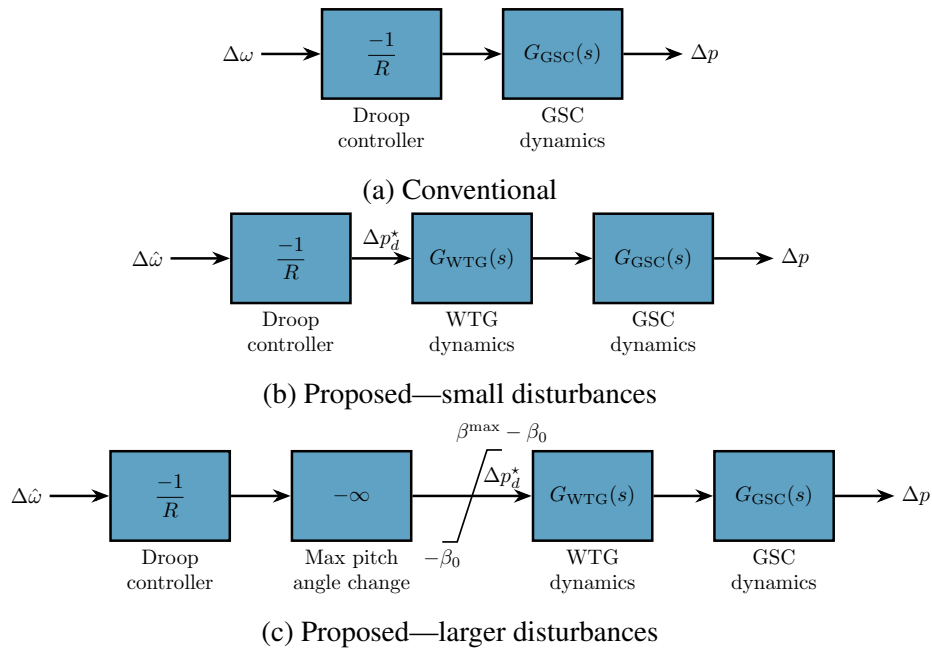
Figure 5.54: Conventional and proposed SFR models of a variable-speed wind turbine generator for droop response below the rated wind speed.

the other hand, the proposed SFR model accurately predicts the frequency behaviour, and the maximum instantaneous error between the proposed SFR model and the RMS model is < 30 mHz.

The difference exists because WTG acts as a low-pass filter with a cut-off frequency between 10^{-3} and 10^{-2} Hz, as shown in Fig. 5.56, due to a large effective time constant compared to just modelling the WTG with a simple first-order converter dynamics which has a cut-off frequency at around 150 Hz (assuming ≈ 1 ms closed-loop time constant). Fig. 5.56 also shows that the attenuation reduces by increasing the wind speed. The impact of K_P^p and K_i^p on the pole-zero map of (5.46) is shown in Fig. 5.57, where it can be seen that reducing the K_P^p results in the appearance of complex-conjugate pairs of poles near the imaginary axis that will cause the oscillations of the output power. However, K_P^p and K_i^p must not be tuned too aggressively since this can also cause oscillations of the WTG output power when in a closed-loop with an external power system.
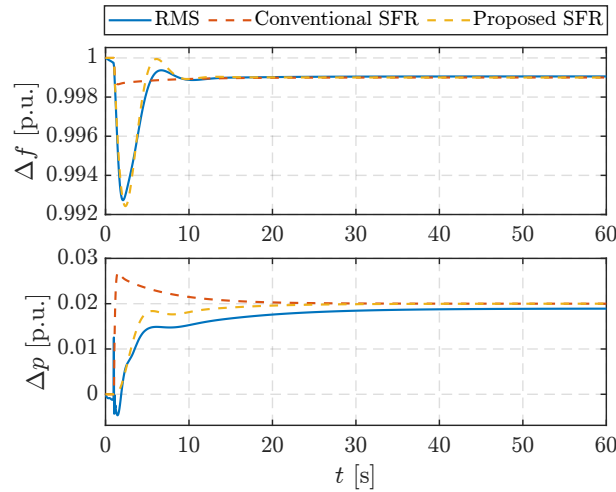
Figure 5.55: Comparison and validation of WTG droop SFR models below the rated wind speed: system frequency (top) and WTG power output change (bottom).
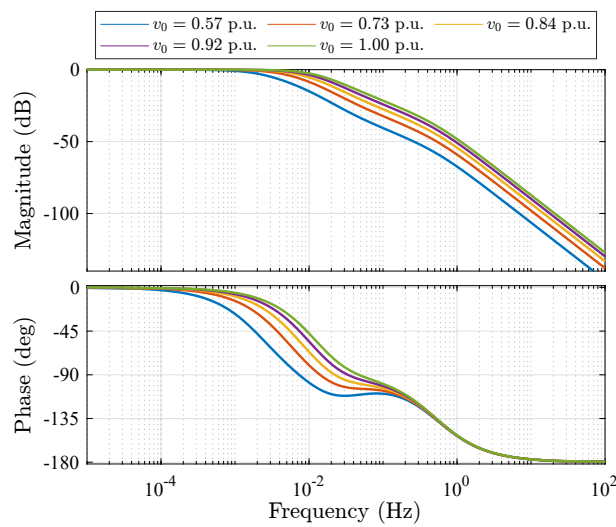
Figure 5.56: Bode plot of $G_{\text{WTG}}^{\text{droop}}(s)$ sensitivity to v_0 for below-rated wind speeds: magnitude (top) and phase (bottom).
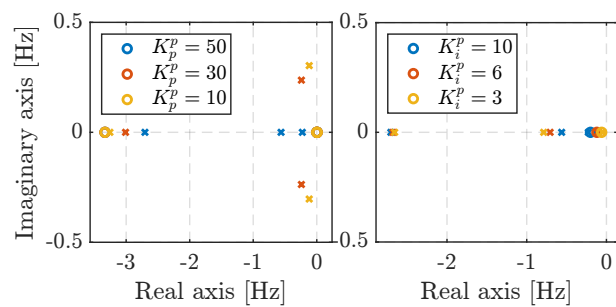
Figure 5.57: Root locus of $G_{\text{WTG}}^{\text{droop}}(s)$ as a function of pitch controller parameters: K_p^p (left) and K_i^p (right).

5.5.2.4 Droop response under deloaded control above the rated wind speed

Above the rated wind speed, Equation (5.46) still holds as the pitch controller will keep the rotor speed below the maximum to ensure a spinning reserve. Therefore, K_p^ω and K_i^ω can be ignored. Fig. 5.58 shows the open-loop validation of the SFR model. It can be seen that for small disturbances the SFR model is accurate (Fig. 5.58a), while for larger disturbances (Fig. 5.58b) the SFR model becomes more inaccurate with increasing wind speed due to the high nonlinearity of the model. Fig. 5.59 shows the closed-loop validation against the full nonlinear model in PowerFactory. It can be seen that the conventional model provides significantly more optimistic results by ignoring the WTG mechanical dynamics. On the other hand, the proposed SFR model provides a more accurate estimation of the system frequency. Frequency domain analysis is omitted since the results are essentially identical to the ones in section 5.5.2.3.

(a) Small-disturbance

(b) Large disturbance
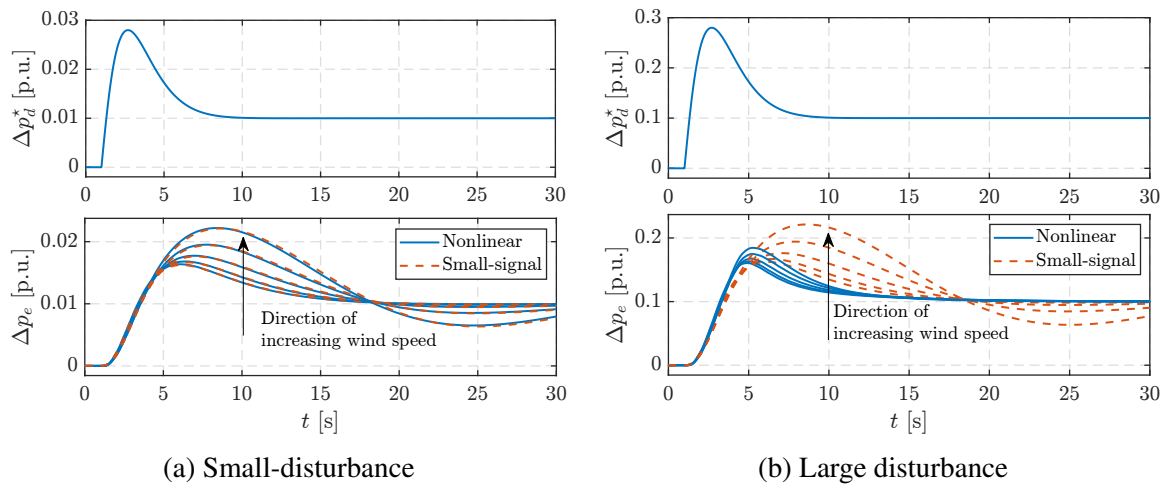
Figure 5.58: Comparison of droop control open-loop responses of the nonlinear and small-signal model above the rated wind speed.
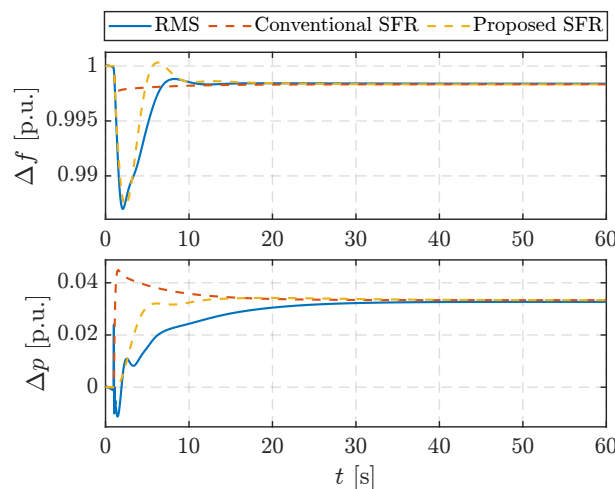
Figure 5.59: Comparison and validation of WTG droop SFR models above the rated wind speed: system frequency (top) and WTG power output change (bottom).

5.6 Summary

In the first part of the chapter, we performed a sensitivity analysis of frequency control performance to grid-following DFIG parameters. These parameters are: initial operating point, machine-side and line-side converter controller parameters, pitch angle control parameters and PLL parameters.

The impact of the wind speed on the strength of the inertial response depends on the type of machine-side converter control. For total power controlled WECS, the response is weaker with increasing wind speed, while for the speed control with inverse MPPT characteristics, the response is stronger with increasing wind speed. Once the pitch control becomes active, the peak is initially slightly higher than the instance before pitch angle control activation. Then, the response also becomes weaker with increasing wind speed. On the other hand, primary frequency control results in a larger power deviation for the same disturbance while pitch control is active.

Small values of PLL PI gains will result in more oscillatory behaviour and weak damping of the local mode. Following a disturbance, the DFIG power is momentarily reduced, further aggravating the grid frequency, although the actual peak value is higher. Additionally, large gains result in strong tracking and no oscillations in the power response. Generally, PLL dynamics can be neglected if the PLL is fast and the modes are well-damped. Furthermore, a too aggressive tuning of PLL can lead to instability, but it also depends on the system characteristics. As illustrated in Chapter 4, the RMS simulation can result in a stable performance, while it is unstable in the EMT simulation. In low inertia systems, PLL should not be neglected.

The outer control loop of MSC has an impact on frequency response provision. If the outer loop has smaller PI gains, the power output is stronger and peak time is shorter. This is because it will take a longer time for the weaker controller to restrain the power changes towards the set-point. The inner loop of the MSC control, DC voltage loop and the inner loop of the LSC and the DC capacitor dynamics can be neglected in the frequency control studies since they are very fast.

Between all the parameters of the pitch control subsystem, proportional gain of the PI controller has the most significant impact. Larger proportional gain will result in bigger power output. Frequency control performance is not significantly sensitive to integral gain nor to the pitch servo time constant for the studied cases. Nevertheless, low gains of pitch controller can result in undesirable swinging of stator and rotor power, which is not visible in their total sum.

It is difficult to draw generalised conclusions about WTG performance since it very much depends on the active control system design which can vary significantly between vendors and in the scientific literature.

In the second part of the chapter, we derive an SFR model of a generic variable-speed

wind turbine generator in which the primary frequency control is achieved solely through pitch angle control. The used nonlinear model is simplified by neglecting fast converter control loops according to conclusions from the first part of the chapter. The performance of the SFR model is verified against the simplified nonlinear model in open-loop as well as against full nonlinear RMS model in DIgSILENT PowerFactory in closed-loop.

Three transfer functions were derived: wind speed change to power output, virtual inertial response power reference to power output, and droop control power reference to power output. All the transfer functions in their most generic form are of third order and, unfortunately, the analytical form does not lend itself to any intuitive insight. The order, however, can be reduced depending on if the pitch controller is active or not. Here, the most interesting result is for the below-rated wind speed provision of virtual inertial response, where it was shown that the WTG acts as a high-pass filter $(sT/(sT+1))$ in which the time constant depends on WTG inertia, initial generator speed and MPPT curve characteristics. Therefore, the conventional assumption in literature that any converter-interfaced device is described by a first order current control transfer function is invalid. In this particular example, modulating the MPPT reference by the measured frequency signal results in a reduction of turbine speed which in turn reduces the power output. In other words, the WTG electromechanical dynamics become coupled to the grid dynamics.

Nevertheless, in all cases the proposed model is more accurate than the conventional approach in the literature that gives overly optimistic results. However, for larger disturbances (more than 10%) the SFR model loses accuracy due to nonlinearities in the physical model, as well as in the pitch controller subsystem.

Chapter 6

Unified low-order system frequency response model of a low-inertia power system

Based on the results from Chapter 4 and Chapter 5, we propose a unified SFR model (Fig. 6.1) for low-inertia power systems that provides a more accurate estimation of grid frequency dynamics at the expense of a slightly more complex model.
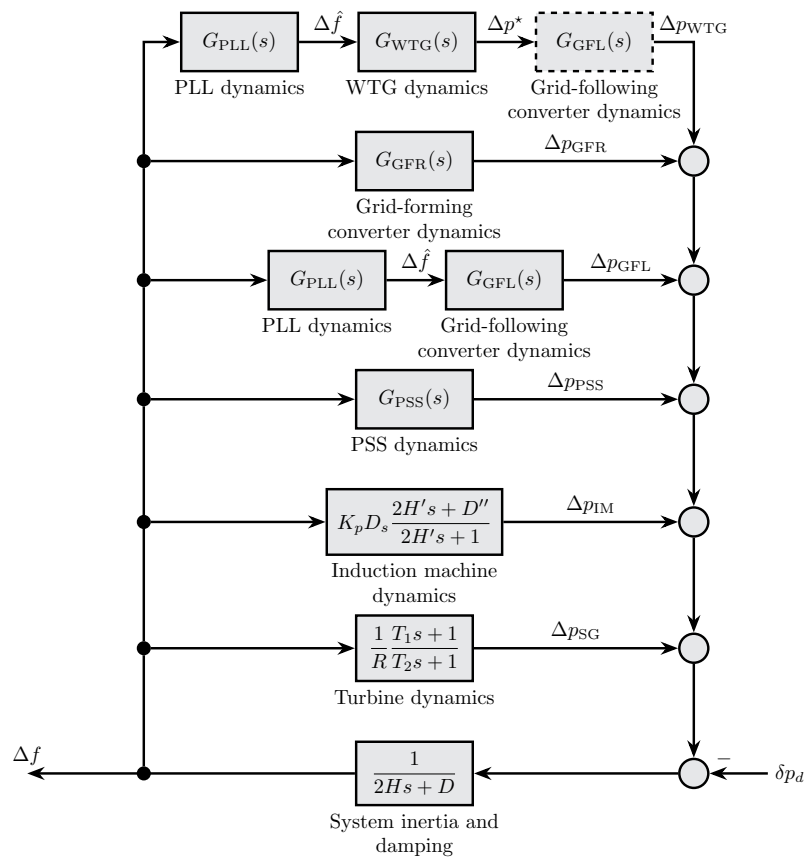
Figure 6.1: Unified SFR model of a low-inertia system.

6.1 Key points of the unified SFR model

Compared to SFR models used in Chapter 4, this representation contains only the main dynamics of each unit type and neglects nonlinearities such as rate limiters and saturation. Nonetheless, these can be added by inserting them in series with unit dynamics at the appropriate places. Likewise, Fig. 6.1 shows only one of each unique unit type, and representing multiple instances of a single unit type is easily achieved by stacking the transfer functions in parallel. Finally, the representation shown in Fig. 6.1 implicitly assumes that all relevant base conversions and input/output signs have been taken care of (i.e., conversion to a common system base and making sure that all Δf inputs and Δp outputs have correct positive or negative signs in the feedback loop).

6.1.1 System inertia and damping

System inertia (H) consists only of synchronous machine inertia (generators and motors) per (4.22), while damping (D) depends on the load structure (e.g., motor mechanical load characteristics, electrical load composition, losses, etc.) per (4.15). Virtual inertia from grid-forming devices is subsumed in the numerator of the $G_{\mathrm{GFR}}(s)$ transfer function to keep the physical inertia and control action separate (as used in [25]). However, this approach results in a non-standard SFR model format when synchronous inertia is zero in which the virtual inertia constant is in the numerator of the upper blocks. Furthermore, it requires the existence of a first-order denominator to avoid improper transfer functions in the model. This, generally, is not an issue since this denominator reflects the converter inner control time constant. Nevertheless, it will make the virtual inertia effect non-instantaneous (which in fact it is, since this behaviour is emulated in the control software and technically subject to control & measurement time lags, however small). This can cause issues in RoCoF calculations using derivative blocks due to numerical instability (both at the instance of the disturbance and in steady-state). Alternatively, grid-forming virtual inertia can be added to synchronous inertia without introducing a significant error, while other terms are kept in the upper $G_{\mathrm{GFR}}(s)$ block, as was shown in Chapter 4.

6.1.2 Synchronous turbine-governor dynamics

Turbine dynamics are represented by a simple lead-lag filter with the time constants T_1 and T_2, and droop R. This is, in most cases, sufficient to in the simplest manner model steam and hydro turbines by setting the appropriate time constants. Nevertheless, more detailed turbine-governor models can be used by replacing this transfer function. We note that this is a very crude representation of turbine-governor dynamics which are complex nonlinear systems and

the fidelity of the model should suit the type of study [230]. For qualitative/screening studies that SFR models are intended for, the simplified models are sufficient to capture the system-wide characteristics such as overall time lags, non-minimum phase behaviour of hydro turbines, etc.

6.1.3 Induction machine dynamics

The induction machine SFR model is derived in Section 4.2 per (4.47). The loss factor $K_p D_{\text{loss}} \omega_{r0}$ is not explicitly shown in Fig. 6.1 since it can be subsumed under the system damping D. The main point here is that the inertial effect of induction motors is not instantaneous with respect to the system frequency disturbance due to the operational principle of induction machines, i.e., slip. The described model is valid for both generators and motors, taking into account the appropriate direction of output Δp_{IM}. In modern and future power systems, this effect may not be relevant since most grid-connected electric drives are converter-interfaced.

6.1.4 Power system stabilizer dynamics

PSS dynamics can technically have an influence on the frequency response as shown in 4.1 since the excitation voltage is modulated based on the frequency deviation signal which impacts the active power output in the transient state. The system-wide effect of this depends on the type of stabilizer and its tuning as well as on the cumulative size of SMs equipped with a PSS with respect to the overall system size.

6.1.5 Generic grid-following CID dynamics

The generic (not considering any particular DC-side device dynamics) grid-following CID is described by two transfer functions: $G_{\text{PLL}}(s)$ describing the PLL dynamics (3.12) which produces the grid frequency estimate for the frequency controller, and $G_{\text{GFL}}(s)$ describing the combined effect of frequency controller and current controller. Without losing generality, $G_{\text{GFL}}(s) = \left(R^{-1} + \frac{2Hs}{T_f s+1} \right) \cdot G_{\text{GSC}}(s)$, where $G_{\text{GSC}}(s)$ is either (3.28) or (3.31) depending on whether the internal d-axis current reference is set directly or through the DC link controller. PLL impact can be significant in case of reduced synchronous inertia since the PLL bandwidth is relatively low. Therefore, the assumption that a CID operates arbitrarily fast may not always be correct since the limiting factor is not the inner current control, but the effectiveness (bandwidth) of frequency measurement and filtering (PLL). Both converter-interfaced sources and loads can be modelled with this model.

6.1.6 Generic grid-forming CID dynamics

Three models have been derived based on the synchronisation approach: PQ-VSM, indirect matching and ViSynC, as described in Section 4.5 and Section 4.6. The SFR models described by Fig. 4.44 (PQ-VSM) and Fig. 4.53 are rearranged to (6.1) to be consistent with the form of Fig. 6.1. For a PQ-VSM, $K_D \in \mathbb{R}$. For the *indirect matching* scheme, $K_D = 0$ and $H = \frac{C_{\text{DC}}}{4R_{\text{DC}}}$ and $R = \frac{R_{\text{DC}}}{K_p^{\text{DC}}}$ per (4.80). In the case of ViSynC, (4.88) is valid. Note that all three variations additionally include the multiplication term $(T_{\text{GSC}}s + 1)^{-1}$ to avoid an improper transfer function in the branch. As in the case of an SFR model of a generic grid-following converter, no particular device dynamics are considered here (assuming that there is enough stored energy to deliver the required power). The model is valid for grid-forming loads as well. Alternatively, as presented in Chapter 4, the $2Hs$ term can be added to the system inertia without a significant error in order to avoid time derivative operator in the numerator.

$$G_{\text{GFR}}(s) = \frac{2Hs + R^{-1} + K_D \left(G_{\text{PLL}}(s) - 1 \right)}{T_{\text{GSC}}s + 1} \tag{6.1}$$

6.1.7 Grid-following WTG dynamics

This can be considered a special case of a grid-following SFR model in which the dynamics of the ECS on the device-side are included. It captures the relevant dynamics of the variable-speed wind turbine generator that provides virtual inertial response through temporary overloading or underloading of the generator, and droop control based on pitch angle modulation. The dynamics of the converter can often be neglected (dashed line in Fig. 6.1) since the time constants are several orders of magnitude smaller than time constants of the PLL and WTG dynamics. Generally, $G_{\text{WTG}}(s)$ depends on the wind speed conditions and type of support control mechanism active (inertia and/or droop) as described by (5.42)–(5.43) in Section 5.5. This SFR model does not discern between DFIG and Type IV WTGs. Except for the case of virtual inertia provision below the rated wind speed, the SFR model is still relatively complex due to the number of parameters and the accuracy strongly decreases for larger disturbances, since it is obtained by linearisation of a highly nonlinear model.

6.2 Characteristics of frequency dynamics of a low-inertia system

In this section we shall discuss some properties of frequency dynamics in the context of low-inertia systems compared to a legacy system.

6.2.1 Physical vs. virtual inertia

The first important point is to discern physical from virtual inertia (and grid-following from grid-forming). The former is a physical property of a rotating electrical machine whose speed changes are driven by the imbalance between mechanical and electrical torque. Frequency dynamics in the simplest way can be written as (6.2):

$$\Delta f(s) = \frac{\Delta p_d(s)}{2Hs + R^{-1}G_{\text{TG}}(s)} \tag{6.2}$$

where $\Delta p_d(s)$ is the generation-load disturbance, R is the droop and $G_{\text{TG}}(s)$ is the turbine-governor transfer function. Using the initial value theorem (e.g., refer to Section 4.1 for a similar discussion), the initial RoCoF ($t = 0^+$) for a step disturbance is calculated as (6.3). What this shows is the instantaneous effect of physical inertia: the initial (and maximum) RoCoF is largest at the instant of a disturbance and depends on the inertia and the size of the disturbance. In other words, the acceleration changes instantly, while the speed initially remains constant.

$$\left\| \frac{df}{dt} \right\|_{t \to 0^+} = \frac{\|\Delta p_d\|}{2H} \tag{6.3}$$

Grid-forming converters can emulate the same behaviour. In an inductive network, the active power of a controlled voltage source will be determined by phase angle dynamics which are governed by the swing equation. Therefore, the device-level control (voltage and current controllers) will be of little importance here. However, the swing equation is not a mathematical description of the physical operating principle of the VSC, but a user-written code implemented in the digital control system, which has two important consequences:

1. It requires a converter output power measurement as input, which is inherently subject to time lag and bandwidth of the measuring+filtering device.
2. The whole thing lives in the discrete time-domain since it is implemented on a digital microcontroller.

Therefore, (6.2) is a discrete time system sampled with T_s in which Δp_d is subject to a measurement time lag T_m. With $G_{\text{TG}}(s) = 1$ (since there is no turbine-governor), the modified swing equation can be written (6.4), which can then be discretised by one of the available methods (zero-order hold, first-order hold, Tustin, etc.) into $\Delta f(z)$ in the z-domain (6.5).

$$\Delta f(s) = \frac{\Delta \hat{p}_d(s)}{2Hs + R^{-1}} = \frac{\Delta p_d(s)}{(2Hs + R^{-1})(T_m s + 1)} = \frac{\Delta p_d(s)}{2HT_m s^2 + (2H + R^{-1}T_s)s + R^{-1}} \tag{6.4}$$

$$\Delta f(z) = \mathcal{Z}\{\Delta f(s)\}_{T_s} \tag{6.5}$$

Applying the initial value theorem to (6.4) results in (6.6), i.e., the RoCoF does not change instantaneously as is the case with synchronous machines. This is because the information

about the disturbance does not propagate to the control system instantaneously.

$$\left\| \frac{df}{dt} \right\|_{t \to 0^+} = 0 \tag{6.6}$$

Assuming $G_{\text{TG}}(s) = 1$ of a synchronous machine swing equation for the sake of comparison (ideal turbine-governor), Fig. 6.2 shows the impact of the discretisation method and sampling time T_s. The impact on Δf is negligible, while the time lag of the initial RoCoF is clearly visible. As the sampling frequency increases, the difference between different discretisation methods decreases. The initial RoCoF transient diminishes very quickly and converges to the continuous time-domain model of an SM, assuming a kHz sampling rate.
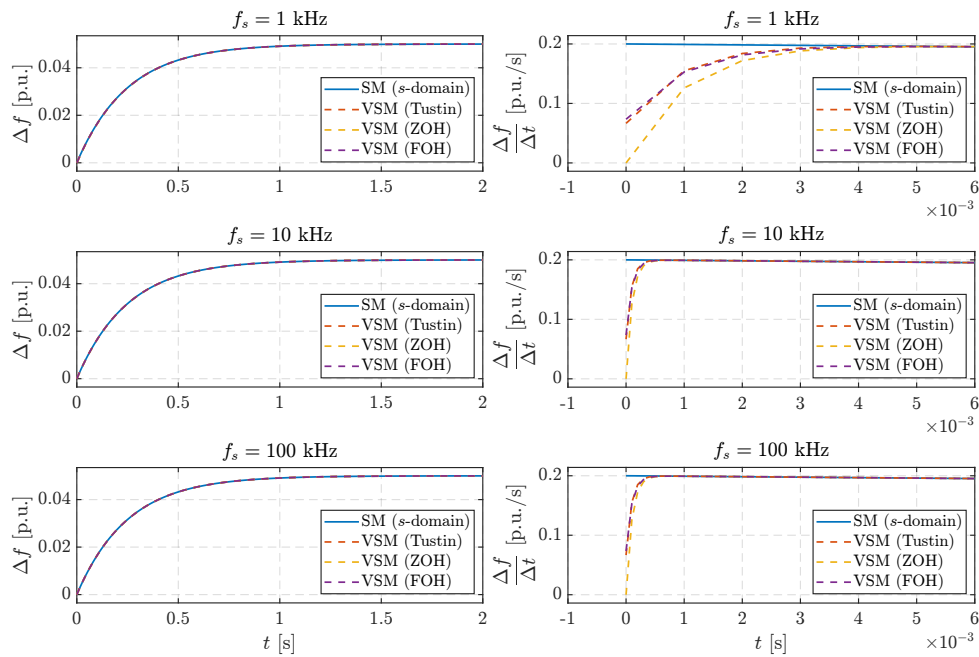
Figure 6.2: Impact of the VSM discretisation method and sampling frequency $f_s = T_s^{-1}$ on frequency characteristics ($T_m = 1$ ms).

Fig. 6.3 shows the effect of the power measurement time constant T_m in the range 1–100 ms (10–1000 Hz bandwidth). The model was discretised with a 10 kHz sampling rate. A decrease of the measurement bandwidth results in a retarded response of the VSM internal frequency. Note that decreasing the measurement bandwidth does not mean that the grid side dynamics will improve as Fig. 6.3 suggests. It only means that the VSM control subsystem will have a reduced response to the physical conditions in the grid, which can be severe, but the signal to the VSM is attenuated due to measurement bandwidth. If not managed properly, it can lead to instability, large excursions of the DC voltage and subsequently converter malfunction.

The discussion above is irrelevant from a practical standpoint because a) initial or instantaneous RoCoF measurement is not used in practice, but usually averaged over a longer time period by RoCoF relays; b) modern digital signal processors are fast which would mean that
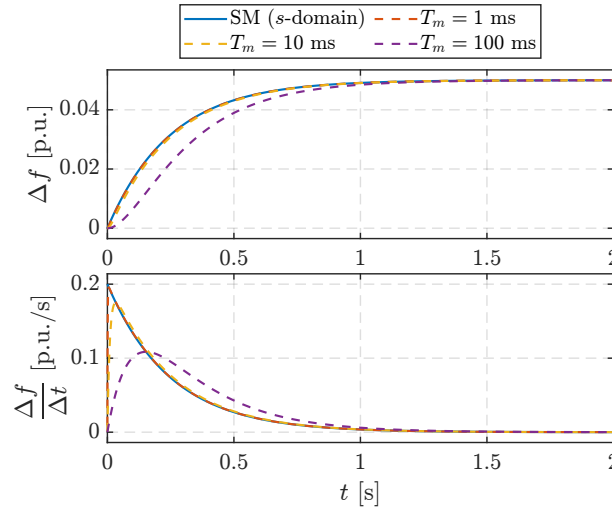
Figure 6.3: Impact of the VSM power measurement bandwidth on frequency characteristics.

the VSM behaviour is identical to an actual synchronous machine for all practical intents and purposes as suggested by Fig. 6.2 (in the frequency control timescale). Furthermore, virtual inertia from grid-forming converters can be considered mathematically equivalent to the physical inertia as suggested in Sections 4.5 and 4.6. Nevertheless, the main purpose of the examples above was to precisely discern between an inherent physical behaviour of a machine and its software emulation on a microprocessor (no matter how fast).

Finally, the virtual inertia effect from grid-following devices is not at all instantaneous since it works on the principle of modulating the power reference based on the measured RoCoF signal, which is subject to PLL lag (for frequency estimation) and additional low-pass filtering (for the time derivative calculation).

6.2.2 Available inertia from various sources

Power system inertia represents an energy buffer of a grid-connected device through which initial imbalances between the prime mover and the electrical load are supplied (without the automatic control action). It is not the stored energy of the "fuel" itself. Changes of values of some quantity of the energy buffer signalizes that an imbalance is happening. This can be used as an input signal to the feedback control that will balance the generation and load. In conventional power plants, inertia comes from the rotating masses of the turbine and generator rotor, therefore, we are talking about kinetic energy. In inverter-based plants, it is the energy of the DC link, so we are talking about the energy in electric and magnetic fields. Certain CIDs, such as WTGs, also have inherent mechanical inertia opposing the changes in turbine speed (but not grid frequency).

Since the mechanical speed of synchronous machines defines the electrical frequency of the power system, their physical inertia defines the overall system inertia. On the other hand, the

inertia of CIDs is essentially hidden since the grid-side converter does not naturally react to AC frequency changes unless specifically controlled in that way. The only natural reaction is the variation of the converter DC link voltage or current due to imbalances between the ECS and GSC power injections, which is decoupled from the synchronous inertia on the AC side. Therefore, if a GSC is analogous to a synchronous generator and the ECS+DSC are analogous to a prime mover, the DC inductor or capacitor are analogous to the rotating mass, as shown in Fig. 6.4.
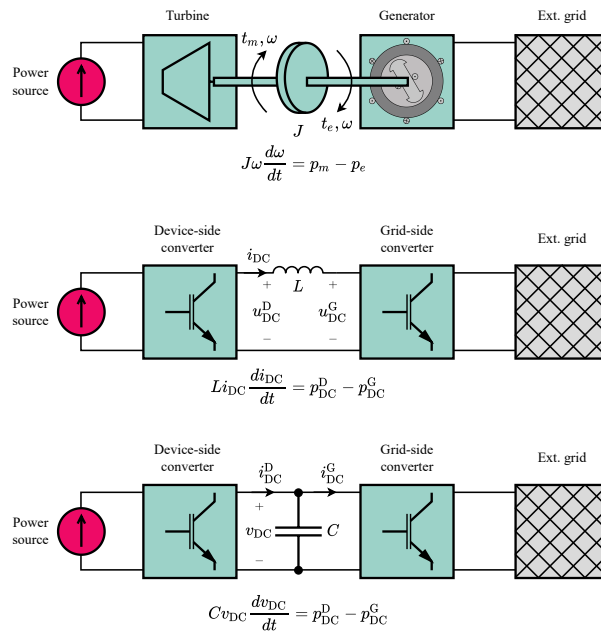
Figure 6.4: Analogy between synchronous inertia and DC inertia.

The effect of inertia is usually expressed through the inertia constant which is the stored energy at rated conditions divided by the rated power. Fig. 6.5 shows the possible ranges of the inertia constant (whether hidden or synchronous) of various technologies to illustrate the amount of stored energy in their mechanical and electrical parts. Note that the data has been consolidated from publicly available sources [13, 16, 38, 106, 231–239] as well as from proprietary generator data from steam, hydro and gas generators in the Croatian power system (courtesy of HOPS ltd.), therefore it is possible that these sources contain erroneous data. Thus, Fig. 6.6 shows the median, upper and lower quartiles, outliers, and minimum and maximum values that are not outliers.

One can see that the inertia constant of conventional synchronous technologies averages between 3–5 s, while the available "inertia" of power electronic converters is three orders of magnitude smaller than that of rotating machinery, thus seen as lying on the x-axis. Generally, stored energy in the DC link is in the order of 1–10 ms with the exception of MMC HVDC where the stored energy ranges between 30 and 40 ms due to bigger equivalent DC-side capacitance. Table 6.1 summarizes the data numerically in a min-max range excluding outliers. Fig. 6.5 and
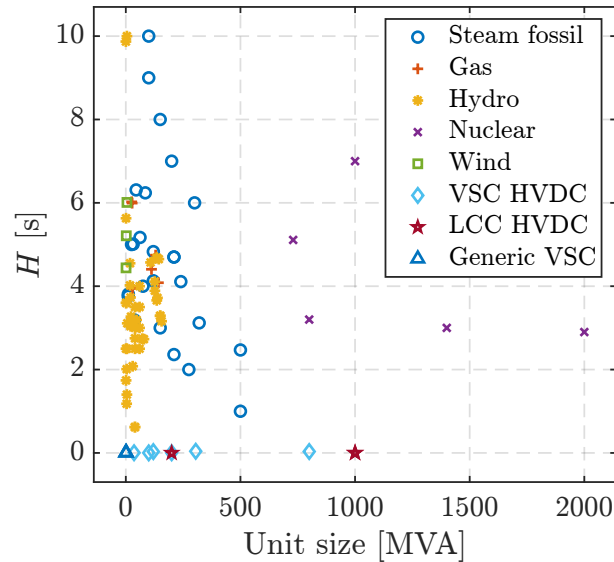
Figure 6.5: Scatter chart of inertia constants of various technologies.
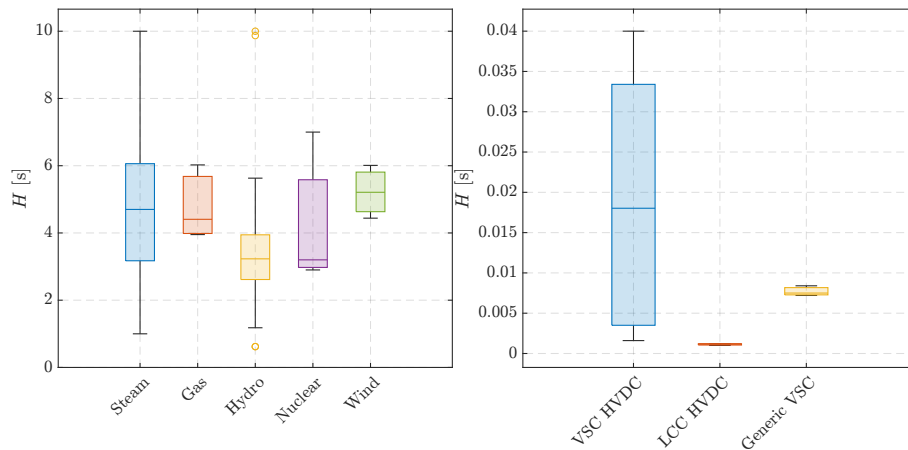
Figure 6.6: Box chart of inertia constants of various technologies.

Table 6.1 only show the "inertia" related to the electromechanical or electromagnetic conversion interface between the ECD and the grid. It does not encapsulate the energy of the primary fuel or storage, i.e., water reservoir, battery, fuel cell, flywheel, etc. since they do not react inherently (considering them as a constant power source) to power-in power-out mismatch. In that sense, the WTG is more akin to a converter-interfaced flywheel since the rotation is decoupled from the grid frequency. Nevertheless, ECD energy can be tapped into via automatic control actions in order to balance the grid frequency or DC link.

6.2.3 Is inertia important?

Grid frequency is tightly controlled mainly to mechanically protect the synchronous turbine-generators in power plants: subsynchronous speed can trigger mechanical resonance of multi-

---

*Decoupled from the grid. Energy in converter DC link not included.

†Single station. Energy in DC lines/cables not included.

Table 6.1: Ranges of inertia constants of various technologies.

Technology	$H = \frac{J\omega_n^2}{2S_n}$	$H = \frac{CV_n^2}{2S_n}$ or $H = \frac{LI_n^2}{2S_n}$
Steam turbines (Coal/Oil/Biomass/Geothermal)	1–10 s	0
Steam turbines (Nuclear)	3–7 s	0
Hydro turbines	1–6 s	0
Gas turbines	4–6 s	0
Wind turbines*	3–6 s	0
Solar PV	0	0
Generic VSC	0	7–8 ms
LCC HVDC[†]	0	1–1.2 ms
VSC HVDC[†]	0	1–40 ms

mass turbines while supersynchronous speed exerts large forces on the shaft. Both can damage the generator and trigger cascade outages. Other reasons include V/Hz limitations, power quality, load impacts and time correction [240]. The V/Hz ratio defines the magnetic flux density in the generator and transformer core which is proportional to heat losses. Too high a V/Hz ratio will cause the core laminations to overheat and the unit will eventually fail. In the context of power quality, a low AC supply frequency causes visible flickering, which is not acceptable. Load impact is not as relevant today since most industrial processes use variable frequency drives, as they are insensitive to variations in the supply frequency. Time correction is necessary for clocks or timers that utilise the AC supply frequency for time calculation.

Inertia essentially provides a time buffer for the power plants to balance out a generation/load mismatch since the turbine power output cannot change instantaneously due to the slowness of thermodynamic or hydrodynamic phenomena, as well as governor time lag. Consider the simplest power system model described by (6.2) with $G_{\text{TG}}(s) \rightarrow G(s) = \frac{1}{Ts+1}$ being the transfer function of the generation power balancing. We use the equation to describe a generic device that behaves as a synchronous generator, without making a distinction between synchronous machines and converters or the type of power source / prime mover.

Frequency quality criteria defined by the grid code depend on the power system characteristics. Without referring to any particular grid code, it is sufficiently accurate to say that most bulk power systems will have a normal frequency operating range inside ±100 mHz (0.002 p.u. for 50 Hz system), maximum instantaneous frequency deviation (nadir) under 1000 mHz (0.02 p.u.) for the largest single contingency and maximum steady-state deviation under 500 mHz (0.01 p.u.). Therefore, one can see that, percentage-wise, frequency is very tightly controlled even for these relatively loose limits.

For a power system with $\Delta p_d = 0.075$ p.u., $D = 0$ p.u., $R = 0.05$ p.u. and $T = 9$ s, Fig. 6.7 shows the impact of reducing the inertia constant from $H = 5$ s to $H = 1$ s. Clearly, inertia reduction causes a sharper frequency decline and violation of the nadir limit for $H = [1,3]$ s as well as an increased oscillation frequency.
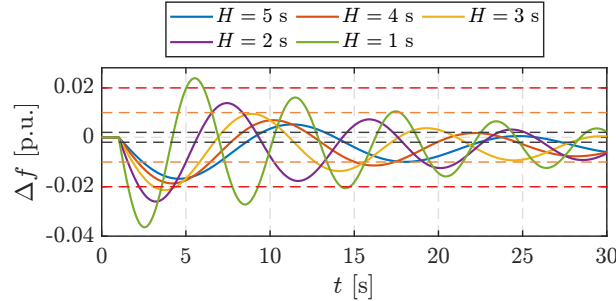
Figure 6.7: Impact of H reduction in a slow power system ($T = 9$ s).

There are three ways to mitigate this effect: decreasing the droop R (Fig. 6.8), reducing the time constant T (Fig. 6.9), or both. Fig. 6.8 shows that the droop needs to be reduced to 1% in order for frequency to stay inside the nadir limits, however the oscillations are still persistent when the lag time constant is large. Fig. 6.9 illustrates that reducing the time constant decreases the instantaneous frequency deviation as well as damps the oscillations. That is because the damping effect of R is constrained by the time constant of the actuation mechanism without any other damping sources in the system ($D = 0$), i.e., R does not contribute to damping unless $T = 0$. Physically speaking, R is the tunable parameter since it is the user-defined gain of the regulator, while T is a consequence of the physical properties of the online units (steam, hydro, battery, etc.) and cannot be tuned except by controlling the instantaneous generation mix.
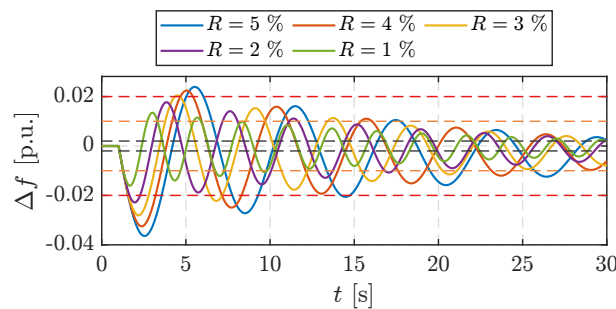
Figure 6.8: Impact of R reduction in a slow, low-inertia power system ($T = 9$ s, $H = 1$ s).

The transfer function $H(s) = \Delta f(s)/\Delta p_d(s)$ (6.2) can be written as (6.7), where ζ and ω_n are damping and the natural frequency is defined as (6.8) and (6.9), respectively.

$$H(s) = \frac{\dfrac{1}{2H}s + \dfrac{1}{2HT}}{s^2 + \left(\dfrac{1}{T} + \dfrac{D}{2H}\right)s + \dfrac{D + R^{-1}}{2HT}} = \frac{\dfrac{\omega_n^2}{D + R^{-1}}(sT + 1)}{s^2 + 2\zeta\omega_n s + \omega_n^2} \tag{6.7}$$
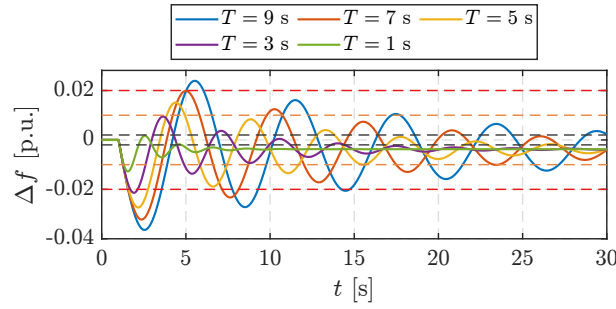
Figure 6.9: Impact of T reduction in a low-inertia power system ($H = 1$ s, $R = 0.05$ p.u.).

$$\zeta = \frac{\sqrt{2}}{2\sqrt{D+R^{-1}}}\left(\sqrt{\frac{H}{T}} + \frac{D}{2}\sqrt{\frac{T}{H}}\right) \tag{6.8}$$

$$\omega_n = \sqrt{\frac{D+R^{-1}}{2HT}} \tag{6.9}$$

Thus, a decrease of R actually decreases damping and increases the natural frequency as shown by Fig. 6.10. One can see that ζ decreases significantly with the increase of T, while the effect of R is less pronounced. In a low-inertia system, adequate damping can only be achieved by fast actuation. Furthermore, Fig. 6.11 illustrates that systems with small T are more sensitive to the reduction of damping due to inertia reduction than slower systems are. For slower systems, the effect of D becomes more important as inertia reduces.
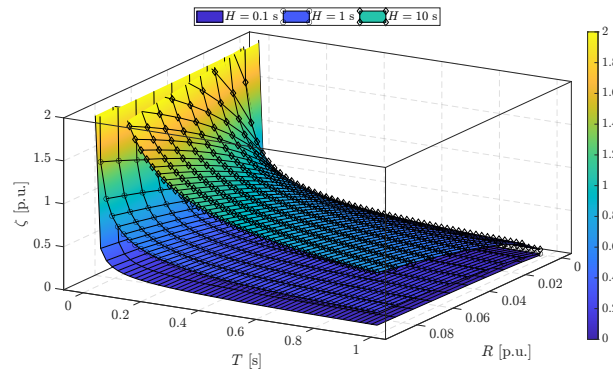
Figure 6.10: ζ as a function of R, T and H ($D = 0$ p.u.).

Implicitly expressing H as a function of remaining variables from (6.8) results in:

$$H^2 + H\left[TD - 2\zeta^2 T\left(D+R^{-1}\right)\right] + \frac{D^2 T^2}{4} = 0 \tag{6.10}$$

to which the solution is:

$$H = -\frac{B}{2} \pm \frac{1}{2}\sqrt{B^2 - D^2 T^2} \tag{6.11}$$

where:

$$B = TD - 2\zeta^2 T\left(D+R^{-1}\right) \tag{6.12}$$
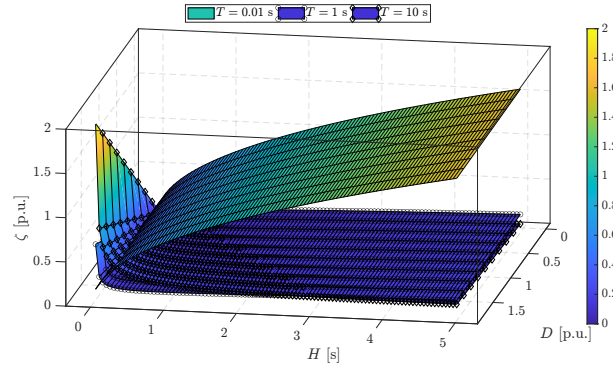
Figure 6.11: ζ as a function of H, D and T ($R = 0.01$ p.u.).

Obviously, $\{H, T, D, R, \zeta\} \in \mathbb{R}_{\geq 0}$ and $B^2 \geq D^2 T^2$ for the equation to be valid. For a special case of $D = 0$, (6.12) further simplifies to:

$$H = 2\zeta^2 T R^{-1} \tag{6.13}$$

Additionally, to achieve a standard damping value of $\zeta = \frac{\sqrt{2}}{2}$, (6.10) simplifies to:

$$HTR^{-1} = H^2 + \frac{T^2 D^2}{4} \tag{6.14}$$

where solving for H gives:

$$H = \frac{T}{2}\left(R^{-1} + \sqrt{R^{-2} - D^2}\right) \tag{6.15}$$

which is valid for $R \leq D^{-1}$, and $H = TR^{-1}$ for $D = 0$.

The main point (6.10)–(6.15) are trying to illustrate is that the reduction of inertia can be compensated by increasing the share of fast-acting sources in the grid, while keeping the same damping level in the system (or improving it). Therefore, the reduction of inertia in and of itself may not be an issue from a frequency containment perspective as illustrated by Fig. 6.12. This shows that the frequency excursions are identical in all cases with respect to the maximum instantaneous deviation and steady-state value. Therefore, damping is preserved and frequency deviation is contained in the same range. However, the natural frequency of the system significantly increases per (6.9) and this could lead to instability if resonances exist at those frequencies. Furthermore, frequency tracking of grid-following devices becomes difficult and such devices, potentially, could not react to frequency excursions quickly enough.

To further stress the point of inertia reduction not inherently causing a small-signal frequency instability, Fig. 6.13 shows the root locus plots of $H(s)$ for varying T and H. It shows that the reduction of H or T generally moves the complex-conjugate roots away from the positive half-plane, thus increasing damping and natural frequency. The complex-conjugate roots
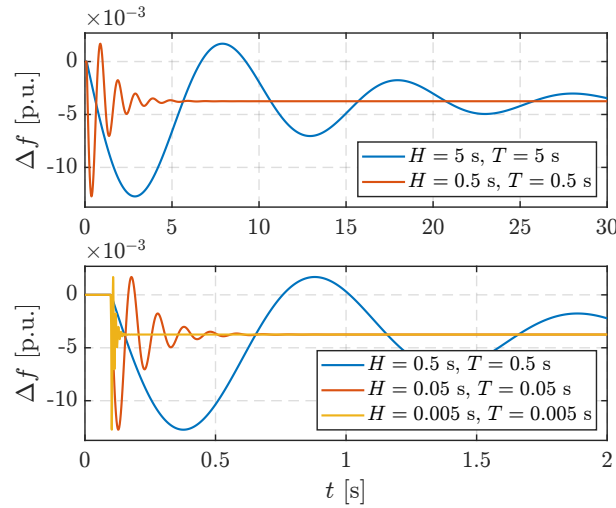
Figure 6.12: Compensating reduced inertia by reducing the system time constant: normal-to-low inertia (top) and low-to-extremely-low inertia (bottom).

of (6.7) are calculated per (6.16).

$$\lambda_{1,2} = -\frac{1}{2}\left(\frac{1}{T} + \frac{D}{2H}\right) \pm \frac{1}{2}\sqrt{\left(\frac{1}{T} + \frac{D}{2H}\right)^2 - \frac{4}{T}\left(\frac{R^{-1}}{2H} + \frac{D}{2H}\right)} \qquad (6.16)$$
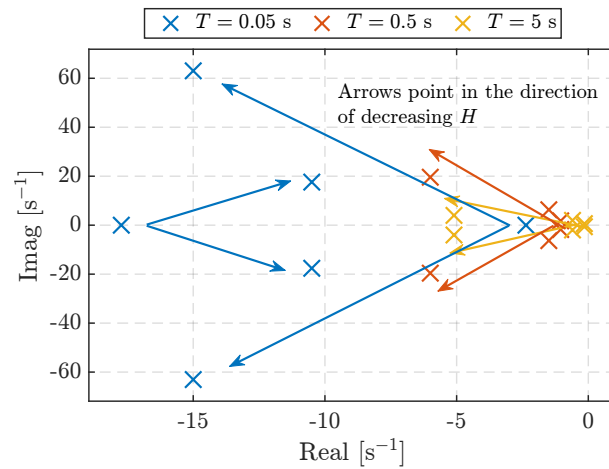
Figure 6.13: Root loci of (6.7) for varying H and T ($D = 1$ p.u., $R = 0.05$ p.u.).

What has not yet been mentioned in the discussion above is the impact of H reduction on the RoCoF ($sH(s)$). The RoCoF withstand capability is important from a system stability perspective because grid-connected units need to remain online to stabilise the system. Reducing the system inertia increases the RoCoF for the same disturbance size (visible by looking at the initial slope of Δf in Fig. 6.12) and therefore units might trip. Fig. 6.14 illustrates the nonlinear impact of H reduction on the initial RoCoF increase (6.3).

Although (6.3) provides an elegant and conservative way to calculate the minimum amount of system inertia, the value it provides (theoretical maximum) is of little practical importance
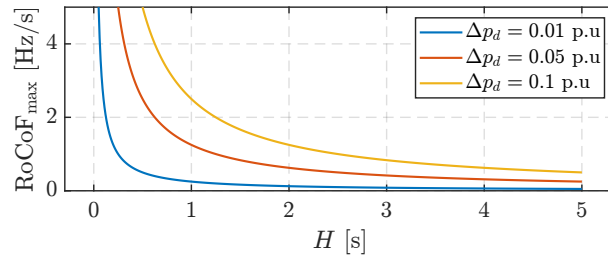
Figure 6.14: Inertia vs. maximum RoCoF (6.3) for various disturbance sizes.

since all RoCoF relays inevitably contain filtering of the frequency measurement which reduces bandwidth [241]. Therefore, the theoretical maximum may not be sensed at all. This is not a limitation of the measuring equipment, but a programmed behaviour since initial the RoCoF transient is very local and prone to voltage waveform disturbances at the point of measurement [242]. It takes between several milliseconds to several hundred milliseconds for the RoCoF to converge to a coherent value (refer to Fig. 4.2). Therefore, the measurement time window over which the RoCoF is averaged is as important as the inertia itself [243]. Furthermore, for $t > 0^+$ all parameters (droop, system time constant, load self-regulation) begin to have an influence on the RoCoF as well.

The question, then, naturally arises: what is the adequate RoCoF measurement performance? Some recent Pan-European studies and guidelines on RoCoF withstand capabilities [241, 243–245] in the context of reduction of synchronous inertia recommend the following:

- "Any frequency measurement technique which would result to ± 1 mHz/s error for a 500 ms rolling time window is considered adequate for the compliance monitoring."
- "500 ms is an appropriate time frame to calculate RoCoF, as it usually takes this length of time for the generators to return to a coherent state."
- RoCoF withstand capability in the future will need to be increased.
- RoCoF triggered synthetic inertia calculated over 500 ms was not found to have suitable performance, and a response time of ≈ 100 mHz would be required to prevent RoCoF events > 0.5 Hz/s.

Table 6.2 shows some typical RoCoF values that grid-connected units must withstand. Generally, if the sliding window decreases, the RoCoF requirements should be relaxed.

Table 6.2: Power generating unit RoCoF withstand capability.

RoCoF [Hz/s]	Time window [ms]
± 2 (± 1 in [243, 245])	500
± 1.5	1000
± 1.25	2000

Fig. 6.15 shows the maximum measured RoCoF for different sliding windows according to

Table 6.2 plotted against the theoretical maximum. It can be seen that for $H \approx 0.5$ s:

- a 2000 ms sliding window outputs $\text{RoCoF}_{\text{max}} \approx 0.75$ Hz/s,
- a 1000 ms sliding window outputs $\text{RoCoF}_{\text{max}} \approx 1.35$ Hz/s,
- a 500 ms sliding window outputs $\text{RoCoF}_{\text{max}} \approx 2.5$ Hz/s,
- 100 ms and 50 ms sliding windows output $\text{RoCoF}_{\text{max}} \approx 4$ Hz/s and are closest to the theoretical limit.
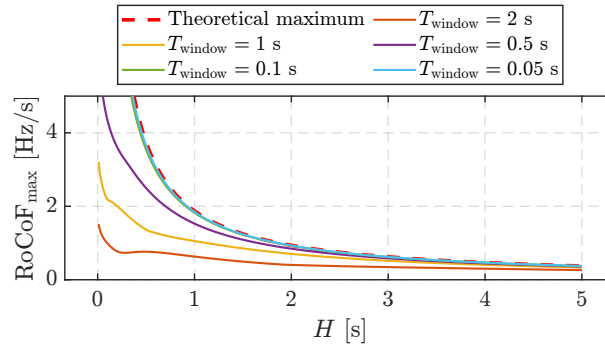
Figure 6.15: Estimation of the maximum RoCoF for various sliding average time windows ($D = 1$ p.u., $R = 0.05$ p.u., $T = 5$ s).

Therefore, degradation of inertia is only a part of the issue as the way RoCoF is estimated for control or protection actions significantly depends on the time window used. Although initial the RoCoF is high in a low-inertia scenario, it will bounce back quickly to a lower value and the length of the sliding window will determine the observed maximum. Fig. 6.16 illustrates that as inertia decreases 10 times, the initial RoCoF will increase 10 times. However, by reducing the time constant of the system, the steady-state is reached faster with fewer oscillations. Additionally, one can see that for extremely low inertia scenarios, the initial RoCoF reaches values of over 40 Hz/s, but when the RoCoF is measured as a sliding average over 500 ms, these extreme initial values are not captured. Hence, if these large initial transients can be neglected without jeopardizing the equipment then extremely low inertia scenarios might be feasible if the actuation is fast enough.

Furthermore, a high RoCoF can be conditionally mitigated by decreasing the droop value if the system is still overdamped ($\zeta > 1$), otherwise the RoCoF is deteriorated since decreasing the droop reduces the damping as illustrated by Fig. 6.17, which shows an amplification of the first overshoot. Additionally, having as large D as possible positively contributes as well, but to a limited extent in the real world since it means having a lot of frequency-sensitive loads, i.e., directly connected synchronous and induction motors. Since it is fairly accurate to say that all new industrial drives are interfaced via frequency converters, no other load remains in the system whose power consumption is inherently sensitive to frequency deviation. Generally, even in a legacy system, the value of D is at least an order of magnitude smaller than R^{-1}.
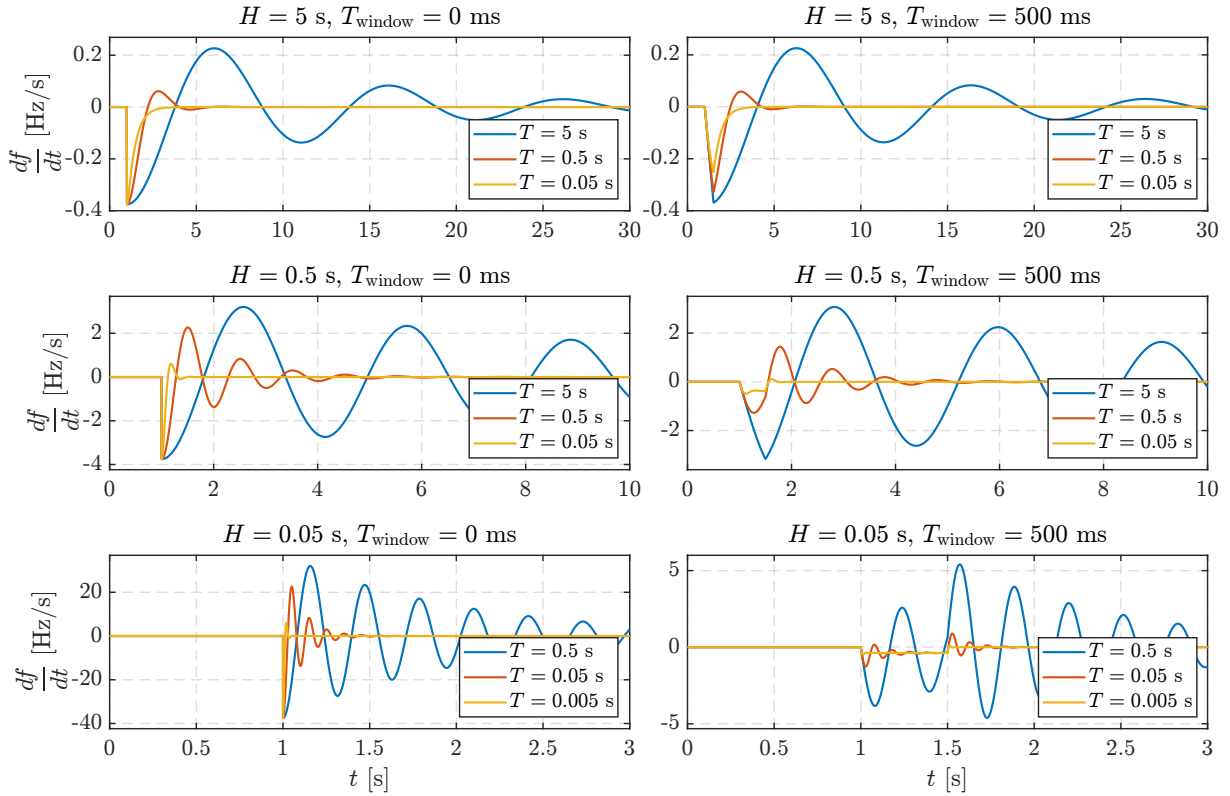
Figure 6.16: Time-domain plot of the RoCoF for varying magnitudes of H and T: ideal instantaneous RoCoF (left column) and average RoCoF measured over a 500 ms window (right column).

6.2.4 Effect of PLLs

We now modify (6.7) such that the virtual inertia and primary frequency control is provided solely by a grid-following CID with a three-phase SRF PLL (6.17). Synchronous units provide only inertia and no droop control. This model will serve to isolate the impact of PLL dynamics on grid frequency dynamics in order to illustrate the efficacy of grid-following units in fast frequency control. G_{GSC} is modelled as (3.28). Notice that for $H_v = 0$ and $G_{\text{PLL}}(s) = 1$ (6.17) reduces to (6.2).

$$\Delta f(s) = \frac{\Delta p_d(s)}{2Hs + \left(R^{-1} + \dfrac{2H_v s}{T_f s + 1}\right) G_{\text{PLL}}(s) G_{\text{GSC}}(s)} \tag{6.17}$$

First, we shall consider only droop provision ($H_v = 0$) from a converter with $T = 10$ ms. The wide range of the PLL bandwidth can be found in the literature from < 1 Hz to > 30 Hz [246, 247], and it is not always clear how this bandwidth is defined [248]. Nevertheless, generally it is sufficiently smaller than the fundamental frequency [249]. Here, we define the bandwidth simply as the natural frequency $f_n^{\text{PLL}} = \frac{\omega_n^{\text{PLL}}}{2\pi}$ of the closed-loop PLL transfer function (4.68). We vary f_n^{PLL} from 0.5 Hz to 25 Hz, which seems to cover a sufficiently wide range of possible bandwidths. K_p^{PLL} is tuned to achieve a constant damping of $\zeta^{\text{PLL}} = \frac{\sqrt{(2)}}{2}$, i.e., $K_p^{\text{PLL}} = 2\zeta^{\text{PLL}} \omega_n^{\text{PLL}} = \sqrt{2}\omega_n^{\text{PLL}}$. Hence, green areas in Fig. 6.18 illustrate the instability
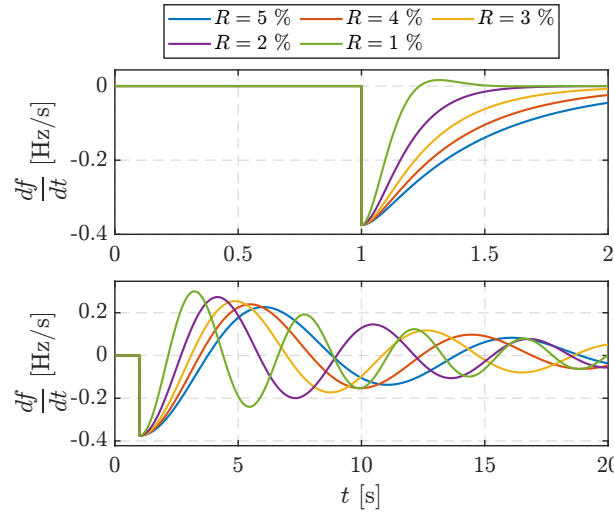
Figure 6.17: Impact of R on RoCoF: overdamped system (top) and underdamped system (bottom).

regions (i.e., pole in the right half-plane) of the closed-loop system (6.17) as a function of inertia, PLL bandwidth and droop. It can be seen that decreasing the droop, PLL bandwidth and inertia constant increases the instability region, i.e., as inertia of the system decreases, the PLL bandwidth and/or droop need to be increased to maintain stability. However, the PLL bandwidth cannot be arbitrarily increased because its performance would degrade and be less robust to voltage waveform disturbances due to, e.g., asymmetric conditions, phase jumps, noise, harmonics, as well as destructive interactions with the grid impedance [250]. To the contrary, the PLL bandwidth is usually decreased in weak grids (low SCR). Moreover, increasing the bandwidth increases the frequency region in which the VSC has negative resistance, as seen from the grid terminals [249]. Therefore, Fig. 6.18 only shows a part of the whole picture as the problem is much deeper than just frequency dynamics that happen on a longer time scale. However, electromagnetic phenomena are not captured by SFR models since electrical networks and voltage dynamics are not modelled. One of the shortcomings of the SFR model is that one could just increase the PLL bandwidth arbitrarily to keep the stability, but that may not reflect the actual system performance, which could prove to be unstable.
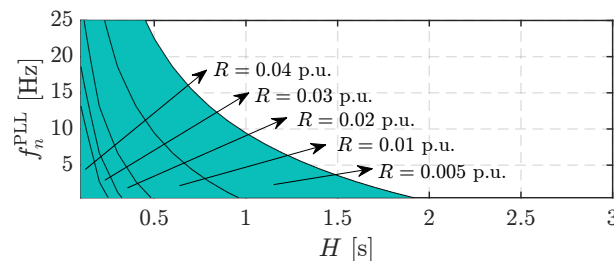
Figure 6.18: Instability region for the most critical mode of (6.17) as a function of H, f_n^{PLL} and R ($H_v = 0$, $D = 0$, $T = 0.01$ s).

Fig. 6.19 shows the damping ($\zeta = -\frac{\sigma}{\|\omega_n\|}$) of the critical mode ($\lambda = \sigma \pm j\omega_n$) where negative damping regions indicate instability. It can be seen that reducing the droop, PLL bandwidth and

inertia decreases damping of this mode. Damping can be increased by increasing K_p^{PLL}, but this can degrade the overall performance of the actual system, as argued in the previous paragraph.
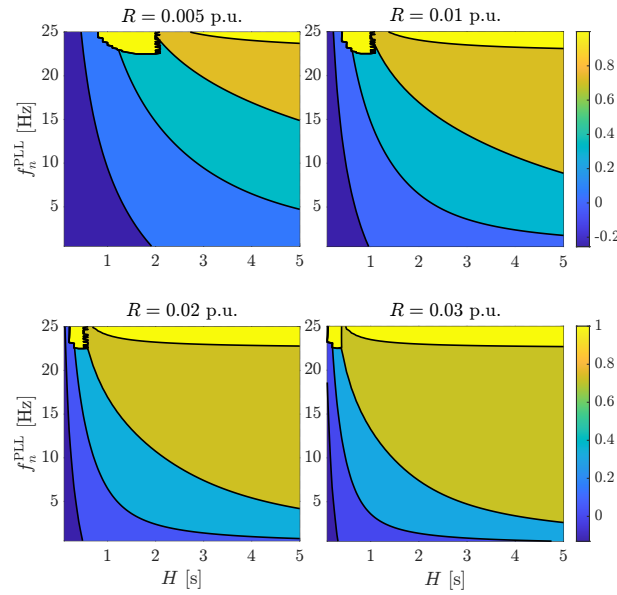
Figure 6.19: Damping ($-\frac{\sigma}{\|\omega_n\|}$) for the most critical mode of (6.17) as a function of H, f_n^{PLL} and R ($H_v = 0$, $D = 0$, $T = 0.01$ s).

Next, we shall analyse the effectiveness of virtual inertia provision by the grid-following CID, considering PLL dynamics and additional filtering. There are two time lag sources impacting the virtual inertial response—the first time lag is due to the frequency estimation by the PLL, as discussed previously. The second time lag is due to the low-pass filtering of the time derivative operation for RoCoF calculation from the previously estimated frequency. The effect of virtual inertia on the RoCoF is shown in Fig. 6.20. The benchmark case is for $H = 5$ s and $H_v = 0$; then, H is sequentially reduced by 1 s which is added to the H_v (i.e., $H + H_v = 5$ s). The simulations are repeated for different PLL bandwidths and time constants of the time derivative's low-pass filter. The instantaneous RoCoF is shown (no averaging). All cases clearly show that virtual inertia does not simply replace physical inertia as the RoCoF degrades with the reduction of H. Moreover, the combination of f_n^{PLL} and T_f will determine how damped the response is, which is particularly visible in low-inertia scenarios: a lower bandwidth results in stronger oscillations of frequency and can sometimes even exacerbate the problem. It is important to note that f_n^{PLL} and T_f^{-1} are inversely proportional: if f_n^{PLL} is large, then T_f^{-1} needs to be small and vice versa, but both do not need to be small and cannot be large. That is because the PLL firstly estimates the grid frequency from a voltage waveform prone to high-frequency disturbances and then the time derivative of that signal needs to be calculated, which further amplifies the noise. Therefore, the combined effect of f_n^{PLL} and T_f^{-1} needs to be such that an adequate low-pass behaviour is exhibited in order to reject the noise in the frequency signal.
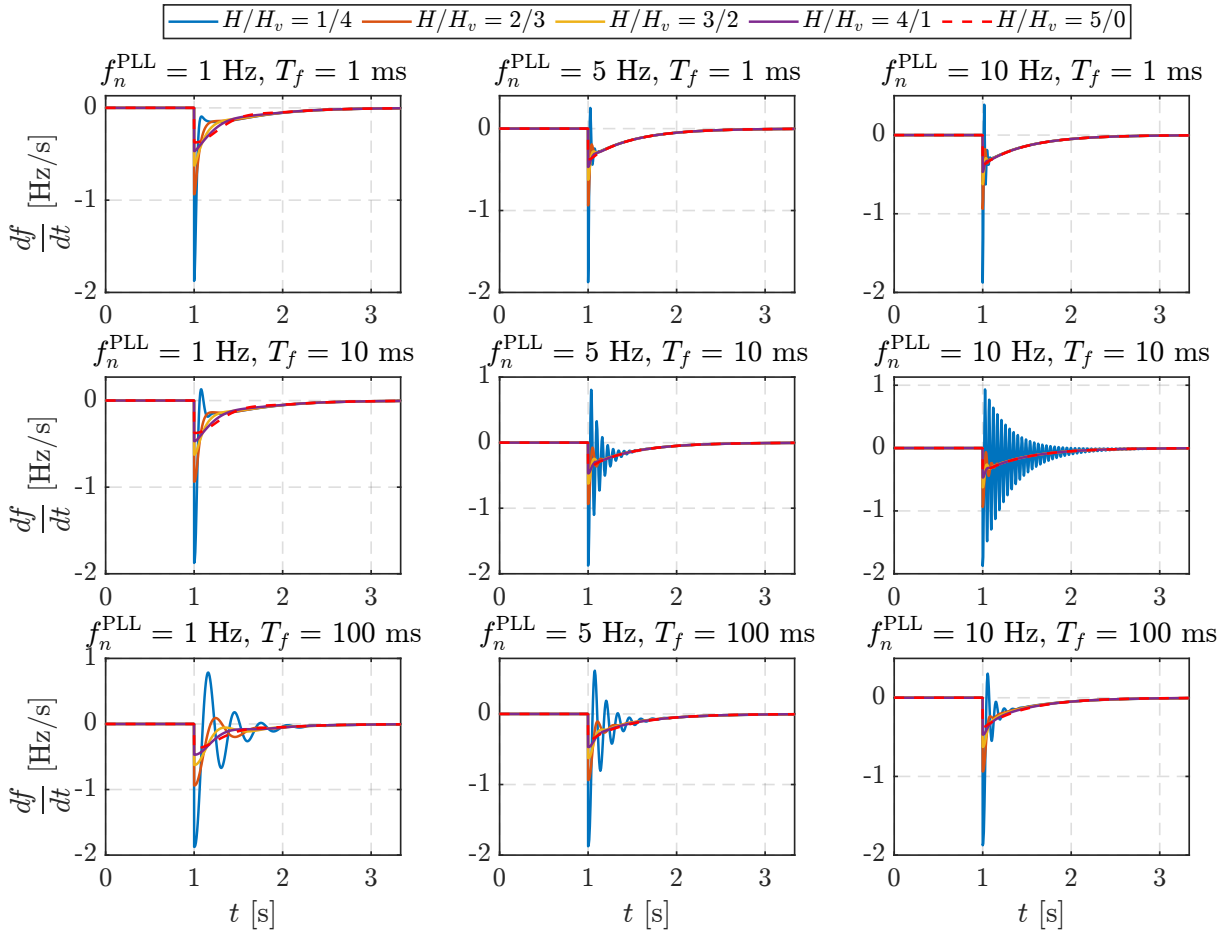
Figure 6.20: System RoCoF as a function of the physical/virtual inertia ratio H/H_v, f_n^{PLL} and T_f ($D=0$ p.u., $R=0.05$ p.u., $T=0.01$ ms).

6.2.5 Effect of induction machines

Here, we shall illustrate the contribution of directly-connected induction machines using their SFR model derived in Section 4.2 by using a simple system (6.18) where $D_\mu = K_p D_{\mathrm{loss}} \omega_{r0}$. Refer to (4.48) for the definition of all other parameters.

$$\Delta f(s) = \frac{\Delta p_d}{2Hs + D + R^{-1}\dfrac{1}{Ts+1} + D_\mu + K_p D_s \dfrac{2H's+D''}{2H's+1}} \tag{6.18}$$

Usually, all load self-regulation is subsumed under a single damping constant D since the system-wide instantaneous load composition and its characteristics are not known. For a simple system consisting only of induction machine loads, we shall compare the difference between modelling load dynamics with just D to a more detailed model $G_{\mathrm{IM}}(s) = D_\mu + K_p D_s \frac{2H's+D''}{2H's+1}$ in which the load inertia constant is considered. Fig. 6.21 shows the results for some values of rotor resistance per Table 4.3. The base case (blue curves) is without any load dynamics ($D = 0$, $G_{\mathrm{IM}}(s) = 0$). For the case when load dynamics are modelled by a damping constant (orange curves), D is chosen such that $D = D_\mu + K_p D_s D''$ (i.e., equal steady-state contribution).
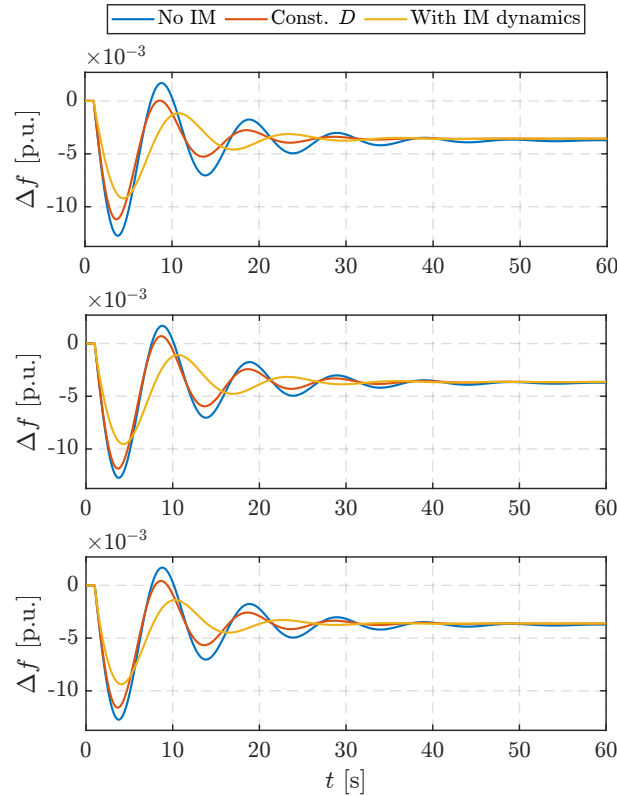
Figure 6.21: Impact of induction machine dynamics modelling on the system frequency response ($H = 5$ s, $T = 5$ s, $R = 0.05$ p.u.): $R'_r = 0.01$ p.u. (top), $R'_r = 0.05$ p.u. (middle), $R'_r = 0.1$ p.u. (bottom).

It can be seen that load self-regulation positively affects frequency containment, but using a constant D representation gives more conservative results than including more complete dynamics through $G_{\mathrm{IM}}(s)$. Fig. 6.21 does not show any substantial impact of rotor resistance on the frequency response. Nonetheless, its impact is more clearly visible on the RoCoF chart shown in Fig. 6.22. Although there is no impact on the initial RoCoF due to the time lag $2H'$, very quickly the RoCoF is more damped than in the case when constant D is used. Fig. 6.22 also shows that lower R'_r leads to stronger RoCoF damping since larger values of R'_r mean the connection of the machine to the grid is less stiff.

Finally, Fig. 6.23 illustrates how larger motors increase the damping of the frequency changes.

The usefulness of $G_{\mathrm{IM}}(s)$ in practice is arguable. First, it adds more complexity to the SFR model and the need to calculate the parameters. Depending on the usage of the model, it seems that in most cases using constant D along with an appropriate increase of synchronous inertia constant H will provide sufficiently accurate results. If it is necessary to distinguish synchronous from asynchronous inertia, using the high-pass filter representation should do the trick as discussed. Secondly, as stressed before, almost all induction motor drives today are converter-interfaced so in that case using this model is irrelevant. At the very least, by using constant D, one should not arrive to overly optimistic results.
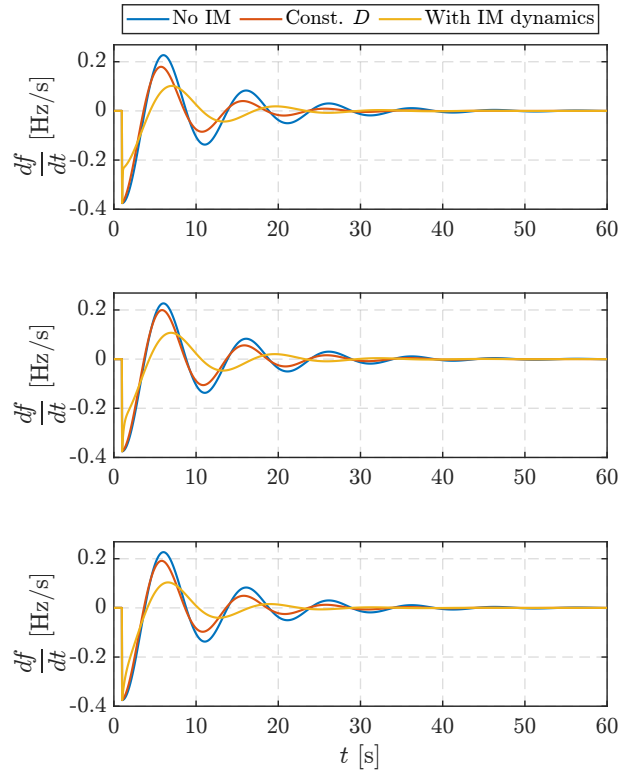
Figure 6.22: Impact of induction machine dynamics modelling on the RoCoF ($H = 5$ s, $T = 5$ s, $R = 0.05$ p.u.): $R_r' = 0.01$ p.u. (top), $R_r' = 0.05$ p.u. (middle), $R_r' = 0.1$ p.u. (bottom).
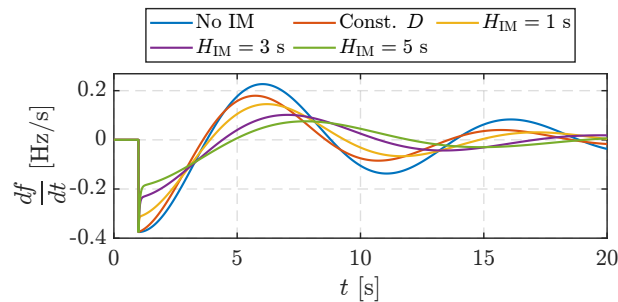
Figure 6.23: Impact of the induction machine dynamics inertia constant H_{IM} on the RoCoF.

6.2.6 Effect of WTGs

A more accurate low-order model of a variable-speed WTG has been derived in Chapter 5. Here, we shall briefly show the impact of WTG parameters on the system frequency response. A WTG in parallel with a generic turbine model is considered per (6.19). Parameters are fixed as follows: $D = 0$, $R = 0.05$ p.u. and $T = 5$ s. The converter time constant is set to 5 ms.

$$\Delta f(s) = \frac{\Delta p_d}{2Hs + D + R^{-1}\dfrac{1}{Ts+1} + G_{\text{PLL}}(s)G_{\text{WTG}}(s)G_{\text{GFL}}(s)} \quad (6.19)$$

First, provision of only the synthetic inertial response ($H_v = 5$, $T_f = 0.01$ s) is considered below the rated wind speed, which means that $G_{\text{WTG}}(s)$ is simplified to (5.44) in which $T_{\text{wtg}} \in [4,7]$

214

s. Fig. 6.24 shows how different SFR modelling approaches impact the system frequency for both a high-inertia and a low-inertia system. It can be seen that the WTG improves the system frequency response, but neglecting $G_{\text{WTG}}(s)$ results in a more optimistic response, especially in the low-inertia scenario in which the grid frequency oscillations are more persistent.
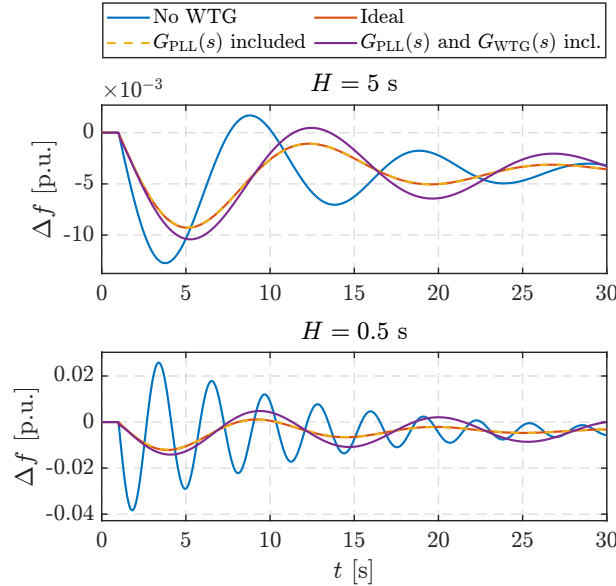
Figure 6.24: Impact of WTG modelling on the system frequency response (synthetic inertia below the rated wind speed): high-inertia (top) and low-inertia (bottom).

Fig. 6.25 illustrates how reducing T_{WTG} (it reduces as wind speed increases) reduces the system damping. Impact is not so significant in a high-inertia scenario, but it can lead to instability in a low-inertia scenario, as illustrated by the purple curve. Therefore, additional sources of damping need to be present in the system (e.g., load self-regulation or effective time constant).

Fig. 6.26 – Fig. 6.28 show the system frequency response once the pitch control becomes active. Fig. 6.26 shows it for synthetic inertia during above-rated wind speed, while Fig. 6.27 and Fig. 6.28 show it for the droop control for below-rated and above-rated wind speed, respectively. Fig. 6.26 shows that the behaviour is similar to the below-rated wind speed scenario (Fig. 6.24). On the other hand, Fig. 6.27 and Fig. 6.28 show that neglecting WTG dynamics including pitch control severely overestimates the performance of WTGs, which is significantly less damped. Moreover, the system frequency is unstable in low-inertia conditions. Therefore, representing WTGs as a first-order transfer function of a converter is not adequate since power reference modulation based on frequency signal actually influences the turbine speed and conditionally activates the pitch control, which all have influence on the WTG power output.
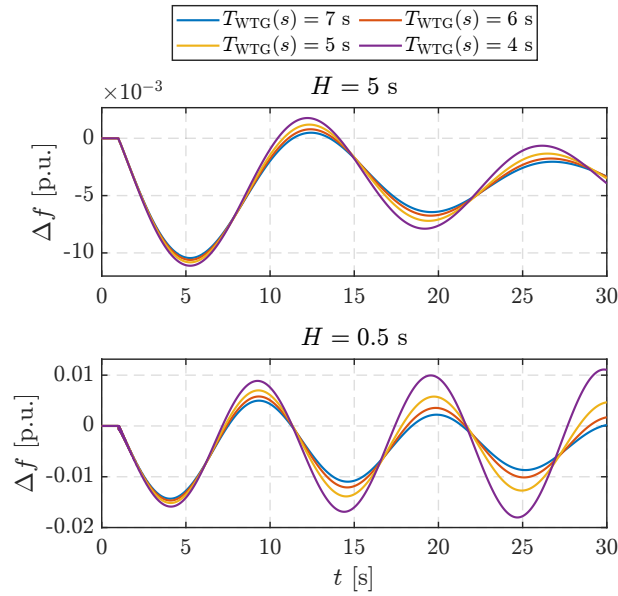
Figure 6.25: Impact of T_{WTG} on system frequency response (synthetic inertia below the rated wind speed): high-inertia (top) and low-inertia (bottom).
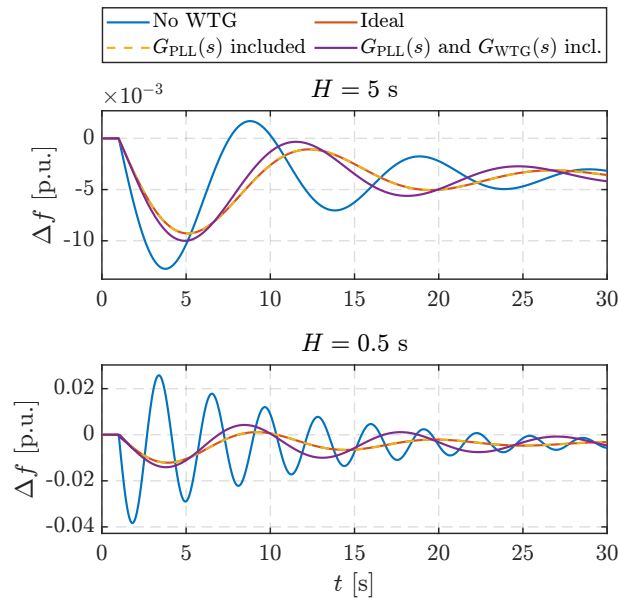
Figure 6.26: Impact of WTG modelling on system frequency response (synthetic inertia above the rated wind speed): high-inertia (top) and low-inertia (bottom).
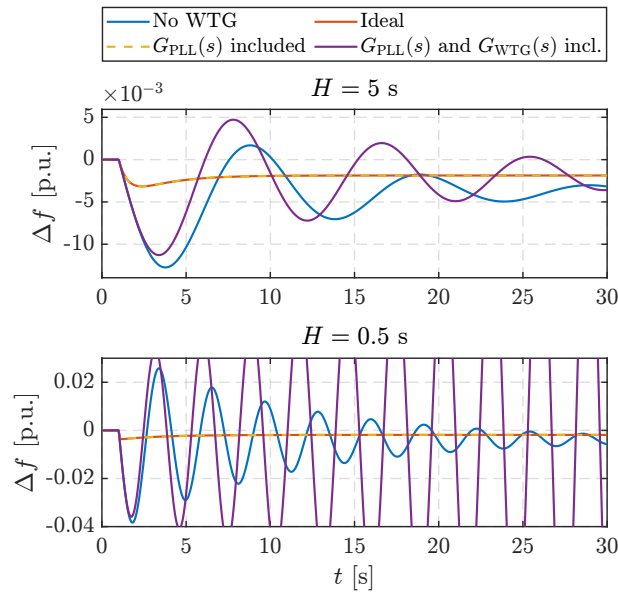
Figure 6.27: Impact of WTG modelling on the system frequency response (droop control below the rated wind speed): high-inertia (top) and low-inertia (bottom).
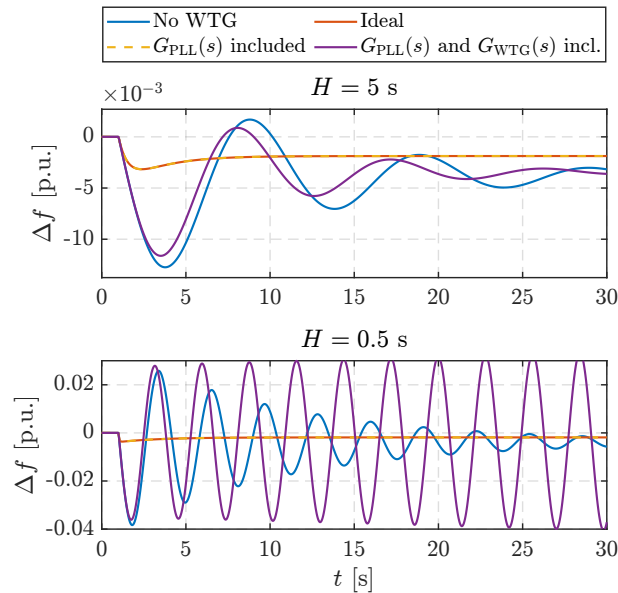
Figure 6.28: Impact of WTG modelling on the system frequency response (droop control above the rated wind speed): high-inertia (top) and low-inertia (bottom).

6.2.7 Effect of converter control approach

In this section we shall briefly discuss the effect of 5 different converter control approaches analysed in this thesis: two grid-following approaches (DCVC on device-side and DCVC on grid-side) and three grid-forming approaches (PQ-VSM, indirect matching and ViSynC).

First, we compare the two grid-following approaches providing droop only ($H_v = 0$) for which the system is described by (6.17). In the case of DCVC implementation on the DSC, $G_{\text{GFL}}(s)$ is described by (3.28), otherwise by (3.31). K_p^{DC} and K_i^{DC} are tuned to achieve damping $\zeta = \sqrt{2}/2$ and bandwidth 1/5 of the current loop bandwidth $1/T$. In both approaches, $D = 0$, $T = 0.005$ s, $R = 0.05$ p.u. and the PLL bandwidth is 5 Hz with damping $\zeta = \sqrt{2}/2$. Fig. 6.29 shows that both approaches behave identically in a high-inertia scenario, while in the low-inertia scenario, the grid-side DCVC has visible (but well-damped) oscillations due to higher-order behaviour. Depending on the combination of system and converter parameters, they may behave identically or one may show instability over the other (usually DCVC due to more complex dynamics). This is illustrated in Fig. 6.30 in which the GSC DCVC is unstable in the low-inertia scenario with inertia emulation alongside droop ($H_v = 3$ s, $T_f = 0.01$ s).
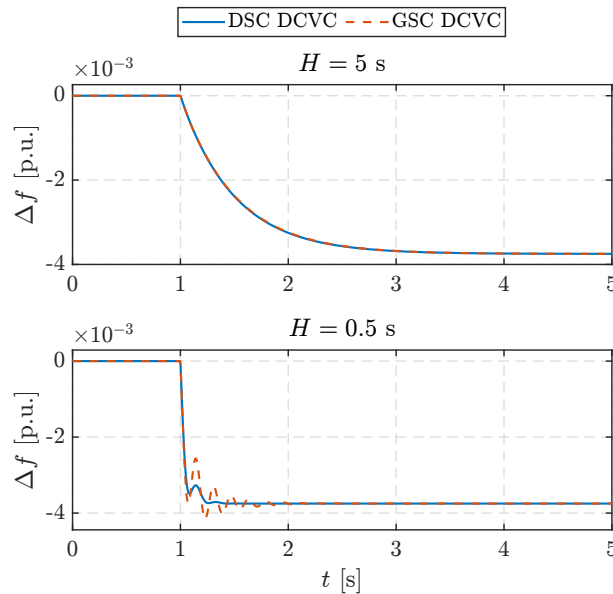
Figure 6.29: Impact of the grid-following converter control approach on system frequency dynamics (only droop): high-inertia (top) and low-inertia (bottom).

The three grid-forming schemes can theoretically behave identically as follows: if PQ-VSM is defined by H and R with $K_D = 0$ (6.1), then the indirect matching scheme can be tuned to achieve the same inertia and droop through (4.80). ViSynC cannot operate standalone, as per definition it does not provide any droop control, i.e., it requires another unit for power balancing or an existence of an external network. To achieve the same frequency dynamics with ViSynC, the power disturbance must be temporary with dynamics $\Delta p_d(s) = \Delta p_d \frac{s}{s+K_T}$ resulting in $\Delta p_d^\infty = \Delta p_d(t \to \infty) = 0$. Then $2Hs + R^{-1} = H_{\text{ViSynC}} \omega_b^{-1} C_{\text{DC}} s + K_D \omega_b^{-1} C_{\text{DC}}$ per
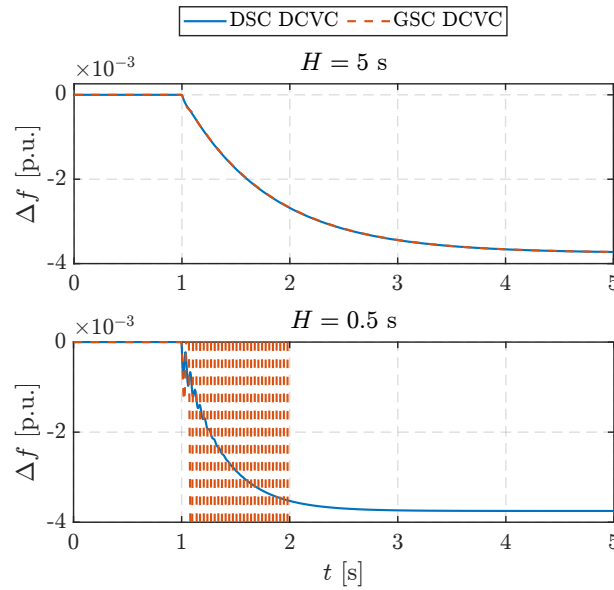
Figure 6.30: Impact of the grid-following converter control approach on system frequency dynamics (droop + virtual inertia): high-inertia (top) and low-inertia (bottom).

(4.87). Fig. 6.31 shows that even though identical frequency dynamics are achieved for the three control schemes, indirect matching and ViSynC results in a total DC voltage collapse. It also shows that the frequency collapses as well in the ViSynC scheme when the power disturbance is persistent $\Delta p_d^\infty = \Delta p_d$ since there is no power balancing mechanism on the device-side. On the other hand, PQ-VSM DC voltage is stable because it is governed by a dedicated DC voltage controller on the device-side, but it assumes an existence of a very fast dispatchable unit such as a battery.
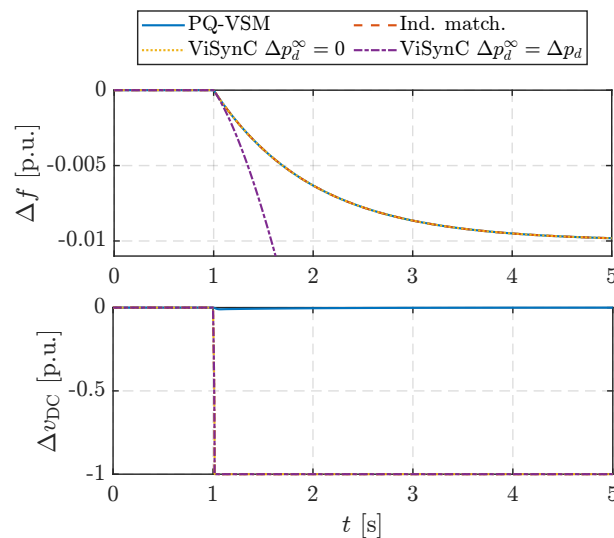
Figure 6.31: Comparison of grid-forming converter control schemes for equivalent frequency dynamics: frequency deviation (top) and DC voltage deviation (bottom).

Since indirect matching and ViSynC utilise DC link dynamics to emulate inertia, the converter gains would need to be extremely large to achieve the effective inertia constant of several

seconds, and there is simply not enough energy in DC link for that (Table 6.1). For indirect matching, $R_{\mathrm{DC}}^{-1} = 0.25\omega_b^{-1}C_{\mathrm{DC}}H^{-1} \approx 6.3 \cdot 10^3$ p.u. and $K_p^{\mathrm{DC}} \approx 0.0016$, i.e., the DC controller has to be very weak to achieve the desired droop, which needs to compensate for small value of capacitance. For ViSynC, $K_D \approx 6.3 \cdot 10^3$ p.u. and $H_{\mathrm{ViSynC}} \approx 3.1 \cdot 10^3$ s.

Since the stability of DC voltage is imperative for converter operation, we can instead try to limit the DC voltage deviation, which will constrain the virtual inertia parameters that we can use. If we limit the DC voltage deviation to 1%, then K_p^{DC} is defined first, resulting in $R_{\mathrm{DC}}^{-1} \approx 2$ p.u. and the effective inertia constant $0.25\omega_b^{-1}C_{\mathrm{DC}}R_{\mathrm{DC}}^{-1} \approx 0.0016$ s. In the case of ViSync, we need to assume it is connected to a stiff grid and that the electrical power out of the GSC behaves according to the power swing equation $V_1 V_2 X^{-1}\sin\delta$, where $\omega_b^{-1}\dot\delta = \delta\omega$. Then, $\Delta\omega(s)$ and Δv_{DC}^2 are defined by (6.20) and (6.21), respectively, where $K_\delta = V_1 V_2 X^{-1}\cos\delta_0$. Eq. (6.20) and (6.21) show that there will be zero frequency and voltage deviation in steady-state, while the transient dynamics are governed by the converter parameters. To comply with the small permissible voltage deviation, $H_{\mathrm{ViSynC}} \approx 1.6 \cdot 10^{-4}$s, $K_D = 320$ and $K_T = 4$.

$$\Delta f(s) = \Delta p_d(s)\frac{s^2 + K_T s}{\omega_b^{-1}C_{\mathrm{DC}}H_{\mathrm{ViSynC}}s^3 + 0.5\omega_b^{-1}C_{\mathrm{DC}}K_D s^2 + sK_\delta\omega_b + K_T K_\delta\omega_b} \qquad (6.20)$$

$$\Delta v_{\mathrm{DC}}^2(s) = \Delta p_d(s)\frac{2H_{\mathrm{ViSynC}}s^2 + K_D s}{\omega_b^{-1}C_{\mathrm{DC}}H_{\mathrm{ViSynC}}s^3 + 0.5\omega_b^{-1}C_{\mathrm{DC}}K_D s^2 + sK_\delta\omega_b + K_T K_\delta\omega_b} \qquad (6.21)$$

Fig. 6.32 shows the results for constrained DC voltage deviation. In both PQ-VSM and ViSynC, the DC voltage deviation diminishes in steady-state, while there is a steady-state deviation for the indirect matching control proportional to the frequency deviation. Once can see that by mapping inertia to DC link capacitance, one cannot achieve a conventional value of the inertia constant, i.e., the system inertia becomes very small (in the order of milliseconds) which in turn causes a high instantaneous RoCoF. These issues were discussed in Section 6.2.3. ViSynC control shows a sharp and large temporary internal frequency deviation of 0.2 p.u. before returning back to the grid frequency value (right y-axis in Fig. 6.32). ViSynC control, as shown here as well as in Chapter 4, is not suitable for standalone operation as it has no power balancing mechanism. It can be used to emulate inertia to a certain extent, but its contribution is limited since it maps the frequency dynamics to limited DC link energy.
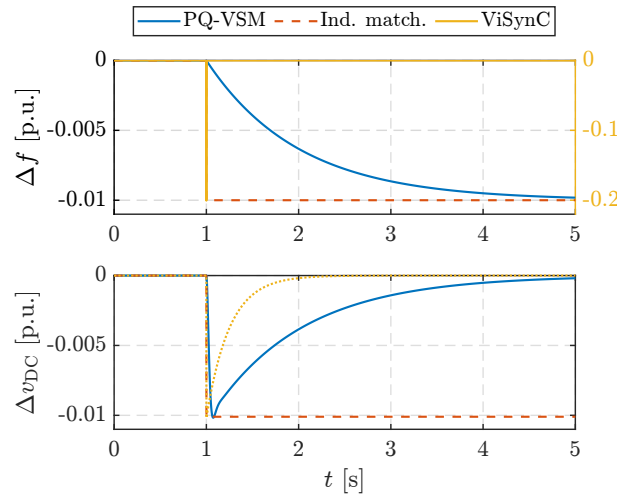
Figure 6.32: Comparison of the grid-forming converter control approach for limited DC voltage deviation: frequency deviation (top) and DC voltage deviation (bottom).

6.3 Summary

We presented a unified SFR model of a low-inertia power system based on analysis in chapters 3–5. It considers relevant synchronous and induction machine dynamics, PSS dynamics, generic grid-following and grid-forming converter dynamics, and variable-speed WTG dynamics as a special case of a grid-following device. The SFR model is far from comprehensive since it does not take into account the specific dynamic behaviour of other devices such as solar PV, grid-forming turbines, energy storage, etc. The key points of each of the sub-blocks above were summarised.

Using the developed SFR model, several studies on the characteristics of frequency dynamics of low-inertia systems were conducted. The difference between physical inertia and virtual (grid-forming) inertia was defined. It was shown that for sufficient discretisation steps, grid-forming inertia is indiscernible from physical inertia for practical intents and purposes. However, terminal power measuring and filtering bandwidth may have an impact that requires further scrutiny.

After we quantified inertia from various sources and described the analogy between rotational inertia (turbine-generators) and electromagnetic inertia (power electronic converters), the importance of inertia was discussed. It was shown that reduced inertia is not necessarily important from a small-signal stability perspective since its reduction increases damping of electromechanical modes. The issue, however, is the increase of RoCoF which can trigger protective relays. Here, the sliding window for RoCoF estimation has an important role. Increasing the sliding window will reduce the estimated average as individual device electrical speeds converge to a uniform value. If equipment can temporarily withstand high RoCoF, then the requirements can be relaxed and the effect of reduced inertia should not be substantial. The main point is that the effect of reduced inertia can be compensated by a small system time con-

stant (many fast-acting devices) in terms of frequency containment. The initial RoCoF value cannot be reduced by anything other than inertia; however, the small time constant will make sure that the initial RoCoF transient diminishes quickly. Therefore, the equipment in extremely low inertia systems should withstand high RoCoF only in the first several hundred milliseconds after a large disturbance. Nevertheless, decreased inertia results in higher frequency oscillations which may induce other resonances in the system which are beyond the applicability of this model.

Then, it was shown how the combination of PLL bandwidth, droop and reduced inertia can cause frequency instability, so these instability regions were calculated for some combinations of parameters. Furthermore, the impact of the PLL bandwidth and additional filtering on system RoCoF was analysed. It was shown that the effect of grid-following inertia emulation cannot replace synchronous inertia during the initial transient state due to inherent time lag in frequency estimation.

It was shown that lumping load self-regulation in the *D* constant gives conservative results. In reality, induction machines will provide more help in arresting frequency deviations and RoCoF. However, since most industrial drives today are grid-interfaced via frequency converters, these effects are not as relevant today and in the future. Controlling the converters of these drives to support the grid frequency will be necessary in the future which means that the presented conclusions on different converter dynamics apply.

On the one hand, it was illustrated how grid-following WTG dynamics can both improve system frequency response in high-inertia conditions and destabilise the frequency in low-inertia conditions depending on the operating point.

Finally, the five analysed converter control modes were compared (two grid-following and three grid-forming). In terms of grid-following devices, the DC voltage controller on the grid-side converter can result in less-damped behaviour or even instability in low inertia conditions due to additional second-order dynamics in the feedback loop. In terms of grid-forming control, emulating a high-inertia device in the grid-side converter requires a very fast DC voltage controller, as well as a fast-acting energy source this controller regulates. Moreover, matching virtual inertia to the DC link energy in the other two grid-forming designs inherently means that the effective inertia constant is extremely low, which substantially increases the initial RoCoF. Setting very large virtual inertia constants is not feasible in these schemes because it will result in a DC voltage collapse and consequently converter failure.

Chapter 7

Modelling and control of supercapacitor banks for power system dynamic studies

In this chapter, an adequate model fidelity of a supercapacitor/ultracapacitor bank for RMS simulations will be derived and discussed. The idiosyncrasy of a supercapacitor is that its capacitance is voltage-dependent, which also has an impact on the stored energy. This may have consequences for the provision of virtual inertia or fast frequency control services, as the amount of stored energy is in the order of several seconds up to a minute. The content of this chapter is based on [68–72].

7.1 Modelling of supercapacitor banks for power system applications

7.1.1 Supercapacitor theory

The core of the SC bank model is the SC cell. An overview of different SC models can be found in [251] while the state-of-the-art SC models are available in [66, 251, 252]. Basically, all these models are based on RC circuit identification using impedance spectroscopy. They can be described with the same type of RC circuit consisting of three parallel sections, as shown in Fig. 7.1. The first branch {M1} models fast dynamics, parallel branches {M2} model slower recombination phenomena after a fast charge or discharge and the third branch {M3} models the long-term self-discharge phenomena [66].

The time constants of the RC circuits in the parallel branches (ranging from a minute or several minutes up to an arbitrary amount of time as reported in [66, 251]) are much longer than the timescale investigated in this paper (up to around 30 s), hence they can be neglected in SC models developed here, as will be shown in section 7.1.2.

The important characteristics of SCs for model development can be summarised as follows:

i) the majority of the ultracapacitor capacitance comes from C_{sc}; ii) series combination of parallel branches $R_1^s C_1^s$–$R_n^s C_n^s$ is actually an infinite series of these parallel groups. However, it has been shown in [66] that five groups are sufficient to obtain an accurate model; iii) capacitance C_{sc} as well as infinite sum elements R_k^s, C_k^s are dependent on the ultracapacitor voltage $u_C(t)$. This dependence is nonlinear, hence the model has the time-varying parameters. That is why an ideal capacitor representation used in many papers in the past is not always appropriate; iv) the number of parallel branches in the {M2} group is also theoretically infinite, though it has been shown that between two and four branches are sufficient to achieve accurate results [66].

In order to simplify the model further, the following assumptions are made: i) R_s is the equivalent series, voltage dependent resistance (ESR) determined at very high frequency [66]. Considering that R_s is small (< 10 mΩ) and its impact on the model performance is insignificant, it is typically considered to be constant; ii) temperature dependence of the parameters is neglected, i.e., the temperature is considered to be constant. The assumption is that the cooling of the system is adequate and that the system operates at room temperature. Although this effect can be included in the model, it was considered that, for the initial derivation of the model for power system dynamic studies, the temperature can be considered to be constant.

The parameters of the first branch are calculated according to (7.1)–(7.3) [66].

$$C_{sc}(u_C) = C_0 + k_v u_C(t) \tag{7.1}$$

$$C_k^s = \frac{1}{2} C_{sc}, \quad k \in \{1...n\} \tag{7.2}$$

$$R_k^s = \frac{2\tau(u_C)}{k^2 \pi^2 C_{sc}} \tag{7.3}$$

C_0 is the ultracapacitor capacitance at 0 V and k_v is a constant expressed in F/V. $\tau(u_C)$ is another experimentally determined parameter (it has a dimension of time) that can be expressed as a function changing linearly with the voltage u_C: $\tau(u_C) = \tau_0 + k_\tau u_C(t)$ [66]. However, it can also be approximated by (7.4) [66]:

$$\tau(u_C) \approx 3 C_{sc}(R_{dc} - R_s), \tag{7.4}$$

where R_{dc} is the resistance experimentally obtained at very low frequencies (essentially DC). Naturally, $R_{dc} > R_s$.

All the parameters of the {M1} branch can be identified using manufacturer's data sheet.

However, parameters of the branches M2 and M3 are more difficult to obtain since they must be obtained experimentally. Furthermore, these parameters are not universal and they depend on the time scale of the phenomena to be observed (described by the RC time constant $\tau_{RC} = RC$). The time scales are arbitrary, however they usually imply a range from several
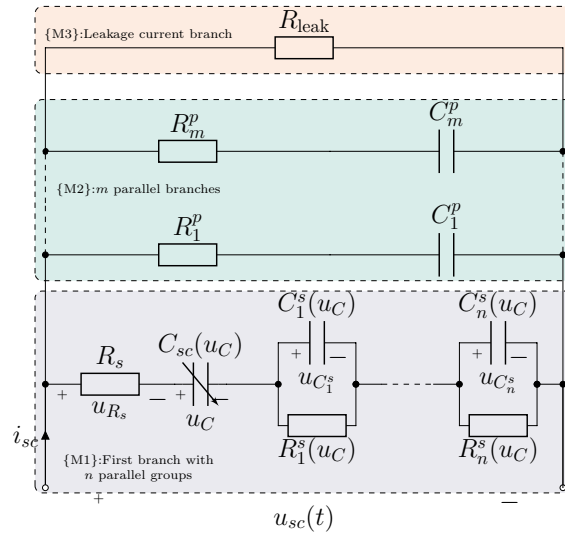
Figure 7.1: Detailed RC circuit of a supercapacitor cell.

minutes to several weeks or even longer [66, 251].

7.1.2 Simplification of the supercapacitor cell model

This section shows that the SC model for power system dynamics studies can be simplified and described by only the {M1} branch and with at least one parallel group $R_k^s C_k^s$. The experimental data from [66, 251] are used to develop dedicated models in Matlab/Simulink and used in simulations for model simplification. The simulation results are related to two commercial SCs (Epcos 110 F and Maxwell 140) represented by different models with varying levels of detail to validate model simplification.

Different model responses are produced in MATLAB-Simulink using the *Simscape Electrical* toolbox. The number of branches in {M2} and {M3} groups is being sequentially reduced and the different model responses to the charge/discharge test are compared. Input to the model is the current $i_{sc}(t)$ and output of the model is the SC terminal voltage $u_{sc}(t)$. Results are shown in Fig. 7.2. For clarification, the 6 branch model represents the total number of branches (first branch {M1}, 4 parallel branches {M2} and a self-discharge branch {M3}). Results for both SCs with different levels of detail (Fig. 7.2 middle and Fig. 7.2 bottom) show that the branches {M2} and {M3} do not have an impact on the model accuracy for the time scale of interest. Therefore, all the branches except the first branch can be neglected.

In the next step, the adequate number of parallel RC groups in the first branch is determined. Results obtained for the Maxwell 140 model are shown in Fig 7.3 (top). The significance of parallel RC groups depends on the difference between R_{dc} and R_s. If those resistances are very close together (e.g., $< 1\text{m}\Omega$ as in Epcos model) then the impact on the accuracy is negligible. However, if the difference between R_{dc} and R_s is larger (e.g. $> 2\text{m}\Omega$ as in Maxwell 140 model) then the accuracy is significantly impacted, which is important from both the available energy
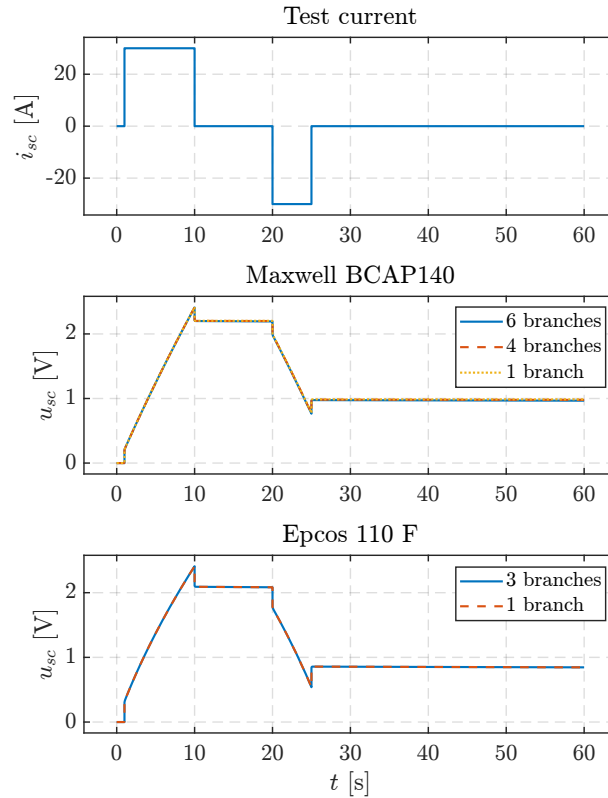
Figure 7.2: Comparison of the supercapacitor model response for different number of branches: test current (top), Maxwell BCAP140 cell voltage (middle) and Epcos 100 F cell voltage (bottom).

perspective and control perspective. The mean absolute percentage error for the Maxwell model with different numbers of groups is shown in Table 7.1. Since R_{dc} and R_s in reality depend on the cell in question, it can be conservatively concluded that at least one parallel group should be included: both R_s and the parallel RC groups will cause voltage drops and energy losses in the circuit, thus should be included. Since the only voltage that can be measured is the one across the supercapacitor terminals (u_{sc}), R_s and parallel RC groups will impact both the estimation of SoC and the DC voltage dynamics which determine the operating range of the supercapacitor module.

Table 7.1: Accuracy of the supercapacitor model (Maxwell) with different numbers of parallel RC groups in the first branch.

Number of RC groups	Mean absolute percentage error [%]	
	Voltage	Energy
1 (relative to 5 group model)	2.6	6.5
0 (relative to 5 group model)	6.7	12.9
0 (relative to 1 group model)	4.3	10.3

Fig. 7.3 (bottom) compares the voltage response between the ideal capacitor and the non-
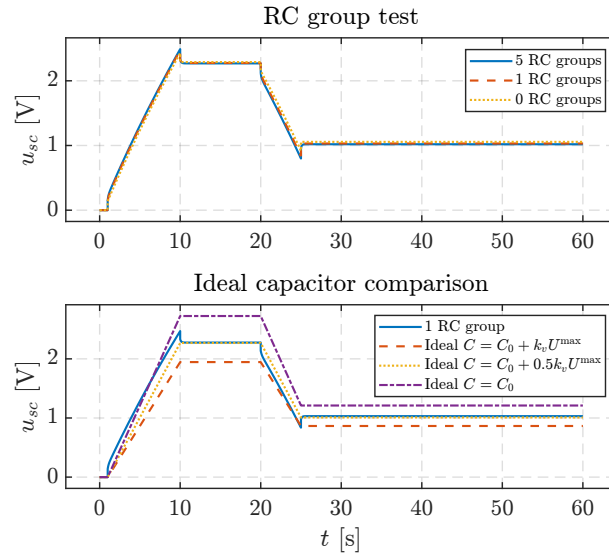
Figure 7.3: Maxwel BCAP0140 model response: voltage response to different numbers of RC groups (top), voltage response compared to ideal capacitor (bottom).

linear model with 1 RC group. The closest voltage profile was obtained when the capacitance of the ideal capacitor was set to the SC capacitance at half the rated voltage. Nevertheless, the ideal representation will not reflect the voltage transient effect due to the ESR which occurs when the charging or discharging current is discontinued. This voltage transient is important from the control perspective because it impacts the logic that enables or disables the charging/discharging based on state-of-voltage. More importantly, Fig. 7.4 shows the difference between stored energy in a nonlinear model and in the ideal capacitor. Using capacitance at rated voltage is overly optimistic regarding the stored energy for the same applied voltage, while using capacitance at 0 V is closest to the nonlinear model (mean absolute percentage error in energy for the operating points between 0.5 V and 2.5 V is 27%). This overestimation of the charge of the ideal ultracapacitor is coming from i) Different initial stored energy in the steady-state (capacitance of the ideal capacitor is constant while the real capacitor has a constant and variable, i.e., proportional to voltage, component); ii) Different rate of discharge because of the variable capacitance; iii) Internal losses due to equivalent series resistance and the parallel RC groups of the first branch in Fig. 7.1.
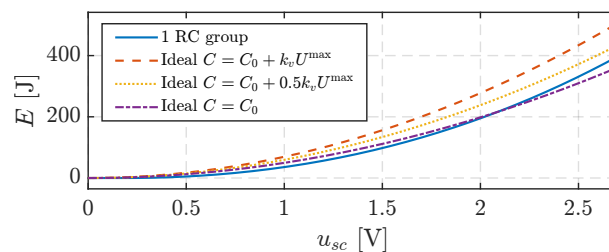
Figure 7.4: Energy stored in a supercapacitor with respect to voltage (Maxwel BCAP0140 model).

7.1.3 Building a supercapacitor bank model

In section 7.1.2 it was shown that the SC dynamics can be accurately represented using first branch only {M1} with at least one parallel RC group. To build a capacitor bank of a higher power rating, a certain number of cells n_s can be connected in series to form a string and a certain number of strings n_p can be connected in parallel to form a module. Modules can then be connected in parallel to form a bank. Assuming completely identical cells, it is easily shown using Kirchoff's voltage and current laws that the voltage of the string u_{sc}^s and the current of the module i_{sc}^m are equal to (7.5) and (7.6), respectively.

$$u_{sc}^s(t) = n_s u_{sc}(t) \tag{7.5}$$

$$i_{sc}^m(t) = n_p i_{sc}(t) \tag{7.6}$$

The assumption of identical and balanced cells is reasonable for bulk power system simulations, otherwise the modelling would have to be done on an electronic component level. Commercial solutions always have some sort of cell balancing system implemented to keep the cell usage and aging uniform. Cell aging is reflected in the change of parameters, so that can be accounted for if the parameters of an older system are known.

Finally, the dynamic model of the bank can be built using circuit analysis in the time domain for the first branch only by setting $u_{sc}(t)$ as an output $y(t)$, $i_{sc}(t)$ as an input $u(t)$. Capacitor voltages are chosen as state variables. A complete nonlinear model of the SC bank in the analytic form is described by (7.7)–(7.12) and shown in Fig. 7.5, where R_k^s and C_k^s are defined by (7.2) and (7.3), respectively.

$$u_{sc}(t) = i_{sc}(t)R_s + u_C(t) + \sum_{k=1}^{n} u_{C_k^s} = y(t) \tag{7.7}$$

$$i_{sc}(t) = u(t) \tag{7.8}$$

$$u_{sc}^s(t) = n_s u_{sc}(t) = n_s y(t) \tag{7.9}$$

$$i_{sc}^m(t) = n_p i_{sc}(t) = n_p u(t) \tag{7.10}$$

$$\frac{du_C}{dt} = \frac{i_{sc}(t)}{C_0 + k_v u_C(t)} \tag{7.11}$$

$$\frac{du_{C_k^s}}{dt} = -\frac{u_{C_k^s}}{R_k^s C_k^s} + \frac{i_{sc}(t)}{C_k^s} \tag{7.12}$$

Note that (7.11)–(7.12) assumes the relation $dQ = C_{sc} \cdot du_C$ per [251] instead of $Q = C_{sc} \cdot u_C$. This is an alternative definition of capacitance for voltage-dependent capacitors [253]. Nevertheless, in both definitions the expression for capacitance in the denominator of (7.11)–(7.12) remains linearly proportional to voltage, only differing in the magnitude of k_v. The behaviour remains the same and the capacitance is varied by varying k_v in the case studies
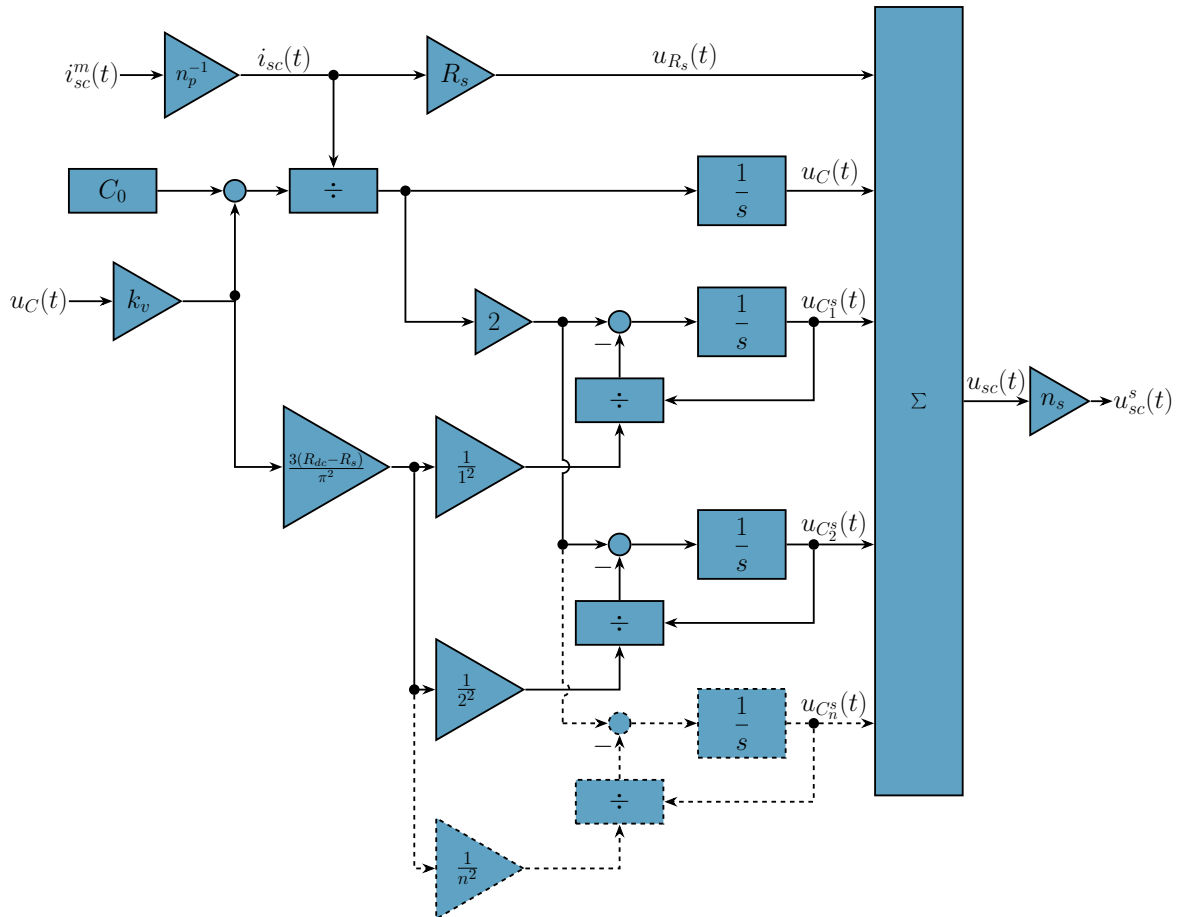
Figure 7.5: Block diagram of the nonlinear supercapacitor module model.

presented here.

SC cells are very low voltage devices (rated voltage up to 2.5–3 V) and they have to be scaled up to form a bank of grid-scale power rating, e.g., 1 MW to 100 MW. The number of cells necessary to form a grid-scale SC bank is in the order of 10^3 for a 1 MW bank, and up to 10^5 for the 100 MW scale. Table 7.2 shows an example of the supercapacitor bank system sizing for providing the rated power for 15 s [254].

7.1.4 Supercapacitor control system

The complete control system consists of inverter PQ control, charge/discharge control, DC current calculation and frequency control loop. The block diagram of the complete SC bank energy storage system is shown in Fig. 7.6. p and q are the active and reactive power injected or absorbed by the inverter to or from the grid, while $\star$ denotes a set-point value. v_{ac}^{grid} is the AC voltage of the bus the inverter is connected to. i_d and i_q are the direct and quadrature axis currents of the inverter. The inverter is controlled in the grid voltage reference frame in which the grid voltage phase is estimated by the PLL (model version 3 in PowerFactory). The PLL also estimates the system frequency for the frequency control block. The DC current calculation

Table 7.2: Sizing of supercapacitor bank.

Bank size [MW]	DC voltage range [V]	Max. cont. current (single string) [A]	Rated cell voltage [V]	# of series cells (string)	# of parallel strings	Cell capacitance [F]
1	250–500	200	2.5	200	20	1920
10	250–500	200	2.5	200	200	1920
100	500–1000	312.5	2.5	400	640	3000

block calculates the SC current for charging or discharging. It should be noted that the presented SC control system is similar to a battery control system [255] since the requirements are the same (constant power output). The difference from the other control schemes however, is that the voltage measurement is directly used as a measure of energy (State-of-Voltage, SoV) rather than State-of-Charge (SoC) through current integration, since the energy of a capacitor is directly proportional to the voltage. Furthermore, capacitors are much more sensitive to applied voltage, which varies significantly more than in batteries. Therefore, special care must be taken not to overcharge the SC, since even the voltage, which is only 5% above the rated voltage, can damage the cell. Similarly, the SC should not overly discharge because of current limitations for constant power. The individual controller blocks are further elaborated in the following subsections.
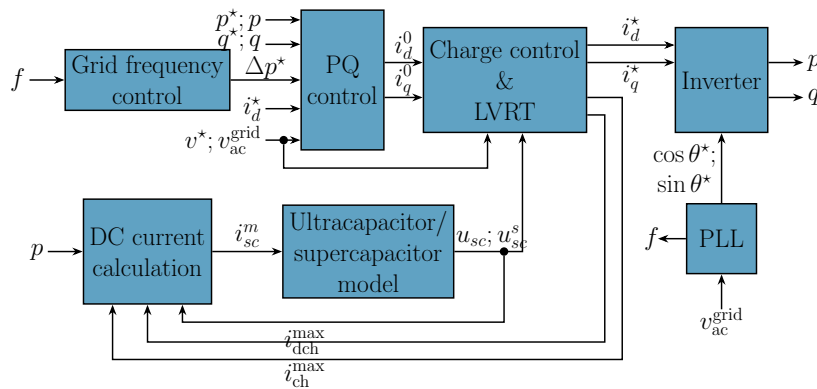
Figure 7.6: Complete model of the supercapacitor bank system.

7.1.4.1 Charge control

Fig. 7.7 shows the structure of this block. The State-of-Voltage (SoV) measurement is used to control the charging and discharging process. Charging is stopped if the SC bank is charged to nominal voltage, while discharging is stopped when the SC voltage falls below a user defined

low voltage threshold. Charging/discharging is enabled again when the voltage reaches a user defined minimum voltage level for charging/discharging. The input to the block are the d and q axis currents i_d^0 and i_q^0 from the PQ control, while the final inverter current set-points $i_d^\star$ and $i_q^\star *$ are determined by this block. Simple low-voltage ride through logic and current limitation are also implemented in this block. They are not shown here since they are available in many papers, e.g. [57, 179, 255].
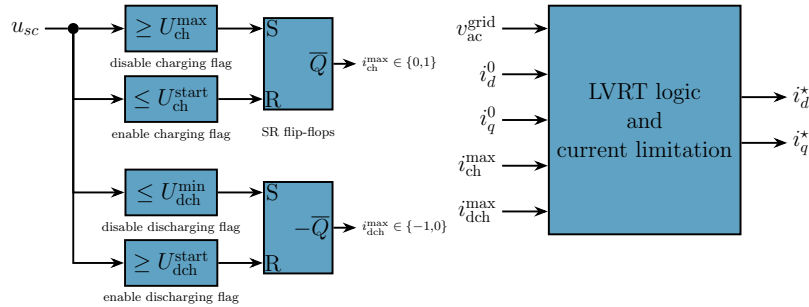
Figure 7.7: Charge control, LVRT and current limitation block.

7.1.4.2 DC current calculation

The input to the SC model is the current, however in power system applications the power is usually controlled and not the current. This block calculates the charging or discharging DC current based on the actual inverter power output. A block diagram of this subsystem is shown in Fig. 7.8. It should be noted that this module as well as the SC model works with SI units, while other subsystems work in p.u. I_{ch}^{max} and I_{dch}^{max} are the maximum single cell charging and discharging current in A (e.g. ± 100 A).
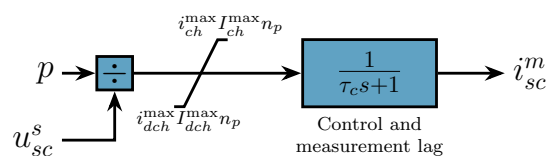
Figure 7.8: DC current calculation block.

7.1.5 PQ control

Fig. 7.9 shows the PQ control structure of the SC bank inverter. In this case, the inverter is modelled as a controlled current source and the d and q axis currents are obtained from the active and reactive power control error, respectively. Measurement/control lag is also included in this block diagram. The term $i_d^\star - i_d^0$ is a compensation term for active power during low-voltage ride through, when the active power should be low and reactive power high. The reactive power or terminal voltage control can be both chosen. However, if the reactive power control

is chosen it will be overridden by terminal voltage control during low-voltage ride through. A simplified structure of the converter and its control applicable for electromechanical transient simulations of large networks (integration step size 1–10 ms), which neglects fast inner current control loops and AC-side filter/grid dynamics, was used in this study [179]. Other or more detailed models could be used for different studies, e.g., EMT, single-machine infinite bus or smaller systems [58, 60, 63].
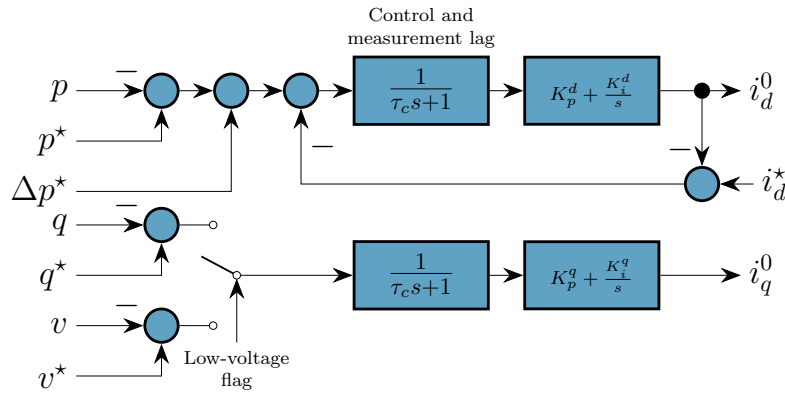
Figure 7.9: Supercapacitor bank inverter PQ control.

7.1.6 Grid frequency control

This block is shown in Fig. 7.10. The input to this block is the grid frequency signal estimated by the PLL and the output is the requested change in power. The type of implemented algorithm for frequency response can be arbitrary. However, based on the SC characteristics, in this study two control loops are used. The bottom loop is a standard virtual inertial response with a washout filter to make the output signal smoother, since the time derivative operation inherently amplifies noise. The upper loop is more akin to a standard droop control, but it also has a washout filter which means this contribution will diminish in steady-state, hence the name *quasi-droop*.

The reasoning for this choice is the following: the SC does not have a lot of stored energy—if the standard droop control is employed then the SC output power is initially proportional to the frequency deviation. However, once the SC is discharged, the output power will fall to zero which will cause a bigger secondary frequency drop. By setting a large washout filter time constant, the output power will slowly diminish while the conventional units pick up. Therefore, the difference between the inertia control loop and quasi-droop control loop is in the washout filter time constant ($\tau_w^d \gg \tau_w^i$).
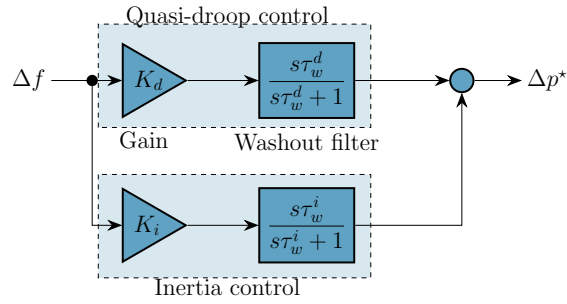
Figure 7.10: Supercapacitor bank grid frequency control module.

7.1.7 Simulation and results

The performance of the proposed model is implemented and tested on a standard IEEE 14-bus test system included in DIgSILENT PowerFactory (Fig. 7.11). Two scenarios are tested: loss of generating unit and low-voltage ride through event. Results obtained with the ideal model and the proposed nonlinear model are compared for different capacitor sizes and initial conditions. A 100 MW SC bank is connected to bus 06. Parameters of the SC bank system are given in the Appendix.
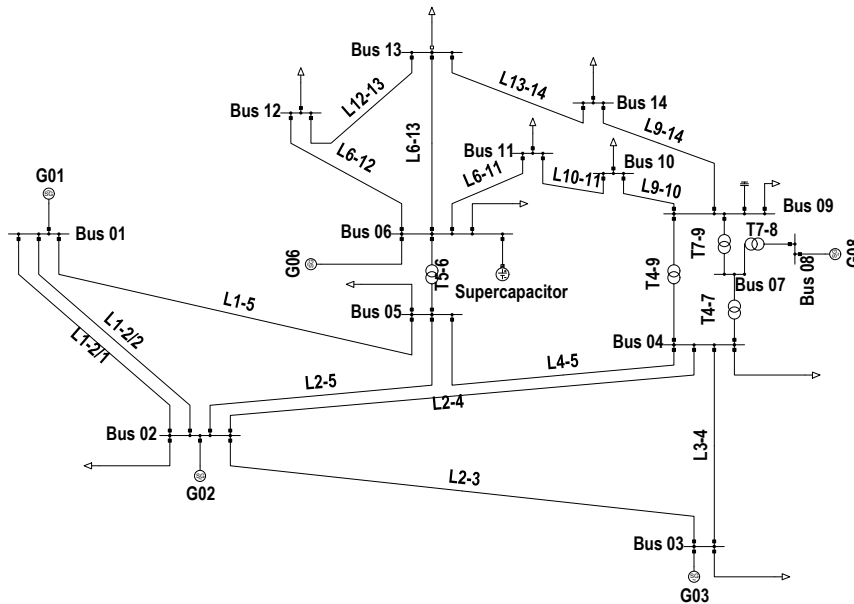
Figure 7.11: IEEE 14-bus test system.

An actual supercapacitor system was not available for validation hence experimentally validated models were used for the validation of model reduction. There is no complete control system model of SC in the open literature that can be easily reproduced in system studies. The model proposed here is modular and generic enough to be implemented in standard power system simulation software or modified if necessary. It can adequately capture the relevant SC

dynamics as the modelled SC control is generic/flexible with the capacitor model based on past experimentally validated results [66, 251].

7.1.7.1   Loss of generating unit

Two cases are analysed to trigger an underfrequency event: i) at $t = 1$ s, generator G02 delivering 95 MW is disconnected; ii) at $t = 1$ s, generator G02 delivering 190 MW is disconnected. The performance of the ideal model is compared to the performance of the nonlinear model. There are several parameters which may affect the performance of both models: initial capacitor voltage, ideal capacitor capacitance, and how much the SC capacitance varies with voltage (i.e., ratio of capacitance at 0 V to capacitance at rated voltage). The SC bank size is 100 MW. Characteristics of the system frequency response were observed and results for VIR control and quasi-droop control for the 95 MW disturbance are shown separately in Fig. 7.12 and Fig. 7.13, respectively (shown separately because parameters of quasi-droop control impact the frequency response differently; nonetheless, the two control loops can be used simultaneously as shown in Fig. 7.10).

There is no significant difference in the frequency nadir between using the ideal and nonlinear model for a range of initial SC voltage values and capacitance models (Fig. 7.12a–7.12c, 7.13a–7.13b); however, the actual range depends on the size of the disturbance and control system parameters. Table 7.3 shows the operating range in terms of SoC in which the ideal model does not adequately represent the nonlinear model (inaccurate range) meaning that the range in which the ideal model is indeed adequate (accurate range) is complementary to the shown range. The criterion for selection of the inaccurate range is the relative error between the nonlinear and ideal model for maximum frequency deviation (if this error is $> 5\%$, then the ideal model does not adequately represent the nonlinear model). In Table 7.3, the best ideal model is highlighted by a shaded cell. Generally, for the same size of SC bank, the ideal model is accurate in a wider range for a smaller disturbance, and in a narrower range for a larger disturbance. Furthermore, smaller gain and a longer washout time constant of the quasi-droop control increase the accurate range of the ideal model. In all cases, the inaccurate range is wider for a larger capacitance of ideal model, although the values obtained with quasi-droop control are not as sensitive to the value of capacitance of the ideal model.

For a smaller disturbance, the inaccurate range is between 20% and 50% SoC for VIR control and between 20% and 30% for quasi-droop control, meaning that the ideal model inaccurately represents the nonlinear model for low to medium SoC. When the disturbance exceeds the size of the SC, the inaccurate range is between 25% and 70% for VIR, although this range can be shifted to the higher SoC range if the variable part of SC capacitance is bigger (e.g., 71% to 85% SoC for 25% variable capacitance and 70% to 90% SoC for 40% variable capacitance). The inaccurate range for quasi-droop control is between 20% and 40% SoC. Note that for both

(a) $C_{sc} = 900 + 40u_C$; $C_0/C_{max} = 0.9$

(b) $C_{sc} = 750 + 90u_C$; $C_0/C_{max} = 0.75$

(c) $C_{sc} = 600 + 150u_C$; $C_0/C_{max} = 0.6$

(d) Average RoCoF for $C_{sc} = 600 + 150u_C$
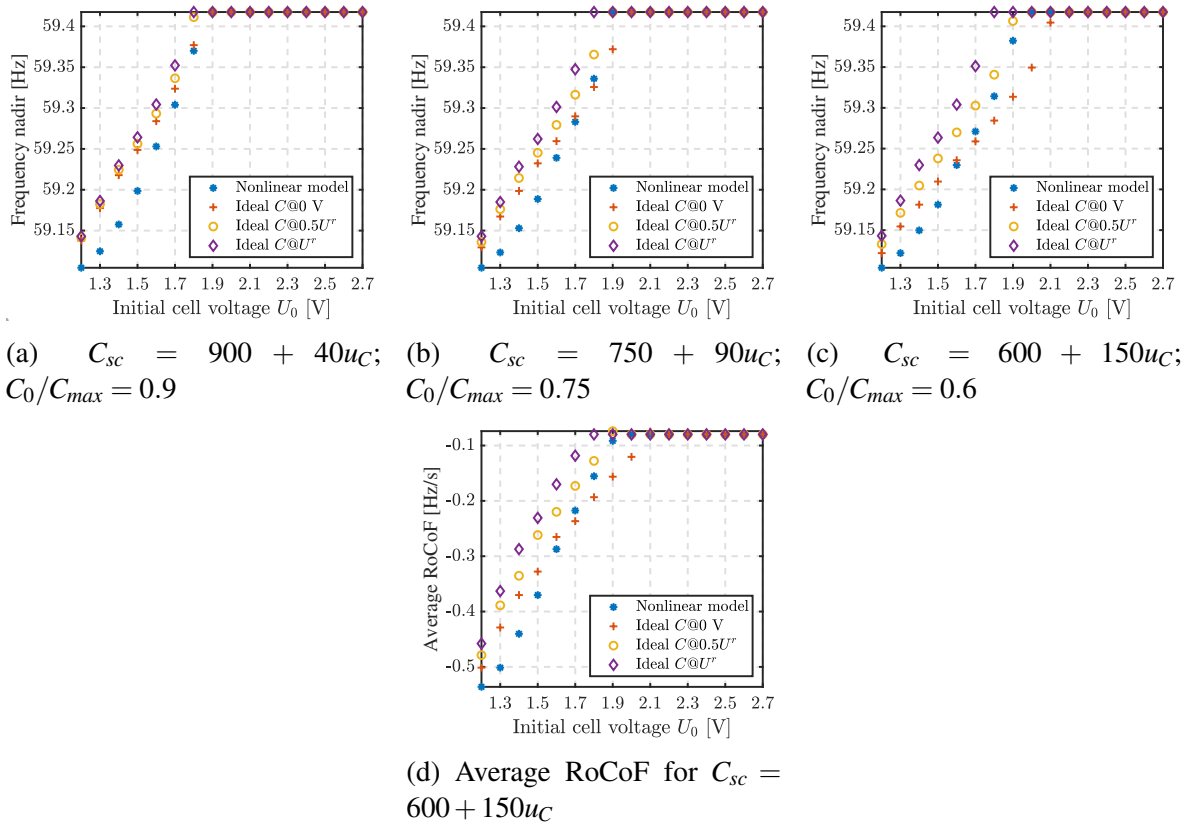
Figure 7.12: Frequency nadir with different supercapacitor models for virtual inertial response control.

(a) $C_{sc} = 900 + 40u_C$; $C_0/C_{max} = 0.9$

(b) $C_{sc} = 600 + 150u_C$; $C_0/C_{max} = 0.6$

(c) $C_{sc} = 900 + 40u_C$; $C_0/C_{max} = 0.9$

(d) $C_{sc} = 600 + 150u_C$; $C_0/C_{max} = 0.6$
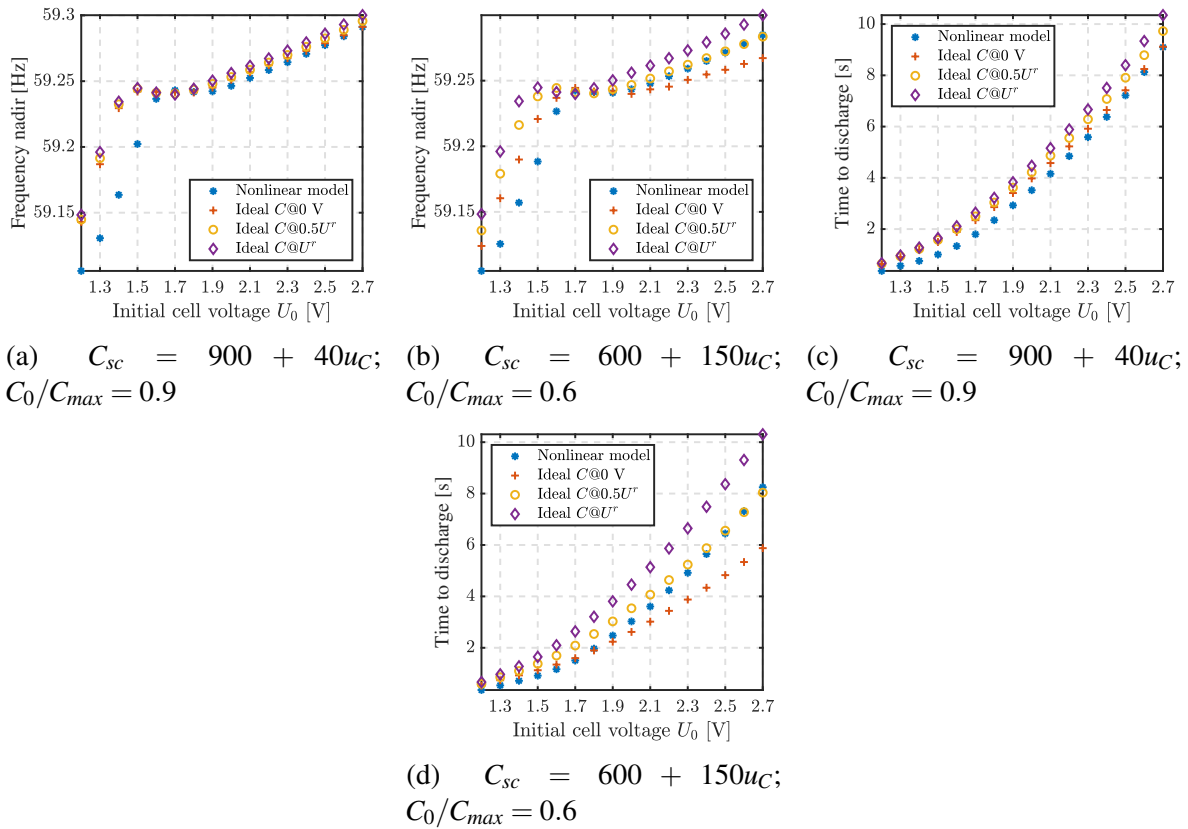
Figure 7.13: Frequency nadir and time to discharge with different supercapacitor models for quasi-droop control.

Table 7.3: Operating range (SoC) in which the ideal model does not describe the nonlinear model accurately with respect to the maximum frequency deviation ($> \pm 5\%$ error); the narrower range is better.

Designed operating range: 1.1 V – 2.7 V (40%–100% $U_r \sim$ 15%–100% SoC)						
Disturbance size: 95 MW						
Model	VIR control			Quasi-droop control		
	$C@0$ V	$C@0.5U_r$	$C@U_r$	$C@0$ V	$C@0.5U_r$	$C@U_r$
$C_0/C_{max} = 0.9$	22%–30%	22%–43%	22%–43%	22%–30%	22%–30%	22%–30%
$C_0/C_{max} = 0.75$	21%–28%	21%–33%	21%–42%	21%–28%	21%–28%	21%–28%
$C_0/C_{max} = 0.6$	40%–50%	20%–35%	20%–45%	-	20%–27%	16%–27%
Disturbance size: 190 MW						
Model	VIR control			Quasi-droop control		
	$C@0$ V	$C@0.5U_r$	$C@U_r$	$C@0$ V	$C@0.5U_r$	$C@U_r$
$C_0/C_{max} = 0.9$	26%–43%	26%–48%	26%–66%	26%–39%	21%–39%	21%–39%
$C_0/C_{max} = 0.75$	71%–85%	25%–47%	25%–71%	-	25%–42%	21%–42%
$C_0/C_{max} = 0.6$	70%–90%	23%–45%	23%–70%	-	23%–40%	20%–40%

disturbance sizes, there are empty cells in the table which mean that the ideal model in those cases accurately represents the nonlinear model for the whole operating range. One must keep in mind that the results are shown for an underfrequency event—for an overfrequency event the observed behaviour is complementary, i.e., the inaccurate range is in higher SoC because the capacitor is charging in that case and is limited by the maximum voltage.

Fig.7.12d shows the average RoCoF for the SC with 40% variable capacitance. It can be seen that the RoCoF increases with lower SoC because the SC bank will not be able to deliver the requested power before reaching the minimum SoV. The RoCoF plots correspond to the frequency nadir plot (e.g., compare Fig. 7.12d and Fig. 7.12c) for all SC models. Generally, larger variable capacitance will result in larger RoCoF and larger nadir for the same initial conditions (e.g., compare the nadir at 1.7 V in Fig. 7.12). The observed differences in nadir and RoCoF between different SC expressions are < 0.05 Hz and < 0.05 Hz/s, respectively.

The maximum possible difference in the frequency nadir for all analysed scenarios is shown in Table 7.4. In 34 out of 36 analysed cases, the ideal model with minimum capacitance will yield the best results (error is ≤ 0.1 Hz) for both types of control. However, if the variable capacitance is larger (e.g., 40% model), than the smallest maximum difference was achieved for the ideal model with average capacitance ($C@0.5U^r$).

Fig. 7.13c and Fig. 7.13d show the time to discharge of 10% and 40% variable capacitance models. The size of the variable capacitance impacts which ideal model adequately describes

Table 7.4: Maximum absolute difference in the frequency nadir for all analysed cases (smaller is better).

Disturbance size: 95 MW						
Model	VIR control			Quasi-droop control		
	$C@0$ V	$C@0.5U_r$	$C@U_r$	$C@0$ V	$C@0.5U_r$	$C@U_r$
$C_0/C_{max} = 0.9$	0.060 Hz	0.067 Hz	0.072 Hz	0.066 Hz	0.069 Hz	0.071 Hz
$C_0/C_{max} = 0.75$	0.046 Hz	0.062 Hz	0.082 Hz	0.050 Hz	0.065 Hz	0.074 Hz
$C_0/C_{max} = 0.6$	0.069 Hz	0.057 Hz	0.103 Hz	0.035 Hz	0.059 Hz	0.077 Hz
Disturbance size: 190 MW						
Model	VIR control			Quasi-droop control		
	$C@0$ V	$C@0.5U_r$	$C@U_r$	$C@0$ V	$C@0.5U_r$	$C@U_r$
$C_0/C_{max} = 0.9$	0.096 Hz	0.104 Hz	0.117 Hz	0.101 Hz	0.113 Hz	0.124 Hz
$C_0/C_{max} = 0.75$	0.089 Hz	0.101 Hz	0.134 Hz	0.080 Hz	0.102 Hz	0.130 Hz
$C_0/C_{max} = 0.6$	0.149 Hz	0.094 Hz	0.167 Hz	0.065 Hz	0.099 Hz	0.137 Hz

the nonlinear model in terms of time to discharge. The mean relative error in discharge time between the ideal model and the nonlinear model with 10% variable capacitance is 16.4% for the ideal model with $C@U^r$, 12.8% for the ideal model with $C@0.5U^r$ and 8.7% for the ideal model with $C@0$ V. The same error for 40% variable capacitance is 24.5%, 9.9% and 10.4%, respectively. As the variable part of capacitance increases, so does the error of the ideal models with minimum and maximum capacitance, and the average model will be the most accurate on average in terms of time to discharge, while also taking into account the whole operating range.

Considering the frequency nadir, RoCoF and time to discharge, the best ideal model for SC with up to 25% variable capacitance is the ideal model with minimum capacitance ($C@0$ V) and this model is the same for both types of control. However, if the variable capacitance is larger than that, e.g. 40%, the best ideal model may actually be the model with the average capacitance for both types of control (for VIR control, this is with respect to the maximum absolute difference in the frequency nadir, while for quasi-droop control, this is with respect to time to discharge).

The observed differences are important to accurately predict the performance of an SC bank during all operating points, and therefore the grid frequency dynamics during large load-generation disturbances. For example, if the frequency is to be contained after the loss of a generator, using an ideal model might lead to a conclusion that the frequency will indeed be contained, while in reality, the SC will not be able to deliver the necessary power output, thus underfrequency load-shedding (UFLS) will be triggered (e.g., see Fig. 7.12a and Fig. 7.13a at 1.5 V if the first stage of UFLS is set at 59.2 Hz). The SC can sustain an output power pro-

file for a limited amount of time and it is necessary to accurately estimate the stored energy in order to guarantee the requested provision of system services. Choosing an inadequate capacitance value may lead to a difference in calculated frequency of over 0.1 Hz (e.g. Fig. 7.12c capacitance at rated voltage) as well as the RoCoF (Fig. 7.12d).

7.1.7.2 Discussion on power and energy of a supercapacitor for a loss of generating unit

An ideal capacitor will extract the maximum amount of energy between two voltage levels without any losses. However, in a real supercapacitor, a part of the stored energy will be dissipated as a thermal loss that is time-variant as the discharging current changes to maintain the requested power profile. Thus, the effective capacitance of an ideal model would have to be recalculated for each operating point, which is not practical. Since the real supercapacitor is nonlinear and the requested power profile depends on external factors (i.e., size of disturbance, grid dynamics and frequency controller tuning), this is also practically impossible to do both analytically and a priori. In a general case, the ideal model will behave identically to the realistic model in terms of output power profile if the energy requested during the transient is less than the minimum of stored effective energy in an ideal model and a in realistic model:

$$E_{\text{tran}} < \min\{E_{\text{ideal}}, E_{\text{real}}\} \tag{7.13}$$

Considering the same loss of a 95 MW generating unit G02 at $t = 1$ s, the power profile and SoC are observed for a fully (100% SoC) and partially ($\sim 45\%$ SoC) charged supercapacitor for different ideal model representations. Frequency controller parameters are set to $K_i = 100$ p.u., $K_d = 50$ p.u., $\tau_w^i = 1$ s, $\tau_w^d = 30$ s to induce a complete discharge of the supercapacitor bank.

Fig. 7.14 shows the results for a supercapacitor with 10% variable capacitance. It can be seen that in the case of a fully charged supercapacitor, the model with average capacitance is the most accurate in terms of power profile and SoC (Fig. 7.14a and Fig. 7.14b): the ideal model with average capacitance can sustain the output power only for a fraction of a second longer than the nonlinear model (14.85 s compared to 14.38, or 3.3%). On the other hand, the ideal model with rated capacitance sustains the output power 1.6 s longer (15.99s compared to 14.38 s or 11.2% longer), while the ideal model with minimum capacitance sustains the output power 0.6 s shorter (13.77 s compared to 14.38 s, or -4.2%). Fig. 7.14b shows that energy depletes faster in the case of the ideal model with minimum capacitance and slower in the case of the ideal model with maximum capacitance, while the ideal model with average capacitance is fairly accurate in this case. If the supercapacitor is only partially charged when the disturbance happens, the differences are more pronounced (Fig. 7.14c and Fig. 7.14d) and all ideal models overestimate the available energy: ideal models with minimum, average and rated capacitance sustain the output power for 0.5 s (+13.9%), 0.74 s (+20.6%) and 0.98 s (+27.3%) longer, respectively.

Furthermore, the initial SoC is overestimated by ideal models by 1.1%, it depletes slower, and the total change of SoC is 15.4% bigger using ideal models.

(a) Power profile for full charge

(b) SoC profile for full charge

(c) Power profile for partial charge

(d) SoC profile for partial charge
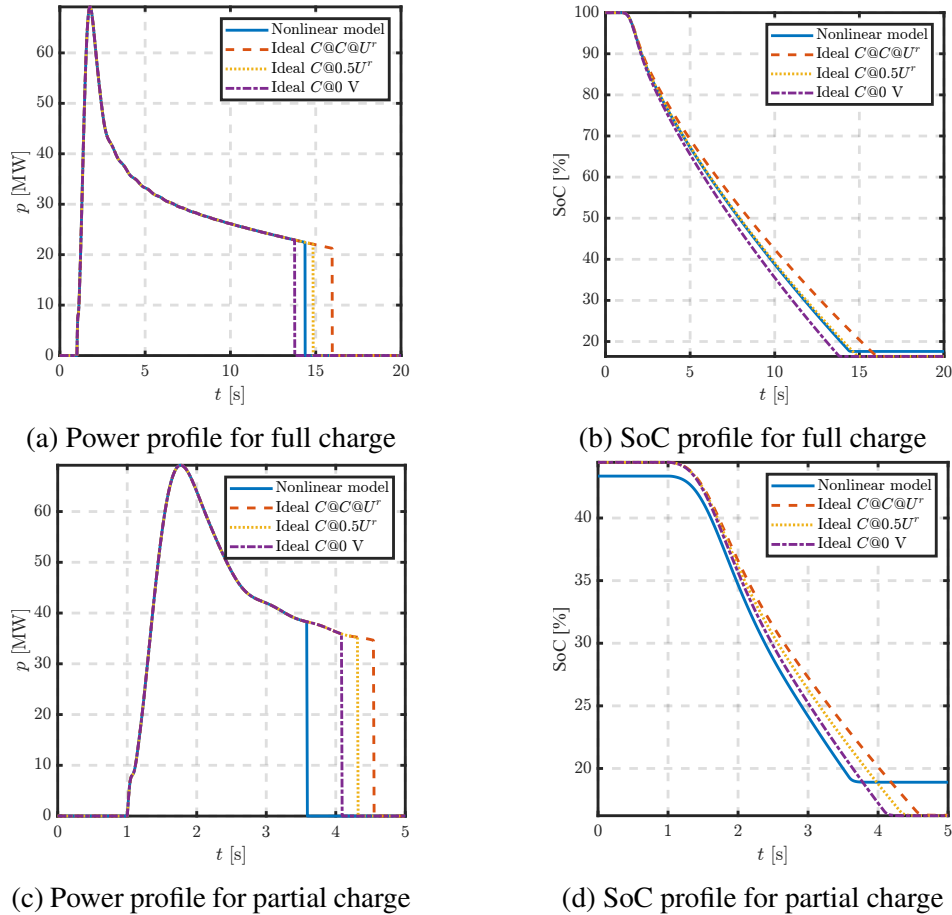
Figure 7.14: Power and SoC profiles for a fully charged (top) and partially charged (bottom) supercapacitor for 10% variable capacitance ($C_{sc} = 900 + 40u_C$).

Fig. 7.15 shows the results for a supercapacitor with 40% variable capacitance. In the case of a fully charged supercapacitor, the most accurate ideal model in terms of power profile and SoC is again the ideal model with average capacitance (Fig. 7.15a and Fig. 7.15b): it can sustain the output power profile for 1 s shorter (11.88 s compared to 12.95 s or -8.3%), while the ideal model with minimum capacitance can sustain the output power for 4.5 s shorter (8.43 s compared to 12.95 s, or -35.1%) and the ideal model with maximum capacitance can sustain the output power for 3 s longer (15.9 s compared to 12.95 s, or +22.8%). Fig. 7.15b shows that the SoC can deplete at significantly different rates depending on the choice of ideal capacitance. For a partially charged supercapacitor (Fig. 7.15c and Fig. 7.15d), the most accurate ideal model with respect to the power profile and SoC is the one with minimum capacitance: it discharges 0.22 s earlier (-7.0%) than the nonlinear model. Ideal models with average and rated capacitance overestimate the stored energy, and they can sustain the power output for a longer time: 0.54 s longer (+17.1%) and 1.37 s longer (+43.3%). The ideal model overestimates the initial SoC by 4.6% and the total change of SoC is 21.4% bigger using the ideal model.

(a) Power profile for full charge

(b) SoC profile for full charge

(c) Power profile for partial charge

(d) SoC profile for partial charge
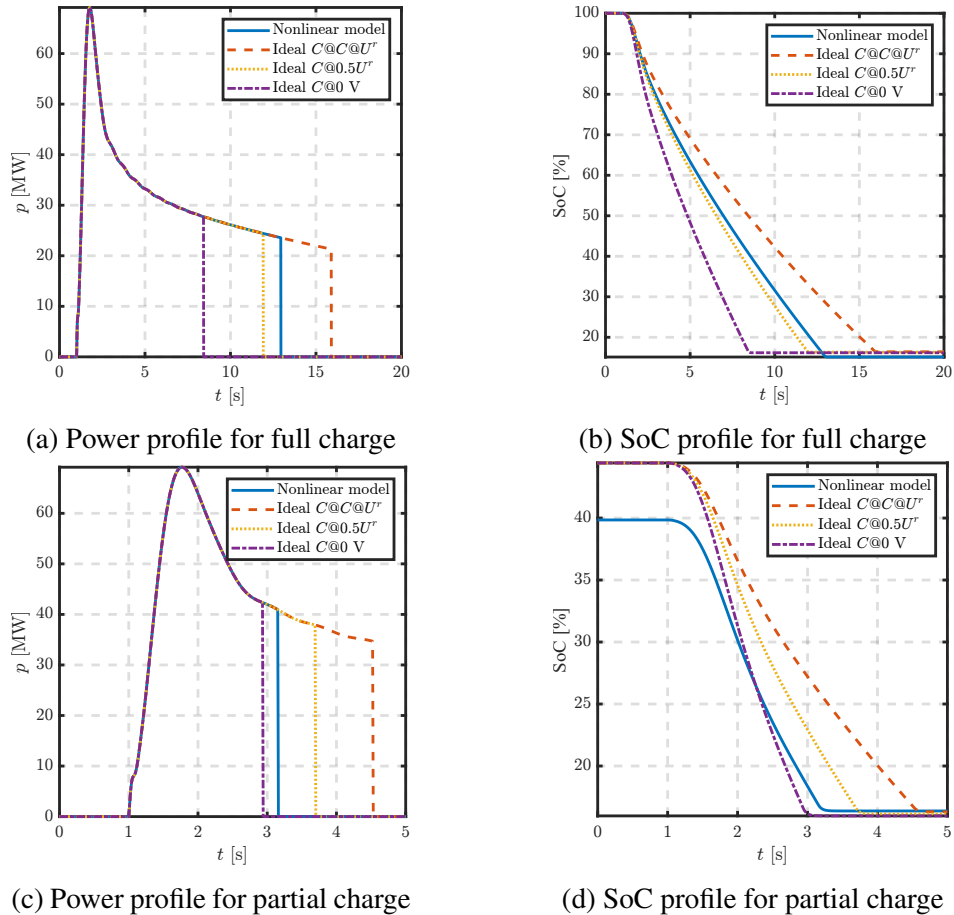
Figure 7.15: Power and SoC profiles for a fully charged (top) and partially charged (bottom) supercapacitor for 40% variable capacitance ($C_{sc} = 600 + 150u_C$).

It can be concluded that as the variable part of capacitance increases, there is a bigger error in the estimation of initial SoC, as well as in the depletion rate of energy between ideal models and nonlinear model. Also, as the initial SoC decreases, different ideal models describe the nonlinear model better. Therefore, the nonlinear voltage dynamics and losses of a real supercapacitor cell make the modelling using ideal or simplified models problematic.

7.1.7.3 Low voltage ride through

The performance of different models has also been evaluated for balanced three-phase faults near Bus 06. In the first scenario, a 500 ms three-phase self-clearing fault has been applied to Bus 02, and Fig. 7.16 shows the SC DC voltage for different initial voltages and SC models. In all cases, the initial voltage and SC voltage dependence do not influence the model performance significantly. The difference between the ideal and nonlinear model (IM,NM) is more visible at first glance: the nonlinear model has a greater voltage change due to the voltage drop on the ESR. However, the maximum difference is less than 10 V so it can also be neglected.

The Bus 06 AC voltage profile is shown in Fig. 7.17. Similarly, the initial voltage, SC voltage dependence and the type of model do not have a significant impact on the post-fault voltage

(a) $C_{sc} = 900 + 40u_C$; $C_{ideal} = 900$ F

(b) $C_{sc} = 600 + 150u_C$; $C_{ideal} = 600$ F
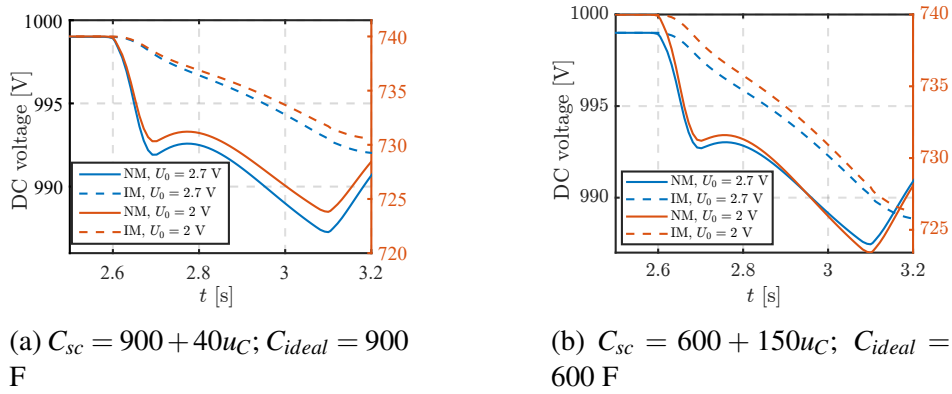
Figure 7.16: DC voltage of a supercapacitor bank during fault for different initial voltages and supercapacitor models.

transient, while the profiles are identical during the fault. The maximum observed difference of absolute voltage values is 0.03 p.u. between the nonlinear and ideal model (both fully charged) for both SC capacitance expressions. For a partially charged SC ($U_0 = 2$ V), this difference is 0 for both capacitance expressions. This is because the system is initially accelerating after the fault clears, so the SC is charging and the fully charged SC is the worst-case scenario since it cannot accept much more charge (a small tolerance of $< 1\%$ exists between the rated voltage and cut-off voltage). Therefore, the SC with low SoC will behave identically to the partially charged SC (e.g., $U_0 = 2$ V or about 50% SoC). The maximum observed difference of absolute voltage values between partially charged and fully charged SCs is 0.07 p.u.

(a) $C_{sc} = 900 + 40u_C$; $C_{ideal} = 900$ F

(b) $C_{sc} = 600 + 150u_C$; $C_{ideal} = 600$ F
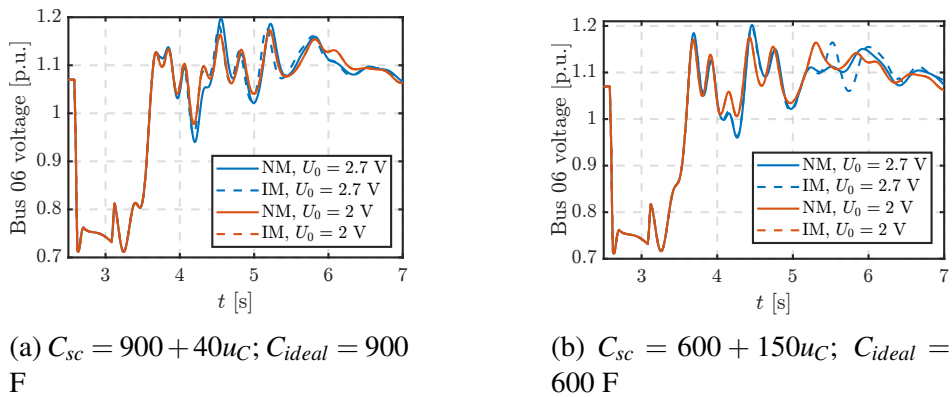
Figure 7.17: AC voltage at Bus 06 after a disturbance.

The impact of different faults and durations has also been analysed. Fig. 7.18a shows the difference in model performance for different durations (100, 200 and 300 ms) of a fault, resulting in a 37% voltage dip at Bus 06. The initial SoC of the SC is 76–78%. It can be seen that the nonlinear model will have a somewhat higher voltage spike and a more oscillatory behaviour after the fault clears due to the ESR. Practically, this means that the overvoltage protection may be triggered sooner when a nonlinear model is used, compared to an ideal model. Again, the difference between the IM and NM is in tens of V and will not play a significant role

in grid dynamics. The longer the fault duration, the bigger the voltage spike and the bigger the difference between models.

(a) $C_{sc} = 600 + 150u_C$; $C_{ideal} = 600$ F

(b) $C_{sc} = 600 + 150u_C$; $C_{ideal} = 600$ F
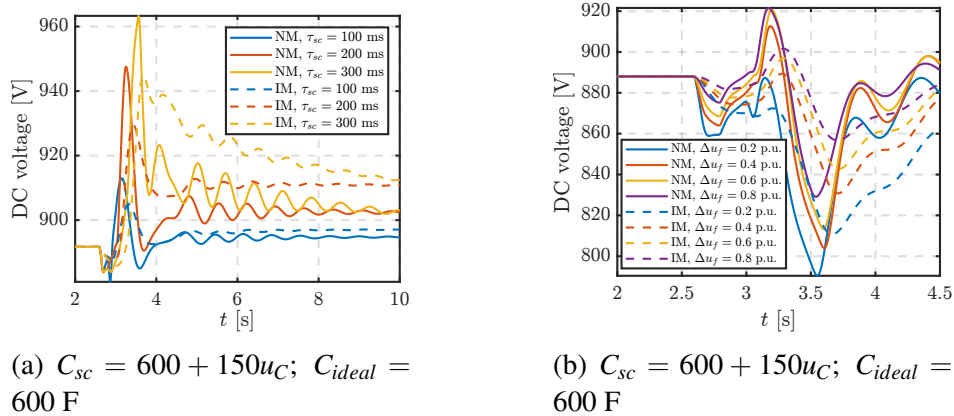
Figure 7.18: DC voltage of an SC bank for a): different fault durations τ_f for a 37% voltage dip; b): different sizes of the voltage dip Δu_f for a 200 ms fault.

The size of the voltage dip (20% to 80%) has a similar impact (Fig. 7.18b). The ideal model will have smaller and smoother transients than the nonlinear mode due to the lack of ESR, but the observed differences will not significantly impact the grid dynamics. Same as before, depending on the operating point of the SC, the undervoltage or overvoltage protection may be triggered sooner when the nonlinear model is used.

In summary, the ideal model representation of SC is adequate for transient stability simulations. The difference in internal dynamics behaviour is small enough that it should not have any impact on the grid results.

7.2 Sizing of supercapacitor banks and the impact of modelling on calculating energy yield

This section will discuss the implications of supercapacitor modelling on its energy yield and a simple method for supercapacitor sizing will be presented. The two main supercapacitor models used in power engineering literature are an ideal model with constant capacitance (Fig. 7.19a), and a constant capacitance model with an equivalent series resistance (nonideal model, Fig. 7.19b). These two models will be compared to the nonlinear model described in 7.1 consisting only of the first branch (Fig. 7.19c) since it was shown that this branch is sufficient for modelling transient behaviour. In this section, the impact of modelling on sizing and the energy yield are discussed in the context of providing shot-term frequency control services (timescale of primary frequency control and faster).

(a) Ideal model

(b) Nonideal model

(c) Nonlinear model (first branch only)
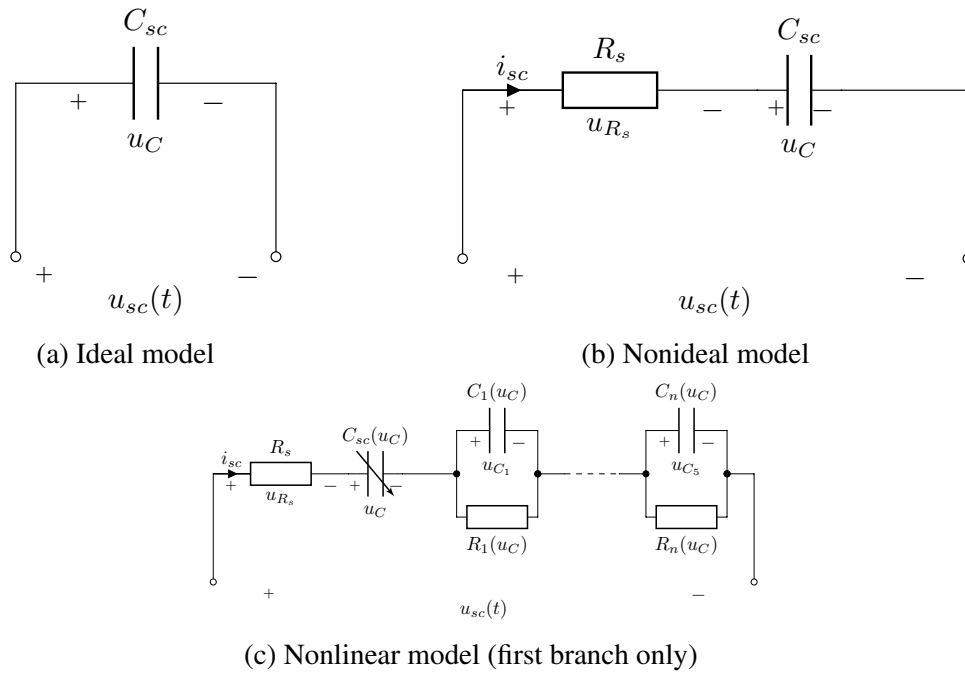
Figure 7.19: Common supercapacitor models.

7.2.1 Implications of supercapacitor modelling on energy yield and efficiency

Voltage and current dynamics of the ideal and nonideal models are described by (7.14), while the energy stored in steady-state ($u_C = U_{sc}$) is calculated by (7.15). Then, for constant discharging power (replacing i_{sc} from (7.14) with P/u_C and solving for u_C), the voltage decay time profile (7.16) is obtained [256], where T is the discharging time and u_{C0} is the initial SC voltage.

$$i_{sc} = C_{sc}\frac{du_C}{dt} \tag{7.14}$$

$$E_{\text{id}} = \frac{1}{2}C_{sc}U_{sc}^2 \tag{7.15}$$

$$u_C(t) = \sqrt{u_{C0}^2 - \frac{2PT}{C_{sc}}} \tag{7.16}$$

However, for a realistic SC model, (7.14) is equal to (7.17) [66]. Then, the steady-state stored energy can be calculated by integrating $u_C i_{sc} dt$ to arrive to (7.18). The voltage decay profile is then given in the implicit form (7.19).

$$i_{sc} = (C_0 + k_v u_C)\frac{du_C}{dt} \tag{7.17}$$

$$E_{\text{real}} = \frac{1}{2}C_0 U_{sc}^2 + \frac{1}{3}k_v U_{sc}^3 \tag{7.18}$$

$$2k_v u_C^3(t) + 3C_0 u_C^2(t) = 2k_v u_{C0}^3 + 3C_0 u_{C0}^2 - 6PT \tag{7.19}$$

According to literature [66, 251], the ratio of (minimum) capacitance at 0 V C_0 and (maximum) capacitance at rated voltage U_r, $\frac{C_0}{C_0+k_vU_r}$ can range between 50% and 80%, although an example of a datasheet of modern cells [257] puts it around 80%. Based on (7.15) and (7.18), the absolute and relative errors in stored energy can be expressed by (7.20) and (7.21), respectively.

$$\Delta E = E_{\text{id}} - E_{\text{real}} = \frac{U_{sc}^2}{6}\left[3(C_{sc} - C_0) - 2k_vU_{sc}\right] \tag{7.20}$$

$$e_E = \frac{\Delta E}{E_{\text{real}}} \times 100\% \tag{7.21}$$

To calculate error in stored energy, three different voltage-dependent characteristics of a realistic SC were used, differing in the magnitude of voltage-dependent capacitance defined as $\gamma = C_0/C_{\text{max}}$—see Table 7.5. For each SC characteristic, three ideal/nonideal models were used, differing in the capacitance value: minimum ($C_{\text{min}} = C_0$), average ($C_{\text{avg}} = \frac{C_{\text{min}}+C_{\text{max}}}{2}$) and maximum ($C_{\text{max}} = C_0 + k_vU_r$). The SC module consists of ≈ 370 cells in series with a rated voltage of 2.7 V each. Note that the equivalent capacitance of N_s identical cells in series can be calculated by (7.22).

$$C_{\text{eqv}} = \frac{C_0}{N_s} + \frac{k_v}{N_s^2}u_C(t) \tag{7.22}$$

Table 7.5: Supercapacitor models with different voltage-dependent characteristics used for energy error calculations.

Model	C_0 [F]	k_v [F/V]	C_{max} [F]	U_r [V]
$\frac{C_0}{C_{\text{max}}} = 0.6$	2160	533.3	3600	2.7
$\frac{C_0}{C_{\text{max}}} = 0.8$	3000	222.2	3600	2.7
$\frac{C_0}{C_{\text{max}}} = 0.95$	3420	66.7	3600	2.7

The relative error in stored energy when the ideal/nonideal model is used relative to the realistic model is shown in Fig. 7.20 ($\gamma = 0.6$—blue curves, $\gamma = 0.8$—orange curves, $\gamma = 0.95$—yellow curves). Firstly, it can be observed that the smaller the voltage-dependent capacitance, the better the ideal/nonideal models represent the SC in terms of stored energy. For 40% voltage-dependent capacitance, the error ranges between: 15% and 60% when maximum capacitance is used, -8% and 30% when average capacitance is used and -30% and -2% when minimum capacitance is used. For 20% voltage-dependent capacitance, the error ranges between: 6% and 20% when maximum capacitance is used, -3% and 10% when average capacitance is used and -12% and 0% when minimum capacitance is used. For 5% voltage-dependent capacitance, the errors for all cases are inside $\pm 5\%$.

Hence, one should be careful when modelling a SC with a constant capacitance model
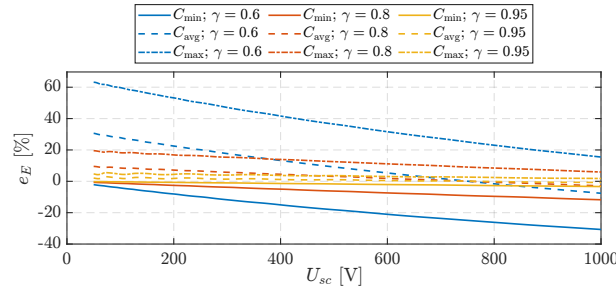
Figure 7.20: Relative error in stored energy for different models.

because the actual stored energy may vary significantly depending on the actual cell in question, i.e., how much the capacitance is truly constant. The issues of sizing are dealt with in the next section.

Voltage discharge profiles of realistic, nonideal and ideal models for different discharge powers are shown in Fig. 7.21. This figure shows the 20% voltage-dependent capacitance model with ideal/nonideal models with average capacitance representation. The SCs are discharged to 10% rated voltage. It can be observed that the nonideal model accurately represents the realistic model in this case, while the ideal model has a slightly longer constant power discharge time (between 2% and 15%, depending on the discharge power). However, these differences may be much more significant depending on the actual cell characteristics, initial voltage and discharge power.
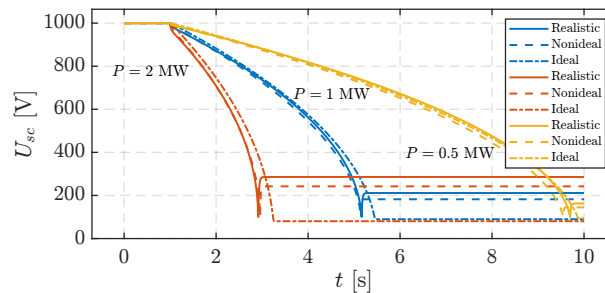
Figure 7.21: Voltage profile for various discharge powers.

Fig. 7.22 illustrates this by showing the voltage discharge profiles (constant 0.5 MW discharge power) for a 40% variable capacitance for different ideal/nonideal representations differing in capacitance value. For the nonideal model, the discharge time difference relative to the realistic model varies between -30% (minimum capacitance) and 17% (maximum capacitance). For the ideal model, this difference is between -27% (minimum capacitance) and 20% (maximum capacitance). In this case, the average capacitance was again the most precise in terms of voltage dynamics (-7% for nonideal model, -3% for ideal model). Notice that the nonideal and realistic models will have the voltage bounce back effect due to the equivalent series resistance (ESR): The measured voltage is smaller than the actual capacitor voltage because of the voltage drop on the ESR during discharging.
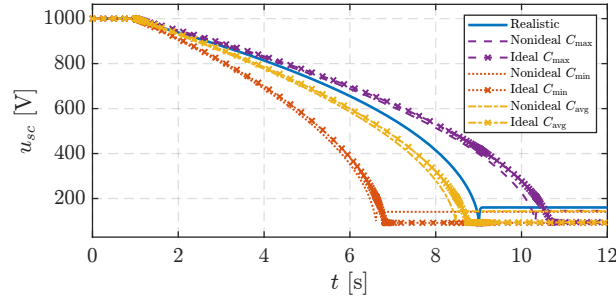
Figure 7.22: Voltage profile for various ideal/nonideal model capacitance values.

The issue with constant power discharging is that the current increases as voltage decreases, which will increase losses on the ESR. The ESR increases when the cells are connected in series, thus when designing an SC bank for high-voltage high-power applications, a certain number of strings must be connected in parallel for two reasons:

1. to decrease the ESR;
2. to reduce the current that flows through each string.

Those two reasons will reduce the power losses and increase efficiency. ε curves are shown in Fig. 7.23. The higher the depth of discharge, the bigger the losses due to higher current demand. Moreover, for the same depth of discharge, a higher discharge power results in bigger losses also due to higher current demand for the same voltage.

$$\varepsilon(t) = \frac{p_C(t)}{p_{sc}(t)} = \frac{i_{sc}u_C(t)}{i_{sc}u_{sc}(t)} = \frac{u_C(t)}{u_{sc}(t)} \tag{7.23}$$
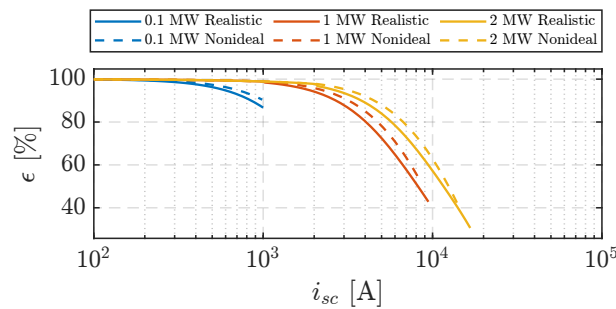
Figure 7.23: Discharge efficiency for various discharge powers.

Minimum achieved efficiencies are shown in Table 7.6. They correspond to the maximum depth-of-discharge, which is in this case 90%. The realistic and nonideal model have the same ESR, but the difference arises from the series combination of parallel RC groups (Fig. 7.19c). The ideal model has 100% efficiency in all cases because it has no losses as it is an ideal capacitor.

Table 7.6: Minimum discharge efficiency for different models.

Model	Discharge power [MW]		
	0.1	1	2
Realistic	87%	45%	33%
Nonideal	90%	53%	39%
Ideal	100%	100%	100%

7.2.2 Supercapacitor bank sizing

In this section, it will be shown how to size an SC bank for constant power operation for frequency control services by taking into account realistic characteristics of an SC cell. The procedure is based on methodology in [254].

Although the complete voltage range of an SC (from 0V to rated) can be exploited, for constant power operation this is not possible since the current would tend towards infinity. Considering an ideal capacitor (7.15), 75% of energy is used between rated voltage and half the rated voltage (7.24).

$$\frac{E_{0.5}}{E_{\max}} = \frac{\frac{1}{2}C\left(\frac{U_{\max}}{2}\right)^2}{\frac{1}{2}CU_{\max}^2} = \frac{1}{4} \tag{7.24}$$

For a realistic super capacitor, (7.24) changes to (7.25).

$$\frac{E_{0.5}}{E_{\max}} = \frac{1}{4}\frac{\frac{1}{2}C_0 + \frac{1}{2}\frac{k_v}{3}U_{\max}}{\frac{1}{2}C_0 + \frac{k_v}{3}U_{\max}} < \frac{1}{4} \tag{7.25}$$

This means that a realistic SC will use slightly more energy between some arbitrary voltage value and rated voltage than the equivalent ideal model. Therefore, it is not necessary to have a deep depth of discharge which increases current and losses. Approximately 84% of energy is used between $40\%U_{\max}$ and $U_{\max}$, and 91% between $30\%\ U_{\max}$ and $U_{\max}$.

When sizing a storage for frequency support services, the design parameters are rated power P and duration of rated power Δt. Consider a 1 MW/30 s SESS. The DC voltage range must be appropriately chosen to deliver the required power. The DC-DC converter must then be able to operate in that voltage range and be able to withstand the maximum current. For this power, an appropriate voltage range is $500 - 1000\ \mathrm{V}_{dc}$. The first approximation of sizing is done using a

nonideal representation. First, minimum, maximum and average currents are calculated:

$$I_{\min} = \frac{P}{V_{\max}} = 1000 \text{ A} \tag{7.26}$$

$$I_{\max} = \frac{P}{V_{\min}} = 2000 \text{ A} \tag{7.27}$$

$$I_{\text{avg}} = \frac{I_{\max} + I_{\min}}{2} = 1500 \text{ A} \tag{7.28}$$

Since the ESR is unknown, in the first approximation it can be estimated using an RC time constant $\tau_{RC} = RC \approx 1$ s according to commercial datasheets. Linearising the circuit equation from Fig. 7.19b, the total voltage change is equal to:

$$\begin{aligned} \Delta u_{sc} &= \Delta u_{R_s} + \Delta u_C \\ &= I_{\text{avg}} R_s + I_{\text{avg}} \frac{\Delta t}{C} \\ &= \frac{I_{\text{avg}}}{C} (\tau_{RC} + \Delta t) \end{aligned} \tag{7.29}$$

Solving for C and substituting $\Delta u_{sc} = V_{\max} - V_{\min}$:

$$\begin{aligned} C &= \frac{I_{\text{avg}}}{V_{\max} - V_{\min}} (\tau_{RC} + \Delta t) \\ &= \frac{1500}{1000 - 500} (1 + 30) = 93 \text{ F} = C_{\text{eqv}} \end{aligned} \tag{7.30}$$

The rated cell voltage of an SC is between 2.5 and 3 V on average. Considering a 2.7 V cell, to obtain 1000 V DC, it will require $N_s = 1000/2.7 \approx 370$ cells in series. If we have only one string ($N_p = 1$), the required cell capacitance would be $C_{cell} = C_{eqv} N_s = 34410$ F. Obviously, such a cell does not exist, but this capacitance can be obtained by connecting cells in parallel. For $N_p = 10$, average cell capacitance is:

$$C_{\text{cell}} \approx C_{\text{eqv}} \frac{N_s}{N_p} = 93 \frac{370}{10} = 3441 \text{ F} \tag{7.31}$$

The ESR of a such a cell is around 0.29 mΩ [257], which means the equivalent ESR is:

$$R_{\text{eqv}} \approx R_s \frac{N_s}{N_p} = 0.29 \cdot 10^{-3} \frac{370}{10} \approx 10.7 \text{ m}\Omega \tag{7.32}$$

Since there are effectively 10 strings in parallel, each string will carry only a tenth of power, i.e., a tenth of total current, therefore, the losses on ESR are reduced by a factor of 100. Considering a 20% voltage-dependent capacitance, k_v and C_0 can be approximated from (7.33) and

(7.34) and they are equal to 283.2 F/V and 3058.7 F, respectively.

$$C_{\text{cell}} = C_{\text{avg}} = C_0 + k_v \frac{U_{\text{max}}}{2} \tag{7.33}$$

$$\frac{C_0}{C_0 + k_v U_{\text{max}}} = 0.8 \tag{7.34}$$

Now this SC bank can be simulated with a realistic model to test the performance. Results are shown in Fig. 7.24. This SC bank can sustain the rated power output for ≈ 35 seconds which is a 16% margin of error compared to the requested 30 s (Fig. 7.24a). This power is discharged between the $0.5U_{\text{max}}$ and U_{max} which can be measured at the SC bank terminals (Fig. 7.24b). The discharging efficiency is between 94% and 98.5% (Fig. 7.24c), while the ESR losses are between 0.01 p.u. and 0.045 p.u. (Fig. 7.24d), which is satisfactory.

(a) Power

(b) DC Voltage

(c) Efficiency

(d) ESR losses
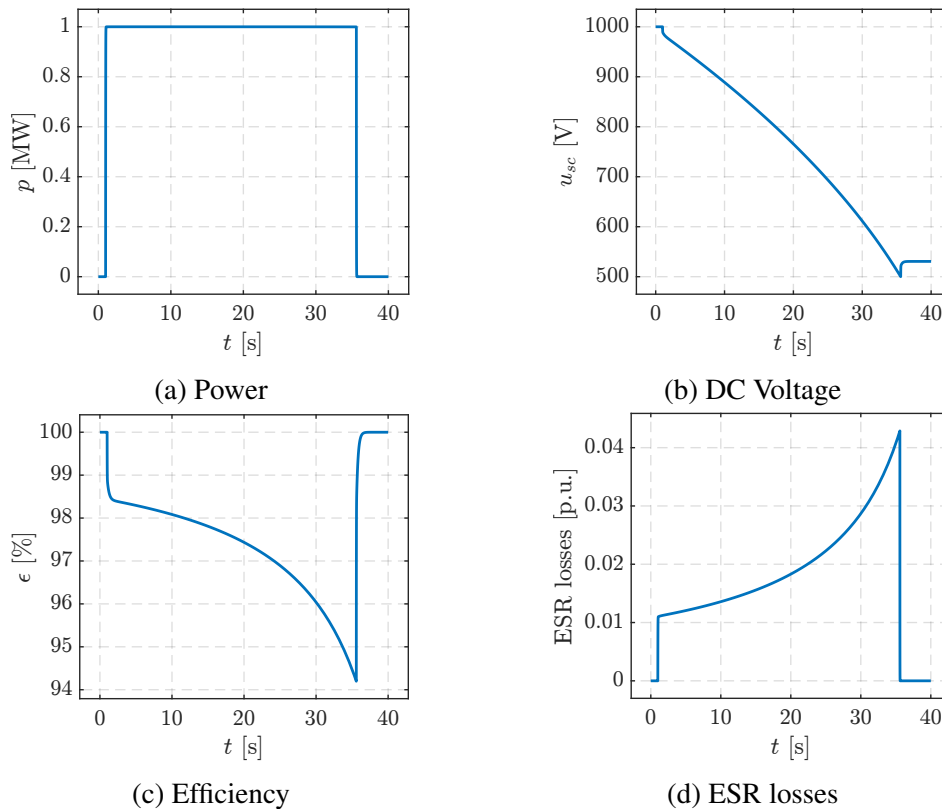
Figure 7.24: Performance test of SESS design.

The presented design procedure can be applied iteratively until satisfactory performance is achieved or if a larger margin for error is needed due to variable capacitance (e.g., 30% variable capacitance). The benefit of the presented method is that it is quite straightforward to do, even by hand, and it is based on a few simple assumptions and data that is easy to obtain from datasheets. Simulation on a realistic model then serves as a performance test for the first approximation after which the process can be repeated iteratively until desired accuracy is achieved.

7.3 Coordinated control of a supercapacitor and a wind turbine generator for the provisioning of fast frequency control services

We modify the virtual inertia controller from Fig. 5.12 such that, when the rotor speed of a wind turbine falls below the minimum speed, the inertial response is blocked (Fig. 7.25) to avoid further slowing down of the turbine and potential stalling. The inertial response is blocked for 30 s to avoid control signal oscillation as the rotor speed oscillates. The time of 30 s was chosen because in this case it is enough for the wind turbine to reach a stable operating point (or steady-state speed for constant wind speed). When the wind turbine generator operates at rated power, stator windings and converter thermal limits may limit the extra power injection for the inertial response.
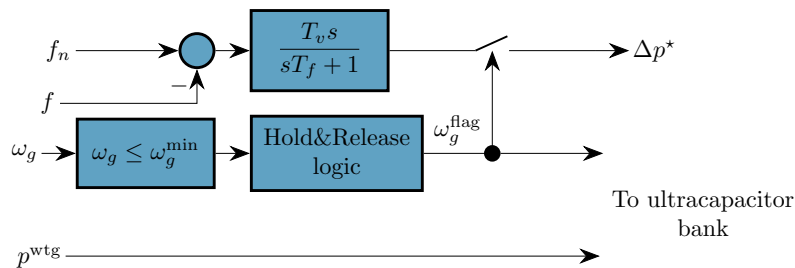
Figure 7.25: Modified virtual inertia controller of a wind turbine.

The rotor speed flag (along with the WTG output power) is propagated to the ultracapacitor bank (UCBS) control system (Fig. 7.6) to enable the inertial response of the bank. The rotor speed signal acts as a flag that enables the inertial response during low wind speeds, while the WTG power signal acts as a flag that enables the inertial response during high wind speeds when rated power is achieved. Modified virtual inertia control of the UCBS system is shown in Fig. 7.26. When either one of those flags is logically true (OR gate), inertial response provision is enabled. Communication delay between the DFIG WTG and UCBS system is taken into account ($e^{-s\tau_d}$ block in Fig. 7.26). Also, there are two frequency control blocks: the upper one is similar to droop control (although it also diminishes in steady-state) and the bottom one is similar to the natural inertial response. Different behaviour is achieved by setting the washout filter time constant T_w^d and T_w^i, respectively. A larger washout time constant means that the output signal will converge to 0 more slowly (when the frequency deviation Δf is reaching steady-state, $s\Delta f \rightarrow 0$)—therefore, $T_w^d \gg T_w^i$.

The simulations are done on a 9-bus system in DIgSILENT PowerFactory following a 20 MW load increase event (see [72] for details). The base case scenario corresponds to the situation when both WTG and UCBS are not participating in frequency control. The wind farm and UCBS size is 100 MW and 10 MW, respectively.
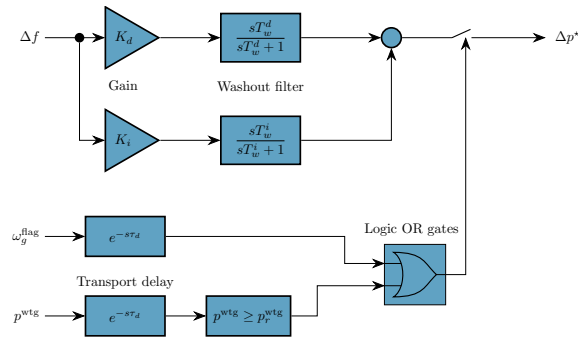
Figure 7.26: Virtual inertial controller of the ultracapacitor bank system.

7.3.1 Low wind speed

Simulation results for a low wind speed scenario are shown in Fig. 7.27. When the inertial response from WTG is activated, the wind turbine rotor will start to slow down. When the rotor speed falls below the lower threshold, the inertial response is disabled (Fig. 7.27, 2nd from the top). However, the same figure shows that the output power does not immediately return to the pre-disturbance value because of the inertia of the rotor. The generator power vs. rotor speed curve is very steep around cut-in wind speed, which means that for a small change in rotor speed there is a big change in output power. Momentarily, the WTG output power is a lot smaller than the pre-disturbance value and this can further aggravate the drop in frequency. On the other hand, if an energy storage system such as an ultracapacitor bank takes over the inertial response (Fig. 7.27, 3rd from the top), the drop in power is much less pronounced and the inertial response lasts longer (Fig. 7.27, bottom). Consequently, this results in a smaller frequency nadir, as seen in Fig. 7.27 top.

7.3.2 Above the rated wind speed

Simulation results for a high wind speed scenario is shown in Fig. 7.28. Here, the generator is operating at its rated power and, when the inertial response is requested, there is no increase in WTG output power because the control system limits the output power to 1 p.u. This is done in order to obey stator and converter maximum current limits. However, power reduction is still possible during the increase of frequency (around the 15 s mark in Fig. 7.28, 2nd from the top). Therefore, there is no significant difference between the base case and the case when only the WTG is participating in frequency control (Fig. 7.28, top). However, if the WTG is coordinated with an UCBS, it knows when the WTG is operating near rated power and it takes over the inertial response (Fig. 7.28, 3rd from the top, and Fig. 7.28, bottom). This extra power injection helps restrain the frequency nadir (Fig. 7.28, top).
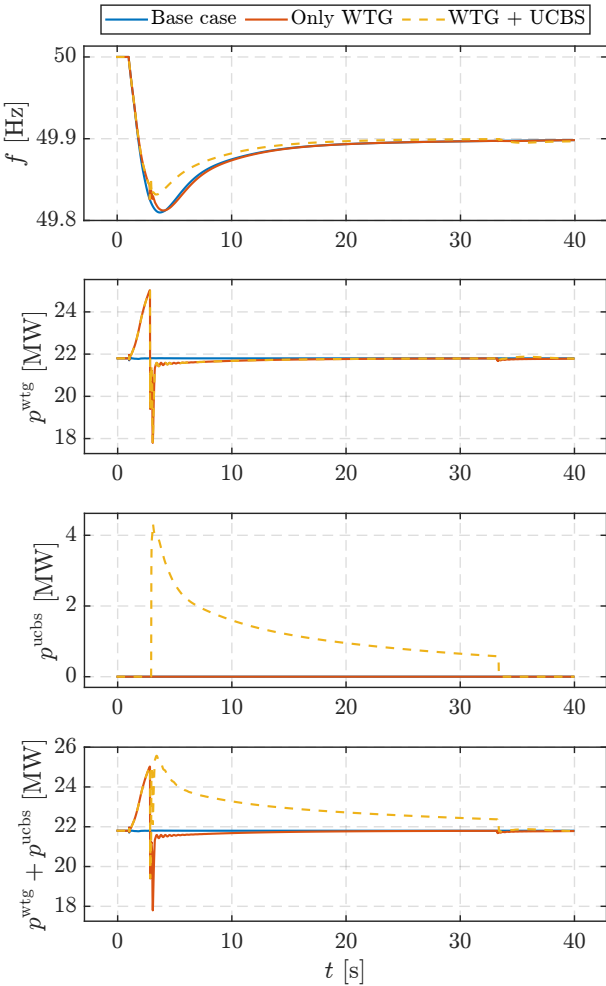
Figure 7.27: Simulation results for the low wind speed scenario (top to bottom): grid frequency, wind turbine output power, ultracapacitor bank output power, total output power.
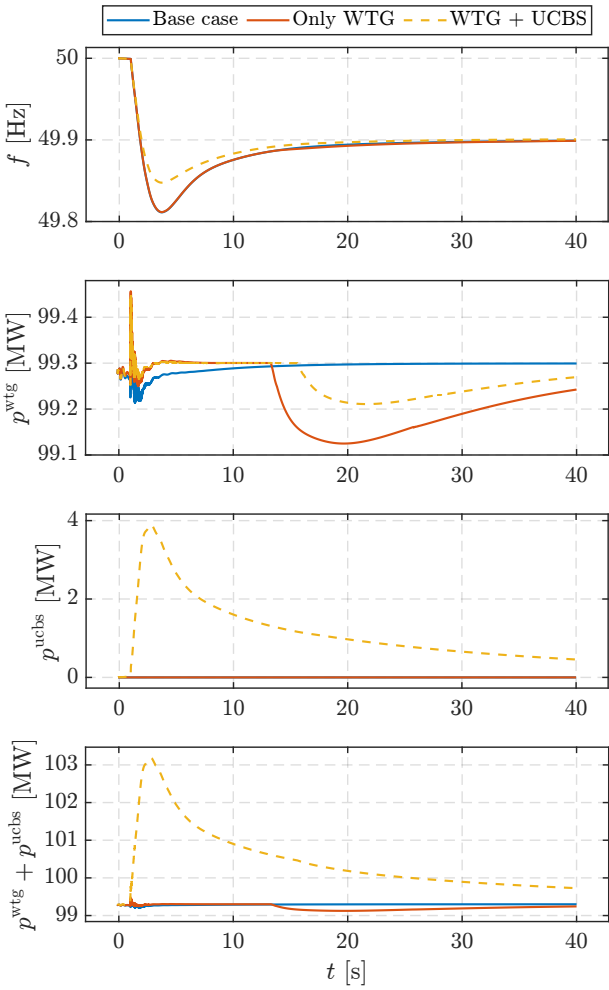
Figure 7.28: Simulation results for the high wind speed scenario (top to bottom): grid frequency, wind turbine output power, ultracapacitor bank output power, total output power.

7.4 A model predictive control approach to the operation optimisation of an ultracapacitor bank for frequency control

7.4.1 Motivation for the MPC approach

Automatic control of active power and frequency in power systems is almost exclusively achieved by standard Proportional-Integral-Derivative (PID) control, which is well-known and reliable [106]. Conventional power plants and large-scale batteries have more than enough energy in normal operation in the time scale of inertial response (IR) and primary frequency control (PFC, tens of seconds) so that PID control can most of the time give adequate performance. However, this is not the case when UCs are utilised. UCs are energy-limited so they can sustain an output power profile only for a limited time (rated power can be sustained for tens of seconds up to a minute, which is the time scale of the IR and PFC). The power output of a UC depends on the PID controller parameters, as well as on the size of the frequency disturbance. Therefore, the PID-controlled UC can likely discharge (i.e., reach the minimum voltage limit) while still providing some amount of power. This can cause additional disturbances to the grid and a larger frequency nadir [61], as well as overvoltages in the UC system. Since disturbances and their size cannot be predicted, PID parameters cannot be optimally chosen or tuned in real-time to provide maximum active power support while avoiding abrupt discontinuation of power for all possible operating scenarios. Thus, in order to address these issues, we adopt an MPC approach to inherently consider UC system constraints in the control system formulation and to obtain a smooth power response to a disturbance of any size. The proposed MPC approach is compared to a standard PID controller for various disturbance sizes to demonstrate the benefits of MPC over PID controllers.

A significant body of literature exists that utilizes ultracapacitor technology for various power system purposes. In the context of control approach, we can roughly divide the literature into two groups:

1. PID control: [56, 58–62, 64, 65, 72, 256, 258, 259]
2. MPC: [260–269].

More details about each source cited above can be found in [71], but their similarities and shortcomings can be summarised as follows:

- realistic supercapacitor model is not considered;
- MPC is used to predict system frequency instead of supercapacitor behaviour;
- supercapacitor is used as a part of a hybrid system as opposed to standalone operation;
- papers that utilise MPC for supercapacitor control are mostly concerned with automotive applications or some general energy management of hybrid systems.

Hence, we use the MPC approach to fast frequency control by a standalone UC bank while also considering a realistic UC model. The main argument against using MPC for fast frequency control can be the computational cost and thus the possibility that the solution cannot be always found within reasonable time. We adopt an implicit MPC framework, which always calculates feasible solutions with solver's average solving time under 100 ms.

The advantages of using MPC for UC banks providing frequency control is that the disturbance uncertainty of any size can be mitigated by inherently incorporating UC system constraints and predictive capabilities into the control design, which is particularly relevant in today's context, where power systems have increasing shares of stochastic renewable energy sources. By doing this, the control action is more robust against the uncertainty coming from the renewable power generation, hence an improved frequency response to disturbances can be obtained. UC only has energy available for tens of seconds, which is also the timescale of frequency containment control. On the one hand, increasing the contribution of UCs to frequency response through PID gain tuning is risky because the system frequency can be aggravated even more if the stored energy is depleted while still providing a significant power output (as shown in the simulation studies). On the other hand, if the PID gains are tuned more conservatively, the advantage of a fast and high-power output is lost. In both cases, the PID controller cannot be tuned to optimise the contribution of a UC to frequency response for all possible disturbance sizes. On the contrary, MPC is able to optimise the behaviour of the control system against the desired criteria, thus making the control system more flexible and responsive to the time-varying power system conditions. Additionally, one of the benefits of MPC is that system limitations are inherently considered in the MPC formulation, and issues such as integral wind-up, which are present in PID controllers, can be avoided. Our MPC control scheme is devised to always guarantee that the UC bank discharges smoothly and that maximum energy is extracted while meeting the constraints of the UC system.

7.4.2 Control design

The proposed hierarchical control architecture applied to the UC bank consists of two control levels defined as follows:

- upper control level—controller at this level calculates the active and reactive power set-points which are passed on to the lower control level. Reactive power control by UC is out of the scope because the focus is on frequency control (thus, this set-point is always 0). Furthermore, reactive power control is related to the inverter and is independent of active power control. The main purpose of this level is to provide a viable solution for power system frequency control using a UC bank.
- lower control level—controllers at the inverter level are used for tracking set points received from the upper control level.

The lower-level controls and those at the inverter level are not analysed in detail since numerous relevant examples can be found in the literature. Here, the UC inverter is modelled as a grid-following current source where the inverter current references are directly determined by fast PI control loops based on *PQ* control errors [255]. The upper control level is in charge of the UC bank frequency control. Fig. 7.29 illustrates the introduced hierarchical control structure. The overall ultracapacitor control structure is shown in Fig. 7.6. The PID frequency controller and the MPC based frequency controller are defined in the following subsections.
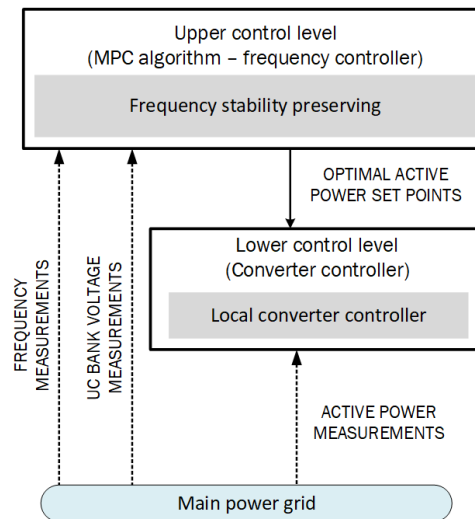
Figure 7.29: Hierarchical control structure.

7.4.2.1 PID frequency controller

The PID frequency controller is the one shown in Fig. 7.10. The input to this block is a grid frequency signal estimated by the PLL and the output is the requested change in power. The type of implemented control algorithm for frequency response can be arbitrary. In the literature, the frequency controller is usually a proportional or a derivative controller, or a combination of both (PD). However, the UC does not have a large amount of stored energy available. If the standard droop control (pure proportional controller) is employed, the UC output power is proportional to the frequency deviation both during the transient state as well as in the steady-state. Once the UC reaches the lower voltage limit during discharging, the output power will instantaneously drop to zero, which will cause a higher secondary frequency drop. This can be mitigated to a certain extent by only allowing the UC to provide support during the transient state. This is achieved through a washout filter, which is more akin to a derivative controller. Hence, in the PID formulation, this controller has the form of a derivative controller with a low-pass filter to smooth out high-frequency noise, since differentiating in time is a process that inherently amplifies the noise.

Although not always guaranteed, the UC will not be completely discharged this way and the

additional frequency drop will not always occur. This depends on the required energy during the transient process, which not only depends on the parameters of the frequency controller, but also on the size of the disturbance, which is something that cannot be controlled. This issue will be tackled using MPC, which will always guarantee that the UC bank discharges smoothly and that the maximum energy is extracted while satisfying the constraints of the UC system.

7.4.2.2 Predictive model of a UC bank

The predictive model of a UC bank in the form of a transfer function that relates the UC bank output voltage v with the charging/discharging power p is expressed as

$$\frac{v(z)}{p(z)} = G(z) = \frac{a_3 z + a_4}{z^2 + a_1 z + a_2} \tag{7.35}$$

The transfer function coefficients a_1, a_2, a_3 and a_4 are identified by conducting simulations on the nonlinear simulation model (7.7)–(7.12) of the UC bank (nonlinearities are due to (7.11)–(7.12)). The identification procedure has been conducted using the Matlab System Identification Toolbox. The prediction model coefficients a_1–a_4 are given in [71]. The sampling time T_s used to discretise the identified linear UC bank model is set to 50 ms (the root square mean error over 30 s, hence a validation data-set of 30000 samples, was 30.21). Fig. 7.30 and 7.31 show the training and validation data sets used to conduct the linear model identification, while Fig. 7.32 shows the response of the nonlinear UC model (black line) compared to the identified linear model (blue line). The identified linear model response has a fitness of 82.59%. In terms of the prediction model quality, the identified linear model fitness level is satisfying.
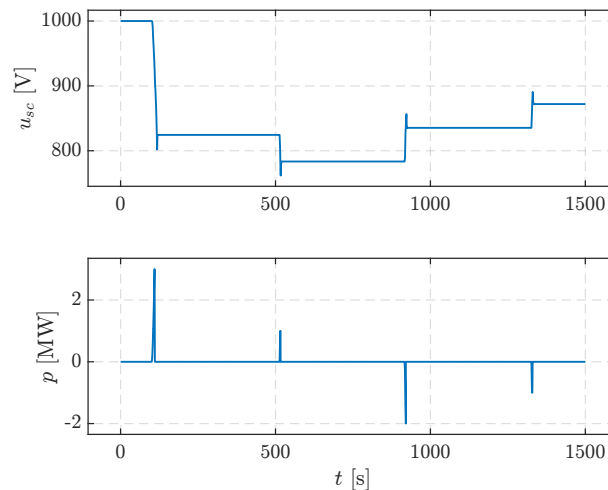
Figure 7.30: Training set.

The state-variables vector is defined based on the availability of direct measurements. Namely, the energy of the UC bank is directly proportional to the square of the UC bank terminal voltage in steady-state. It is not necessary to perform a state estimation since voltage measurements at
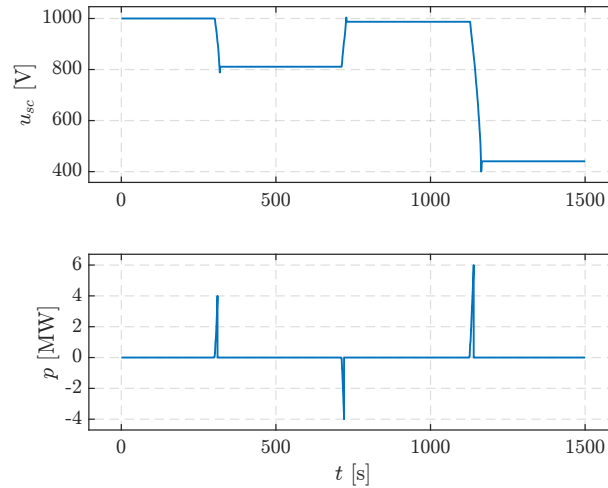
Figure 7.31: Validation set.
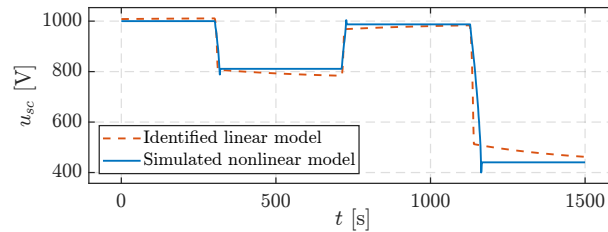
Figure 7.32: Simulated nonlinear (validation set) and identified linear model output.

the UC bank terminals are available. The use of an observer is therefore not needed.

Furthermore, the discrete-time predictive model used within the MPC controller in this paper is derived by using the generalised formulation of the Controlled Auto Regressive Integrated Moving Average (CARIMA) model expressed as

$$a(z)\Delta y_k = b(z)\Delta u_k + T(z)\varepsilon(z) \tag{7.36}$$

Since the output, i.e., voltage, can be directly measured, the prediction model uses variables of the output and input increment and assumes the best estimate of future random term $T(z)\varepsilon(z) = 0$. In (7.36), $a(z)$ and $b(z)$ are polynomials that represents denominator and numerator of the transfer function, respectively. These polynomials are expressed as:

$$a(z) = 1 + a_1 z^{-1} + \cdots + a_n z^{-n} \tag{7.37}$$

$$a(z)\Delta = a(z)(1 - z^{-1}) = A(z) \tag{7.38}$$

$$b(z) = b_1 z^{-1} + \cdots + b_m z^{-m} \tag{7.39}$$

Since the disturbance estimate is implicit within the use of increments, there is no need for a disturbance estimate in this prediction model. The UC bank output voltage predictions can be

found by using the following compact matrix/vector form:

$$\underrightarrow{\mathbf{v}_{k+1}} = \mathbf{H}\Delta\underrightarrow{p_k^\star} + \mathbf{K}\Delta\underleftarrow{p_{k-1}^\star} + \mathbf{Q}\underleftarrow{v_k} \tag{7.40}$$

Where the **H**, **K** and **Q** matrices are expressed as:

$$\mathbf{H} = \mathbf{C_A}^{-1}\mathbf{C_b}, \mathbf{K} = \mathbf{C_A}^{-1}\mathbf{H_b}, \mathbf{Q} = \mathbf{C_A}^{-1} \tag{7.41}$$

in which the matrices C_A, C_b, H_A and H_b are defined by (7.42)–(7.45):

$$\mathbf{C_A} = \begin{pmatrix} 1 & \cdots & 0 & 0 \\ A_1 & 1 & 0 & 0 \\ \vdots & \ddots & \vdots & 0 \\ A_{N-1} & A_{N-2} & \cdots & 1 \end{pmatrix} \tag{7.42}$$

$$\mathbf{H_A} = \begin{pmatrix} A_1 & A_2 & \cdots & A_{n-4} & A_{n-3} & \cdots & A_{n-1} & A_n \\ A_2 & A_3 & \cdots & A_{n-3} & A_{n-2} & \cdots & A_n & 0 \\ \vdots & \cdots & \cdots & A_{n-2} & A_{n-1} & \cdots & 0 & 0 \\ A_N & A_{N+1} & \cdots & A_{n-1} & A_n & \cdots & 0 & 0 \end{pmatrix} \tag{7.43}$$

$$\mathbf{C_b} = \begin{pmatrix} b_1 & 0 & 0 & 0 \\ b_2 & b_1 & 0 & 0 \\ \vdots & \ddots & \vdots & 0 \\ b_N & b_{N-1} & \cdots & b_1 \end{pmatrix} \tag{7.44}$$

$$\mathbf{H_b} = \begin{pmatrix} b_2 & b_3 & \cdots & b_{m-4} & b_{m-3} & \cdots & b_{m-1} & b_m \\ b_3 & b_4 & \cdots & b_{m-3} & b_{m-2} & \cdots & b_m & 0 \\ \vdots & \cdots & \cdots & b_{m-2} & b_{m-1} & \cdots & 0 & 0 \\ b_{N+1} & b_{N+2} & \cdots & b_{m-1} & b_m & \cdots & 0 & 0 \end{pmatrix} \tag{7.45}$$

Furthermore, in (7.40), the vector $\underrightarrow{v_{k+1}}$ represents the predicted output voltage of a UC bank,

while the vector $\Delta p_{\underrightarrow{k}}^{\star}$ represents the control sequence in a form of active power increments of the converter's active power set-point. These vectors are expressed as (7.46)–(7.47):

$$\mathbf{v}_{\underrightarrow{k+1}} = [v(k+1)\ v(k+2)\ ...\ v(k+N)]^{\top} \tag{7.46}$$

$$\Delta \mathbf{p}_{\underrightarrow{k}}^{\star} = [\Delta p^{\star}(k)\ \Delta p^{\star}(k+1)\ ...\ \Delta p^{\star}(k+N-1)]^{\top} \tag{7.47}$$

Since the MPC formulation in this paper is set up in a way that the control signal increment, i.e., the power increment, is calculated at each time step, the control signal produced by the controller at the time instant k is calculated by (7.48).

$$p^{\star}(k) = p^{\star}(k-1) + \Delta p^{\star}(k). \tag{7.48}$$

7.4.2.3 Novel autonomous frequency controller based on voltage reference trajectory and MPC

In this section, we introduce a novel autonomous frequency controller which is shown in Fig. 7.33. If either the frequency deviation or RoCoF are outside user-defined limits (modelled by deadzones in Fig. 7.33), the UC system switches to fast discharge mode in which the DC voltage trajectory is equal to $v_s(\Delta f) = v_0 + K_V \Delta f$, where v_0 is the initial voltage reference (SoC) of the UC, and K_V is the DC voltage – frequency droop gain in V_{DC}/Hz. The change in voltage due to the change in frequency $K_V \Delta f$ is limited to only negative gradients, and to some desired negative maximum change Δv_{min} which corresponds to some user-defined maximum change of SoC for a change in frequency.
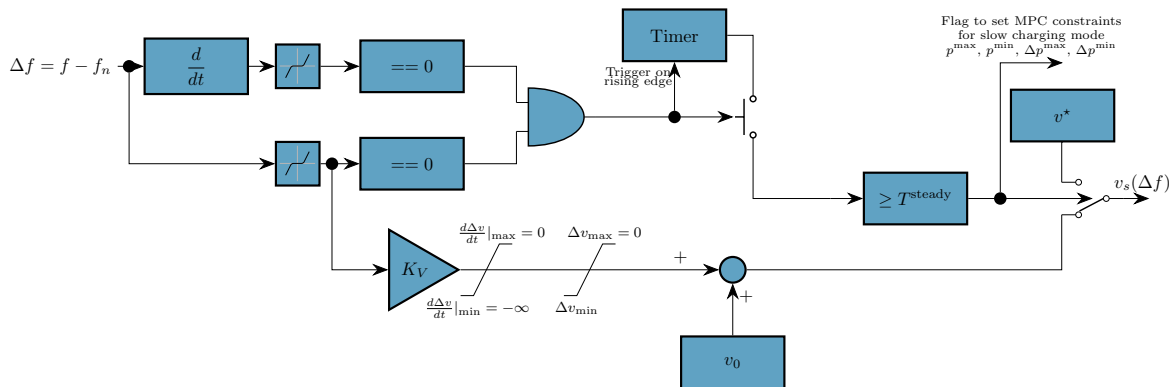
Figure 7.33: Novel autonomous frequency controller based on voltage reference trajectory and MPC.

On the other hand, once the frequency is stabilised, i.e., both the frequency deviation and the RoCoF are inside the user-defined limits, the timer is triggered. If the frequency deviation and RoCoF are inside the user-defined limits for a user-defined period of time T^{steady}, the UC system switches to the slow charging mode in which the voltage reference trajectory is set to the user-specified value $v_s = v^{\star}$, e.g., maximum voltage for a full charge. Simultaneously, a flag is

triggered which induces a change of MPC constraints for the control signal: p^{max}, p^{min}, Δp^{max}, Δp^{min}. These constraints are set conservatively which will reduce the charging power so that it does not cause additional grid frequency excursions.

The slow-charging mode is not enabled before the frequency is stable for some time T^{steady} because both the frequency deviation and RoCoF can temporarily pass through the defined deadbands during the frequency containment process. Without this time delay, an oscillatory behaviour between charging and discharging modes can be triggered, which will be reflected in grid frequency oscillations. This time delay can be set from 30 seconds up to around tens of minutes, which is usually the time range in which the frequency is theoretically stabilised and returned to nominal value.

The presented control is superior to classic active power – frequency droop control because the latter can cause a sudden reduction of output power if UC energy is depleted, which will be shown in the study cases. On the other hand, the proposed approach directly determines how much energy will be used for a certain frequency deviation, while the MPC framework calculates the required power set-points to the lower-level converter control such that all system constraints are satisfied. This results in a smoother discharge curve and better performance in arresting the frequency excursions.

The parameters of the proposed controller are set as follows: the frequency deviation deadband is set to $\pm\,50$ mHz, the RoCoF deadband is set to ±100 mHz/s, $T^{\mathrm{steady}} = 30$ s, $K_V = 1050$ $V_{\mathrm{DC}}/$Hz, $\Delta v_{\mathrm{min}} = -600$ V, $v_0 = V^\star = 1000$ V.

7.4.2.4 MPC problem formulation

The objective function to be minimised at each current point in time k is defined as:

$$J = [v_s \mathbf{1} - \underset{\longrightarrow}{\mathbf{v}_{k+1}}]^\top \mathbf{Q_y}[v_s \mathbf{1} - \underset{\longrightarrow}{\mathbf{v}_{k+1}}] + \Delta \mathbf{p}_{\underset{\rightarrow}{k}}^{\star T} \mathbf{Q_u} \Delta \mathbf{p}_{\underset{\rightarrow}{k}}^{\star} + \mathbf{S}^\top \mathbf{R} \mathbf{S}, \tag{7.49}$$

where $\mathbf{1}$ is a column vector of N ones, v_s is the UC bank output voltage reference trajectory defined as $v_s(\Delta f) = v_0 + K_V \Delta f$.

The objective function (7.49) has a quadratic form that consists of two terms: i) the first term is used to express the error between the output voltage reference trajectory v_s and the predicted UC bank voltage output v; ii) the second term models the control effort. The optimal control sequence resulting from the MPC algorithm consists of active power increments. At each time step, an optimisation problem is solved, and the first element of the resulting control sequence is then sent to the local controller that controls the converter. The matrices $\mathbf{Q_y}$ and $\mathbf{Q_u}$ in (7.49) contain the weighting factors: q_y penalizes the predicted UC bank voltage output deviations from the reference trajectory, while q_u penalizes the change of the control signals.

The weighting matrices $\mathbf{Q_y}$ and $\mathbf{Q_u}$ over the prediction horizon N can be built as follows:

$$\mathbf{Q_y} = \begin{pmatrix} q_y & \cdots & 0 \\ \vdots & \ddots & \vdots \\ 0 & \cdots & q_y \end{pmatrix} \tag{7.50}$$

$$\mathbf{Q_u} = \begin{pmatrix} q_u & \cdots & 0 \\ \vdots & \ddots & \vdots \\ 0 & \cdots & q_u \end{pmatrix} \tag{7.51}$$

One of the main advantages of MPC schemes is their ability to incorporate different types of constraints on control and output signals into the control design. By doing so, the optimal control sequence is calculated taking into account relevant system constraints. However, one should be very careful in constraint formulation since they can lead to infeasibility issues. In order to ensure the feasibility of the optimisation problem within an MPC scheme, its constraints can be formulated as 'hard' and 'soft' constraints. Hard constraints must always be satisfied, while soft constraints can be ignored to a certain extent so that it is possible to find a feasible solution at each MPC iteration. In the proposed MPC algorithm, hard constraints are considered for the control signals (charging/discharging power and the incremental charging/discharging power), whilst the output constraints on the UC bank terminal voltage can be softened since UC bank voltage violations are permissible. These constraints are softened by introducing a vector of N slack variable, $\mathbf{S}$, which is penalised in the objective function (7.49) by adding the term $\mathbf{S}^\top \mathbf{R} \mathbf{S}$, with $\mathbf{R}$ being a diagonal matrix of penalties over the prediction horizon N defined as (7.52).

$$\mathbf{R} = \begin{pmatrix} r & \cdots & 0 \\ \vdots & \ddots & \vdots \\ 0 & \cdots & r \end{pmatrix} \tag{7.52}$$

The constraints of the objective function are expressed as

$$\mathbf{p}^{\min} \leq \mathbf{p}^\star \leq \mathbf{p}^{\max} \tag{7.53a}$$

$$-\Delta\mathbf{p}^{\min} \leq \Delta\mathbf{p}^\star \leq \Delta\mathbf{p}^{\max} \tag{7.53b}$$

$$\mathbf{v}^{\min} - \mathbf{S} \leq \mathbf{v} \leq \mathbf{v}^{\max} + \mathbf{S} \tag{7.53c}$$

where $\mathbf{p}^{\min}$, $\mathbf{p}^{\max}$, $\Delta\mathbf{p}^{\min}$, $\Delta\mathbf{p}^{\max}$, $\mathbf{v}^{\min}$ and $\mathbf{v}^{\max}$ are column vectors with N elements of $p^{\min}$, $p^{\max}$, $\Delta p^{\min}$, $\Delta p^{\max}$, $v^{\min}$ and $v^{\max}$, respectively.

7.4.3   Results and discussion

The effectiveness of the proposed hierarchical control structure is validated on a nonlinear simulation model of the UC bank. The quality of the upper-level controller based on the MPC algorithm is compared with the response of 3 standard PID control approaches: i) virtual inertia + transient droop (Fig. 7.10, $K_d > 0$; $K_i > 0$; $T_w^d \gg T_w^i > 0$); ii) virtual inertia only ($K_d = 0$; $K_i > 0$; $T_w^i > 0$); iii) virtual inertia and droop with dynamic power limitation based on SoC estimation from [65] ($K_d > 0$; $K_i > 0$; $T_w^d = T_w^i = 0$)*. Four study cases are analysed: three different disturbance sizes with automatic generation control (AGC) enabled in the power system and one study case for the largest disturbance without AGC enabled. MPC and PID controller settings used in all simulation cases are given in Table 7.7.

The PID parameters were chosen such that the desired response to changes in system frequency is obtained while having gain and phase margins of an open-loop system (frequency input to converter power output). The MPC parameters were chosen to obtain a smooth and fast discharging profile. Closed-loop stability can be guaranteed by adopting standard approaches in the literature, i.e., by adding a terminal cost to the cost function or a terminal set [270]. It should be emphasised that the controller settings do not represent optimal settings for PID nor MPC controllers. Nonetheless, different tuning of the PID controller does not lead to significant differences in control performance. The main MPC controller tuning parameters are the prediction horizon N and the weighting factors q_y, q_u and r. Constraints are defined based on system limitations in the simulation setup. Namely, the maximum permissible UC bank voltage is 1000 V, while the minimum permissible UC bank voltage is 400 V. In addition, it is also necessary to include constraints on the control signals due to the physical limitations of the converter used to couple the UC bank with the grid.

The power system is modelled as an equivalent single machine described by an inertia (H), a damping (D) and a steam turbine with governor to simulate a power system dominated by thermal units (see [71]).

---

*$T_w^d = T_w^i = 0$ in this context denotes that the washout blocks are replaced with unity gain, not that they are zero; see [65] for details of the implementation we reproduced for the comparison.

†Parameters for 3 different PID layouts used for comparison are delimited with a slash: e.g., for virtual inertia control [layout ii)]: $K_d = 0$, $K_i = 150$, $\tau_w^d = 0$, $\tau_w^i = 1$.

‡Control signal constraints for fast discharge / slow charge are delimited with a slash, e.g., for fast discharge the constraints are: $p^{\max} = 10$ MW, $p^{\min} = -10$ MW, $\Delta p^{\max} = 0.1$ MW, $\Delta p^{\min} = -0.1$ MW.

Table 7.7: Controller settings for simulation comparison.

Controller	Settings	
PID[†]	$K_d = 20/0/20$	$K_i = 150/150/150$
	$T_w^d = 30/0/0$	$T_w^i = 1/1/0$
MPC[‡]	$N{=}50$	
	$p^{\max} = 10/0.5$ MW	$p^{\min} = -10/-0.5$ MW
	$\Delta p^{\max} = 0.1/0.1$ MW	$\Delta p^{\min} = -0.1/-0.1$ MW
	$v^{\max} = 1000$ V	$v^{\min} = 400$ V
	$q_y = 1000$	$q_u = 150$
	$r = 1500$	

7.4.3.1 Case 1—Disturbance exceeds the size of the UC bank

A 15 MW disturbance is applied at $t = 5$ s, causing a frequency drop. Results are shown in Fig. 7.34. It can be seen that both the PID and MPC controllers satisfy the physical constraints in terms of the UC bank permissible voltage range (Fig. 7.34 voltage) and power (Fig. 7.34 power, Fig. 7.34 current) limitations of the converter. However, the MPC controller has a significantly stronger power injection and discharges completely in a smooth manner around 25 s. Consequently, the frequency nadir is significantly reduced compared to PID controllers (Fig. 7.34 frequency): MPC-based control results in 0.07 Hz (-10%) smaller nadir compared to virtual inertia + (transient) droop controllers, and approximately 0.17 Hz (-23%) smaller nadir compared to only virtual inertia control. Moreover, the MPC controller visibly reduces the drop of frequency and it delays the occurrence of nadir. On the other hand, the initial ROCOF is worse for the MPC control (around 0.03 Hz/s higher initial ROCOF or $+25\%$, Fig. 7.34 RoCoF). However, this is due to the fact that all other PID controllers are sensitive to the frequency time derivative, while MPC operates only on the frequency deviation. This can potentially be mitigated by introducing a d/dt term in the proposed frequency controller. Nevertheless, around 7 s mark the RoCoF is quickly reduced by the MPC controller and after a few oscillations the frequency is stabilised. In terms of RoCoF, the behaviour between PID controllers is similar, while MPC controllers shows somewhat more oscillatory behaviour in this case. It can be seen that once the frequency is stabilised around the 80 s mark, the MPC controller switches to the slow charging mode and the SoC is slowly brought back to full charge, ready for the next disturbance (Fig. 7.34 SoE).
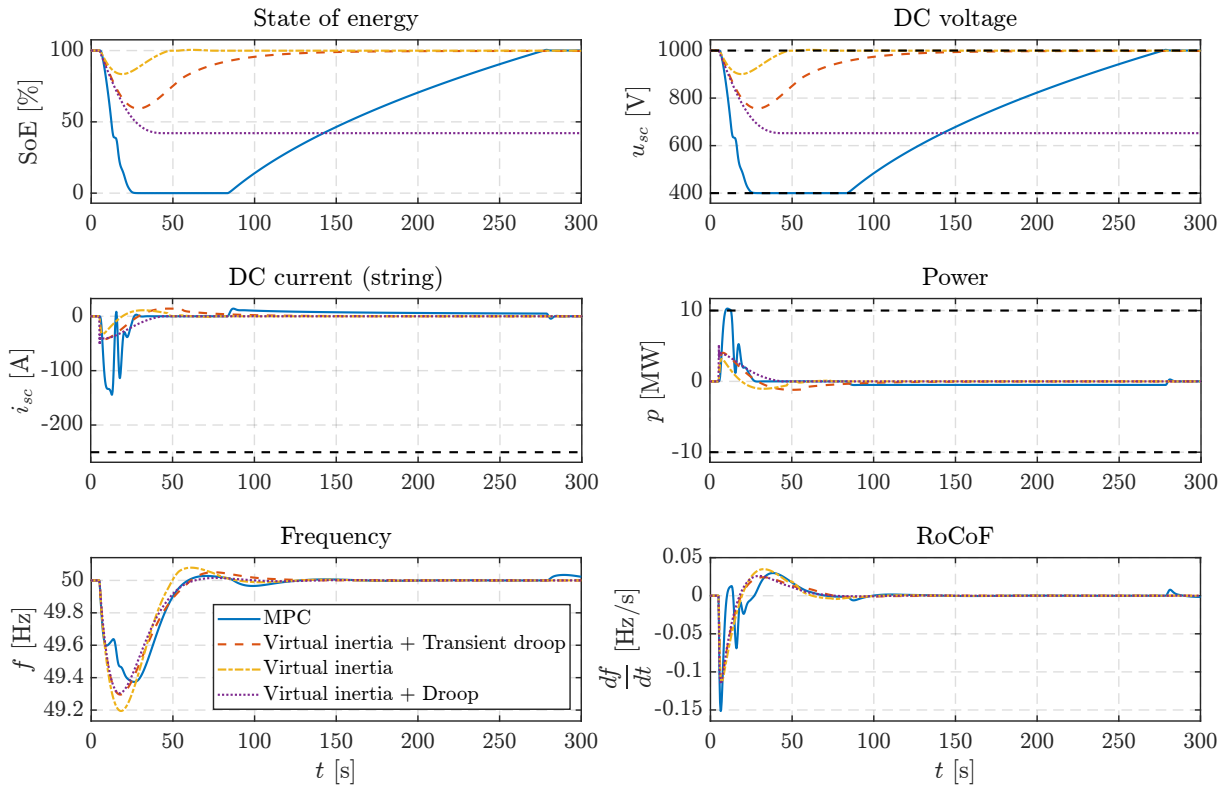
Figure 7.34: Results of study case 1.

7.4.3.2 Case 2—Disturbance is equal to the size of the UC bank

A 10 MW disturbance is applied at $t = 5$ s. Results are shown in Fig. 7.35. Both controllers satisfy the physical constraints in terms of the permissible voltage range (Fig. 7.35 voltage) and power (Fig. 7.35 power, Fig. 7.35 current) limitations of the converter. The MPC controller shows superior performance in terms of the frequency nadir (Fig. 7.35 frequency), resulting in a 0.1 Hz (-22%) lower nadir compared to virtual inertia + (transient) droop controllers, and in a 0.17 Hz (-32%) lower nadir compared to virtual inertia only. In this case, the performance of the MPC controller in terms of RoCoF is similar to conventional PID controllers (Fig. 7.35 RoCoF). The initial RoCoF is marginally worse in the case of the MPC controller (0.085 Hz/s compared to 0.08 Hz/s, or $+6\%$). On the other hand, the MPC controller strongly reduces the RoCoF around the 7 s mark, delaying the nadir and resulting in a generally smaller RoCoF afterwards. Slow charging starts around the 80 s mark and finishes around the 220 s mark, which does not violate the defined frequency controller limits, and the UC is slowly charged to 100% ready for the next disturbance (Fig. 7.35 SoE). It is interesting to note that both virtual inertia and virtual inertia + transient droop controllers charge back to 100% fairly quickly. This is due to the df/dt action with a low pass filter in their respective controllers which will charge the UC up to a certain point on the positive frequency gradient. On the other hand, the purely proportional part (droop) of the virtual inertia + droop controller will discharge the UC to a certain point, but it will not autonomously recharge the UC bank back to nominal voltage, a

problem solved by the proposed MPC controller.
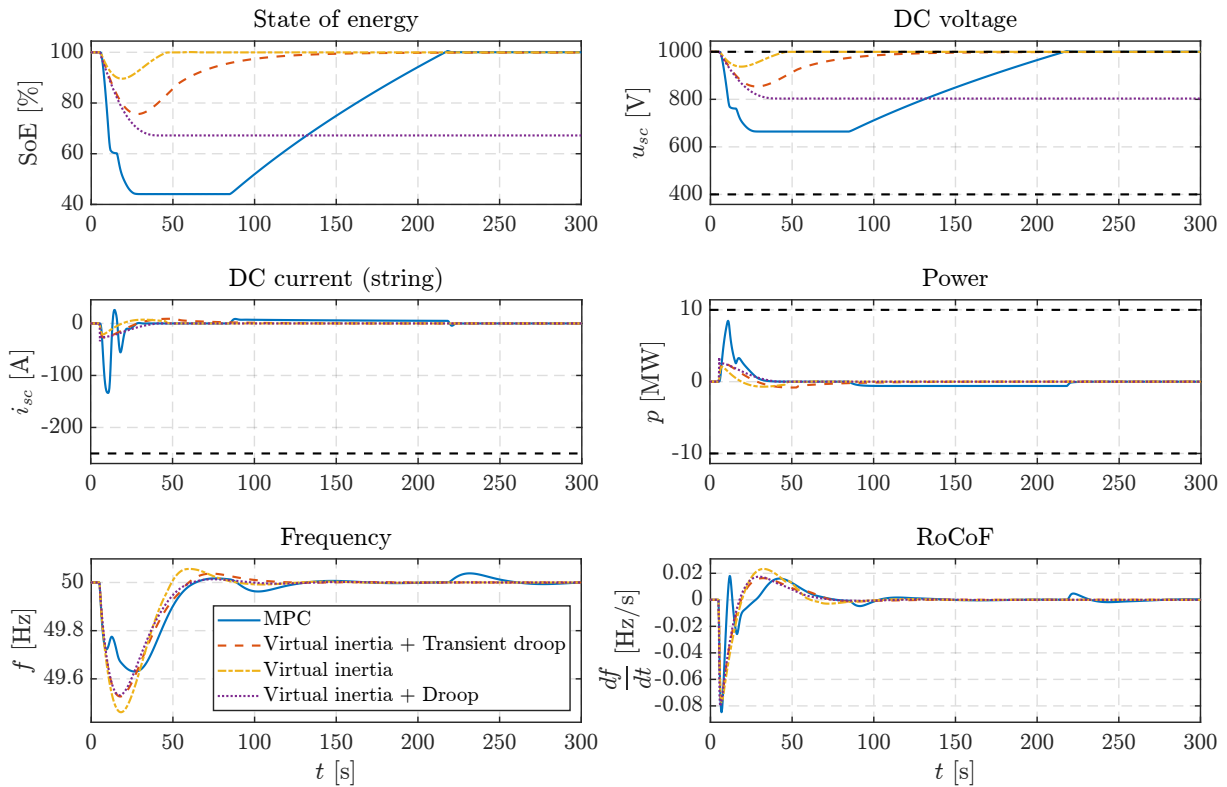
Figure 7.35: Results of study case 2.

7.4.3.3 Case 3—Disturbance is smaller than the size of UC bank

A 5 MW disturbance is applied at $t = 5$ s. Results are compared in Fig. 7.36. Once again, all controllers satisfy the physical constraints in terms of the permissible voltage range (Fig. 7.36 voltage) and power limitations of the converter (Fig. 7.36 power, Fig. 7.36 current). As in the previous cases, the MPC controller has a stronger response to system frequency excursion, resulting in a significantly lower frequency nadir: 0.19 Hz compared to 0.24 Hz (-20%) by virtual inertia + (transient) droop controllers and 0.19 Hz compared to 0.27 Hz by virtual inertia controllers (-30%). The initial RoCoF is marginally higher compared to the virtual inertia and virtual inertia + transient droop controllers ($+7\%$) and 19% higher than the virtual inertia + droop controller, however the MPC controller damps the ROCOF much more quickly than the conventional controllers.

7.4.4 Case 4—No automatic generation control

In this study case, AGC is disabled (integral term in the power system model is zero) to illustrate the benefits of the proposed MPC controller even further. In previous study cases, AGC will pick up the generation-load mismatch to drive the frequency error to zero, thus decreasing
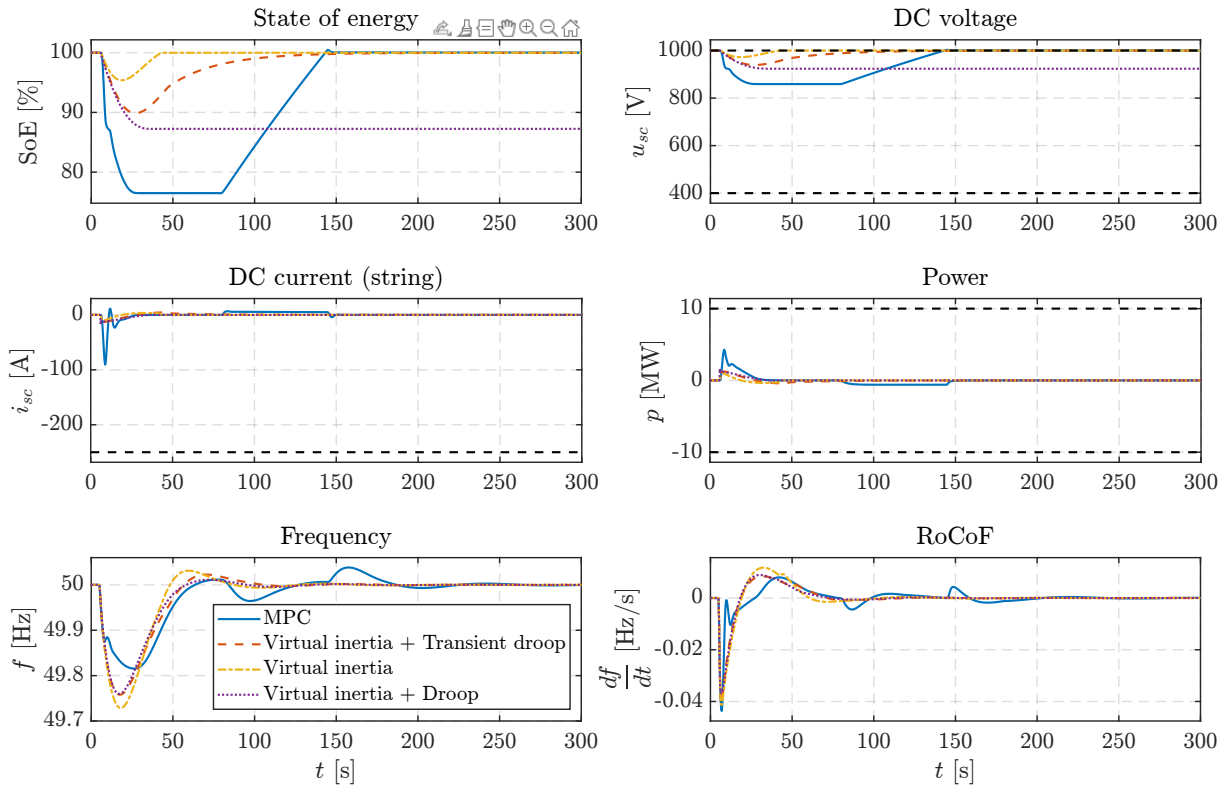
Figure 7.36: Results of study case 3.

the contribution of the ultracapacitor. Additionally, all PID controllers were tuned more aggressively so that the power injection to grid frequency change is greater (all gains were scaled by a factor of 4). A 15 MW disturbance is applied at $t = 5$ s. The MPC controller shows a better performance compared to traditional PID approaches (Fig. 7.37 frequency and Fig. 7.37 RoCoF). The virtual inertia + droop controller exhibits an oscillatory behaviour due to high gains (Fig. 7.37 power), while the problem of sudden power loss once the energy is depleted is visible in virtual inertia + transient droop and pure virtual inertia controllers, which causes an additional disturbance. In terms of the grid frequency response (Fig. 7.37 frequency and Fig. 7.37 RoCoF) it can be seen that initially the PID controllers have a stronger response, which results in a smaller frequency deviation compared to the MPC controller up to the 15 s mark. However, once the energy of the UC bank controlled by the PID controller is depleted, a secondary frequency drop occurs which reduces the frequency even further. On the other hand, the MPC controller brings the frequency to steady-state in a more controlled manner. Around the 28 s mark, the frequency drops to 49.0 Hz in the case of virtual inertia + (transient) droop controllers, while in the case of the MPC controller the frequency at this instant is 0.2 Hz higher, or 49.2 Hz, which is significant. Similarly, the initial RoCoF is higher for the MPC controller but is initially damped more quickly. On the other hand, a secondary frequency drop around the 20 s mark in cases with virtual inertia + (transient) droop controllers causes a 50% to 100% higher RoCoF than with the MPC controller at the same time instant.
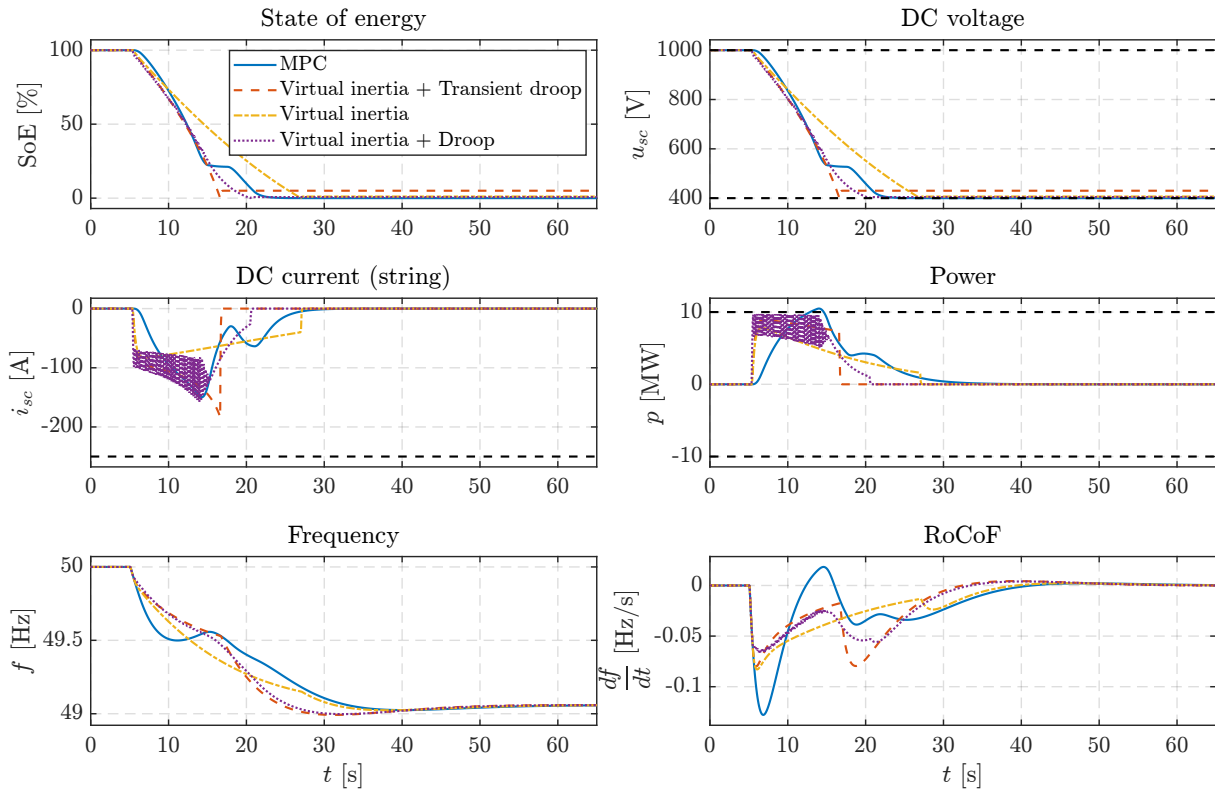
Figure 7.37: Results of study case 4.

7.5   Summary

An accurate supercapacitor bank model and associated control system has been presented for the use in power system dynamics simulations. Starting from the most detailed RC model of a supercapacitor cell, the model has been gradually reduced until arriving to the simplest representation which adequately describes the supercapacitor dynamics, as confirmed by simulation experiments. The proposed model is described with only 4 parameters which are easily obtained from the manufacturer's data sheet: capacitance at zero voltage, voltage-dependent capacitance, DC resistance and high-frequency resistance. The performance of the presented model compared to an ideal model has been tested in an IEEE 14-bus test system in frequency control and LVRT scenarios.

For frequency control, the ideal model does not always represent the nonlinear model adequately depending on the initial supercapacitor voltage and disturbance size. For an underfrequency event, a fully to partially charged supercapacitor may be adequately represented by an ideal model in terms of system frequency response, but nearing the minimum voltage limit the ideal model may yield overly optimistic or pessimistic results (a frequency nadir difference of over 0.1 Hz can be observed depending on the ideal capacitor capacitance value). Similar behaviour is observed for an overfrequency event. Generally, the equivalent series resistance and parallel RC groups of the first branch reduce the efficiency of the supercapacitor, while the voltage-dependent capacitance changes the amount of stored energy during charg-

ing/discharging and influences the charge/discharge rate. The observed mean relative error in the discharge time between the ideal and nonlinear model ranges from 9% to 16% for a 10% variable capacitance and between 10% and 25% for 40% variable capacitance, while the maximum observed relative error in discharge time can go up to 27% for 10% variable capacitance and 43% for 40% variable capacitance. The best ideal model for most observed cases for both types of presented control schemes is the ideal model with the capacitance set between minimum and average supercapacitor capacitance, with the ideal model with average capacitance being usually more accurate for high initial SoC. Losses and nonlinear voltage dynamics complicate representing a real supercapacitor with an ideal model for all operating points.

For low-voltage ride through, the impact of modelling is not significant and the ideal model will be adequate, although the undervoltage and overvoltage protective circuits may be triggered sooner for the nonlinear model.

Next, we have presented a simple iterative procedure for sizing a SESS which uses model simplifications for the approximation and the realistic model simulation for performance testing. We have also discussed the supercapacitor characteristics and how different modelling approaches have an impact on predicted SC performance:

- the variable capacitance of the SC cell can have significant impact on the amount of energy stored and therefore on the voltage dynamics during charging/discharging;
- SC cells are very low voltage devices which need to be connected in series for high-voltage application. However, this increases losses so a balance has to be achieved with parallel strings to reduce losses;
- constant power operation can be achieved only for a limited voltage range due to current limitations—around 75% of energy can be utilised between half the rated voltage and rated voltage.

Furthermore, we have presented a coordinated control framework of a wind turbine generator and a supercapacitor bank system in order to address the shortcomings of providing the virtual inertial response by WTG during low and high wind speeds. During low wind speeds, the virtual inertial response from WTG is disabled so the minimum rotor speed limit is not violated and the virtual inertial response is taken over by the supercapacitor bank. During high (above rated) wind speeds, the generator and converter are operating at rated power and additional available power is limited by the converter and/or generator thermal limits (maximum current limits). However, the shortcoming of the framework is that the wind farm is modelled as a lumped model of identical WTGs.

Finally, we have proposed an MPC control framework for operation optimisation of a supercapacitor bank for frequency control. The algorithm is based on a linear prediction model of an SC bank, while a nonlinear model of the SC bank is used as a simulation model to validate the algorithm. An autonomous frequency controller based on voltage reference trajectory and

MPC has been proposed and compared against three classical PID control layouts for different sizes of disturbances and with or without automatic generation control in the power system. The proposed controller autonomously and slowly recharges the UC bank in the steady-state by changing the MPC formulation constraints, while providing a strong and smooth response during disturbances in the grid. The main conclusion is that the MPC provides a smoother power decrease and improves the system frequency response (in terms of frequency deviations and RoCoF), since it takes into account constraints on the discharging power change rate. For the simulated study cases, the proposed MPC controller reduces the frequency nadir between 10%–30%. On the other hand, although the initial RoCoF for the MPC controller is 6% to 25% higher, it is damped more quickly. Moreover, this somewhat inferior behaviour is due to the fact that the used PID controllers all have the d/dt term, which reacts more strongly to RoCoF. Finally, aggressive tuning of PID controllers can lead to unwanted oscillatory behaviour and sudden loss of power once the energy is depleted, causing another frequency disturbance and a 50% to 100% higher RoCoF at that point. This behaviour has been mitigated with the use of the proposed MPC controller which behaves consistently across all simulated study cases. In addition, a smooth power decrease also prevents over-voltage issues, which can occur in the converter due to instantaneous current reduction. An additional strength of the introduced MPC algorithm is that it is based only on direct measurements (i.e. supercapacitor terminal voltage and power) and therefore state estimation is not necessary, making it less computationally intensive.

Chapter 8

On the feasibility of distributed control of energy storage assets for frequency regulation

8.1 Consensus-based primal-dual algorithm for optimal storage dispatch

In this section, we present the distributed control approach implemented in the laboratory. This employs a primal-dual algorithm solving a saddle-point problem for the optimised storage response. Laplacian averaging is embedded into the framework for a fully distributed storage control.

8.1.1 Problem formulation

The storage assets are managed as a VSP, whose control approach is derived based on a multiagent framework, where the storage units are regarded as intelligent agents with computational capabilities. We use a graph model to describe the communication network denoted as $\mathcal{G} = (\mathcal{N}, \mathcal{E})$, where the storage units are collected in the set $\mathcal{N}$; the edge set $\mathcal{E}$ represents the communication links among the storage agents. The characteristic matrices of the graph $\mathcal{G}$ can be obtained: the adjacency matrix $A \in \mathbb{R}^{N \times N}$ is defined as $A = \{a_{ij}\}$, whose elements $a_{ij} = 1$ if $(i, j) \in \mathcal{E}$, and 0 otherwise. Note that the pair (i, j) is ordered to represent a direct graph. Define the in-degree matrix $D = \mathbf{diag}\{d_i\} \in \mathbb{R}^{N \times N}$, with $d_i = \sum_{j \in \mathcal{N}_i} a_{ij}$, where $\mathcal{N}_i$ is the set of neighbours of agent i. The Laplacian matrix is defined as $L = \{l_{ij}\} = D - A$. We consider a leader-follower setup, where the leader nodes are collected in $\mathcal{N}_l \in \mathcal{N}$.

The provision of frequency restoration services is formulated as an optimisation problem

considering storage security constraints.

$$\min_{P_i} \sum_{i \in \mathcal{N}} \left[a_i(P_i)^2 + b_i P_i \right] + c(P^d)^2 \tag{8.1a}$$

$$P_i^{\min} \leq P_i \leq P_i^{\max} \tag{8.1b}$$

$$E_i^{\min} \leq E_i = E_i^0 - \frac{P_i}{\eta_i} \Delta t \leq E_i^{\max}, \forall i \tag{8.1c}$$

$$\sum_{i \in \mathcal{N}} P_i + P^d = P^*. \tag{8.1d}$$

The parameters (a_i, b_i) in (8.1a) give fixed storage costs in the objective function, where P^d captures the deviations from the aggregated-level reference and is penalised with the coefficient c. The discharging power of individual storage devices is P_i and bounded by $(P_i^{\min}, P_i^{\max})$ as in (8.1b). The constraint (8.1c) shows that the storage energy is limited by $(E_i^{\min}, E_i^{\max})$, and E_i^0 is the storage energy at the beginning of the dispatch period, whose length is Δt, the storage discharging efficiency is η_i; the VSP is scheduled to deliver the requested power P^* as described in (8.1d).

Remark 1 *The formulated optimisation problem* (8.1) *targets the automatic and manual frequency restoration reserve (aFRR, mFRR). In the European grid code [271], the full activation time of restoration reserves (secondary and tertiary reserves) must be under 12.5 minutes for mFRR [272] and 7.5 minutes (will be reduced to 5 minutes in the future) for (aFRR) [273]. Additionally, the maximum time to restore frequency to the nominal value is 15 minutes per the ENTSO-E grid code [274], while the standard frequency range is ± 50 mHz around the nominal value. Consequently, if a VSP participates in the mFRR and aFRR of a bulk power system, the activation of its scheduled reserves must be under the specified times (12.5/5 min). Moreover, if a VSP is used to restore the frequency to the nominal value, it must do so in under 15 minutes with a ± 50 mHz maximum steady-state error. In this regard, the optimisation problem has a static nature, considering a single full activation time (5 minutes) for storage devices. We mainly consider a discharging case for the underfrequency event; however, the framework works just as well for charging during overfrequency events.*

8.1.2 Distributed solution

Efficient coordinated control of many geographically dispersed units motivates the utilisation of advanced distributed control approaches, which provides the desired scalability and plug-and-play capabilities for large-scale storage integration [275]. Similar formulations in existing approaches [276, 277] do not involve a global slack variable P^d for power mismatch, which accounts for scenarios where the VSP cannot fulfil the requested power.

In this paper, we adopt an approach based on [278], which can handle a more general opti-misation problem with global and coupled local variables in the objective and constraints. The Lagrangian of the optimisation problem (8.1) is given first as

$$
\begin{aligned}
\phi(P_i, \cdots, P_N, P^d, z) = & \\
{\scriptstyle P_i \in \mathcal{X}_i, \forall i} \\
= \sum_{i \in \mathcal{N}} \left[a_i(P_i)^2 + b_i P_i \right] &+ c(P^d)^2 + z^T \left(\sum_{i \in \mathcal{N}} P_i + P^d - P^* \right) \\
= \sum_{i \in \mathcal{N}} \left[a_i(P_i)^2 + b_i P_i &+ c\frac{(P^d)^2}{N} + z^T \left(P_i + \frac{P^d}{N} - P_i^* \right) \right],
\end{aligned}
\tag{8.2}
$$

where we dualise the coupled constraint (8.1d) and represent the remaining local constrains as the feasible set $\mathcal{X}_i$, the dual variable is denoted as z, whose transpose is z^T. The knowledge of the VSP power reference by individual storage units is denoted as P_i^*, where $P_i^* = P^*/|\mathcal{N}_l|$ for the leader storage devices that have access to the VSP power reference and $P_i^* = 0$ for the non-leader nodes. The cardinality is defined as $|\mathcal{N}| = N$.

Strong duality holds for problem (8.1) since it is convex and satisfies Slater's condition [279]. Therefore, the solution of problem (8.1) can be obtained by solving a constrained convex-concave min-max problem whose optimal is the saddle point

$$
\begin{aligned}
\min_{\substack{P_i \in \mathcal{X}_i \\ P_i^d = P_j^d}} \max_{\substack{z_i = z_j \\ \forall i j \in \mathcal{E}}} \sum_{i \in \mathcal{N}} &\left[a_i(P_i)^2 + b_i(P_i) + c\frac{P_i^d}{N} \right. \\
&\left. + z_i^T \left(P_i + \frac{P_i^d}{N} - P_i^* \right) \right].
\end{aligned}
\tag{8.3}
$$

Here, the global variables P^d and z are replaced by their local copies P_i^d, z_i with the imposed consensus constraints $P_i^d = P_j^d, z_i = z_j, \forall (i,j) \in \mathcal{E}$. It can been proven [278] that the following dynamics with Laplacian averaging in (8.4b), (8.4c) solve the saddle-point problem (8.3)

$$
\hat{P}_{i,t+1} = P_{i,t} - \alpha_t g_{P_i}
\tag{8.4a}
$$

$$
\hat{P}_{i,t+1}^d = P_{i,t}^d - \sigma \sum_{j \in \mathcal{N}_i} l_{ij} P_{j,t}^d - \alpha_t g_{P_i^d}
\tag{8.4b}
$$

$$
\hat{z}_{i,t+1} = z_{i,t} - \sigma \sum_{j \in \mathcal{N}_i} l_{ij} z_{j,t} + \alpha_t g_{z_i}
\tag{8.4c}
$$

$$
(P_{i,t+1}, P_{i,t+1}^d, z_{i,t+1}) = \mathcal{P}_{\mathcal{X}_i}(\hat{P}_{i,t+1}, \hat{P}_{i,t+1}^d, \hat{z}_{i,t+1})
\tag{8.4d}
$$

where t is the time index, σ is the consensus step size, α_t is the learning rate, and

$$
g_{P_i} = \frac{\partial \phi}{\partial P_i}\big|_{P_{i,t}}, \qquad g_{P_i^d} = \frac{\partial \phi}{\partial P_i^d}\big|_{P_{i,t}^d}, \qquad g_{z_i} = \frac{\partial \phi}{\partial z_i}\big|_{z_{i,t}}
$$

are the subgradients evaluated at each operating point. The estimates of the primal and dual variables are $(\hat{P}_{i,t+1}, \hat{P}^d_{i,t+1}, \hat{z}_{i,t+1})$, and the projection into the feasible set is denoted as $\mathcal{P}_{\mathcal{X}_i}$, which are evaluated as $\mathcal{P}_{\mathcal{X}_i}(x) = \mathbf{arg}\min_{\hat{x} \in \mathcal{X}_i} ||\hat{x} - x||_2$.

The evolution of variables in (8.4) is called primal-dual dynamics [280] or the saddle-point dynamics, whose convergence can be established with Laplacian averaging [278]. With a suitable choice of the decreasing learning rates α_t, the saddle-point evaluation error

$$\phi(P_{i,t+1}, P^d_{i,t+1}, z_{i,t+1}) - \phi(P^*_i, P^{d*}_i, z^*_i), \forall i$$

decreases in proportion to $1/\sqrt{t}$, assuming the connectivity of the graph and boundness of the subgradients.

8.2 Experimental setup

The experimental setup has been developed at the University of Zagreb's Smart Grid Laboratory (SGLab) and is illustrated in Fig. 8.1a (highlighted in yellow). The laboratory-scale VSP consists of heterogeneous units: five 2.5 kW / 6 kWh Li-Ion residential battery energy storage systems (BESS) and a 20 kVA synchronous generator (SG) driven by a Pelton hydraulic turbine emulating a pumped-hydro storage. BESS and the hydraulic turbine-generator (HTG) are synchronised to the external power grid in the SGLab on a 400/230 V level. Since these are low-voltage/low-power devices, their voltage level and output power are scaled accordingly in the real-time simulator (Section 8.2.0.4). The experimental setup is shown in Fig. 8.1b. Relevant device data is given in Table 8.1.

Table 8.1: SGLab storage units parameters.

	Rated voltage [V]	$P_{\mathbf{max}}$ [kW]	$P_{\mathbf{min}}$ [kW]
HTG	380 (3ph, L-L, RMS)	11.8	1.0
BESS$_1$–BESS$_5$	230 (1ph, L-N, RMS)	2.3	-2.3

8.2.0.1 Controller setup

Each storage device has a dedicated programmable logic controller (PLC) in which the consensus-based distributed control algorithm has been implemented. The used PLCs are Siemens S7-1200 (for controlling the batteries) and S7-1500 (for controlling the HTG). These PLCs are external devices to the BESS, with which they communicate via MODBUS TCP; external meaning that the batteries have their own internal control system which is unknown, thus the batteries are a black-box that can receive external set-points. The HTG is completely controlled by the

274

(a) Block diagram   (b) Photo
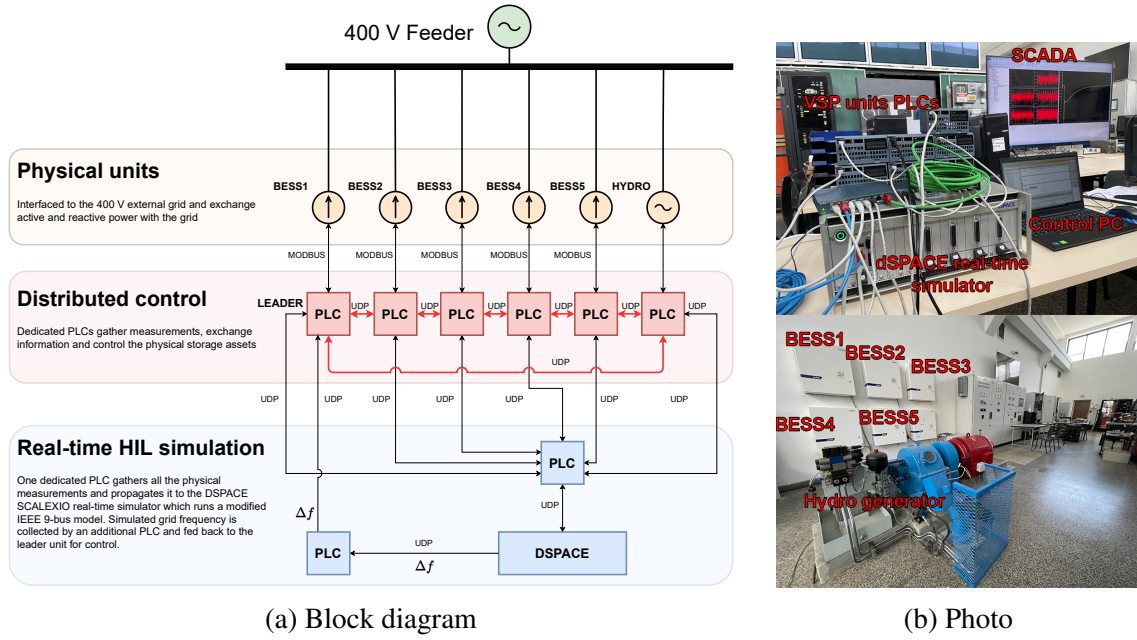
Figure 8.1: The experimental HIL setup in SGLab.

S7-1500 CPU with the corresponding modules, i.e., this PLC is the lowest level control for the HTG. These PLCs also gather active power measurements that are injected to the real-time simulator on a signal level.

The pseudo-code of the described multi-agent consensus distributed control framework implementation on each PLC of unit i is described by Algorithm 1. The PLC code runs in a loop, in which one iteration is also called a scan cycle. The length of the scan cycle depends on the complexity of the code and can vary from cycle to cycle as different functions are executed. To achieve algorithm execution at consistent time intervals, all code related to the VSP is wrapped inside what is called a *cyclic interrupt*, which will execute all the code inside every T milliseconds (e.g. 50 ms). The total convergence time depends on other factors such as communication delays in the system, which will be discussed in Section 8.3.

The PLC always communicates with its storage device and the real-time simulator (steps 1–4 of Algorithm 1) in order to propagate measurements. Once the preconditions are met, i.e., all communication lines are established (steps A–F of Algorithm 1) and the start time is reached ($t^{\text{local}} \geq t^{\text{start}}$), the VSP algorithm is started by each PLC which consists of send/receive commands in order to exchange states with neighbouring controllers (steps 5–8 of Algorithm 1). Then, the states P_i, z_i, P_i^d, t_i are updated (step 9 of Algorithm 1). Every time the states are updated, one iteration of the algorithm is considered to be executed, which also corresponds to one scan cycle of the PLC (time step t).

Once the new power set-point is calculated, it is sent to the internal (lower-level) controller of each unit. The lower-level controller of each unit is device-specific, but it is a PI controller which runs with its own cycle, which can range from several ms to several hundred ms. Prop-

agation of the power set-point to low-level controller essentially boils down to writing the new set-point value to a specific internal register which the lower-level PI controller periodically reads.

Algorithm 1 Distributed control framework PLC pseudo-code

Require: A. Storage device i communication established
Require: B. SCALEXIO PLC communication open
Require: C. Comm. towards Neighbours $j \in \mathcal{N}_i$ open (NAC_j)
Ensure: D. Parameters a_i, b_i, α_t, σ, $P_i^{\max}$, $P_i^{\min}$ are set
Ensure: E. Initialise states $z_{i,t}$, $P_{i,t}^d$ and $P_{i,t}$

    $z_{i,t} \leftarrow z_{i,0}$
    $P_{i,t}^d \leftarrow P_{i,0}^d$
    $P_{i,t} \leftarrow P_{i,0}$
    repeat every T_{cycle} ms
        1. Receive device i active power measurement $p_{i,t}$
        2. Send active power setpoint $P_{i,t}$ to device i
        3. Rec. Δf_t signal from SCALEXIO PLC   ▷ Leader
        4. Send $p_{i,t}$ signal to SCALEXIO PLC
        if NAC_y AND $t^{\text{local}} \geq t^{\text{start}}$ **then**
            5. Send $z_{i,t}$, $P_{i,t}^d$, t to Neighbours $j \in \mathcal{N}_i$
            6. Receive $z_{j,t}$, $P_{j,t}^d$, t from Neighbours $j \in \mathcal{N}_i$
            if $t_i = t_j$ **then**   ▷ Condition is optional (state sync)
                7. Update $P_{i,t+1}$, $z_{i,t+1}$, $P_{i,t+1}^d$, t
            end if
        end if
    until manually stopped

8.2.0.2 Communication setup

All the devices are connected in the local network via gigabit Ethernet switches. The distributed communication between storage PLCs is developed as a ring topology as shown in Fig. 8.1a (bold red lines), i.e., each agent communicates with two of its neighbours. The communication is based on UDP because it is connectionless and allows for much faster data exchange on the account that some packets may be dropped. The insights about the practical impact of communication setup will be further discussed in Section 8.3.

8.2.0.3 Real-time simulator setup

The real-time simulator is a dSPACE SCALEXIO platform which runs an EMT simulation of a modified IEEE 9-bus test system in real-time (Fig.8.1a and Fig. 8.2, refer to Section 8.2.0.4). Six active power measurement signals are sent to one central PLC (from here on out—SCALEXIO PLC, also a S7-1200 unit) which propagates this data to the SCALEXIO platform (highlighted in blue). Likewise, the grid frequency measurements from the simulation

model are collected by an additional PLC (due to the limitation on the number of simultaneous connections) and fed back to the leader PLC.

8.2.0.4 Modified IEEE 9-bus system and simulation setup

The test system is shown in Fig. 8.2. The six storage units from the SGLab are interfaced to the test grid through six three-phase dynamic loads controlled by an external signal. These are labelled as $BESS_1$–$BESS_5$ and HTG. Since the laboratory units are on kW scale, their measured active power signals are scaled by a factor of 1000 to obtain a MW level VSP before being injected into the grid through the controllable loads. An additional 20 MW PV plant is added to Bus 9 for simulating an instantaneous power mismatch by cloud covering. The rated power of the three SGs (SG_1–SG_3) is 247.5 MVA, 192 MVA and 128 MVA respectively. All are equipped with an IEEE T1 excitation system and a tandem compound steam turbine (single mass) with governor. All SGs have the same parameters (6 s inertia constant, 5% droop and ± 0.1 p.u./s rate limit on the governor). All other parameters have default values from the Simscape Power Systems library in MATLAB-Simulink so they are omitted for brevity. Loads L_A–L_C are modelled as constant PQ loads: 125 MW / 50 Mvar, 90 MW / 30 Mvar and 100 MW / 35 Mvar, respectively.

The model uses a discrete-type simulation which discretizes the three-phase electrical system in the time domain with a 100 μs fixed-step size, thus capturing the electromagnetic phenomena and simulating the behaviour of a real system as close as possible. An ODE1 solver (forward Euler method) is used.
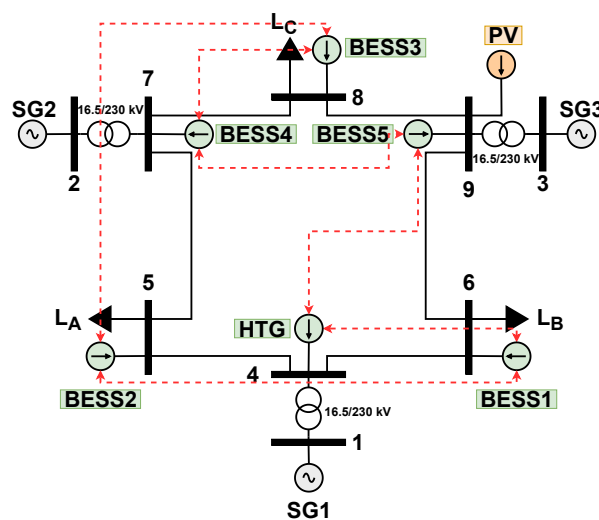
Figure 8.2: Modified IEEE 9-bus system (dashed lines are communication links).

8.3 Experimental results and discussion

The VSP secondary control capability will be analysed from the aspects of scheduled power activation time and the capability to restore the frequency to nominal value, while the VSP tertiary control capability will be analysed only from the aspect of scheduled power activation time. It will be shown that the consensus-based distributed control of VSP assets provides a combination of secondary and tertiary response, since the nominal frequency is attained with optimal resource allocation. To this end, the following four case studies are conducted:

- Case A: Analysis of controller scan cycle and communication time delay impact on control performance (Section 8.3.1)
- Case B-I: Reference tracking for secondary and tertiary reserves provision without state synchronisation (Section 8.3.2)
- Case B-II: Reference tracking for secondary and tertiary reserves provision with state synchronisation (Section 8.3.2)
- Case C: Frequency restoration service (FRS) by a VSP using distributed control (Section 8.3.3)

For secondary and tertiary reserve provision (Section 8.3.2), the most important requirement is to accurately converge to the scheduled power. The experimental results are compared to simulations of the VSP performance to provide insights into the difference between a practical implementation and an ideal desired behaviour. For frequency restoration (Section 8.3.3), the requirement is to drive the frequency inside the normal operational range within 15 minutes. The performance of providing frequency restoration service by a VSP is experimentally compared to the case when frequency restoration is provided centrally by a single unit.

Cost parameters (a, b) introduced in Section 8.1 generally describe the cost of operating a plant. These parameters take into account costs of fuel, personnel, maintenance, etc. Since there are no such costs associated with operating laboratory assets used for experimental validation, (a, b) are set to arbitrary values. These parameters only determine how the total power is divided among individual units and have no impact on the conclusions. All the used parameters are provided in Table 8.2.

8.3.1 Case A: Impact of controller scan cycles and (non)uniform time delays on distributed control performance

The controller scan cycle T_{cycle} determines the frequency of code execution. The communication time delay T_{delay} determines when the information that was sent by an agent is received by its neighbour.

Uniform time delay means that all agents have identical communication delays. In the context of discrete control systems, Fig. 8.3a shows that both the scan cycle and the time delay

Table 8.2: VSP parameters.

	$P_i^{\max}$ [W]	$P_i^{\min}$ [W]	a_i	b_i	σ	α_t
BESS$_1$			0.7431	0.0462		
BESS$_2$			0.3922	0.0971		
BESS$_3$	2300	0	0.5071	0.0657	0.2	0.1
BESS$_4$			0.6012	0.0213		
BESS$_5$			0.4501	0.0585		
HTG	11800	1000	0.4212	0.0324		

have the same effect as a time lag in continuous systems. Existence of uniform time delays does not impact the convergence accuracy, only settling time as all four cases converge to the set-point value of 10 MW. On the other hand, if every agent has a slightly different time delay, we are dealing with nonuniform time delays, illustrated by Fig. 8.3b for two examples defined by the mean value and standard deviation (5 ± 1 ms and 500 ± 104 ms, respectively). When the delay is small enough, the convergence accuracy is not significantly impacted, as shown by blue and yellow lines in Fig. 8.3b. However, if the communication delays are non-uniform and significant, the VSP converges to an erroneous value because each agent is using incorrect neighbouring states in the consensus protocol (orange and purple lines in Fig. 8.3b).

The following sections will show that the time delays are nonuniform in practice. That is because a simulation has a single global source of time reference. In reality, physically distributed units all have different local time definitions. This is not because time measuring is inaccurate, but because every unit is slightly different, or it started operating at a different global time, or it was impacted by a local disturbance not affecting other units. Therefore, time synchronisation is of utmost importance for application of DCS in frequency control.

(a) Uniform time delays

(b) Nonuniform time delays
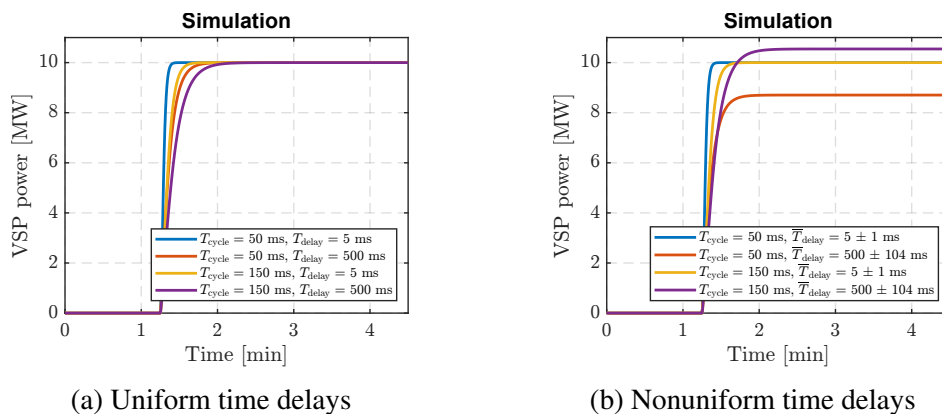
Figure 8.3: Case A—Impact of controller scan cycle and communication time delays.

8.3.2 Case B: Capability of VSP to provide tertiary and secondary reserves

8.3.2.1 Case B-I: no forced state synchronisation

Consider that the VSP is scheduled to activate $P^* = 10$ MW at $t \approx 1.25$ min. The cycle time of the distributed control algorithm is 50 ms. Results are shown in Fig. 8.4. The steady-state is reached within 2 minutes (Fig. 8.4a, Fig. 8.4c) thus satisfying the full activation time. However, the measured VSP power has a large steady-state error (1.8 MW or 18%) also confirmed by the simulation (Fig. 8.4b, Fig. 8.4d). The reason for the discrepancy between the simulation and the experiment is mostly caused by the existence of nonuniform time delays in the communication subsystem, as explained in Section 8.3.1, which presents the same scenario. In other words, the time delays itself are not an issue if they are all equal as this will only cause slower convergence of distributed control. In reality, however, each agent receives the information at different global time, which can cause convergence to an incorrect value.

Existing literature assumes that during each iteration of the algorithm, all states are perfectly exchanged and new states are precisely calculated, even with time delays. However, it cannot be guaranteed that all information packets will be received by every unit during every scan cycle of the controller and sometimes it takes several scan cycles for the information to be received. Therefore, the states of every agent and of its neighbours will go out of sync and this will increase error in the consensus. This is pronounced even in a relatively small communication network without much latency as reported in this paper, thus it would be even more pronounced in a utility scale network.

This uncovers a potential flaw of the distributed control approach based on multi-agent consensus: an error in any agent may propagate throughout the multi-agent system and accumulate. The cause of the error may range from a simple non-uniform communication delay to bugs during operation or malicious attacks. The latter is especially crucial if the VSP consists of units dispersed over large areas that communicate over the internet. The communication delay is a non-negligible factor when implementing a distributed algorithm and, special attention needs to be given to data exchange between controllers and error correction. Nevertheless, it has been theoretically proven that the effects of the communication delays on the distributed algorithms can be reduced or even eliminated when the communication delay is bounded, and efficient approaches are undertaken to design the communication network [281, 282]. Further research efforts will be focused on experimentally validating the theoretical findings.

Another factor that needs to be considered is the design choice of the communication protocol. We chose UDP because it is faster and connectionless (handshake between two devices is not necessary for the data transmission to start), which is inherently more suitable for a plug&play distributed control approach. However, the UDP is unreliable as packets may come

out of order and there is no error checking, which can contribute to error propagation. On the other hand, TCP/IP is more reliable and all information is received in correct order, but it is slower and a dropped connection will cause a timeout, blocking the execution of the next line of code, which is especially important in real-time applications. Based on the experimental results, UDP package loss was not found to have a significant impact on the steady-state power compared to the synchronisation issue.

(a) Laboratory units   (b) Simulated units

(c) Measured VSP total power   (d) Simulated VSP total power
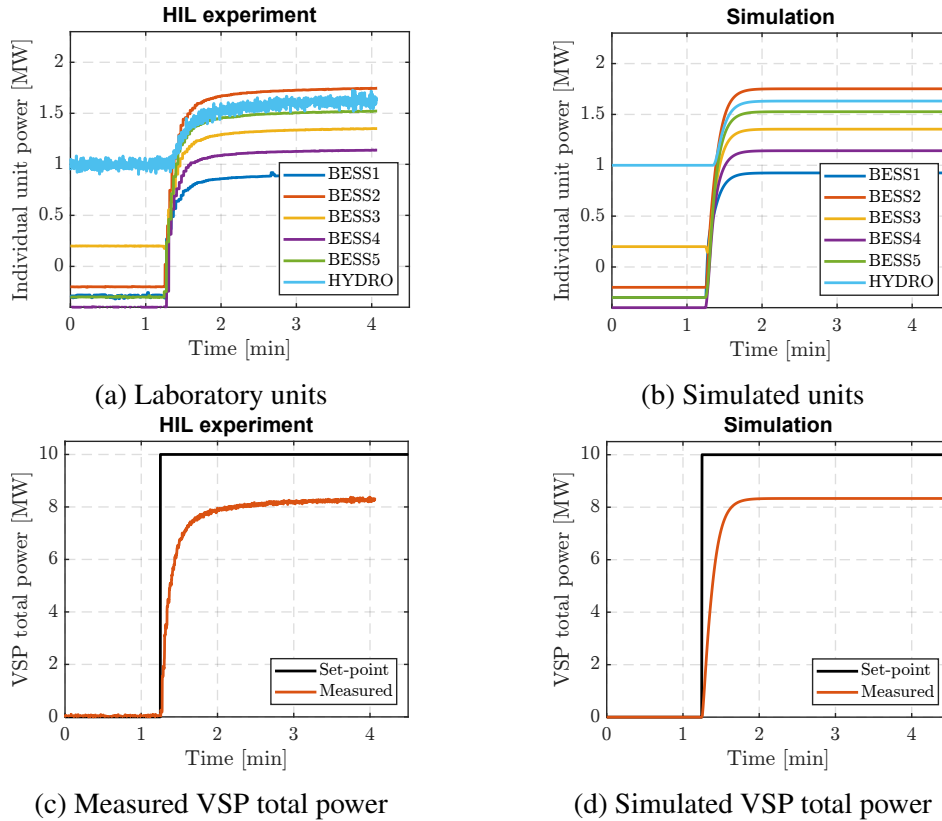
Figure 8.4: Case B-I—Measured and simulated results for reference tracking without state syncing.

8.3.2.2   Case B-II: with forced state synchronisation

With regard to the errors caused by non-uniform communication delays, one simple solution is to increase the cycle time of each iteration of the algorithm to ensure that all states are sent and received correctly. This cycle time should take into account the worst delays that are expected in the system. Furthermore, each agent should check that its timestamp is equal to the received timestamps of its neighbours. The next cycle of the algorithm is not executed until all the timestamps are equal. In this context, a timestamp may be a simple counter that is incremented at each iteration. This way, the states can be synchronised correctly and the steady-state error is reduced, and the whole system behaves as though it has uniform time delays (estimated to be ≈ 600 ms in this case, which normally depends on the slowest agent). It was noticed during the experiments that each agent should read the incoming data at a faster rate than it is sending

data. This guarantees that all the latest information has been received. Sending data too quickly may fill up the UDP socket buffers and the performance will be inevitably reduced with time. Additionally, sometimes the execution of the algorithm can even halt. Further inquiry into the best choice of the communication protocol between the agents is needed.

A simple state synchronisation method has been implemented in the unit PLCs: the cycle time of the algorithm has been increased from 50 ms to 150 ms and the timestamps (t_i) are compared each scan cycle (refer to Algorithm 1). Results are shown in Fig. 8.5. Both the full activation time and the accuracy of the reference tracking are now satisfied (< 1 min and $< 1\%$ error in steady-state, respectively: shown in Fig. 8.5a and Fig. 8.5b). Furthermore, the experimental results accurately correspond to the simulation (Fig. 8.5b, Fig. 8.5d).

(a) Laboratory units

(b) Simulated units

(c) Measured VSP total power

(d) Simulated VSP total power
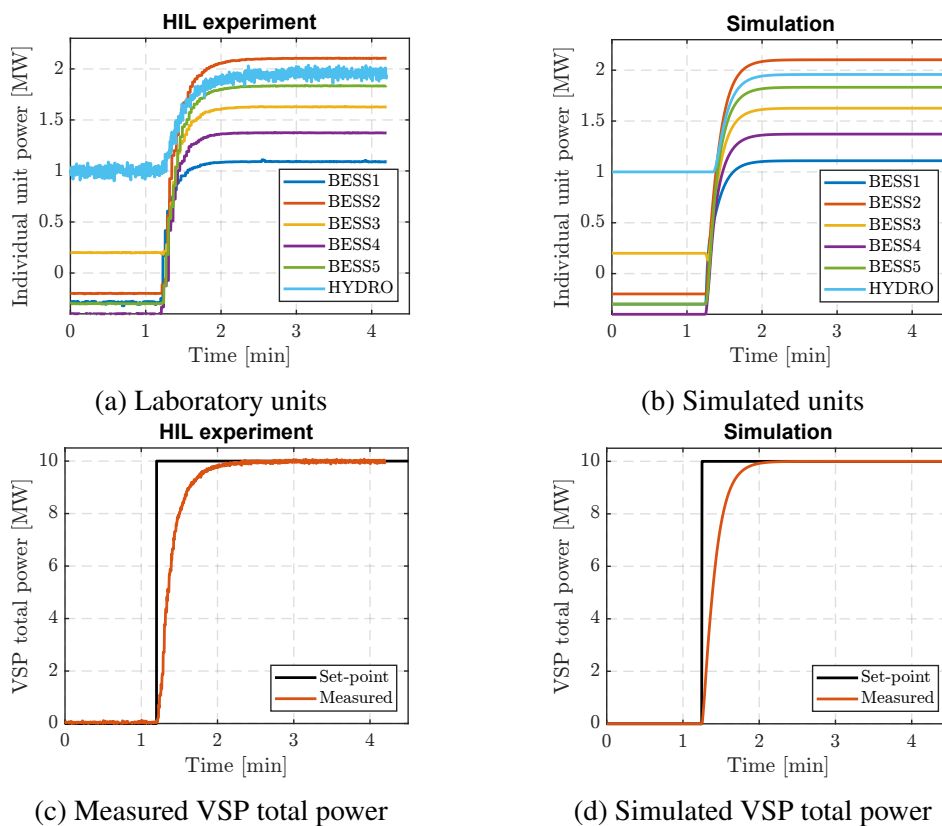
Figure 8.5: Case B-II—Measured and simulated results for reference tracking with state syncing.

In the HIL experiment in both cases (B-I and B-II) the convergence is reached in around 100 iterations and 1 min (Fig. 8.4c, Fig. 8.5c). This corresponds to an average cycle of 600 ms instead of 50 ms and 150 ms, respectively, confirmed by simulations (Fig. 8.4b, Fig. 8.5d). This is precisely because a send command in one scan cycle does not guarantee that the same information will be received by another agent in the same cycle. Therefore, the effective system time delay is significantly larger as the information propagates around the communication graph. This is why proper communication design is imperative for the distributed control to work properly.

Note that the agents update their respective power references under the assumption that the lower-level control will realise the set-point, thus there is no feedback of the measured power to the consensus algorithm of each unit to check if the total VSP setpoint has been indeed realised. Hence, the plug&play ability and fault tolerance were not validated in this paper.

8.3.3 Case C: Capability of VSP to restore the frequency of an isolated system

to nominal value The maximum time to restore the frequency to nominal value is 15 minutes per ENTSO-E grid code [274] while the standard frequency range is ± 50 mHz around nominal value. In this experiment, the cycle time of the distributed control algorithm is 50 ms without state synchronisation. This slightly differs from the bulk power system AGC, where a central controller updates the signal every 1–5 seconds. However, it will show whether the performance is adequate for faster cycle times, which is a more demanding case.

State synchronisation was not found to be as relevant in this scenario as the leader unit's states are dynamically updated each cycle based on the global frequency error signal, so any errors in the state propagation will eventually be corrected by the PI controller, assuming the system is stable. However, this way it cannot be guaranteed that the VSP cost is minimised in the steady-state (this can be mitigated by including state synchronisation constraints).

Distributed automatic secondary control is achieved by implementing a PI controller in the leader unit (8.5) which regulates the change in output power reference ΔP (in p.u.) with respect to the change in system frequency Δf (the frequency signal is obtained inside the real-time simulation via PLL model, in p.u. as well).

$$G(s) = \frac{\Delta P}{\Delta f} = 10 + \frac{0.2}{s} \tag{8.5}$$

To implement this PI regulator on the PLC, it was discretised with a 10 ms step using the Tustin method (8.6).

$$G(z) = \frac{\Delta P}{\Delta f} = \frac{10.001z - 9.999}{z - 1} \tag{8.6}$$

Finally, the change in power reference at the time step $t + 1$ is described by (8.7).

$$\Delta P_{t+1} = \Delta P_t + 10.001\Delta f_{t+1} - 9.999\Delta f_t \tag{8.7}$$

ΔP_{t+1} is added to the $P_{i,t+1}^d$ state of the leader ($i = L$):

$$\hat{P}_{L,t+1}^d = P_{L,t}^d - \sigma \sum_{j \in \mathcal{N}_i} l_{Lj} P_{j,t}^d - \alpha_t g_{P_L^d} - \Delta P_{t+1} P_L^{\max} \tag{8.8}$$

The PI parameters were chosen according to the operational handbook of the European network code [283,284]: the integration time constant is between 50 s and 200 s ($T_I = K_P/K_I = 10/0.2 = 50$ s), and the proportional gain should not be too large in order to avoid inducing network oscillations.

At $t \approx 1$ min, a there is a sudden 20 MW power reduction in the PV plant at Bus 9 due to cloud covering. Results are compared to the case when only BESS1 provides the frequency restoration service (FRS). Results are shown in Fig. 8.6.

(a) Using distributed control

(b) Using only 1 unit

(c) Grid frequency
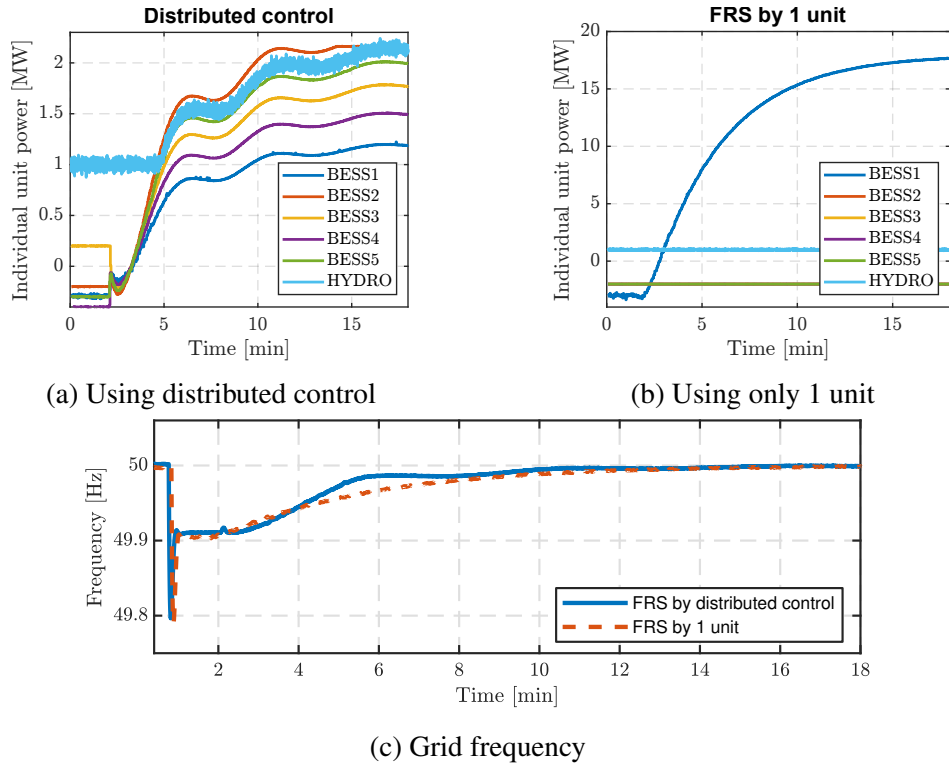
Figure 8.6: Case B—Experimental validation of frequency restoration service (FRS).

FRS starts at the $t \approx 2$ min mark and the frequency is restored to the nominal value in ≈ 10 minutes, thus satisfying the requirement of the 15 min maximum restoration time (Fig. 8.6c). The performance is similar compared to the case when only 1 unit performs the FRS in terms of restoration time (Fig. 8.6b). The reason why the battery shows a slow response, even though batteries are fast, is because the secondary controller (PI) was tuned conservatively as in a real system [283, 284]. Too aggressive tuning of the integral gain would increase oscillations and eventually destabilise the system. This effect is even more pronounced in the case of distributed control where additional delays between the agents due to data transmission also need to be considered. Therefore, more conservative tuning of the AGC controller due to stability reasons is reflected in a longer time needed to restore the frequency to the nominal value.

It can also be seen that the proposed framework reduces the steady-state frequency deviation more quickly between the 2 min mark and 6 min mark. However, the distributed approach does not seem to substantially outperform a centralised approach. The centralised approach ineffi-

ciently uses only one unit by not taking advantage of the decentralised assets. Nevertheless, the goal of this experiment was not to demonstrate that the proposed framework is superior in every way, but to investigate whether the distributed control for automatic frequency restoration is compliant with the grid code requirements, which it is. True superiority of the distributed control would come to light if hundreds of units were dispatched centrally, but this was not possible to emulate with the existing laboratory setup.

One noticeable difference is that visible power oscillations are present in the distributed control scenario (Fig. 8.6a) due to time delays in communication and control (as explained in the previous sections), and possibly also due to no explicit state synchronisation between the agents. The oscillations can also be related to the α_t and σ control parameters which can be tuned to achieve a less aggressive storage response. The parameters were tuned based on the satisfying response in offline simulations. Nevertheless, these oscillations were not reflected in the grid frequency since the size of the VSP is small compared to the size of the power system.

8.4   Summary

The distributed control framework based on a consensus algorithm for the provision of automatic and manual frequency restoration services was experimentally verified on a small-scale laboratory VSP consisting of 6 devices. Results show that VSP assets controlled using the proposed approach are compliant with the grid code requirements because the power reference tracking under 1 minute was achieved and the isolated system frequency can be restored under 15 minutes. It was experimentally shown that the distributed control can achieve optimal dispatching of the VSP portfolio in a computationally efficient way, while still satisfying the requirements placed upon the aggregated plant. Therefore, distributed control allows for secondary and tertiary control to happen on the same timescale, assuming correct state synchronisation.

The main challenges identified during the laboratory validation were issues with erroneous states being propagated between the agents which can cause oscillations and/or inaccuracy in reference tracking due to non-uniform time delays. Thus, making the consensus algorithms robust to faults and errors is crucial for grid-compliance. State synchronisation, global time consensus or the existence of a global time reference ensures accurate operation of the consensus algorithm. Even a very rudimentary state synchronisation scheme can achieve the scheduled power under 1 minute, which is well under the maximum full activation time of secondary and tertiary reserves. The choice of the most suitable communication protocol requires further research.

Chapter 9

Concluding remarks and future work

In this thesis, power system frequency dynamics were explored in the presence of converter-interfaced devices. The main goal was to revisit the applicability of low-order system frequency response (SFR) models in converter-dominated power systems, challenge existing assumptions and propose solutions that can extend the SFR model applicability range. The main motivation behind the research is the fact that certain parts of converter control happen in the electromagnetic transient (EMT) time scale and may adversely interact with the power grid and other sources. Although frequency control traditionally happens on a slower time scale than EMT, new fast frequency control services from converters may shift it to an extent towards the EMT scale.

In Chapter 2, it was shown that phasor-domain simulation (RMS) can still adequately capture frequency oscillations up to 200 Hz under the requirement that the integration time step is adequately reduced (obeying the Nyquist criterion). For higher frequency phenomena, line dynamics play into account and the RMS model loses accuracy. Nevertheless, even if the bandwidth of frequency control increases several times from what it is today, the existing simulation tools should still be adequate. However, the drawback of the conducted studies is that an ideal controllable voltage source supplying a passive load was used, thus neglecting more possible complex interactions between converters, control systems and machines.

In Chapter 3, different common converter control systems and synchronisation approaches were modelled and discussed in terms of similarities and differences between them. It was explained that the first-order transfer function representation of converters originates from tuning the current control loop based on the impedance between the converter and the grid, which is prone to change under different grid conditions. Simplified converter models for SFR studies were derived based on converter power balance equations.

In Chapter 4, first the system frequency dynamics of conventional systems were explained, along with the aggregated machine representation that is an SFR model. The impacts of power system stabilizers, induction and synchronous motors were analysed and analytical models were

derived. The SFR model was then extended to include converter dynamics. Simulations with up to 90% penetration of grid-following converters were conducted for two types of converter control designs. It was shown that neglecting phase-locked loop (PLL) dynamics when converter share was > 40% will cause inaccuracies in the system frequency estimated by the conventional SFR model. The proposed SFR model with included PLL dynamics shows improved accuracy, however, for very high penetration levels (> 80%) the accuracy is somewhat reduced. Nevertheless, the inaccuracy was on the conservative side (results reported by the SFR model were worse than results from the EMT/RMS models) indicating that there is more inherent damping in the system than captured by the SFR model. Simulations up to 100% penetration of grid-forming converters were conducted for three different control designs. The SFR model of a virtual synchronous machine was accurate for all converter penetration levels, while the SFR model of indirect matching scheme exhibited a more damped behaviour than the EMT model when there is a mix of synchronous machines and converters, but the accuracy wasn't significantly affected. On the other hand, for 100% penetration it was as accurate as the EMT model in estimating the system frequency. The ViSynC scheme which emulates the swing equation in the DC link controller had the worst performance in arresting grid frequency, and the derived SFR model was inaccurate for penetration levels > 50%. In all simulated cases, the SFR model was compared against the full EMT model of the benchmark grid. Moreover, the accuracy of the RMS model was compared against the EMT model as well, and the results have shown that RMS modelling is still very accurate for simulating system frequency dynamics, even for very high converter penetration levels. However, it was shown that PLL can cause frequency instability which is captured by the EMT simulation, but not by the RMS simulation. The drawbacks of the conducted studies are (i) the dynamics of the converter-interfaced "prime mover" were neglected, i.e., they were replaced by a controllable power source so any distinction between, e.g., wind, solar PV or energy storage was not captured; and (ii) the benchmark model was well-interconnected and the grid impedance was relatively low so the effect of varying grid strength or topology was not analysed. Additionally, all lines were modelled with π-sections so any additional frequency dependency was not taken into account.

In Chapter 5, the drawback of not considering "prime mover" dynamics in Chapter 4 was addressed on an example of a grid-following variable-speed wind turbine generator. An analytical SFR model was derived for various operating conditions and it was shown that the conventional assumption of wind turbine dynamics decoupled from the grid does not hold in the context of frequency support. By operating on a maximum power point, modulating the power reference through virtual inertia control causes a turbine speed reduction which consequently reduces the power output. Furthermore, droop control or above-rated wind speed operation introduces pitch control dynamics into the loop, which has an impact on power output dynamics. It was shown by comparison to a full-order RMS model that representing wind turbine generators in

SFR studies with a first order converter transfer function is not adequate and results in overly optimistic system frequency dynamics. On the other hand, the proposed SFR models are more accurate. However, high nonlinearity of a wind turbine system makes the SFR model accurate for very small disturbances and the number of required transfer function parameters is significant if the pitch control system is active.

In Chapter 6, a unified system frequency response model was presented based on the analysis from previous chapters. It was shown that the effect of virtual inertia from PLL-based converters is not instantaneous due to the time lag of frequency estimation and filtering. On the other hand, the inertia of grid-forming converters can be considered instantaneous under the assumption of a small discretisation time step and a not too large power filter time constant (e.g., < 10 ms). That means that the grid-forming inertia can be algebraically added to the synchronous inertia without losing accuracy, as illustrated in Chapter 4. Moreover, it was illustrated how the reduction of system inertia is not necessarily important from a purely frequency stability perspective, since it can be compensated by faster acting devices. The relationship between inertia, droop and the system time constant was explored here analytically: a decrease of inertia increases the damping of system modes, as well as the natural frequency, but it does not shift the system poles towards the right half-plane. However, a reduction of inertia also results in a RoCoF increase which is a protection triggering signal. Still, it is measured over a specific time window, so any instantaneous effects of reduced inertia are attenuated. Systems with very low inertia, but with a very small time constant will have a large instantaneous RoCoF which will quickly diminish. Therefore, by appropriately increasing the measuring window, the RoCoF relays will not be triggered prematurely, but pushing these limits and the effects it can have on the equipment requires further research.

Numerical simulations identified potential instability regions due to a combination of PLL bandwidth, droop and system inertia. Generally, a low PLL bandwidth with low inertia and small droop can result in frequency instability. The effect of additional frequency filtering for inertia emulation on frequency dynamics has been explored. It was shown that virtual inertia from grid-following units cannot replace the synchronous inertia with the same efficacy and can even result in stronger oscillations. The provision of virtual inertia by wind turbine generators can even cause frequency instability in low-inertia scenarios. There are certain equivalences between different grid-forming designs, but the practical limitation is the DC link voltage stability. Emulating a synchronous machine using inertia constants in the order of seconds requires fast independent DC voltage balancing and a fast-acting energy source (e.g., a battery). Matching the emulated inertia to DC link dynamics inherently means that the emulated inertia needs to be very small and the damping high in order to preserve DC voltage stability. However, this causes a large initial RoCoF as mentioned previously. Other grid-forming schemes such as ViSynC are not effective in standalone operation for frequency stabilisation and require an existence of

a strong external grid.

In Chapter 7, it was concluded that an ideal capacitor model can accurately represent the nonlinear supercapacitor dynamics in frequency control studies if the disturbance is small enough, i.e., if the required energy from the ideal model is less than the minimum of stored energy in the ideal and realistic models. In fault ride through studies, the supercapacitor model had no significant effect on the results. It was also concluded that if using a constant capacitance representation, at least the equivalent series resistance should be considered due to losses. Furthermore, a simple coordination algorithm between a supercapacitor and a wind turbine generator was proposed that can compensate for the limitations of the wind turbine in providing the inertial response during low and high wind speeds. Finally, a novel model predictive control algorithm based on frequency-DC voltage droop was shown to be an effective alternative to standard proportional-derivative control in maximizing the response to frequency disturbances and smooth charging/discharging of the supercapacitor bank.

In Chapter 8, the feasibility of utilizing distributed consensus control for secondary and tertiary frequency regulation was experimentally proven. However, it was shown that such a control is very sensitive to nonuniform time delays. Robust state synchronisation is imperative for practical applications in order to guarantee the accurate convergence to the set-point.

To summarise, it has been shown that frequency dynamics will become increasingly complicated with the increase of converter-interfaced devices. Conventional assumptions of almighty and fast converters will not be appropriate anymore as system inertia decreases. The main bottleneck of grid-following converters is the phase-locked loop or any other frequency estimation device, while for the grid-forming design, DC voltage stability is the main limitation. Regardless of the type of control, dynamics of the energy conversion system behind the converter become coupled to the grid behaviour and need to be considered in order to have the complete picture of the power balance (as illustrated in the wind turbine example). In the end, here are some directions for further research:

- analysing and quantifying the impact of grid impedance and controller tuning on converter performance;
- analysing the impact of different converter control approaches to system frequency regulation considering specific device dynamics (wind turbine, solar PV panel, energy storage, HVDC, etc.) and identifying the limitations to the provision of frequency control services under DC voltage stability constraints and device stability constraints;
- developing faster and more robust grid frequency estimators;
- further researching the developed system frequency response models to improve the accuracy of grid frequency estimation depending on the converter control design;
- more experimental work in identifying and designing robust communication protocols for consensus control of geographically dispersed energy storage assets.

Appendix A

Two-machine system parameters

The parameters of the test system used in Section 5.3 are listed below.

Wind turbine and shaft parameters: nominal/base power: 2 MVA; rotor radius: 37.5 m; gearbox ratio: 87; nominal wind speed: 12 m/s; turbine inertia constant: 4.33 s; shaft-stiffness: 0.46 p.u./el. rad.; shaft-damping: 0 p.u.

DFIG parameters: stator voltage: 690 V (line-to-line, RMS); rated apparent power: 2.28 MVA; frequency: 50 Hz; number of pole-pairs: 2; stator resistance/reactance: 0.01/0.1 p.u.; rotor resistance/reactance (referred to stator): 0.01/0.1 p.u.; magnetizing reactance: 3.5 p.u.; inertia constant: 0.6 s; DC capacitor: 10 mF.

RSC parameters: outer control loop: $K_p = 4$, $K_i = 10$; inner control loop: $K_p = 1$, $K_i = 100$.

GSC parameters: apparent power: 0.8 MVA; rated AC voltage:0.69 kV; rated DC voltage: 1.5 kV; DC voltage control loop: $K_p = 8$, $K_i = 40$; inner control loop: $K_p = 1$, $K_i = 100$.

Line-side filter: apparent power: 2 MVA; short-circuit voltage: 10%.

PLL parameters: $K_p = 50$, $K_i = 150$.

Pitch angle controller parameters: $K_p = 150$, $K_i = 25$; servomechanism time constant: 0.3 s; max. rate-of-change-of-pitch: ± 10 deg/s.

Auxilliary frequency controller parameters: $T_v = 10$; $T_f = 1$ s; $R^{-1} = 0$.

Synchronous generator parameters: Apparent power: 75 MVA; nominal voltage: 20 kV (line-to-line, RMS); Inertia constant: 3 s; stator resistance/reactance: 0.05/0.1 p.u.; synchronous reactance x_d/x_q: 1.5/1.5 p.u.; transient reactance x'_d/x'_q: 0.256/0.3 p.u.

AVR parameters (IEEET1): default parameters in DIgSILENT PowerFactory.

Turbine-governor (TGOV1) parameters: high-pressure fraction F_H: 0.3, reheat time constant T_r: 8 s; droop: 5 %; governor time constant T_g: 0.3 s.

0.69/20 kV transformer parameters: nominal power: 100 MVA; short-circuit voltage: 10%; copper losses: 500 kW.

20/220 kV transformer parameters: nominal power: 3 MVA; LV/HV voltage ratio: 0.69/20 kV; short-circuit voltage: 10%; copper losses: 30 kW.

Overhead line parameters: rated voltage: 220 kV; rated current: 0.4 kA; resistance: 0.05 Ω/km; reactance: 0.488 Ω/km; length: 10 km.

Appendix B

Supercapacitor bank parameters

The parameters of the test system used in Section 7.1 are listed below.

$n_s = 370$, $n_p = 400$

Bank rated power: 100 MW

$C_{\max} \approx 1000$ F, $R_{dc} = 0.5$ mΩ, $R_s = 0.25$ mΩ

$I_{\mathrm{ch}}^{\max} / I_{\mathrm{dch}}^{\max} = \pm 615 A$

$U_{\mathrm{ch}}^{\max} = 2.71$ V, $U_{\mathrm{ch}}^{\mathrm{start}} = 2.4$ V, $U_{\mathrm{dch}}^{\min} = 1.1$ V, $U_{\mathrm{dch}}^{\mathrm{start}} = 1.4$ V

$\tau_c = 50$ ms, $K_i = 150$ p.u., $K_d = 100$ p.u., $\tau_w^i = 1$ s, $\tau_w^d = 30$ s

$K_p^d = K_p^q = 1$ p.u., $K_i^d = K_i^q = 100$ p.u.

Bibliography

[1] F. Milano, F. Dorfler, G. Hug, D. J. Hill, and G. Verbic, "Foundations and Challenges of Low-Inertia Systems," in *2018 Power Systems Computation Conference (PSCC)*. IEEE, jun 2018, pp. 1–25. [Online]. Available: https://ieeexplore.ieee.org/document/8450880/

[2] Y. Ji, W. He, S. Cheng, J. Kurths, and M. Zhan, "Dynamic Network Characteristics of Power-electronics-based Power Systems," *Scientific Reports 2020 10:1*, vol. 10, no. 1, pp. 1–16, jun 2020. [Online]. Available: https://www.nature.com/articles/s41598-020-66635-0

[3] M. Paolone, T. Gaunt, X. Guillaud, M. Liserre, S. Meliopoulos *et al.*, "Fundamentals of power systems modelling in the presence of converter-interfaced generation," *Electric Power Systems Research*, vol. 189, p. 106811, dec 2020.

[4] N. Holjevac, T. Baškarad, J. Đaković, M. Krpan, M. Zidar *et al.*, "Challenges of High Renewable Energy Sources Integration in Power Systems—The Case of Croatia," *Energies 2021, Vol. 14, Page 1047*, vol. 14, no. 4, p. 1047, feb 2021. [Online]. Available: https://www.mdpi.com/1996-1073/14/4/1047/htmhttps://www.mdpi.com/1996-1073/14/4/1047

[5] T. Ackermann, T. Prevost, V. Vittal, A. J. Roscoe, J. Matevosyan *et al.*, "Paving the Way: A Future Without Inertia Is Closer Than You Think," *IEEE Power and Energy Magazine*, vol. 15, no. 6, pp. 61–69, 2017.

[6] U. Markovic, O. Stanojev, P. Aristidou, E. Vrettos, D. S. Callaway *et al.*, "Understanding Small-Signal Stability of Low-Inertia Systems," *IEEE Transactions on Power Systems*, vol. 36, no. 5, pp. 3997–4017, 2021. [Online]. Available: https://ieeexplore.ieee.org/document/9361257/

[7] J. Rocabert, A. Luna, F. Blaabjerg, and P. Rodríguez, "Control of power converters in AC microgrids," *IEEE Transactions on Power Electronics*, vol. 27, no. 11, pp. 4734–4749, 2012.

[8] R. Rosso, X. Wang, M. Liserre, X. Lu, and S. Engelken, "Grid-Forming Converters: Control Approaches, Grid-Synchronization, and Future Trends—A Review," *IEEE Open Journal of Industry Applications*, vol. 2, pp. 93–109, apr 2021.

[9] A. Tayyebi, F. Dörfler, F. Kupzog, Z. Miletic, and W. Hribernik, "Grid-Forming Converters – Inevitability, Control Strategies and Challenges in Future Grid Applications," in *CIRED 2018 Ljubljana Workshop on Microgrids and Local Energy Communities*, Ljubljana, 2018, pp. 1–5.

[10] B. Barac, M. Krpan, T. Capuder, and I. Kuzle, "Modeling and Initialization of a Virtual Synchronous Machine for Power System Fundamental Frequency Simulations," *IEEE Access*, vol. 9, pp. 160 116–160 134, 2021.

[11] P. Kundur, J. Paserba, V. Ajjarapu, G. Andersson, A. Bose *et al.*, "Definition and Classification of Power System Stability IEEE/CIGRE Joint Task Force on Stability Terms and Definitions," *IEEE Transactions on Power Systems*, vol. 19, no. 3, pp. 1387–1401, aug 2004. [Online]. Available: http://ieeexplore.ieee.org/document/1318675/

[12] N. Hatziargyriou, J. V. Milanovic, C. Rahmann, V. Ajjarapu, C. Canizares *et al.*, "Definition and Classification of Power System Stability – Revisited & Extended," *IEEE Transactions on Power Systems*, vol. 34, no. 4, pp. 3271–3281, 2021. [Online]. Available: https://ieeexplore.ieee.org/document/9286772/

[13] A. Yazdani and R. Iravani, *Voltage-sourced converters in power systems: modeling, control, and applications.* John Wiley & Sons, 2010.

[14] P. Tielens and D. Van Hertem, "The relevance of inertia in power systems," *Renewable and Sustainable Energy Reviews*, vol. 55, pp. 999–1009, mar 2016. [Online]. Available: https://www.sciencedirect.com/science/article/pii/S136403211501268X

[15] G. A. Munoz-Hernandez, D. I. Jones *et al.*, *Modelling and controlling hydropower plants.* Springer Science & Business Media, 2012.

[16] J. Machowski, Z. Lubosny, J. W. Bialek, and J. R. Bumby, *Power system dynamics: stability and control*, 3rd ed. John Wiley & Sons, 2020.

[17] C. K. Aravind, B. Indu Rani, C. Manickam, J. M. Guerrero, S. I. Ganesan *et al.*, "Performance evaluation of type-3 plls under wide variation in input voltage and frequency," *IEEE Journal of Emerging and Selected Topics in Power Electronics*, vol. 5, no. 3, pp. 971–981, 2017.

[18] "WINDLIPS project," https://windlips.com/, [Online; accessed 21-April-2022].

[19] "CROSSBOW project," http://http://crossbowproject.eu, [Online; accessed 21-April-2022].

Bibliography

[20] P. Anderson and M. Mirheydar, "A low-order system frequency response model," *IEEE Transactions on Power Systems*, vol. 5, no. 3, pp. 720–729, 1990.

[21] "Smart Grid Laboratory," https://sglab.fer.hr/, accessed: 2022-02-19.

[22] Powersystems UK, "National Grid ESO debuts new fast frequency service," https://www.powersystemsuk.co.uk/news/national-grid-eso-launches-fast-frequency-response-service/, 2020, [Online; accessed 21-April-2022].

[23] National Grid, "Product Roadmap For Frequency Response and Reserve," https://www.nationalgrideso.com/sites/eso/files/documents/Product%20Roadmap%20for%20Frequency%20Response%20and%20Reserve.pdf, 2017, [Online; accessed 21-April-2022].

[24] P. Tielens, "Operation and control of power systems with low synchronous inertia," Ph.D. dissertation, KU Leuven, 2017.

[25] U. Marković, "Towards reliable operation of converter-dominated power systems: dynamics, optimization and control," Ph.D. dissertation, ETH Zürich, 2020.

[26] I. Kuzle, T. Tomisa, and S. Tesnjak, "A mathematical model for studying power system frequency changes," in *2004 IEEE Africon. 7th Africon Conference in Africa (IEEE Cat. No.04CH37590)*. IEEE, 2004, pp. 761–764. [Online]. Available: http://ieeexplore.ieee.org/document/1406786/

[27] L. Gao, J. Xia, and Y. Dai, "Analysis of power system frequency responses with hydro turbines incorporating load shedding," in *2010 5th IEEE Conference on Industrial Electronics and Applications*. IEEE, 6 2010, pp. 893–897. [Online]. Available: http://ieeexplore.ieee.org/document/5515638/

[28] M. Krpan and I. Kuzle, "The mathematical model of a wind power plant and a gas power plant," *Journal of Energy*, vol. 66, pp. 69–86, 2017. [Online]. Available: http://journalofenergy.com/

[29] Q. Zhang and P. So, "Dynamic modelling of a combined cycle plant for power system stability studies," in *2000 IEEE Power Engineering Society Winter Meeting. Conference Proceedings (Cat. No.00CH37077)*, vol. 2. IEEE, 2020, pp. 1538–1543. [Online]. Available: http://ieeexplore.ieee.org/document/850211/

[30] K. Weimin, X. Junrong, G. Lian, and D. Yiping, "Study on the mathematical model and primary frequency regulation characteristics of combined cycle plants," *2011 Second International Conference on Mechanic Automation and Control Engineering*, pp.

2632–2635, 2011. [Online]. Available: http://ieeexplore.ieee.org/lpdocs/epic03/wrapper. htm?arnumber=5987524

[31] S. A. Pourmousavi and M. H. Nehrir, "Introducing dynamic demand response in the lfc model," *IEEE Transactions on Power Systems*, vol. 29, pp. 1562–1572, 7 2014. [Online]. Available: http://ieeexplore.ieee.org/document/6717056/

[32] Q. Shi, F. Li, and H. Cui, "Analytical method to aggregate multi-machine sfr model with applications in power system dynamic studies," *IEEE Transactions on Power Systems*, vol. 33, pp. 6355–6367, 11 2018.

[33] K. V. Vidyanandan and N. Senroy, "Simplified dynamic models of variable speed wind turbines for frequency regulation studies," in *2013 IEEE Innovative Smart Grid Technologies-Asia (ISGT Asia)*. IEEE, 11 2013, pp. 1–6. [Online]. Available: http://ieeexplore.ieee.org/document/6698708/

[34] H. Ye, W. Pei, and Z. Qi, "Analytical modeling of inertial and droop responses from a wind farm for short-term frequency regulation in power systems," *IEEE Transactions on Power Systems*, vol. 31, pp. 3414–3423, 9 2016.

[35] J. Hu, L. Sun, X. Yuan, S. Wang, and Y. Chi, "Modeling of type 3 wind turbines with df/dt inertia control for system frequency response study," *IEEE Transactions on Power Systems*, vol. 32, pp. 2799–2809, 7 2017. [Online]. Available: http://ieeexplore.ieee.org/document/7585076/

[36] R. Quan and W. Pan, "A low-order system frequency response model for dfig distributed wind power generation systems based on small signal analysis," *Energies*, vol. 10, p. 657, 2017. [Online]. Available: http://www.mdpi.com/1996-1073/10/5/657

[37] M. Krpan and I. Kuzle, "Linearized model of variable speed wind turbines for studying power system frequency changes," in *17th IEEE International Conference on Smart Technologies, EUROCON 2017 - Conference Proceedings*, 2017, pp. 393–398. [Online]. Available: http://ieeexplore.ieee.org/document/8011141/

[38] M. Krpan and I. Kuzle, "Inertial and primary frequency response model of variable-speed wind turbines," *Published in The Journal of Engineering*, vol. 2017, pp. 844–848, 2017. [Online]. Available: http://digital-library.theiet.org/content/journals/10.1049/joe. 2017.0449

[39] M. Krpan and I. Kuzle, "Towards the new low-order system frequency response model of power systems with high penetration of variable-speed wind turbine generators," in

2018 IEEE Power & Energy Society General Meeting (PESGM). IEEE, 8 2018, pp. 1–5. [Online]. Available: https://ieeexplore.ieee.org/document/8586570/

[40] T. Ackermann, *Wind Power in Power Systems*, 2nd ed. Wiley, 2012.

[41] M. Krpan and I. Kuzle, "Introducing low-order system frequency response modelling of a future power system with high penetration of wind power plants with frequency support capabilities," *IET Renewable Power Generation*, vol. 12, pp. 1453–1461, 10 2018. [Online]. Available: https://digital-library.theiet.org/content/journals/10.1049/iet-rpg.2017.0811

[42] A. D. Hansen, C. Jauch, P. Sørensen, F. Iov, F. Blaabjerg *et al.*, "Dynamic wind turbine models in power system simulation tool digsilent," Technical University of Denmark, Tech. Rep., 2007. [Online]. Available: http://www.risoe.dtu.dk/rispubl/VEA/veapdf/ris-r-1400.pdf

[43] Z. Wu, W. Gao, T. Gao, W. Yan, H. Zhang *et al.*, "State-of-the-art review on frequency response of wind power plants in power systems," *Journal of Modern Power Systems and Clean Energy*, vol. 6, pp. 1–16, 1 2018. [Online]. Available: http://link.springer.com/10.1007/s40565-017-0315-y

[44] E. I. Batzelis, G. E. Kampitsis, and S. A. Papathanassiou, "Power reserves control for pv systems with real-time mpp estimation via curve fitting," *IEEE Transactions on Sustainable Energy*, vol. 8, pp. 1269–1280, 7 2017.

[45] T. Pavlovic, T. Bjazi, and Željko Ban, "Simplified averaged models of dc-dc power converters suitable for controller design and microgrid simulation," *IEEE Transactions on Power Electronics*, vol. 28, pp. 3266–3275, 2013.

[46] W. Xiao, W. G. Dunford, P. R. Palmer, and A. Capel, "Regulation of photovoltaic voltage," *IEEE Transactions on Industrial Electronics*, vol. 54, pp. 1365–1374, 6 2007.

[47] Y. Yang, K. A. Kim, F. Blaabjerg, and A. Sangwongwanich, *Advances in Grid-Connected Photovoltaic Power Conversion Systems*, 1st ed. Elsevier, 2019.

[48] T. Baskarad, I. Kuzle, and N. Holjevac, "Photovoltaic system power reserve determination using parabolic approximation of frequency response," *IEEE Transactions on Smart Grid*, vol. 12, pp. 3175–3184, 7 2021.

[49] R. Rajan and F. M. Fernandez, "Power control strategy of photovoltaic plants for frequency regulation in a hybrid power system," *International Journal of Electrical Power & Energy Systems*, vol. 110, pp. 171–183, 9 2019.

[50] J. Fang, H. Li, Y. Tang, and F. Blaabjerg, "Distributed power system virtual inertia implemented by grid-connected power converters," *IEEE Transactions on Power Electronics*, vol. 33, pp. 8488–8499, 10 2018.

[51] U. Markovic, Z. Chu, P. Aristidou, and G. Hug, "Lqr-based adaptive virtual synchronous machine for power systems with high inverter penetration," *IEEE Transactions on Sustainable Energy*, vol. 10, pp. 1501–1512, 7 2019.

[52] X. Luo, J. Wang, M. Dooner, and J. Clarke, "Overview of current development in electrical energy storage technologies and the application potential in power system operation," *Applied Energy*, vol. 137, pp. 511–536, 1 2015. [Online]. Available: https://www.sciencedirect.com/science/article/pii/S0306261914010290

[53] Maxwell Technologies, "Ultracapacitors frequency response application brief," 2018, technical brochure.

[54] A. Tahri, H. E. Fadil, F. Belhaj, K. Gaouzi, A. Rachid *et al.*, "Management of fuel cell power and supercapacitor state-of-charge for electric vehicles," *Electr. Power Syst. Res.*, vol. 160, pp. 89 – 98, 2018. [Online]. Available: http://www.sciencedirect.com/science/article/pii/S0378779618300403

[55] T. Zhou and W. Sun, "Optimization of battery–supercapacitor hybrid energy storage station in wind/solar generation system," *IEEE Trans. Sustain. Energy*, vol. 5, no. 2, pp. 408–415, April 2014.

[56] M. F. M. Arani and E. F. El-Saadany, "Implementing virtual inertia in dfig-based wind power generation," *IEEE Trans. Power Syst.*, vol. 28, no. 2, pp. 1373–1384, May 2013.

[57] S. I. Gkavanoudis and C. S. Demoulias, "A combined fault ride-through and power smoothing control method for full-converter wind turbines employing supercapacitor energy storage system," *Electr. Power Syst. Res.*, vol. 106, pp. 62 – 72, 2014. [Online]. Available: http://www.sciencedirect.com/science/article/pii/S0378779613002174

[58] J. Fang, Y. Tang, H. Li, and X. Li, "A battery/ultracapacitor hybrid energy storage system for implementing the power management of virtual synchronous generators," *IEEE Trans. Power Electron.*, vol. 33, no. 4, pp. 2820–2824, April 2018.

[59] M. H. Fini and M. E. H. Golshan, "Determining optimal virtual inertia and frequency control parameters to preserve the frequency stability in islanded microgrids with high penetration of renewables," *Electr. Power Syst. Res.*, vol. 154, pp. 13 – 22, 2018. [Online]. Available: http://www.sciencedirect.com/science/article/pii/S0378779617303255

[60] V. Gevorgian, E. Muljadi, Y. Luo, M. Mohanpurkar, R. Hovsapian *et al.*, "Supercapacitor to provide ancillary services," in *2017 IEEE Energy Conversion Congress and Exposition (ECCE)*, Oct 2017, pp. 1030–1036.

[61] L. Sigrist, I. Egido, E. Lobato Miguélez, and L. Rouco, "Sizing and controller setting of ultracapacitors for frequency stability enhancement of small isolated power systems," *IEEE Trans. Power Syst.*, vol. 30, no. 4, pp. 2130–2138, July 2015.

[62] J. Cao, W. Du, H. Wang, and M. McCulloch, "Optimal sizing and control strategies for hybrid storage system as limited by grid frequency deviations," *IEEE Trans. Power Syst.*, vol. 33, no. 5, pp. 5486–5495, Sep. 2018.

[63] M. G. Molina and P. E. Mercado, "Modeling of a DSTATCOM with ultra-capacitor energy storage for power distribution system applications," in *XIII Eriac Décimo Tercer Encuentro Regional Iberoamericano de CIGRÉ*, May 2009, pp. 1–8.

[64] G. Delille, B. Francois, and G. Malarange, "Dynamic frequency control support by energy storage to reduce the impact of wind and solar generation on isolated power system's inertia," *IEEE Transactions on Sustainable Energy*, vol. 3, no. 4, pp. 931–939, 2012.

[65] I. Egido, L. Sigrist, E. Lobato, L. Rouco, and A. Barrado, "An ultra-capacitor for frequency stability enhancement in small-isolated power systems: Models, simulation and field tests," *Applied Energy*, vol. 137, pp. 670 – 676, 2015. [Online]. Available: http://www.sciencedirect.com/science/article/pii/S0306261914008447

[66] V. Musolino, L. Piegari, and E. Tironi, "New full-frequency-range supercapacitor model with easy identification procedure," *IEEE Trans. Ind. Electron.*, vol. 60, no. 1, pp. 112–120, Jan 2013.

[67] F. Rafik, H. Gualous, R. Gallay, A. Crausaz, and A. Berthon, "Frequency, thermal and voltage supercapacitor characterization and modeling," *Journal of Power Sources*, vol. 165, no. 2, pp. 928 – 934, 2007, iBA – HBC 2006. [Online]. Available: http://www.sciencedirect.com/science/article/pii/S0378775306025110

[68] M. Krpan and I. Kuzle, "Impact of ultracapacitor modelling on fast frequency control performance," in *2020 International Conference on Smart Grids and Energy Systems (SGES)*, 2020, pp. 326–331.

[69] M. Krpan and I. Kuzle, "On modelling and sizing a supercapacitor energy storage for power system frequency control," *IET Conference Proceedings*, pp. 404–409(5), January 2021. [Online]. Available: https://digital-library.theiet.org/content/conferences/10.1049/icp.2021.1242

[70] M. Krpan, I. Kuzle, A. Radovanovic, and J. V. Milanovic, "Modelling of Supercapacitor Banks for Power System Dynamics Studies," *IEEE Transactions on Power Systems*, vol. 36, no. 5, pp. 3987–3996, 2021.

[71] M. Beus, M. Krpan, I. Kuzle, H. Pandzic, and A. Parisio, "A Model Predictive Control Approach to Operation Optimization of an Ultracapacitor Bank for Frequency Control," *IEEE Transactions on Energy Conversion*, vol. 36, no. 3, pp. 1743–1755, 2021.

[72] M. Krpan and I. Kuzle, "Coordinated control of an ultracapacitor bank and a variable-speed wind turbine generator for inertial response provision during low and above rated wind speeds," in *2019 IEEE Sustainable Power and Energy Conference (iSPEC)*, 2019, pp. 1693–1698.

[73] T. Zhao, A. Parisio, and J. V. Milanović, "Distributed control of battery energy storage systems for improved frequency regulation," *IEEE Transactions on Power Systems*, vol. 35, no. 5, pp. 3729–3738, 2020.

[74] E. Mallada, C. Zhao, and S. Low, "Optimal load-side control for frequency regulation in smart grids," *IEEE Transactions on Automatic Control*, vol. 62, no. 12, pp. 6294–6309, 2017.

[75] N. Li, C. Zhao, and L. Chen, "Connecting automatic generation control and economic dispatch from an optimization view," *IEEE Transactions on Control of Network Systems*, vol. 3, no. 3, pp. 254–264, 2016.

[76] F. Dörfler, S. Bolognani, J. W. Simpson-Porco, and S. Grammatico, "Distributed control and optimization for autonomous power grids," in *2019 18th European Control Conference (ECC)*, 2019, pp. 2436–2453.

[77] D. K. Molzahn, F. Dörfler, H. Sandberg, S. H. Low, S. Chakrabarti *et al.*, "A survey of distributed optimization and control algorithms for electric power systems," *IEEE Transactions on Smart Grid*, vol. 8, no. 6, pp. 2941–2962, 2017.

[78] T. Morstyn, B. Hredzak, and V. G. Agelidis, "Control strategies for microgrids with distributed energy storage systems: An overview," *IEEE Transactions on Smart Grid*, vol. 9, no. 4, pp. 3652–3666, 2018.

[79] S. Kar and G. Hug, "Distributed robust economic dispatch in power systems: A consensus + innovations approach," in *2012 IEEE Power and Energy Society General Meeting*, 2012, pp. 1–8.

[80] R. Mudumbai, S. Dasgupta, and B. B. Cho, "Distributed control for optimal economic dispatch of a network of heterogeneous power generators," *IEEE Transactions on Power Systems*, vol. 27, no. 4, pp. 1750–1760, 2012.

[81] M. Andreasson, D. V. Dimarogonas, K. H. Johansson, and H. Sandberg, "Distributed vs. centralized power systems frequency control," in *2013 European Control Conference (ECC)*, 2013, pp. 3524–3529.

[82] M. Andreasson, D. V. Dimarogonas, H. Sandberg, and K. H. Johansson, "Distributed pi-control with applications to power systems frequency control," in *2014 American Control Conference*, 2014, pp. 3183–3188.

[83] A. Bidram, F. L. Lewis, and A. Davoudi, "Distributed control systems for small-scale power networks: Using multiagent cooperative control theory," *IEEE Control Systems Magazine*, vol. 34, no. 6, pp. 56–77, 2014.

[84] W. Lin and E. Bitar, "Decentralized stochastic control of distributed energy resources," *IEEE Transactions on Power Systems*, vol. 33, no. 1, pp. 888–900, 2018.

[85] R. Sebastián and J. Quesada, "Distributed control system for frequency control in a isolated wind system," *Renewable Energy*, vol. 31, no. 3, pp. 285–305, 2006. [Online]. Available: https://www.sciencedirect.com/science/article/pii/S0960148105000819

[86] T. Logenthiran, D. Srinivasan, A. M. Khambadkone, and H. N. Aung, "Multiagent system for real-time operation of a microgrid in real-time digital simulator," *IEEE Transactions on Smart Grid*, vol. 3, no. 2, pp. 925–933, 2012.

[87] J. Hu, J. Cao, J. M. Guerrero, T. Yong, and J. Yu, "Improving frequency stability based on distributed control of multiple load aggregators," *IEEE Transactions on Smart Grid*, vol. 8, no. 4, pp. 1553–1567, 2017.

[88] R. Fu, Y. Wu, H. Wang, and J. Xie, "A distributed control strategy for frequency regulation in smart grids based on the consensus protocol," *Energies*, vol. 8, no. 8, pp. 7930–7944, 2015. [Online]. Available: https://www.mdpi.com/1996-1073/8/8/7930

[89] Y. Duan, L. Luo, Y. Li, Y. Cao, C. Rehtanz *et al.*, "Co-simulation of distributed control system based on jade for smart distribution networks with distributed generations," *IET Generation, Transmission & Distribution*, vol. 11, pp. 3097–3105(8), August 2017. [Online]. Available: https://digital-library.theiet.org/content/journals/10.1049/iet-gtd.2016.1382

[90] E. Hammad, A. Farraj, and D. Kundur, "On effective virtual inertia of storage-based distributed control for transient stability," *IEEE Transactions on Smart Grid*, vol. 10, no. 1, pp. 327–336, 2019.

[91] M. Ayar, S. Obuz, R. D. Trevizan, A. S. Bretas, and H. A. Latchman, "A distributed control approach for enhancing smart grid transient stability and resilience," *IEEE Transactions on Smart Grid*, vol. 8, no. 6, pp. 3035–3044, 2017.

[92] X. Wang, T. Zhang, and A. Parisio, "Virtual storage plant aggregating electrical energy storages and hvac systems providing regulating reserve and voltage regulation," *IFAC-PapersOnLine*, vol. 54, no. 6, pp. 1–7, 2021, 7th IFAC Conference on Nonlinear Model Predictive Control NMPC 2021. [Online]. Available: https://www.sciencedirect.com/science/article/pii/S240589632101291X

[93] G. Qu and N. Li, "Optimal distributed feedback voltage control under limited reactive power," *IEEE Transactions on Power Systems*, vol. 35, no. 1, pp. 315–331, 2020.

[94] Z. Tang, D. J. Hill, and T. Liu, "Fast distributed reactive power control for voltage regulation in distribution networks," *IEEE Transactions on Power Systems*, vol. 34, no. 1, pp. 802–805, 2019.

[95] T. Xu and W. Wu, "Accelerated admm-based fully distributed inverter-based volt/var control strategy for active distribution networks," *IEEE Transactions on Industrial Informatics*, vol. 16, no. 12, pp. 7532–7543, 2020.

[96] M. Prodanovic and T. Green, "High-quality power generation through distributed control of a power park microgrid," *IEEE Transactions on Industrial Electronics*, vol. 53, no. 5, pp. 1471–1482, 2006.

[97] Y. Du, H. Tu, S. Lukic, D. Lubkeman, A. Dubey *et al.*, "Development of a controller hardware-in-the-loop platform for microgrid distributed control applications," in *2018 IEEE Electronic Power Grid (eGrid)*, 2018, pp. 1–6.

[98] Y. Du, H. Tu, and S. Lukic, "Distributed control strategy to achieve synchronized operation of an islanded mg," *IEEE Transactions on Smart Grid*, vol. 10, no. 4, pp. 4487–4496, 2019.

[99] V. Nasirian, Q. Shafiee, J. M. Guerrero, F. L. Lewis, and A. Davoudi, "Droop-free distributed control for ac microgrids," *IEEE Transactions on Power Electronics*, vol. 31, no. 2, pp. 1600–1617, 2016.

[100] Q. Shafiee, V. Nasirian, J. C. Vasquez, J. M. Guerrero, and A. Davoudi, "A multifunctional fully distributed control framework for ac microgrids," *IEEE Transactions on Smart Grid*, vol. 9, no. 4, pp. 3247–3258, 2018.

[101] F. Guo, L. Herrera, R. Murawski, E. Inoa, C.-L. Wang *et al.*, "Comprehensive real-time simulation of the smart grid," *IEEE Transactions on Industry Applications*, vol. 49, no. 2, pp. 899–908, 2013.

[102] G. D. Carne, M. Langwasser, M. Ndreko, R. Bachmann, R. W. D. Doncker *et al.*, "Which deepness class is suited for modeling power electronics?: A guide for choosing the right model for grid-integration studies," *IEEE Industrial Electronics Magazine*, vol. 13, pp. 41–55, 6 2019.

[103] G. D. Carne, G. Lauss, M. H. Syed, A. Monti, A. Benigni *et al.*, "On modeling depths of power electronic circuits for real-time simulation - a comparative analysis for power systems," *IEEE Open Access Journal of Power and Energy*, vol. 9, pp. 76–87, 2022.

[104] D. Baimel, J. Belikov, J. M. Guerrero, and Y. Levron, "Dynamic modeling of networks, microgrids, and renewable sources in the dq0 reference frame: A survey," *IEEE Access*, vol. 5, pp. 21 323–21 335, 2017.

[105] R. Henriquez-Auba, J. D. Lara, D. S. Callaway, and C. Barrows, "Transient simulations with a large penetration of converter-interfaced generation: Scientific computing challenges and opportunities," *IEEE Electrification Magazine*, vol. 9, pp. 72–82, 6 2021.

[106] P. Kundur, *Power system stability and control*. McGraw-Hill, 1994.

[107] A. Stankovic, S. Sanders, and T. Aydin, "Dynamic phasors in modeling and analysis of unbalanced polyphase ac machines," *IEEE Transactions on Energy Conversion*, vol. 17, no. 1, pp. 107–113, 2002.

[108] T. H. Demiray, "Simulation of power system dynamics using dynamic phasor models," Ph.D. dissertation, ETH Zürich, 2008.

[109] J. Belikov and Y. Levron, "Uses and misuses of quasi-static time-varying phasor models in power systems," *IEEE Transactions on Power Delivery*, vol. 33, pp. 3263–3266, 12 2018. [Online]. Available: https://ieeexplore.ieee.org/document/8403297/

[110] A. Derviskadic, G. Frigo, and M. Paolone, "Beyond phasors: Modeling of power system signals using the hilbert transform," *IEEE Transactions on Power Systems*, vol. 35, pp. 2971–2980, 7 2020.

[111] DIgSILENT GmbH, "DIgSILENT PowerFactory," 2022, user manual.

[112] C. L. Fortescue, "Method of symmetrical co-ordinates applied to the solution of polyphase networks," *Transactions of the American Institute of Electrical Engineers*, vol. 37, pp. 1027–1140, 1918.

[113] Siemens PTI, "PSS E," 2017, program Operation Manual.

[114] A. Clark, P. Mitra, N. Johansson, and M. Ghandhari, "Development of a base model in rms and emt environment to study low inertia system," in *2021 IEEE Power & Energy Society General Meeting (PESGM)*, vol. 2021-July.   IEEE, 7 2021, pp. 1–5. [Online]. Available: https://ieeexplore.ieee.org/document/9637883/

[115] P. Krause, O. Wasynczuk, S. Sudhoff, and S. Pekarek, *Analysis of Electric Machinery and Drive Systems*, 3rd ed.   Wiley, 2013.

[116] G. Diaz, C. Gonzalez-Moran, J. Gomez-Aleixandre, and A. Diez, "Complex-valued state matrices for simple representation of large autonomous microgrids supplied by *pq* and *vf* generation," *IEEE Transactions on Power Systems*, vol. 24, pp. 1720–1730, 11 2009. [Online]. Available: http://ieeexplore.ieee.org/document/5262954/

[117] J. Belikov and Y. Levron, "A sparse minimal-order dynamic model of power networks based on dq0 signals," *IEEE Transactions on Power Systems*, vol. 33, no. 1, pp. 1059–1067, 2018.

[118] Y. Levron and J. Belikov, "Observable canonical forms of multi-machine power systems using dq0 signals," in *2016 IEEE International Conference on the Science of Electrical Engineering (ICSEE)*, 2016, pp. 1–5.

[119] R. D. Zimmerman, C. E. Murillo-Sánchez, and R. J. Thomas, "Matpower: Steady-state operations, planning, and analysis tools for power systems research and education," *IEEE Transactions on Power Systems*, vol. 26, no. 1, pp. 12–19, 2011.

[120] R. D. Zimmerman and C. E. Murillo-Sánchez, "Matpower," Oct. 2020. [Online]. Available: https://doi.org/10.5281/zenodo.4074135

[121] R. D. Zimmerman and C. E. Murillo-Sánchez, "Matpower user's manual," Oct. 2020. [Online]. Available: https://doi.org/10.5281/zenodo.4074122

[122] T. Demiray and G. Andersson, "Comparison of the efficiency of dynamic phasor models derived from abc and dqo reference frame in power system dynamic simulations," *IET Conference Proceedings*, pp. 204–204(1), January 2006. [Online]. Available: https://digital-library.theiet.org/content/conferences/10.1049/cp_20062077

[123] M. Hannan and K. Chan, "Modern power systems transients studies using dynamic phasor models," in *2004 International Conference on Power System Technology, 2004. PowerCon 2004.*, vol. 2, 2004, pp. 1469–1473 Vol.2.

[124] R. R. O. Yang, "A Comparison of EMT, Dynamic Phasor, and Traditional Transient Stability Models," Master's thesis, University of Manitoba, 2014.

[125] K. Mudunkotuwa and S. Filizadeh, "Co-simulation of electrical networks by interfacing emt and dynamic-phasor simulators," *Electric Power Systems Research*, vol. 163, pp. 423–429, 2018. [Online]. Available: https://www.sciencedirect.com/science/article/pii/S0378779618301858

[126] F. Plumier, "Co-simulation of electromagnetic transients and phasor models of electric power systems," Ph.D. dissertation, Université de Liège, 2015.

[127] A. Constantin, A. Ellerbrock, F. Fernandez, and J. Rueß, "Co-simulation of power electronic dominated networks," *IEEE Power and Energy Magazine*, vol. 18, no. 2, pp. 84–89, 2020.

[128] G. Grdenić, M. Delimar, and J. Beerten, "Ac grid model order reduction based on interaction modes identification in converter-based power systems," *IEEE Transactions on Power Systems*, pp. 1–10, 2022.

[129] G. Grdenic, F. Cifuentes-Garcia, N. d. M. D. Campos, F. Villella, and J. Beerten, "Model order reduction of voltage source converters based on the ac side admittance assessment: from emt to rms," *IEEE Transactions on Power Delivery*, pp. 1–1, 2022.

[130] A. Alassi, S. Bañales, O. Ellabban, G. Adam, and C. MacIver, "Hvdc transmission: Technology review, market trends and future outlook," *Renewable and Sustainable Energy Reviews*, vol. 112, pp. 530–554, 9 2019. [Online]. Available: https://linkinghub.elsevier.com/retrieve/pii/S1364032119302837

[131] B. Wu, J. Pontt, J. Rodríguez, S. Bernet, and S. Kouro, "Current-source converter and cycloconverter topologies for industrial medium-voltage drives," *IEEE Transactions on Industrial Electronics*, vol. 55, no. 7, pp. 2786–2797, 2008.

[132] S. Debnath, J. Qin, B. Bahrani, M. Saeedifard, and P. Barbosa, "Operation, control, and applications of the modular multilevel converter: A review," *IEEE Transactions on Power Electronics*, vol. 30, pp. 37–53, 1 2015. [Online]. Available: https://ieeexplore.ieee.org/document/6757006/

[133] S. Liu, Z. Xu, W. Hua, G. Tang, and Y. Xue, "Electromechanical transient modeling of modular multilevel converter based multi-terminal hvdc systems," in *2014 IEEE PES General Meeting*. IEEE, 7 2014, pp. 1–1. [Online]. Available: http://ieeexplore.ieee.org/document/6938791/

[134] A. Beddard, C. E. Sheridan, M. Barnes, and T. C. Green, "Improved accuracy average value models of modular multilevel converters," *IEEE Transactions on Power Delivery*, vol. 31, pp. 2260–2269, 10 2016. [Online]. Available: http://ieeexplore.ieee.org/document/7464846/

[135] H. Saad, S. Dennetiere, J. Mahseredjian, P. Delarue, X. Guillaud *et al.*, "Modular multilevel converter models for electromagnetic transients," *IEEE Transactions on Power Delivery*, vol. 29, pp. 1481–1489, 6 2014. [Online]. Available: http://ieeexplore.ieee.org/document/6676832/

[136] A. Jamshidifar and D. Jovcic, "Small-signal dynamic dq model of modular multilevel converter for system studies," *IEEE Transactions on Power Delivery*, vol. 31, pp. 191–199, 2 2016. [Online]. Available: https://ieeexplore.ieee.org/document/7279188/

[137] D. Jovcic and A. J. Far, "Phasor model of modular multilevel converter with circulating current suppression control," *IEEE Transactions on Power Delivery*, vol. 30, pp. 1889–1897, 8 2015. [Online]. Available: http://ieeexplore.ieee.org/document/6977938/

[138] M. Liserre, F. Blaabjerg, and S. Hansen, "Design and control of an lcl-filter-based three-phase active rectifier," *IEEE Transactions on Industry Applications*, vol. 41, pp. 1281–1291, 9 2005.

[139] S. D'Arco, J. A. Suul, and O. B. Fosso, "A virtual synchronous machine implementation for distributed control of power converters in smartgrids," *Electric Power Systems Research*, vol. 122, pp. 180–197, 5 2015. [Online]. Available: https://www.sciencedirect.com/science/article/pii/S0378779615000024

[140] Q.-C. Zhong and G. Weiss, "Synchronverters: Inverters that mimic synchronous generators," *IEEE transactions on industrial electronics*, vol. 58, no. 4, pp. 1259–1267, 2010.

[141] H.-P. Beck and R. Hesse, "Virtual synchronous machine," in *2007 9th International Conference on Electrical Power Quality and Utilisation*. IEEE, 2007, pp. 1–6.

[142] F. Blaabjerg, R. Teodorescu, M. Liserre, and A. V. Timbus, "Overview of control and grid synchronization for distributed power generation systems," *IEEE Transactions on Industrial Electronics*, vol. 53, pp. 1398–1409, 10 2006.

[143] S. Golestan, J. M. Guerrero, and J. C. Vasquez, "Three-phase plls: A review of recent advances," *IEEE Transactions on Power Electronics*, vol. 32, pp. 1894–1907, 3 2017.

[144] A. Ortega and F. Milano, "Comparison of different pll implementations for frequency estimation and control," *Proceedings of International Conference on Harmonics and Quality of Power, ICHQP*, vol. 2018-May, pp. 1–6, 6 2018.

[145] L. Huang, H. Xin, Z. Wang, K. Wu, H. Wang *et al.*, "A virtual synchronous control for voltage-source converters utilizing dynamics of dc-link capacitor to realize self-synchronization," *IEEE Journal of Emerging and Selected Topics in Power Electronics*, vol. 5, pp. 1565–1577, 12 2017.

[146] C. Arghir, T. Jouini, and F. Dörfler, "Grid-forming control for power converters based on matching of synchronous machines," *Automatica*, vol. 95, pp. 273–282, 9 2018.

[147] S. Curi, D. Gros, and F. Dorfler, "Control of low-inertia power grids: A model reduction approach," *2017 IEEE 56th Annual Conference on Decision and Control, CDC 2017*, vol. 2018-January, pp. 5708–5713, 1 2018.

[148] M. Yu, A. J. Roscoe, C. D. Booth, A. Dyśko, R. Ierna *et al.*, "Use of an inertia-less virtual synchronous machine within future power networks with high penetrations of converters," *19th Power Systems Computation Conference, PSCC 2016*, 8 2016.

[149] A. J. Roscoe, M. Yu, R. Ierna, J. Zhu, A. Dyśko *et al.*, "A vsm (virtual synchronous machine) convertor control model suitable for rms studies for resolving system operator/owner challenges," in *15th Wind Integration Workshop*, 11 2016, this paper was presented at the 15th Wind Integration Workshop and published in the workshop's proceedings. [Online]. Available: https://strathprints.strath.ac.uk/58053/

[150] R. Ofir, U. Markovic, P. Aristidou, and G. Hug, "Droop vs. virtual inertia: Comparison from the perspective of converter operation mode," in *2018 IEEE International Energy Conference (ENERGYCON)*. IEEE, 6 2018, pp. 1–6. [Online]. Available: https://ieeexplore.ieee.org/document/8398752/

[151] M. Van Wesenbeeck, S. De Haan, P. Varela, and K. Visscher, "Grid tied converter with virtual kinetic storage," in *2009 IEEE Bucharest PowerTech*. IEEE, 2009, pp. 1–7.

[152] H. Bevrani, T. Ise, and Y. Miura, "Virtual synchronous generators: A survey and new perspectives," *International Journal of Electrical Power & Energy Systems*, vol. 54, pp. 244–254, 1 2014. [Online]. Available: https://www.sciencedirect.com/science/article/pii/S0142061513003062

[153] S. D'Arco, J. A. Suul, and O. B. Fosso, "Small-signal modelling and parametric sensitivity of a virtual synchronous machine," in *2014 Power Systems Computation Conference*. IEEE, 2014, pp. 1–9.

[154] M. Yu, A. Dyśko, A. Roscoe, C. Booth, R. Ierna *et al.*, "Effects of swing equation-based inertial response (SEBIR) control on penetration limits of non-synchronous generation in

the GB power system," in *International Conference on Renewable Power Generation (RPG 2015)*, 2015, pp. 1–6.

[155] L. A. Lopes *et al.*, "Self-tuning virtual synchronous machine: A control strategy for energy storage systems to support dynamic frequency control," *IEEE Transactions on Energy Conversion*, vol. 29, no. 4, pp. 833–840, 2014.

[156] S. V. Dhople, B. B. Johnson, and A. O. Hamadeh, "Virtual oscillator control for voltage source inverters," in *2013 51st Annual Allerton Conference on Communication, Control, and Computing (Allerton)*, 2013, pp. 1359–1363.

[157] S. Jayalath and M. Hanif, "Generalized lcl-filter design algorithm for grid-connected voltage-source inverter," *IEEE Transactions on Industrial Electronics*, vol. 64, pp. 1905–1915, 3 2017.

[158] G. Majic, M. Despalatovic, and B. Terzic, "Lcl filter design method for grid-connected pwm-vsc," *Journal of Electrical Engineering and Technology*, vol. 12, pp. 1945–1954, 9 2017.

[159] R. Peña-Alzola, M. Liserre, F. Blaabjerg, M. Ordonez, and Y. Yang, "Lcl-filter design for robust active damping in grid-connected converters," *IEEE Transactions on Industrial Informatics*, vol. 10, pp. 2192–2203, 11 2014.

[160] A. Reznik, M. G. Simoes, A. Al-Durra, and S. M. Muyeen, "Lcl filter design and performance analysis for grid-interconnected systems," *IEEE Transactions on Industry Applications*, vol. 50, pp. 1225–1232, 2014.

[161] R. Meyer and A. Mertens, "Design of lcl filters in consideration of parameter variations for grid-connected converters," *2012 IEEE Energy Conversion Congress and Exposition, ECCE 2012*, pp. 557–564, 2012.

[162] P. Channegowda and V. John, "Filter optimization for grid interactive voltage source inverters," *IEEE Transactions on Industrial Electronics*, vol. 57, pp. 4106–4114, 12 2010.

[163] K. Jalili and S. Bernet, "Design of lcl filters of active-front-end two-level voltage-source converters," *IEEE Transactions on Industrial Electronics*, vol. 56, pp. 1674–1689, 2009.

[164] T. C. Wang, Z. Ye, G. Sinha, and X. Yuan, "Output filter design for a grid-interconnected three-phase inverter," *PESC Record - IEEE Annual Power Electronics Specialists Conference*, vol. 2, pp. 779–784, 2003.

[165] M. Liserre, F. Blaabjerg, and S. Hansen, "Design and control of an lcl-filter based three-phase active rectifier," *Conference Record - IAS Annual Meeting (IEEE Industry Applications Society)*, vol. 1, pp. 299–307, 2001.

[166] W. Wu, Y. Liu, Y. He, H. S. H. Chung, M. Liserre *et al.*, "Damping methods for resonances caused by lcl-filter-based current-controlled grid-tied power inverters: An overview," *IEEE Transactions on Industrial Electronics*, vol. 64, pp. 7402–7413, 9 2017.

[167] R. Wolf, *Osnove električnih strojeva*, 4th ed. Školska knjiga, 1995.

[168] DIgSILENT GmbH, "Asynchronous machine," 2022, technical reference.

[169] M. Krpan, I. Erceg, I. Kuzle, and H. Pandžić, "Three-phase srf pll model for system frequency response studies in low-inertia systems," in *2022 IEEE PES Innovative Smart Grid Technologies - Asia (ISGT Asia)*, 2022, pp. 155–159.

[170] Y. Wang, G. Delille, X. Guillaud, F. Colas, and B. François, "Real-time simulation: The missing link in the design process of advanced grid equipment," in *IEEE PES General Meeting*, 2010, pp. 1–8.

[171] J. Ma, Y. Qiu, Y. Li, W. Zhang, Z. Song *et al.*, "Research on the impact of DFIG virtual inertia control on power system small-signal stability considering the phase-locked loop," *IEEE Transactions on Power Systems*, vol. 32, no. 3, pp. 2094–2105, 2017.

[172] F. Hans, W. Schumacher, and L. Harnefors, "Small-signal modeling of three-phase synchronous reference frame phase-locked loops," *IEEE Transactions on Power Electronics*, vol. 33, no. 7, pp. 5556–5560, 2018.

[173] A. D. Hansen, P. Sørensen, F. Iov, and F. Blaabjerg, "Initialisation of grid-connected wind turbine models in power-system simulations," *Wind Engineering*, vol. 27, pp. 21–38, 2003.

[174] G. Abad, J. Lopez, M. A. Rodriguez, L. Marroyo, and G. Iwanski, *Doubly fed induction machine: modeling and control for wind energy generation*, 1st ed. John Wiley & Sons, 2011.

[175] J. Slootweg, S. de Haan, H. Polinder, and W. Kling, "General model for representing variable speed wind turbines in power system dynamics simulations," *IEEE Transactions on Power Systems*, vol. 18, pp. 144–151, 2003. [Online]. Available: http://ieeexplore.ieee.org/lpdocs/epic03/wrapper.htm?arnumber=1178790

[176] J. Slootweg, S. de Haan, H. Polinder, and W. Kling, "Modeling wind turbines in power system dynamics simulations," in *2001 Power Engineering Society Summer Meeting.*

Conference Proceedings (Cat. No.01CH37262). IEEE, 2001, pp. 22–26 vol.1. [Online]. Available: http://ieeexplore.ieee.org/document/969976/

[177] A. Honrubia-Escribano, E. Gómez-Lázaro, J. Fortmann, P. Sørensen, and S. Martin-Martinez, "Generic dynamic wind turbine models for power system stability analysis: A comprehensive review," *Renewable and Sustainable Energy Reviews*, vol. 81, pp. 1939–1952, 2018. [Online]. Available: http://dx.doi.org/10.1016/j.rser.2017.06.005

[178] J. J. Sanchez-Gasca, "Generic wind turbine generator models for WECC - a second status report," in *2015 IEEE Power Energy Society General Meeting*, Denver, USA, July 2015, pp. 1–5.

[179] WECC REMTF, "WECC wind plant dynamic modeling guidelines," WECC, Tech. Rep., April 2014.

[180] P. Sørensen, B. Andresen, J. Fortmann, and P. Pourbeik, "Modular structure of wind turbine models in IEC 61400-27-1," in *2013 IEEE Power Energy Society General Meeting*, Vancouver, Canada, July 2013, pp. 1–5.

[181] IEC, "IEC61400-27-1," IEC Technical Committee 88: Wind turbines, Tech. Rep., February 2015.

[182] P. Sørensen, J. Fortmann, F. J. Buendia, J. Bech, A. Morales *et al.*, "Final draft international standard IEC 61400-27-1," in *Proc. of the 13th Wind Integration Workshop*, Berlin, Germany, November 2014, pp. 1–5.

[183] K. Clark, N. W. Miller, and J. J. Sanchez-Gasca, "Modeling of ge wind turbine-generators for grid studies," GE Energy, Tech. Rep., 2010.

[184] J. Slootweg, H. Polinder, and W. Kling, "Dynamic modeling of a wind turbine with direct drive synchronous generator and back to back voltage source converter," in *European Wind Energy Conference*, 7 2001, pp. 1–4.

[185] J. Slootweg, H. Polinder, and W. Kling, "Dynamic modelling of a wind turbine with doubly fed induction generator," in *2001 Power Engineering Society Summer Meeting. Conference Proceedings (Cat. No.01CH37262).* IEEE, 2001, pp. 644–649. [Online]. Available: http://ieeexplore.ieee.org/document/970114/

[186] J. G. Slootweg, H. Polinder, and W. L. Kling, "Representing wind turbine electrical generating systems in fundamental frequency simulations," *IEEE Transactions on Energy Conversion*, vol. 18, pp. 516–524, 2003.

[187] D. GmbH, "Dynamic modelling of doubly-fed induction machine wind-generators," DIgSILENT GmbH, Tech. Rep., 2003.

[188] D. GmbH, "Digsilent powerfactory application guide dfig template," DIgSILENT GmbH, Tech. Rep., 2013.

[189] D. GmbH, "Digsilent powerfactory application guide frcwtg template," DIgSILENT GmbH, Tech. Rep., 2013.

[190] NEPLAN, "Wind turbine models-IEC61400-27-1," NEPLAN AG, Tech. Rep., 2015.

[191] Siemens PTI, "PSS/E 34 Program Application Guide," Siemens Industry Inc., Tech. Rep., 2015.

[192] Siemens PTI, "PSS/E 34 Model Library," Siemens Industry Inc., Tech. Rep., 2015.

[193] M. Singh and S. Santoso, "Dynamic models for wind turbines and wind power plants," NREL, Tech. Rep., 2011.

[194] J. Slootweg, H. Polinder, and W. Kling, "Initialization of wind turbine models in power system dynamics simulations," in *2001 IEEE Porto Power Tech Proceedings (Cat. No.01EX502)*, vol. vol.4. IEEE, 2001, pp. 1–6. [Online]. Available: http://ieeexplore.ieee.org/document/964827/

[195] L. Holdsworth, X. Wu, J. Ekanayake, and N. Jenkins, "Direct solution method for initialising doubly-fed induction wind turbines in power system dynamic models," *IEE Proceedings - Generation, Transmission and Distribution*, vol. 150, p. 334, 2003.

[196] M. Krpan, "Sudjelovanje vjetroelektrana u regulaciji frekvencije elektroenergetskog sustava," 2018, kvalifikacijski doktorski ispit, Fakultet elektrotehnike i računarstva.

[197] T. Petru and T. Thiringer, "Modeling of wind turbines for power system studies," *IEEE Transactions on Power Systems*, vol. 17, pp. 1132–1139, 2002.

[198] V. Akhmatov, "Analysis of dynamic behaviour of electric power systems with large amount of wind power," Ph.D. dissertation, Technical University of Denmark, 2003.

[199] S. Achilles and M. Pöller, "Direct drive synchronous machine models for stability assessment of wind farms," 2011. [Online]. Available: https://www.researchgate.net/publication/228888515_1_Direct_Drive_Synchronous_Machine_Models_for_Stability_Assessment_of_Wind_Farms

[200] F. M. González-Longatt, P. Wall, and V. Terzija, "A simplified model for dynamic behavior of permanent magnet synchronous generator for direct drive wind turbines," in *2011 IEEE Trondheim PowerTech*, 2011, pp. 1–7.

[201] J. Zhang, M. Cheng, Z. Chen, and X. Fu, "Pitch angle control for variable speed wind turbines," in *2008 Third International Conference on Electric Utility Deregulation and Restructuring and Power Technologies*, 2008, pp. 2691–2696. [Online]. Available: http://ieeexplore.ieee.org/lpdocs/epic03/wrapper.htm?arnumber=4523867

[202] E. Muljadi, V. Gevorgian, M. Singh, and S. Santoso, "Understanding inertial and frequency response of wind power plants," in *2012 IEEE Power Electronics and Machines in Wind Applications*. IEEE, 7 2012, pp. 1–8. [Online]. Available: http://ieeexplore.ieee.org/document/6316361/

[203] L. Holdsworth, J. B. Ekanayake, and N. Jenkins, "Power system frequency response from fixed speed and doubly fed induction generator-based wind turbines," *Wind Energy*, vol. 7, pp. 21–35, 2004.

[204] K. Watanabe and T. Nanahara, "Study on inertial response of fix-speed wind turbine generator," in *2014 49th International Universities Power Engineering Conference (UPEC)*, Cluj-Napoca, Romania, September 2014, pp. 1–6.

[205] J. Morren, J. Pierik, and S. W. H. de Haan, "Inertial response of variable speed wind turbines," *Electric Power Systems Research*, vol. 76, pp. 980–987, 2006.

[206] Z.-S. Zhang, Y.-Z. Sun, J. Lin, and G.-J. Li, "Coordinated frequency regulation by doubly fed induction generator-based wind power plants," *IET Renewable Power Generation*, vol. 6, pp. 38–47, 2012. [Online]. Available: https://digital-library.theiet.org/content/journals/10.1049/iet-rpg.2010.0208

[207] P. Tielens and D. van Hertem, "Grid inertia and frequency control in power systems with high penetration of renewables," in *Young Researchers Symposium in Electrical Power Engineering*, 2012, pp. 1–6. [Online]. Available: https://lirias.kuleuven.be/handle/123456789/345286

[208] E. Muljadi, M. Singh, and V. Gevorgian, "Fixed-speed and variable-slip wind turbines providing spinning reserves to the grid," in *2013 IEEE Power & Energy Society General Meeting*. IEEE, 2013, pp. 1–5. [Online]. Available: http://ieeexplore.ieee.org/document/6672228/

[209] G. Ramtharan, J. B. Ekanayake, and N. Jenkins, "Frequency support from doubly fed induction generator wind turbines," *IET Renewable Power Generation*, vol. 1, no. 1, pp. 3–9, March 2007.

[210] S. D. Rijcke, P. Tielens, B. Rawn, D. V. Hertem, and J. Driesen, "Trading energy yield for frequency regulation: Optimal control of kinetic energy in wind farms," *IEEE Transactions on Power Systems*, vol. 30, pp. 2469–2478, 9 2015. [Online]. Available: http://ieeexplore.ieee.org/document/6926873/

[211] R. de Almeida and J. Lopes, "Participation of doubly fed induction wind generators in system frequency regulation," *Power Systems, IEEE Transactions on*, vol. 22, pp. 944–950, 2007.

[212] Z. Wu, W. Gao, J. Wang, and S. Gu, "A coordinated primary frequency regulation from permanent magnet synchronous wind turbine generation," in *2012 IEEE Power Electronics and Machines in Wind Applications*, 7 2012, pp. 1–6. [Online]. Available: http://ieeexplore.ieee.org/lpdocs/epic03/wrapper.htm?arnumber=6316405

[213] K. V. Vidyanandan and N. Senroy, "Primary frequency regulation by deloaded wind turbines using variable droop," *IEEE Transactions on Power Systems*, vol. 28, pp. 837–846, 2013.

[214] M. Hwang, E. Muljadi, J. W. Park, P. Sorensen, and Y. C. Kang, "Dynamic droop-based inertial control of a doubly-fed induction generator," *IEEE Transactions on Sustainable Energy*, vol. 7, pp. 924–933, 2016.

[215] M. Hwang, E. Muljadi, G. Jang, and Y. C. Kang, "Disturbance-adaptive short-term frequency support of a dfig associated with the variable gain based on the rocof and rotor speed," *IEEE Transactions on Power Systems*, vol. 32, pp. 1873–1881, 5 2017. [Online]. Available: http://ieeexplore.ieee.org/document/7517363/

[216] M. Abbes and M. Allagui, "Participation of pmsg-based wind farms to the grid ancillary services," *Electric Power Systems Research*, vol. 136, pp. 201–211, 2016. [Online]. Available: http://dx.doi.org/10.1016/j.epsr.2016.02.028

[217] A. Attya, J. Dominguez-Garcia, and O. Anaya-Lara, "A review on frequency support provision by wind power plants: Current and future challenges," *Renewable and Sustainable Energy Reviews*, vol. 81, no. 2, pp. 2071 – 2087, January 2018. [Online]. Available: http://www.sciencedirect.com/science/article/pii/S1364032117309553

[218] N. Ullah, T. Thiringer, and D. Karlsson, "Temporary primary frequency control support by variable speed wind turbines— potential and applications," *IEEE Transactions*

on Power Systems, vol. 23, pp. 601–612, 5 2008. [Online]. Available: http://ieeexplore.ieee.org/document/4480153/

[219] J. Ekanayake, N. Jenkins, and G. Strbac, "Frequency response from wind turbines," *Wind Engineering*, vol. 32, pp. 573–586, 2008. [Online]. Available: http://journals.sagepub.com/doi/10.1260/030952408787548811

[220] R. G. de Almeida, E. D. Castronuovo, and J. A. P. Lopes, "Optimum generation control in wind parks when carrying out system operator requests," *IEEE Transactions on Power Systems*, vol. 21, pp. 718–725, 2006.

[221] S. Ghosh, S. Kamalasadan, N. Senroy, and J. Enslin, "Doubly fed induction generator (dfig)-based wind farm control framework for primary frequency and inertial response application," *IEEE Transactions on Power Systems*, vol. 31, pp. 1861–1871, 2016.

[222] I. Erlich and M. Wilch, "Primary frequency control by wind turbines," in *IEEE PES General Meeting*. IEEE, 7 2010, pp. 1–8. [Online]. Available: http://ieeexplore.ieee.org/document/5589911/

[223] S. Engelken, A. Mendonca, and M. Fischer, "Inertial response with improved variable recovery behaviour provided by type 4 wts," *IET Renewable Power Generation*, vol. 11, pp. 195–201, 2017. [Online]. Available: http://digital-library.theiet.org/content/journals/10.1049/iet-rpg.2016.0333

[224] X. Zhaoxia, H. Yu, J. M. Guerrero, and F. Hongwei, "Frequency participation by using virtual inertia in wind turbines including energy storage," in *IECON 2017 - 43rd Annual Conference of the IEEE Industrial Electronics Society*. IEEE, 10 2017, pp. 2492–2497. [Online]. Available: http://ieeexplore.ieee.org/document/8216419/

[225] M. Krpan, I. Kuzle, and Y. Liu, "Analysing frequency support from dfig-based wind turbines - impact of parameters and initial conditions," in *11th Mediterranean Conference on Power Generation,Transmission, Distribution and Energy Conversion*. Institution of Engineering and Technology (IET), 10 2018, pp. 1–7.

[226] M. Krpan and I. Kuzle, "Dynamic characteristics of virtual inertial response provision by dfig-based wind turbines," *Electric Power Systems Research*, vol. 178, p. 106005, 1 2020. [Online]. Available: https://www.sciencedirect.com/science/article/pii/S0378779619303244

[227] M. Kayikçi and J. V. Milanović, "Assessing transient response of dfig-based wind plants - the influence of model simplifications and parameters," *IEEE Transactions on Power Systems*, vol. 23, pp. 545–554, 2008.

[228] Z. Wang, C. Shen, and F. Liu, "Impact of dfig with phase lock loop dynamics on power systems small signal stability," in *2014 IEEE PES General Meeting | Conference Exposition*, July 2014, pp. 1–5.

[229] P. Tielens, M. Reza, A. Marinopoulos, and J. Driesen, "Frequency support by wind power plants in isolated grids with varying generation mix," in *2012 IEEE Power and Energy Society General Meeting*. IEEE, 7 2012, pp. 1–8. [Online]. Available: http://ieeexplore.ieee.org/document/6344690/

[230] IEEE PES Task Force on Turbine-Governor Modeling, "Dynamic models for turbine-governors in power system studies," IEEE, Tech. Rep., 2013.

[231] P.M. Anderson and A.A. Fouad, *Power System Control and Stability*. Wiley-IEEE Press, 2002, iSSN: 00135127.

[232] M. M. C. Merlin, T. C. Green, P. D. Mitcheson, F. J. Moreno, K. J. Dyke *et al.*, "Cell capacitor sizing in modular multilevel converters and hybrid topologies," in *2014 16th European Conference on Power Electronics and Applications*, 2014, pp. 1–10.

[233] C. Spallarossa, M. Merlin, and T. Green, "Augmented inertial response of multi-level converters using internal energy storage," in *2016 IEEE International Energy Conference (ENERGYCON)*, 2016, pp. 1–6.

[234] M. R. Hasan, "Development, calibration and simulation of generic VSC-HVDC high level controls for DC grid Simulation," Master's thesis, KTH Stockholm, 2014.

[235] B. Yang, L. Jiang, T. Yu, H. Shu, C.-K. Zhang *et al.*, "Passive control design for multi-terminal vsc-hvdc systems via energy shaping," *International Journal of Electrical Power & Energy Systems*, vol. 98, pp. 496–508, 2018. [Online]. Available: https://www.sciencedirect.com/science/article/pii/S0142061516318130

[236] S. Casoria, "VSC-Based HVDC Transmission System." [Online]. Available: https://www.mathworks.com/help/sps/ug/vsc-based-hvdc-transmission-system-detailed-model.html

[237] J. R. Lluch, "Modelling, control and simulation of LCC-HVDC systems for stability studies," Master's thesis, Escola Técnica Superior d'Enginyeria Industrial de Barcelona, 2017.

[238] Mathworks, "Thyristor-Based HVDC Link." [Online]. Available: https://www.mathworks.com/help/sps/powersys/ug/thyristor-based-hvdc-link.html

[239] M. Faruque, Y. Zhang, and V. Dinavahi, "Detailed modeling of cigre hvdc benchmark system using pscad/emtdc and psb/simulink," *IEEE Transactions on Power Delivery*, vol. 21, no. 1, pp. 378–387, 2006.

[240] B. J. Kirby, J. Dyer, C. Martinez, R. A. Shoureshi, R. Guttromson *et al.*, "Frequency Control Concerns In The North American Electric Power System," Oak Ridge National Laboratory, Tech. Rep., December 2002.

[241] ENTSO-E, "Rate of Change of Frequency (RoCoF) withstand capability," ENTSO-E, Tech. Rep., January 2018.

[242] RG-CE System Protection & Dynamics Sub Group, "Frequency Measurement Requirements and Usage," ENTSO-E, Tech. Rep., January 2018.

[243] EirGrid and SONI, "RoCoF Modification Proposal—TSOs' Recommendations," EirGrid and SONI, Tech. Rep., September 2012.

[244] EirGrid and SONI, "DS3 Rate of Change of Frequency Modification Recommendation to the CER," EirGrid and SONI, Tech. Rep., December 2012.

[245] EirGrid and SONI, "RoCoF Alternative & Complementary Solutions Project: Phase 2 Study Report," EirGrid and SONI, Tech. Rep., March 2016.

[246] F. Liccardo, P. Marino, and G. Raimondo, "Robust and fast three-phase pll tracking system," *IEEE Transactions on Industrial Electronics*, vol. 58, no. 1, pp. 221–231, 2011.

[247] B. Liu, F. Zhuo, Y. Zhu, H. Yi, and F. Wang, "A three-phase pll algorithm based on signal reforming under distorted grid conditions," *IEEE Transactions on Power Electronics*, vol. 30, no. 9, pp. 5272–5283, 2015.

[248] M. J. Korytowski, "Effects of the phase locked loop on the stability of a voltage source converter in a weak grid environment," Ph.D. dissertation, University of Pittsburgh, 2014.

[249] B. Wen, D. Dong, D. Boroyevich, R. Burgos, P. Mattavelli *et al.*, "Impedance-based analysis of grid-synchronization stability for three-phase paralleled converters," *IEEE Transactions on Power Electronics*, vol. 31, no. 1, pp. 26–38, 2016.

[250] D. Dong, B. Wen, D. Boroyevich, P. Mattavelli, and Y. Xue, "Analysis of phase-locked loop low-frequency stability in three-phase grid-connected power converters considering impedance interactions," *IEEE Transactions on Industrial Electronics*, vol. 62, no. 1, pp. 310–321, 2015.

[251] R. Faranda, M. Gallina, and D. T. Son, "A new simplified model of double-layer capacitors," in *2007 International Conference on Clean Electrical Power*, May 2007, pp. 706–710.

[252] S. Buller, E. Karden, D. Kok, and R. W. De Doncker, "Modeling the dynamic behavior of supercapacitors using impedance spectroscopy," *IEEE Trans. Ind. Appl.*, vol. 38, no. 6, pp. 1622–1626, Nov 2002.

[253] I. Zeltser and S. Ben-Yaakov, "On spice simulation of voltage-dependent capacitors," *IEEE Trans. Power Electron.*, vol. 33, no. 5, pp. 3703–3710, 2018.

[254] Maxwell Technologies, "Maxwell technologies®BOOSTCAP®ultracapacitor cell sizing," 2009, applications note.

[255] DIgSILENT GmbH, "Battery energy storing system template," 2017, template documentation.

[256] J. Kim, V. Gevorgian, Y. Luo, M. Mohanpurkar, V. Koritarov *et al.*, "Supercapacitor to provide ancillary services with control coordination," *IEEE Trans. Ind. Appl.*, vol. 55, no. 5, pp. 5119–5127, Sep. 2019.

[257] Maxwell Technologies, "2.7v 650-3000f ultracapacitor cells," 2019, datasheet.

[258] L. Yang, Z. Hu, S. Xie, S. Kong, and W. Lin, "Adjustable virtual inertia control of supercapacitors in pv-based ac microgrid cluster," *Electr. Power Syst. Res.*, vol. 173, pp. 71 – 85, 2019.

[259] Y. Liu, W. Du, L. Xiao, H. Wang, S. Bu *et al.*, "Sizing a hybrid energy storage system for maintaining power balance of an isolated system with high penetration of wind generation," *IEEE Trans. Power Syst.*, vol. 31, no. 4, pp. 3267–3275, July 2016.

[260] A. Santucci, A. Sorniotti, and C. Lekakou, "Model predictive control for the power-split between supercapacitor and battery for automotive applications," in *2013 IEEE International Electric Vehicle Conference (IEVC)*, Oct 2013, pp. 1–7.

[261] P. Golchoubian and N. L. Azad, "Real-time nonlinear model predictive control of a battery–supercapacitor hybrid energy storage system in electric vehicles," *IEEE Trans. Veh. Technol.*, vol. 66, no. 11, pp. 9678–9688, Nov 2017.

[262] Amin, R. T. Bambang, A. S. Rohman, C. J. Dronkers, R. Ortega *et al.*, "Energy management of fuel cell/battery/supercapacitor hybrid power sources using model predictive control," *IEEE Trans. Ind. Informat.*, vol. 10, no. 4, pp. 1992–2002, Nov 2014.

[263] B. Hredzak, V. G. Agelidis, and M. Jang, "A model predictive control system for a hybrid battery-ultracapacitor power source," *IEEE Trans. Power Electron.*, vol. 29, no. 3, pp. 1469–1479, March 2014.

[264] M. D. Mufti, S. J. Iqbal, S. A. Lone, and Q. Ain, "Supervisory adaptive predictive control scheme for supercapacitor energy storage system," *IEEE Systems Journal*, vol. 9, no. 3, pp. 1020–1030, Sep. 2015.

[265] Y. Luo, C. Wang, L. Tan, G. Liao, M. Zhou *et al.*, "Application of generalized predictive control for charging super capacitors in microgrid power systems under input constraints," in *2015 IEEE International Conference on Cyber Technology in Automation, Control, and Intelligent Systems (CYBER)*, 2015, pp. 1708–1713.

[266] Y. Luo, M. Panwar, M. Mohanpurkar, and R. Hovsapian, "Real time optimal control of supercapacitor operation for frequency response," in *2016 IEEE Power and Energy Society General Meeting (PESGM)*, 2016, pp. 1–5.

[267] M. Darabian and A. Jalilvand, "A power control strategy to improve power system stability in the presence of wind farms using facts devices and predictive control," *International Journal of Electrical Power & Energy Systems*, vol. 85, pp. 50–66, 2017.

[268] M. S. Masaki, L. Zhang, and X. Xia, "A hierarchical predictive control for supercapacitor-retrofitted grid-connected hybrid renewable systems," *Applied Energy*, vol. 242, pp. 393–402, 2019.

[269] U. Akram and M. Khalid, "A coordinated frequency regulation framework based on hybrid battery-ultracapacitor energy storage technologies," *IEEE Access*, vol. 6, pp. 7310–7320, 2018.

[270] D. Mayne, J. Rawlings, C. Rao, and P. Scokaert, "Constrained model predictive control: Stability and optimality," *Automatica*, vol. 36, no. 6, pp. 789 – 814, 2000. [Online]. Available: http://www.sciencedirect.com/science/article/pii/S0005109899002149

[271] ENTSO-E, "The proposal of all Transmission System Operators performing the reserve replacement for the implementation framework for the exchange of balancing energy from Replacement Reserves in accordance with Article 19 of Commission Regulation (EU) 2017/2195 of 23 November 2017 establishing a guideline on electricity balancing," ENTSO-E, Tech. Rep., 2018.

[272] ENTSO-E, "All TSOs' proposal for the implementation framework for a European platform for the exchange of balancing energy from frequency restoration reserves with manual

activation in accordance with Article 20 of Commission Regulation (EU) 2017/2195 establishing a guideline on electricity balancing," ENTSO-E, Tech. Rep., 2018.

[273] ENTSO-E, "Explanatory Document to All TSOs' proposal for the implementation framework for a European platform for the exchange of balancing energy from frequency restoration reserves with automatic activation in accordance with Article 21 of Commission Regulation (EU) 2017/2195 of 23 November 2017 establishing a guideline on electricity balancing," ENTSO-E, Tech. Rep., 2018.

[274] European Commission, "COMMISSION REGULATION (EU) 2017/1485 of 2 August 2017 establishing a guideline on electricity transmission system operation," EC, Tech. Rep., 2021.

[275] R. Olfati-Saber, J. A. Fax, and R. M. Murray, "Consensus and cooperation in networked multi-agent systems," *Proceedings of the IEEE*, vol. 95, no. 1, pp. 215–233, 2007.

[276] S. Yang, S. Tan, and J.-X. Xu, "Consensus based approach for economic dispatch problem in a smart grid," *IEEE Transactions on Power Systems*, vol. 28, no. 4, pp. 4416–4426, 2013.

[277] Y. Xu, W. Zhang, G. Hug, S. Kar, and Z. Li, "Cooperative control of distributed energy storage systems in a microgrid," *IEEE Transactions on Smart Grid*, vol. 6, no. 1, pp. 238–248, 2015.

[278] D. Mateos-Núñez and J. Cortés, "Distributed saddle-point subgradient algorithms with laplacian averaging," *IEEE Transactions on Automatic Control*, vol. 62, no. 6, pp. 2720–2735, 2017.

[279] S. Boyd and L. Vandenberghe, *Convex optimization*. Cambridge University Press, 2004.

[280] D. Feijer and F. Paganini, "Stability of primal–dual gradient dynamics and applications to network optimization," *Automatica*, vol. 46, no. 12, pp. 1974–1981, 2010. [Online]. Available: https://www.sciencedirect.com/science/article/pii/S0005109810003596

[281] R. Huang and Z. Ding, "Robustness to delay mismatch in consensus control under undirected graphs," *IFAC-PapersOnLine*, vol. 53, no. 2, pp. 7671–7676, 2020, 21st IFAC World Congress. [Online]. Available: https://www.sciencedirect.com/science/article/pii/S2405896320321054

[282] A. V. Proskurnikov and G. Calafiore, "New results on delay robustness of consensus algorithms," 2020, arXiv preprint, 2009.02714.

[283] UCTE, "P1 – Policy 1: Load-Frequency Control and Performance," UCTE, Tech. Rep., 2009.

[284] UCTE, "Appendix 1: Load-Frequency Control and Performance," UCTE, Tech. Rep., 2004.

Nomenclature

Abbreviations

APC   Active power control

AVR   Automatic voltage regulator

CID   Converter-interfaced devices

CSC   Current-sourced converter

DCS   Distributed control system

DCVC DC voltage control

DFIG Doubly-fed induction generator

DSC   Device-side converter

ECS   Energy conversion system

EES   Elektroenergetski sustav (*Electric power system*, in Croatian)

EMT Electromagnetic transient

ESO   Electricity system operator

ESR   equivalent series resistance

ESS   Energy storage systems

EV   Electric vehicle

FACTS Flexible alternating current transmission system

GSC   Grid-side converter

HIL   Hardware-in-the-loop

HVDC High-voltage direct current

Nomenclature

IGBT Insulated-gate bipolar transistor

IM   Induction machine

LCC   Line-commutated converter

MMC Modular multilevel converter

MPC Model predictive control

PI   Proportional-integral

PLL   Phase-locked loop

PMSG Permanent magnet synchronous generator

PSS   Power system stabilizer

PV   Photovoltaic

PWM Pulse-width modulation

RES   Renewable energy sources

RMS Root mean square

ROCOF Rate-of-change-of-frequency

RPC   Reactive power control

SC   Supercapacitor

SCIG Squirrel cage induction generator

SCR   Short-circuit ratio

SFR   System frequency response

SG   Synchronous generator

SGlab Smart Grid Laboratory [21]

SRF-PLL Synchronous reference frame PLL

SSCI Subsynchronous control interaction

SSR   Subsynchronous resonance

STATCOM Static synchronous compensator

SVC   Static var compensator

THD   Total harmonic distortion

UC   Ultracapacitor (supercapacitor)

UCBS Ultracapacitor (supercapacitor) bank system

VSC   Voltage-sourced converters

VSG   Virtual synchronous generator

VSM   Virtual synchronous machine

VSP   Virtual storage plant

WECS Wind energy conversion system

WRIG Wound rotor induction generator

WTG   Wind turbine-generator

List of Figures

List of Tables

Biography

Matej Krpan was born in Zagreb in 1992. He graduated from the Ruđer Bošković Technical School in 2011 with a computer technician degree. He obtained BEng and MEng degrees in electrical engineering at the University of Zagreb, Faculty of Electrical Engineering and Computing (FER), in 2014 and 2016, respectively. From October 2016 to May 2023 he was with the Department of Energy and Power Systems of FER as a research and teaching assistant. He enrolled in the doctoral program in March 2017 under the supervision of prof. Igor Kuzle. Since July 2023, he works in Hitachi Energy Sweden AB as an HVDC system performance engineer.

He coauthored seventeen journal papers and nineteen conference papers. He won the best paper award in the Study Committee C2 at the 13th HRO CIGRE session in 2017. He won third place in the best paper category at the IET 6th International Conference on Renewable Power Generation in 2017. He won the excellent paper award at the IEEE Sustainable Power & Energy Conference in 2019 and best presenter award at IEEE ENERGYCON in 2022. He is a reviewer for several international journals.

He coauthored over 30 grid integration studies for transmission and distribution system operators. He was a teaching assistant for the Power System Dynamics and Control and Power System Operation and Planning graduate courses. He co-supervised several student projects, seminars, bachelor and graduate theses. His area of scientific interest is the dynamics, stability and control of power systems with a high share of power electronic converters.

List of publications

The work presented in this thesis has been reported in the following publications:

Articles in peer-reviewed journals

[1] B. Barac, M. Krpan, T. Capuder, and I. Kuzle, "Modeling and Initialization of a Virtual Synchronous Machine for Power System Fundamental Frequency Simulations," *IEEE Access*, vol. 9, pp. 160 116–160 134, 2021.

[2] M. Krpan, I. Kuzle, A. Radovanovic, and J. V. Milanovic, "Modelling of Supercapacitor Banks for Power System Dynamics Studies," *IEEE Transactions on Power Systems*, vol. 36, no. 5, pp. 3987–3996, 2021.

[3] M. Beus, M. Krpan, I. Kuzle, H. Pandzic, and A. Parisio, "A Model Predictive Control Approach to Operation Optimization of an Ultracapacitor Bank for Frequency Control," *IEEE Transactions on Energy Conversion*, vol. 36, no. 3, pp. 1743–1755, 2021.

[4] M. Krpan and I. Kuzle, "Dynamic characteristics of virtual inertial response provision by DFIG-based wind turbines," *Electric Power Systems Research*, vol. 178, p. 106005, jan 2020. [Online]. Available: https://www.sciencedirect.com/science/article/pii/S0378779619303244

[5] J. Đaković, M. Krpan, P. Ilak, T. Baškarad, and I. Kuzle, "Impact of wind capacity share, allocation of inertia and grid configuration on transient RoCoF: The case of the Croatian power system," *International Journal of Electrical Power and Energy Systems*, vol. 121, p. 106075, oct 2020.

[6] M. Krpan and I. Kuzle, "Introducing low-order system frequency response modelling of a future power system with high penetration of wind power plants with frequency support capabilities," *IET Renewable Power Generation*, vol. 12, no. 13, pp. 1453–1461, oct 2018. [Online]. Available: https://digital-library.theiet.org/content/journals/10.1049/iet-rpg.2017.0811

[7] M. Krpan and I. Kuzle, "Inertial and primary frequency response model of variable-speed wind turbines," *Published in The Journal of Engineering*, vol. 2017, no. 3, pp. 844–848, 2017. [Online]. Available: http://digital-library.theiet.org/content/journals/10.1049/joe.2017.0449

Conference papers

[1] M. Krpan, I. Erceg, I. Kuzle, and H. Pandžić, "Three-phase srf pll model for system frequency response studies in low-inertia systems," in *2022 IEEE PES Innovative Smart Grid Technologies - Asia (ISGT Asia)*, 2022, pp. 155–159.

[2] M. Krpan, M. Beus, I. Kuzle, and H. Pandžić, "Laboratory testbed for advanced grid applications of interconnected battery energy storage systems in smart grids," in *2022 IEEE International Conference on Power Systems Technology (POWERCON)*, 2022, pp. 1–6.

[3] M. Krpan, I. Kuzle, and M. Beus, "Istraživanje i razvoj naprednih metoda za regulaciju elektroenergetskog sustava u laboratoriju za napredne elektroenergetske mreže," in *15. simpozij o vođenju EES-a*, 2022, pp. 1–10.

[4] M. Krpan and I. Kuzle, "Impact of ultracapacitor modelling on fast frequency control performance," in *2020 International Conference on Smart Grids and Energy Systems (SGES)*, 2020, pp. 326–331.

[5] M. Krpan and I. Kuzle, "On modelling and sizing a supercapacitor energy storage for power system frequency control," *IET Conference Proceedings*, pp. 404–409(5), January 2021. [Online]. Available: https://digital-library.theiet.org/content/conferences/10.1049/icp.2021.1242

[6] M. Beus, H. Pandzic, M. Krpan, and I. Kuzle, "Korištenje modelskog prediktivnog upravljanja za optimizaciju pogona superkondenzatora u svrhu pružanja primarne regulacije frekvencije," in *14. simpozij o sustavu vođenja EES-a*, Opatija, Croatia, 2020, pp. 1–10.

[7] M. Krpan and I. Kuzle, "Coordinated control of an ultracapacitor bank and a variable-speed wind turbine generator for inertial response provision during low and above rated wind speeds," in *2019 IEEE Sustainable Power and Energy Conference (iSPEC)*, 2019, pp. 1693–1698.

[8] M. Krpan, I. Kuzle, and Y. Liu, "Analysing Frequency Support from DFIG-based Wind Turbines - Impact of Parameters and Initial Conditions," in *11th Mediterranean Conference on Power Generation,Transmission, Distribution and Energy Conversion*. Institution of Engineering and Technology (IET), oct 2018, pp. 1–7.

[9] J. Dakovic, P. Ilak, T. Baskarad, M. Krpan, and I. Kuzle, "Effectiveness of Wind Turbine Fast Frequency Response Control on Electrically Distanced Active Power Disturbance Mitigation," in *11th Mediterranean Conference on Power Generation,Transmission, Distribution and Energy Conversion*. Institution of Engineering and Technology (IET), oct 2018, pp. 1–7.

[10] M. Krpan and I. Kuzle, "Towards the new low-order system frequency response model of power systems with high penetration of variable-speed wind turbine generators," in *2018 IEEE Power Energy Society General Meeting (PESGM)*, 2018, pp. 1–5.

[11] M. Krpan and I. Kuzle, "Sudjelovanje vjetroelektrana s promjenjivom brzinom vrtnje u primarnoj regulaciji frekvencije," in *13. savjetovanje HRO CIGRE*, Šibenik, 2017, pp. 1–10. [Online]. Available: https://www.researchgate.net/publication/322069323_Sudjelovanje_vjetroelektrana_s_promjenjivom_brzinom_vrtnje_u_primarnoj_regulaciji_frekvencije

[12] M. Krpan, "Koncept virtualne konstante tromosti i regulacija frekvencije u elektroenergetskim sustavima s visokom penetracijom obnovljivih izvora energije," in *HKIE 10. Dani inženjera elektrotehnike*, Pula, 2017, pp. 1–11.

[13] M. Krpan and I. Kuzle, "Linearized model of variable speed wind turbines for studying power system frequency changes," in *17th IEEE International Conference on Smart Technologies, EUROCON 2017 - Conference Proceedings*, Ohrid, Macedonia, 2017, pp. 393–398. [Online]. Available: http://ieeexplore.ieee.org/document/8011141/

Other publications

[1] X. Wang, T. Zhao, A. Parisio, D. Rayo, R. de Arriba *et al.*, "Techno-economic framework and algorithms for advanced coordinated use of distributed storage technologies," CROSSBOW consortium, Tech. Rep. Deliverable D7.2, aug 2019.

The following works have been published during the course of the doctoral studies, but their content is not included in this thesis:

Articles in peer-reviewed journals

[1] B. Barać, M. Krpan, and T. Capuder, "Modelling of pem fuel cell for power system dynamic studies," *IEEE Transactions on Power Systems*, pp. 1–13, 2023.

[2] M. Miletić, M. Krpan, I. Pavić, H. Pandžić, and I. Kuzle, "Optimal primary frequency reserve provision by an aggregator considering nonlinear unit dynamics," *IEEE Transactions on Power Systems*, pp. 1–14, 2023.

[3] T. Capuder, B. Barać, M. Kostelac, and M. Krpan, "Three-stage modeling framework for analyzing islanding capabilities of decarbonized energy communities," *Energies*, vol. 16, no. 11, p. 4321, May 2023. [Online]. Available: http://dx.doi.org/10.3390/en16114321

[4] A. Secic, M. Krpan, and I. Kuzle, "Using Deep Neural Networks for On-Load Tap Changer Audio-based Diagnostics," *IEEE Transactions on Power Delivery*, 2021.

[5] N. Holjevac, T. Baškarad, J. Đaković, M. Krpan, M. Zidar *et al.*, "Challenges of High Renewable Energy Sources Integration in Power Systems—The Case of Croatia," *Energies 2021, Vol. 14, Page 1047*, vol. 14, no. 4, p. 1047, feb 2021. [Online]. Available: https://www.mdpi.com/1996-1073/14/4/1047

[6] M. Brezovec, I. Kuzle, M. Krpan, and N. Holjevac, "Improved dynamic model of a bulb turbine-generator for analysing oscillations caused by mechanical torque disturbance on a runner blade," *International Journal of Electrical Power and Energy Systems*, vol. 119, p. 105929, jul 2020.

[7] M. Brezovec, I. Kuzle, M. Krpan, and N. Holjevac, "Analysis and treatment of power oscillations in hydropower plant dubrava," *IET Renewable Power Generation*, vol. 14, no. 1, pp. 80–89, jan 2020.

[8] A. Secic, M. Krpan, and I. Kuzle, "Vibro-Acoustic Methods in the Condition Assessment of Power Transformers: A Survey," *IEEE Access*, vol. 7, pp. 83 915–83 931, 2019.

[9] M. Krpan and I. Kuzle, "The mathematical model of a wind power plant and a gas power plant," *Journal of Energy*, vol. 66, no. 1, pp. 69–86, 2017. [Online]. Available: https://hrcak.srce.hr/file/294107

[10] M. Brezovec, I. Kuzle, and M. Krpan, "Detailed mathematical and simulation model of a synchronous generator," *Journal of Energy*, vol. 64, no. 1, pp. 102–129, 2015. [Online]. Available: https://www.researchgate.net/publication/322364716_Detailed_mathematical_and_simulation_model_of_a_synchronous_generator

Conference papers

[1] B. Barać, M. Krpan, and T. Capuder, "Aggregated model of a flexible multi-energy distribution system for coordinated tso-dso fast frequency services provision," in *2023 International Conference on Smart Energy Systems and Technologies (SEST)*, 2023, pp. 1–6.

[2] M. Krpan, M. Miletić, I. Kuzle, and H. Pandžić, "Incorporating settling time constraints of energy storage systems in frequency containment control optimization problems," in *2022 IEEE 7th International Energy Conference (ENERGYCON)*, 2022, pp. 1–6.

[3] I. Kuzle, M. Krpan, and M. Beus, "Razvoj laboratorija za napredne elektroenergetske mreže," in *15. savjetovanje HRO CIGRE*, 2021, pp. 1–11.

[4] T. Capuder, M. Kostelac, M. Krpan, and I. Pavic, "Multi-energy microgrid ability to provide flexibility services to the system operator and security of supply to end-users," in *SEST 2020 - 3rd International Conference on Smart Energy Systems and Technologies*, 2020.

[5] I. Pavić, M. Krpan, I. Kuzle, and Y. Liu, "Effect of Stochastic Variables on Balancing Mechanism," in *2019 International Conference on Modeling, Simulation, Optimization and Numerical Techniques (SMONT 2019)*. Atlantis Press, may 2019, pp. 211–214.

[6] N. Holjevac, M. Zidar, M. Krpan, and I. Kuzle, "Optimizing the Grid Connection Scheme of the Wind Power Plant," in *14th Conference on Sustainable Development of Energy, Water and Environment Systems (SDEWES)*, Oct 2019, pp. 1–17.

In addition to the aforementioned publications, the content of this thesis is also based on the following master's seminars, master's projects and master's theses conducted at the Department of Energy and Power Systems, Faculty of electrical engineering and computing, University of Zagreb.

Master's seminar

[1] B. Barać, "Mikromreže izmjenične struje u otočnom pogonu," Zagreb, Croatia, May 2020, University of Zagreb, Faculty of electrical engineering and computing.

Master's project

[1] B. Barać, "Virtualni sinkroni generator," Zagreb, Croatia, Jan. 2021, University of Zagreb, Faculty of electrical engineering and computing.

Master's thesis

[1] I. S. Alfageme, "Dynamic modelling of a solar pv plant with a battery storage system," Master's thesis, University of Zagreb, Faculty of electrical engineering and computing, Zagreb, Croatia, Jun. 2022.

[2] B. Barać, "Converter-based microgrid providing system ancillary services with dynamically stable off-grid transition & operation," Master's thesis, University of Zagreb, Faculty of electrical engineering and computing, Zagreb, Croatia, Jun. 2021.

[3] I. M. A. Mohamed, "Modeling and control of dc-dc converters for power system applications," Master's thesis, University of Zagreb, Faculty of electrical engineering and computing, Zagreb, Croatia, Jun. 2021.

Životopis

Matej Krpan rođen je u Zagrebu 1992. godine. Završio je Tehničku školu Ruđera Boškovića 2011. godine, smjer tehničar za računalstvo. Preddiplomski i diplomski sveučilišni studij završio je na Sveučilištu u Zagrebu na Fakultetu elektrotehnike i računarstva (FER) 2014., odnosno 2016. godine, smjer elektrotehnika i informacijska tehnologija, profil elektroenergetika. Od listopada 2016. do svibnja 2023. godine bio je zaposlen na FER-u na Zavodu za visoki napon i energetiku kao asistent. Doktorski studij upisao je u ožujku 2017. godine pod mentorstvom prof. dr. sc. Igora Kuzle. Od srpnja 2023. zaposlen je u Hitachi Energy Sweden AB na poziciji HVDC system performance engineer.

Objavio je sedamnaest radova u časopisima i devetnaest radova na konferencijama. Dobitnik je nagrade za najbolji referat u SO C2 na 13. savjetovanju HRO CIGRE 2017. godine. Osvojio je treće mjesto u kategoriji za najbolji rad na međunarodnoj konferenciji IET 6th International Conference on Renewable Power Generation 2017. godine, dobitnik je nagrade za odličan rad na međunarodnoj konferenciji IEEE Sustainable Power & Energy Conference 2019. godine te nagrade za najbolju prezentaciju na međunarodnoj konferenciji IEEE ENERGYCON 2022. godine. Recenzent je u nekoliko međunarodnih časopisa.

Koautor je na preko trideset tehničkih studija i elaborata za operatore prijenosnog i distribucijskog sustava. Bio je asistent je na kolegijima Dinamika i regulacija elektroenergetskog sustava i Planiranje pogona elektroenergetskog sustava. Bio je suvoditelj na nekoliko studentskih projekata te seminarskih, završnih i diplomskih radova. Područje znanstvenog interesa mu je dinamika, regulacija i stabilnost EES-a s visokim udjelom elektroničkih energetskih pretvarača.

Popis radova

Sadržaj ove disertacije objavljen je u sljedećim radovima:

Radovi u časopisima

[1] B. Barac, M. Krpan, T. Capuder, and I. Kuzle, "Modeling and Initialization of a Virtual Synchronous Machine for Power System Fundamental Frequency Simulations," *IEEE Access*, vol. 9, pp. 160 116–160 134, 2021.

[2] M. Krpan, I. Kuzle, A. Radovanovic, and J. V. Milanovic, "Modelling of Supercapacitor Banks for Power System Dynamics Studies," *IEEE Transactions on Power Systems*, vol. 36, no. 5, pp. 3987–3996, 2021.

[3] M. Beus, M. Krpan, I. Kuzle, H. Pandzic, and A. Parisio, "A Model Predictive Control Approach to Operation Optimization of an Ultracapacitor Bank for Frequency Control," *IEEE Transactions on Energy Conversion*, vol. 36, no. 3, pp. 1743–1755, 2021.

[4] M. Krpan and I. Kuzle, "Dynamic characteristics of virtual inertial response provision by DFIG-based wind turbines," *Electric Power Systems Research*, vol. 178, p. 106005, jan 2020. [Online]. Available: https://www.sciencedirect.com/science/article/pii/S0378779619303244

[5] J. Đaković, M. Krpan, P. Ilak, T. Baškarad, and I. Kuzle, "Impact of wind capacity share, allocation of inertia and grid configuration on transient RoCoF: The case of the Croatian power system," *International Journal of Electrical Power and Energy Systems*, vol. 121, p. 106075, oct 2020.

[6] M. Krpan and I. Kuzle, "Introducing low-order system frequency response modelling of a future power system with high penetration of wind power plants with frequency support capabilities," *IET Renewable Power Generation*, vol. 12, no. 13, pp. 1453–1461, oct 2018. [Online]. Available: https://digital-library.theiet.org/content/journals/10.1049/iet-rpg.2017.0811

[7] M. Krpan and I. Kuzle, "Inertial and primary frequency response model of variable-speed wind turbines," *Published in The Journal of Engineering*, vol. 2017, no. 3, pp. 844–848, 2017. [Online]. Available: http://digital-library.theiet.org/content/journals/10.1049/joe.2017.0449

Radovi na konferencijama

[1] M. Krpan, I. Erceg, I. Kuzle, and H. Pandžić, "Three-phase srf pll model for system frequency response studies in low-inertia systems," in *2022 IEEE PES Innovative Smart Grid Technologies - Asia (ISGT Asia)*, 2022, pp. 155–159.

[2] M. Krpan, M. Beus, I. Kuzle, and H. Pandžić, "Laboratory testbed for advanced grid applications of interconnected battery energy storage systems in smart grids," in *2022 IEEE International Conference on Power Systems Technology (POWERCON)*, 2022, pp. 1–6.

[3] M. Krpan, I. Kuzle, and M. Beus, "Istraživanje i razvoj naprednih metoda za regulaciju elektroenergetskog sustava u laboratoriju za napredne elektroenergetske mreže," in *15. simpozij o vođenju EES-a*, 2022, pp. 1–10.

[4] M. Krpan and I. Kuzle, "Impact of ultracapacitor modelling on fast frequency control performance," in *2020 International Conference on Smart Grids and Energy Systems (SGES)*, 2020, pp. 326–331.

[5] M. Krpan and I. Kuzle, "On modelling and sizing a supercapacitor energy storage for power system frequency control," *IET Conference Proceedings*, pp. 404–409(5), January 2021. [Online]. Available: https://digital-library.theiet.org/content/conferences/10.1049/icp.2021.1242

[6] M. Beus, H. Pandzic, M. Krpan, and I. Kuzle, "Korištenje modelskog prediktivnog upravljanja za optimizaciju pogona superkondenzatora u svrhu pružanja primarne regulacije frekvencije," in *14. simpozij o sustavu vođenja EES-a*, Opatija, Croatia, 2020, pp. 1–10.

[7] M. Krpan and I. Kuzle, "Coordinated control of an ultracapacitor bank and a variable-speed wind turbine generator for inertial response provision during low and above rated wind speeds," in *2019 IEEE Sustainable Power and Energy Conference (iSPEC)*, 2019, pp. 1693–1698.

[8] M. Krpan, I. Kuzle, and Y. Liu, "Analysing Frequency Support from DFIG-based Wind Turbines - Impact of Parameters and Initial Conditions," in *11th Mediterranean Conference on Power Generation,Transmission, Distribution and Energy Conversion*. Institution of Engineering and Technology (IET), oct 2018, pp. 1–7.

[9] J. Dakovic, P. Ilak, T. Baskarad, M. Krpan, and I. Kuzle, "Effectiveness of Wind Turbine Fast Frequency Response Control on Electrically Distanced Active Power Disturbance Mitigation," in *11th Mediterranean Conference on Power Generation,Transmission, Distribution and Energy Conversion*. Institution of Engineering and Technology (IET), oct 2018, pp. 1–7.

[10] M. Krpan and I. Kuzle, "Towards the new low-order system frequency response model of power systems with high penetration of variable-speed wind turbine generators," in *2018 IEEE Power Energy Society General Meeting (PESGM)*, 2018, pp. 1–5.

[11] M. Krpan and I. Kuzle, "Sudjelovanje vjetroelektrana s promjenjivom brzinom vrtnje u primarnoj regulaciji frekvencije," in *13. savjetovanje HRO CIGRE*, Šibenik, 2017, pp. 1–10. [Online]. Available: https://www.researchgate.net/publication/322069323_Sudjelovanje_vjetroelektrana_s_promjenjivom_brzinom_vrtnje_u_primarnoj_regulaciji_frekvencije

[12] M. Krpan, "Koncept virtualne konstante tromosti i regulacija frekvencije u elektroenergetskim sustavima s visokom penetracijom obnovljivih izvora energije," in *HKIE 10. Dani inženjera elektrotehnike*, Pula, 2017, pp. 1–11.

[13] M. Krpan and I. Kuzle, "Linearized model of variable speed wind turbines for studying power system frequency changes," in *17th IEEE International Conference on Smart Technologies, EUROCON 2017 - Conference Proceedings*, Ohrid, Macedonia, 2017, pp. 393–398. [Online]. Available: http://ieeexplore.ieee.org/document/8011141/

Ostale publikacije

[1] X. Wang, T. Zhao, A. Parisio, D. Rayo, R. de Arriba *et al.*, "Techno-economic framework and algorithms for advanced coordinated use of distributed storage technologies," CROSSBOW consortium, Tech. Rep. Deliverable D7.2, aug 2019.

U sklopu doktorskog studija objavljeni su sljedeći radovi, ali njihov sadržaj nije uključen u ovu disertaciju:

Radovi u časopisima

[1] B. Barać, M. Krpan, and T. Capuder, "Modelling of pem fuel cell for power system dynamic studies," *IEEE Transactions on Power Systems*, pp. 1–13, 2023.

[2] M. Miletić, M. Krpan, I. Pavić, H. Pandžić, and I. Kuzle, "Optimal primary frequency reserve provision by an aggregator considering nonlinear unit dynamics," *IEEE Transactions on Power Systems*, pp. 1–14, 2023.

[3] T. Capuder, B. Barać, M. Kostelac, and M. Krpan, "Three-stage modeling framework for analyzing islanding capabilities of decarbonized energy communities," *Energies*, vol. 16, no. 11, p. 4321, May 2023. [Online]. Available: http://dx.doi.org/10.3390/en16114321

[4] A. Secic, M. Krpan, and I. Kuzle, "Using Deep Neural Networks for On-Load Tap Changer Audio-based Diagnostics," *IEEE Transactions on Power Delivery*, 2021.

[5] N. Holjevac, T. Baškarad, J. Đaković, M. Krpan, M. Zidar *et al.*, "Challenges of High Renewable Energy Sources Integration in Power Systems—The Case of Croatia," *Energies 2021, Vol. 14, Page 1047*, vol. 14, no. 4, p. 1047, feb 2021. [Online]. Available: https://www.mdpi.com/1996-1073/14/4/1047

[6] M. Brezovec, I. Kuzle, M. Krpan, and N. Holjevac, "Improved dynamic model of a bulb turbine-generator for analysing oscillations caused by mechanical torque disturbance on a runner blade," *International Journal of Electrical Power and Energy Systems*, vol. 119, p. 105929, jul 2020.

[7] M. Brezovec, I. Kuzle, M. Krpan, and N. Holjevac, "Analysis and treatment of power oscillations in hydropower plant dubrava," *IET Renewable Power Generation*, vol. 14, no. 1, pp. 80–89, jan 2020.

[8] A. Secic, M. Krpan, and I. Kuzle, "Vibro-Acoustic Methods in the Condition Assessment of Power Transformers: A Survey," *IEEE Access*, vol. 7, pp. 83 915–83 931, 2019.

[9] M. Krpan and I. Kuzle, "The mathematical model of a wind power plant and a gas power plant," *Journal of Energy*, vol. 66, no. 1, pp. 69–86, 2017. [Online]. Available: https://hrcak.srce.hr/file/294107

[10] M. Brezovec, I. Kuzle, and M. Krpan, "Detailed mathematical and simulation model of a synchronous generator," *Journal of Energy*, vol. 64, no. 1, pp. 102–129, 2015. [Online]. Available: https://www.researchgate.net/publication/322364716_Detailed_mathematical_and_simulation_model_of_a_synchronous_generator

Radovi na konferencijama

[1] B. Barać, M. Krpan, and T. Capuder, "Aggregated model of a flexible multi-energy distribution system for coordinated tso-dso fast frequency services provision," in *2023 International Conference on Smart Energy Systems and Technologies (SEST)*, 2023, pp. 1–6.

[2] M. Krpan, M. Miletić, I. Kuzle, and H. Pandžić, "Incorporating settling time constraints of energy storage systems in frequency containment control optimization problems," in *2022 IEEE 7th International Energy Conference (ENERGYCON)*, 2022, pp. 1–6.

[3] I. Kuzle, M. Krpan, and M. Beus, "Razvoj laboratorija za napredne elektroenergetske mreže," in *15. savjetovanje HRO CIGRE*, 2021, pp. 1–11.

[4] T. Capuder, M. Kostelac, M. Krpan, and I. Pavic, "Multi-energy microgrid ability to provide flexibility services to the system operator and security of supply to end-users," in *SEST 2020 - 3rd International Conference on Smart Energy Systems and Technologies*, 2020.

[5] I. Pavić, M. Krpan, I. Kuzle, and Y. Liu, "Effect of Stochastic Variables on Balancing Mechanism," in *2019 International Conference on Modeling, Simulation, Optimization and Numerical Techniques (SMONT 2019)*. Atlantis Press, may 2019, pp. 211–214.

[6] N. Holjevac, M. Zidar, M. Krpan, and I. Kuzle, "Optimizing the Grid Connection Scheme of the Wind Power Plant," in *14th Conference on Sustainable Development of Energy, Water and Environment Systems (SDEWES)*, Oct 2019, pp. 1–17.

Uz prethodno navedene publikacije, sadržaj ove disertacije temelji se i na sljedećim diplomskim seminarima, diplomskim projektima i diplomskim radovima koji su izrađeni na Zavodu za visoki napon i energetiku Fakulteta elektrotehnike i računarstva Sveučilišta u Zagrebu.

Diplomski seminari

[1] B. Barać, "Mikromreže izmjenične struje u otočnom pogonu," Zagreb, Croatia, May 2020, University of Zagreb, Faculty of electrical engineering and computing.

Diplomski projekti

[1] B. Barać, "Virtualni sinkroni generator," Zagreb, Croatia, Jan. 2021, University of Zagreb, Faculty of electrical engineering and computing.

Diplomski radovi

[1] I. S. Alfageme, "Dynamic modelling of a solar pv plant with a battery storage system," Master's thesis, University of Zagreb, Faculty of electrical engineering and computing, Zagreb, Croatia, Jun. 2022.

[2] B. Barać, "Converter-based microgrid providing system ancillary services with dynamically stable off-grid transition & operation," Master's thesis, University of Zagreb, Faculty of electrical engineering and computing, Zagreb, Croatia, Jun. 2021.

[3] I. M. A. Mohamed, "Modeling and control of dc-dc converters for power system applications," Master's thesis, University of Zagreb, Faculty of electrical engineering and computing, Zagreb, Croatia, Jun. 2021.